



# Durham E-Theses

---

## *The Dynamics of Upland River Confluences*

TANCOCK, MATTHEW,JAMES

### How to cite:

---

TANCOCK, MATTHEW,JAMES (2014) *The Dynamics of Upland River Confluences*, Durham theses, Durham University. Available at Durham E-Theses Online: <http://etheses.dur.ac.uk/10527/>

### Use policy

---

The full-text may be used and/or reproduced, and given to third parties in any format or medium, without prior permission or charge, for personal research or study, educational, or not-for-profit purposes provided that:

- a full bibliographic reference is made to the original source
- a [link](#) is made to the metadata record in Durham E-Theses
- the full-text is not changed in any way

The full-text must not be sold in any format or medium without the formal permission of the copyright holders.

Please consult the [full Durham E-Theses policy](#) for further details.

# **The Dynamics of Upland River Confluences**

Matthew James Tancock

**Department of Geography  
Durham University**

Thesis submitted for the degree of Doctor of Philosophy

2014

# **The Dynamics of Upland River Confluences**

## **Abstract**

River confluences are common features of the landscape as a result of the dendritic nature of river catchments. Much of the research to date has investigated flow at lowland confluences, whereas the most dynamic river confluences are likely to be found in upland areas. Therefore, in order to improve the understanding of the flow, sediment transport and morphological processes at river confluences, it is necessary to investigate the applicability of the findings from lowland confluences to their upland counterparts.

This thesis uses field and numerical modelling experiments to increase the understanding of the dynamics of these upland river confluences. Flow and particle tracking data have been obtained from two different field sites: the more stable upland river confluences of Moor House National Nature Reserve and the steeper confluences of the Borgne d'Arolla braid plain. These data have been used to test two new numerical modelling developments. The first is the application of an explicit free surface model within a Computational Fluid Dynamics framework to enable the simulation of flow in natural rivers with steep water surface slopes. The second is the development of a new, reduced-complexity Discrete Particle Model that uses the three-dimensional flow data to simulate individual particle trajectories and the Generalised Likelihood Uncertainty Estimation method to estimate the uncertainty in these trajectories.

There are three main findings in this thesis. Firstly, at upland confluences changes in the flow direction over the less well-defined banks have the greatest impact on individual particle trajectories and thus the morphological evolution of these confluences. Secondly, as water surface slopes increase, topographic features have less impact on the flow field than undulations in the water surface. Finally, turbulent flow structures and helical flow cells are found to be less important for the dynamics of these upland river confluences.

**The Dynamics of Upland River Confluences**  
**Volume 1**

Matthew James Tancock

**Department of Geography**  
**Durham University**

Thesis submitted for the degree of Doctor of Philosophy

2014



# Table of Contents

## **Volume 1**

<b>Abstract</b> .....	i
<b>Table of Contents</b> .....	iii
<b>List of Figures</b> .....	x
<b>List of Tables</b> .....	xxi
<b>List of Symbols</b> .....	xxiii
<b>List of Abbreviations</b> .....	xxvii
<b>Statement of Copyright</b> .....	xxviii
<b>Acknowledgements</b> .....	xxix
<b>Chapter 1: Introduction</b> .....	1
1.1 Introduction.....	1
1.2 The Classical Model of River Confluences .....	3
1.3 Recent Developments in the Study of River Confluences.....	5
1.4 Research Rationale.....	7
1.5 Research Question, Aims and Objectives .....	9
1.6 Field Site Location .....	11
1.6.1 Trout Beck and the River Tees, Moor House Nature Reserve .....	12
1.6.2 The Borgne d’Arolla Braid Plain .....	15
1.7 Thesis Structure .....	17
<b>Chapter 2: River Confluences</b> .....	20
2.1 Introduction.....	20
2.2 Major Flow and Morphological Zones at River Confluences .....	20
2.3 Flow Dynamics in River Confluences .....	23
2.3.1 Shear Layer/Mixing Layer Zone .....	23
2.3.2 Shear Zones in the CHZ .....	24
2.3.3 Mixing in the CHZ .....	27
2.3.4 Speed of Mixing in the CHZ .....	30
2.3.5 Helical Cells .....	32
2.3.6 Stagnation Zone.....	36
2.3.7 Flow Separation Zone.....	36
2.3.8 Flow Acceleration Zone .....	38
2.4 Key Factors Affecting Flow Dynamics at River Confluences.....	39
2.4.1 Junction Angle.....	39
2.4.2 Discharge Ratio .....	40
2.4.3 Symmetry .....	42
2.4.4 Bed Discordance.....	43
2.4.5 Additional Controls on Confluence Flow Fields.....	45
2.5 Summary of Research into Flow at River Confluences.....	47

2.6	Morphology and Sediment Dynamics of River Confluences .....	47
2.6.1	River Confluence Sediment Dynamics at the Catchment Scale.....	48
2.6.2	Scour Holes .....	49
2.6.3	Mid-Channel Bar Development .....	50
2.6.4	Deposition Bars in Flow Separation Zones and the Stagnation Zone.....	51
2.6.5	Hypotheses on Sediment Dynamics .....	51
2.7	Factors Affecting Sediment Dynamics at River Confluences .....	52
2.7.1	Junction Angle.....	52
2.7.2	Discharge Ratio .....	53
2.7.3	Symmetry .....	55
2.7.4	Bed Discordance.....	55
2.7.5	Additional Controls on the Sediment Dynamics at River Confluences .....	56
2.8	Summary of Morphological and Sediment Dynamics Research .....	57
2.9	Conclusions.....	57
	<b>Chapter 3: Numerical Modelling and Field Methodology .....</b>	<b>60</b>
3.1	Introduction.....	60
3.2	Computational Fluid Dynamics (CFD).....	61
3.3	The Navier-Stokes Equations and Their Solution .....	62
3.3.1	The Navier-Stokes Equations .....	62
3.3.2	Discretisation.....	63
3.3.3	Solution Algorithms .....	64
3.4	Auxiliary Modelling within the CFD Framework .....	65
3.4.1	The Reynolds-Averaged Navier-Stokes (RANS) Equations.....	66
3.4.2	Turbulence Models .....	67
3.4.3	The $\kappa$ - $\epsilon$ Model and Variants .....	68
3.4.4	Large Eddy Simulation (LES) .....	70
3.4.5	Selecting an Appropriate Turbulence Model .....	72
3.4.6	Accounting for Bed Roughness.....	72
3.4.7	Limitations of Methods of Accounting for Bed Roughness.....	75
3.4.8	The Mass Flux Scaling Algorithm (MFSA).....	77
3.4.9	Representing Channel Planform in CFD .....	79
3.4.10	Representing the Free Surface.....	80
3.4.11	Summary of Auxiliary Models within CFD Simulations.....	82
3.5	Good Practice in Numerical Modelling .....	83
3.5.1	Code Verification .....	84
3.5.2	Solution Verification .....	85
3.5.3	The Grid Convergence Index .....	86
3.6	A Review of the CFD Methodology .....	88
3.7	Numerical Methodology for This Thesis.....	89

3.8	Field Methodology .....	92
3.8.1	Methods for Obtaining Topographic Data .....	94
3.8.2	Flow Data .....	98
3.8.3	Methods for Determining Roughness Height.....	102
3.8.4	Particle Tracking Experiments .....	106
3.8.5	Summary of Field Methodology .....	109
3.9	Conclusions.....	110
<b>Chapter 4: Investigating Flow at Stable and Dynamic Upland River</b>		
	<b>Confluences .....</b>	<b>113</b>
4.1	Introduction.....	113
4.2	Field Conditions and Flow Regime at Moor House .....	114
4.3	Topographical Data from the Moor House Confluences .....	118
4.3.1	Individual Point Quality .....	119
4.3.2	Topographic Data Point Densities.....	122
4.3.3	Lower Confluence Topography.....	123
4.3.4	Upper Confluence Topography .....	124
4.3.5	Discussion of Topographic Data .....	126
4.4	Characterising Roughness in the Moor House Confluences.....	127
4.4.1	Obtaining Roughness Heights from Velocity Profile Data .....	128
4.4.2	Obtaining Roughness Heights from a Characteristic Grain Size .....	131
4.4.3	Discussion of the Roughness Values.....	134
4.5	Flow Data from the Moor House Confluences .....	135
4.5.1	Comparison of Discharge Measurements.....	138
4.5.2	Mean Flow Results .....	140
4.5.3	Discussion of the Mean Flow at the Moor House Confluences .....	151
4.6	Turbulence in the Three-Dimensional Flow Results .....	155
4.6.1	Turbulent Kinetic Energy in the Moor House Confluences .....	158
4.6.2	Spectral Analysis of the Flow Data .....	160
4.6.3	Discussion of Flow Turbulence.....	166
4.7	Discussion of Flow at the Moor House Confluences.....	169
4.8	Borgne d'Arolla Field Site Conditions and Data Collection .....	170
4.8.1	Data Collection Process.....	173
4.8.2	Characteristics of the Flow at the Arolla Confluences .....	177
4.9	Topographic Data at the Arolla Confluences.....	177
4.9.1	Data Quality.....	178
4.9.2	Topographic Data .....	181
4.9.3	Discussion of Topographic Data .....	184
4.10	Grain Size Distribution and Roughness Data .....	185
4.10.1	Comparison of Wolman Counts and Photosieving .....	186
4.10.2	Calculating Roughness Heights from Grain Size Distributions .....	187

4.10.3	Discussion of Roughness Data .....	189
4.11	Flow Data .....	190
4.11.1	Flow Data Quality and Stationarity Tests .....	190
4.11.2	Mean Flow Data .....	195
4.11.3	Discussion of Flow Data .....	197
4.12	Comparison of the Arolla and Moor House confluences.....	198
4.13	Conclusions.....	200

## **Volume 2**

<b>Chapter 5: Free Surface Modelling of Flow at Upland River Confluences</b>	205
5.1 Introduction	205
5.2 Description of the Height of Liquid (HOL) Free Surface Model	206
5.3 Testing the HOL Model	209
5.3.1 Model Verification	209
5.3.2 Model Validation	210
5.3.3 Errors Associated with Geolocation	211
5.4 Model Verification Using Arolla Confluence E	212
5.5 Model Calibration and Sensitivity Tests	216
5.5.1 Results from the Model Calibration and Sensitivity Tests	218
5.5.2 Discussion of Model Calibration and Sensitivity Testing	222
5.6 Model Validation Using Straight, Gravel-Bed Channels	223
5.6.1 Validation Using the Upper Confluence Inlets	224
5.6.2 Validation Using the Lower Confluence Inlets	229
5.6.3 Discussion of Model Validation in Straight, Gravel-Bed Channels	234
5.7 Model Validation Using the Moor House Confluences	234
5.7.1 Model Setup	235
5.7.2 Results from Modelling the Upper Moor House Confluence	235
5.7.3 Results from Modelling the Lower Moor House Confluence	241
5.7.4 Discussion of the Moor House Confluence Validation Tests	246
5.8 Model Validation Using the Arolla Datasets	247
5.8.1 Validation Using Confluence G	248
5.8.2 Validation Using Confluence H	252
5.8.3 Discussion of the Arolla Confluence Validation Tests	257
5.9 Discussion of Overall HOL Model Performance	258
5.10 Interpreting the Flow Dynamics at the Moor House Confluences	259
5.10.1 Flow Dynamics at the Upper Confluence	259
5.10.2 Flow Dynamics at the Lower Confluence	265
5.10.3 Discussion of the Low Flow Dynamics of the Moor House Confluences	269
5.11 HOL Scenario Modelling at the Moor House Confluences	271

5.11.1	High Discharges at the Upper Confluence .....	272
5.11.2	High Discharges at the Lower Confluence.....	281
5.11.3	Discussion of High Discharge Flows at the Moor House Confluences .....	290
5.12	Interpreting the Flow Dynamics at the Arolla Confluences .....	294
5.12.1	Flow Dynamics at Confluence G .....	294
5.12.2	Flow Dynamics at Confluence H .....	299
5.12.3	Discussion of the Flow Dynamics at the Arolla Confluences.....	304
5.13	Discussion of Flow at Upland River Confluences .....	307
5.14	Conclusions.....	309
<b>Chapter 6:</b>	<b>Bedload Transport at Upland River Confluences .....</b>	<b>312</b>
6.1	Introduction.....	312
6.2	Particle Tracking at Moor House Nature Reserve .....	313
6.2.1	Particle Tracking Experiment Design at Moor House .....	314
6.2.2	Data Quality and Recovery Rates.....	317
6.2.3	Particle Survey Dates .....	317
6.2.4	Particle Tracks at the Upper Confluence.....	318
6.2.5	Upper Confluence Particle Densities and Near-Bed Streamlines .....	324
6.2.6	Particle Tracks at the Lower Confluence .....	329
6.2.7	Lower Confluence Particle Densities and Near-Bed Streamlines.....	333
6.2.8	Discussion of Particle Tracks at the Moor House Confluences .....	336
6.3	Grain Size and Roundness Effects on Bedload Transport.....	338
6.3.1	Results from the Particle Size and Roundness Experiments.....	338
6.3.2	Discussion of Particle Size and Roundness Effects on Bedload Transport.....	344
6.4	Particle Tracking at the Borgne d'Arolla Confluences.....	345
6.4.1	Particle Tracking Experiment Design on the Borgne d'Arolla .....	345
6.4.2	Results from the Particle Tracking Experiments at Confluence G.....	347
6.4.3	Results from the Particle Tracking Experiments at Confluence H.....	349
6.4.4	Discussion of Arolla Particle Trajectory Data.....	350
6.5	Comparison of the Moor House and Arolla Confluences.....	352
6.6	Conclusions.....	354
<b>Chapter 7:</b>	<b>Discrete Particle Modelling of Upland River Confluences .....</b>	<b>356</b>
7.1	Introduction.....	356
7.2	Modelling Bedload Transport in Natural Rivers .....	357
7.2.1	Eulerian Sediment Transport Models .....	358
7.2.2	Discrete Particle Models.....	361
7.2.3	Modelling Saltation Using DPMs .....	362
7.2.4	Uncertainty in the DPMs .....	364
7.2.5	Discussion of Bedload Transport Models .....	365

7.3	Model Development and Implementation .....	365
7.3.1	Model Physics .....	366
7.3.2	Flow Turbulence.....	368
7.3.3	Particle Initiation .....	369
7.3.4	Particle Density and Values for the Friction and Drag Co-efficients....	371
7.3.5	The GLUE Methodology.....	373
7.3.6	Number of Parameter Sets and Time Step Variables .....	376
7.4	Model Calibration and Evaluation Using the Arolla Confluences .....	379
7.4.1	Model Calibration Using the Confluence G Particle Patches .....	379
7.4.2	Model Evaluation Using the Borgne d'Arolla Data .....	384
7.4.3	Discussion of the Arolla Confluence Results .....	390
7.5	Modelling Bedload Transport at the Moor House Confluences .....	392
7.5.1	First Simulations of the Upper and Lower Confluences .....	392
7.5.2	Second Simulations of the Upper and Lower Confluences.....	397
7.5.3	Discussion of the Model Results from the Moor House Confluences .....	403
7.6	Conclusions.....	406
<b>Chapter 8:</b>	<b>Conclusions .....</b>	<b>408</b>
8.1	Introduction.....	408
8.2	Evaluation of the Research Objectives .....	409
8.2.1	Research Objective 1: To obtain and to present high quality field data on the morphology, flow field and particle transport at a range of upland river confluences .....	409
8.2.2	Research Objective 2: To develop the application of numerical approaches to improve the understanding of steep river confluence flow dynamics .....	411
8.2.3	Research Objective 3: To use the topographic and flow data obtained as part of Objective 1 to test the performance of the numerical flow model developed in Objective 2.....	412
8.2.4	Research Objective 4: To create a sediment transport and morphology model which uses the three-dimensional flow modelling developed in Objective 2 to determine the major processes driving particle movement in upland river confluences.....	413
8.2.5	Research Objective 5: To use the particle tracking data collected as part of Objective 1 to test the sediment transport model developed in Objective 4 .....	415
8.3	The Dynamics of Upland River Confluences .....	416
8.4	Further Research .....	421
8.4.1	Field Experiments.....	421
8.4.2	Numerical Modelling.....	423

8.4.3	River Confluence Dynamics.....	423
8.5	Conclusions.....	424
<b>Reference List</b> .....		425

# List of Figures

## Volume 1

Figure 1.1:	Diagrams showing the interaction between flow, sediment transport and bed morphology. ....	2
Figure 1.2:	Conceptual diagrams of Best (1986) showing the major flow structure zones in a 90° confluence. ....	4
Figure 1.3:	Diagram showing the relationship between the research question, aims and objectives. ....	10
Figure 1.4:	Map of the locations of the EA gauging station and two confluence sites on Trout Beck in Moor House Nature Reserve. ....	13
Figure 1.5:	Photograph of the lower confluence at Moor House Nature Reserve during low flow, looking upstream. ....	14
Figure 1.6:	Photograph of the upper confluence at Moor House Nature Reserve during a medium discharge. ....	14
Figure 1.7:	Aerial view of the Borgne d’Arolla braid plain field site, with the village of La Monta visible at the bottom of the picture. ....	16
Figure 1.8:	Confluence on the Borgne d’Arolla braid plain on 28 <sup>th</sup> August 2011, with visibly steeper water surface slopes than the Moor House confluences. ....	17
Figure 2.1:	A hypothetical river confluence showing the major flow and morphological zones compared to the original diagram of Best (1986). ....	22
Figure 2.2:	Diagram highlighting the CHZ, split into a central region and downstream region (Rhoads and Kenworthy, 1998). ....	24
Figure 2.3:	Diagram from Rhoads and Sukhodolov (2008) showing the differences between shallow mixing layers (or shear layers, <i>top</i> ), wake flow ( <i>middle</i> ) and jet flow ( <i>bottom</i> ). ....	26
Figure 2.4:	Diagrams from Constantinescu <i>et al.</i> (2011) showing vertical vorticity at 0.1 <i>d</i> ( <i>left</i> ) and 0.5 <i>d</i> below the water surface, determined from numerical modelling using a Detached Eddy Simulation treatment of turbulence. ....	26
Figure 2.5:	Photograph of the Kaskaskia River-Copper Slough confluence showing clearly the position of the mixing layer as a result of differences in turbidity between the tributaries (Rhoads and Sukhodolov, 2008). ....	28
Figure 2.6:	False-colour satellite image showing the confluence of the Negro and Solimoes Rivers near Manaus in the Amazon basin. ....	29
Figure 2.7:	Diagram showing three different definitions of primary and secondary flow direction (Lane <i>et al.</i> , 2000). ....	33



Figure 2.8:	Diagram showing water depth and flow streamlines from numerical simulations of confluences with increasing confluence angles (Huang <i>et al.</i> , 2002). .....	37
Figure 2.9:	The key flow parameters and boundary conditions in a river confluence. ....	39
Figure 2.10:	The position of the Kaskaskia River-Copper Slough mixing layer for three different flow conditions (Rhoads and Kenworthy, 1995). ....	41
Figure 2.11:	Plan view of the flow field at the bed of a discordant river confluence (Best and Roy, 1991). ....	44
Figure 2.12:	Comparison of streamlines for discordant and concordant laboratory river confluences (Biron <i>et al.</i> , 1996a). ....	45
Figure 2.13:	Conceptual model of the sediment dynamics at the Kaskaskia River and Copper Slough confluence for high and low discharge ratios (Rhoads <i>et al.</i> , 2009). ....	54
Figure 3.1:	An idealised logarithmic velocity profile, with a roughness height, $z_0$ . ....	73
Figure 3.2:	Comparison of the traditional method of representing topography by mesh distortion with the Mass Flux Scaling Algorithm approach from Hardy <i>et al.</i> (2005). ....	78
Figure 3.3:	Diagram showing the mesh used in a simulation of a simple, asymmetric, $30^\circ$ confluence (Biron <i>et al.</i> , 2004a). ....	79
Figure 3.4:	Diagram showing different possible treatments of the free surface.....	81
Figure 3.5:	Photograph showing the collection of topographic data using electronic tacheometry. ....	97
Figure 3.6:	Photograph showing the bulk seeding of tracer particles into a confluence tributary. ....	107
Figure 4.1:	Photographs of the lower and upper confluences at Moor House Nature Reserve, with a field assistant for scale. ....	115
Figure 4.2:	Discharge measurements from the Environment Agency (EA) gauging station at Moor House from 1 <sup>st</sup> February 2011 to 31 <sup>st</sup> July 2012 (data provided by the EA). ....	116
Figure 4.3:	Cumulative frequency plot of the discharge data from the Moor House gauging station. ....	117
Figure 4.4:	Scatter plots showing the horizontal positions (relative to the mean) for each of the quality control points at the lower and upper confluences. ....	121
Figure 4.5:	Point densities for the lower confluence DEM, with the channel outline from 7 <sup>th</sup> October 2011 (blue line) provided for reference. ....	122

Figure 4.6:	Point densities for the upper confluence DEM, with the water edge for 20 <sup>th</sup> September 2011 (blue line) for reference. ....	123
Figure 4.7:	DEM of the lower confluence, with the channel outline from 7 <sup>th</sup> October 2011 (a medium flow stage and discharge). ....	124
Figure 4.8:	DEM of the upper confluence, with the channel outline from 20 <sup>th</sup> September 2011 (a medium flow stage and discharge). Flow is from left to right. The black dashed circle highlights the low profile bar referred to in the text. ....	125
Figure 4.9:	Vertical velocity profiles for the upper confluence on 20 <sup>th</sup> September 2011 (during medium flow conditions). ....	129
Figure 4.10:	Vertical velocity profiles for the lower confluence on 7 <sup>th</sup> October 2011 (during medium flow conditions). ....	130
Figure 4.11:	Grain Size Distributions (GSDs) determined from Wolman counts and photosieving for the sites on the true left, true right and middle (upstream corner) banks of the lower confluence. ....	132
Figure 4.12:	GSDs determined from Wolman counts and photosieving for the upper confluence. ....	132
Figure 4.13:	Graphs showing the variation in mean velocity with length of time series for a velocity profile from the lower confluence (Profile W). ....	136
Figure 4.14:	Graphs plotting the standard deviation of velocity against length of time series for the aDv data in Profile W. ....	137
Figure 4.15:	Flow directions and velocities at the lower confluence for the medium flow of 7 <sup>th</sup> October 2011. ....	141
Figure 4.16:	Flow directions and velocities for the upper confluence in a medium flow of 20 <sup>th</sup> September 2011. ....	142
Figure 4.17:	Radar plots showing deviations from the mean flow angle for each dataset (given as the elevation above the bed) of the velocity profiles at the lower confluence. ....	145
Figure 4.18:	Radar plots for the velocity profiles at the upper confluence from the dataset of 20 <sup>th</sup> September 2011. ....	148
Figure 4.19:	Velocity time series for Profile W at the lower confluence, measured at heights of 0.05m, 0.1m, 0.15m, 0.2m and 0.25m above the bed. ....	157
Figure 4.20:	Turbulent kinetic energy (TKE) and Reynolds Stress (RS) values for the lower confluence.....	159
Figure 4.21:	Turbulent kinetic energy (TKE) and Reynolds Stress (RS) values for the upper confluence on 20 <sup>th</sup> September 2011. ....	160
Figure 4.22:	Spectral analysis plots for Profile W at the lower confluence. ....	162
Figure 4.23:	Spectral analysis plot for lower confluence aDv dataset 61, the dataset with the highest calculated TKE in Figure 4.22 ( $k = 82.2\text{kJ}$ ). ....	163

Figure 4.24: Spectral analysis plots for Profile E at the upper confluence. ....	164
Figure 4.25: Spectral analysis plot for upper confluence aDv dataset 49, the dataset with the highest calculated TKE in the downstream channel ( $k = 37.0\text{kJ}$ ). ....	166
Figure 4.26: Plots of TKE with depth for velocity profiles W and E. ....	167
Figure 4.27: Merged photographs of the Borgne d’Arolla braid plain on 24 <sup>th</sup> August 2011, showing the purges at 11:10am and 1:40pm local time. ....	171
Figure 4.28: Merged photographs of the Arolla braid plain on 25 <sup>th</sup> August 2011 and 28 <sup>th</sup> August 2011, before and after a large flood. ....	172
Figure 4.29: Photographs of the three confluences to be analysed in this section: E, G and H. ....	176
Figure 4.30: Point densities for the DEM of Confluence E. ....	180
Figure 4.31: Point densities for the DEM of Confluence G. ....	180
Figure 4.32: Point densities for the DEM of Confluence H. ....	181
Figure 4.33: The DEM for Confluence E, with the dark blue line showing the water edge. ....	182
Figure 4.34: The DEM for Confluence G, with the blue line marking the water edge. ....	183
Figure 4.35: The DEM for Confluence H, with the water edge given by the blue line. ....	184
Figure 4.36: Grain Size Distributions for three sites on the Borgne d’Arolla braid plain, calculated from both a field Wolman count and photosieving. ....	187
Figure 4.37: Velocity time series for an example aDv dataset from Confluence I. ....	191
Figure 4.38: Velocity time series for four of the aDv datasets from Confluence E. ....	193
Figure 4.39: Stationarity plots of mean velocity against length of time series for datasets 4 and 14. ....	194
Figure 4.40: Stationarity plots of standard deviation against length of time series for datasets 4 and 14. ....	195
Figure 4.41: Flow velocities and calculated discharges for the inlets and outlets of Confluence G. ....	196
Figure 4.42: Flow velocities and calculated discharges for the inlets and outlets of Confluence H. ....	197

## **Volume 2**

Figure 5.1: Model output showing the pressure distribution of a steeply sloped flume (bed slope = 0.1) modelled without an explicit treatment of the free surface. ....	207
---	-----

Figure 5.2:	Digital Elevation Models (DEMs) for Arolla Confluence E, using a 2cm grid, 4cm grid and 8cm grid. ....	213
Figure 5.3:	Graphs showing the change in water surface elevation through time for three locations in Confluence E: in the true left, true right and downstream channels. ....	215
Figure 5.4:	An example of the position of the model cross-section used for comparison with the field data. ....	217
Figure 5.5:	Modelled water surface elevations for the six test runs at the true left tributary of the upper confluence. ....	219
Figure 5.6:	Contour plots of downstream flow velocity for each of the test runs at the upper confluence true left tributary. ....	220
Figure 5.7:	Velocity profiles for each of the upper confluence true left tributary test runs. ....	222
Figure 5.8:	Modelled and measured water surface elevations for the inlets at the upper Moor House confluence. ....	224
Figure 5.9:	Contour plots showing the modelled and measured flow velocities for the upper confluence tributaries. ....	225
Figure 5.10:	Modelled and measured velocity profiles for the upper confluence true left and true right tributaries. ....	226
Figure 5.11:	Modelled and measured velocities for the upper confluence tributaries, with error bars giving the potential geolocation errors. ...	228
Figure 5.12:	Modelled and measured water surface elevations for the inlets at the lower Moor House confluence. ....	229
Figure 5.13:	Contour plots showing the modelled and measured (filled circles) flow velocities for the lower confluence tributaries. ....	230
Figure 5.14:	Modelled and measured velocity profiles for the lower confluence true left and true right tributaries. ....	231
Figure 5.15:	Modelled and measured velocities plotted for the lower confluence tributaries, with error bars showing the potential geolocation errors. ....	233
Figure 5.16:	Three-dimensional view of modelled and measured water surface elevations for the upper Moor House confluence. ....	236
Figure 5.17:	Modelled water surface extent compared to the measured water edge from 20 <sup>th</sup> September 2011 and modelled minus measured water surface elevations for the upper confluence. ....	237
Figure 5.18:	Comparison of modelled and measured water surface elevations at the upper confluence, with points within 2m of the outlet marked in red. ....	238
Figure 5.19:	Depth-averaged modelled flow velocities for the upper confluence at Moor House Nature Reserve. ....	239
Figure 5.20:	Modelled and measured downstream and cross-stream velocities for the upper confluence at Moor House Nature Reserve. ....	240

Figure 5.21: Three-dimensional view of modelled and measured water surface elevations for the lower Moor House confluence. ....	241
Figure 5.22: Two-dimensional plot of modelled water extent at the lower confluence compared to the measured water edge from 7 <sup>th</sup> October 2011 and a diagram showing the difference between modelled and measured water surface elevations. ....	242
Figure 5.23: Modelled and measured water surface elevations for the lower confluence, with the points located within 2m of the outlet marked in red. ....	243
Figure 5.24: Depth-averaged modelled flow velocities for the lower confluence at Moor House Nature Reserve. ....	244
Figure 5.25: Modelled and measured downstream and cross-stream velocities for the lower confluence, with RMA regression lines, 1:1 lines and error bars showing the range of values in the adjacent model cells. ....	245
Figure 5.26: Modelled and measured water surface elevations for Confluence G on the Borgne d'Arolla braid plain, shown in three-dimensional form. ....	249
Figure 5.27: Confluence G modelled water extent and a comparison of modelled and measured water surface elevations. ....	250
Figure 5.28: Plot showing modelled and measured water surface elevations for Confluence G. ....	251
Figure 5.29: Contour plot showing modelled downstream velocity at the outlet of Confluence G. ....	251
Figure 5.30: Modelled and measured downstream velocities for Confluence G, plotted with the RMA regression line and errors bars. ....	252
Figure 5.31: Three-dimensional modelled and measured water surface elevations for Confluence H on the Borgne d'Arolla braid plain. ....	253
Figure 5.32: Two-dimensional plot of modelled water extent at Confluence H compared to the surveyed water edge and a diagram showing the difference between modelled and measured water surface elevations. ....	254
Figure 5.33: Modelled and measured water surface elevations for Confluence H. ....	255
Figure 5.34: Modelled downstream flow velocities at Confluence H with measured velocities superimposed for comparison. ....	256
Figure 5.35: Modelled and measured downstream flow velocities at Confluence H plotted with geolocation error bars. ....	256
Figure 5.36: Contour and vector plots for three cross-sections through the centre of the upper Moor House confluence. ....	261
Figure 5.37: Helicity plots for three cross-sections through the centre of the upper Moor House confluence. ....	262

Figure 5.38: Plot of helicity index with distance downstream at the upper Moor House confluence. ....	263
Figure 5.39: Turbulent kinetic energy and bed shear stress from the modelled data of the upper confluence. ....	264
Figure 5.40: Contour and vector plots for three cross-sections in the middle of the lower confluence. ....	266
Figure 5.41: Helicity plots for three cross-sections at the lower Moor House confluence. ....	267
Figure 5.42: Plot of helicity index with distance downstream at the lower Moor House confluence. ....	268
Figure 5.43: Turbulent kinetic energy and bed shear stress plots using the modelled data from the lower confluence. ....	269
Figure 5.44: Three-dimensional view of the modelled water surface elevations for high flows at the upper Moor House confluence. ....	273
Figure 5.45: Depth-averaged flow velocities for the true-left dominated and true right dominated floods at the upper confluence. ....	274
Figure 5.46: Contour and vector plots for the three cross-sections at the upper confluence, derived from the model output of UpperRun007. ....	275
Figure 5.47: Helicity plots for three cross-sections at the upper Moor House confluence, taken from the output data of UpperRun007. ....	276
Figure 5.48: Contour and vector plots for the three upper confluence cross-sections, taken from the model output of UpperRun008. ....	277
Figure 5.49: Helicity plots for the upper Moor House confluence, derived from the model output of UpperRun008. ....	278
Figure 5.50: Variations in helicity index with distance downstream for UpperRun007 and UpperRun008. ....	279
Figure 5.51: Calculated TKE for UpperRun007 and UpperRun008. ....	280
Figure 5.52: Calculated bed shear stress for UpperRun007 and UpperRun008. ....	281
Figure 5.53: Modelled water surface elevations for the lower confluence in floods dominated by the true right tributary (LowerRun005) and the true left tributary (LowerRun007). ....	282
Figure 5.54: Depth-averaged flow velocities for the lower confluence in high discharges dominated by the true right and true left tributaries. ....	283
Figure 5.55: Contour and vector plots for the three lower confluence cross-sections, taken from the model output of LowerRun005. ....	284
Figure 5.56: Helicity plots for the lower Moor House confluence, derived from LowerRun005. ....	285
Figure 5.57: Contour and vector plots for the three cross-sections at the lower confluence, derived from the model output of LowerRun007. ....	286
Figure 5.58: Helicity plots for the three lower confluence cross-sections, using the model output from LowerRun007. ....	287

Figure 5.59: Helicity index plot for LowerRun005 (true right tributary dominant) and LowerRun007 (true left tributary dominant) at the lower Moor House confluence. ....	288
Figure 5.60: Modelled TKE for LowerRun005 and LowerRun007. ....	289
Figure 5.61: Bed shear stress calculations for the true right and true left dominated flows at the lower confluence. ....	290
Figure 5.62: Plan view of the depth-averaged flow velocities from the model of Confluence G. ....	294
Figure 5.63: Contour and vector plots for three cross-sections in Confluence G, with downstream velocity given by the contours. Local deviations from the depth-averaged cross-stream and vertical velocities are shown by the vectors. ....	295
Figure 5.64: Helicity plots for the three Confluence G cross-sections. ....	296
Figure 5.65: Turbulent kinetic energy and bed shear stress plots using the modelled data from Confluence G. ....	297
Figure 5.66: Variations in helicity index in Confluence G and a plot of turbulent kinetic energy, bed shear stress and water surface elevation against distance downstream. ....	298
Figure 5.67: Depth-averaged flow velocities for Confluence H calculated from the model output. ....	300
Figure 5.68: Contour and vector plots for three cross-sections in the centre of Confluence H. ....	301
Figure 5.69: Helicity plots for the three Confluence H cross-sections. ....	302
Figure 5.70: Calculated TKE and bed shear stress for the Confluence H model data. ....	303
Figure 5.71: Graph showing helicity index plotted against distance downstream for Confluence H, alongside equivalent plots for turbulent kinetic energy, bed shear stress and water surface elevation. ....	304
Figure 6.1: Grain size distributions for the tracer and bed particles at the Moor House confluences. ....	314
Figure 6.2: Photograph of the upper confluence at the beginning of the second particle tracking experiment. ....	316
Figure 6.3: Discharge data from the EA gauging station, with the dates of particle surveys marked by dashed lines. ....	318
Figure 6.4: Particle positions for the first experiment at the upper confluence. ...	319
Figure 6.5: Particle positions for the second upper confluence experiment. ....	322
Figure 6.6: Near-bed (25mm) streamlines from UpperRun007 (true left tributary dominant) superimposed on the particle densities from Experiment 1 at the upper confluence. ....	325

Figure 6.7:	Near-bed streamlines from UpperRun008 and particle densities from Experiment 1 at the upper confluence. ....	326
Figure 6.8:	Near-bed streamlines from UpperRun007 superimposed on particle densities calculated from the results of Experiment 2 at the upper confluence. ....	327
Figure 6.9:	Near-bed streamlines from UpperRun008 and particle densities from Experiment 2 at the upper confluence. ....	328
Figure 6.10:	Particle positions for the second experiment at the lower confluence. ....	330
Figure 6.11:	Near-bed streamlines from LowerRun005 (flow predominantly from the true right tributary) superimposed on the particle densities from Experiment 2 at the lower confluence. ....	334
Figure 6.12:	Near-bed streamlines from LowerRun007 and particle densities from Experiment 2 at the lower confluence. ....	335
Figure 6.13:	Particle density plots for the rounded and angular particles during Experiment 2 at the upper confluence. ....	338
Figure 6.14:	Tracer grain size distributions in each patch for the zones marked in Figure 6.4e (from Experiment 1 at the upper confluence). ....	340
Figure 6.15:	Bar charts showing the grain size distributions for each patch in the second upper confluence experiment. ....	342
Figure 6.16:	Photograph of Arolla Confluence B during a purge, showing the difference in turbidity between the purge flow in the true left tributary and the low flow in the true right tributary. ....	346
Figure 6.17:	Results from particle tracking experiments for Confluence G using individual particle tracks and pebble patches. ....	348
Figure 6.18:	Results from particle tracking experiments using individual particle tracks and pebble patches at Confluence H. ....	350
Figure 7.1:	Diagram showing the major forces acting on a particle placed on a flat surface. ....	358
Figure 7.2:	Diagram showing the tracer particle at rest in the pocket between two bed particles. ....	370
Figure 7.3:	Plot of the vertical distribution of drag co-efficients for a sphere. ....	373
Figure 7.4:	Dotty plots showing the distribution of NSE values for the sliding friction co-efficient in a preliminary version of the model. ....	378
Figure 7.5:	Plot showing the change in the number of behavioural simulations with the number of time steps. ....	378
Figure 7.6:	Plot showing the spread of particle paths for the true right patch of Confluence G. ....	380
Figure 7.7:	Dotty plots for simulations of the true right patch of Confluence G, with the red line showing the threshold for a parameter set to be considered behavioural. ....	381



Figure 7.8:	Plot showing the spread of particle paths for the true left patch of Confluence G. ....	382
Figure 7.9:	Dotty plots for simulations of the true left patch of Confluence G, with the red line showing the threshold for a parameter set to be considered behavioural. ....	383
Figure 7.10:	Modelled and measured particle trajectories for the true right patch of Confluence H. ....	384
Figure 7.11:	Dotty plots for simulations of the true right patch of Confluence H, with the threshold to be considered behavioural given by the red line. ....	385
Figure 7.12:	Plot showing the modelled and measured (orange polygon) spread of particle paths for the true left patch of Confluence H. ....	386
Figure 7.13:	Dotty plots for simulations of the true left patch of Confluence H. ...	387
Figure 7.14:	Plot showing the spread of particle paths for the additional tests in the true left and true right tributaries of Confluence G, with the observed individual particle tracks given by the black lines. ....	389
Figure 7.15:	Plot showing the particle paths for the additional tests in both tributaries at Confluence H, with the observed individual particle tracks given in black. ....	390
Figure 7.16:	Plot showing the spread of particle paths for patches seeded in the true left and true right halves of the lower Moor House confluence tributaries, using the flow data from LowerRun005. ....	393
Figure 7.17:	Plot showing the percentage chance of particle initiation and the spread of particle paths for patches seeded in the true left and true right halves of the lower Moor House confluence tributaries, using the flow data from LowerRun007. ....	394
Figure 7.18:	Plot showing the spread of particle paths for patches seeded in the true left and true right halves of the upper Moor House confluence tributaries, using the flow data from UpperRun007. ....	395
Figure 7.19:	Plot showing the likelihood of particle initiation and the spread of particle paths for patches seeded in the true left and true right halves of the upper Moor House confluence tributaries, using the flow data from UpperRun008. ....	396
Figure 7.20:	Three-dimensional water surface plot and the depth-averaged flow velocities for LowerRun008. ....	399
Figure 7.21:	Plot showing the spread of particle paths for patches seeded in the true left and true right halves of the lower Moor House confluence tributaries, using the flow data from LowerRun008. ....	400
Figure 7.22:	Three-dimensional view of the water surface and plan view of the depth-averaged flow velocities for UpperRun009. ....	401
Figure 7.23:	Plot showing the spread of particle paths for patches seeded in the true left and true right halves of the upper Moor House confluence tributaries, using the flow data from UpperRun009. ....	402

Figure 7.24: Photographs showing the upper confluence before and after the very large flood ( $26\text{m}^3/\text{s}$ ) of 22 <sup>nd</sup> June 2012. ....	404
Figure 8.1: Schematic diagrams of flow and sediment dynamics at upland river confluences. ....	418

## List of Tables

### **Volume 1**

Table 3.1:	Descriptions, advantages and limitations of different types of sub-grid scale turbulence models. ....	71
Table 4.1:	Flow and channel characteristics of the upper and lower confluences at Moor House Nature Reserve during medium discharge conditions. ....	118
Table 4.2:	Mean errors and standard deviations for each quality control point placed at the Moor House site, along with the total Root Mean Squared Error for each. ....	120
Table 4.3:	Summary statistics of the roughness heights calculated from the upper and lower confluence velocity profiles. ....	131
Table 4.4:	Comparison of characteristic grain sizes determined from Wolman counts and photo sieving for each site of the lower and upper confluences. ....	133
Table 4.5:	Roughness heights calculated from the characteristic grain sizes given in Table 4.4 using the three alternative methods presented in Section 3.8.3. ....	134
Table 4.6:	Comparison between EA gauging station data and the discharges calculated from ECM and aDv data. ....	139
Table 4.7:	Summary of data collected for each of the nine Arolla confluences (A to I). ....	174
Table 4.8:	Flow and channel characteristics of the three Arolla confluences (E, G and H) to be studied in depth. ....	177
Table 4.9:	Differences between the horizontal distances recorded by tape measure and their equivalents from the Leica Total Station data. ....	179
Table 4.10:	Comparison of the characteristic grain sizes (in mm) obtained using the Wolman count and photosieving methods for three sites on the Borgne d'Arolla. ....	187
Table 4.11:	D <sub>50</sub> and D <sub>84</sub> values for the four confluences analysed in this chapter. ....	188
Table 4.12:	Roughness heights calculated from the characteristic grain sizes given in Table 4.11. ....	188

### **Volume 2**

Table 5.1:	Model runtimes (in hours) for each of the models to be discussed in this chapter. ....	208
Table 5.2:	Calculated Grid Convergence Index (GCI) values for the medium and finest resolution grids at Confluence E. ....	216

Table 5.3:	Details of the model sensitivity tests using the true left tributary of the upper confluence. ....	218
Table 5.4:	Mean absolute and normalised difference values for the modelled water surface elevations at the true left tributary of the upper confluence. ....	219
Table 5.5:	Mean absolute differences for the modelled flow velocities in the true left tributary of the upper confluence. ....	222
Table 5.6:	Discharges for the true left (TL) and true right (TR) inlets in the upper and lower confluence scenario models. ....	272
Table 6.1:	Summary of research previously conducted into bedload dynamics at river confluences. ....	312
Table 6.2:	Mean positions and standard deviations (in metres) for the angular and the rounded particles in each of the four surveys of Experiment 2 at the upper confluence. ....	339
Table 6.3:	Distribution of tracer particle sizes in each patch at the end of the first experiment at the upper confluence. ....	340
Table 6.4:	Tracer particle sizes for each patch during the second experiment at the upper confluence. ....	343
Table 6.5:	The tracer particle size results from Table 6.4 converted into percentages for ease of comparison. ....	343
Table 7.1:	The mass, volume and calculated density for five randomly-selected tracer particles. ....	371
Table 7.2:	Table showing the results from tests to determine the static friction co-efficient.....	372
Table 7.3:	The range of parameter values used in the particle tracking model. All values are dimensionless unless stated.....	375

## List of Symbols

$A$	Cross-sectional area
$A_D$	Effective cross-sectional area in the drag equation
$A_L$	Effective cross-sectional area in lift equation
$A_i$	Cross-sectional area of the cell
$B$	Subscript relating to the bottom of the tracer particle
$C$	Constant of proportionality relating roughness length scale to roughness height
$C_{I\varepsilon}$	Constant in the RNG turbulence model (value of 1.42)
$C_{2\varepsilon}$	Constant in the RNG turbulence model (value of 1.68)
$C_D$	Drag co-efficient
$C_L$	Lift co-efficient
$C_m$	Added mass co-efficient
$C_\mu$	Constant in the $\kappa$ - $\varepsilon$ turbulence model (value of 0.09)
$D_n$	$n$ th percentile of the grain size distribution
$E_1$	Estimated error due to grid resolution
$F_D$	Drag force
$F_L$	Lift force
$Fr$	Froude number
$F_R$	Friction
$F_s$	Safety factor for GCI calculations
$GCI_i$	Grid convergence index for the grid at resolution $i$
$H$	Helicity
$HI$	Helicity Index
$L$	Turbulent length scale
$M_r$	Momentum ratio
$NSE$	Nash-Sutcliffe Efficiency measure
$Q$	Discharge
$Q_A$	Discharge for channel A
$R_N$	Force normal to the bed slope
$R$	Rate of strain
$R^2$	Goodness of fit of a regression line
$RS$	Reynolds Stress
$S$	Modulus of the mean rate of strain tensor

$S_{ij}$	Mean rate of strain tensor
$T$	Subscript relating to top of the tracer particle
$U$	Velocity of the fluid
$V$	Velocity of the particle
$a$	y-intercept of a regression line
$b$	Gradient of a regression line
$c$	Helicity index constant
$c_1$	Constant in the $\kappa$ - $\varepsilon$ turbulence model (value 1.55)
$c_2$	Constant in the $\kappa$ - $\varepsilon$ turbulence model (value 2.0)
$d$	Depth
$d_A$	Depth of channel A
$e$	Mathematical constant
$f_{exact}$	Exact cell value from model output
$f_i$	Cell value from model output at grid resolution $i$
$h_d$	Bed discordance
$h_w$	Surface wave height
$k$	Turbulent kinetic energy
$k_s$	Roughness length scale
$m$	Mass of a tracer particle
$m_f$	Equivalent mass of fluid for a given particle volume
$m_l$	Mass of liquid in a cell column
$n_i$	Surface normal vector of the face $i$
$p$	Pressure
$p_c$	Pearson's correlation
$p_o$	Order of the solution
$r$	Grid refinement ratio
$r_B$	Radius of a bed particle
$r_T$	Radius of a tracer particle
$s$	Slope between the bottom of a tracer particle and the top of the adjacent bed particle
$t$	Time
$\bar{u}$	Mean velocity
$u$	Velocity in the $x$ direction

$u'$	Instantaneous velocity fluctuation about the mean in the $x$ direction
$u_*$	Shear velocity
$u_0$	Ambient flow velocity
$\bar{u}_A$	Mean velocity for channel A
$u_f$	Velocity of the fluid
$u_i$	Velocity in the $i$ direction
$u'_i$	Instantaneous velocity fluctuation about the mean in the $i$ direction
$u_s$	Particle velocity
$v$	Velocity in the $y$ direction
$v'$	Instantaneous velocity fluctuation about the mean in the $y$ direction
$w$	Velocity in the $z$ direction
$w'$	Instantaneous velocity fluctuation about the mean in the $z$ direction
$w_c$	Channel width
$w_A$	Width of channel A
$x$	Distance in the downstream direction
$\bar{x}$	Mean of the observed data
$x_a$	Depth of a tracer particle below the surface
$x_b$	Protrusion height of a bed particle
$x_i$	Distance in the $i$ direction
$x_{mod}$	Modelled value at a given timestep or location
$x_{obs}$	Individual observed data value at a given timestep or location
$y$	Distance in the cross-stream direction
$z$	Distance in the vertical direction
$z_0$	Roughness height
$\Phi_L$	Latitude
$\Phi_i$	Upwind value of the volume of fluid (VFOL) variable
$\alpha$	Inverse Prandtl number for turbulent transport
$\varepsilon$	Turbulent dissipation
$\varepsilon_f$	Error band between co-located cell values of different sized grids
$\zeta$	Angular rotation of the earth
$\theta$	Angle between the centre of a tracer and the adjacent bed particle

$\theta_C$	Confluence angle
$\kappa$	The von Karman constant
$\mu$	Co-efficient of friction
$\mu_T$	Turbulent viscosity
$\nu$	Kinematic viscosity
$\rho$	Density
$\rho_A$	Water density for channel A
$\rho_L$	Density of the liquid
$\sigma$	Standard deviation
$\sigma^2$	Variance
$\sigma_k$	Constant in the $\kappa$ - $\varepsilon$ turbulence model (value of 1.0)
$\sigma_\varepsilon$	Constant in the $\kappa$ - $\varepsilon$ turbulence model (value of 1.3)
$\tau$	Shear stress
$\tau_{ij}$	Shear stress acting in the $ij$ plane.
D	Ordinary differential
$\Delta$	Finite difference
$\partial$	Partial differential



## List of Abbreviations

2D	Two-Dimensional
3D	Three-Dimensional
aDcp	acoustic Doppler current profiling/profiler
aDv	acoustic Doppler velocimetry/velocimeter
ASME	American Society of Mechanical Engineers
BFC	Boundary Fitted Co-ordinates
CAFE	Cumulative Area Fraction Error
CFD	Computational Fluid Dynamics
CHZ	Confluence Hydrodynamic Zone
CPU	Central Processing Unit
DEM	Digital Elevation Model
DES	Detached Eddy Simulation
dGPS	Differential GPS
DNS	Direct Numerical Simulation
DPM	Discrete Particle Model (or Discrete Element Model)
DS	Downstream
EA	Environment Agency
ECM	Electromagnetic Current Meter
EP	Dissipation Rate
GCI	Grid Convergence Index
GLUE	Generalised Likelihood Uncertainty Estimation
GPU	Graphics Processing Unit
GSD	Grain Size Distribution
HEP	Hydroelectric Power
HOL	Height-of-Liquid
LES	Large Eddy Simulation
LiDAR	Light Detection and Ranging
MAE	Mean Absolute Error
MFSA	Mass Flux Scaling Algorithm
MMS	Method of Manufactured Solutions
NSE	Nash-Sutcliffe Efficiency
PDE	Partial Differential Equations

PISO	Pressure Implicit with Split Operator
PIT	Passive Integrated Transponder
PIV	Particle Image Velocimetry
PRIME	Pressure Implicit Momentum Explicit
PS	Photo Sieving
RAM	Random Access Memory
RANS	Reynolds-Averaged Navier-Stokes
RMA	Reduced Major Axis
RMSE	Root Mean Squared Error
RNG	Renormalisation Group
RR	Recovery Rate
RS	Reynolds Stress
RSM	Reynolds Stress Model
RTK	Real Time Kinematic
SGS	Sub-Grid Scale
SIMPLE	Semi-Implicit Method for Pressure-Linked Equations
SIMPLER	SIMPLE Revised
SIMPLEST	SIMPLE Shortened
SOV	Streamwise Oriented Vortical
SS	Bed Shear Stress
TIN	Triangular Irregular Network
TKE	Turbulent Kinetic Energy
TL	True Left
TR	True Right
VoF	Volume of Fluid
WC	Wolman Count
WSE	Water Surface Elevation

## **Statement of Copyright**

The copyright of this thesis rests with the author. No quotation from it should be published without the author's prior written consent and information derived from it should be acknowledged.

## Acknowledgements

There are many people and organisations that have provided me with assistance throughout this thesis and without them it would not have been possible to complete the research. I would like to extend my gratitude to all of them here.

Firstly, I want to thank the Environment Agency for providing the Moor House Nature Reserve gauging station data. In addition, the services of the Natural Environment Research Council (NERC) British Isles continuous GNSS Facility (BIGF) in providing archived GNSS data to this study, are gratefully acknowledged. I would also like to note my gratitude to JBA Consulting, on whose laptop the particle modelling experiments were conducted.

Secondly, I wish to extend a general thank you to all of the academic, technical and support staff in the Geography Department at Durham University. Their help with ideas, laboratory access, field equipment and logistics throughout my period of study have gone a long way to ensuring the completion of this thesis. In particular, Dr Samantha Waugh helped to arrange the analysis of the GPS data from BIGF and also provided very useful advice on surveying techniques. I am also grateful to Dr Patrice Carbonneau for giving me access to his photosieving Matlab code.

Thirdly, I would like to thank my supervisors, Prof Stuart Lane and Dr Rich Hardy. I cannot begin to describe how immensely helpful their constant flow of ideas and suggestions was, nor how grateful I am for their seemingly endless patience when reading drafts of this thesis.

Fourthly, I would like to thank Dr Tim Marjoribanks, who willingly braved the ice of Moor House and the heat wave of Arolla as a much-trusted field assistant. In addition, his role as a general sounding board, assistant pebble painter and proof reader when the occasion demanded meant that the research for this thesis has encountered far fewer obstacles than might otherwise have been the case.

The final thanks go to my wife, Mrs Devon Tancock. Her help as an occasional field assistant, pebble painter and proof reader were much appreciated, but not as much as the unending support she has given throughout the last four years.

# Chapter 1:

## Introduction

*‘Confluences can seem unruly places, their morphologies complex, even untidy, frequently unstable and shifting’ Ettema (2008: 95)*

### 1.1 Introduction

When viewed at the larger scale, a river catchment can be described as a network made up of a series of linked nodes (Rice *et al.*, 2008). A number of studies have therefore treated the catchment as a dendritic network, where the nodes are river confluences (*e.g.* De Serres and Roy, 1990; Hu and Richards, 2008). In this network, an increasing number of tributaries branch off from the main channel as distance upstream increases, meaning that river confluences are common features of the fluvial system.

Whilst some tributaries will join a river channel with limited impacts on the main channel flow field (Ferguson and Hoey, 2008), other confluences are areas of highly variable velocity, turbulence, sediment dynamics, planform geometry and bed morphology (Best and Roy, 1991, Miori, 2008). This makes confluences important areas of study for fluvial flows (*e.g.* Bradbrook *et al.*, 1998, 2001; De Serres *et al.*, 1999; Rhoads and Sukhodolov, 2001, 2008; Biron *et al.*, 2002, 2004a; Boyer *et al.*, 2006; Parsons *et al.*, 2007; Szupiany *et al.*, 2009; Laraque *et al.*, 2009; Bouchez *et al.*, 2010; Sukhodolov *et al.*, 2010; Constantinescu *et al.*, 2011), sediment dynamics (*e.g.* Best, 1988; Roy and Bergeron, 1990; Szupiany *et al.*, 2009; Musselman, 2011; Leite Ribeiro *et al.*, 2012), pollution (Gaudet and Roy, 1995) and fluvial ecosystem dynamics (Fernandes *et al.*, 2004; Gascon and Smith, 2004; Wallis *et al.*, 2008).

In many fluvial environments geomorphologists have sought to explain the importance of the three-way interactions between the flow field, sediment dynamics and bed morphology. Figure 1.1a shows Leeder’s (1983) diagram of this three-way interaction (the flow ‘trinity’). The morphology (bedform development) is an important control on the flow field, which in turn drives the sediment transport that determines how this morphology will evolve. A more complex interpretation of these interactions from Ashworth and Ferguson (1986) is given in Figure 1.1b, which includes an input from the river discharge. However, whilst these two diagrams highlight different

processes, the principle of both is that the flow dynamics, geomorphology and sediment dynamics cannot be studied in isolation if the system is to be understood as a whole (Leeder, 1983). At river confluences, with the meeting and mixing of two tributary flows, these interactions become highly complex and variable in both space and time. Understanding the complexity of these linkages is the focus of this thesis.

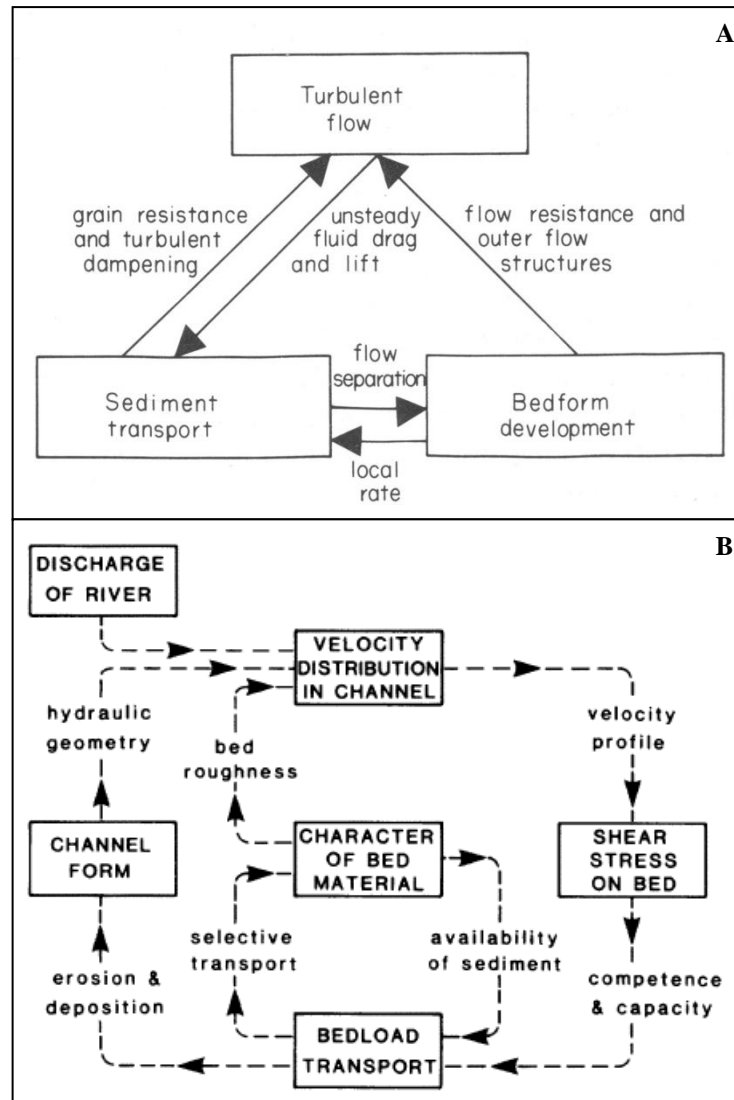


Figure 1.1: Diagrams showing the interaction between flow, sediment transport and bed morphology. The flow trinity of Leeder (1983) is shown in (a), with the more detailed interpretation of Ashworth and Ferguson (1986) given in (b). Neither figure specifically includes the effects of bed slope, but this will have an important impact on the velocity distribution in the channel.

Research has focused on the mixing process at river confluences for some decades (*e.g.* Mackay, 1970). However, the first major advances in understanding the flow processes at river confluences resulted from the laboratory research of Mosley (1976). In these flume experiments, Mosley (1976) investigated the major controls on

the scouring of bed material as the two tributaries join, finding that (i) larger junction angles, (ii) similar discharges between the two tributaries and (iii) higher levels of turbulence encouraged larger scour holes to develop. This work also provided evidence for the presence of helix-shaped flow cells in the centre of the river confluence helping to maintain the size of the scour holes (Mosley, 1976). Subsequent advances in understanding were largely the result of further laboratory studies. Following on from Mosley's work, Ashmore and Parker (1983) developed the idea that the flow field at river confluences resembled back-to-back meander bends, with two helix-shaped flow cells rotating in opposite directions. Subsequent research by Best and Roy (1991), however, disproved this for confluences where there is a disparity in bed elevation between the two tributaries (*i.e.* a discordant river confluence).

This laboratory work was supplemented by early field experiments, which attempted to apply some of the findings from the laboratory to the more variable morphologies of natural river confluences (*e.g.* Best, 1988; Ashmore *et al.*, 1992). This included some early work which addressed the issue of bedload transport in natural river confluences using tracer particles (Best, 1988; Roy and Bergeron, 1990). The result of this early laboratory and field research was the development of a conceptual model of river confluences, which in this thesis is referred to as the classical river confluence model. This conceptual model is summarised in the following section.

## **1.2 The Classical Model of River Confluences**

The classical model of river confluences is based on the separation of the river confluence into a series of commonly-identifiable zones. Figure 1.2 shows these zones, which are based on either characteristic geomorphological features or flow structures, as defined by Best (1986).

The classical model of river confluence morphology can be described as follows. When two flows meet they interact, generating a shear layer (shown in Figure 1.2). This shear layer (also referred to as a mixing layer) is the major area for the generation of turbulent flow structures and secondary circulation cells (Best, 1986). As the two tributaries join, there is an increase in the water pressure at the surface. This pressure increase induces superelevation of the water surface and directs the flow of water towards the bed (Mosley, 1976; Biron *et al.*, 2002). This water then flows along the bed towards the banks, where it resurfaces to complete a secondary circulation cell (Miori,

2008). As shown in Figure 1.2b, this secondary circulation cell may take the form of two adjacent, but counter-rotating, helix-shaped cells (Mosley, 1976).

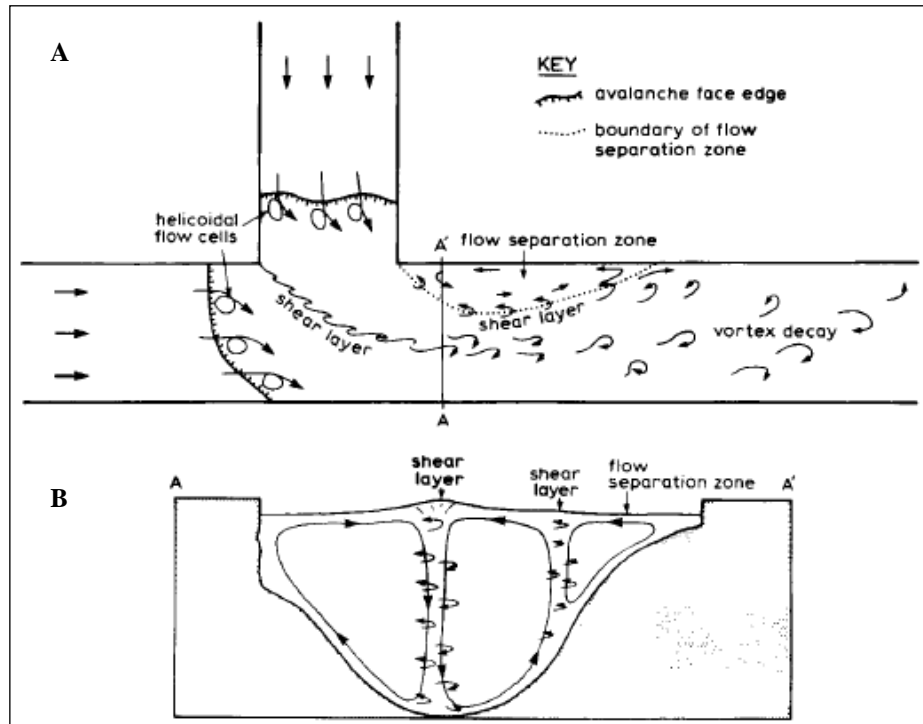


Figure 1.2: Conceptual diagrams of Best (1986) showing the major flow structure zones in a 90° confluence. Diagram (a) shows the plan view of the confluence, with a cross-section through the shear layer given in (b).

In addition, as the two tributaries join any disparity in velocity will result in shear between the two flows, which will encourage the development of turbulent vortices, as shown in Figure 1.2a (Best, 1986; Rhoads and Sukhodolov, 2004). These turbulent vortices will increase the local turbulent kinetic energy and therefore encourage greater mixing between the two tributary flows.

As a result of the development of helical secondary circulation cells and turbulent flow structures in the shear zone, there is increased shear stress at the bed under the mixing layer which encourages the development of a scour hole. In the classic model of river confluences, the scour hole and the steep avalanche faces into it are maintained as a result of the downwelling and near-bed flow divergence of the secondary circulation cells (Mosley, 1976). Furthermore, these helical cells help to route the flow and bedload around the edges of the scour hole, rather than through the centre of it (Best, 1988). The bedload routed around the scour hole in this way joins into a single transport zone at the downstream edge of the scour hole (Mosley, 1976; Best, 1986; Parsons *et al.*, 2008). This, combined with sediment eroded from the scour hole,

provides the potential for a mid-channel bar to develop downstream of the scour hole (Best, 1986).

Where the cross-sectional area is reduced downstream (often assisted by the formation of sediment bars in flow separation zones at the downstream corners), flow acceleration will occur (Rhoads and Kenworthy, 1995). At the downstream end of the confluence is the flow recovery zone, which can be considered to be the point at which the vortices shown in Figure 1.2a have decayed and the two tributary flows are fully mixed. The position of the flow recovery zone can be a considerable distance (hundreds of channel widths) downstream (Gaudet and Roy, 1995; Parsons *et al.*, 2008) and will depend on both the speed of flow mixing and the downstream channel morphology and bed roughness.

This classical model of river confluences provided a good initial understanding of the flow and sediment transport processes operating at river confluences. However, the model was devised from research on a relatively limited number of confluences, some of which used idealised geometries developed for controlled flume experiments. The work of Best and Roy (1991) and Biron *et al.* (1993) has already demonstrated that this classical model does not necessarily apply at river confluences with discordant beds, whilst the sediment transport research of Roy and Bergeron (1990) has shown that particles can be transported through the scour hole. Further research took advantage of technological developments to show the additional complexity which characterised the flow fields (and by implication the sediment transport process) of many natural river confluences. Therefore, the current level of understanding of river confluences has moved beyond the conceptual model set out above.

### **1.3 Recent Developments in the Study of River Confluences**

The early work on river confluences which led to the development of the classical model highlighted the complexity of the flow field at these confluences. The nature of the secondary circulation cells and turbulent vortices means that to obtain a complete understanding of river confluences requires a comprehensive knowledge of what drives the flow in all three spatial dimensions and through time.

Since the early river confluence research using laboratory flumes, there have been significant advances in the methods available to fluvial geomorphologists in the field. It is now possible to get high resolution topographic data using GPS systems



(Brasington *et al.*, 2000), terrestrial LiDAR (*e.g.* Hodge *et al.*, 2009), photographic methods (*e.g.* Lane *et al.*, 1994) or sub-surface sound-based techniques (Lane *et al.*, 2008). Spatially distributed, three-dimensional flow data can be obtained using acoustic methods (*e.g.* Rhoads and Sukhodolov, 2001; Lane *et al.*, 2008) and particles can be tracked using electromagnetic tags (Lamarre and Roy, 2008b). The more recent river confluence research has therefore taken advantage of these technological advances to expand on the initial laboratory studies.

For research using field experiments, two confluences have been extensively studied over the past two decades: the Bayonne-Berthier confluence in Quebec, Canada (Biron *et al.*, 1993, 2002, 2004a; De Serres *et al.*, 1999; Boyer *et al.*, 2006) and the Kaskaskia River-Copper Slough in Illinois, USA (Bradbrook *et al.*, 2000a; Rhoads and Sukhodolov, 2001, 2008; Rhoads *et al.*, 2009; Constantinescu *et al.*, 2011). These are both relatively small-scale (channel widths of <25m) lowland river confluences, with the Bayonne-Berthier being distinguished by its discordant beds. More recently, there has been an increased interest in understanding the processes operating at confluences on much larger rivers, such as on the Rio Parana in Argentina (*e.g.* Orfeo *et al.*, 2006; Parsons *et al.*, 2007; Lane *et al.*, 2008; Szupiany *et al.*, 2009) and on tributaries of the Amazon River (Laraque *et al.*, 2009; Bouchez *et al.*, 2010).

These field studies have added greatly to the knowledge of the flow and turbulent mixing processes operating at river confluences (Rice *et al.*, 2008, Roy, 2008). However, whilst much can be gained from research on natural rivers and in laboratory flumes, it is still far from straightforward to obtain three-dimensional flow data at both high spatial and temporal resolutions. There has therefore been an increased interest in the development of numerical modelling methods to simulate the flow processes at river confluences.

River confluences, as components of multi-thread channels, have been modelled numerically using both reduced-complexity methods (*e.g.* Murray and Paola, 1994) and two-dimensional approaches based on the shallow water equations (*e.g.* Lane and Richards, 1998). However, the use of depth-averaged numerical modelling approaches is arguably an over-simplification in cases where there is a significant vertical velocity component to the flow field due to the helical flow cells. A comparison of two- and three-dimensional numerical modelling approaches by Lane *et al.* (1999a) demonstrated that for river confluences, three-dimensional methods provided more reliable predictions of the flow field. Computational advances (in terms of processing power

and memory) have increased the viability of these three-dimensional flow models. As a result, much research in the past two decades has involved the development and use of three-dimensional Computational Fluid Dynamics (CFD) models to simulate the confluence flow field (*e.g.* Bradbrook *et al.*, 1998, 2000a, 2000b, 2001; Lane *et al.*, 2000; Huang *et al.*, 2002; Biron *et al.*, 2004a; Constantinescu *et al.*, 2011).

The earlier research of Bradbrook *et al.* (1998) applied CFD models to relatively simple confluence geometries, whereas more recent research has used natural river confluences such as the Bayonne-Berthier (Biron *et al.*, 2002, 2004a) and Kaskaskia River-Copper Slough (Bradbrook *et al.*, 2000a; Constantinescu *et al.*, 2011). There have also been advances in the complexity of the turbulence models used within the CFD framework, from models which determine the impact of turbulence on the mean flow field (Bradbrook *et al.*, 1998, 2000a, 2001) to those which resolve the larger turbulent eddies directly (*e.g.* Bradbrook *et al.*, 2000b; Constantinescu *et al.*, 2011). By incorporating more complex turbulence models into the CFD model, the dynamics of individual turbulent eddies within the shear layer can be studied.

High-resolution numerical modelling has therefore become an important tool in the drive to understand the complex nature of the flow at river confluences. However, it is generally agreed that although there is now a good knowledge of flow processes at river confluences, there is still much work to be done to increase the understanding of the interactions between flow, sediment transport and confluence morphology (Ashmore and Gardner, 2008; Roy, 2008, Biron and Lane, 2008; Best and Rhoads, 2008). It is this lack of understanding which is the motivation for the research conducted in this thesis.

## **1.4 Research Rationale**

The current state of our understanding of river confluence processes can therefore be summarised as follows: the quantity of research into the sediment dynamics of river confluences (Best, 1988; Roy and Bergeron, 1990; Szupiany *et al.*, 2009) is vastly outweighed by the work on the flow dynamics (Mosley, 1976; Best and Roy, 1991; Biron *et al.*, 1993, 1996a, 1996b, 2002, 2004a; Bradbrook *et al.*, 1998, 2001; De Serres *et al.*, 1999; Rhoads and Sukhodolov, 2001, 2008; Boyer *et al.*, 2006; Parsons *et al.*, 2007; Szupiany *et al.*, 2009; Laraque *et al.*, 2009; Bouchez *et al.*, 2010; Sukhodolov *et al.*, 2010; Constantinescu *et al.*, 2011). This has meant that of the three major

components of Leeder's (1983) trinity (Figure 1.1a), only for the flow component can we truly be considered to be approaching a full understanding.

However, in addition to the well documented need for research into the interactions between sediment dynamics and the resultant evolution in confluence morphology (Ashmore and Gardner, 2008; Roy, 2008, Biron and Lane, 2008; Best and Rhoads, 2008), it is notable that the majority of the field sites studied to date are located in lowland areas (the Bayonne-Berthier, Kaskaskia-Copper Slough and sites on the Rio Parana and Amazon can all be considered lowland). The branching nature of the river network implies that upland river confluences should be more common than lowland junctions within a given catchment. It could be argued, therefore, that a complete understanding of the flow field has yet to be attained as the flow processes at upland confluences, in particular those with steep water surface slopes, have yet to be fully investigated. Furthermore, upland confluences, such as those studied by Lane and Richards (1998), are characterised by gravel or cobble beds, steep water surface slopes and rapidly evolving morphologies. In short, it is in upland areas that we might expect to find good examples of river confluences which demonstrate the complexities of the three-way interactions and the dynamics between flow, sediment transport and confluence morphology.

Three-dimensional numerical modelling has been an important tool for improving our understanding of flow at lowland river confluences (*e.g.* Constantinescu *et al.*, 2011) and has great potential for disentangling the interactions between the flow field, sediment dynamics and morphology at these dynamic, upland river confluences. However, to date, the vast majority of CFD simulations of river confluences have represented the water surface with a fixed boundary (a 'rigid-lid' approach) or made only minor modifications to this assumption (*e.g.* Bradbrook *et al.*, 1998, 2000a, 2000b, 2001; Biron *et al.*, 2002, 2004a; Constantinescu *et al.*, 2011). This can be considered to be a reasonable approximation for the lowland confluence field sites investigated in those studies. However, in order to develop a realistic representation of dynamic, upland river confluences, it is necessary to explicitly account for the steeply-sloping water surface.

The rationale for this thesis is therefore driven by two key gaps in the current understanding of river confluences. The first is the lack of in-depth research into the interactions between flow, sediment dynamics and morphology at river confluences, whilst the second is the relative paucity of the knowledge of processes at dynamic,

upland river confluences with steep water surface slopes. The aims and objectives set out in the following section have therefore been drawn up with heavy reference to this underlying rationale.

## **1.5 Research Question, Aims and Objectives**

Given the current state of the understanding of river confluence processes set out above, and the rationale in Section 1.4, a two-part research question can be devised for this thesis, namely: what processes drive the dynamism of upland river confluences and how do these processes differ from those currently known to shape lowland river confluences?

This research question can be subdivided into three aims for the thesis, as set out below:

- To improve our understanding of the feedback mechanisms operating between flow, sediment dynamics and morphology at steep river confluences.
- To investigate the flow processes at upland river confluences characterised by steep water surface slopes.
- To investigate the way in which the flow field drives the sediment transport and the resultant implications for morphological evolution in dynamic, upland river confluences.

In order to meet these aims, a set of five specific objectives have been drawn up which are set out below. In addition, Figure 1.3 provides a graphical representation of how these objectives relate directly to the research aims set out above:

1. To obtain and to present high-quality field data on the morphology, flow field and particle transport at a range of upland river confluences.
2. To develop the application of numerical approaches to improve the understanding of steep river confluence flow dynamics.
3. To use the topographic and flow data obtained as part of Objective 1 to test the performance of the numerical flow model developed in Objective 2.

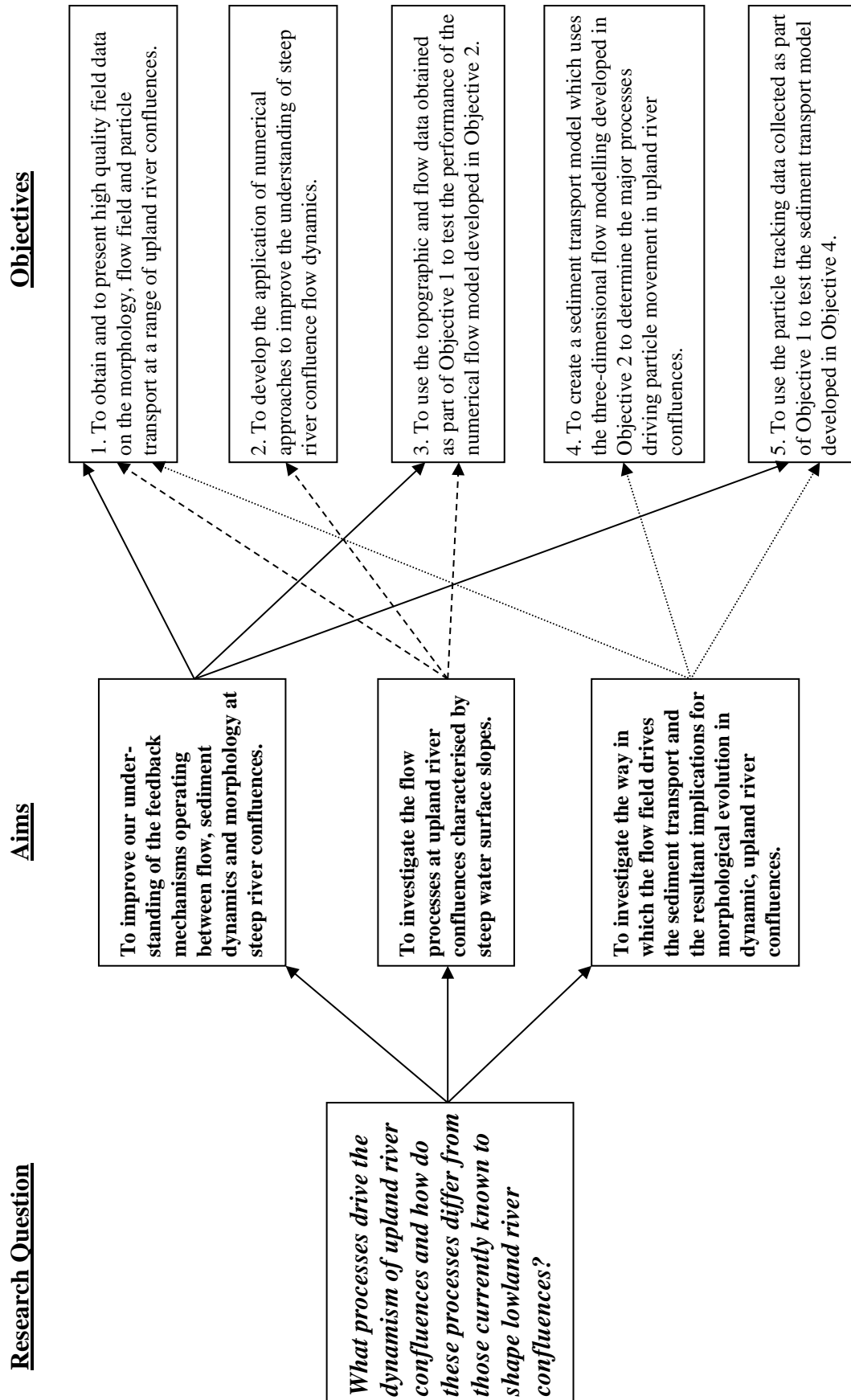


Figure 1.3: Diagram showing the relationship between the research question, aims and objectives.

4. To create a sediment transport model which uses the three-dimensional flow modelling developed in Objective 2 to determine the major processes driving particle movement in upland river confluences.
5. To use the particle tracking data collected as part of Objective 1 to test the sediment transport model developed in Objective 4.

By fulfilling each of these objectives, the thesis will address the three research aims. It is suggested that this will increase our current understanding of the processes operating at dynamic, upland river confluences, thus enabling a comprehensive answer to be provided to the research question set out at the beginning of this section.

## **1.6 Field Site Location**

In the previous section, it was set out as part of Objective 1 that high quality field data were required to increase the understanding of the flow, sediment transport and morphological processes operating at upland river confluences. Obtaining these datasets on a variety of different sloping river confluences is also a crucial component to Objectives 3 and 5 and can be directly linked to all three research aims (as shown in Figure 1.3). The selection of appropriate field sites is therefore an important task and must be undertaken with a clear set of requirements. As such, given the objectives set out in the previous section, the following criteria have been determined for the selection of field sites. These are as follows:

1. Data should be collected from a range of confluences which have different water surface slopes and hydraulic characteristics.
2. Some of the confluences should be highly dynamic such that particle tracks can be obtained in real time.
3. Confluences should be chosen where it is possible to obtain discharge measurements for the flows in which bedload transport is active.
4. There should be at least two examples of confluences with steep water surface slopes, in order to fully test the numerical modelling of steep river confluences.
5. For at least some of the confluences it should be possible to obtain high quality boundary condition data and three-dimensional velocity data with good spatial coverage.

Given the criteria set out above, it is suggested that no single field site would be able to provide the range of confluences to fulfil all of these criteria. Furthermore, dynamic confluences where water surface slopes are steep and bedload transport is active (as required for Criteria 2 and 4) will almost certainly be too unstable to be able to obtain the high-quality three-dimensional velocity and topography data for Criterion 5. Therefore, the possibility of finding a single field site to satisfy all of the criteria was rejected in favour of looking for two field sites with complementary hydrological and geomorphological characteristics. By taking this approach, it would also ensure greater variability in the sites as required by Criterion 1.

The first field site would be selected primarily for its ability to satisfy Criterion 5. This meant finding a more stable, less steep river confluence with bedload transport that was only active in high discharge events. This stability would enable boundary conditions and input data to be obtained at higher resolutions and on multiple days, as the confluence would not change substantially on a weekly or monthly basis. However, in order to satisfy Criterion 3, the field site would have to be chosen so that it would be possible to obtain data on the range of discharges for the high flow events in which any tracer particles are entrained and transported.

The second field site would be selected to fulfil Criteria 2, 3 and 4, being a site of much more dynamic and steeper confluences with active bedload transport. This would enable particle tracks to be obtained for the discharges and flow velocities measured *in situ*. The ever-changing nature of these confluences, however, would mean they would be less likely to satisfy Criterion 5.

As a result of this, two field sites were chosen for data collection. The first, at Moor House Nature Reserve in the North Pennines, was selected for its more stable nature and shallower water surface slopes. This would contrast with the second field site, the Borgne d'Arolla braid plain in the Valais canton of Switzerland, which has much steeper water surface slopes and a far more dynamic morphology.

#### *1.6.1 Trout Beck and the River Tees, Moor House Nature Reserve*

Moor House Nature Reserve is located in the North Pennines on the border between Durham and Cumbria, and is shown on the map in Figure 1.4. The River Tees and its tributary Trout Beck flow through Moor House Nature Reserve, joining at the 'lower' confluence marked in Figure 1.4. Another confluence (the 'upper' confluence in

Figure 1.4) is located on Trout Beck approximately 640m upstream of the lower confluence. In the reach that separates these two confluences is an Environment Agency gauging station, which records river level and discharge at 15 minute intervals.

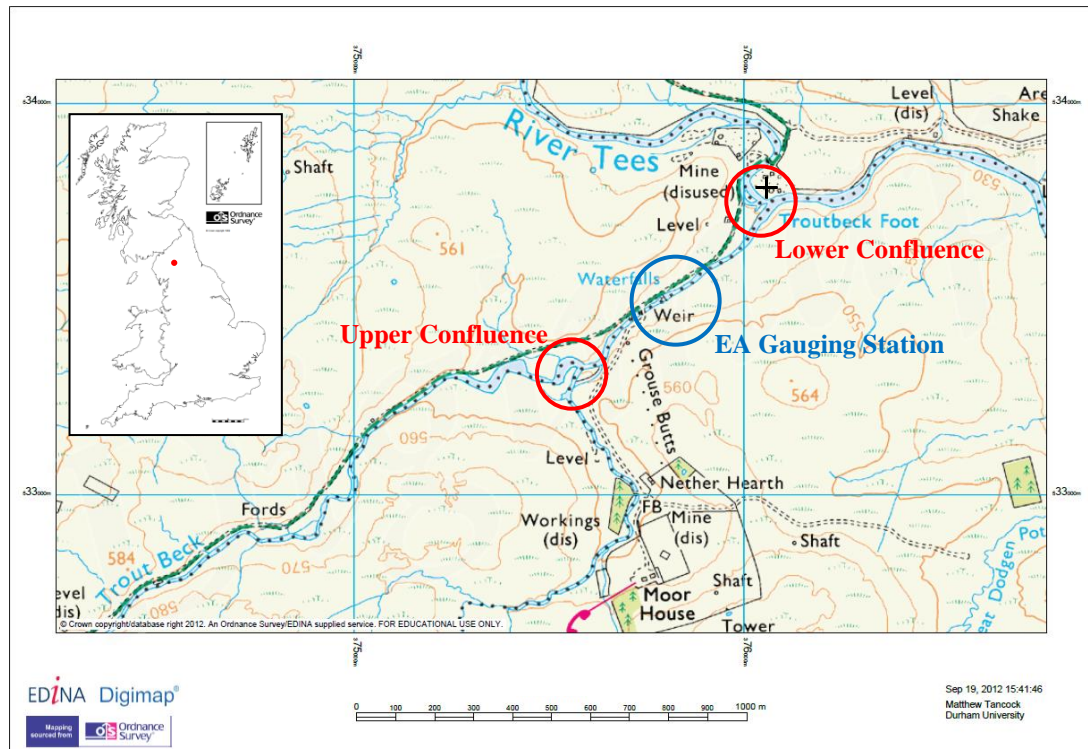


Figure 1.4: Map of the locations of the EA gauging station (circled in blue) and two confluence sites (circled in red) on Trout Beck in Moor House Nature Reserve. The inset map shows the location of the site within Great Britain and the black cross the location of the base station (at 54.698385°N, 2.3730057°W). Source: EDINA Digimap and Ordnance Survey (© Crown Copyright and database rights 2012. An Ordnance Survey/EDINA supplied service).

The location of the gauging station means that recorded discharges should be equivalent to those in the downstream channel of the upper confluence and the true right tributary of the lower confluence. The gauging station data can therefore be used to determine the range of discharges at which bedload transport is active, as required by Criterion 3. Photographs of the lower and upper confluences are given in Figure 1.5 and Figure 1.6 respectively.

The vegetated banks seen in Figure 1.5 and Figure 1.6 ensure that the morphology of the confluences is relatively stable at most discharges, meaning that it is possible to obtain high-resolution topographic and velocity data. Both confluences have slight water surface slopes which, in the photographs, can be seen most clearly where the true left tributaries join the main channels. The upland nature of the confluences means that both have gravel or cobble beds and that bedload transport is inactive during



low flows. However, particles will move during high flow events that occur on an approximately monthly basis.



Figure 1.5: Photograph of the lower confluence at Moor House Nature Reserve during low flow, looking upstream. Downstream channel width is approximately 10m (as scaled by the field assistant in the photo).



Figure 1.6: Photograph of the upper confluence at Moor House Nature Reserve during a medium discharge. Downstream channel width is approximately 8m, whilst the field assistant in the photograph provides scale.

Being located further downstream, the lower confluence is the larger of the two, with typical main channel and tributary widths of 10m and 6m respectively, compared to 8m and 3m for the upper confluence. The discharges experienced at the lower confluence will also be correspondingly higher than those at the upper confluence. This provides some of the variability required as part of Criterion 1, whilst the two confluences can both be considered to fulfil Criteria 3 and 5.

### *1.6.2 The Borgne d'Arolla Braid Plain*

The village of Arolla is located within the Valais canton in Switzerland, close to the Italian border. The Borgne d'Arolla is the proglacial stream which begins at the tongue of the Bas Glacier d'Arolla at the head of the valley and ends at its confluence with the Rhône in the town of Sion. The Arolla valley has been used in the past for a variety of glaciological (*e.g.* Sharp *et al.*, 1993; Hubbard *et al.*, 1995; Nienow *et al.*, 1996) and hydraulic research (*e.g.* Warburton, 1990, 1992, 1994; Clifford *et al.*, 1995; Lane *et al.*, 1995). The research in this thesis is conducted on the braid plain between the hamlets of La Monta and Pramousse, shown in Figure 1.7. The channel enters and leaves the braid plain as a single thread, but in between there are numerous river bifurcations and confluences which can be studied.

The flow through the Borgne d'Arolla is heavily regulated as a result of glacial meltwater being used for the Grande Dixence hydro-electric power (HEP) scheme. Water is collected from the proglacial streams, transported into the Lac Des Dix and stored until needed for electricity generation.

For the Borgne d'Arolla field site, water that would normally flow through the channel from the Bas Glacier d'Arolla and the Glacier de Tsidjoire Nouve is pumped up to the Lac Des Dix via the Arolla pumping station. For the vast majority of the time, therefore, the flow in the Borgne d'Arolla is kept artificially low. However, when the inlet structure sediment traps are full, they must be purged of their sediments by allowing the glacial water to flow through them and into the downstream channel. On warm mid-summer afternoons, this can release a sudden, large flood downstream for around 45 minutes that has the potential to significantly modify the braid plain geomorphology.



Figure 1.7: Aerial view of the Borgne d'Arolla braid plain field site, with the village of La Monta ( $46.031806^{\circ}\text{N}$ ,  $7.486067^{\circ}\text{E}$ ) visible at the bottom of the picture. Flow is from south to north. *Source: Google Earth (Imagery: Digital Globe, Map data: Google).*

Even without the purges, flow through the braid plain is often supercritical, with steep water surface slopes and much faster low flow velocities than are seen in the confluences of Moor House Nature Reserve. An example of a confluence on the Borgne d'Arolla braid plain is given in Figure 1.8. The confluences on this braid plain are very unstable, either constantly evolving throughout the day due to erosion of the unvegetated banks (seen in Figure 1.8) or being destroyed as purges are sent through the system. This dynamism means that sediment transport is almost always active on summer days, allowing individual particles to be tracked in real time. Using the confluences of the Borgne d'Arolla therefore clearly satisfies Criteria 2, 3 and 4, providing flow measurements are taken shortly before or after any particle tracking experiments. Furthermore, the nature of the braid plain as a constantly evolving system means that on any given day confluences with different morphologies are found, very much adding to the variability required in Criterion 1.





Figure 1.8: Confluence on the Borgne d'Arolla braid plain on 28<sup>th</sup> August 2011, with visibly steeper water surface slopes than the Moor House confluences. Downstream channel flow widths are approximately 3m, as scaled by the field assistant in the photograph.

Therefore, the Moor House and Arolla field sites can be considered to complement each other in such a way that between them, they fulfil all five of the criteria set out at the beginning of this section. By selecting these sites, a wide range of data on sloping river confluences can be obtained to help to validate the numerical models being developed as part of Objectives 2 and 3. Furthermore, the comparisons that can be made between the sites mean that the experiments should be able to significantly add to the current understanding of sediment dynamics at river confluences, thus fulfilling the requirements of Objective 1.

## 1.7 Thesis Structure

In order to achieve the research aims set out in Section 1.5, the following thesis structure has been devised. Following on from this chapter, Chapter 2 provides an extensive review of the river confluence literature, to give context for the thesis and outline in detail the current state of understanding of river confluence dynamics. As a result of this review, it is suggested that numerical modelling is a highly promising

methodological tool for improving our understanding of flow at steep river confluences. Therefore, Chapter 3 will provide a review of the main numerical modelling techniques to be used in this thesis, with particular emphasis on three-dimensional Computational Fluid Dynamics (CFD) models. This is followed by a full review of potential field methods and an explanation of the field methodology adopted in this thesis.

Having provided the context for the thesis in Chapter 2 and a review of the methodology in Chapter 3, Chapter 4 presents the first set of results from the thesis. Flow data from the more stable and less steep Moor House Nature Reserve confluences are compared with the flow at the more dynamic and steeper confluences of the Borgne d'Arolla braid plain. This chapter will therefore primarily address Objective 1 in Section 1.5. Having demonstrated the complexity of the flow field at upland river confluences and its imperfect fit with the classical river confluence model, Chapter 5 introduces the results from three-dimensional numerical modelling of the Moor House and Arolla confluences. This includes the testing and application of a numerical method for simulating steep water surface slopes. The results from the numerical modelling are compared to the field data obtained in Chapter 4, thus addressing Objectives 2 and 3 in Section 1.5.

With a much fuller understanding of the flow at the Moor House and Arolla confluences, Chapter 6 provides an opportunity to begin to address the other aspects of Leeder's (1983) flow trinity (Figure 1.1a). In Chapter 6, the particle tracking results are presented from the river confluences at Moor House Nature Reserve and on the Borgne d'Arolla braid plain. The results are discussed with reference to the flow data obtained in Chapter 4 and the numerical modelling results of Chapter 5. As with Chapter 4, this chapter mainly addresses Objective 1 from Section 1.5. Having presented the particle tracking data in Chapter 6, Chapter 7 reviews the methods of modelling bedload transport at the grain scale and presents a new reduced-complexity particle transport model. This model uses a basic treatment of the force balance on an individual particle to determine its change of momentum. The particle transport model is tested against the data from Chapter 6 to determine whether it can reproduce the particle transport paths found in natural confluences. It is then used as a tool for understanding the dynamics of sediment transport more generally, in particular in response to changes in the boundary conditions. Objectives 4 and 5 will therefore be the main focus of Chapter 7.

Chapter 8 will discuss all of the results presented in the thesis and evaluate the success of the new numerical modelling methods introduced. The results of the thesis

will be compared to the original research aims and objectives, before the final concluding remarks address the overarching research question set out in Section 1.5.

# Chapter 2:

## River Confluences

### 2.1 Introduction

In the previous chapter, it was emphasised that river confluences can be fully understood only by considering the complex interactions between the ‘trinity’ of flow structures, morphology and sediment dynamics (Leeder, 1983). To date, however, the three-dimensional nature of the flow at river confluences has led to much greater focus on researching the turbulent flow structures and secondary circulation cells (*e.g.* Bradbrook *et al.*, 2001; Biron *et al.*, 2007; Parsons *et al.*, 2007; Laraque *et al.*, 2009; Szupiany *et al.*, 2009; Constantinescu *et al.*, 2011). This work has led to a very good understanding of the flow dynamics at a range of river confluences and is examined in detail in this chapter. However, this emphasis on the flow has meant that the links with sediment transport and the resultant morphological evolution of river confluences are less well understood. The current state of this understanding and the areas in which further research is required are also examined in this chapter.

This chapter provides an over-arching review of the river confluence literature. The first section defines the major morphological and flow structure zones within river confluences. The current level of understanding of flow structures is then set out in detail, followed by a section addressing how confluence planform and channel shape affect the flow. The research conducted into river confluence sediment dynamics at the catchment scale and at the scale of individual confluence morphological zones is then discussed. In the following section, the effect of confluence planform and channel shape on both the morphology and sediment dynamics is investigated, with particular focus on the scour hole. The final section of the chapter summarises the overall state of river confluence research and highlights the current gaps in the understanding which this thesis intends to address.

### 2.2 Major Flow and Morphological Zones at River Confluences

The major flow structure and geomorphological zones within river confluences have been identified by a number of authors (Best, 1987, 1988; Best and Rhoads, 2008;

Biron and Lane, 2008; Parsons *et al.*, 2008). Figure 2.1a reproduces the original diagram of Best (1986), as shown in the previous chapter as Figure 1.2, along with two new diagrams which have been developed from the review which follows in this chapter. Figure 2.1b defines the confluence as a series of key flow structure zones and Figure 2.1c separates the confluence into a number of geomorphological features.

This chapter will investigate river confluences from these two different perspectives: the confluence as areas of different flow structures and the confluence as a series of morphological zones. The following sections will therefore review the research into the flow structure zones and morphological zones separately.

From Figure 2.1b, five major flow structure zones can be identified: the shear or mixing layer, the helical secondary circulation cells, flow in the stagnation zone, the flow separation zones and the zone of maximum velocity, or flow acceleration zone. The zone of flow recovery is excluded because its location at the downstream extent of the confluence is largely dependent on the speed of flow mixing, which will be covered in the review of the mixing layer.

By contrast, there are four major morphological zones which can be identified from Figure 2.1c: the scour hole and associated avalanche faces, lateral bars, mid-channel bars and the upstream corner bar. Although, in general, there has been far more research into the flow structures at river confluences, the processes that drive the formation and evolution of the scour hole have been particularly well researched. This will become evident in review of the river confluence sediment dynamics literature in Sections 2.6 and 2.7.



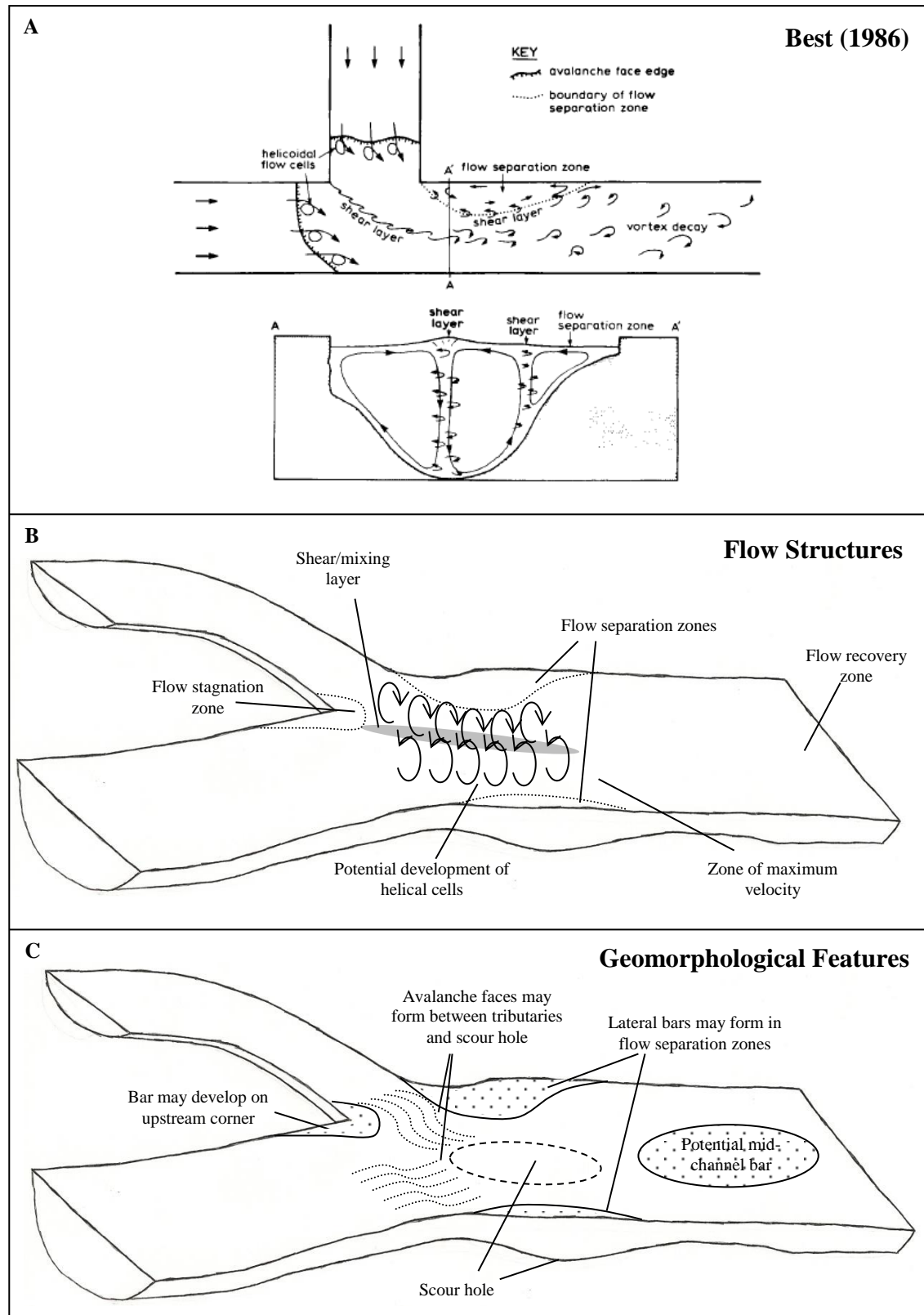


Figure 2.1: A hypothetical river confluence showing the major flow (b) and morphological (c) zones (after Best, 1986 and Biron and Lane, 2008). These are compared to, in (a), the original diagram of Best (1986), which focused largely on flow structures.

## 2.3 Flow Dynamics in River Confluences

This section presents a review of the research into the dynamics of the key flow structure zones identified in Figure 2.1b, setting out the current level of understanding for each. The first four subsections address the shear and mixing processes, reflecting the wide-ranging nature of research into this feature of river confluences. The remaining subsections review, in turn, helical flow cells, the flow stagnation zone, the flow separation zone and the flow acceleration zone.

### 2.3.1 Shear Layer/Mixing Layer Zone

The zone referred to in Figure 2.1 as the ‘shear/mixing layer’ is considered to be the major zone of river confluences and can extend for a significant distance downstream, from the flow stagnation zone to the flow recovery zone (Biron and Lane, 2008). Shear layers are considered to be highly turbulent, with high shear stresses and well-defined coherent flow structures such as Kelvin-Helmholtz instabilities (Boyer *et al.*, 2006). However, when referring to this zone of the confluence, it is not ideal to use either of the terms ‘shear layer’ and ‘mixing layer’, as the two are different and will not necessarily occur in the same place in a confluence (Sukhodolov *et al.*, 2010). A shear layer implies that flows of different velocities are flowing next to each other, encouraging the development of Kelvin-Helmholtz instabilities which can pair up, split or join together as they move downstream (Best and Roy, 1991). This will almost certainly cause some mixing of the two flows, but it is not the only method by which mixing occurs. Therefore the definition of the Confluence Hydrodynamic Zone (CHZ) by Rhoads and Kenworthy (1998) (shown in Figure 2.2) provides a more generic term which can be used to avoid implying any particular physical properties of the flow field.

The CHZ has been the subject of a large amount of research, covering the nature of the shear and mixing processes as well as the dynamics of helical cells. Helical cells are discussed in detail in Section 2.3.5, whilst the following three sections deal with the presence of shear in the CHZ, the causes and development of the mixing layer and factors affecting the speed of mixing.

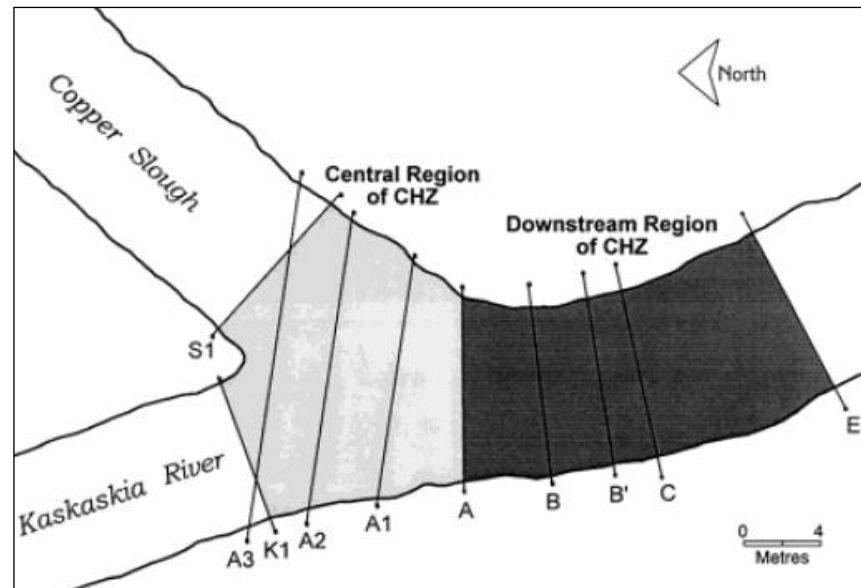


Figure 2.2: Diagram highlighting the CHZ, split into a central region and downstream region (Rhoads and Kenworthy, 1998). The letters denote positions of cross-sections on the Kaskaskia River-Copper Slough confluence.

### 2.3.2 Shear Zones in the CHZ

The development of a shear layer encourages vertical vortices to develop which are similar to Kelvin-Helmholtz instabilities (Rhoads and Sukhodolov, 2004). Babarutsi and Chu (1998) produced aerial photographs of the Nottaway River-Broadback River confluence in Québec, where large-scale turbulent structures (horizontal lengths of 100m) can be seen due to differences in water turbidity. These large-scale structures are restricted by the depth of the water and therefore they are considered to be quasi-2D, as their movement is restricted to the horizontal plane (Babarutsi and Chu, 1998; Rhoads and Sukhodolov, 2008). These large eddies can increase in size through vortex coalescence, although eventually they will destabilise and decay into smaller, three-dimensional structures (Uijttewaal and Booij, 2000).

In natural river confluences, these shear layers will also have interactions with the bed (through the effect of friction and the bedforms) and so have been described as ‘shallow mixing layers’ (*e.g.* Sukhodolov *et al.*, 2010). Shallow mixing layers are also characterised by the presence of smaller turbulent structures which are generated by bedforms and are three-dimensional, as their length scales are similar to the water depth (Babarutsi and Chu, 1998). These turbulent structures will form in all shallow water flows, but their effect on confluences is more marked due to the interactions with larger coherent structures in the CHZ.

Rhoads and Sukhodolov (2004) conducted experiments in the Kaskaskia River-Copper Slough confluence (Illinois, USA) with two acoustic Doppler velocimeter (aDv) probes placed at different lengths apart in the downstream direction. Their analysis of data from the two probes found that the strongest correlations were between the downstream and cross-stream velocities, thus supporting the view that these structures are mostly two-dimensional. Furthermore, the separation distance at which the correlations started to markedly decrease (0.6m) was found to be similar to the 0.5-1.0m structures visible from dye tracing experiments (Rhoads and Sukhodolov, 2004).

Much of this understanding of shear at confluences and the generation of Kelvin-Helmholtz instabilities has come from work on parallel junctions (*e.g.* Best and Roy, 1991). However, it has been realised that natural confluences are far more complex than parallel flows with different velocities (Vermaas *et al.*, 2011). The most recent research is beginning to account for this, with Rhoads and Sukhodolov (2008) finding that the CHZ contained not just shear-generated coherent flow structures, but also wake flow and jet flow (as shown in Figure 2.3). From aDv measurements at the Kaskaskia River-Copper Slough confluence, they found that the stagnation zone acted like an obstacle, encouraging the development of wake flow around it. Further downstream this was replaced with flow resembling a shallow mixing layer before a weak jet flow formed around the scour hole due to flow constriction and deepening (Rhoads and Sukhodolov, 2008).

Constantinescu *et al.* (2011) used numerical modelling to devise a conceptual model of the mixing layer. Figure 2.4 shows the calculated vertical vorticities at two different depths of the flow. Areas of high positive vorticity include a small separation zone off the true left downstream corner and the true left bank of the Kaskaskia River, whilst high negative vorticity is seen around a separation zone on the true right bank and on the true right bank of Copper Slough.

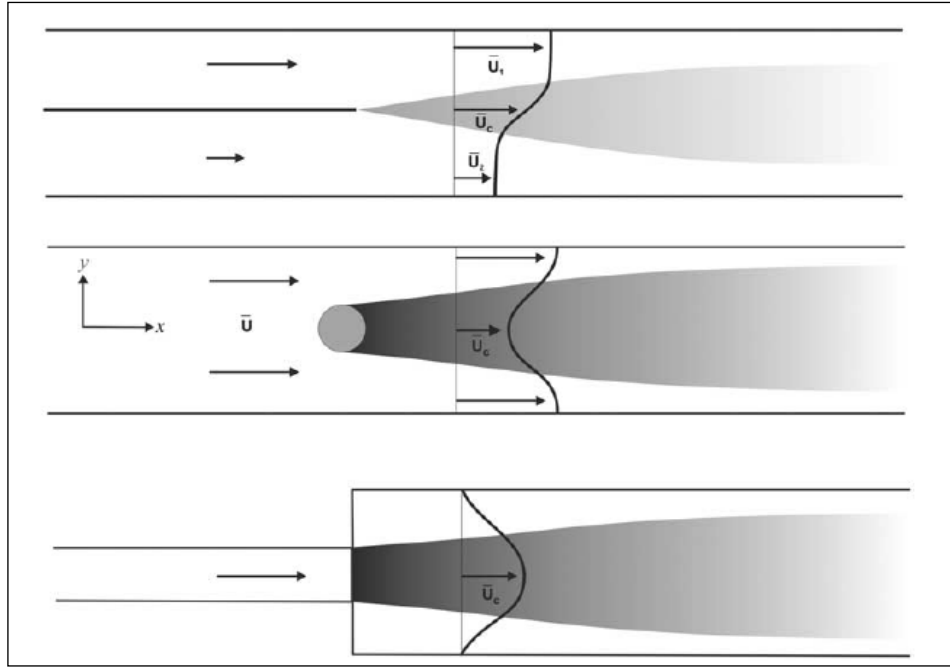


Figure 2.3: Diagram from Rhoads and Sukhodolov (2008) showing the differences between shallow mixing layers (or shear layers, *top*), wake flow (*middle*) and jet flow (*bottom*). Coherent flow structures are likely to be generated where there are sharp lateral differences in depth-averaged velocity, as shown by the solid black line.

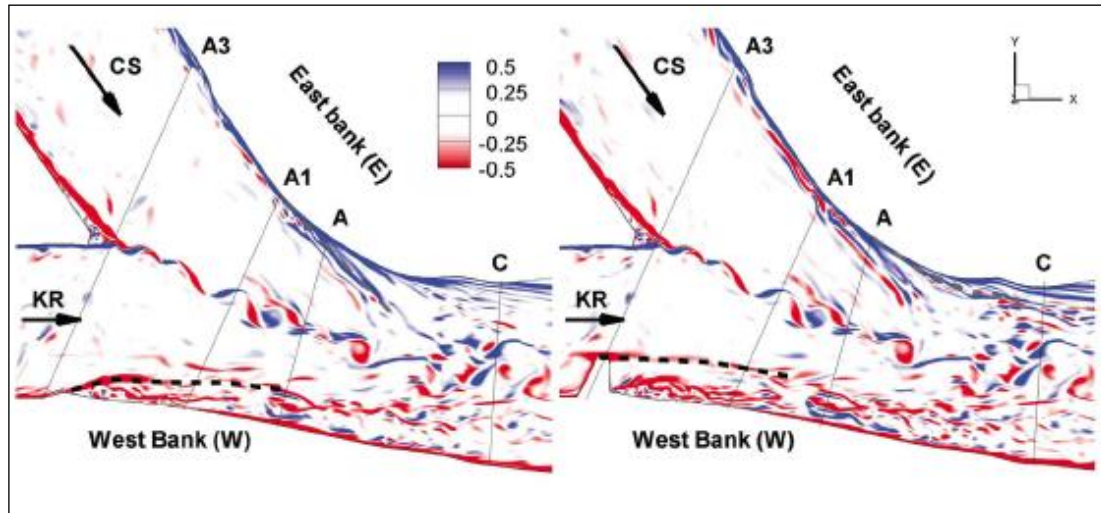


Figure 2.4: Diagrams from Constantinescu *et al.* (2011) showing vertical vorticity at  $0.1d$  (*left*) and  $0.5d$  below the water surface, determined from numerical modelling using a Detached Eddy Simulation treatment of turbulence. Counter-rotating vortices can be seen to be shedding off the stagnation zone and pairing up in the centre of the CHZ. The dashed lines highlight areas of shear layer formation due to channel curvature on the true left bank (grey) and a topographic obstacle on the true right bank (black).

The mixing zone theory of Constantinescu *et al.* (2011) is derived from these results and suggests that with a velocity ratio much greater than 1, the shear between the flows encourages Kelvin-Helmholtz instabilities and thus eddy generation. However,

given a sufficiently high junction angle and a velocity ratio of approximately 1, Kelvin-Helmholtz instabilities will develop either side of the stagnation zone, generating eddies there instead. As these eddies come from either side of the stagnation zone, they rotate in opposite directions and then join together in the CHZ (Constantinescu *et al.*, 2011). These findings are consistent with the observations of wake-generated coherent flow structures around the stagnation zone (Rhoads and Sukhodolov, 2008). However, this theory has largely been formulated from research on one particular confluence. Further research would be required to determine how dependent this is on the topography, planform and momentum ratio of the individual confluence.

### 2.3.3 Mixing in the CHZ

In terms of driving the mixing process in confluences, four main methods can be identified: the quasi-2D vortices discussed in the previous section, helical secondary circulation cells, the effects of bed discordance (where one tributary joins the main channel at a higher elevation than the other) and mass transfer from faster, decelerating flow to slower, accelerating flow (Best and Roy, 1991; Lane *et al.*, 2008; Parsons *et al.*, 2008; Rhoads and Sukhodolov, 2008; Sukhodolov *et al.*, 2010; Vermaas *et al.*, 2011). The fourth of these processes occurs in order to satisfy conservation of mass requirements (Uijttewaal and Booij, 2000).

The position of the mixing interface within the CHZ can sometimes be visible due to the turbidity of the water (Figure 2.5) or can be found indirectly by using a proxy method such as electronic conductivity (*e.g.* Biron *et al.*, 2004a), differences in the chemical isotope composition (*e.g.* Bouchez *et al.*, 2010) or, as on the Kaskaskia River-Copper Slough confluence, by small differences in temperature between the two tributaries (*e.g.* Rhoads and Kenworthy, 1995). From this, changes to mixing layer position can be seen over time.



Figure 2.5: Photograph of the Kaskaskia River-Copper Slough confluence showing clearly the position of the mixing layer as a result of differences in turbidity between the tributaries (Rhoads and Sukhodolov, 2008).

Fitting with the classic model of river confluences, Rhoads and Kenworthy (1998) found that the mixing interface at the Kaskaskia River-Copper Slough is vertical for many different discharges and extends from the junction apex to a position near the scour hole. However, there are many instances where this is not the case.

Where there is bed discordance at confluences, the mixing interface (or area of highest turbulent kinetic energy) is not vertical, but is angled so that it is located closer to the tributary at the bed and nearer the main channel at the surface (De Serres *et al.*, 1999; Biron *et al.*, 1996b, 2004a). Additionally, as the mixing interface migrates in response to changes in momentum ratio, the tributary mouth bar can advance or retreat, as Boyer *et al.* (2006) found for the Bayonne-Berthier confluence. This would potentially have an additional effect on the flow field through topographic steering.

There are, however, factors other than bed discordance which will affect the mixing interface position and size. From quasi-3D flow measurements, De Serres *et al.* (1999) found the zone of high turbulent kinetic energy in the centre of the Bayonne-Berthier CHZ widened and moved towards the surface with distance downstream. This widening is expected in the CHZ as vortices of different sizes join together to form bigger vortices (Rhoads and Sukhodolov, 2004). These structures should grow at a constant rate in deep water (Uijttewaalt and Booij, 2000), but in shallow water, the



growth rate decreases with distance downstream (Uijttewaal and Booij, 2000; Rhoads and Sukhodolov, 2004, 2008).

The slower growth of the vortices in a shallow mixing layer is due to the presence of the bed and the effect of friction. Bed friction causes extra turbulent dissipation, which results in slower growth of the Kelvin-Helmholtz instabilities (Uijttewaal and Booij, 2000). Rhoads and Sukhodolov (2004) found that the Kolmogorov relationship for turbulent dissipation (the  $-5/3$  gradient of the energy cascade) did not apply when the flow was depth-limited, in particular for the largest coherent flow structures. Therefore, shallower water will result in less effective mixing at river confluences.

One of the most famous examples of a flow mixing zone is that of the Solimoes-Negro confluence in Figure 2.6. At this confluence the visible boundary between the waters has led to the common belief that there is no significant mixing of the two tributary flows for a considerable distance downstream. In fact, the higher density water from the deeper Solimoes River has been found to pass under the water from the Negro River, causing friction between the two flows and encouraging some, admittedly very slow, mixing (Laraque *et al.*, 2009). Similar research by Bouchez *et al.* (2010) used isotope analysis to demonstrate that the waters of the Purus and Solimoes Rivers are still not fully mixed many hundreds of kilometres downstream of their confluence.



Figure 2.6: False-colour satellite image showing the confluence of the Negro and Solimoes Rivers near Manaus in the Amazon basin. The mixing interface between the dark waters of the Negro River and the much lighter waters of the Solimoes River can be seen to extend many kilometres downstream. *Source: Google Earth (Imagery: Landsat, Map data: Google).*



Of all the studies into mixing at large confluences, however, it is the research at the Rio Parana-Rio Paraguay confluence by Lane *et al.* (2008) that provides the most interesting results, with mixing shown to take place over 400km (*i.e.* approximately 150x channel width), or over 8km (approximately 3x channel width). In the case of the rapid mixing, the Rio Paraguay has a higher relative discharge, higher suspended sediment content and appears to pass under the waters of the Rio Parana, causing a horizontal shear layer that gives highly effective mixing (Lane *et al.*, 2008). By comparison, in the slow mixing case the horizontal shear layer does not develop, meaning mixing occurs only at a small turbulent mixing layer near the junction that weakens quickly (Lane *et al.*, 2008). Although more research at a range of discharges would be needed to confirm this, Lane *et al.* (2008) hypothesise that faster mixing occurs when an increase in momentum of the Rio Paraguay overrides the normal topographic steering of the flow, allowing sufficient ejection of fluid into the Rio Parana to force overturning.

#### 2.3.4 *Speed of Mixing in the CHZ*

At a river confluence, the pattern of downstream velocity changes from two areas of higher velocities either side of a lower velocity area to a single zone of higher velocity further downstream (Rhoads and Kenworthy, 1998; Rhoads and Sukhodolov, 2001). The distance downstream required for this transformation can vary, with a discharge ratio close to unity encouraging two separate high-velocity cores to persist for longer, whilst a dominant tributary will see its core last longer than a weaker tributary (Rhoads and Kenworthy, 1998). Although the complete mixing of two flows requires more than the development of this single core of high velocity, in situations where the individual cores persist downstream for a considerable distance, the complete mixing of the two tributary flows would be expected to take some time.

In most cases, the absence of strong turbulent flow structures or secondary circulation cells will lead to slower mixing of the waters from the two tributaries, as the molecular diffusion of particles is considered a far less effective process than turbulent mixing (Bouchez *et al.*, 2010). However, it is not entirely clear which of the other processes identified in the previous section will result in the fastest mixing. Uijttewaai and Booij (2000) found that the large turbulent structures contributed most to momentum transfer, although their work was on a 0° confluence, where the secondary

helical cells are less likely to develop. Alternatively, Rhoads and Sukhodolov (2001, 2008) provide evidence that helical cells contribute most to mixing, with the bed friction effect restricting the impact of quasi-2D coherent flow structures. Without the secondary circulation cells, the mixing interface could continue downstream for a considerable distance (Rhoads and Sukhodolov, 2001).

Lane *et al.* (2008) suggested that both shear layers and secondary circulation cells had the potential to result in effective mixing. However, mixing within the shear layer would tend to be limited to the immediate vicinity of the shear, whereas secondary circulation cells had the potential to encourage mixing of the flows over a much greater proportion of the channel width. More recently, the results of the flume experiments of Vermaas *et al.* (2011) suggested that (in the case of flow over adjacent rough and smooth beds) water depth played a key role, with increasing contributions to lateral momentum transfer from secondary circulation cells (at the expense of the turbulent mixing layer) as depth increases.

Other possible factors which can affect confluence mixing lengths include channel width, junction angle, width-to-depth ratio and the presence of meander bends or mid-channel bars in the downstream channel (Gaudet and Roy, 1995; Bouchez *et al.*, 2010; Biron *et al.*, 2004a). The width-to-depth ratio is thought to be a key control on the speed of mixing through its effect on the development of large-scale secondary circulation cells across the full channel width. Parsons *et al.* (2007, 2008), for example, showed that in the very wide, shallow river confluence-diffuence units of the Rio Parana, there is very little evidence of secondary flow cells. A higher width-to-depth ratio would therefore be expected to discourage fast mixing of the flows. By contrast, bed discordance has been found to encourage much more rapid mixing, potentially by up to two orders of magnitude, due to the tendency for the mixing interface to be distorted (Gaudet and Roy, 1995; Biron *et al.*, 2004a; Lane *et al.*, 2008). The effect of bed discordance on the confluence flow field and mixing process is discussed in greater detail in Section 2.4.2.

In all of these cases, the distance required to get a fully-mixed flow will depend entirely on the flow field in the confluence and the extent to which it encourages the lateral mixing of water masses. Shallow flows will restrict the depth and therefore the growth of the quasi-2D vortices in the shear layer, whilst wider rivers increase the amount of lateral movement necessary to achieve a fully mixed flow. On the other hand, complete mixing becomes more likely whenever the topography or planform

encourages large-scale secondary circulation to develop, such as in the case of mid-channel bars, meander bends and bed discordance. The effect of a higher junction angle, as noted by Biron *et al.* (2004a), will be to increase the curvature of both flows, thus encouraging stronger secondary circulation cells to develop. Secondary circulation cells are therefore of high importance to the dynamics of river confluences and are discussed in the following section.

### 2.3.5 Helical Cells

Helical cells were identified in laboratory confluences by Mosley (1976), but there is still some debate and controversy about the nature and proliferation of these cells in natural river confluences (Rhoads and Sukhodolov, 2001). The concept of the helical secondary flow in confluences is relatively straightforward, with one common description being that it resembles back-to-back meander bends (*e.g.* Ashmore and Parker, 1983). As the two tributaries join, there is mutual deflection of the flows, which causes the same imbalances between the pressure gradient and centrifugal forces found in meander bends, thus encouraging helical cells to form (Ashmore *et al.*, 1992; Rhoads and Kenworthy, 1998; Parsons *et al.*, 2007). As the tributary flows are deflected in opposite directions, the helical flow cells are counter-rotating and back-to-back, as shown previously in Figure 2.1.

The concept of the development of helical flow in a confluence may be relatively straightforward, but in reality helical flow cells are difficult to define. This is largely due to the problems associated with defining the primary flow direction, a problem exacerbated in confluences as two primary flow directions merge (Lane *et al.*, 2000). As Rhoads and Kenworthy (1998) point out, in some confluences two high-velocity cores can persist downstream for a considerable distance. In this situation, using a single primary flow direction would be an oversimplification. Figure 2.7 shows three different methods of defining the primary flow direction. The choice of method will naturally have some impact on the detection of any helical flows within the confluence and can be controversial. This is demonstrated by the debate between Lane *et al.* (2000) and Rhoads and Kenworthy (1999) regarding whether the Rozovskii method will always imply the presence of secondary flow, and specifically the upwelling and downwelling process, as a methodological artefact. Even with an acceptable definition of the primary flow direction, determining conclusively the

presence of helical cells requires a large amount of evidence, with three-dimensional flow measurements necessary for a number of vertical profiles on at least two cross-sections (Lane *et al.*, 2000).

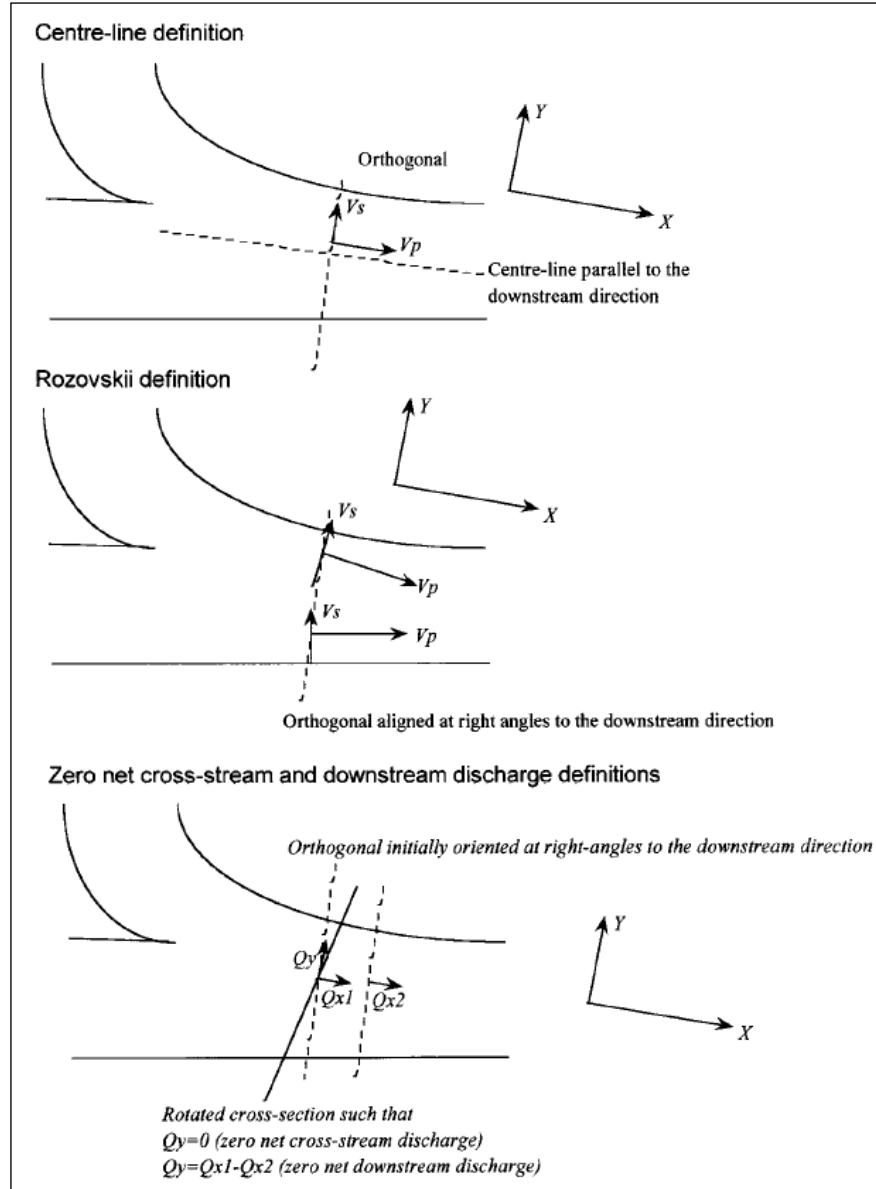


Figure 2.7: Diagram showing three different definitions of primary and secondary flow direction (Lane *et al.*, 2000). The centre line definition (*top*) sets the primary direction as the tangent of the channel centre line. The Rozovskii method (*middle*) sets the primary flow direction for individual vertical profiles such that secondary discharge for the profile equals zero. The zero net cross-stream and downstream discharge definitions (*bottom*) set the primary flow direction for the cross-section so that either the overall secondary discharge for that cross-section is zero (cross-stream definition) or the net secondary discharge between two adjacent cross-sections is zero (downstream definition).

The first to quantify helical flow cells in the field were Ashmore *et al.* (1992). Even though they specifically chose two Y-shaped confluences (planforms which would

be expected to encourage the development of helical cells) one of the confluences had much weaker helical flow and had more persistent tributary high velocity cores (Ashmore *et al.*, 1992). This was attributed to a more complex upstream topography and less well-defined tributary banks, compared to the other confluence (Ashmore *et al.*, 1992). A later study by Rhoads and Sukhodolov (2001) on three concordant river confluences demonstrated that the helical cells are not common features in such confluences, with the Kaskaskia River-Copper Slough the only confluence with a clear helical cell pattern.

Early research by Best (1986) and Best and Roy (1991) suggested that flow separation over the avalanche faces or in the presence of discordant beds could initiate or cause the helical secondary flow cells. However, more recent evidence has encouraged the view that bed discordance is likely to disrupt the helical cells, although the processes causing this are still not fully understood (Biron *et al.*, 1993, 1996a; Bradbrook *et al.*, 2001; Biron and Lane, 2008; Constantinescu *et al.*, 2011). Given that bed discordance is not unusual in natural confluences, it is fair to suggest that strong back-to-back helical cells are relatively uncommon features in natural river confluences. This hypothesis, however, has implications regarding the formation of scour holes, as, according to the classical model, the morphology of scour holes is dependent on the strength of the helical flow cells. Scour holes are considered to be a major morphological feature of river confluences and therefore, if helical cells are not as common as the classic model suggests, important questions are raised about how scour holes are formed and maintained.

Where back-to-back helical cells do exist, they are by no means equal in strength or found as complete circulation cells. The numerical modelling of Bradbrook *et al.* (2000a), found evidence of the existence of back-to-back helical cells in more symmetrical flume confluences, but only weak and incomplete secondary cells in simulations of the Kaskaskia River-Copper Slough junction. Ashmore *et al.* (1992), meanwhile, found that the helical cell strength declines with increasing distance downstream and away from the thalweg, whilst the cell forming on the side of the larger tributary will tend to override the other cell. Similarly, Rhoads and Kenworthy (1995) found that a single, stronger cell existed on the Kaskaskia River-Copper Slough confluence when the momentum ratio was high (*i.e.* a stronger tributary). When a single cell dominates in this way, there can be upwelling of main channel water at the downstream corner, a process normally associated with discordant confluences (Rhoads

and Kenworthy, 1995). By contrast, a dominant Kaskaskia River has been found to give a dual helical circulation cell which transforms into a single cell further downstream (Rhoads *et al.*, 2009).

Therefore, current research suggests that where helical cells do exist, they are not necessarily in the back-to-back counter-rotating form proposed by Mosley (1976). However, this variability has improved the understanding of the conditions favourable to their development. Helical cells appear to be caused primarily by flow curvature, the loss of kinetic energy involved as the two flows meet and the resultant superelevation in the CHZ (Rhoads and Kenworthy, 1995; Constantinescu *et al.*, 2011). Confluence planform has therefore been highlighted as a key factor in determining whether back-to-back helical cells or a shear layer will form (Biron *et al.*, 2002). Constantinescu *et al.* (2011) note that both momentum ratio and junction angle are key factors in the formation, duration and strength of helical cells. Both of these are linked to flow curvature, with higher angles encouraging greater mutual flow deflection (and thus the development of stronger cells) and momentum ratio capable of significantly modifying the flow deflection of the individual tributaries. Bed discordance has also been highlighted as a key factor in the strength of helical flow cells (Bradbrook *et al.*, 2001). The effects of junction angle, momentum ratio and bed discordance on the flow structures at river confluences are discussed in more detail in Section 2.4.

The most recent confluence research has highlighted the importance of width-to-depth ratio to helical cell development. At large confluences, where the width-to-depth ratio can be very high, any helical cells present are less likely to cover the full width (Parsons *et al.*, 2007, 2008). Szupiany *et al.* (2009) suggest that the secondary flow covers less than 20% of the channel width, with the lack of widespread secondary circulation thought to be due to both the large width-to-depth ratio (Lane *et al.*, 2008) and topographic steering by sand dunes at the bed (Parsons *et al.*, 2008). Biron and Lane (2008), meanwhile, suggest that twin helical cells seem to be found where width-to-depth ratios are lower than those normally found in natural confluences. The laboratory experiments of Vermaas *et al.* (2011) also support this view, with increases in depth encouraging the development of secondary flow. However, further research is required to determine the relative importance of width-to-depth ratio with respect to other factors such as planform curvature and momentum ratio.

### 2.3.6 Stagnation Zone

In contrast to the CHZ, the stagnation (or ‘dead’) zone has seen less research. It is known to be an area of low or recirculating flow at the upstream corner of the junction (Rhoads and Kenworthy, 1998; Rhoads and Sukhodolov, 2004), which, as has been noted in Section 2.3.2 above, can act as an obstacle encouraging the development of wake-generated shear flows around it (Rhoads and Sukhodolov, 2004, 2008; Constantinescu *et al.*, 2011). However it is still not clear how widespread these zones are in natural confluences, what causes them to form and whether these causes vary depending on the type of confluence.

Rhoads and Kenworthy (1998) suggested that the stagnation zone is caused by the confluence of low velocity flows from near the tributary banks. An alternative explanation is that superelevation in the CHZ or even in the stagnation zone itself results in a negative pressure gradient towards the upstream corner, which encourages the lower or negative velocities in this zone (Rhoads and Sukhodolov, 2001; Biron *et al.*, 2002). However, the understanding of this confluence zone will remain incomplete until enough confluence stagnation zones have been investigated for their prevalence and dynamics.

### 2.3.7 Flow Separation Zone

The flow separation zone is an area of lower pressure and flow recirculation at the downstream corner that is known to increase in size with larger junction angles and higher tributary discharges (Best and Reid, 1984). From their three-dimensional numerical experiments, Huang *et al.* (2002) found that flow separation was minimal for a 30° confluence but increased substantially as the confluence angle approached 90°. The results from these simulations are shown in Figure 2.8. Huang *et al.* (2002) argue that as junction angle increases, more lateral momentum has to be converted into downstream momentum. This causes a greater loss of energy, which increases the size of the zone and deepens the water surface depression. The loss of energy hypothesis may also explain the increase in tributary water depths seen in Figure 2.8.

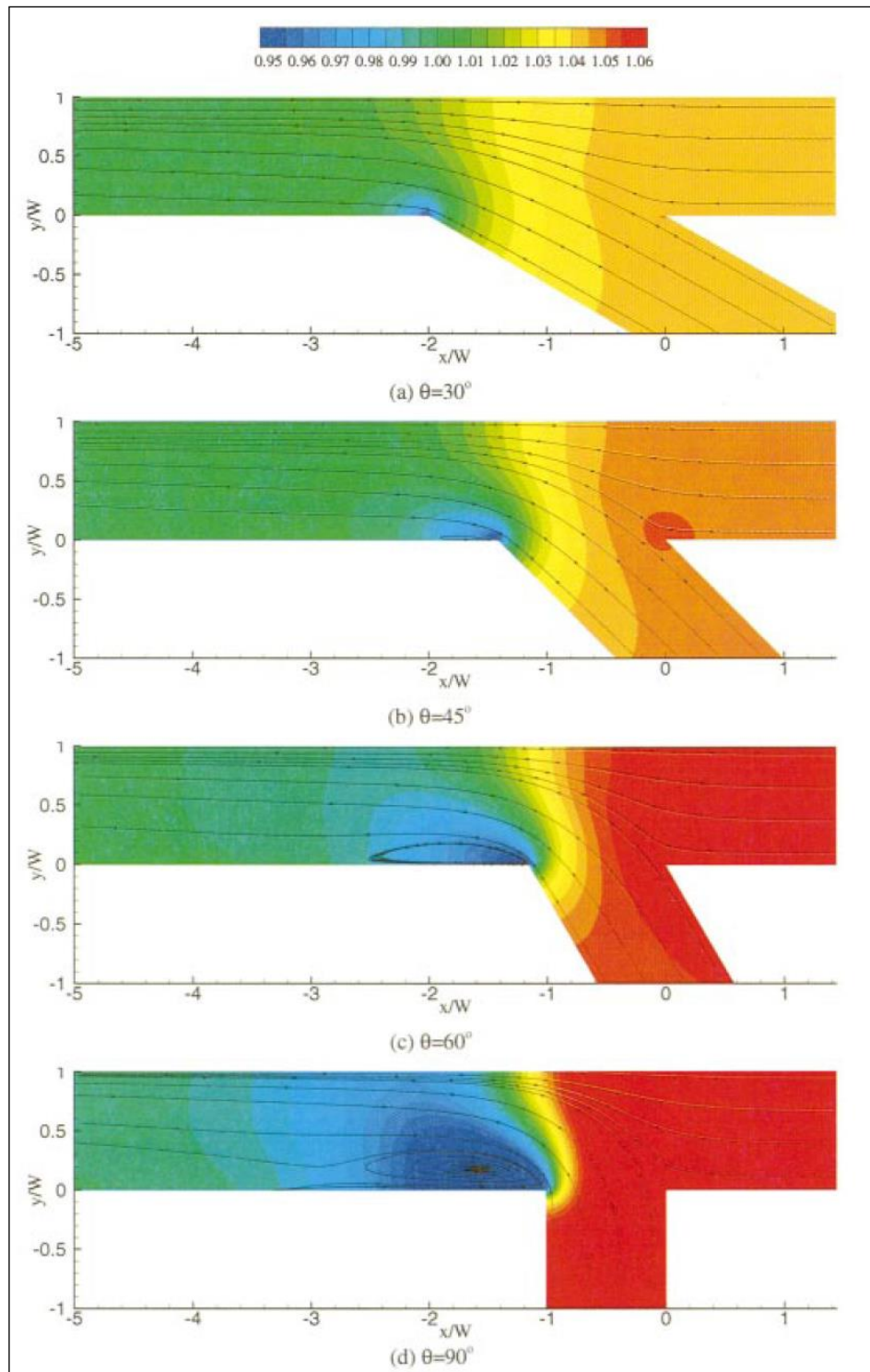


Figure 2.8: Diagram showing water depth and flow streamlines from numerical simulations of confluences with increasing confluence angles (Huang *et al.*, 2002). There is a clear expansion in the width and depth of the flow separation zone with higher junction angle. Additionally, the higher angle seems to encourage the backing up of water in the tributaries.

Ashmore *et al.* (1992) argue that in reality, natural confluences have limited or no flow separation due to their banks changing direction more gradually than in simplified flume experiments. Although more recent field research has found evidence



of flow separation zones (*e.g.* Unde and Dhakal, 2009), as yet it is not clear if the causes proposed by Huang *et al.* (2002) apply to natural confluences.

In the case of discordant confluences, it has been found that flow separation on the downstream corner is very limited (Biron *et al.*, 1993; De Serres *et al.*, 1999; Bradbrook *et al.*, 2001), with the flume experiments of Biron *et al.* (1996a) demonstrating that a concordant confluence has a small flow separation zone that is not present in a similar, discordant case. Biron *et al.* (2002) found superelevation at the downstream corner of the discordant Bayonne-Berthier confluence and suggested that the upwelling of flow from the main channel disrupts the formation of a flow separation zone. Other possible causes, however, include the erosion of the downstream corner (giving the aforementioned gradually curving banks) or the presence of a bar on the downstream corner disrupting the flow separation (Biron *et al.*, 1993; De Serres *et al.*, 1999).

It is clear, therefore, that whilst flow separation zones may exist at river confluences, they are by no means ubiquitous. The presence of flow separation is very dependent on channel planform and topography, implying that each confluence will be unique in terms of the amount of flow separation present.

#### 2.3.8 Flow Acceleration Zone

From the classic river confluence conceptual model, the flow acceleration zone is believed to exist due to the constriction of two tributary flows into a smaller total cross-sectional area. Indeed, the early research by Best and Reid (1984) found that flow separation zones encourage this acceleration by further constricting the flow, with near-bed velocities at a 90° confluence up to 1.3 times larger than those at a 15° confluence. Flow acceleration will increase the bed shear stresses and has therefore been highlighted as a potential contributing factor to the development or maintenance of scour holes (Rhoads *et al.*, 2009).

The principle of continuity requires that a decrease in channel cross-sectional area results in flow acceleration in the downstream channel. However, the complexity of natural river confluence morphologies has meant that the flow acceleration zone is not always clearly present or consistent in its form (Ashmore *et al.*, 1992; Wallis *et al.*, 2008; Szupiany *et al.*, 2009). Therefore, there is a need for further research which aims to explain this variability in the nature of the flow acceleration zone.

## 2.4 Key Factors Affecting Flow Dynamics at River Confluences

From the earliest research into the fluid dynamics of river confluences (*e.g.* Mosley, 1976), certain aspects of river confluence morphology or geometry have been identified as key controlling factors for the confluence flow field. These factors are shown in Figure 2.9, which has been developed from the following review.

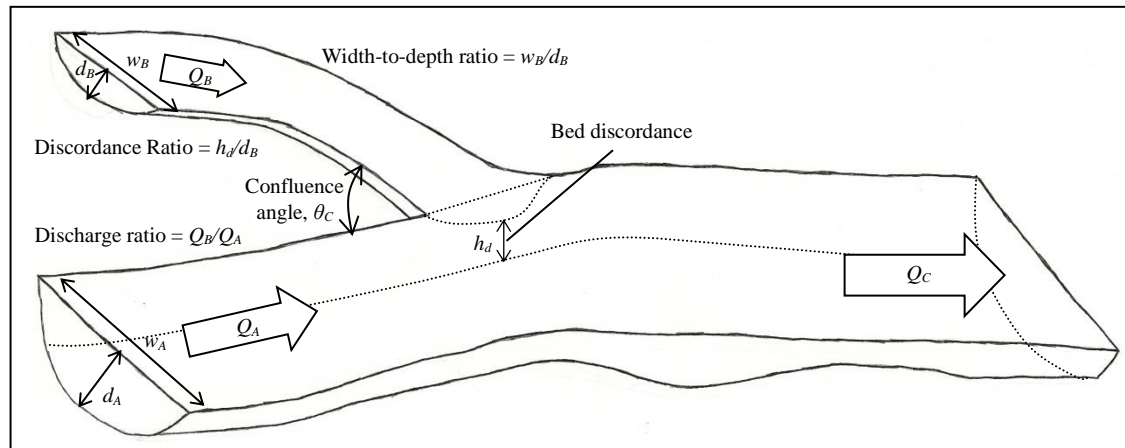


Figure 2.9: The key flow parameters and boundary conditions in a river confluence. A symmetrical confluence will have the centre of the downstream channel on a line bisecting the confluence angle, although a completely symmetrical flow field will also require the discharge ratio to equal one.

Of the key factors identified in Figure 2.9, this section will focus primarily on the effects of junction angle, symmetry, discharge ratio and bed discordance on flow structures in river confluences. Although the effects of these factors have been researched over many years, as Parsons *et al.* (2003) note, at present there is still a debate about whether bed discordance or channel planform controls coherent flow structure generation in confluences. The final part of this section will summarise other factors which have been identified as affecting confluences under specific conditions.

### 2.4.1 Junction Angle

Much of the early research into the effects of junction angle on river confluences focused on the impact of the changes on the confluence scour hole. However, junction angle can also be an important control on the strength of secondary flow. Mosley (1976) suggested that a greater junction angle would result in more turbulence generation as the flow in each of the tributaries was deflected more. This is the effect described by Ashmore and Parker (1983) as a decrease in curvature radius, where a higher junction

angle results in the flows from the two tributaries effectively being forced to flow around a tighter bend. A tighter bend implies that the force imbalances identified in Section 2.3.5 will be greater, thus increasing the strength of the helical cells. Results from the numerical modelling of Bradbrook *et al.* (2001) support this hypothesis, showing that secondary circulation was much stronger for a confluence with a junction angle of  $30^\circ$  compared to one with a  $0^\circ$  angle.

#### 2.4.2 Discharge Ratio

Many confluence studies consider the effect of one tributary dominating another due to differences in inputs. Depending on the study, this will be accounted for by the velocity ratio ( $\bar{u}_B/\bar{u}_A$ ), the discharge ratio ( $Q_B/Q_A$ ) or momentum ratio. Rhoads and Kenworthy (1995) define the momentum ratio ( $M_r$ ) as:

$$M_r = \frac{(\rho_B Q_B \bar{u}_B)}{(\rho_A Q_A \bar{u}_A)} \quad (2.1)$$

where the subscripts *A* and *B* represent the two tributaries,  $Q$  is discharge ( $\text{m}^3/\text{s}$ ),  $\bar{u}$  is mean velocity ( $\text{m/s}$ ) and  $\rho$  is the water density ( $\text{kg/m}^3$ ).

From the research of Ashmore and Parker (1983) and Bradbrook *et al.* (2001), it has been suggested that large disparities in the tributary velocities (*i.e.* where the velocity ratio is much greater or much less than one) will affect the confluence flow field more than the junction angle, especially where this angle exceeds  $30^\circ$ . However, when the junction angle is smaller, this does not seem to be the case. The work of Bradbrook *et al.* (1998) found very little cross-stream flow at parallel confluences, even when there were large differences in flow velocity between the tributaries. Therefore, the extent to which the velocity ratio affects the flow field appears to vary depending on the confluence planform.

Another effect of the discharge ratio is to encourage the migration of flow structures in river confluences. An example of this is given in Figure 2.10, where Rhoads and Kenworthy (1995) demonstrate how the position of the mixing layer at the Kaskaskia River-Copper Slough confluence changes with different momentum ratios. From Figure 2.10, it can be seen that a high momentum ratio (*i.e.* Copper Slough dominating) pushes the mixing interface towards the true right bank, especially at low

flow. With a low momentum ratio, meanwhile, the Kaskaskia River dominates and the mixing interface moves closer to the centre.

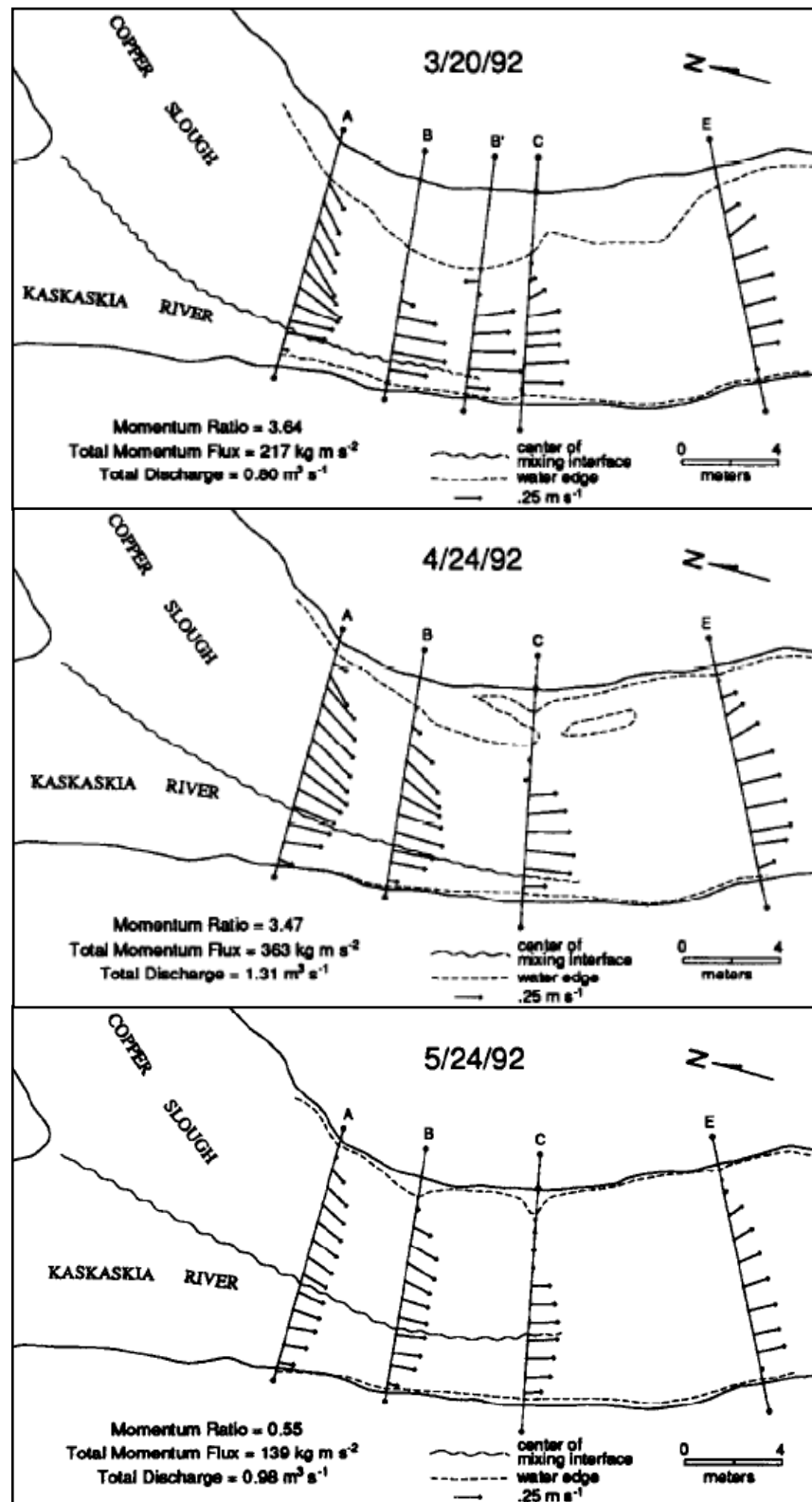


Figure 2.10: The position of the Kaskaskia River-Copper Slough mixing layer for three different flow conditions (Rhoads and Kenworthy, 1995). The mixing layer position is determined from temperature data (taking advantage of differences in temperature between the tributaries).

In addition to the effects on the position of the mixing interface, as noted in Section 2.3.5, momentum ratio is a key factor in the formation, duration and strength of helical cells (Constantinescu *et al.*, 2011). Examples of this effect include the research of Rhoads and Kenworthy (1995) on the Kaskaskia River-Copper Slough confluence. They found that a dominant Copper Slough encouraged a single, strong helical cell to develop on the tributary side (much like in a meander bend), whilst a dominant Kaskaskia River gave only a weak convergence at the surface of the mixing interface (Rhoads and Kenworthy, 1995).

Therefore, the discharge ratio can be considered to play an important role in determining the strength and location of any secondary circulation cells, as well as the position of the mixing layer and its associated zone of higher turbulence and shear stress. This makes it an important factor not just for the flow dynamics of river confluences, but also the consequent effects on the sediment transport and morphology.

#### 2.4.3 Symmetry

A confluence is described as symmetric if it has a planform that resembles a ‘Y’ shape (Best, 1986). Asymmetry in confluences adds an extra level of complexity to the confluence flow structure and it is by far the dominant form in natural rivers (Ashmore *et al.*, 1992).

The major difference between symmetric and asymmetric confluences (assuming other variables such as the tributary discharges and junction angle are the same) is the angle between the primary flow directions in the tributaries and that in the downstream channel. In a symmetric confluence, both tributary flows will turn through equal and opposite angles to align with the downstream flow direction. In an asymmetric confluence, however, one of the tributary flows will be forced to turn through a much greater angle than the other. As noted in Section 2.4.3, this will encourage a stronger helical circulation cell to develop in that tributary (Ashmore and Parker, 1983). Therefore, assuming the discharge ratio is around 1, an asymmetric confluence would be expected to have one tributary with a much stronger helical cell than the other.

This process led Rhoads and Kenworthy (1995) to argue that the classic back-to-back helical cells tend not to be found in asymmetrical confluences. The results from the numerical modelling of both laboratory and natural confluences by Bradbrook *et al.*

(2000a, 2000b) supported this view, with the back-to-back helical cell structure thought to become less representative of the flow field as asymmetry increases.

It should be noted, however, that the effects of confluence asymmetry on the flow field cannot be treated in isolation. As shown in Figure 2.10, for example, if the discharge of the main tributary channel (*i.e.* that aligned closest to the direction of the downstream channel) is much higher than that of the other tributary, the flow field may become similar to that of a symmetrical confluence (Rhoads and Kenworthy, 1995). The flow field of any asymmetric confluence, therefore, is also very much dependent on variables such as the discharge ratio and junction angle.

#### 2.4.4 Bed Discordance

Bed discordance, as labelled on Figure 2.9, occurs when the two tributaries have different bed elevations. Best and Roy (1991) suggest that bed discordance is commonly caused by the formation of tributary mouth bars, which have steep avalanche faces descending into the confluence scour hole. However, one of the key features of the discordant Bayonne-Berthier confluence is that it has no obvious scour hole (Biron *et al.*, 1993) and subsequent flume experiments on a 30° confluence found no evidence of scour hole development or the helical cells thought to maintain it (Biron *et al.*, 1996a). There is therefore no clear causal relationship between bed discordance and confluence scour holes or any associated geomorphological features.

The first investigations of bed discordance were conducted on a parallel, discordant flume confluence by Best and Roy (1991), with results showing that the flow separates over the step, disrupting the mixing layer and giving far more rapid mixing in the shallow tributary. The flow separation is caused by low dynamic pressure in the lee of the step (Bradbrook *et al.*, 1998) and results in clear changes to the flow field, as shown by the streamlines in Figure 2.11.

Discordant confluences are considerably different from concordant confluences, as shear layer distortion is considered more important than the presence of scour holes and helical cells (Szupiany *et al.*, 2009). The flow separation that occurs at discordant confluences distorts the vortices in the mixing layer (Best and Roy, 1991; Biron *et al.*, 1996a, 1996b; Rhoads and Sukhodolov, 2001), which encourages faster mixing of the two flows, especially at low flows (Gaudet and Roy, 1995; De Serres *et al.*, 1999; Rhoads and Sukhodolov, 2001; Biron *et al.*, 2004a). This increase in mixing speed at

low flows may well be a function of the increased relative size of the step (compared to the water depth). Gaudet and Roy (1995) argue that when river levels are shallow, water from the tributary with the higher bed elevation can flow over the water from the deeper tributary, giving more rapid mixing of the two flows.

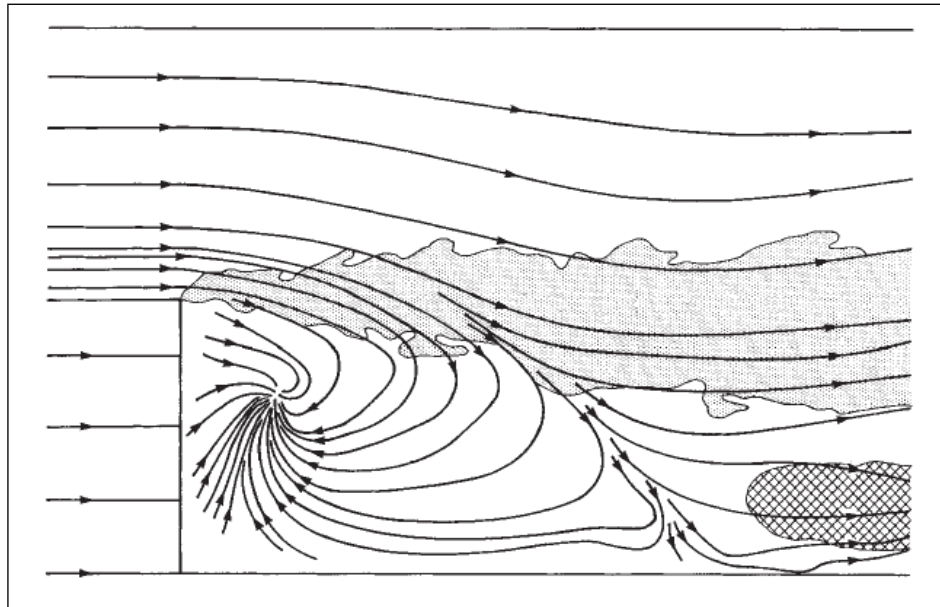


Figure 2.11: Plan view of the flow field at the bed of a discordant river confluence (Best and Roy, 1991). The shaded area shows the shear layer, whilst the cross-hatched area is a zone of upwelling.

The flow field at a discordant confluence has key features not present at concordant confluences. Providing the bed discordance is sufficiently large relative to the water depth, flow separation over the step means that near-bed flow from the main channel will not be deflected, as would happen in a concordant confluence (Biron *et al.*, 1993, 1996a). Instead, this near-bed flow passes under the tributary flow, resurfacing at the downstream corner (Biron *et al.*, 1993, 1996a, 1996b; De Serres *et al.*, 1999). This leads to the zone of upwelling highlighted in Figure 2.11 and shown from side-on in Figure 2.12. A side-effect of this upwelling is the reduction in size or loss of the lateral flow separation zone, which in turn increases the cross-sectional area of the downstream channel and thus reduces flow acceleration (Biron *et al.*, 1996a).

The amount of bed discordance required to have a significant effect on the flow field was investigated in numerical modelling work by Bradbrook *et al.* (1998). Their CFD modelling suggested that a difference in bed height of 25% was required to get strong secondary circulation, although this could be reduced with much higher velocities in the shallower tributary (Bradbrook *et al.*, 1998). Once the bed discordance

is sufficient, however, the confluence flow field appears to be less sensitive to changes in both discharge ratio (Biron *et al.*, 1993) and junction angle (Bradbrook *et al.*, 2001).

Therefore, bed discordance is potentially a major factor in river confluences, with up to four of the six major confluence flow features given in Figure 2.1 affected (the flow separation zone, maximum velocity zone, shear/mixing layer and helical flow cells). Nevertheless, the complexity of the flow at natural confluences means there are many other minor factors that have also been found to affect the confluence flow field.

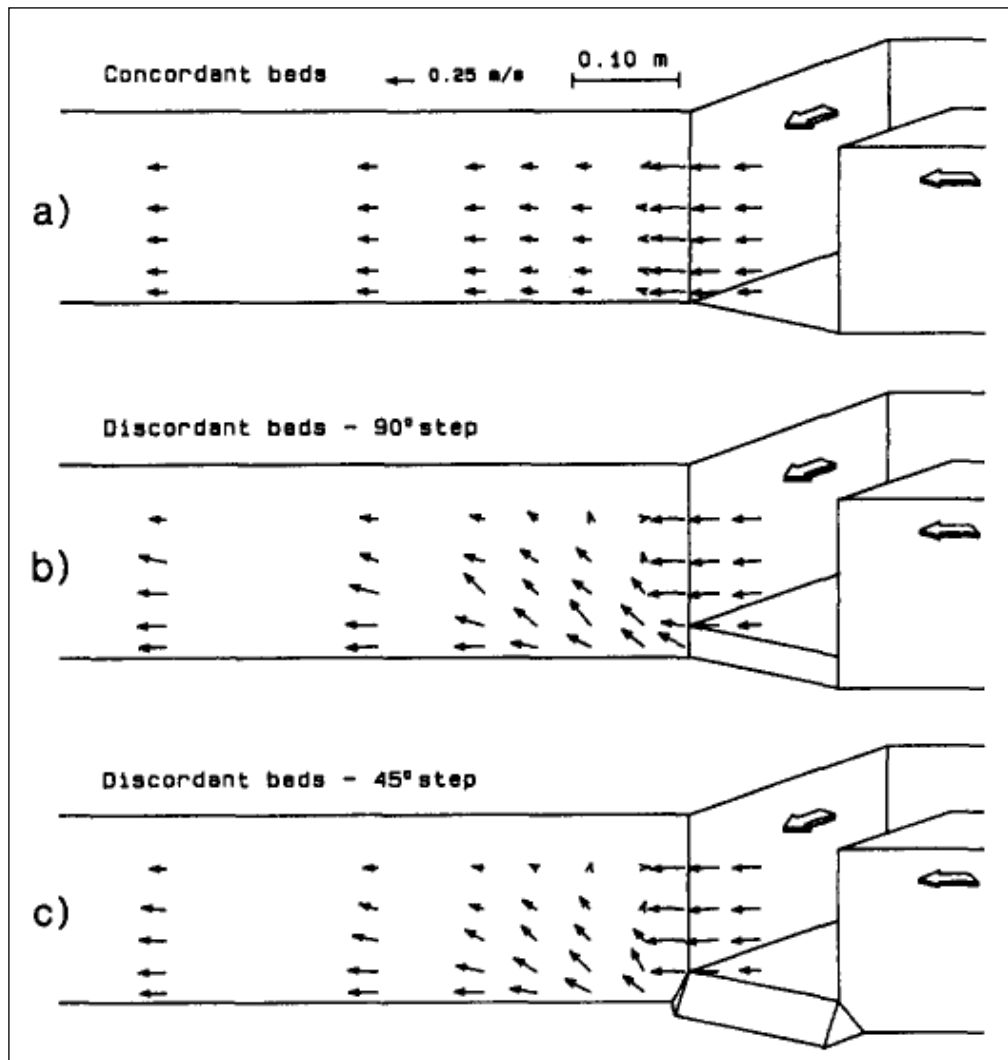


Figure 2.12: Comparison of streamlines for discordant and concordant laboratory river confluences (Biron *et al.*, 1996a). The upwelling of water from the lee of the step can be clearly seen.

#### 2.4.5 Additional Controls on Confluence Flow Fields

A number of other factors have been identified in the literature as potentially having an important controlling effect on the flow field at river confluences. The effects of topographic steering and the upstream planform of the tributaries have tended to



receive the most attention, but there are other variables which can have an effect on the flow field under certain conditions and should therefore not be discounted.

Changes in bed morphology have been shown to be important for the development of flow structures at river confluences (De Serres *et al.*, 1999). It is now generally recognised that in most cases bed topography is the major control on the flow field at low flows (Roy and Bergeron, 1990; Rhoads and Kenworthy, 1995). Topographic changes from the most recent high flow event will therefore be important for determining the nature of the flow field at subsequent low flows (Rhoads and Kenworthy, 1995).

An example of the effects of topographic steering is given by Rhoads and Kenworthy (1998), who find a lower than expected (based on momentum ratio) deflection of the Kaskaskia River on one day due to the migration of the scour hole towards the Copper Slough tributary. This reduced the capacity of the channel on the Kaskaskia River side, forcing this water further towards the centre of the channel and causing greater than expected deflection of the Copper Slough flow (Rhoads and Kenworthy, 1998).

The importance of the upstream channel direction on the flow at river confluences was recognised by Mosley (1976) in his laboratory experiments and more recent research has supported this (Rhoads and Kenworthy, 1995; Biron *et al.*, 2002; Biron and Lane, 2008). The curvature of the Copper Slough tributary has been demonstrated to give stronger helical cells on the tributary side of the confluence, even with a momentum ratio favouring the Kaskaskia River (Rhoads and Kenworthy, 1995). Furthermore, the numerical modelling of Biron *et al.* (2002) showed significant differences in results depending on whether the upstream curvature was included in the model. The change in direction of the upstream channel is therefore a key factor in determining confluence flow fields.

Another factor that has been emphasised as important, especially at large river confluences, is the effect of differences in tributary densities (Best and Rhoads, 2008; Biron and Lane, 2008). The numerical modelling of Biron and Lane (2008) demonstrated that these disparities will affect the nature of the mixing layer. Additional factors that have been highlighted for their potential effects on confluence flow fields include the presence of ice jams (Ettema *et al.*, 2008), large inputs of sediment (*e.g.* as a debris fan) which can cause flow constriction (Benda *et al.*, 2003) and obstructions due to large boulders or woody debris (Wallis *et al.*, 2008).

## **2.5 Summary of Research into Flow at River Confluences**

This review has shown that the extent of research into the flow field at river confluences is substantial. Nevertheless, there are still aspects of the confluence flow dynamics which have received limited attention. The flow stagnation, separation and acceleration zones, for example, have been the subject of far less research than the shear/mixing layer and the helical flow cells. This may be partly explained, however, by the greater complexity of the flow structures in the central part of the confluence.

However, it is argued that it is not a lack of research into the flow stagnation, separation and acceleration zones which is the major limiting factor on our understanding of the flow dynamics at river confluences. Instead, it is the limited amount of research into the dynamics of confluences with much steeper water surface slopes. Given the dendritic nature of the catchment system, upland confluences would be expected to outnumber lowland confluences. However, the Kaskaskia River-Copper Slough, Bayonne-Berthier, Rio Parana and Amazon basin field sites, on which much of the research into natural river confluences has been conducted, can all be considered to be lowland confluences. Therefore, it is unclear the extent to which the flow structures set out in the preceding two sections are generic to both lowland and upland river junctions. As such, it is steeper, upland river confluences which are the main focus of this thesis.

## **2.6 Morphology and Sediment Dynamics of River Confluences**

The previous two sections have demonstrated the vast amount of research that has been conducted into the mean flow field and turbulent flow structures at river confluences. For all the research into the flow at river confluences, however, there have been few studies which have explicitly addressed the issue of sediment transport (Biron and Lane, 2008). This contrasts markedly with river units such as meanders, pools, riffles and even the tributaries leading into confluences (Bridge and Gabel, 1992; Unde and Dhakal, 2009). Nevertheless, there has been some research which has addressed the sediment dynamics of river confluences at the river catchment scale, whilst a limited number of other studies have addressed the geomorphological features at river confluences and the sediment transport processes that affect their formation and evolution.

This section, therefore, reviews research conducted into sediment dynamics at the catchment scale before looking in more detail at the sediment dynamics in the four major morphological features identified in Section 2.2 (from Figure 2.1). Given the similarities between and limited nature of research into depositional bars in both the flow separation and flow stagnation zones, these features are both covered within a single sub-section. The section concludes with a review of the various hypotheses that have been made about the sediment transport processes at river confluences. These hypotheses have been suggested as part of studies into the confluence flow field but have yet to be investigated more fully, so provide a good indication of areas in which the understanding of river confluence sediment dynamics is more limited.

### *2.6.1 River Confluence Sediment Dynamics at the Catchment Scale*

A number of studies have looked at the sediment dynamics of river confluences on a catchment scale. Some of these have looked at the impact of sediment influxes from tributaries into the main channel and have found that it interrupts the general process of downstream fining in the main channel (Rice, 1998; Benda *et al.*, 2004; Ferguson and Hoey, 2008; Rice, 2008; Wallis *et al.*, 2008). In the case of Rice (1998) and Benda *et al.* (2004), their conclusions were drawn from large sample sizes of well over 100 different confluences. Benda *et al.* (2004) concluded that it is the larger tributaries (those for which the drainage area approaches that of the main channel) which will have a greater chance of causing a sediment discontinuity in the main channel. However, Unde and Dhakal (2009) suggest that for the very largest tributaries, the grain sizes are likely to be similar in both channels, thus reducing the effect of the tributary sediment input. Other factors that have been highlighted for their impacts on the main channel sediments include the presence of dams (by artificially restricting flow and sediment flux upstream) and the shape of the catchment (Benda *et al.*, 2004; Curtis *et al.*, 2010; Musselman, 2011).

The influx of sediment is also seen to affect the morphology of the confluence, with large debris fans capable of rerouting the main channel, whilst significant sediment inputs change the main channel slope (Benda *et al.*, 2004; Ferguson and Hoey, 2008; Curtis *et al.*, 2010). The slope will tend to decrease upstream of a large sediment influx from a tributary, with a corresponding increase downstream (Curtis *et al.*, 2010).

Research has also addressed the evolution of river confluences over longer timespans. Confluences can rotate, evolve through lateral and streamwise migration or change in size, processes that are often linked to the evolution of the scour hole (Ashmore and Gardner, 2008). On braid plains, there is a tendency for confluence evolution to occur in above-average flows, whereas larger floods will cause more comprehensive changes to the planform (Bertoldi *et al.*, 2010). If a braid plain is more susceptible to avulsion, then confluences will be reworked more frequently, whilst sediments are less likely to be stored for long periods (Lancaster *et al.*, 2010).

All of these studies provide useful insights into the possible workings of the sediment dynamics at river confluences. However, developing a full conceptual model of the flow, sediment dynamics and the resultant morphological changes at individual river confluences is still a major challenge in the field of geomorphology. This requires a more detailed analysis of the processes operating at the scale of individual morphological features within river confluences.

### 2.6.2 Scour Holes

As noted in Section 1.2, the classic conceptual model of river confluences suggests that particles from each tributary will be routed around the scour hole, leading to maintenance of the scour hole and a zone of maximum sediment transport just downstream of it (Best, 1988; Ashmore and Gardner, 2008). The helical flow cells discussed in Section 2.3.5 and high levels of turbulence also help to maintain the morphology of the scour hole by ensuring that it is an area of high bed shear stress.

However, from the work of Roy and Bergeron (1990) it was found that particles, regardless of size, could travel through the scour hole, with particles from both tributaries capable of doing so depending on the river stage. More recently, research on the Bayonne-Berthier by Boyer *et al.* (2006) found that maximum bedload transport values were at the edge of the shear layer, rather than in the zone of maximum turbulence. This suggests that the link between high levels of turbulence in the centre of the CHZ and maintenance of the scour hole may be not be as straightforward as the classical model suggests. For the Rio Parana confluences, Szupiany *et al.* (2009) found that suspended sediment transport did not correlate well with bed shear stress, but occurred in narrow zones linked to the flow field, the upstream sources of sediment and in some cases, topographic steering. However, their research did agree with the classical

model by finding that the highest suspended sediment concentrations were in the areas around the scour hole (Szupiany *et al.*, 2009).

This ambiguity in the links between the scour hole and sediment dynamics may well explain why scour holes have not been found to be universal features of river confluences. Wallis *et al.* (2008), for example, found that only five of the eight confluences they studied had scour holes present. Additionally, it has already been noted in Section 2.4.4 that bed discordance can result in the absence or reduction in size of scour holes. There is, therefore, still a significant amount of research required to determine how variations in the sediment dynamics control the characteristics of confluence scour holes and the links to variations in the confluence flow field.

### 2.6.3 Mid-Channel Bar Development

Mosley (1976) was the first to identify the potential for mid-channel bars to develop in higher angle ( $>60^\circ$ ) confluences, finding that higher bed elevations and transport rates either side of the scour hole combined downstream into an area of deposition. It is the combination of scour hole erosion and sediment routing around it which gives the conditions for deposition in this zone (Best, 1986), with sediment thought to accumulate slightly downstream of the area of maximum bedload transport (Ashmore and Gardner, 2008).

Orfeo *et al.* (2006) found that for a confluence-diffuence unit on the Rio Parana, the flow started to diverge at a location that was a significant distance upstream from the front of the mid-channel bar. Once a mid-channel bar is in place, therefore, the flow field would appear to be conducive to the further deposition of sediment on the front of the bar, thus encouraging growth. However, in order for sediment to accumulate in the first place, there must be some initial cause of flow divergence or an alternative process that reduces the downstream flow velocities and encourages sediment deposition. As such, confluence symmetry is believed to be an important factor in determining whether a mid-channel bar will form, due to its impact on flow divergence downstream of the scour hole (Parsons *et al.*, 2008). The effect of channel planform symmetry on the morphology and sediment dynamics at river confluences is discussed in more detail in Section 2.7.3.

#### 2.6.4 Deposition Bars in Flow Separation Zones and the Stagnation Zone

There has been very little research into the development of depositional bars in river confluences in both the flow stagnation and flow separation zones. The flow separation zone is known to be an area of lower pressure and recirculating flow which encourages sediment deposition (Leite Ribeiro *et al.*, 2012). The same is true for the lower velocities in the flow stagnation zone at the upstream corner of many confluences.

Parsons *et al.* (2008) suggest that lateral bars are more common features on asymmetric confluences where there is flow separation at the downstream corners. However, it is still not clear how often such bars are present at asymmetric confluences and how they evolve with changes in the flow conditions.

#### 2.6.5 Hypotheses on Sediment Dynamics

As well as research that directly addresses sediment dynamics at river confluences, a significant body of work has developed hypotheses from other data, such as the flow field, the bed shear stresses and the sediments themselves (*e.g.* Biron *et al.*, 1993).

Many studies have highlighted the role played by turbulence in bedload transport. The turbulent structures generated in the CHZ are considered to be crucial for potential entrainment and transportation of particles (Best, 1986; Biron *et al.*, 1996b; De Serres *et al.*, 1999). In particular, it has been noted how the mean velocity and Reynolds shear stress do not accurately explain bedload transport, with variations in the instantaneous values considered more important (Biron *et al.*, 1996b).

A number of authors have attempted to find links between bed shear stress and sediment transport, although as noted in Section 2.6.2 above, this may not always be a reliable guide to actual transport rates. Nevertheless, some studies have hypothesised the link on the grounds that other units in the river system have a connection between sediment transport and bed shear stress (Bridge and Gabel, 1992; Biron *et al.*, 2002). Assuming that there is a link, Bradbrook *et al.* (1998) suggested from their CFD results that, under the right circumstances, confluences with a small difference in bed elevation experienced sufficient bed shear stress to cause erosion and thus deepening of the tributary step. However, as yet no studies have followed this up and tested the hypothesis.

The formation and maintenance of confluence scour holes encourages much debate in the river confluence literature. Rhoads *et al.* (2009) note that helical flow, shear layer turbulence and flow acceleration all increase bed shear stress, so it is understandable that disagreements exist over the major cause of scour. Constantinescu *et al.* (2011) argue from their numerical modelling that it is helical or ‘streamwise oriented vortical’ (SOV) cells that are most important to maintaining scour, although they concede that this could change if the CHZ starts to shear and produce Kelvin-Helmholtz instabilities. On a larger scale, Best and Rhoads (2008) hypothesised that the migration of a tributary bar into the junction as the dominance of the two channels changes could provide a mechanism for scour hole infill. However, much of this is based on conjecture and there is, as yet, no clear evidence for the causal mechanisms behind scour hole formation, maintenance and infilling.

## **2.7 Factors Affecting Sediment Dynamics at River Confluences**

Much of the early river confluence research investigated the factors affecting confluence geomorphology and in particular, the form of the scour hole. As in Section 2.4, this section will review how the junction angle, planform symmetry, discharge ratio and bed discordance affect river confluence morphology and the sediment dynamics that drive its evolution.

### *2.7.1 Junction Angle*

From the laboratory experiments of Mosley (1976), increases in junction angle were found to increase both the depth and cross-sectional area of scour holes. Smaller junction angles can have no obvious scour, with Best (1988) finding scour non-existent at junctions of less than 15°. The increase in scour hole depth with junction angle is considered to be non-linear (Best and Rhoads, 2008), with Mosley (1976) finding the greatest increases in scour depth as the angle approached 90°. Possible explanations for the increase in scour with junction angle include those covered in Section 2.4.1: the increase in turbulence generation suggested by Mosley (1976) and the decrease in curvature radius highlighted by Ashmore and Parker (1983). However, an alternative explanation offered by Best (1988) is that the greater routing of sediment around the scour hole at higher angles encourages a larger scour hole to be maintained. However,

the likelihood is that all three factors (turbulence, helical cells and sediment routing) are interdependent and will have varying effects depending on the specific confluence geometry.

There is also evidence that the junction angle influences scour hole position and shape. Best and Rhoads (2008) noted that the deepest scour tends to be positioned on a line bisecting the junction angle, while Ashmore and Parker (1983) found that scour holes move from trough to basin shapes at larger junction angles. Junction angle is therefore an important factor in determining the morphology of river confluences.

### 2.7.2 Discharge Ratio

Mosley (1976) found from his laboratory experiments that a discharge ratio close to unity gave the largest scour holes. However, there is also evidence that scour will increase at asymmetric confluences if the tributary discharge becomes higher than that of the main channel (Best, 1988). In both cases, the cause will be similar to that highlighted in Section 2.7.1, with a combination of greater turbulence, stronger secondary circulation and sediment routing around the scour hole responsible. Variations in discharge ratio will also have an impact on the position of the scour hole. When one channel dominates the other, the scour hole is expected to migrate to align with the dominant channel (Ashmore and Parker, 1983; Best 1986).

In terms of deposition, recent research has highlighted the potential role played by the timing of the flood peaks from the two channels. If the tributary flood peak arrives first, then deltas can form at the mouth of the tributary (Musselman, 2011). On the other hand, when the flow peaks in the main channel, there can be a backwater effect in the tributary, with this slack water being an ideal place for the deposition of fine sediments (Unde and Dhakal, 2009; Curtis *et al.*, 2010; Musselman 2011; Thompson *et al.*, 2011). These tributary mouth bars may also be affected by the discharge ratio, with the bar expected to migrate into the main channel, or to retreat in line with the main channel bank, depending on the momentum ratio (De Serres *et al.*, 1999). This migration could then have a corresponding effect on the nature of the scour hole downstream (Boyer *et al.*, 2006).

Variations in the discharge ratio were also found to affect the sediment dynamics of the Kaskaskia River-Copper Slough confluence, as shown in Figure 2.13. A dominant Copper Slough results in the confluence becoming more like a meander, with



the coarser Copper Slough sediments able to reach the true right bank and a narrow scour hole developing near this bank (Rhoads *et al.*, 2009). In addition, fine Kaskaskia River sediments can cross over to the true left bank where a lateral bar forms (Rhoads *et al.*, 2009). By contrast, if the Kaskaskia River dominates the scour hole moves towards the centre, with bedload from the respective tributaries splitting either side of the scour hole (Rhoads *et al.*, 2009).

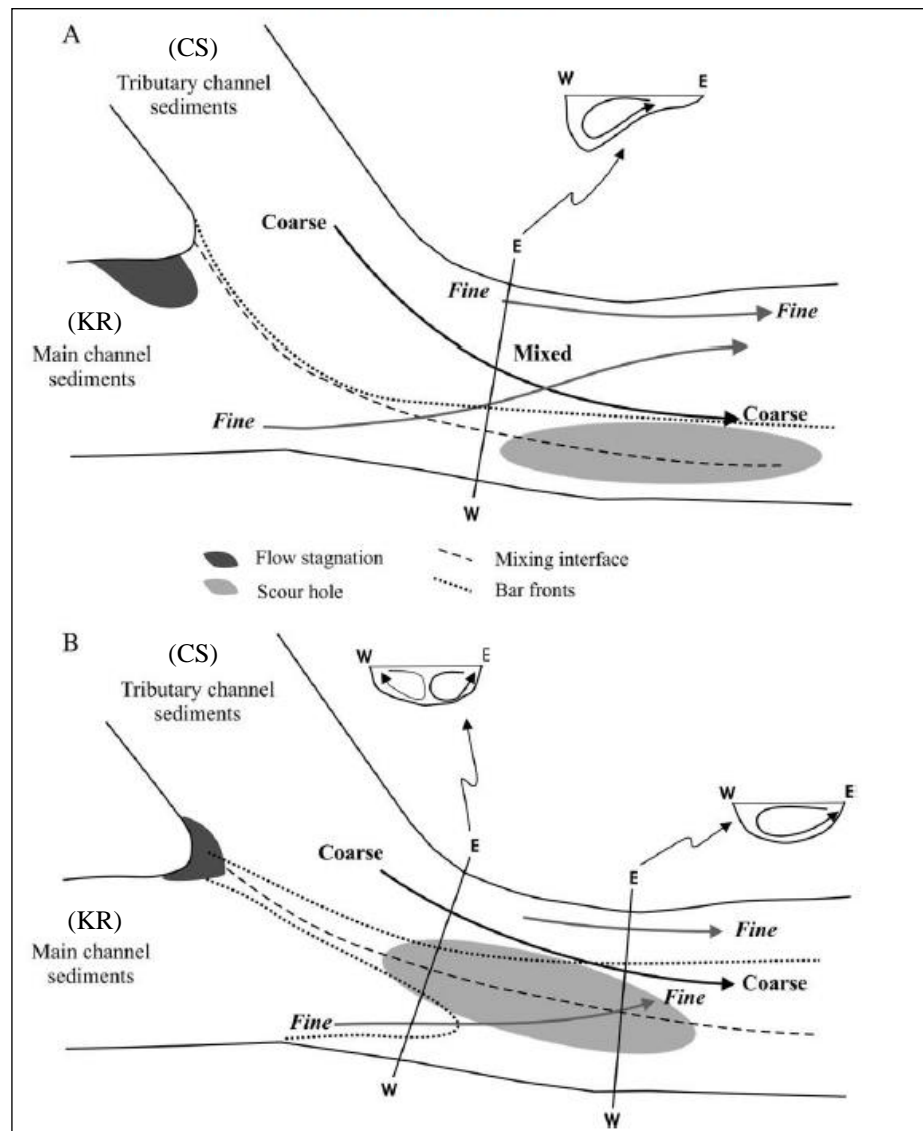


Figure 2.13: Conceptual model of the sediment dynamics at the Kaskaskia River (KR) and Copper Slough (CS) confluence for high (a) and low (b) discharge ratios (Rhoads *et al.*, 2009). With a stronger single helical cell (a), the fine sediments in the Kaskaskia River (main channel) can travel along the bed to the far downstream corner. With a weaker back-to-back helical circulation (b), the sediments tend to be routed around the scour hole.

Discharge ratio can therefore be seen as a key factor in determining the characteristics and evolution of morphological features within river confluences, as a result of its impact on the sediment dynamics of the confluences.

### 2.7.3 Symmetry

An asymmetric confluence planform will have a significant effect on the morphological features present and their form. Mosley (1976) found that at an asymmetric confluence, the scour hole will be positioned on a line that bisects the junction angle, erosion will occur on the bank opposite the tributary and deposition will occur on the downstream corner of the tributary. This encourages the development of a lateral bar on this corner, rather than the mid-channel bars that tend to develop at symmetric confluences (Best, 1986; Parsons *et al.*, 2008). The combined effects of these factors could be to encourage the lateral migration of the downstream channel, of which the ultimate result is the eventual evolution of a symmetrical confluence planform (Bryan and Kuhn, 2002; Best and Rhoads, 2008).

Parsons *et al.* (2008) suggest that confluence symmetry is the key factor in the development of mid-channel bars, with bars tending to form at symmetrical confluences with discharge ratios nearing unity. An example of this is the approximately symmetrical Mula-Kas confluence, where a partly vegetated mid-channel bar has developed (Unde and Dhakal, 2009). However, Rhoads *et al.* (2009) found that although the asymmetric Kaskaskia River-Copper Slough confluence doesn't have a stable mid-channel bar, when the Kaskaskia River is dominant, two separate sediment transport paths are seen combining downstream of the scour hole.

Therefore, it is likely that it is not specifically the symmetry of the confluence which is important, but the probability of the flow deflection in the CHZ being symmetrical. If there is sufficient, and equal, deflection of the two tributary flows, then the downstream flow is more likely to diverge, providing the potential development of a zone of deposition. Additional numerical or laboratory simulations may help to test this hypothesis.

### 2.7.4 Bed Discordance

It has already been noted in Section 2.4.4 that bed discordance can have a significant impact on the nature of the flow field at river confluences. Arguably the most important effect on the sediment dynamics and morphology, however, is the tendency for a discordant bed to discourage the development of a scour hole. It has already been noted in Section 2.4.4 that the Biron *et al.* (1996a) flume experiments on a

30° confluence found no evidence of helical cell formation or scour hole development. Given that discordant beds are far from rare in natural confluences, this may partly explain the observation in Section 2.6.2 that scour holes are not as common in confluences as the classical model would suggest. However, there is evidence that not all discordant confluences are lacking a scour hole. De Serres *et al.* (1999), for example, found that in the highest flows on the Bayonne-Berthier a small but clear scour hole developed. A possible explanation for this is that the higher water depths decreased the relative importance of the bed discordance.

Bed discordance at river confluences can also affect the development of other morphological features such as lateral bars. Where there is a significant step, it is known that the near-bed flow from the main channel passes under the tributary flow before upwelling at the downstream corner (Biron *et al.*, 1993, 1996a, 1996b; De Serres *et al.*, 1999). This naturally provides a potential sediment transport path for main channel sediments to reach the downstream junction corner and form a lateral bar. Leite Ribeiro *et al.* (2012) suggest that where bed discordance is particularly large, this process is helped by coarse sediment from the tributary being carried into the main channel and joining this near-bed flow towards the downstream corner.

Therefore, bed discordance can have a significant effect on the sediment dynamics and as a result the morphological features present in river confluences. Furthermore, given the evidence that the effect of bed discordance varies with river stage (*e.g.* De Serres *et al.*, 1999), it also provides a possible cause for river confluence evolution. Changes to the overall discharge flowing through the confluence can reduce the relative importance of the bed discordance, potentially leading to a change in the nature of the flow field in the CHZ and thus the sediment dynamics.

#### 2.7.5 Additional Controls on the Sediment Dynamics at River Confluences

The limited number of studies into the sediment dynamics at natural river confluences has meant that there are very few other factors which have been found to impact on the sediment dynamics. However, it has been suggested that large inputs of sediment (*e.g.* as a debris fan) can affect the morphology in the confluence through flow constriction, changes to sediment supply and changes to slope (Benda *et al.*, 2003). This contrasts with the earlier work of Ashmore and Parker (1983), which suggested that the confluence slope had little effect on the amount of scour. However, a much more

detailed study of the effects of slope on the sediment dynamics at river confluences would be required to test this hypothesis. A final potential limiting factor on the development of scour holes is identified by Rhoads *et al.* (2009) as being the level of the underlying bedrock, which can inhibit further erosion and thus restrict the depth of the scour hole.

## **2.8 Summary of Morphological and Sediment Dynamics Research**

The preceding two sections have set out the current state of research into the sediment dynamics and morphological evolution of river confluences. Unlike the research into the flow field, studies of the sediment dynamics have been much more limited in both scope and depth. Much of this research has focused on the confluence as part of a catchment network (as set out in Section 2.6.1), with fewer studies on the dynamics of individual confluences. Furthermore, the majority of research into the sediment dynamics and morphology of individual confluences has addressed the evolution of one specific feature, the scour hole (Sections 2.6.2 and 2.7). Therefore, an holistic understanding of the sediment transport processes at river confluences (and the resultant effects on confluence morphology) is still a long way off.

In Section 2.5, it was argued that a major gap in our understanding of the flow dynamics of natural river confluences was the limited knowledge of the flow processes at steep, upland river junctions. The depth of research into the sediment dynamics at these confluences is similarly limited, with the bedload transport work of Best (1988) and Roy and Bergeron (1990) arguably the most relevant. Even so, these studies were conducted before the widespread availability of field and numerical methods for obtaining three-dimensional flow data. Therefore, there is a clear opportunity to make use of these technological advances to improve our understanding of the sediment dynamics at steep, upland river confluences.

## **2.9 Conclusions**

This chapter has provided a comprehensive review of the river confluence literature in order to set out the overall context for this thesis. In Section 2.2, the major flow and morphological zones at river confluences were defined, with each zone discussed in turn throughout the rest of the chapter. Section 2.3 provided an in-depth

analysis of the understanding of the flow structure zones defined in Section 2.2, whilst the following section addressed the major external controls (*e.g.* channel planform and discharge ratio) on the confluence flow field. The overall state of the research into flow at river confluences was summarised in Section 2.5, with the argument made that it is the lack of studies at upland river confluences which is currently providing the greatest limitation on progress.

In Section 2.6, the focus switched to the sediment dynamics and morphological research, discussing in turn the morphological zones defined in Section 2.2. In a similar form to Section 2.4, Section 2.7 analysed the effects of external controls such as confluence planform, bed discordance and discharge ratio on the sediment dynamics. Section 2.8 provided an overall summary of the state of this research and argued that there has been much less research into the sediment dynamics and morphological evolution of river confluences than their flow dynamics. Studies of the bedload transport in upland river confluences were found to be particularly rare and those studies which had been conducted were done so without the ability to get detailed three-dimensional flow fields.

From the review of research into river confluences presented in this chapter, it has been demonstrated that whilst the understanding of the mean flow field and turbulent flow structures at river confluences is good, very little research has been conducted on upland river confluences. Therefore, it is still not known whether the processes identified as being prevalent in lowland river confluences are applicable when water surface slopes increase. This is a particularly important question, as steep, upland river confluences are more likely to have active bedload transport and morphological change over short timescales. In other words, to improve our understanding of the three-way interactions between flow, sediment transport and morphological change at river confluences, the first step is to increase our knowledge of the environments in which these interactions are the most pronounced. Therefore, the research question set out in Chapter 1 is fully justified given the current state of research into river confluences.

However, if the aims and objectives set out in Section 1.5 are to be realised, it will be necessary to take advantage of the most recent methodological advances in both field equipment and numerical modelling. If the sediment dynamics at upland river confluences are to be investigated, an understanding of the three-dimensional flow field is imperative. There is, therefore, an important role for the application and development of three-dimensional numerical modelling to complement the flow data collected in the

field. In addition, new applications and developments of numerical models need to be tested using high quality field datasets. The following chapter therefore discusses in detail the methodological developments in three-dimensional numerical modelling of natural rivers, before presenting an in-depth review of the methods to be employed at the Moor House and Arolla field sites.

# Chapter 3:

## Numerical Modelling and Field Methodology

### 3.1 Introduction

Within the research aim and objectives set out in Section 1.5, it was emphasised that using both numerical modelling and field methods would be necessary to obtain a greater understanding of the sediment dynamics at natural river confluences. Field studies of natural river junctions were considered desirable because it would enable experiments to be conducted on confluences that are known to be highly dynamic and experience rapid morphological change (over the course of minutes or hours). However, field data have another important function by providing boundary conditions and validation data for numerical models. Numerical modelling has become an increasingly popular tool for understanding the flow at natural river confluences, as demonstrated by the number of confluence studies reviewed in Chapter 2 that used Computational Fluid Dynamics (CFD) models (*e.g.* Bradbrook *et al.*, 1998, 2000a, 2000b, 2001; Lane *et al.*, 2000; Huang *et al.*, 2002; Biron *et al.*, 2004a; Constantinescu *et al.*, 2011). Numerical modelling has three major benefits: it can provide greater spatial density in the data than field measurements will allow, it can increase the understanding of the processes operating in a system and it enables a much more in-depth analysis of the manner in which these processes change in response to variations in the boundary conditions (Lane *et al.*, 1999a).

This chapter is therefore divided into two major sections, with the first introducing the methodology for the numerical modelling of flow and the second discussing the field methodology. Numerical modelling methods for particle transport are covered separately in Section 7.2 ahead of the development of a new reduced-complexity discrete particle model. In each section of this chapter, the available methods are analysed and the most applicable chosen with reference to the objectives set out in Section 1.5. The complete methodology for this thesis is summarised in the concluding remarks at the end of the chapter, along with a short discussion of the potential limitations and uncertainties that this methodology implies.

## 3.2 Computational Fluid Dynamics (CFD)

Numerical models vary in their levels of sophistication, depending on the underlying equations and the number of dimensions in which these equations are applied (Hardy, 2006a). However, whilst greater sophistication might seem desirable, other factors must be considered when determining the optimal numerical modelling approach. These considerations include the complexity of the processes being modelled, the quality of boundary condition and validation data available, model robustness, the computational cost and the temporal and spatial scales at which the modelling is required.

In Chapter 2 it has been demonstrated that flow at river confluences is highly complex, with secondary circulation cells and coherent turbulent structures commonplace. This complexity leads to a wide variability in vertical velocities and pressures, meaning that simpler, two-dimensional models based on the shallow water equations may be insufficient (Lane *et al.*, 1999a; Bradbrook *et al.*, 2000a). Three-dimensional CFD models are therefore the most appropriate numerical method for understanding river confluence dynamics.

CFD was developed in the 1960s and has now been widely applied within fluvial geomorphology (Hardy, 2008). Three-dimensional versions of these models can provide much better predictions of flow at river units (such as confluences) where secondary flows are important (Lane *et al.*, 1999a; Hardy, 2006a). The number of commercial codes available and the extensive research into fluvial applications of CFD means fluvial geomorphologists do not need to consider modifying the governing equations of these CFD packages (Lane, 1998). Instead, the focus is on developing the application of these models to the individual geomorphological investigation whilst minimising any limitations.

This first part of this chapter presents the numerical modelling methodology for this thesis. It begins by addressing the more generic aspects of CFD modelling that apply to simulations of all Newtonian fluids. This includes setting out the governing Navier-Stokes equations, the process of discretisation and the algorithms used to solve the equations numerically. The focus then switches to the auxiliary models which must be set up in a more specific way depending on the geomorphological problem. This includes methods for modelling turbulence, modifications to the turbulence models in the near-wall region, representing the channel morphology at a range of scales and



approaches for including variability in the free surface. The following section addresses issues of good practice in CFD modelling, which includes the procedures for verification and validation of the model or individual simulation. A review of the CFD modelling approach is then set out, followed by a description of the methods to be used in this study.

The choice of numerical methodology for this thesis is based on three broad principles. The first is that the methods chosen should reflect the priorities for the flow modelling set out in the thesis objectives of Section 1.5. The second is that unless a new method is specifically required in the objectives of Section 1.5, the methods used should be those with a proven track record in simulations of natural rivers. The final principle concerns the complexity of the models being used. As Lane (1998) notes, it is not necessarily the case that predictions will be improved by using more complex models. Therefore the final principle is that if there are multiple methods which would satisfy these first two criteria, more simple methods should be used in the first instance. Additional complexity will be introduced only if it is demonstrated that the simpler methods underperform.

### 3.3 The Navier-Stokes Equations and Their Solution

#### 3.3.1 The Navier-Stokes Equations

Fluid dynamics is based on three fundamental physical principles: the conservation of mass, the conservation of energy and Newton's Second Law of Motion (Anderson, 1995). These fundamental principles are accounted for through a continuity equation and three momentum equations (Ferziger and Peric, 1999). The fluid is treated as a continuum and therefore it is the Eulerian transformation of the Newtonian laws which are used to describe fluid motion (Lane *et al.*, 1999a).

The conservation of mass equation for an incompressible fluid is given as (Lane *et al.*, 1999a):

$$\frac{\partial u}{\partial x} + \frac{\partial v}{\partial y} + \frac{\partial w}{\partial z} = 0 \quad (3.1)$$

where  $u$ ,  $v$  and  $w$  are the velocity components in the  $x$ ,  $y$  (horizontal) and  $z$  (vertical) directions respectively. The Navier-Stokes momentum equations for an incompressible fluid are given below (Lane *et al.*, 1999a):

$$\frac{\partial}{\partial t}(\rho u) + \frac{\partial}{\partial x}(\rho u^2) + \frac{\partial}{\partial y}(\rho uv) + \frac{\partial}{\partial z}(\rho uw) - 2\rho u\zeta \sin \Phi_L + \frac{\partial p}{\partial x} - \frac{\partial \tau_{xx}}{\partial x} - \frac{\partial \tau_{xy}}{\partial y} - \frac{\partial \tau_{xz}}{\partial z} = 0 \quad (3.2)$$

$$\frac{\partial}{\partial t}(\rho v) + \frac{\partial}{\partial x}(\rho uv) + \frac{\partial}{\partial y}(\rho v^2) + \frac{\partial}{\partial z}(\rho vw) - 2\rho v\zeta \sin \Phi_L + \frac{\partial p}{\partial y} - \frac{\partial \tau_{xy}}{\partial x} - \frac{\partial \tau_{yy}}{\partial y} - \frac{\partial \tau_{yz}}{\partial z} = 0 \quad (3.3)$$

$$\frac{\partial}{\partial t}(\rho w) + \frac{\partial}{\partial x}(\rho uw) + \frac{\partial}{\partial y}(\rho vw) + \frac{\partial}{\partial z}(\rho w^2) - \rho g + \frac{\partial p}{\partial z} - \frac{\partial \tau_{xz}}{\partial x} - \frac{\partial \tau_{yz}}{\partial y} - \frac{\partial \tau_{zz}}{\partial z} = 0 \quad (3.4)$$

where  $\rho$  is density,  $p$  is the pressure,  $\zeta$  is the angular rotation of the earth,  $\Phi_L$  is latitude and  $\tau_{ij}$  is a shear stress term. When applying these equations to natural rivers at the scale of interest for this study, factors such as atmospheric pressure, wind stress and the Coriolis force can be ignored as having a negligible effect (Lane *et al.*, 1999a). Even so, as it is rarely possible to solve the Navier-Stokes equations analytically at the Reynolds numbers encountered in natural river systems, numerical methods must be used (Ferziger and Peric, 1999).

### 3.3.2 Discretisation

As the Navier-Stokes equations consist of partial differential equations for which an analytical solution is usually not possible, any numerical solution of the equations will require some form of discretisation. Discretisation is the process of converting the partial differential equations into discrete algebraic equations (Ferziger and Peric, 1999). The three major discretisation methods used to solve these equations are the finite difference, finite volume and finite element approaches (Hardy, 2008). Of these, the finite difference method is the oldest and is usually better suited to regular, structured grids, whilst finite volume approaches are the most popular, especially where the topography is complex (Ferziger and Peric, 1999; Biron and Lane, 2008).

The popularity of finite volume discretisation methods may be due to their reputation as fast and numerically stable, at least with a structured grid and simple topography (Lane *et al.*, 2004). Each cell in the finite volume method has a cell centre value from which the cell surface values are interpolated, meaning that any shape of grid can be used (Ferziger and Peric, 1999). However, it is generally advisable to avoid steep angles between gridlines when using a finite volume discretisation (Lane *et al.*, 1999a). Therefore, if the topography is particularly irregular, it may be better to implement a finite element approach, which can use tetrahedral as well as hexahedral cells (Ferziger and Peric, 1999).

Finite difference methods have an advantage in that they allow higher-order solutions of the Navier-Stokes equations to be developed, but they are less suitable when trying to model complex topographies (Ferziger and Peric, 1999). Therefore, it is understandable that high-resolution CFD models of river confluences have tended to use finite volume discretisation methods (*e.g.* Bradbrook *et al.*, 2001; Huang *et al.*, 2002; Biron *et al.*, 2004a). PHOENICS, the commercial CFD code used within this thesis, employs a finite volume discretisation of the Navier-Stokes equations (CHAM, 2013).

### *3.3.3 Solution Algorithms*

The inability to solve the Navier-Stokes momentum equations analytically means that iterative numerical methods are required. A number of solution algorithms have been developed for this purpose, for example PISO (Issa, 1986), PRIME (Maliska and Raithby, 1984), SIMPLE (Patankar and Spalding, 1972) and modified versions of SIMPLE such as SIMPLER (Patankar, 1981) and SIMPLEST (Spalding, 1980, from CHAM, 2013). However, even though there are slight variations in these numerical methods, the broad principles of solving the Navier-Stokes equations remain the same. The SIMPLEST algorithm is the solver used by PHOENICS and therefore SIMPLE is explained in more detail here.

The SIMPLE algorithm starts by determining the pressure field, usually with some form of estimate (Patankar and Spalding, 1972; Lane *et al.*, 2000). With the pressure field given, it is then straightforward to determine the velocities from the momentum equations (Weerakoon *et al.*, 2003). However, this first estimate of the pressure field will give velocity values that are highly unlikely to fit the continuity equation (Patankar and Spalding, 1972). Having determined the required corrections to

the velocity field, it is then possible to derive a pressure correction equation from the momentum equations (Weerakoon *et al.*, 2003). An iterative sequence is created, therefore, with the corrections giving a new estimate of the pressure field for the next iteration (Patankar and Spalding, 1972; Lane *et al.*, 2000)

With numerical methods such as SIMPLE, there is a risk that any error can propagate through the domain and lead to numerical instability. Therefore, models will include an option to set the relaxation, which is the percentage of the calculated corrections that is allowed between iterations (Hodkinson, 1996). By permitting only small changes between iterations, the risk of the solution diverging (rather than converging to a solution) is reduced. The iterative process of the SIMPLE algorithm will continue until the model is deemed to have converged sufficiently (iterative convergence is discussed in Section 3.5.2).

SIMPLER is an updated version of SIMPLE which uses the pressure correction equation only to provide corrections to the velocity values and uses an alternative equation for obtaining the pressure values (Patankar, 1980). SIMPLEST, meanwhile, is an update to SIMPLE that makes changes to the ways the diffusive and convective terms are dealt with in the momentum equation (CHAM, 2013). Both of these updates are designed to improve the efficiency and stability of the solver.

### 3.4 Auxiliary Modelling within the CFD Framework

The Navier-Stokes equations can be applied to the flow of any Newtonian fluid (defined by Anderson (1995) as a fluid in which the shear stress is proportional to the velocity gradient), whether laminar or turbulent. The generic form of the Navier-Stokes equations, the process of discretisation and the algorithm used to solve the equation can all be considered widely applicable to simulations of any fluid. These more general aspects of CFD modelling have been addressed in the previous section. However, beyond this there are a number of other considerations which must be taken into account when applying the model specifically to river confluences.

The river confluences of interest to this research will have flow that is characterised by turbulent structures, irregular channel planforms, rough bed topography and sloping water surfaces. Some of these characteristics are found widely in CFD applications (*e.g.* turbulent flow) and therefore have received greater attention within the literature, whereas others are more particular to this research (*e.g.* the steep

water surface slopes). Nevertheless, the way in which all of these characteristics are modelled within the more generic CFD code is a critical component of the numerical modelling methodology that is covered within this section.

#### 3.4.1 The Reynolds-Averaged Navier-Stokes (RANS) Equations

With an algorithm such as SIMPLE, the Navier-Stokes equations can be solved providing the grid size and time step are small enough to resolve the smallest and shortest-duration turbulent structures (Hodkinson, 1996; Lane, 1998). This is known as ‘Direct Numerical Simulation’ (DNS). The nature of turbulent flows is that they have interactions between many turbulent structures of different sizes (Roy *et al.*, 1999). Therefore, resolving all turbulence structures directly is only possible at low Reynolds numbers (Rogallo and Moin, 1984; Keylock *et al.*, 2005).

Reynolds averaging of the Navier-Stokes (RANS) equations is the classic approach used to overcome this issue, with individual turbulent structures ignored and the focus switched to the effect of these turbulent structures on the transfer of momentum in the mean flow (Hodkinson, 1996; Lane, 1998; Lane *et al.*, 1999a). Reynolds averaging results in the removal of the time-dependent terms from Equations (3.2) to (3.4) and instead splits each variable into a mean and fluctuating component (Lane *et al.*, 1999a). Additionally, in the RANS equations, the shear stress term ( $\tau_{ij}$ ) from Equations (3.2) to (3.4) is defined as (Bradbrook *et al.*, 2001):

$$\tau_{ij} = \nu \left( \frac{\partial u_j}{\partial x_i} + \frac{\partial u_i}{\partial x_j} \right) - \overline{u'_i u'_j} \quad (3.5)$$

where  $\nu$  is kinematic viscosity,  $u$  is velocity,  $x$  is distance, the subscripts  $i$  and  $j$  refer to the  $x$ ,  $y$  or  $z$  directions and  $\overline{u'_i u'_j}$  is the Reynolds shear stress. The Reynolds shear stress terms are added to the Navier-Stokes equations as a result of the Reynolds averaging process (Lane, 1998; Lane *et al.*, 2000; Keylock *et al.*, 2005). As these terms are added without a corresponding increase in the number of equations, the only way to obtain values for the Reynolds shear stress terms is through the use of a turbulence model (Bradbrook *et al.*, 2000a). There are many different turbulence modelling approaches available and these are discussed in the following subsections.

### 3.4.2 Turbulence Models

As noted in Section 3.4.1, DNS is not a feasible approach for modelling the turbulence in most flows. As such, a number of methods have been devised to model flow turbulence. Use of the RANS equations requires the eddy viscosity (the constant of proportionality in the relationship between Reynolds shear stress and mean strain rate) to be determined (Lane *et al.*, 2000). This can be done using a zero-equation model, where the eddy viscosity is specified as a constant and an implicit assumption is that any turbulence dissipates at the place of generation (Lane, 1998, Lane *et al.*, 2000). Alternatively, one- or two- equations models will contain differential equations that allow turbulent structures to be transported (Lane, 1998). Examples of two-equation turbulence models are the RNG  $\kappa$ - $\epsilon$  model (*e.g.* Bradbrook *et al.*, 2000a) and the  $\kappa$ - $\omega$  model used by Huang *et al.* (2002). The use of Reynolds Stress Models (RSMs) has also been considered in recent studies (Miori *et al.*, 2012; Sandbach *et al.*, 2012). RSMs have the advantage that they provide a more valid representation of anisotropic turbulence (Miori *et al.*, 2012). However, within PHOENICS there is a conflict in variable storage between the method of topographic representation, which is discussed in detail in Section 3.4.8, and the RSM model (Miori *et al.*, 2012; Sandbach *et al.*, 2012). Given the highly variable bed morphology of upland river confluences, it is considered more important to accurately and robustly represent the topography than to use RSMs.

The  $\kappa$ - $\epsilon$  model and its variants (described in Section 3.4.3) are some of the most popular turbulence models, although there has been an increase in the use of Large Eddy Simulation (LES) in river confluence studies. LES is a hybrid model that directly simulates the larger turbulent structures but uses RANS-based approaches (*e.g.* the  $\kappa$ - $\epsilon$  model) for the smaller scale fluctuations (Rogallo and Moin, 1984; Lane *et al.*, 2000). Between them, LES and  $\kappa$ - $\epsilon$  modelling approaches are used in the vast majority of CFD applications to river confluence studies. Therefore, although there are a wide range of turbulence models available, the  $\kappa$ - $\epsilon$  model and LES models are considered the two most applicable methods for this research and are explained in more detail here.

### 3.4.3 The $\kappa$ - $\varepsilon$ Model and Variants

Of the two-equation turbulence models available, versions of the  $\kappa$ - $\varepsilon$  model have been by far the most popular for river confluence studies. The  $\kappa$ - $\varepsilon$  turbulence model is a two equation model which treats turbulence as isotropic (Rodriguez *et al.*, 2004). The standard  $\kappa$ - $\varepsilon$  model was developed by Jones and Launder (1972) and has been widely used in hydraulic modelling. The basic principle behind the model is that the turbulent shear stress is related to mean strain rate by a turbulent viscosity (Jones and Launder, 1972):

$$-\rho \overline{u'v'} = \mu_T \frac{\partial u}{\partial y} \quad (3.6)$$

where  $(\overline{u'v'})$  is the turbulent shear stress,  $\rho$  is the density,  $\mu_T$  is the turbulent viscosity and  $(\frac{\partial u}{\partial y})$  is mean strain rate. In the  $\kappa$ - $\varepsilon$  turbulence model, the turbulent viscosity,  $\mu_T$ , is related to a length scale,  $L$ , the turbulent kinetic energy,  $k$ , and dissipation,  $\varepsilon$ , in the following equation (Ferziger and Peric, 1999):

$$\mu_T = \rho C_\mu \sqrt{k} L = \rho C_\mu \frac{k^2}{\varepsilon} \quad (3.7)$$

where  $C_\mu$  is a constant given the value 0.09. In the standard  $\kappa$ - $\varepsilon$  turbulence model, for flows with high Reynolds numbers, the values for  $k$  and  $\varepsilon$  can be determined from (Jones and Launder, 1972):

$$\rho \frac{Dk}{Dt} = \frac{\partial}{\partial y} \left( \frac{\mu_T \partial k}{\sigma_k \partial y} \right) + \mu_T \left( \frac{\partial u}{\partial y} \right)^2 - \rho \varepsilon \quad (3.8)$$

$$\rho \frac{D\varepsilon}{Dt} = \frac{\partial}{\partial y} \left( \frac{\mu_T \partial \varepsilon}{\sigma_\varepsilon \partial y} \right) + c_1 \frac{\varepsilon}{k} \mu_T \left( \frac{\partial u}{\partial y} \right)^2 - c_2 \frac{\rho \varepsilon^2}{k} \quad (3.9)$$

where  $c_1$ ,  $c_2$ ,  $\sigma_k$  and  $\sigma_\varepsilon$  are constants with values of 1.55, 2.0, 1.0 and 1.3 respectively.

The standard  $\kappa$ - $\varepsilon$  turbulence model has been very popular in CFD studies, but this extensive research revealed that it has limitations in certain circumstances. Tritthart

and Gutknecht (2007), for example, suggest the under-prediction of superelevation on the outside of a river bend is partly due to the standard  $\kappa$ - $\epsilon$  model being unable to reproduce the strength of the secondary circulation cells. This is part of a wider issue for two-equations models, which tend to work well unless dealing with anisotropic turbulence (Nicholas, 2001). The standard  $\kappa$ - $\epsilon$  model is also known to have difficulties when there is shear in the flow or flow separation (Hodkinson, 1996; Bradbrook *et al.*, 2001; Rodriguez *et al.*, 2004). This is problematic for the use of the model at river confluences, where secondary flow, anisotropic turbulence and flow shear are commonplace.

A solution to this limitation is to evaluate the equations of motion for turbulent kinetic energy ( $k$ ) and dissipation ( $\epsilon$ ) using the Renormalisation Group (RNG) theory approach developed by Yakhot and Orszag (1986). The equations for the RNG version of the  $\kappa$ - $\epsilon$  model are given by Nicholas and Sambrook Smith (1999) and reproduced below:

$$\frac{\partial k}{\partial t} + \frac{\partial}{\partial x_i}(u_i k) = \frac{\partial}{\partial x_i} \left( \alpha v_t \frac{\partial k}{\partial x_i} \right) + v_t S^2 - \epsilon \quad (3.10)$$

$$\frac{\partial \epsilon}{\partial t} + \frac{\partial}{\partial x_i}(u_i \epsilon) = \frac{\partial}{\partial x_i} \left( \alpha v_t \frac{\partial \epsilon}{\partial x_i} \right) + C_{1\epsilon} \frac{\epsilon}{k} v_t S^2 - C_{2\epsilon} \frac{\epsilon^2}{k} - R \quad (3.11)$$

where  $S$  is the modulus of  $S_{ij}$ , the mean rate of strain tensor,  $\alpha$  is the inverse Prandtl number for turbulent transport,  $R$  is the rate of strain and the constants  $C_{1\epsilon}$  and  $C_{2\epsilon}$  have values of 1.42 and 1.68 respectively. It is the presence of these extra terms in the equation which improves the representation of the turbulent flow structures.

The RNG version of the model has been shown by a series of studies to perform better than the standard version when applied to scenarios such as river confluences (Hodkinson, 1996; Bradbrook *et al.*, 1998, 2000a, 2001; Rodriguez *et al.*, 2004; Biron and Lane, 2008). Therefore, except in situations where information on individual turbulent structures is required, the RNG version of the  $\kappa$ - $\epsilon$  model is considered to be a perfectly adequate treatment of turbulence.

Nevertheless, research into alternatives has been encouraged by the limitations of two-equation models in complex flows. Ferziger and Peric (1999) note that whilst Reynolds stress models have not been fully tested, the evidence so far suggests that they



may perform better in swirling flows. However, the alternative method considered most relevant to this study is Large Eddy Simulation (LES), which has been developed to investigate the nature of individual turbulent structures in natural rivers.

#### 3.4.4 Large Eddy Simulation (LES)

Large Eddy Simulation (LES) is a hybrid turbulence modelling method that lies in between Direct Numerical Simulation (DNS) of turbulence and RANS-based approaches (Rogallo and Moin, 1984; Bradbrook *et al.*, 2000b; Keylock *et al.*, 2005). It has been argued by a number of authors that in order to represent the complex nature of the flow in river confluences, and in particular the mixing zone, the use of LES approaches is a necessity (Bradbrook *et al.*, 2000b; Parsons *et al.*, 2003; Biron and Lane, 2008).

Unlike the RANS methods, LES does not split the turbulent structures into mean and fluctuating components of the velocity (Hardy *et al.*, 2003, 2007; Keylock *et al.*, 2005). Instead, LES reintroduces the time dependence normally removed as part of the Reynolds-averaging procedure and uses DNS for the larger turbulent structures (Rogallo and Moin, 1984; Lane *et al.*, 2000). This is based on the principle that the largest structures will give the biggest transfers of energy (Ferziger and Peric, 1999).

In order for LES to provide useful information on the flow field, the cell size must be sufficiently small to represent the key flow structures (Hardy *et al.*, 2007). Any structures smaller than the chosen filter size (usually the grid cell size) are not ‘large eddies’, and so are modelled using a sub-grid scale (SGS) model (Ferziger and Peric, 1999; Abba *et al.*, 2003; Hardy *et al.*, 2003, 2007). There are a number of SGS models available and a summary of their properties is given in Table 3.1.

The choice of SGS model is important as they help to resolve the larger turbulent structures (Hardy *et al.*, 2003). Specifically, they deal with the transfer of energy between the grid and sub-grid scales, predominantly only from the grid scale to the sub-grid scale (Keylock *et al.*, 2005; Hardy *et al.*, 2007). The accuracy of the SGS model will therefore influence the reliability of the simulation of the larger turbulent eddies. As shown in Table 3.1, all of the methods have limitations and therefore there will always be uncertainty in the LES model. However, providing that the SGS model is deemed to perform to a satisfactory level, LES can reveal useful information about flow

structures in natural confluences that may not be possible to observe in the field (Hardy *et al.*, 2007).

	Description	Advantages	Limitations
Smagorinsky model	Most popular SGS model.  Determines an eddy-viscosity parameter and links to mixing length in three dimensions.	Its common usage is largely down to its simplicity.	Transfer of energy only from larger to smaller eddies.  Comparisons with DNS have questioned performance level.  Some issues in the laminar flow near the wall.
Scale-similarity models	Assumes the major unresolved eddies are those just smaller than the chosen filter.	Found to be good for SGS Reynolds Stress.  Can potentially represent the process of energy backscatter.	Difficulties found with complex geometry.  Problems with insufficient energy dissipation mean it is often combined with the Smagorinsky model.
Structure-function models	Similar to scale-similarity, but with a simpler method of determining the effective viscosity.	More applicable in real rivers.  Some evidence of outperforming Smagorinsky.	Has not been tested over a wide range of fluvial applications.
Dynamic models	Covers a range of model types where two different filters are used.  The scale between the two filters is used to test turbulence modelling, with the results used to determine the Smagorinsky constant (or similar) for modelling the smallest scales.  These approaches allow the Smagorinsky constant to be variable through time and space.	Higher accuracy for kinetic energy and SGS dissipation.  Good when dealing with anisotropic turbulence that does not fit an idealised energy cascade.	Still evidence of errors in turbulent intensity predictions.  Numerical instability encountered when dynamic Smagorinsky constant varied considerably locally.  Also got instabilities if model produces localised negative eddy viscosity (which might imply inverse energy transfer in reality).

Table 3.1: Descriptions, advantages and limitations of different types of sub-grid scale turbulence models. Adapted from Ferziger and Peric (1999), Abba *et al.* (2003) and Keylock *et al.* (2005).

An alternative to LES is the Detached Eddy Simulation (DES) method used by Kirkil and Constantinescu (2009) and Constantinescu *et al.* (2011). This is a hybrid approach, with LES used for the main flow and a RANS-based turbulence model used in the region near the wall (Constantinescu *et al.*, 2011). However, much like the Reynolds Stress method mentioned in the previous section, this method is relatively new and any detailed analysis should follow further testing on a wider range of natural rivers.

#### *3.4.5 Selecting an Appropriate Turbulence Model*

When choosing a method for modelling turbulence, there is no single approach which is best suited to all circumstances (Ferziger and Peric, 1999). LES and the RNG  $\kappa$ - $\epsilon$  model have been used in a number of river confluence studies and have been demonstrated to produce reliable representations of the flow. As a result, they are considered to be the two most appropriate methods for this research. The decision about which of these approaches should be used has to be taken with consideration for the level of detail required, the compatibility with other aspects of the model (*e.g.* the treatment of the boundaries and free surface) and the computational cost. Section 3.7 will provide a justification for the numerical methodology to be used in this thesis with consideration of all aspects of the model. However, it is implied from the general philosophy set out in Section 3.2 that the more complex LES approach will be used only if simpler methods such as the RNG  $\kappa$ - $\epsilon$  model are demonstrated to have underperformed.

#### *3.4.6 Accounting for Bed Roughness*

When modelling turbulent flows using CFD, it is necessary to find a method for modelling the near-wall zone, which is characterised by large velocity gradients, the influence of molecular viscosity and anisotropic turbulence (Apsley, 2007). Wall functions are used in this zone to avoid the necessity of having a very fine grid to resolve the turbulent structures (Craft *et al.*, 2002; Apsley, 2007). These wall functions are important, with the performance of the turbulence model in large part determined by the wall treatment used (Chen and Patel, 1988).

The wall function method essentially splits the domain into an outer layer and an inner layer (Sotiropoulos, 2005). For the  $\kappa$ - $\epsilon$  model, the standard  $k$  and  $\epsilon$  equations are used in the outer layer, whereas the inner layer replaces the  $\epsilon$  equation with an equation linking the turbulent length scale to  $k$ , the viscosity of the fluid and the distance from the wall (Sotiropoulos, 2005). It is widely accepted that wall functions do not provide particularly good representations of the flow complexity near the wall, especially where there is flow separation (Chen and Patel, 1988; Craft *et al.*, 2002; Apsley, 2007). However, although their inherent assumptions have been criticised, wall functions are considered to be the only practical option for use in natural river flows (Apsley, 2007).

If the particles that make up a channel bed are larger than the laminar sub-layer of the flow (as in almost all natural rivers), then the bed is hydraulically rough (Lane, 2005). Although a wall function is still needed if the bed is hydraulically smooth, a rough surface results in modifications to the equations with the inclusion of a roughness length scale ( $k_s$ ) term (Sotiropoulos, 2005). The roughness length scale is therefore an important boundary condition for most CFD models of flows over rough beds.

Instead of using the roughness length scale parameter, many wall functions refer to roughness height, which is the height above the bed at which the mean horizontal velocity is zero. Figure 3.1 shows an idealised logarithmic velocity profile, with the roughness height ( $z_0$ ) labelled. The principle behind the roughness height is that a rough boundary layer can be split into a logarithmic layer (where the vertical velocity profile can be represented by a logarithmic law) and a roughness sub-layer where the flow is affected by individual particles or clusters (Stoesser *et al.*, 2004). In the idealised treatment of flow near a wall, the velocity would be considered to be zero up to the roughness height, above which the velocity follows a logarithmic profile. However, this is considered an over-simplification, as flow in the roughness sub-layer is known to be affected differently by the wake around isolated clasts, patches of pebbles and over an armoured bed (Robert *et al.*, 1992; Stoesser *et al.*, 2004).

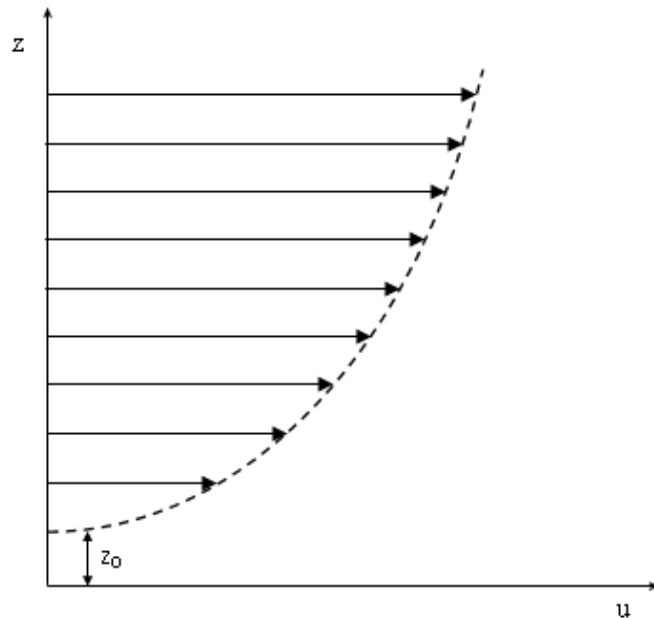


Figure 3.1: An idealised logarithmic velocity profile, with a roughness height,  $z_0$ . The logarithmic layer is the zone above  $z = z_0$ , whilst the roughness sub-layer is the zone below. In reality the flow field will be highly complex in the roughness sub-layer and at the boundary of the logarithmic layer.

The roughness length scale is related to roughness height by the following equation:

$$k_s = Cz_0 \quad (3.12)$$

where  $C$ , the constant of proportionality in Equation 3.12, is given as either 29.7 (*e.g.* Rüther and Olsen, 2007) or 30 (*e.g.* Nicholas, 2001).

There are a number of ways that the roughness height, and by extension roughness length scale, can be determined. The first is to obtain the value of the roughness height from the von Karman-Prandtl law (also known as the law of the wall) and a measured velocity profile. The second is to use an empirical relationship between the roughness height or roughness length scale and a characteristic grain size.

The von Karman-Prandtl law is given by Biron *et al.* (1998, 2004b) as:

$$u = \frac{u_*}{\kappa} \left( \ln \left( \frac{z}{z_0} \right) \right) \quad (3.13)$$

where  $u$  is velocity at height  $z$ ,  $u_*$  is the shear velocity,  $\kappa$  is the von Karman constant and  $z_0$  is the roughness height. Shear velocity is related to shear stress ( $\tau$ ) through the following relationship (Sime *et al.*, 2007):

$$u_* = \sqrt{\tau/\rho} \quad (3.14)$$

where  $\rho$  is the water density. The shear stress can be determined from the velocity profile and therefore the value for roughness height can be found without the need for any additional data.

Using an empirical relationship to obtain the roughness height, meanwhile, is particularly popular when detailed velocity profile data do not exist. A number of empirical relationships have been suggested for determining the roughness height from the bed grain size, but the three most common are  $z_0 = 0.1D_{84}$ ,  $k_s = 3.5D_{84}$  or  $k_s = 6.8D_{50}$  (Nicholas and Sambrook Smith, 1999; Nicholas, 2001; Hardy *et al.*, 2005).

## 3.4.7 Limitations of Methods of Accounting for Bed Roughness

When representing the bed topography in a CFD simulation, the traditional approach is to use the grid to represent the major topographic features and a roughness parameter to account for topographic variations at smaller scales (Lane *et al.*, 2004). Use of a roughness parameter is a necessity because there is a risk of numerical instability if the mesh becomes too warped trying to represent the topography at smaller scales (Hardy *et al.*, 2005, 2007). However, a number of limitations have been raised with this method and alternatives, such as the Mass Flux Scaling Algorithm (MFSA), have been developed to improve on this methodology. This section outlines the major concerns with the use of a roughness value, whilst the following section introduces the MFSA.

There are three major concerns that have been raised with respect to the use of a roughness height value. These are the multiple methods of obtaining the value (as described in the previous section), the interdependence with grid cell size and questions over what is being included in the roughness height.

The first of these issues is the difficulty in determining a definitive value for roughness height when so many different methods are available. Even if it is decided that the roughness height should be determined from a characteristic grain size, there is a choice of at least three separate empirical relationships, as noted in Section 3.4.6. In turn, each of these is based on the use of a single grain size, which in most cases can be argued to be an oversimplification (Hodge, 2007). Additionally, these empirical relationships are not necessarily trusted in all cases, with some studies arguing that for the individual field site in question the roughness has been over- or underestimated (Robert *et al.*, 1996; Rodriguez *et al.*, 2004). This means that for any given value of the roughness height, there will be a significant amount of uncertainty surrounding the final value.

The second issue is the existence of a paradox between the roughness height and the cell size. A larger grid size means less of the topography can be represented through variations in the mesh and therefore more of the smaller-scale topography must be included within the roughness parameter (Nicholas and Sambrook Smith, 1999). Therefore, a higher grid resolution might be considered to be an advantage.

However, due to the nature of the logarithmic law of the wall (Equation 3.13), any value of  $z_0$  greater than half the grid resolution (*i.e.* the centre of the cell nearest the

bed) becomes meaningless (Nicholas and Sambrook Smith, 1999; Nicholas, 2001; Rameshwaran *et al.*, 2011). If the roughness height is equal to the cell centre, then the bottom cell should have a velocity of zero. Therefore, any increase in the roughness height above that is considered to be irrelevant and would potentially risk numerical instability (Lane *et al.*, 2004). As such, a paradox exists for very rough beds: a larger grid size is required to allow for the high value of  $z_0$ , but this reduces the ability to represent the topography using the mesh. Ultimately, this can lead to a smaller than desired value of  $z_0$  being used instead of increasing the cell size (Hodskinson, 1996).

The final issue with the roughness height is that it is not entirely clear which properties the roughness value is trying to represent. Rameshwaran *et al.* (2011) argue that a value of  $k_s$  calculated from  $D_{50}$  or  $D_{84}$  may be inaccurate because there is the additional issue of form roughness to consider (*i.e.* roughness caused by bedforms rather than individual grains). This would be expected to be a more pressing concern in large-scale simulations with cell dimensions that are larger than the size of the river bedforms. Alternatively, the work of Clifford *et al.* (1992) suggested that for grain roughness alone a relationship of  $k_s = 0.4D_{50}$  is more realistic than, for example,  $k_s = 3.5D_{84}$ , which accounts for both bed and grain roughness. Given that the mesh should account for the form roughness to some extent (depending on the cell size), determining precisely which components of roughness are to be represented by  $z_0$  (or  $k_s$ ) is far from straightforward.

With the focus on these limitations, though, there is a risk of overstating the importance of the roughness parameter. When a two-dimensional model is used it is known to be very sensitive to the roughness height (Lane *et al.*, 1999a). However, evidence has suggested that for three-dimensional CFD models the results are less sensitive to the chosen value, at least for relatively small-scale natural river simulations (Lane *et al.*, 2005; Ruether *et al.*, 2005). Therefore, providing the roughness height is of the right magnitude, it may be sufficient to represent the microscale topography.

Given the well-documented limitations with the traditional method of representing roughness, it is understandable that alternative methods have been investigated. Nicholas (2001) developed a method where the mesh near the bed is varied randomly based on a Gaussian distribution. Rameshwaran *et al.* (2011), meanwhile, used a combination of high-resolution topography with a partial solids treatment. This method allowed a much lower roughness value to be used and was found to work well with isolated, protruding particles. However, the alternative method which has been the

most well-tested and widely used to date is the use of a Mass Flux Scaling Algorithm (e.g. Lane *et al.*, 2002, 2004; Hardy *et al.*, 2005; Sandbach *et al.*, 2012).

#### 3.4.8 *The Mass Flux Scaling Algorithm (MFSA)*

Nicholas (2001) describes three separate scales of roughness: those at the bar, pool or riffle scale, the sub-grid scale roughness and an intermediate scale of pebble clusters larger than the cell size. All three scales must be accounted for in CFD simulations of natural rivers. The first of these, roughness at the pool and riffle scale, will largely be accounted for by the channel-scale topography (discussed in Section 3.4.9). However, the remaining two scales must be incorporated into the model using other methods.

Olsen and Stokseth (1995) outline three different methods of modelling bed roughness: the use of a very fine grid, incorporating roughness into a law of the wall function and their porosity method. The first of these methods is usually unfeasible due to the computational cost. The roughness value method, meanwhile, has some important limitations, as noted in the previous section. Therefore porosity-based approaches, such as the MFSA, are becoming increasingly popular.

The increasing interest in methods of representing the bed topography which do not require the grid cells to change in size (such as the MFSA) is a result of the well-documented issues with using a warped mesh and a roughness height value (Lane *et al.*, 2004). Additionally, there has been an interest in developing methods where the sub-grid scale topography affects mass continuity in the Navier-Stokes equations, something that does not happen with the roughness height (Hardy *et al.*, 2005).

The MFSA approach developed by Olsen and Stokseth (1995) provides a way of including the effect of the microtopography in the mass balance. The principle of the MFSA is that a regular grid is used, with each cell (and sometimes cell face) given a porosity value that represents the amount of the cell that needs to be blocked out. This research will test simulations where a single, volume porosity value is used as well as simulations which include porosity values for each of the cell faces. The porosity value is calculated from the proportion of the cell which is not blocked out by the bed, meaning that a value of one represents a cell that is completely filled with water. This is demonstrated in Figure 3.2.



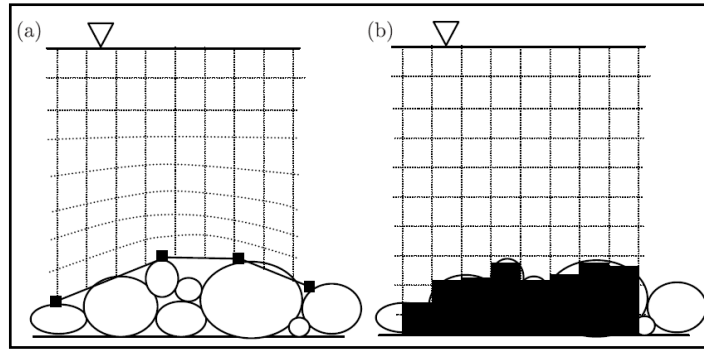


Figure 3.2: Comparison of the traditional method of representing topography by mesh distortion (a) with the Mass Flux Scaling Algorithm approach (b) from Hardy *et al.* (2005). In (b), the topography is represented to a high-resolution without the need to distort the mesh.

Studies using the porosity approach have also modified the momentum equations by scaling the porosity value with the drag term (*e.g.* Hardy *et al.*, 2005). This method works by identifying where the bed height increases in the direction of the flow and accounts for this by scaling the drag co-efficient in that direction (Lane *et al.*, 2002; Hardy *et al.*, 2005; Sandbach *et al.*, 2012).

The ability of the MFSA approach to represent sub-grid scale topography implies that high-resolution topographic data are required. However, Casas *et al.* (2010) demonstrated that the MFSA approach could be used along with artificial sub-grid scale topography generated using fractals (where a simple rule gives a small random variation at each iteration and eventually creates an irregular surface). As ever, the feasibility of this fractal-based method will depend on the spatial scales involved and so further research is required to assess its applicability on a wider range of natural rivers. However, it does open up the possibility of combining the MFSA with some form of stochastic representation of the microtopography.

The major advantage of the MFSA approach is its adaptability, as it can account for complex topography in all three dimensions, such as that found in river confluences (Lane *et al.*, 2004). Furthermore, it has recently been demonstrated to be robust for modelling the large Parana-Paraguay river confluence on the Argentina/Paraguay border (Sandbach *et al.*, 2012). It can do this without having to modify the mesh in any way and therefore reduces the probability of numerical stability problems. Although no single method of representing roughness is perfect, at present the MFSA approach seems to have fewer limitations than the traditional approaches (Miori *et al.*, 2012; Sandbach *et al.*, 2012).

## 3.4.9 Representing Channel Planform in CFD

Modelling straight, regular channels in CFD can be done using a simple, uniform, hexahedral grid, but this is not possible for river units with more complex planforms. The channel planform can be an important factor for the flow in channels with shallow, unconsolidated banks (Nicholas and Sambrook Smith, 1999), meanders (Ferguson *et al.*, 2003) and river confluences (Lane *et al.*, 1999b; Huang *et al.*, 2002; Biron and Lane, 2008).

In many cases, the traditional solution to simulating irregular planforms is to use Boundary Fitted Co-ordinates (BFC) (*e.g.* Weerakoon *et al.*, 2003; Ferguson *et al.*, 2003). With a finite volume discretisation, BFC fits the nodes of the mesh to the topographic variation and therefore setting up the model takes much longer, adding to the simulation time (Bradbrook *et al.*, 2000b). Furthermore, with BFC approaches the mesh is distorted in a way that can affect the numerical stability (Lane *et al.*, 2002; Hardy and Lane, 2004; Hardy, 2008). For minor distortions in the channel shape (and thus the mesh) instability should not be an issue, but if the planform is more irregular or has very shallow areas close to the bank, the near-bank cells can become highly distorted or very small (Nicholas and Sambrook Smith, 1999).

For river confluences, an additional issue is created as two separate channels have to join. One option is to use multiblocking (Figure 3.3), where two separate meshes are created and numerically linked (Huang *et al.*, 2002; Biron and Lane, 2008). As can be seen in Figure 3.3, this creates distortion in the mesh even for the simplest confluence planform. Therefore, whilst a river confluence can be represented in this way, it is still preferable to use a single grid if possible (Lane *et al.*, 1999a).

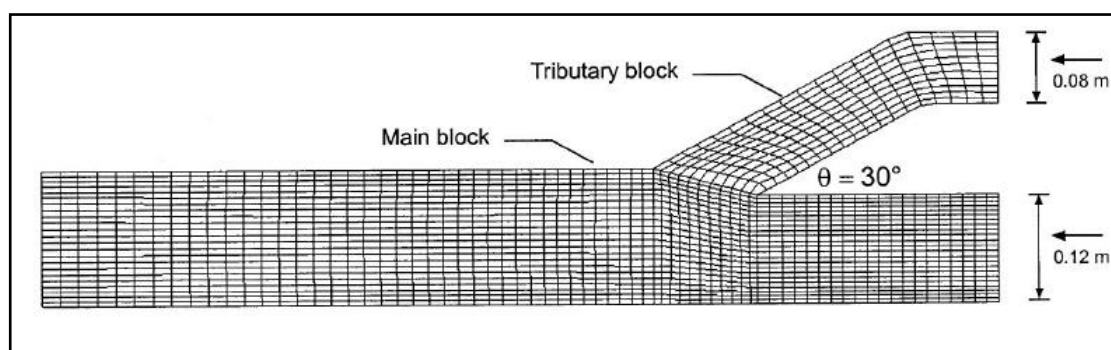


Figure 3.3: Diagram showing the mesh used in a simulation of a simple, asymmetric,  $30^\circ$  confluence (Biron *et al.*, 2004a). BFC allows the main channel to widen downstream, whilst a separate mesh block is used to attach the tributary.

In situations where the mesh would be particularly distorted, an alternative is to use an unstructured form of the mesh with tetrahedral elements rather than the standard hexahedral cells (*e.g.* Nicholas and Sambrook Smith, 1999). However, similar issues with numerical stability may arise, so it is unclear whether such an approach will result in a significant improvement in model performance.

In the last decade, research has focused on using the Mass Flux Scaling Algorithm (MFSA) approach described in the previous section for representing complex river planforms (Lane *et al.*, 2004). Using the MFSA approach can overcome some of the issues surrounding the application of BFC and multiblocking by reducing cell distortion. Furthermore, in situations where the banks are more irregular, such as on steeply sloping braid plains, the MFSA approach removes some of the difficulty associated with defining the limits of the computational domain. Therefore, the development of the MFSA approach has become a useful tool in CFD simulations of natural rivers.

#### 3.4.10 Representing the Free Surface

In CFD simulations, the free surface is important as it is both an unknown and a boundary condition (Rodriguez *et al.*, 2004). The standard approach at the free surface in CFD models is to use a rigid lid (Figure 3.4b), which means the water surface elevation is fixed at a specific level. When using a rigid lid approach, variations in pressure in the top cell will represent the water surface elevation and therefore some of the effects of this will be accounted for in the momentum equations (Lane *et al.*, 2004). However, there will be no change in the continuity equation and therefore the principle of mass conservation will not be adhered to.

Most numerical modelling uses a rigid lid approach (Bradbrook *et al.*, 2000a), which in many cases is a fair assumption. Nicholas (2001) found very little difference in the pressure values at the rigid lid in research on the River Exe and River Culm in Devon, whilst Constantinescu *et al.* (2011) justified the use of the rigid lid approach for their river confluence because of its low Froude number. However, if the rigid lid is used to simulate a flow with significant superelevation, the energy that raises the water surface will instead cause additional, unrealistic secondary flows to be simulated (Keylock *et al.*, 2005). The tendency for superelevation to occur at river confluences means, therefore, that a rigid lid assumption is not ideal (Bradbrook *et al.*, 1998; Biron

and Lane, 2008). As such, a number of alternative methods have been developed (as shown in Figure 3.4).

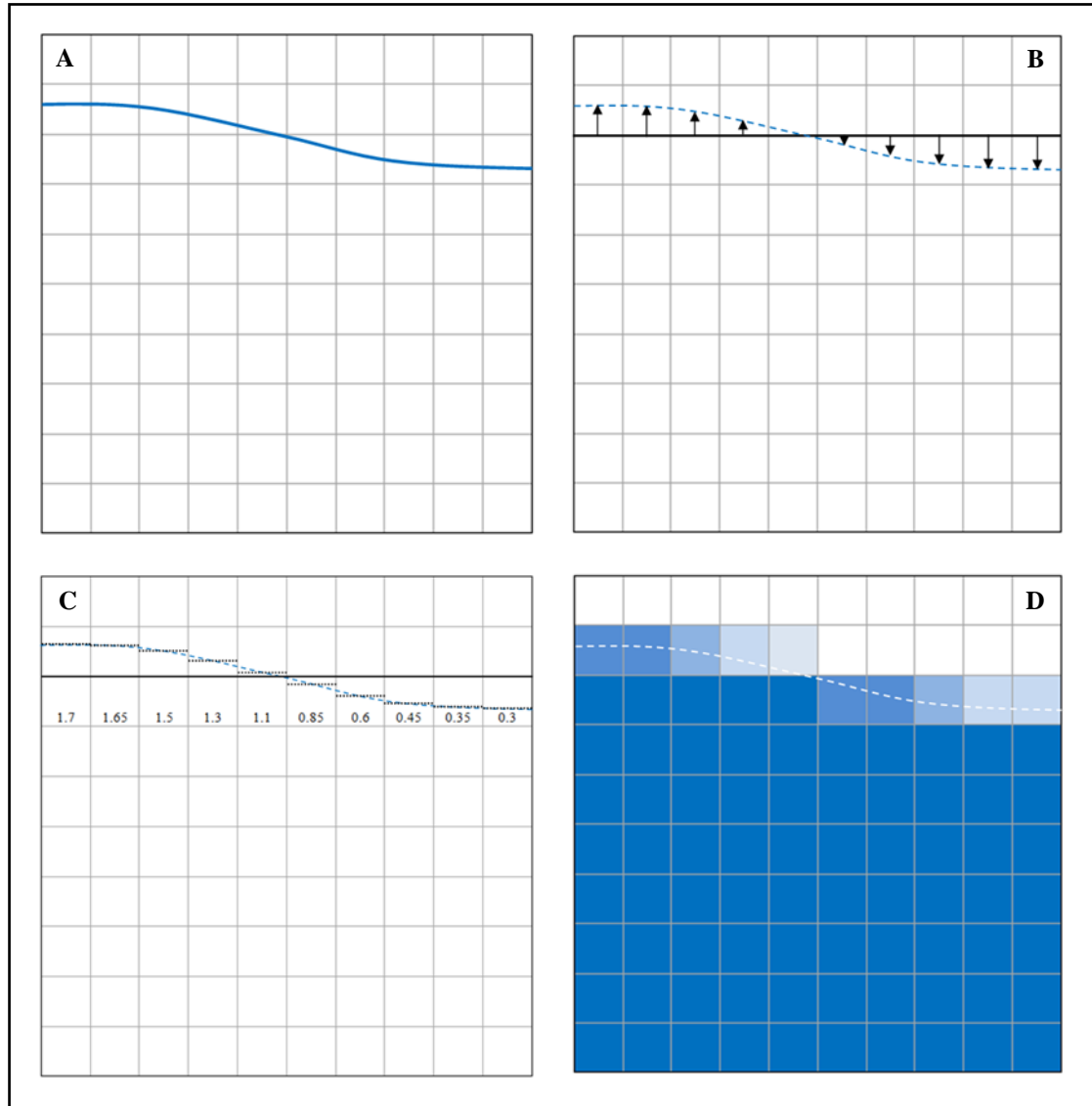


Figure 3.4: Diagram showing different possible treatments of the free surface. The actual water surface is shown in (a), with the rigid-lid approach given in (b). The arrows in (b) represent the force acting on the rigid lid. Diagram (c) shows how porosity values can represent this water surface, whilst (d) demonstrates a VoF (or similar) approach. Darker shading in diagram (d) indicates a greater volume of water in the cell.

The first option is to modify the grid in response to changes in the pressure (*e.g.* Huang *et al.*, 2002; Tritthart and Gutknecht, 2007; Fischer-Antze *et al.*, 2008). The pressure at the rigid lid is used to determine the water superelevation or depression and then the mesh is modified to take this into account. Although this will represent the water surface elevation more accurately, the process of stretching or adding cells to the

domain during the model run is not straightforward and can cause problems for the numerical stability of the model (Bradbrook *et al.*, 2001).

The second option, shown in Figure 3.4c, is to use a porosity-based MFSA approach similar to the flood modelling methods of Bates and Anderson (1993), where a value between zero and one was used to represent the inundation extent. In this method, the top cell in the domain is given a porosity value depending on the amount of water in it, with a value greater than one indicating superelevation. This approach was adapted to river confluences from the work of Spalding (1985) by Bradbrook *et al.* (1998).

The porosity approach has one major advantage over the standard rigid lid approach in that by giving an effective thickness for the top cell, it ensures more accurate values are in the mass conservation equations (Lane *et al.*, 2004). This method has been used and found to be dependable in a number of fluvial CFD studies (*e.g.* Lane *et al.*, 1999a; Lane *et al.*, 2002, 2004; Biron *et al.*, 2002; Ferguson *et al.*, 2003; Hardy and Lane, 2004). The only problems of note have occurred when the porosity values become too high (Bradbrook *et al.*, 2000a, 2001).

However, as Rodriguez *et al.* (2004) note, methods where minor adjustments are made to the rigid lid are fine when small changes are needed, but they are less reliable when the flow is supercritical or there are large changes in water surface elevation. In such situations, it is better to use an explicit representation of the free surface. Volume of Fluid (VoF) approaches provide this by solving the Navier-Stokes equations for both air and water (Ma *et al.*, 2002). Each cell is given a value to represent the extent to which it is full of water and from this the water surface can be calculated. To date, there are very few river confluence studies that have used a full free surface model, with most preferring either a rigid lid or porosity approach. However, if the interest is in steeply sloping upland river confluences that have supercritical flows, the use of a more realistic representation of water surface flow may become a necessity.

#### 3.4.11 Summary of Auxiliary Models within CFD Simulations

This section has set out the various methods available for representing channel planform, topography, roughness and free surface elevation within CFD simulations, as well as the range of turbulence models available. When setting up numerical simulations of natural rivers, it is necessary to determine the most appropriate methods for the study in question. At present, it is not computationally feasible to combine Direct

Numerical Simulation of turbulent structures with the more complex representations of the channel morphology and water surface elevation. Most studies in fluvial geomorphology introduce simplifications in one or more of areas, depending on the aims of the research. Those studies where the primary focus is on the dynamics of individual flow structures (*e.g.* Constantinescu *et al.*, 2012) tend to prioritise a complex representation of the turbulence over the other auxiliary models. Other studies, meanwhile, focus on the effects of the bed topography on the flow field (*e.g.* Hardy *et al.*, 2005) and therefore the representation of the sub-grid scale topography becomes the main priority.

It is therefore a necessary part of numerical modelling to determine the key research aims and the most important factors in driving the flow processes for a given study site. This can then be used to inform the choice of auxiliary models. Section 3.7 will set out and justify the auxiliary modelling methods to be used in this thesis. However, given that the focus of this research (as set out in the research question in Section 1.5) is on steeply-sloping upland river confluences, the use of an explicit free surface model will be the primary requirement for the numerical simulations. The choice of turbulence model and method of representing the topography will therefore take this into consideration.

### **3.5 Good Practice in Numerical Modelling**

The increase in popularity of CFD applications has resulted in a greater emphasis on ensuring good practice in the numerical modelling process. In particular, this includes standards for model verification and validation to help ensure the validity of the model being used. Model validation and verification are important components of any Computational Fluid Dynamics (CFD) study and many journals now specify verification standards which must be satisfied for papers to be published (Lane *et al.*, 2005). However, this is still an area in the field which is often overlooked or given minimal attention by researchers (Stern *et al.*, 2006).

Model validation involves assessing the extent to which a numerical model (and the associated computer code) is capable of simulating a real system (Oberkampf and Trucano, 2002). This usually involves a comparison with data collected either in a laboratory or in the field. Lane *et al.* (2005) argue that field validation of CFD models is particularly important due to there being limits in what the laboratory results can show.

It is for this reason that this thesis concentrates on field studies to provide model validation data.

The process of model verification, on the other hand, is used to assess whether the model code is correctly solving the underlying equations and the uncertainty caused by the discretisation process (Oberkampf and Trucano, 2008). The model verification process can be split into code verification, which attempts to remove bugs from the code, and solution verification, which aims to find the error in a single simulation (Roy, 2005). This section addresses both of these aspects of model verification.

### 3.5.1 Code Verification

Code verification involves attempting to remove any errors in the programming of a computer model (Oberkampf and Trucano, 2002). Naturally this is a task which must be undertaken before the code is put to use. In CFD, this means comparing the model output to highly accurate or exact solutions of the Navier-Stokes equations. The latter are rare, but there are a few examples which exist and are well used for code verification (Kirkman and Metzger, 2008). If exact analytical solutions are not available or insufficient, then highly accurate numerical solutions of ordinary differential equations are the next best option, followed by numerical solutions of partial differential equations (Oberkampf and Trucano, 2008). An alternative method is the Method of Manufactured Solutions (MMS) described by Roy (2005). This involves determining an exact solution to the partial differential equations (PDEs) first and then modifying the governing equations to fit this solution. The performance of the numerical model can then be compared to this manufactured solution (Roy, 2005).

Part of the code verification process should involve determining the formal order of accuracy (also referred to as the order of convergence) of the model. This can be done by comparing the discrete form of the PDEs to the PDEs themselves. One of the criteria for the publication of CFD research in the ASME journals is that the model should be second order accurate spatially (Lane *et al.*, 2005) and so it is necessary to confirm the formal order of convergence before the package is released. This is important as sensitivity analysis by Ruether *et al.* (2005) suggests that model performance improves more by using a second order scheme than by increasing the grid resolution.

In the case of commercial codes, although sufficient code verification pre-release might be expected, independent verification tests have shown some codes to perform poorly (Oberkampf and Trucano, 2008). Nevertheless, whilst it is sensible to treat model results with caution, if any research is to be conducted using numerical models, it is necessary to place a certain amount of trust in the code, at least until there is concrete evidence of the code being invalid.

### 3.5.2 Solution Verification

With the range of commercial CFD codes available and the level of testing that these codes are expected to undergo, it is considered reasonable to presume that code verification has been satisfactorily undertaken on the CFD solver. However, it is still important to verify any additional code entered into the model by the user, such as that required to implement the MFSA.

Nevertheless, for the vast majority of the time it is the verification of the particular solution which should concern the modeller. Solution verification should ideally be undertaken for each individual simulation to determine an estimate of its numerical accuracy (Oberkampf and Trucano, 2008). Three potential sources of error in a CFD simulation identified by Roy (2005) are round-off error (due to the limited number of digits which can be stored by the model), iterative errors (which occur with all iteration-based methods) and truncation errors (as discrete algebraic equations are used to approximate the PDEs). Round-off error is generally considered inevitable and not addressed by researchers (Oberkampf and Trucano, 2008). Therefore, solution verification is concerned primarily with iterative errors, grid resolution errors and time step errors (Stern *et al.*, 2006). As such, the principle of solution verification is to confirm that the model has converged iteratively, spatially and temporally onto a particular solution.

To determine whether iterative convergence has been achieved, it is common to assess the residuals, which will tend to zero as the solution converges and are found by calculating the remainder when the current solution is entered into the discrete equations (Roy, 2005). Celik *et al.* (2008) recommend that the residuals should be shown to have decreased by at least three orders of magnitude before grid and time step convergence is tested. Iterative convergence is especially important in time-dependent solutions as any



iterative errors will increase through subsequent time steps (Oberkampf and Trucano, 2002).

As noted in Section 3.3.2 on discretisation, the numerical methods used to solve the Navier-Stokes equations require time and space to be split into discrete elements. The Lax Theorem suggests that as the mesh size (or time step) tends to zero, the solution will tend towards the true solution of the PDEs (Hardy *et al.*, 2003). For all meshes it is preferable that both the time and grid resolution are sufficiently small that any increase in resolution has a negligible effect on the results. At this point, the solution is considered to be in the ‘asymptotic region’ where the actual order of convergence is approximately constant as the grid or time step size is reduced (Oberkampf and Trucano, 2002, 2008). A simplistic way of testing this is to compare the results when the same simulation is run at different time step and grid resolutions. However, this becomes much more complex for grid resolution if an irregular, boundary-fitted method is used. The use of the MFSA therefore has an additional advantage in that by representing irregular topography within a regular grid, it is possible to conduct grid independence tests (although changes in grid resolution will still lead to differences in the boundary conditions). The principle of grid (and time step) independence tests is to quantify the error due to the discretisation process. There is a considerable body of research on conducting tests for this, especially for the grid resolution.

It would be naïve to believe that it is possible to have a fully converged grid when working on most real simulations. Indeed, Lane *et al.* (1999a) note that grid independence may not be achievable on simulations of gravel-bed rivers (due to the more complex topography). Additionally, computing resources will probably mean that grid-independent solutions are not feasible. Therefore, every effort should be made to reduce and quantify the discretisation error. As there is no straightforward way of getting a traditional statistical error band in CFD studies, Roache (1994) developed the Grid Convergence Index method.

### *3.5.3 The Grid Convergence Index*

The Grid Convergence Index (GCI) is based on the Richardson extrapolation method for estimating the error due to the resolution of the grid. A general form of the Richardson extrapolation is given by Roache (1998):

$$f_{exact} \cong f_1 + \frac{f_1 - f_2}{r^{p_o} - 1} \quad (3.15)$$

where  $f$  is the value of the solution at a particular grid cell (with subscripts 1 and 2 denoting the fine and coarse grids respectively),  $r$  is the grid refinement ratio (*i.e.*  $r = 2$  if the grid resolution has been doubled/halved) and  $p_o$  is the order of the solution. This can be rearranged to give the estimated error (as a fraction),  $E_1$ , as shown below:

$$E_1 = \frac{\varepsilon_f}{r^{p_o} - 1} \quad (3.16)$$

where:

$$\varepsilon_f = \frac{f_2 - f_1}{f_1} \quad (3.17)$$

Roache (1998) argues that the value of  $\varepsilon_f$  would be seen as an acceptable error band by most, providing that the solution is second order accurate and the grid resolution has been doubled (*i.e.*  $r = 2$ ). The GCI aims to provide a way of standardising the value of  $\varepsilon_f$  so that a comparable error value can be given for solutions which have variable  $p_o$  and  $r$  values (Roache, 1994). As such, the GCI for the fine grid is given by (from Roache, 1998):

$$GCI_{fine} = F_s \left( \frac{|\varepsilon_f|}{r^{p_o} - 1} \right) \quad (3.18)$$

If the interest is in the GCI for the coarser grid, then the equation is:

$$GCI_{coarse} = F_s \left( \frac{r^{p_o} |\varepsilon_f|}{r^{p_o} - 1} \right) \quad (3.19)$$

The co-efficient  $F_s$  is a ‘safety factor’, for which Roache (1994) uses a value of 3, although he later accepts that  $F_s = 1.25$  would be sufficient in grid refinement studies

with at least three grids used (Roache, 1998). This is because the use of three grids means it is possible to obtain a better estimate of  $p_o$ , the observed convergence rate (rather than using the theoretical formal convergence rate). Providing  $r$  is constant then Equation 3.20 can be used to give an estimated value of  $p_o$  (Roache, 1997).

$$p_o = \frac{\ln \left( \frac{f_3 - f_2}{f_2 - f_1} \right)}{\ln r} \quad (3.20)$$

The GCI can be determined for a single point, a cross-section or an entire reach (Lane *et al.*, 2005). However, as the GCI is designed to give a value for a single variable at a specific point, a method such as the Cumulative Area Fraction Error (CAFE) curves of Luetlich and Westerink (1994) may need to be used to give the percentage of the domain exceeding a certain error. In general, though, the GCI has proven to be very useful for quantifying the uncertainty in CFD solutions due to the grid resolution (*e.g.* Hardy *et al.*, 2005; Sandbach *et al.*, 2012; Miori *et al.*, 2012).

### 3.6 A Review of the CFD Methodology

CFD models are often considered to be the most physically-based hydraulic models available. However, the solutions obtained from them can still vary quite considerably depending on factors such as the model code, the methods used to simulate turbulence, the representation of the topography, computational cost and data quality.

In general, it might be expected that CFD codes will give acceptable and similar solutions of the governing equations. However, research by Tritthart and Gutknecht (2007) on a river bend found variations in the predicted superelevation levels and velocity values from the FLUENT, SSIIM and RSim 3D models, even though they used the same boundary conditions and were all grid-independent. This demonstrates that whilst commercial codes may be considered to be generally reliable, there is always some uncertainty in numerical solutions of the Navier-Stokes equations. Therefore, whilst a full analysis of the effects of different model codes on the solution is beyond the remit of this research, it is important to take note of the uncertainties caused by the choice of CFD code.

Although CFD models are considered to be physically-based, the reality is that they contain semi-empirical methods for both the turbulence and wall roughness (Nicholas and Sambrook-Smith, 1999; Nicholas, 2001). In addition, when modelling complex flows, the method of accounting for the free surface elevation also becomes important (Rameshwaran *et al.*, 2011). The optimal auxiliary model to use in each of these cases is not always clear and it is often more a question of modelling philosophy than a clear difference in performance.

Computational expense is a consideration in almost all CFD modelling and inevitably results in compromises in the methods used. This is particularly evident in the choice of grid resolution, where a halving in the cell size will result in an eightfold increase in total cells and thus a similar increase in the time required to achieve convergence. This becomes particularly problematic when attempting to test grid-independence, as it may be unfeasible to run simulations with significantly finer grids than those used for the research. Therefore, it is rarely possible to develop new applications of CFD to natural rivers and obtain estimates of the uncertainty caused by the choice of grid resolution for each separate simulation.

Finally, in any model simulation, the quality of the boundary conditions and input data will have an important impact on the solution. In CFD models of natural rivers, the required input data include three-dimensional velocity data (plus an estimate of turbulence intensity), topography data, roughness data, information on the position of the water surface edge and water surface elevation data (Lane *et al.*, 2000). For the upstream inlets, it is possible to allow the flow field to resolve itself from a uniform input, but this will take a number of cells downstream to work and so may need a separate model run to determine (Bradbrook *et al.*, 1998). Obtaining as much high-quality data as possible is a necessity because even a fully verified numerical solution will have significant errors if there is a large amount of uncertainty in the boundary conditions. Therefore, the field methodology should be devised with a careful consideration of the requirements of the numerical models being used. The field methodology for this research is discussed in detail in Section 3.8.

### **3.7 Numerical Methodology for This Thesis**

The modelling approaches used in this research have been determined by the thesis objectives in Section 1.5, which define the priorities for the study, and the general

modelling philosophy set out in Section 3.2. It has already been noted that for river confluences, the highly complex and three-dimensional nature of the flow means that CFD becomes the most appropriate choice for numerical modelling. The use of the commercial CFD code PHOENICS in this thesis means that the Navier-Stokes equations are solved using the SIMPLEST algorithm on a finite volume grid. This is a well-tested approach used in many applications of CFD to river confluences (*e.g.* Bradbrook *et al.*, 2001; Biron *et al.*, 2004a; Sandbach *et al.*, 2012). Beyond that, however, there are a number of options for modelling turbulence, representing the channel topography at a range of scales and accounting for the free surface (as set out in Section 3.4). While it might seem preferable to use the most complex (and therefore by implication most physically realistic) methods available, the computational requirements of this mean that it is almost certainly not possible for studies of natural rivers.

The major focus for the numerical modelling of flow, as set out in Objective 2 in Section 1.5, is to improve the understanding of the flow processes operating at steep river confluences. Therefore, an accurate representation of the free surface elevation is the first priority when choosing the auxiliary models. As such, the choice of turbulence model and the representation of the topography will depend partly on the computational requirements of this free surface model. Given that the steep, upland river confluences of interest to this study tend to be characterised by highly variable gravel beds, topographic steering of the flow is likely to be more important to the overall flow field than the development of large-scale turbulent eddies (Sandbach *et al.*, 2012). Therefore, for the numerical simulations in this thesis, a robust and physically realistic representation of the bed topography and channel planform is a greater priority than the direct simulation of individual turbulent eddies.

With respect to the representation of the free surface, the rigid lid or porosity-based approaches favoured in most river confluence studies become less applicable as the gradients become steeper. This will be explored in detail in Chapter 5, where it will be demonstrated that the standard approaches are insufficient when the water surface slope increases. As such, an explicit free surface model will be used to determine the water surface elevation and satisfy mass conservation. Within the PHOENICS code used in this thesis, the explicit free surface model is referred to as a Height-of-Liquid (HOL) model. A full description of the PHOENICS HOL model will be provided in Chapter 5. However, for the purpose of selecting an appropriate treatment of the

turbulence and channel topography, it is necessary to acknowledge that simulations using the HOL model need to be run in time-dependent mode because there are significant problems with achieving convergence in steady-state mode (CHAM, 2013). As a result, the choice of other auxiliary models must take into account this additional computational cost.

As noted above, a physically realistic and robust representation of the channel morphology is the second priority after the free surface model. Representing the complex topography of upland rivers can be tricky, as it introduces the risk of numerical instability if the computational mesh becomes excessively warped. The Mass Flux Scaling Algorithm (MFSA) approach has been proven to be a robust and stable method of representing complex topography in a number of fluvial geomorphology studies (*e.g.* Hardy *et al.*, 2005; Miori *et al.*, 2012; Sandbach *et al.*, 2012). Given the modelling philosophy set out in Section 3.2, this is considered to be the optimum choice for the CFD modelling in this thesis. In addition, the MFSA approach can be seen as complementary to the HOL free surface method, as both methods allow for cells to be partially filled with water in order to account for complex topographic variations within a regular mesh framework. The use of the MFSA should therefore satisfy the requirement for an accurate representation of the complex river confluence morphology without compromising either model stability or the implementation of the HOL free surface model.

When it comes to the variation of bed topography at the smallest scales, the MFSA will represent some of the sub-grid scale roughness. However, the nature of the beds (gravel and cobble) and the relatively large cell size (on the order of centimetres) means that there will still be a significant roughness component to account for. A fully rough law of the wall model with a specified roughness height (which can be determined in the field) is therefore deemed to be the most appropriate option in these circumstances.

Given the scale of the CFD modelling in this thesis, resolving individual turbulent eddies is not a priority. Therefore a two-equation model which determines the effects of turbulent kinetic energy on the mean flow field is considered sufficient. There are a number of two-equation options available, but this thesis will use the RNG  $\kappa$ - $\epsilon$  model, as it has been well tested in CFD modelling of natural rivers (as noted in Section 3.4.3). It is therefore considered to be a robust method for applications of CFD to river confluences. This choice of turbulence model follows the modelling philosophy set out

in Section 3.2, with the well-tested, simpler model being preferred until such time as it is demonstrated to be insufficient.

Therefore, in summary, the CFD modelling used in this thesis will be run in time-dependent mode with the HOL free surface model. The topography at the medium and larger spatial scales will be represented using the MFSA within a regular mesh, whilst a fully rough law of the wall treatment will account for the topographic variability at scales much smaller than the cell size. Finally, the RNG  $\kappa$ - $\epsilon$  model will be used to simulate the effects of turbulence on the momentum equations.

### **3.8 Field Methodology**

In Section 3.6, it was noted that the performance of numerical models is inextricably linked to the quality of the boundary conditions and input data. In many CFD applications, these models are validated using data obtained in laboratories. However, as Lane *et al.* (2005) argue, when it comes to simulations of natural rivers there are limits to the insights that laboratory experiments can provide and so there is a need to increase the amount of field data available for model validation. Field data would be expected to have larger uncertainties in the results than would be obtained in a controlled laboratory environment. However, the major advantage of field experiments is that it removes scaling issues (Lane *et al.*, 2005).

The use of studies of natural rivers means that the methodology must be carefully considered. The data requirements for the study must be balanced with the feasibility of using different methods at the individual sites in question. Additionally, the sampling strategy must reflect the data requirements, the speed at which data can be collected using any given method and the time available to collect the data in a dynamic system. As Lane *et al.* (1999a) note, in field studies it takes time to collect a spatially and temporally detailed dataset, during which time the processes operating in the system can change significantly. This is a particular problem in more dynamic fluvial environments such as mountain valley braid plains (*e.g.* Ashmore and Parker, 1983; Ashmore *et al.*, 1992). It is therefore important to determine the appropriate balance between the desire for detail and the need to obtain data before the system has experienced significant change. This must be done for each individual field site, with reference to the aims of the research and the reason for selecting that specific field site. The criteria set out in Section 1.6 resulted in the selection of two field sites for which a

methodology must be determined. The first, at Moor House Nature Reserve in the North Pennines, was chosen in order to provide detailed three-dimensional flow data on more stable, upland river confluences. This site also benefitted from the presence of an Environment Agency gauging station on Trout Beck.

The second site was a braid plain on the Borgne d'Arolla river in the Valais canton in Switzerland. This site was selected to provide examples of highly dynamic, steep river confluences where particle transport is active and flow is near-critical or supercritical. The selection of this site would enable particle tracks to be obtained in real time for discharges measured *in situ*.

The different characteristics of the two sites mean that the methodology for each will be subtly different. In most cases, the Moor House site, being more stable and less dynamic, has much more time available for the collection of field data. The sampling regime can therefore be more detailed and the data do not have to be collected simultaneously. The Arolla sites, by contrast, will see significant changes in morphology and discharge over the course of a few hours and therefore the methodology must reflect this. The limited amount of time available for data collection is not unusual in mountainous environments such as these, with Ashmore and Parker (1983) observing changes to the scour holes at their confluences during the measurement process. In addition, Ashmore *et al.* (1992) collected their data in approximately two hours around peak diurnal discharge in order to limit the discharge variability and found that by the following day their first confluence site had been infilled.

In order to provide boundary condition and input data for the numerical modelling, it is necessary to obtain three key datasets. These are topographic data, flow data and information on bed roughness. In addition, particle tracking data must be collected to investigate the sediment dynamics at upland river confluences and to provide validation data for the reduced-complexity particle transport model (as identified in the objectives in Section 1.5). This section will examine the different methods which could be used to obtain each of these four datasets. Within each subsection, the methods available for obtaining data of that type will be explained, along with the criteria and acceptable error margins for each dataset. These requirements will vary depending on the field site and the quality of data required in the criteria of Section 1.6. There will then be an analysis of the methods which can fulfil these requirements and the methods considered most appropriate for this research. The



final part of the section will summarise the methods to be used at both the Moor House and Arolla field sites.

### 3.8.1 *Methods for Obtaining Topographic Data*

A good representation of the channel morphology is an important boundary condition for any numerical model of a natural river. However, the resolution of the topographic data required for numerical modelling will depend on the channel dimensions and the nature of the bed, as well as the best feasible spatial discretisation. In short, it is clearly unnecessary to account for every sand grain when modelling a large lowland river. For each site it is therefore necessary to determine the minimum requirements for DEM quality. The overall quality of the DEM will depend on a combination of the individual point quality, the point density and the point distribution (Lane *et al.*, 2003). Acceptable bounds for each of these must therefore be determined before a decision is made on which method to use. The quality of the point distribution is difficult to quantify as it refers more broadly to how well the individual points represent the topographic highs and lows. Nevertheless, a good point distribution which picks out all of the breaks of slope will increase the DEM quality. Therefore, increases in point density would not necessarily lead to a significant increase in DEM quality at sites where the breaks of slope are easily identified.

In the case of the Moor House confluences, low flow channel widths and depths are of 3-10m and 0.2-0.5m respectively. The size of the confluence means that grid cells in the numerical model will be of the order of centimetres rather than millimetres. Therefore, although large boulders would need to be surveyed accurately because of their impact on the flow field, the elevation model will not include the vast majority of the individual gravel and cobble particles. This means that the average point spacing and individual point error of the survey does not need to be on the scale of millimetres. The work of Brasington *et al.* (2000) demonstrated that for an upland, vegetated braid plain in the UK (the River Feshie, Scotland), minimum point densities of around 1pt/m<sup>2</sup> were necessary to obtain a reliable representation of the major breaks of slope. Given that channels on the River Feshie site are approximately twice the width (10-20m) of those at Moor House Nature Reserve, this would imply a minimum point spacing of 0.5m (point densities of 4pts/m<sup>2</sup>) at the Moor House field sites. However, as noted in Section 1.6, this site was specifically chosen in order to obtain a high-quality dataset on

a more stable river. Therefore, although a point spacing of 0.5m will be considered the minimum for the Moor House confluences, the aim is to achieve an average point spacing of 0.25m (point densities of 16pts/m<sup>2</sup>). However, point densities would be expected to follow a distribution whereby the values are higher in the centre of the channel and lower on the banks. In terms of the mean individual point errors, these should be at most of the same order of magnitude as the minimum feasible grid cell size. Given that this will be on the order of centimetres, mean individual point errors of 0.05m for each site are considered acceptable.

The Arolla confluences, meanwhile, are narrower (channel widths mostly in the range 2-4m) and shallower (maximum depths of 0.3m) with a bed that is largely in motion, even in low flows. This is to be expected, as the site was chosen for its topographic dynamism rather than the ability to obtain high-resolution boundary condition data (see Section 1.6). Nevertheless, it is still important that the DEM represents the major breaks of slope and any large clasts which will affect the flow field, otherwise the quality of the numerical modelling will be adversely affected. The fact that the bed is in motion in most parts of the channel means that topographic variations on the scale of a few centimetres (*i.e.* the  $D_{25}$  value) become largely irrelevant. In addition, although grid cell sizes will be smaller than for the Moor House confluence simulations, they will still be a few centimetres in width. Therefore, in these circumstances, the focus must be on obtaining a good point distribution, with the same magnitude of mean individual point errors as for the Moor House data. In terms of point density, this would be expected to vary depending on the complexity of the bed and the presence of large clasts. However, there will still be a minimum point density below which the representation of the topography will become compromised. Working on the proglacial braid plain of the Haut Glacier d'Arolla (which can be considered a similar site to that used in this study), Lane *et al.* (1994) found that this minimum point density for their Total Station surveys was in the region of 3.5pts/m<sup>2</sup>. Therefore, the minimum point density criterion for the Borgne d'Arolla field site is set at 4pts/m<sup>2</sup>.

There are many different methods available for obtaining elevation data at fluvial field sites. Approaches such as photogrammetry (*e.g.* Lane *et al.*, 1994) and terrestrial LiDAR (*e.g.* Hodge *et al.*, 2009) can provide high-resolution, high-quality data. However, their use of light means they are limited when it comes to surveying underwater topography, as refraction has to be accounted for. Research by Butler *et al.* (2002) demonstrated that through-water photogrammetry is possible on shallow (water

depths of around 0.2m) natural rivers, providing the water surface is made to be flat and reflection from the sun is minimised. However, this method would be unlikely to work reliably on the highly turbulent water surfaces of the Borgne d'Arolla braid plain or the deeper, peat-stained waters of Trout Beck. Furthermore, the resolution that these methods provide is significantly higher than that which can be represented in the numerical modelling. As such, the most appropriate surveying methods for this research are considered to be Real Time Kinematic (RTK) differential GPS (dGPS), as recommended by Brasington *et al.* (2000), and electronic tacheometry using a Total Station, as used for underwater sections by Lane *et al.* (1994).

The principle of dGPS is that whilst determining the position of a receiver from the coarse GPS signal results in inaccuracies, many of these inaccuracies can be reduced if more than one receiver is used (Brasington *et al.*, 2000). The dGPS therefore consists of a base station which is located over a known point, and a rover which is used to take the survey. With the RTK method, the real-time base station position is transmitted to the rover using a radio signal, meaning that it can calculate its relative position to centimetre precision. The individual point data will therefore have error values of around 0.01-0.02m (Leica, 2004a), with the accuracy improved if a larger number of satellites are visible and evenly spread across the sky (Rennie and Rainville, 2006).

Total Stations, on the other hand, provide a means of electronic distance measurement (Keim *et al.*, 1999). A prism is attached to the top of a detail pole and the Total Station records the angles (vertical and horizontal) and distances (using a laser pulse) to the prism. Naturally this requires the prism to be visible at all times. If this is not possible, then a series of control points should be set up to provide a reference between surveys (Keim *et al.*, 1999). Total Stations are capable of centimetre accuracy and can have a range of several kilometres, depending on the individual prism being used (Leica, 2004b). However, problems will also be caused if the prism gets too close to the Total Station, with Leica (2004b) specifying a minimum measuring distance of 1.5m (although previous experience in the field has found anything less than 5m becomes difficult). Total Station surveys are considered to be time consuming (Keim *et al.*, 1999; Westaway *et al.*, 2001), although recent technological advances have improved this (Rumsby *et al.*, 2008). It is also now possible to conduct the survey single-handed with a handset on the detail pole linked by radio to the Total Station itself, as shown in Figure 3.5.



Figure 3.5: Photograph showing the collection of topographic data using electronic tacheometry. The base station tracks the position of the prism (*inset*) and can be controlled remotely using a handset attached to the detail pole. The downstream channel in this picture has an approximate width of 2m, as scaled by the field assistant in the photograph.

The two major advantages of using dGPS rather than electronic tacheometry are its faster speed and the lack of a line of sight requirement, which gives better performance in poor or dark conditions (Higgitt and Warburton, 1999; Brasington *et al.*, 2000). However, as the performance of the dGPS is related to the quantity and spread of the satellites (Rennie and Rainville, 2006), accuracy may be reduced in mountainous environments where the steep valley sides reduce the visible area of sky.

The decision about which method to use at each field site was taken by considering the advantages and limitations of the different methods and the data quality requirements set out in this section. Both the dGPS and Total Station methods will provide individual point data that are accurate to within 0.01-0.02m, so the decision was largely based on the most reliable and fastest method for each site.

For the Moor House confluences, it was decided that the RTK dGPS method would be used to obtain point data for the Digital Elevation Models (DEMs) because of the potential for faster data collection. Although the site was located in an upland area, the surrounding hills were not considered to be steep enough to cause problems with the

satellite signals. Therefore, topographic data from the Moor House sites were obtained using a Leica GPS1200 system.

The site on the Borgne d'Arolla braid plain, by contrast, is located in a valley with steep sides and a much more restricted view of the sky. Previous experience of research on the site has been that the GPS signal was particularly unreliable in the afternoons. As a result, the marginal decrease in speed that is encountered with the Total Station method was deemed to be far less problematic than the possibility that it might not be possible to collect data at all using dGPS. Therefore, topographic data at the Arolla site were obtained using a Leica TPS1200 Total Station.

### 3.8.2 Flow Data

Obtaining good quality flow data is important for both inlet boundary conditions and validation data. There are a number of different methods available for measuring flow velocities in one, two or three dimensions using at-a-point or spatially distributed methods. The methods available for flow measurement tend to use visible light, sound or electricity in order to obtain the data. Visible light techniques include Particle Image Velocimetry (PIV), which has primarily been used within laboratory flumes but has been subsequently developed to measure water surface velocities in the field (Creutin *et al.*, 2003). Sound-based methods include acoustic Doppler velocimetry (aDv) and acoustic Doppler current profiling (aDcp), which have become increasingly popular tools on natural rivers (*e.g.* Rhoads and Sukhodolov, 2001; Parsons *et al.*, 2006; Kostachuk *et al.*, 2005). Methods which use electrical currents, meanwhile, include Electromagnetic Current Meters (ECMs), which are older than the acoustic methods but still popular within fluvial geomorphology (*e.g.* Ashmore *et al.*, 1992; MacVicar *et al.*, 2007)

Field PIV methods have an advantage in that they can provide spatially distributed two-dimensional flow data, but there are limitations. Firstly, the measurement of surface velocities alone will not provide any information on the complex subsurface flow field at natural river confluences or even an indication of the depth-averaged flow velocity at each point. Secondly, Creutin *et al.* (2003) note that PIV is very sensitive to variations in the quality of the light, for example with reflections and shadows. Finally, although PIV has been shown to work on natural rivers, this will not be the case if the water surface has significant waves (Weitbrecht *et*

*al.*, 2002). As such, the distortion of the water surface caused by the turbulent nature of the flow at both the Moor House and Borgne d'Arolla sites makes this method much less suitable than other methods using sound waves and electrical currents.

The aDv and aDcp approaches transmit an acoustic (sound) beam into the water where it is reflected off small particles (Didden, 1987; Lane *et al.*, 1998; Elgar *et al.*, 2001). The Doppler Effect means that the frequency of this acoustic beam will increase if the particle is moving closer and decrease if it is moving away (Kostachuk *et al.*, 2005). By measuring this change in frequency, the velocity parallel to the beam can be determined (Didden, 1987). Three-dimensional velocities can therefore be found by measuring the returns to three beams at different angles (Elgar *et al.*, 2001; Kostachuk *et al.*, 2005).

Acoustic Doppler current profilers (aDcps) are widely used in studies with relatively deep water (*e.g.* large rivers or coastal studies) as they are capable of determining the velocities at different depths by analysing the time taken for the signal to return (Shields *et al.*, 2003; Kostachuk *et al.*, 2005). This ability to obtain three-dimensional velocity values throughout the water depth is a major advantage, as it gives very detailed, spatially-distributed data. However, aDcp methods are better suited to measurements in deeper flows. This can be confirmed by looking at the specification sheets of three commercial suppliers of aDcp equipment. The highest frequency model for Nortek AS will allow measurements in the range 4-10m, for RD Instruments it is 0.2-5.0m and for Sontek it is 0.3-6.0m. Therefore whilst aDcps can be highly valuable tools for obtaining spatially-distributed, three-dimensional flow fields, the shallow nature of the flow at both field sites makes their use unfeasible. As such, of the acoustic methods available, aDvs are more practical for research in shallow flows.

With aDvs, flow is measured in a single sample volume that tends to be approximately  $1\text{cm}^3$  and located 5cm from the transmitter and receiver probes (Lane *et al.*, 1998; Rhoads and Sukhodolov, 2001; Elgar *et al.*, 2005). The two major advantages of the aDv method are the ability to get three-dimensional velocities and the non-intrusive nature of the method (MacVicar *et al.*, 2007). However, the aDv does have limitations, the first of which is that it provides only at-a-point data, which means that some form of interpolation is required before it is used as an input for numerical modelling. The second major limitation is that it is known to be sensitive to the presence of air bubbles in the flow and will also record incorrect velocities if the sensor is too close to the bed (Rodriguez *et al.*, 1999; Elgar *et al.*, 2001, 2005; MacVicar *et al.*,

2007). Finally, past research has found that aDv methods may not be suitable in fast flows (when successive return signals come from different particles) and highly turbulent flows (Elgar *et al.*, 2001; MacVicar *et al.*, 2007).

ECMs are different from the methods discussed so far, as they use electrical currents rather than light or sound waves. They are based on the Faraday principle of electromagnetic induction, which is that water flowing through a magnetic field will generate a voltage that is proportional to its velocity (Rodriguez *et al.*, 1999; MacVicar *et al.*, 2007). As the relationship is one of proportionality, ECMs will require calibration beforehand in known flow velocities. Some ECM models are capable of giving two-dimensional velocities (*e.g.* Ashmore *et al.*, 1992; De Serres *et al.*, 1999), although the Valeport Model 801 available for this research is one-dimensional. The Valeport Model 801 has a flat electromagnetic sensor with a cylindrical measuring volume between the two electrodes up to 10mm above the top of the sensor (Valeport, 2011). In addition to the inability to measure flow in three dimensions, ECMs have the disadvantages that they are intrusive to the flow and can be affected by other magnetic fields (Rodriguez *et al.*, 1999; MacVicar *et al.*, 2007). However, they have advantages over aDv, as they are considered more robust and less sensitive to the presence of air bubbles in the flow (Rodriguez *et al.*, 1999). Indeed, in a comparison of the two methods, MacVicar *et al.* (2007) found that ECMs, in spite of being the older technology, were more reliable in highly turbulent flows.

Studies that have compared aDv and ECM data have found good agreement between the results from the two methods (Lane *et al.*, 1998; Elgar *et al.*, 2001). Therefore, the accuracy of the flow measurements should not be affected by the choice of method. Both methods will also have similar levels of uncertainty due to the movement of the probes on the wading rod or the movement of the wading rod within the water (which for the ECM was found by Ashmore *et al.* (1992) to be approximately 6° in the *xy*-plane).

Although high-resolution, spatially detailed three-dimensional velocity data would be ideal, in practice this is not possible to obtain for the river confluences of interest to these studies. Therefore, the criteria for the flow data to be obtained in this study have taken into account this limitation. The first criterion, which applies to both confluences, is that the method chosen must be the most reliable in the flow conditions. High-resolution or detailed data with large uncertainties are considered less valuable than lower resolution or less detailed data that are more reliable.

For the Moor House confluences, Section 1.6 emphasised the need for high quality data. Therefore, one dataset for each confluence should provide three-dimensional data for the inlets, outlet and at least one other cross-section in the centre of the channel. For the point spacing along the cross-section, a balance must be struck between the level of detail and the need to obtain all flow measurements before the discharge has changed substantially (which can occur quite rapidly in flashy, upland catchments). Therefore, given the width of the channels (on the order of 3-10m), the maximum acceptable point spacing was set at 0.5m. This spacing provides sufficient detail to obtain reliable estimates of discharge through a cross-section whilst at the same time enabling all datasets to be obtained over the course of a few hours (thus limiting the uncertainty due to changing discharge). Furthermore, in order to assess velocity distributions in the vertical direction at least one vertical velocity profile should be obtained from a deep or turbulent location along each cross-section.

The Arolla confluences, by contrast, were selected because they are more dynamic and can provide particle tracking data for which the discharge can be measured *in situ*. The second criterion for this confluence, therefore, is that the flow data are of sufficient quality and reliability that a measurement of discharge at each inlet can be calculated. Additional data from the outlet are also preferable as they provide validation data. In order to obtain reliable estimates of discharge, the data points should be closer together than the Moor House data to account for the smaller channel widths. Scaling with channel width (maximum widths of 4m compared to 10m at Moor House) gives a maximum point spacing of 0.2m. Having more closely spaced point data is considered more important than obtaining detailed velocity profile data at just one or two locations.

Given these criteria, it was decided that aDv would be the method of choice for the Moor House confluences, as the method provides more information than the ECMs and is better suited to the less turbulent flows at these confluences. The model used in this study was a Sontek MicroADV. At the Borgne d'Arolla site, however, the ECM is considered to be the more reliable choice, as the probe faces away from the bed with a sampling volume closer to the probe. Furthermore, its reputation for performing better in turbulent flows with numerous air bubbles makes it the more dependable option. However, it was resolved that at least one attempt would be made to use the aDv in a less turbulent confluence on the Borgne d'Arolla braid plain, to test its performance and see whether it would be possible to obtain accurate and robust three-dimensional velocity data in these highly turbulent flows.



Having selected the aDv and ECM methods, it is necessary to determine the minimum length of time series in order to ensure stationarity in the flow data. A time series is considered to have reached stationarity when any increase in the length of the time series will have no significant effect on the mean velocity. For ECM data, Roy and Bergeron (1990) used time series of 20s to obtain mean values, although more recent in-depth analysis by Buffin-Bélanger and Roy (2005) suggests 60-90s is required. This is quite a large disparity and only in post-processing of the aDv data will it be possible to determine the minimum length of time series for the individual datasets. As such, it was decided that a standard time series length of 60s would be used for the aDv data at the Moor House confluences. In terms of sampling frequency, the research by Buffin-Bélanger and Roy (2005) obtained aDv data at 20-25Hz. However, the sampling frequency in this research is limited to 10Hz due to the aDv model available. Analysis of these data would then provide an indication of the minimum length of time series needed to reach stationarity in upland river confluences. The length of time series to be used on the Arolla confluences (where there are greater time pressures) will be determined from these results. However, any aDv data from the Arolla confluences would still be collected over a 60s period in order to evaluate the uncertainties due to the time series length.

### *3.8.3 Methods for Determining Roughness Height*

In order to account for the roughness effect of the sub-grid scale topography in the numerical models, it is necessary to determine a value for the roughness height at each individual confluence. As noted in Section 3.4.6, the two major ways of determining the roughness height are by using velocity profiles or an empirical relationship using a characteristic grain size.

Determining the roughness height from a vertical velocity profile requires the von Karman-Prandtl law of the wall to be used (as given in Equation 3.13 and reproduced here for convenience).

$$u = \frac{u_*}{\kappa} \left( \ln \left( \frac{z}{z_0} \right) \right) \quad (3.13)$$

This equation can be rearranged to give:

$$\frac{u\kappa}{u_*} = \left( \ln \left( \frac{z}{z_0} \right) \right) \quad (3.21)$$

$$\frac{u\kappa}{u_*} = (\ln z) - (\ln z_0) \quad (3.22)$$

$$u = \frac{u_*}{\kappa} (\ln z) - \frac{u_*}{\kappa} (\ln z_0) \quad (3.23)$$

The term  $(u_*/\kappa)$  can be determined from the slope of a plot of  $u$  against  $(\ln z)$ , thus making the second term in Equation 3.23 the y-intercept (Wilcock, 1996). In other words:

$$u = b(\ln z) + a \quad (3.24)$$

where:

$$b = \frac{u_*}{\kappa} \quad (3.25)$$

and:

$$a = -b(\ln z_0) \quad (3.26)$$

Therefore, for any given velocity profile, fitting a linear trend line to the plot of  $(\ln z)$  versus  $u$  means that the roughness height,  $z_0$ , can be found from the y-intercept,  $a$ , and the gradient,  $b$ :

$$z_0 = e^{\left( \frac{a}{b} \right)} \quad (3.27)$$

Of the methods which use a characteristic grain size, the three most popular empirical relations, as mentioned in Section 3.4.6, are as follows (Nicholas and Sambrook Smith, 1999; Nicholas, 2001; Hardy *et al.*, 2005):

$$z_0 = 0.1D_{84} \quad (3.28)$$

$$k_s = 3.5D_{84} \quad (3.29)$$

$$k_s = 6.8D_{50} \quad (3.30)$$

In order to use these empirical relationships, it is necessary to obtain a reliable Grain Size Distribution (GSD) for the confluence in question. GSDs can be obtained in terms of particle numbers or weights in one of three ways: on a grid, for an area or for a volume (Graham *et al.*, 2005b). A common and traditional method to obtain a GSD is to use a grid-by-number method such as a Wolman count, but these can take up a significant amount of field time (Warrick *et al.*, 2009). Therefore, research has been undertaken into photosieving or automated image analysis methods. These are methods of obtaining grid-by-number or area-by number results through the analysis of photographs of a patch of gravel.

Sime and Ferguson (2003) set out three main stages of automated image analysis: the detection of the grain edges, the cleaning up of this grain edge map and finally the determination of the grain size properties. The early photo digitisation methods of Ibbeken and Schleyer (1986) used a stylus to trace around the grain edges, whereas more recent advances have allowed this to be done automatically (*e.g.* Sime and Ferguson, 2003; Graham *et al.*, 2005a). Once the outlines of individual grains have been determined, the surface area and b-axis of the particle can be calculated, providing a scale (*e.g.* a metre rule) has been included in the photograph.

Although the automatic detection of grains from photographs can give a GSD very quickly, there are limitations associated with the method. These include the need for good lighting conditions, poorer performance when there is shadow, the existence of a lower limit of detectable particle sizes, difficulties if pebbles have unusual colourings or shapes, the inability to get data through water and the reduced performance for partially wet surfaces (Sime and Ferguson, 2003; Carbonneau *et al.*, 2004; Graham *et al.*, 2005a; Warrick *et al.*, 2009).

However, there are alternative photosieving techniques available. Some avoid the need for automatic grain edge detection methods by relating image properties to the grain size distribution (*e.g.* Carbonneau *et al.*, 2004; Verdú *et al.*, 2005; Dugdale *et al.*,

2010). Another is the MATLAB method of Carbonneau *et al.* (2004), where a grid is placed over the photograph and the b-axis of the pebble under each intersection measured by clicking on screen. This essentially provides a photo-based grid-by-number method which can be compared to Wolman counts conducted in the field.

The choice of method for determining roughness height must therefore take into consideration the requirements and limitations set out above. For the Moor House confluence, the focus is on having a high-quality dataset from which the boundary conditions can be determined. Therefore, for this site it is deemed necessary to have data from both the velocity profile method and the empirical grain size method. For the velocity profile method, at least 10 profiles from each confluence should be used to obtain a value for  $z_0$ , in order to account for the variability between individual profiles. For the empirical grain size method, at each confluence three  $1\text{m}^2$  patches should be manually surveyed for the GSD (with at least 100 data points) and photographed for subsequent analysis by photosieving methods. The three sites should be chosen so that they are evenly spread and as close as possible to the channel. A survey of 100 data points should capture the variability within the patch itself, whilst the use of three patches at different locations should account for any larger-scale spatial variability (in particular between tributaries). Given that the data will ultimately be used to determine a single roughness height at each site (for the numerical modelling), the combined sample size of at least 300 for each confluence matches the 300-400 pebbles recommended by Rice and Church (1996).

For the Arolla confluences, a reasonable estimate of the roughness height is needed for each confluence as a boundary condition for the model, but it is not necessary to have the same level of detail as the Moor House site. The highly turbulent and shallow nature of the flow makes it probable that velocity readings taken from near the bed and surface will be unreliable, leading to inaccuracies in the velocity profile method. Therefore, the empirical methods are likely to be more suitable. As such, for each confluence at least one patch with an area of approximately  $1\text{m}^2$  should be surveyed, although two or three patches would be preferable. In addition, for at least two confluences a comparison between the Wolman count and photosieving methods should be undertaken.

Given the criteria set out above, photosieving methods will be the main source of GSD data for both confluences. The advantage of this method is that multiple analysis techniques can be used and the photos can be resampled at leisure (unlike *in*

*situ* Wolman counts). However, this does require the preferred analysis technique to be determined. Of the techniques available, it was decided to use the Carbonneau *et al.*, (2004) method, as it uses human judgement (rather than a computer algorithm) to determine the edge of the grains. This means there are fewer problems encountered in situations where the particles are casting shadows, wetted or underwater. Although this method is still limited by photographic resolution, it does give a more reliable dataset when the conditions are not ideal.

#### 3.8.4 Particle Tracking Experiments

Particle tracking has been used in a number of studies within fluvial geomorphology (*e.g.* Best, 1988; Roy and Bergeron, 1990; Sear, 1996; Ferguson and Wathen, 1998; Lamarre and Roy, 2008a, 2008b). Early examples of applications to river confluences include the work of Best (1988) on Widdale Beck and that of Roy and Bergeron (1990), who tracked painted particles through a river confluence on a tributary of the Eaton North River, Québec. From such studies, it is possible to draw conclusions about the bedload transport from the individual particle trajectories.

Using painted pebbles is not the only way of tracking particle movement through a river unit. More recently, the work of Lamarre and Roy (2008a, 2008b) has used Passive Integrated Transponder (PIT) tags to trace individual particles. PIT tags are magnetic tags drilled into pebbles that, with the help of the appropriate reader, enable individual particles to be recovered and identified. Using PIT tags should improve recovery rates, but there are limitations associated with this method. Aside from the time that it takes to prepare the individual particles, Lamarre and Roy (2008b) found that the minimum clast size (b-axis) for drilling and inserting the PIT tag was 40mm. This restricts the range of potential sizes for the tracers, which may cause problems if the stream power is insufficient to move particles of that size.

For both sites, it was decided that instead of using a small number of tagged particles, a larger number would be painted and tracked as the particle cloud dispersed downstream. Although individual particle tracks could not be found from within the patch and recovery rates would drop slightly, more tracers could be followed and the particle scatter would be more representative. Furthermore, this would reduce the lower limit on particle size from 40mm to approximately 10mm (the minimum size clearly visible on the river bed).

There are two basic options for particle tracking experiments. Either individual particles can be seeded and the paths tracked, or a patch of pebbles can be seeded into the river at the same starting point, with the spread of the particle cloud recorded as it travels downstream (Figure 3.6).

For the Moor House confluences, the cobble beds and episodic nature of the bedload transport (as it is active only in peak flows) would be expected to give significant scatter in the particle paths from the same seeding point. Therefore, greater insight will be provided from using a bulk seeding method than attempting to track individual particles as they are transported in high flow events. For this purpose, it is considered that two patches of pebbles should be seeded into each tributary, giving a total of four particle clouds to be surveyed through time. This allows for the variability between and within tributaries to be investigated.



Figure 3.6: Photograph showing the bulk seeding of tracer particles into a confluence tributary. Two separate patches are visible, with each patch having distinct markings on the individual particles so that the particle origin can be identified in subsequent surveys. For scale, the tributary in the foreground has a channel width of approximately 5m.

The number of particles seeded in such experiments has varied between studies. Sear (1996) tracked 700 particles through three pool-riffle sequences of the North Tyne River (Northumberland, UK). Ferguson and Wathen (1998), meanwhile, tracked 1400

particles across six reaches of a gravel-bed river, Allt Dubhaig, in Scotland, using particle sizes in the range 16-256mm. The subsequent study of Hodge *et al.* (2011) used 200-350 magnetically-tagged particles in each study reach, with sites on the River Calder, the South Fork Eel River and the Allt Dubhaig. Of the river confluence studies, Best (1988) used over 900 particles in a 10-month period of surveys on the River Ure-Widdale Beck confluence, whilst Roy and Bergeron (1990) used 127 painted particles of sizes ranging from 32mm to greater than 128mm. Given the range of particle numbers used in these studies, it was determined that each individual patch at the Moor House confluences should consist of at least 100 particles (giving a total of 400 for each experiment). Furthermore, in light of the findings of Roy and Bergeron (1990) that larger particles followed similar transport paths, but over longer timescales, at least one of these patches should test the variability in particle trajectories with clast size.

The Arolla confluences, as noted in Section 1.6, were chosen in order to fulfil the criteria of being able to track individual particles for known discharges. Therefore, the priority is to obtain a dataset of the tracks of individual particles of known size from a range of different starting points. However, it would also be useful to obtain an indication of the spread of a batch of particles starting in each confluence tributary. Therefore, for at least two confluences individual particle tracks should be obtained with seeding locations across both inlets at a spacing of 0.2m (to complement the spacing of flow measurements prescribed in Section 3.8.2). In most confluences this would give 10-20 individual particle tracks. In addition, for at least one confluence a particle patch should be released into the centre of each tributary to compare the outer extent of the particle cloud with the individual tracks. As these confluences are smaller than those at the Moor House site by at least a factor of 2, the minimum number of particles in each patch will be set at 50.

At the Moor House confluences, the particle positions were surveyed after each high flow event. The range of movement of individual particles could therefore be inferred from the changes in position over a period of weeks. For the Arolla confluences, however, the individual particle experiments allowed each separate particle path to be tracked. The paths were surveyed immediately after the experiments with the assistance of video footage. In the bulk seeding tests, the same method was used to determine the extent of the particle cloud as it moved downstream. The ability to review the footage multiple times in the field as the particle paths were being surveyed was considered to be the best tool available for ensuring accuracy in the data.

### 3.8.5 Summary of Field Methodology

This section has set out the range of methods available for conducting field research into the flow and sediment dynamics of upland river confluences. The thesis objectives in Section 1.5 stressed the need for high-quality field datasets from a range of upland river confluences. This was in order to provide information on the relationship between the flow field and sediment transport at dynamic, upland river confluences. Furthermore, as set out in Objectives 3 and 5, these data are required to test the numerical modelling developments of this thesis.

The field methodology has therefore been determined with reference to these research objectives. In order to investigate the sediment dynamics of upland river confluences, and in particular the three-way interactions of Leeder's (1983) trinity, the particle tracking methodology is very important. However, due to the complexity of the flow at upland river confluences, numerical modelling plays a key role in providing the context for these particle data in the form of detailed three-dimensional flow fields. Given the steep water surface slopes and the need to develop explicit free surface numerical methods, high-quality topographic and flow datasets are required to provide boundary conditions and validation data. The Moor House confluences, with their more stable morphologies, were chosen to provide these high-quality data (as noted in Section 1.6). The criteria for the quality of the topographic and flow data obtained from the Moor House confluences was therefore set higher than that for the Arolla datasets.

For the particle tracking experiments, the decision was made to use the simpler, painted particle method at the Moor House sites rather than inserting magnetic PIT tags into the particles. This was justified on the grounds that seeding a much greater number of particles (with a lower minimum particle size) would provide more useful information on particle dispersal downstream than would be given by a slight improvement in particle recovery rates and an ability to determine individual particle tracks. Instead, the Arolla confluences would provide the best opportunity to track individual particles, with the advantage that this could be done for discharges measured *in situ*. This, in particular, would provide useful data for testing the sediment transport model required in Objective 4 of Section 1.5.

Therefore, although the field methodology and quality criteria set out in this section are different for the Moor House and Arolla sites, they are complementary. The methods take advantage of both the stability of the Moor House confluences and the



dynamism of the Borgne d'Arolla braid plain to obtain a varied and detailed dataset which satisfies the research objectives and field site criteria in Chapter 1.

### **3.9 Conclusions**

This chapter has set out the major options for both the numerical modelling and field methodologies, before determining the most appropriate methods for the research in this thesis. For the numerical modelling, methods which solve the three-dimensional Navier-Stokes equations are considered the only feasible option for simulating the complex flow at natural river confluences. The Navier-Stokes equations, the discretisation process and examples of solution algorithms were discussed in Section 3.3, with particular emphasis on the finite volume approach and the SIMPLEST algorithm (and its predecessors) used in the commercial code (PHOENICS) chosen for this thesis.

Section 3.4 then moved on to discuss the different auxiliary models used in numerical modelling process, specifically those that account for turbulence, bed roughness, channel planform and the free surface. Although there are many turbulence models available, the RNG  $\kappa$ - $\epsilon$  and LES models have undergone substantial testing in river confluence studies and therefore are considered to be the two most dependable options for this research. The chapter therefore explained these two models in detail. The treatment of the wall was considered, with the von Karman-Prandtl 'Law of the Wall' explained. Some of the limitations of this approach were discussed, which led to the introduction of an alternative method, the Mass Flux Scaling Algorithm (MFSA). The MFSA is a particularly useful tool as it can represent the sub-grid scale topography and account for irregular channel patterns without needing to distort the computational mesh. The final part of the section on auxiliary models introduced the different options for representing the free surface, with an explicit free surface model deemed to be the only realistic option for the steep confluences of interest to this study.

Good practice in numerical modelling, through the processes of validation and verification, was discussed in Section 3.5. This included a discussion of iterative, time step and grid convergence. For the last of these, the Grid Convergence Index was introduced as a method for quantifying the error due to the choice of grid resolution.

A review of the CFD methods and limitations in Section 3.6 was followed by an explanation of the numerical modelling methodology chosen (Section 3.7). The choices

were based on the principles outlined in Section 3.2 and the objectives of Section 1.5, which emphasise the importance of correctly modelling the free surface elevation in steep river confluences. Therefore, use of the HOL free surface model is a major aspect of the methodology and other auxiliary model choices were made with this in mind. On this basis the MFSA was chosen to represent the channel shape and confluence topography. However, because the cell size is likely to be larger than most gravel and cobble clasts, it was considered necessary to include a fully rough law of the wall to account for the effects of these clasts on the momentum equations and turbulence production. For turbulence modelling, the RNG  $\kappa$ - $\epsilon$  model was chosen because it is considered robust and has been well tested on a number of river confluence studies.

In Section 3.8, the field data required for this research and the methods available for obtaining these data were described. For the topographic data (Section 3.8.1), it was determined that LiDAR and photogrammetry approaches were insufficiently developed for use through water and therefore that it became a choice between dGPS and electronic tacheometry approaches. With both having similar levels of accuracy for individual point data, the slightly faster speed of the dGPS meant it was considered the best choice for the Moor House confluences. However, the unreliable nature of the satellite signal in the steep-sided Arolla valley led to electronic tacheometry being selected for use on the Borgne d'Arolla braid plain.

For the flow data in Section 3.8.2, the two most feasible methods were found to be three-dimensional aDv and using one-dimensional ECMs. The extra information the aDv provides was considered advantageous at the Moor House confluences. However, the limitations of aDvs in highly turbulent flow mean that the ECM was deemed the more reliable for the Arolla confluences.

In Section 3.8.3, the methods for finding a roughness height value were discussed. Neither the velocity profile method nor the empirical method was considered to be more appropriate for the Moor House confluences, so both methods will be used and compared. For the empirical method, Grain Size Distributions will be obtained from both a Wolman count and the Carbonneau *et al.* (2004) photosieving method. On the Borgne d'Arolla braid plain, the shallow and highly turbulent flow means that the velocity profile method may become unreliable. Therefore empirical methods will be used, primarily through the analysis of scaled photographs but with some manual counts undertaken for comparison.

The final part of this chapter reviewed particle tracking methods. The use of PIT tags to track individual particles was considered, but it was decided that having a lower limit on clast size was more problematic than the potential for a slightly lower recovery rate. Therefore, the experiments will involve tracking painted pebbles through time. At Moor House Nature Reserve, this involves surveying four patches of particles in each confluence before and after high flow events. For the Arolla confluences, individual particles would be tracked in real time for discharges measured *in situ*, although some bulk seeding experiments will also be conducted to determine the particle dispersion.

This chapter has described the methods available for this research and has provided data quality criteria and justifications for the chosen methods. However, as Ferguson *et al.* (2003) note, there is uncertainty inherent in both field measurements and numerical modelling results. Therefore, although the methodology for this thesis is considered the most suitable given the research objectives set out in Section 1.5, it is still important to account for the uncertainties in the data when drawing conclusions from both the field and numerical modelling results.

# **Chapter 4:**

## **Investigating Flow at Stable and Dynamic Upland River Confluences**

### **4.1 Introduction**

In Section 1.5, the research question, aims and objectives were identified. Upland river confluences were selected as the primary area of investigation, as most research into the flow at natural river junctions has been conducted in lowland areas. Therefore it was determined (Section 1.6) that one of the main criteria for the selection of field sites would be that they should include a range of upland river confluences with steep water surface slopes. This, along with the other criteria established in Section 1.6, led to the selection of two field sites: Moor House National Nature Reserve in the North Pennines and the Borgne d'Arolla braid plain in the Valais canton, Switzerland. The confluences at Moor House National Nature Reserve were selected for their steep water surface slopes, turbulent flow and stable channel planform. The Arolla confluences, by contrast, were chosen for their dynamism, with steeper water surface slopes than those at Moor House, highly turbulent flow and active bedload transport. This dynamism results in confluence planforms which can change significantly over the course of several hours.

The data collected in the field served two principal purposes. Firstly, data were collected in order to improve the understanding of the processes operating at upland river confluences with steep water surface slopes. As set out in the research question for this thesis (Section 1.5), there is a need to understand the extent to which our knowledge of lowland confluences is applicable in upland areas. In particular, it is important to understand whether the classic model of river confluences is applicable when the slopes get steeper. Secondly, as noted in Section 3.1, field data are necessary to provide boundary conditions and validation data for the numerical modelling applications of this thesis. Although Computational Fluid Dynamics (CFD) is widely used and a well-tested tool for modelling three-dimensional flow in rivers, its application to steep river confluences is yet to be fully developed with respect to the modelling of the free surface.

High quality field data were therefore considered imperative for testing these developments (to be presented in Chapter 5).

In Chapter 3, the field methodology has been described along with criteria for data quality at both the Moor House and Arolla sites. This chapter will present the results from field experiments at the more stable confluences of Moor House National Nature Reserve (Sections 4.2 to 4.7) before addressing the steeper and more dynamic confluences of the Borgne d'Arolla braid plain (Sections 4.8 to 4.11). For each of these sites, the field conditions are discussed (Sections 4.2 and 4.8) before the topographic, roughness and flow data are presented in turn. At Moor House National Nature Reserve, data were obtained from two confluences (the upper and lower confluences identified in Section 1.6.1). For the Arolla site, however, nine confluence datasets were collected, with the quality and detail of these data depending on the specific flow conditions. As such, Section 4.8 also includes a description of these nine datasets, a discussion of their quality and the justification for their inclusion or exclusion in the analysis that follows. Following the presentation of the results from both sites, the Moor House and Arolla confluences are compared in Section 4.12, before the chapter conclusions are given in Section 4.13.

## **4.2 Field Conditions and Flow Regime at Moor House**

In Section 1.6, the two confluence field sites at Moor House National Nature Reserve were introduced, along with a location map and photographs (Figures 1.5 and 1.6). For ease of reference, these figures are reproduced in Figure 4.1.



Figure 4.1: Photographs of the lower (*a*) and upper (*b*) confluences at Moor House National Nature Reserve, with a field assistant for scale. Discharge is low at the lower confluence and medium at the upper confluence.

This section sets out the weather conditions and flow regime during the data collection period. The experiments at Moor House National Nature Reserve were conducted from February 2011 to July 2012. The weather therefore fluctuated considerably depending on the time of year, although most of the time site visits could be arranged during more benign conditions to ensure this had little impact on data collection. However, the field site is accessible only by a dirt track that is impassable in heavy snow or ice and occasionally blocked by landslips after very wet weather. During the very cold period from December 2011 to February 2012, the site was inaccessible

due to snow and ice, although this had only a very minor impact on the collection of the particle tracking data (which will be discussed in Chapter 6).

Figure 4.2 shows the discharge data obtained from the Environment Agency gauging station on Trout Beck. The river can be seen to have periods which are both rich and poor in high discharge events, with a particularly notable period of low flow from April to May 2011.

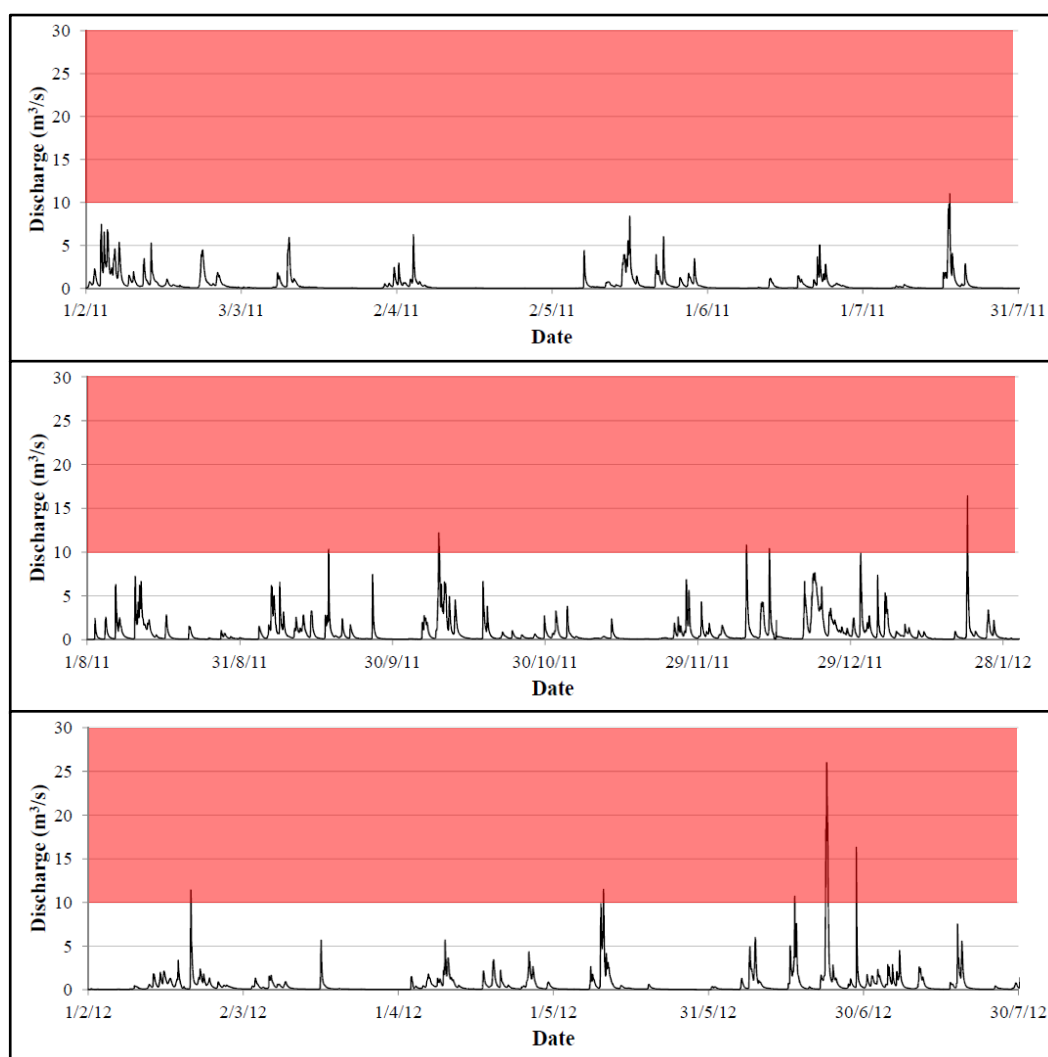


Figure 4.2: Discharge measurements from the Environment Agency (EA) gauging station at Moor House from 1<sup>st</sup> February 2011 to 31<sup>st</sup> July 2012 (data provided by the EA). The area in red indicates the point at which the EA considers the river to have reached bankfull discharge.

From the data in Figure 4.2, Trout Beck can be seen to have a river regime characterised by a series of flashy floods. Flood waters rise very quickly (in hours) and recede slightly more slowly (but still on the scale of hours or days). The minimum and maximum flows recorded in this 18 month period (from February 2011 to July 2012) were  $0.012\text{m}^3/\text{s}$  and  $26\text{m}^3/\text{s}$  respectively, which compares to a mean flow of  $0.63\text{m}^3/\text{s}$

and a median flow of  $0.182\text{m}^3/\text{s}$ . The analysis of flow percentiles (Figure 4.3) also demonstrates the flashy nature of the river regime, with 83% of flows below  $1\text{m}^3/\text{s}$  in the data collection period. Given the data in Figure 4.3, in this thesis low flows at the Moor House site are considered to be those below  $0.2\text{m}^3/\text{s}$ , whilst high discharges are those in the top 5% of flows (*i.e.* greater than  $3\text{m}^3/\text{s}$ ). Flood events, meanwhile, have discharges greater than  $10\text{m}^3/\text{s}$  (in the red zones in Figures 4.2 and 4.3) and account for less than 1% of all flows.

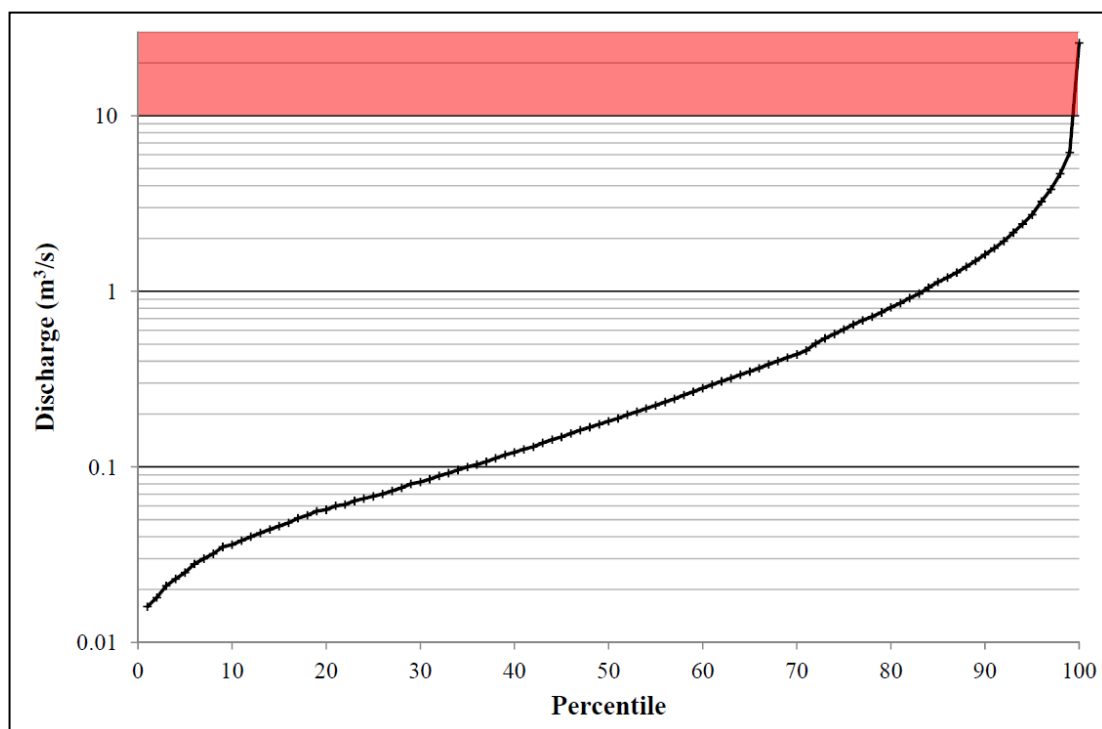


Figure 4.3: Cumulative frequency plot of the discharge data from the Moor House gauging station. Discharges are for the 18 month period of the field experiments (1<sup>st</sup> February 2011 – 31<sup>st</sup> July 2012). Discharge is plotted on a logarithmic scale to ease visual analysis and discharges above bankfull are shown by the red area.

For each confluence, Table 4.1 summarises the channel geometry and flow characteristics during medium discharge conditions (*i.e.* a discharge between the low and high flows set out above). Both confluences are characterised by subcritical flow and maximum water depths which, although shallow, are deep enough to obtain water velocity profiles using an aDv.



		Upper	Lower
Channel Width	TL tributary	4.0m	4.5m
	TR tributary	3.0m	5.0m
	Main Channel	5.0m	8.5m
Channel Depth	TL tributary	0.3m	0.25m
	TR tributary	0.3m	0.4m
	Main Channel	0.45m	0.5m
Cross-sectional area	TL tributary	0.67m <sup>2</sup>	0.78m <sup>2</sup>
	TR tributary	0.55m <sup>2</sup>	1.08m <sup>2</sup>
	Main Channel	1.28m <sup>2</sup>	2.39m <sup>2</sup>
Froude Number		0.29-0.31	0.2-0.26

Table 4.1: Flow and channel characteristics of the upper and lower confluences at Moor House National Nature Reserve during medium discharge conditions. Widths and areas are taken from the cross-sections selected as confluence inlets and outlets, while TL and TR refer to the true left and true right respectively.

### 4.3 Topographical Data from the Moor House Confluences

High resolution topographic data for the Moor House confluences were obtained from a differential Global Positioning System (dGPS) survey, the method considered most appropriate in Section 3.8.1. Due to the stable nature of the channels, the topographic survey could be conducted over a number of consecutive days, whilst the availability of two separate rover units meant data collection could be undertaken by two individuals working concurrently. The survey for the larger, lower confluence took four days to complete (with two people operating dGPS rovers), whilst the upper confluence took just over two days using the same method.

The dGPS data were converted from the WGS 1984 projection to the Ordnance Survey grid using the transformation software Grid InQuest. The data points from both dGPS and Total Station surveys were then rotated and translated onto a local grid for each confluence. This local grid was set up so that the major flow direction was from left to right and so that the inlet and outlet cross-sections were either parallel or perpendicular to this primary flow direction. This was done to improve the orientation of the boundary conditions for the numerical models. Having transformed the data in this way, the individual points were converted to a Triangular Irregular Network (TIN) using Delaunay triangulation. Each TIN was then converted to raster format by linear interpolation and clipped such that the locations of the inlet and outlet cross-sections were on the edges of the domain.

The quality of Digital Elevation Models (DEMs) derived from dGPS data is known to depend on individual point quality, point density and point distribution (Lane *et al.*, 2003). Of these, the quality of the point distribution is more subjective, being determined by the extent to which the recorded points accurately represent the breaks of slope. Unless a much higher resolution DEM is available, for example from terrestrial LiDAR data, then it is difficult to objectively determine the quality of the point distribution. Therefore, before the topographic data are presented in this section, the individual point quality and overall point density will be analysed to determine whether they satisfy the quality criteria set out in Section 3.8.1.

#### *4.3.1 Individual Point Quality*

When determining the individual point quality, the most reliable way to obtain an estimate for the error is to survey fixed quality control points on each occasion that data are recorded and to analyse their variability. Brasington *et al.* (2000) found greater differences in control point positions between days than within days and suggested that variations in atmospheric conditions were the likely cause. Therefore, given that the surveys to obtain the topographic data were conducted over multiple days, it is imperative that the uncertainty caused by reoccupying the base station on separate occasions is quantified.

For this research, four quality control points were set up on each confluence site and surveyed every time a survey was undertaken. Three of the control points at the upper confluence (QC6, QC7 and QC8) became overgrown in the spring and were lost, meaning they had to be replaced partway through the research (with points QCa, QCb and QCc). The dGPS was used to survey these three new points, allowing their position relative to the base station and five remaining quality control points to be determined. Having done this, the three new control points were surveyed on each subsequent field day and therefore variations in their positions could also be analysed.

As the data had to go through multiple transformations from the WGS 1984 projection onto an arbitrary grid, it is the post-transformation positions of the quality control points which are analysed. This implies that the error values being determined will give a reliable indication of the combined error from transformation errors, individual point errors and human errors. For each quality control point the mean

location was found and from those data the mean error was calculated. The error values are given in Table 4.2.

Point	Mean Error (m)				Total RMSE (m)
	x	y	z	Total	
QC1	0.024 ± 0.026	0.035 ± 0.025	0.005 ± 0.004	0.047 ± 0.031	0.056
QC2	0.038 ± 0.035	0.03 ± 0.019	0.005 ± 0.004	0.055 ± 0.03	0.063
QC3	0.037 ± 0.031	0.04 ± 0.034	0.006 ± 0.004	0.059 ± 0.039	0.071
QC4	0.019 ± 0.02	0.038 ± 0.021	0.006 ± 0.007	0.047 ± 0.023	0.052
QC6	0.019 ± 0.017	0.025 ± 0.017	0.003 ± 0.002	0.035 ± 0.02	0.039
QC7	0.028 ± 0.025	0.028 ± 0.029	0.003 ± 0.002	0.042 ± 0.035	0.054
QC8	0.029 ± 0.028	0.025 ± 0.026	0.003 ± 0.003	0.042 ± 0.034	0.052
QC9	0.029 ± 0.034	0.035 ± 0.034	0.006 ± 0.004	0.051 ± 0.042	0.065
QCa	0.041 ± 0.044	0.028 ± 0.033	0.007 ± 0.004	0.054 ± 0.051	0.071
QCb	0.04 ± 0.027	0.021 ± 0.017	0.004 ± 0.003	0.051 ± 0.02	0.054
QCc	0.023 ± 0.016	0.027 ± 0.023	0.003 ± 0.003	0.039 ± 0.022	0.044

Table 4.2: Mean errors and standard deviations for each quality control (QC) point placed at the Moor House site, along with the total Root Mean Squared Error (RMSE) for each. This includes all data obtained using both dGPS and Leica Total Station.

The results in Table 4.2 show that the RMSE values are in the range 0.035-0.075m. The mean error for all quality control points from both confluences was calculated as  $0.049\text{m} \pm 0.032$ . Most of this error is due to differences in the horizontal plane; all mean vertical errors are below 7mm. The variations in the horizontal locations of the quality control points are given in Figure 4.4. From Figure 4.4, it can be seen that there is greater uncertainty for the lower confluence control points, with 56% of points within 0.05m of the mean, compared to 70% of points for the upper confluence. Nevertheless, both confluences have 90% of their horizontal errors within 0.1m of the mean.

The 0.035-0.075m RMSE values account for the 0.02-0.03m accuracy of the dGPS or Total Station (as estimated by the machine during data collection), plus errors of a similar magnitude associated with the positioning of the detail pole and data transformation. The mean individual point error of 0.049m just satisfies the criterion in Section 3.8.1 (that the mean error should be less than 0.05m). However, the presence of some points with anomalously large deviations from the mean position does imply that any conclusions drawn from the topographic data should account for the possibility of individual point errors of up to 0.1m (which in gravel- and cobble-bed rivers will be similar in magnitude to the bed grain size). It should also be noted that although the Moor House beds are relatively stable, there is still the possibility that bedload transport will result in some minor topographic variability.

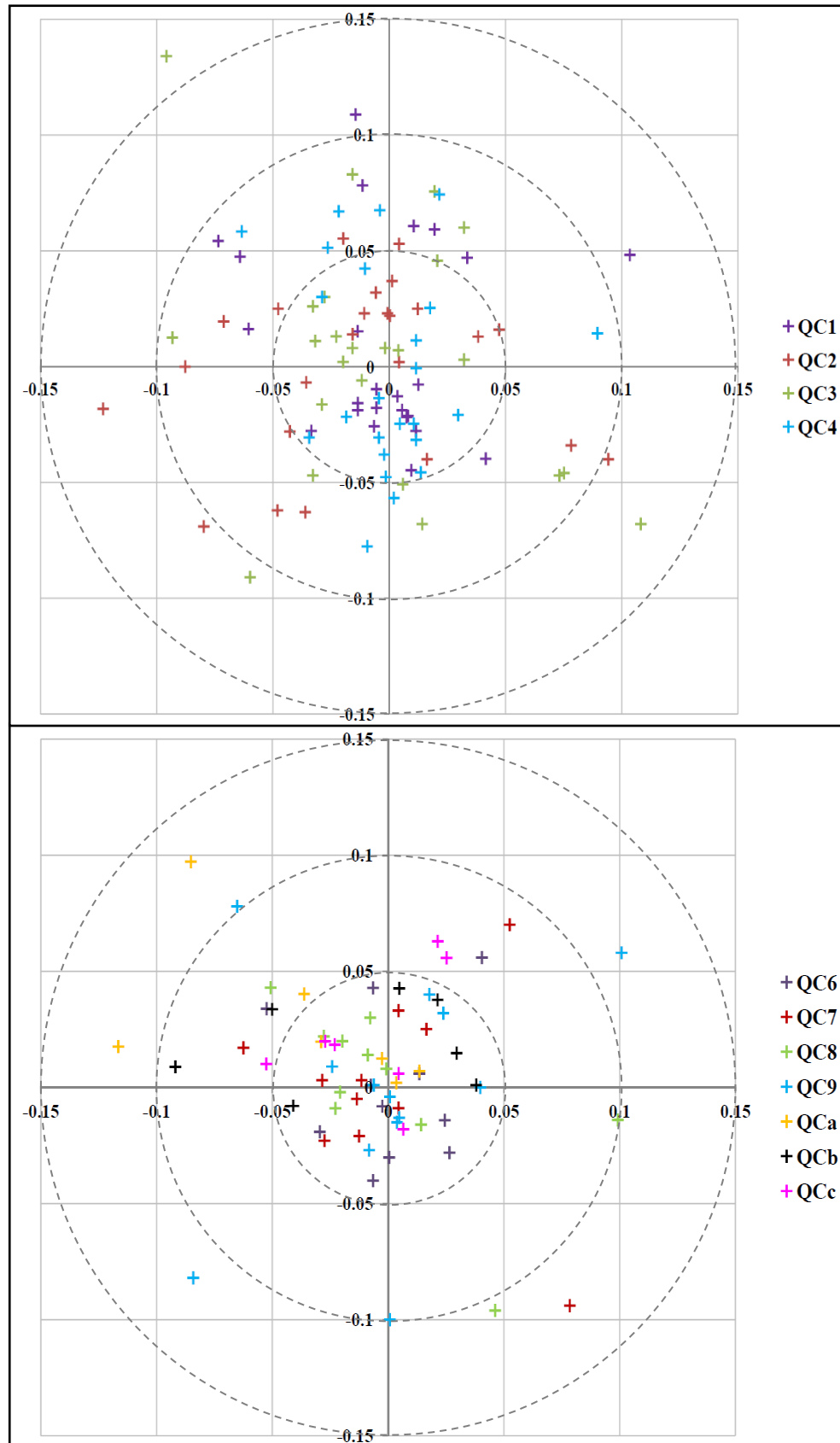


Figure 4.4: Scatter plots showing the horizontal positions (relative to the mean) for each of the quality control points at the lower (*top*) and upper (*bottom*) confluences.

### 4.3.2 Topographic Data Point Densities

Point density plots are given in Figures 4.5 and 4.6 for the lower and upper confluences respectively.

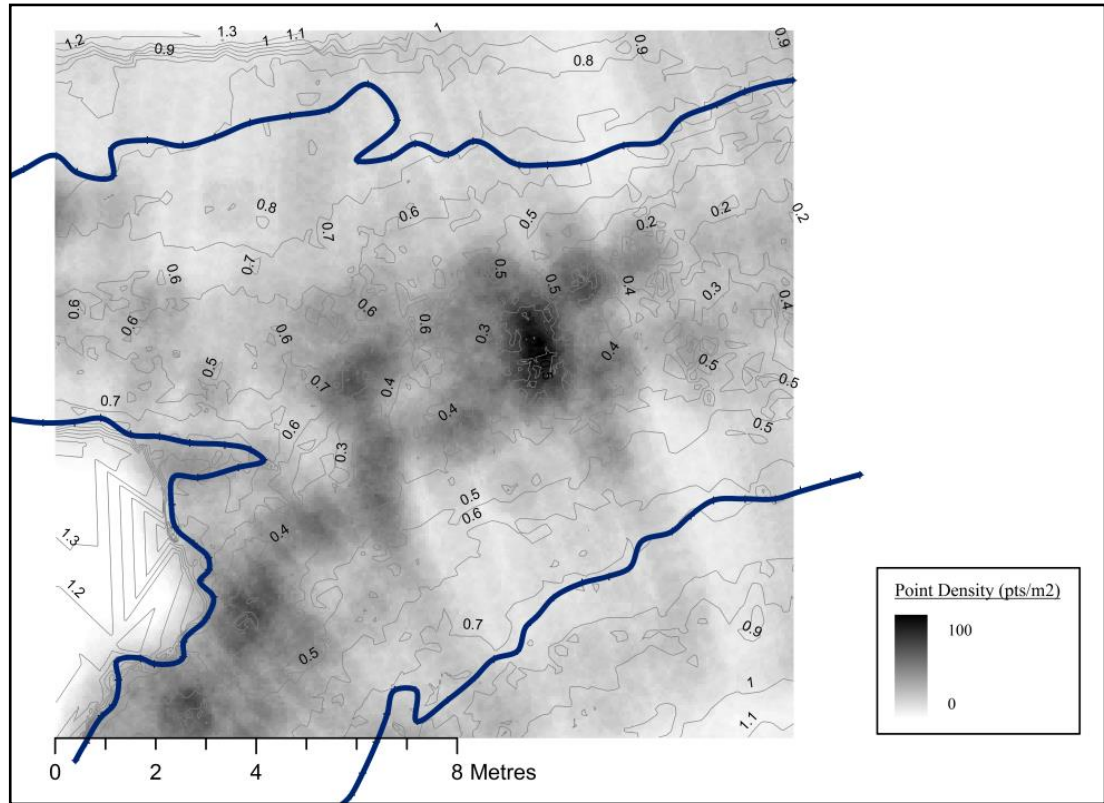


Figure 4.5: Point densities for the lower confluence DEM, with the channel outline from 7<sup>th</sup> October 2011 (blue line) provided for reference. The value of each cell is the number of data points that were located within 0.564m of the cell (*i.e.* the radius of a 1m<sup>2</sup> circle).

The highest point densities for the lower confluence (Figure 4.5) are found in the centre of the confluence and in the deeper parts of the tributaries, whereas the lowest point densities are found away from the water edge, mostly on top of the banks. Meanwhile, at the smaller upper confluence, the point densities are high throughout the inundated area, although the highest values are once again in the centre of the confluence.

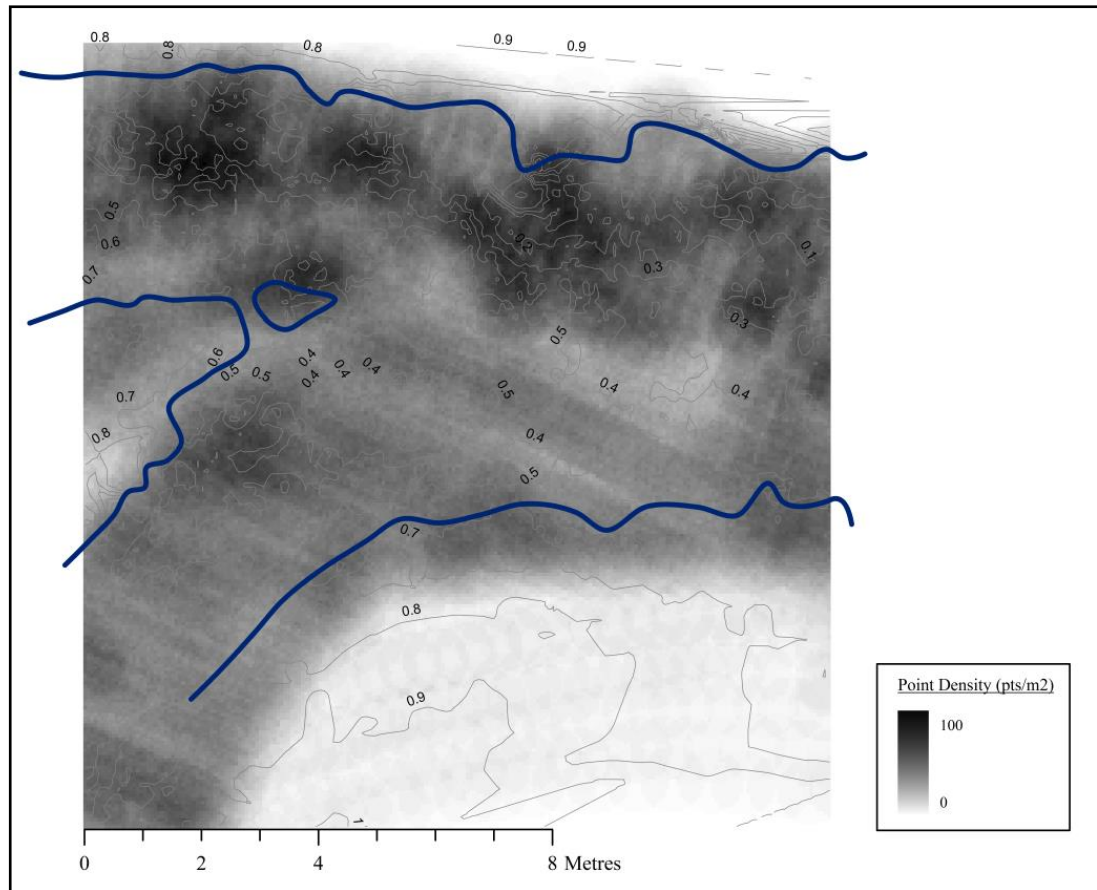


Figure 4.6: Point densities for the upper confluence DEM, with the water edge for 20<sup>th</sup> September 2011 (blue line) for reference.

In Section 3.8.1, the criterion is for point densities in excess of 16pts/m<sup>2</sup>, with a point distribution which has higher point densities in the centre of the channel and lower densities on the banks. Both confluences satisfy these criteria, with point densities higher on the smaller upper confluence. Therefore, given the individual point quality analysis, point density plots and point distribution, the topographic data presented in this section have satisfied the quality criteria from Section 3.8.1.

#### 4.3.3 Lower Confluence Topography

The Digital Elevation Model (DEM) for the lower confluence is given in Figure 4.7.

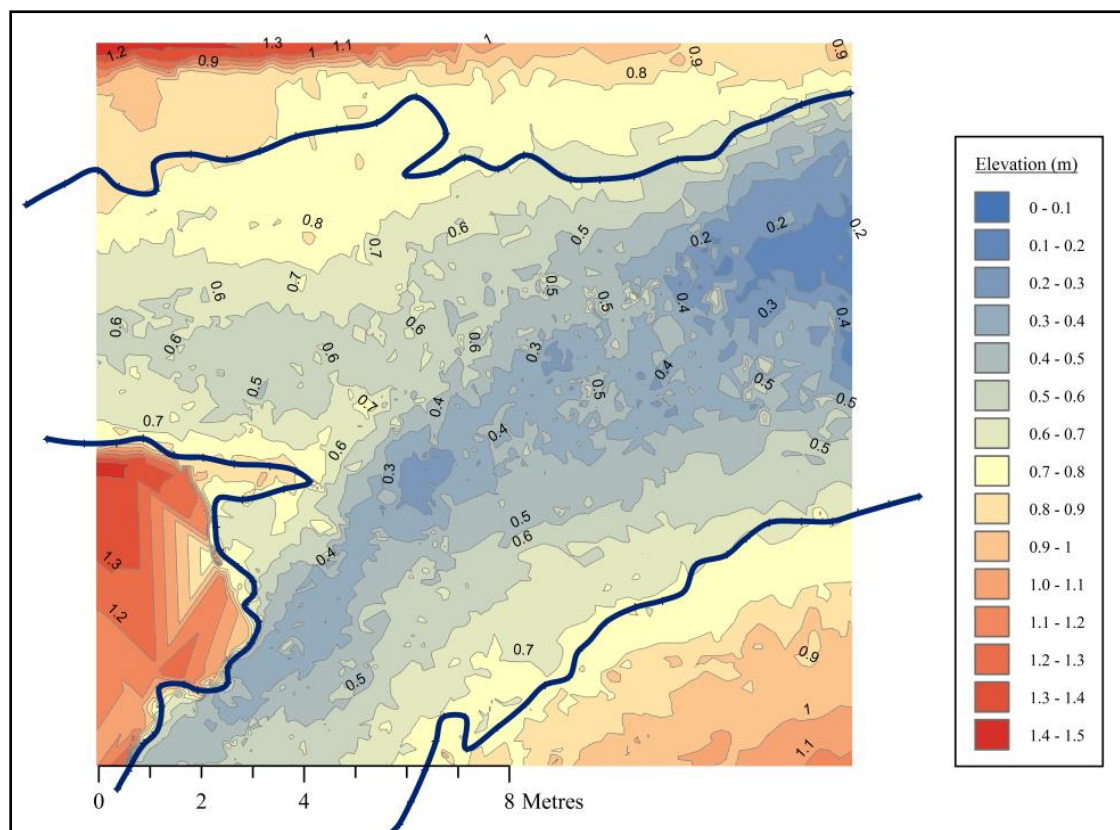


Figure 4.7: DEM of the lower confluence, with the channel outline from 7<sup>th</sup> October 2011 (a medium flow stage and discharge). Flow is from left to right.

The lower confluence is an asymmetric confluence with a junction angle of approximately  $45^\circ$ . Figure 4.7 shows clear evidence of bed discordance between the two tributaries, with differences in the elevation of the two tributary thalwegs of 0.2-0.4m. The true right tributary curves into the confluence, with a thalweg close to the true left bank. This thalweg appears to continue into the main channel, although there is no obvious scour hole present where the true left tributary joins.

The true left tributary is well contained by high, peat-covered banks, as can be seen by the elevations on both sides of the channel in the DEM and also in Figure 4.1. However, this is not the case for the true right bank of the confluence and further downstream on the true left bank, where gravel bars extend for a considerable distance either side of the channel. The lower confluence has a small bar in the stagnation zone, but there is no evidence of lateral or mid-channel bars developing within the confluence.

#### 4.3.4 Upper Confluence Topography

The DEM for the upper confluence is given in Figure 4.8.



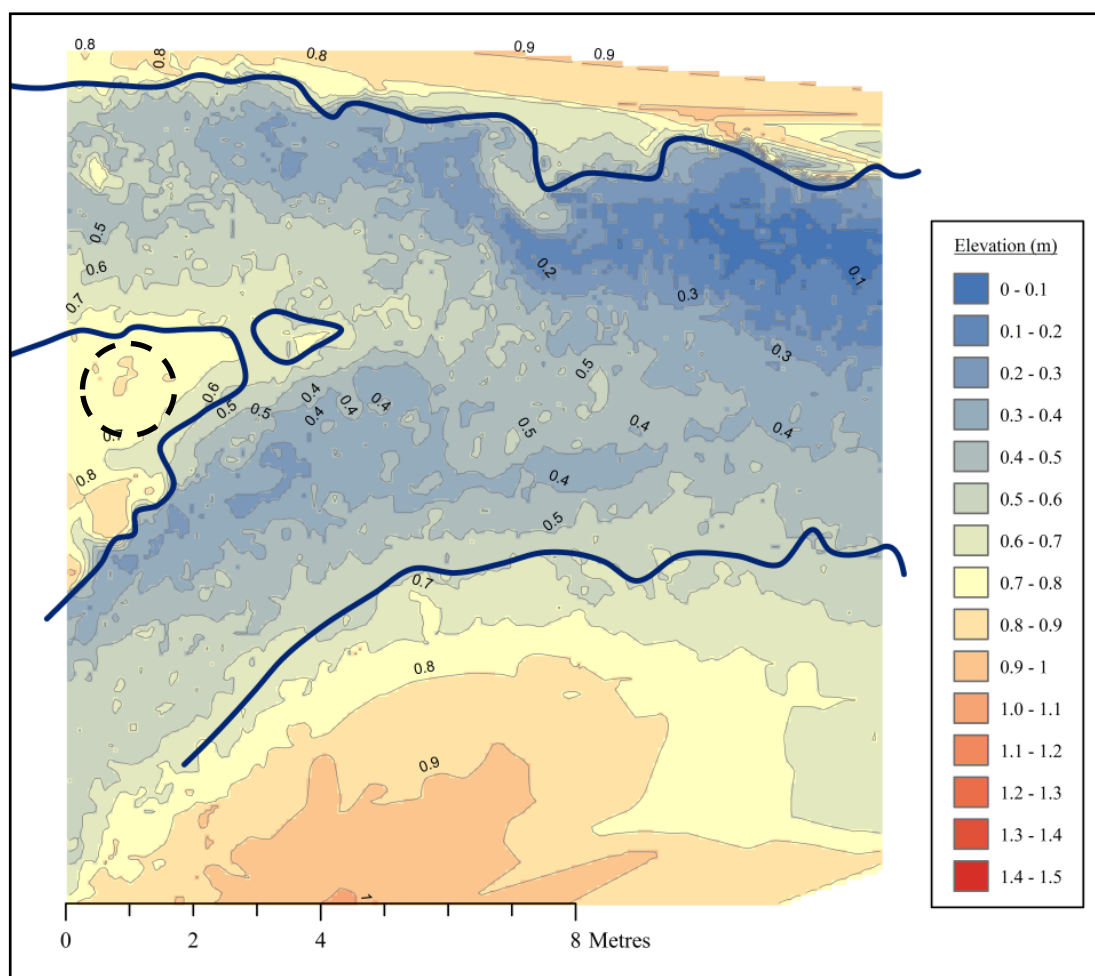


Figure 4.8: DEM of the upper confluence, with the channel outline from 20<sup>th</sup> September 2011 (a medium flow stage and discharge). Flow is from left to right. The black dashed circle highlights the low profile bar referred to in the text.

The upper confluence is an asymmetric confluence, with a junction angle of approximately  $40^\circ$  at low flow. However, the junction angle is variable; during the medium discharges of 20<sup>th</sup> September 2011 (shown by the water outline in Figure 4.8) the junction angle was measured as being closer to  $55^\circ$ . The reason for this is the presence of a large, but relatively low profile bar on the upstream corner (marked with a dashed black circle in Figure 4.8). As the flow level changes, so does the amount of the bar that is submerged, which affects the flow direction of the true left tributary and thus the junction angle.

Much like the lower confluence, the true right tributary of the upper confluence curves into the main channel, with its thalweg close to the true left bank. However, this thalweg is interrupted before it reaches the main channel by a zone of higher topography extending from the end of the upstream corner bar. The true left tributary, meanwhile, flows through a narrow, deeper section close to the true left bank as it enters the main



channel. This thalweg continues into the main channel, but there is again no clear evidence of a scour hole. Although there is a deeper area in the main channel, it is of a similar depth to the true left tributary thalweg and therefore does not have the characteristic avalanche faces descending into it from both tributaries (as shown in Best's (1986) classic schematic diagram of a river confluence in Figures 1.2 and 2.1). Meanwhile, the bed discordance is complex, as the true left tributary is slightly higher than the true right before the flows join, but at the point where the flows meet in the main channel, it is in fact the true right tributary bed which is higher.

The upper confluence has very clearly defined banks along its true left edge, and also further upstream between the two tributaries (as can be seen in Figure 4.1). However, much like the lower confluence, the true right bank is not well-defined and therefore higher flow events will flood onto this bar.

#### *4.3.5 Discussion of Topographic Data*

As noted in Section 4.3.2, the topographic data satisfies the quality criteria set out in Section 3.8.1. The quality of individual points is less easy to control, as it depends on the performance of the equipment and the atmospheric conditions. However, thanks to the morphological stability of these confluences, it was possible to obtain good point densities, with some parts of the confluences having point densities well in excess of the pre-defined minimum. Furthermore, from a qualitative point of view, the point distributions can also be considered good, with Figures 4.5 and 4.6 demonstrating that higher point densities are found in the key hydrodynamic zones in the confluence (as highlighted in Figures 1.2 and 2.1). Therefore, taking these three components of data quality into consideration, this dataset can be considered to be of high quality.

From the topographic data presented in this section, it is clear that both confluences are complex and do not fit particularly well with the classic model of river confluences. The lower confluence is a discordant confluence, which would account for its lack of a scour hole. However, the bed topography is clearly punctuated by a series of small boulders which means that any patterns in the bed topography are inconsistent.

The upper confluence is similar, with large rocks having a significant presence throughout the confluence. Although there is a deeper zone in the main channel, this does not have the characteristic avalanche faces that are associated with a scour hole. Instead, this zone appears to be merely a continuation of the true left tributary thalweg

with some widening. The complexity of the upper confluence is increased by the unusual variability in elevation between the two tributaries, which does not fall neatly into either the concordant or discordant categories.

Neither of the Moor House confluences, therefore, can be considered to have a 'classic' morphology and this reflects the differences that exist between lowland and upland river confluences. The classic model of river confluences (as set out in Section 1.2) and more recent developments in understanding (in Chapter 2) have been largely based on laboratory experiments (*e.g.* Mosley, 1976; Best and Roy, 1991) or research at lowland confluences (*e.g.* Bradbrook *et al.*, 2000a; Biron *et al.*, 2002, 2004a; Constantinescu *et al.*, 2012; Sandbach *et al.*, 2012). The Moor House confluences, however, are both natural upland confluences with steeper water surface slopes, coarser bed material and smaller channel depths. Combined with the relative stability of their morphology, this makes them ideal case studies for understanding the flow and sediment dynamics in environments such as these where idealised channel planforms and topographies tend not to exist.

#### **4.4 Characterising Roughness in the Moor House Confluences**

Flow through a natural river channel will be affected by the nature of the bed over which the water is flowing. It is therefore important to determine the resistance to the flow caused by the rough channel bed. In numerical modelling, roughness at the bed and walls becomes an important boundary condition of the model. At the Moor House confluences, values for the roughness height were found using both the velocity profile and characteristic grain size methods set out in Section 3.8.3. For the velocity profile method, 12 separate profiles were obtained from the lower confluence flow datasets, whilst 15 profiles were available for the upper confluence. In both cases these profiles came from datasets obtained on three separate days.

In addition, Wolman counts were conducted for the bars on the true left, true right and in the middle of the upper confluence, with photographs taken of the same patches to enable subsequent analysis using the Carbonneau *et al.* (2004) photosieving method (as discussed in Section 3.8.3). The same sampling approach was used for the lower confluence, although the central bar was insufficiently exposed to conduct a 1m<sup>2</sup> Wolman count. Nevertheless, a photograph was taken of the bar to determine the Grain Size Distribution (GSD) from photosieving.

This section will therefore compare roughness heights obtained from velocity profiles to those calculated from a characteristic grain size. In addition, there will be a comparison between the GSDs determined from *in situ* Wolman counts and the photosieving method of Carbonneau *et al.* (2004).

#### *4.4.1 Obtaining Roughness Heights from Velocity Profile Data*

The von Karman-Prandtl law of the wall equation is given in Section 3.8.3, along with an explanation of how its derivation can be used to determine a roughness height from a logarithmic velocity profile (Equations 3.21 to 3.27). To provide examples of the shape of the velocity profiles, Figures 4.9 and 4.10 show the six velocity profiles collected from the upper and lower confluences in medium discharge flows using acoustic Doppler velocimetry (aDv).

In both Figures 4.9 and 4.10 there are examples of velocity profiles which follow the standard logarithmic shape and others where the flow data are much more variable. At the upper confluence (Figure 4.9), profiles A, B and E are good examples of logarithmic velocity profiles, while at the lower confluence (Figure 4.10) the same is true for profiles V, X, Y and Z. In some cases (A, E, X and Y), there is also evidence of slower flow near the water surface due to air resistance. In the case of profiles C and U, the velocity profiles are much more anomalous, but in both cases this is likely to be due to the presence of submerged topographic obstacles in the vicinity of the measurement location.

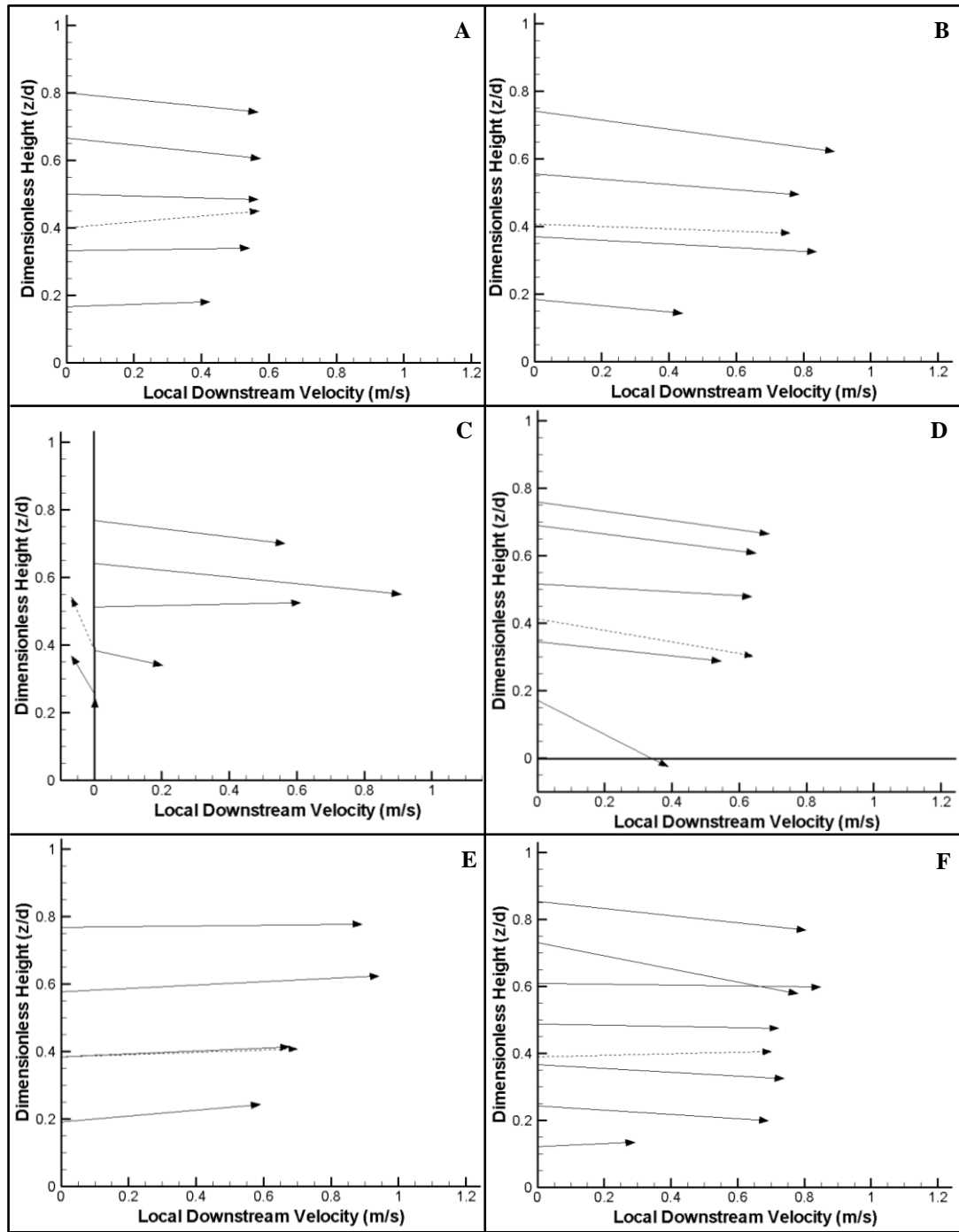


Figure 4.9: Vertical velocity profiles for the upper confluence on 20<sup>th</sup> September 2011 (during medium flow conditions). The dashed arrows are the 0.4d measurements at each location. The profile labels (A-F) correspond to the locations labelled later in Figure 4.16.

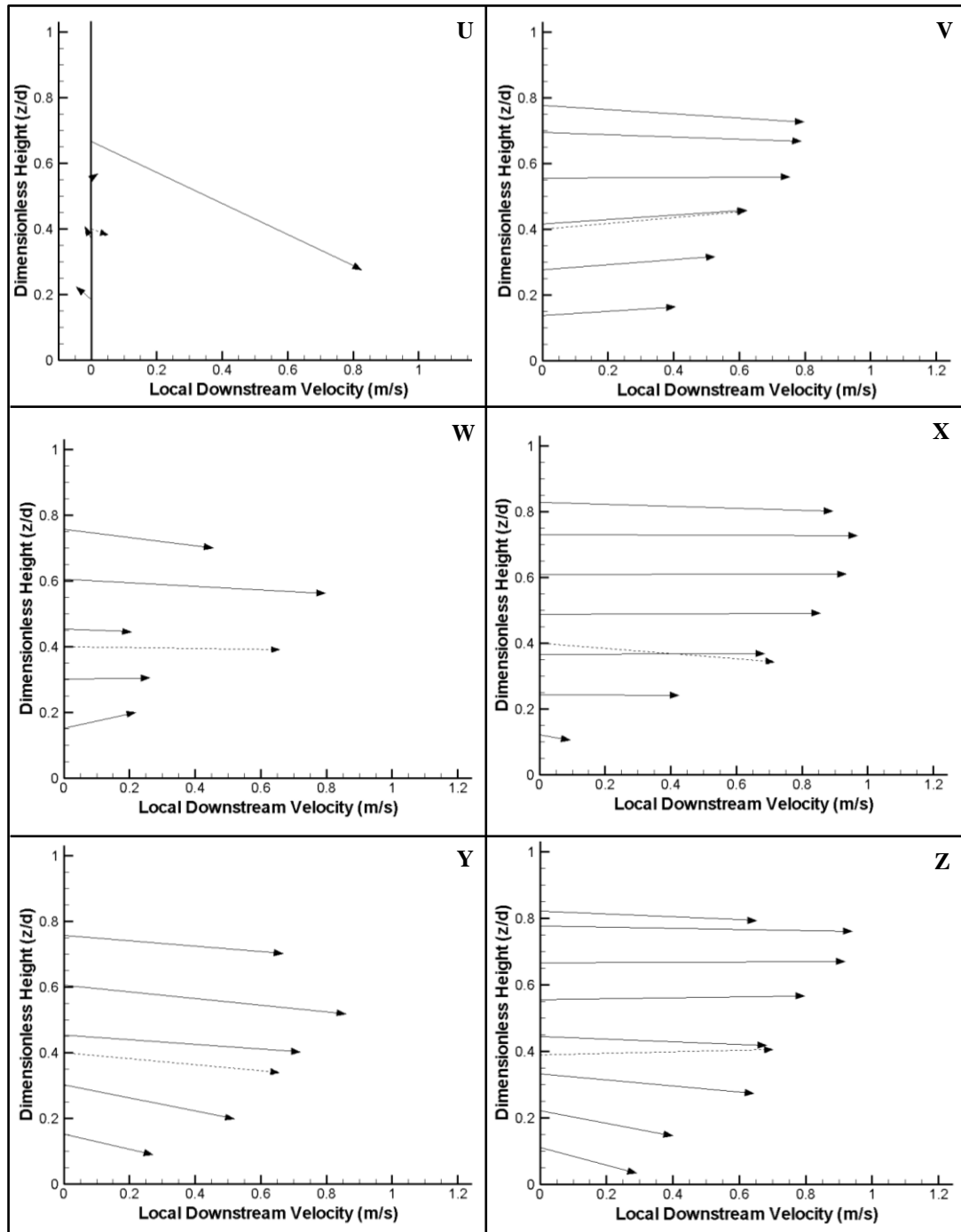


Figure 4.10: Vertical velocity profiles for the lower confluence on 7<sup>th</sup> October 2011 (during medium flow conditions). The profile labels (U-Z) correspond to those in Figure 4.15, while the dashed arrows are the 0.4d measurements at each location.

Having used the methodology in Section 3.8.3 to calculate the roughness height for each individual velocity profile, summary statistics were derived. These statistics are set out in Table 4.3.

	Upper	Lower	All Data
<b>Mean</b>	18 ± 9	29 ± 15	23 ± 9
<b>Minimum</b>	1	2	1
<b>Lower Quartile</b>	4	13	7
<b>Median</b>	12	18	15
<b>Upper Quartile</b>	22	40	30
<b>Maximum</b>	61	91	91

Table 4.3: Summary statistics of the roughness heights calculated from the upper and lower confluence velocity profiles. The final column gives the statistics for all of the datasets from both confluences. The mean values are given along with their respective 95% confidence intervals. All measurements are given in millimetres.

Table 4.3 gives mean  $z_0$  values of 18mm and 29mm for the upper and lower confluences respectively. However, the range of possible values varies considerably for each confluence, with the upper quartile values being up to five times larger than the lower quartile values. There is, therefore, significant uncertainty associated with obtaining roughness heights in this way.

#### 4.4.2 Obtaining Roughness Heights from a Characteristic Grain Size

For each of the 1m<sup>2</sup> quadrats used to determine a characteristic GSD at the upper and lower confluences, particles were sampled every 0.1m within the quadrat. This gave 121 data points for each, although the actual number of pebbles sampled was generally lower due to larger clasts being sampled multiple times. Therefore, the actual numbers of individual particles sampled were 121 and 101 for the true left and true right sites at the lower confluence, and 117, 120 and 121 for the true left, true right and middle sites at the upper confluence. This compares well to Kondolf's (1997) suggested minimum sample size of 60-100 particles.

The results from the Wolman count and photosieving methods of obtaining a GSD are presented in Figures 4.11 (lower confluence) and 4.12 (upper confluence). As explained in Section 3.8.3, in the Carbonneau *et al.* (2004) method a series of regularly spaced crosshairs are placed on the scaled photograph, with the user clicking on screen to identify the lengths of the b-axes of all particles under these crosshairs. This grid-by-number method therefore gives a frequency distribution that can be directly compared to the Wolman counts at the same location. In addition to the frequency distribution

figures, Table 4.4 gives the median, quartile and 84<sup>th</sup> percentile grain sizes for both methods at each of the sites, allowing quantitative comparisons to be made.

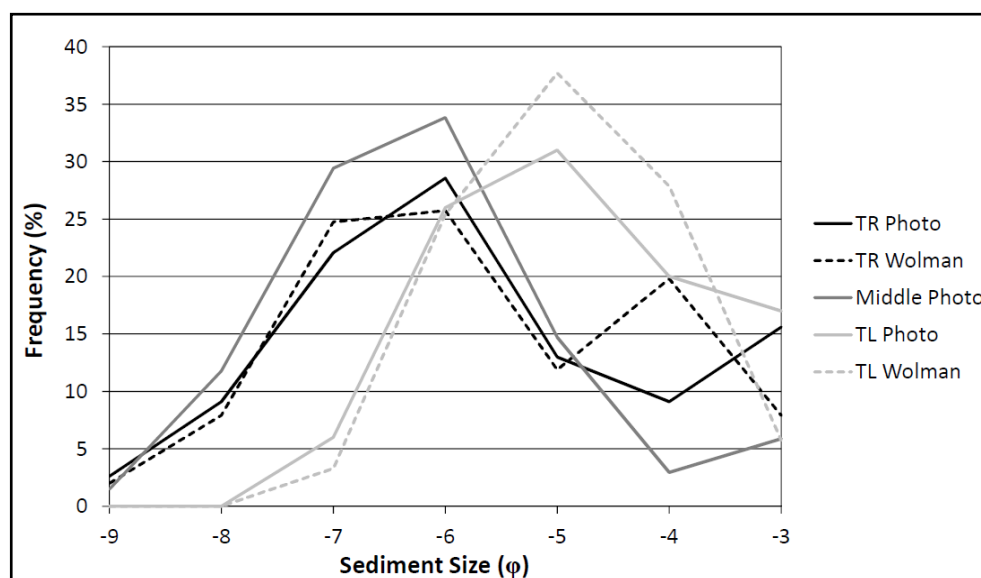


Figure 4.11: Grain Size Distributions (GSDs) determined from Wolman counts ('Wolman') and photosieving ('Photo') for the sites on the true left (TL), true right (TR) and middle (upstream corner) banks of the lower confluence. Grain sizes range from  $-9\phi$  (512mm) to  $-3\phi$  (8mm) and frequencies are the percentages of the grains' b-axes smaller than the  $\phi$  value.

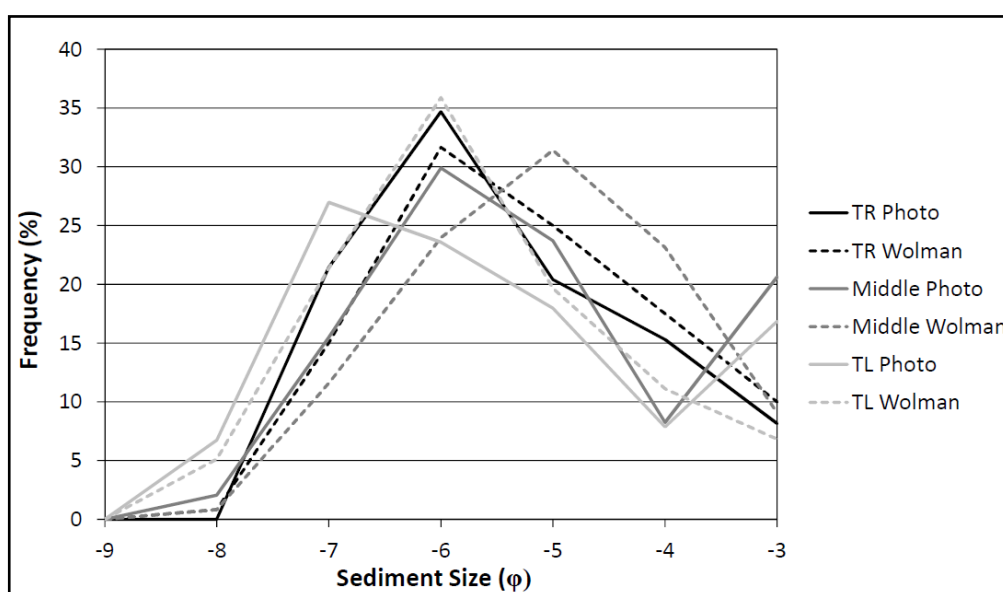


Figure 4.12: GSDs determined from Wolman counts and photosieving for the upper confluence. Notation and grain size range is the same as for Figure 4.11, although no pebbles were recorded in the  $<-8\phi$  (256-512mm) category.

From Figures 4.11 and 4.12, small differences can be seen in the GSDs obtained from the Wolman count and photosieving methods, but the overall pattern is clear in both cases. Of the five datasets where a comparison can be made, the true left and true

right GSDs of the lower confluence and the true right GSD at the upper confluence provide particularly good matches between the two methods.

In Table 4.4, the Root Mean Squared Error (RMSE) values are determined for each of the sites where both methods were used. The RMSE values vary from 2.9mm (true left site on the lower confluence) to 6.5mm (middle and true right sites on the upper confluence). A comparison with the median grain sizes (23.3-53.9mm) shows that these RMSE values are approximately an order of magnitude smaller than the median.

	Lower Confluence					Upper Confluence					
	True Left		Middle	True Right		True Left		Middle		True Right	
	WC	PS	PS	WC	PS	WC	PS	WC	PS	WC	PS
<b>D<sub>25</sub></b>	13.4	9.8	32.0	14.5	17.8	20.8	16.2	13.9	11.5	14.8	16.7
<b>D<sub>50</sub></b>	24.8	23.3	53.9	41.8	44.6	43.8	38.5	24.2	30.4	30.4	38.5
<b>D<sub>75</sub></b>	35.1	38.7	107.7	80.5	78.9	68.7	77.5	45.9	53.4	53.0	59.3
<b>D<sub>84</sub></b>	42.6	45.2	119.6	102.7	96.4	96.6	94.5	58.8	66.9	63.8	71.5
<b>RMSE</b>	2.9			3.9		5.7		6.5		6.5	

Table 4.4: Comparison of characteristic grain sizes determined from Wolman counts (WC) and photosieving (PS) for each site of the lower and upper confluences. All measurements are given in millimetres.

The characteristic grain sizes given in Table 4.4 were used to give an effective roughness height ( $z_0$ ) using Equations 3.28 to 3.30. The calculated  $z_0$  values are given in Table 4.5. In each case, the grain size used is the mean of those determined from the Wolman count and photosieving methods. Averaging between sites gives roughness heights of 9.8mm for the lower confluence and 8.0mm for the upper confluence. Although these roughness height values are lower than the mean values in Table 4.3, they are still within the range of values found from the velocity profile method.



	Location	Method	ks	z0
Lower Confluence	True Left	0.1D <sub>84</sub>		4.39
		3.5D <sub>84</sub>	153.7	5.12
		6.8D <sub>50</sub>	163.5	5.45
	Middle	0.1D <sub>84</sub>		11.96
		3.5D <sub>84</sub>	418.6	13.95
		6.8D <sub>50</sub>	366.5	12.22
	True Right	0.1D <sub>84</sub>		9.96
		3.5D <sub>84</sub>	348.4	11.61
		6.8D <sub>50</sub>	293.8	9.79
Upper Confluence	True Left	0.1D <sub>84</sub>		9.56
		3.5D <sub>84</sub>	334.4	11.15
		6.8D <sub>50</sub>	279.8	9.33
	Middle	0.1D <sub>84</sub>		6.29
		3.5D <sub>84</sub>	220.0	7.33
		6.8D <sub>50</sub>	185.6	6.19
	True Right	0.1D <sub>84</sub>		6.77
		3.5D <sub>84</sub>	236.8	7.89
		6.8D <sub>50</sub>	234.3	7.81

Table 4.5: Roughness heights calculated from the characteristic grain sizes given in Table 4.4 using the three alternative methods presented in Section 3.8.3. All measurements are in millimetres.

#### 4.4.3 Discussion of the Roughness Values

There is good agreement between the GSD results obtained from the Wolman counts and photosieving, meaning that there is little evidence to suggest that the two methods cannot be used interchangeably on these types of surface. However, determining a representative roughness value from these data is far from straightforward. The results in Table 4.3 show that there can be a considerable range in the roughness heights calculated from individual velocity profiles, meaning that the concept of a single roughness height representing a gravel- or cobble-bed river confluence could be considered an over-simplification.

The roughness heights calculated using the D<sub>50</sub> and D<sub>84</sub> values are lower than those using the velocity profiles, although both methods are consistent in recording a lower roughness height for the upper confluence. Part of the issue is that, as noted in Section 3.8.3, it is never entirely clear which components of roughness are being represented. In some cases (*e.g.* Profile C in Figure 4.9 and Profile U in Figure 4.10), the velocity profiles may not follow the standard logarithmic shape due to the presence of topographic obstacles. Although this is likely to give high roughness values, the

cause would be the presence of features which would be at the extremes of the bed GSD and therefore not necessarily located within the sampling area from which the  $D_{50}$  and  $D_{84}$  values were derived. In addition, it should be noted that such obstacles would most likely be represented in the macrotopography of any numerical model (depending on the cell resolution), rather than through the roughness height. Other possible explanations for disparities in the calculated roughness heights are that the bed GSD does not account for effects such as the organisation of the grains, channel form roughness or channel-scale effects on the flow field.

Therefore, if the aim is to provide boundary conditions for numerical models, selecting a single representative value for roughness is difficult. As such, when the roughness height is selected, it should be considered as a reasonable estimate only and just one value from a range of equally valid roughness heights. For this thesis, the results from the velocity profile method will be used in the first instance, although part of the testing of the numerical models (presented in Chapter 5) will include an analysis of the model sensitivity to changes in the roughness parameter.

## **4.5 Flow Data from the Moor House Confluences**

If there is to be any understanding of the sediment transport processes operating in upland river confluences, it is first necessary to understand the flow processes, and especially the shear stress, in these confluences. In particular, as noted in Section 4.1, it is important to determine whether much of the knowledge obtained from lowland river confluences is applicable to upland confluences with steeper water surfaces. Furthermore, if numerical modelling is to be used to further this understanding, reliable input and validation flow data are pre-requisites.

In Section 3.8.2, it was determined that the Moor House confluences would be used to obtain three-dimensional flow data for the inlets, outlets and a cross-section in the middle of the confluence. In addition, the criteria stated that data should be taken at 0.5m spacing across the cross-section (equivalent to an average  $y/w_c$  ratio of less than 0.1) and that a velocity profile should be taken at each cross-section.

As specified in Section 3.8.2,  $aDv$  data were collected for 60s (at 10Hz), with the results to be analysed to determine the minimum length of time series that would have been required to reach stationarity in the data. Figures 4.13 and 4.14 show the mean velocity and standard deviation plotted against length of time series for each

velocity component of Profile W at the lower confluence. These data have already been presented in the form of time-averaged velocity profiles in Figure 4.10, while the raw data themselves are shown later in Figure 4.19 (page 157) as part of the flow turbulence data.

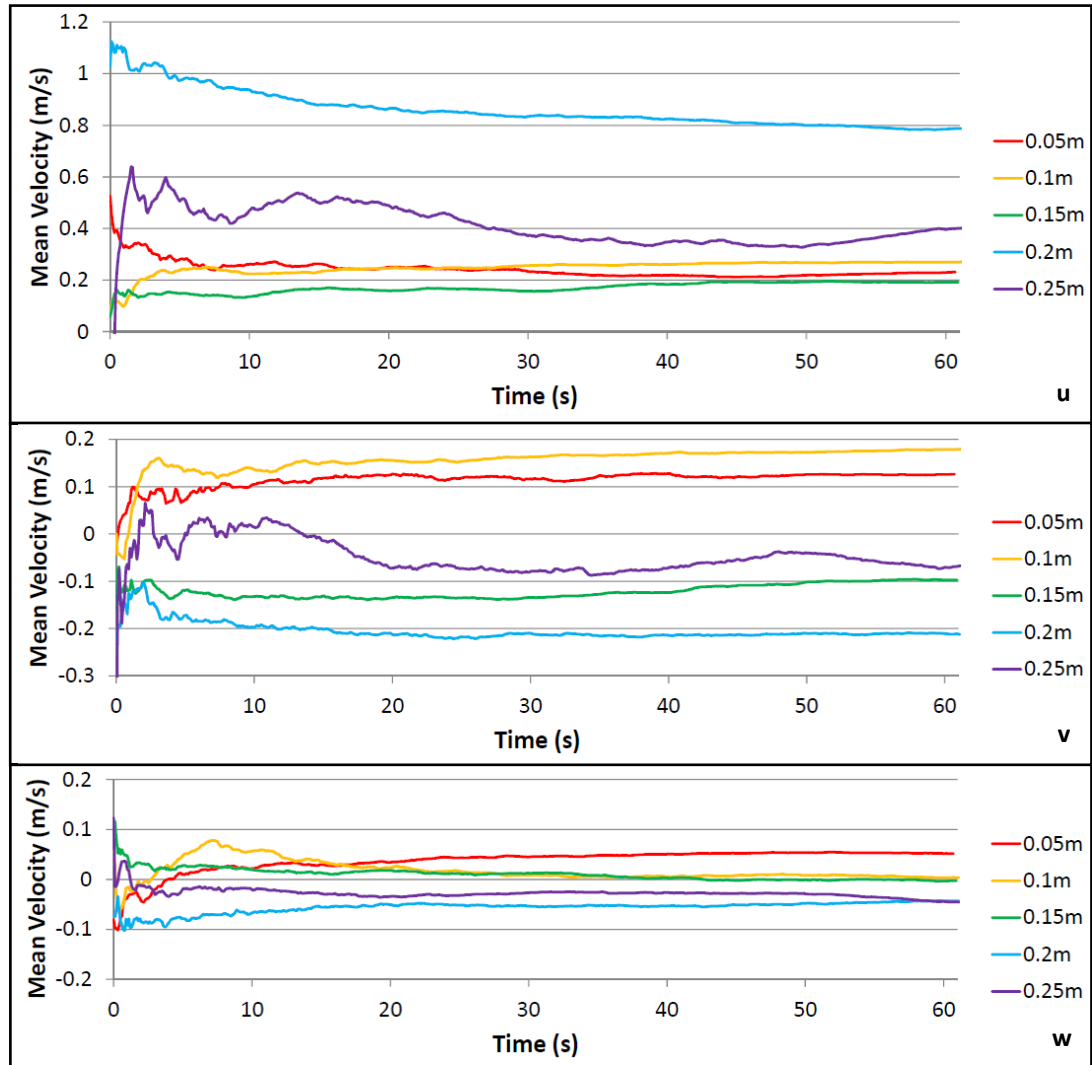


Figure 4.13: Graphs showing the variation in mean velocity with length of time series for a velocity profile from the lower confluence (Profile W). Graphs are plotted for downstream ( $u$ ), cross-stream ( $v$ ) and vertical ( $w$ ) velocities.

In both Figure 4.13 and 4.14, the dataset taken at 0.25m above the bed (*i.e.* nearest the surface) tends to show the greatest variability. This dataset was particularly badly affected by anomalously high velocity fluctuations (see Figure 4.19), which are likely to be due to noise from the presence of air bubbles near the water surface. It is therefore useful as a comparison with the remainder of the profile (which by and large did not suffer these problems).

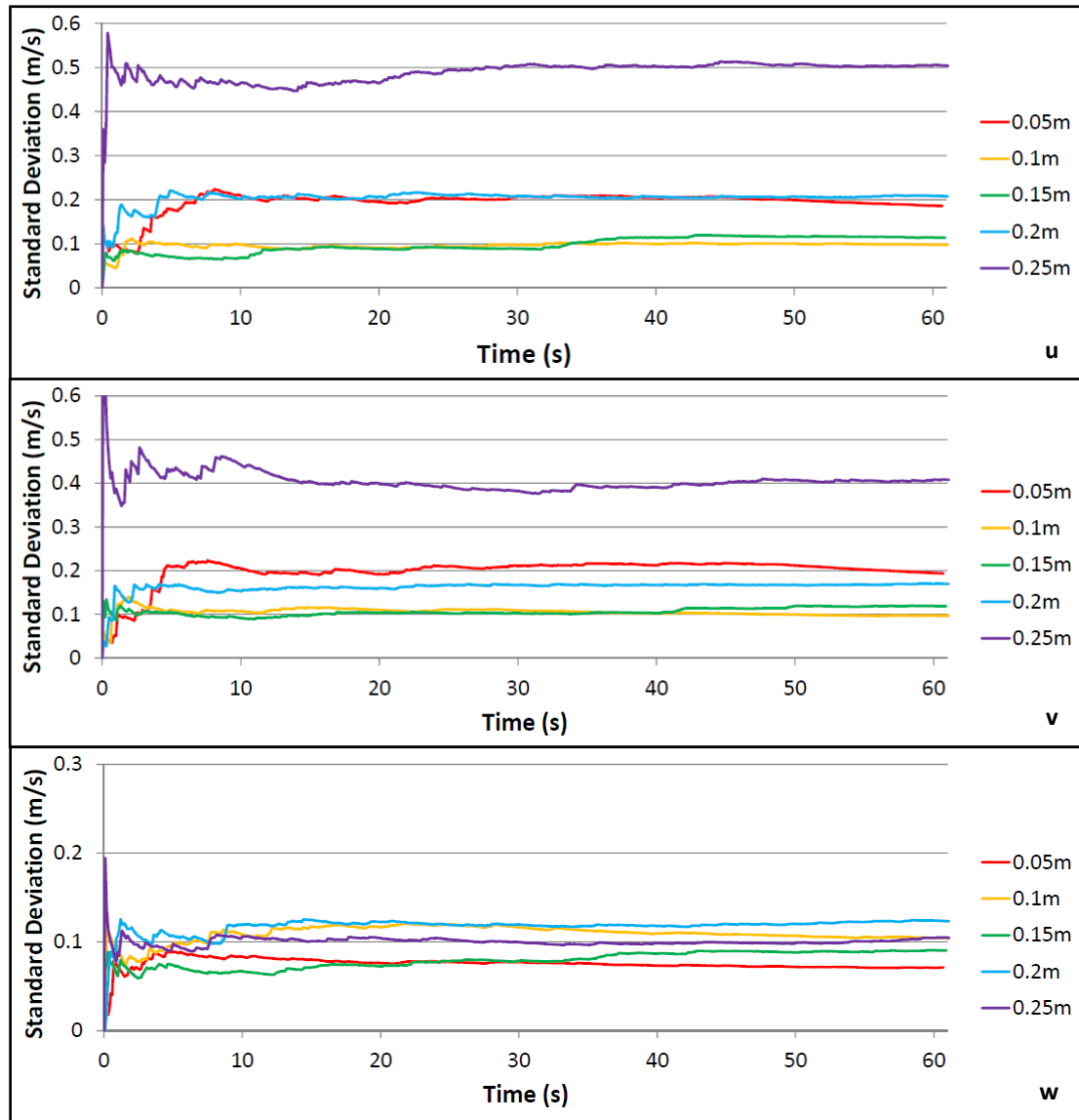


Figure 4.14: Graphs plotting the standard deviation of velocity against length of time series for the aDv data in Profile W.

Whilst the dataset from 0.25m is a clear anomaly for the downstream and cross-stream velocity plots, the vast majority of the remainder of the lines tend to reach a stable value once data have been collected for at least 30s. The 20s time series of Roy and Bergeron (1990) would appear to be slightly too short, although in most cases it would not have had a significantly negative effect on the quality of the mean velocities recorded. Therefore, although the aDv data were collected for 60s to satisfy requirements for a high-quality dataset, a time series of 30s would be sufficient if only the mean flow velocity is required.

When analysing aDv data, any anomalous data points ('spikes') are usually removed before the data are processed (*e.g.* Rodriguez *et al.*, 1999). Determining which

points are considered anomalous is tricky, as a balance has to be struck between retaining poor quality data and the potential removal of good data (Elgar *et al.*, 2005). Rhoads and Sukhodolov (2001) removed all data points where the velocity was more than three standard deviations from the mean and it is this threshold which was used to remove extreme outliers from the aDv data presented in this section. This will ensure the mean velocity is not unduly skewed by large anomalous values, although for these data the effect on the mean was found to be low.

This section begins by presenting the discharge measurements obtained from all cross-sections and comparing the results with data from the Environment Agency gauging station (shown previously in Figure 4.2). This provides an indication of how well the interpolation of point data across a cross-section (using the trapezium rule) agrees with data collected at fixed gauging stations. A good agreement is important as it will increase confidence in both datasets and also justify the use of EA gauging station data when simulating high discharge events through the confluences. The following section then defines six major flow processes from the classical model of river confluences and uses the mean flow data to determine in what form they are present at the Moor House confluences.

#### *4.5.1 Comparison of Discharge Measurements*

Flow velocity datasets were obtained on three separate occasions for each confluence. ECM readings were taken on the 8<sup>th</sup> April 2011 for the inlets and outlets of both confluences, with stream ribbons used to determine the angle of flow. Additional ECM data were taken for the lower confluence on the 22<sup>nd</sup> July 2011, at which point the inlet and outlet positions were modified to provide a better geometry for both the numerical modelling and the second set of particle tracking experiments (which are discussed in Chapter 6). More detailed three-dimensional aDv data were obtained on three occasions: at the upper confluence on 20<sup>th</sup> September 2011 (for a medium discharge) and 23<sup>rd</sup> September 2011 (low discharge), and at the lower confluence on 7<sup>th</sup> October 2011 (medium discharge).

Discharges were calculated for each of the cross-sections for which flow data were collected. Table 4.6 shows the discharges calculated for the tributaries and main channel on each of the surveyed days, with the gauging station data provided for comparison.

Date	Confluence	Discharge (m³/s)							
		True Left		True Right		Main Channel			EA Station
8/4/11	Lower	0.17		0.2		0.32			0.1-0.11
8/4/11	Upper	0.1		0.04		0.12			0.1-0.11
22/7/11	Lower	0.22		0.17		0.32			0.13-0.15
20/9/11	Upper	0.36		0.25		0.55	0.58	0.46	0.5-1.0
23/9/11	Upper	0.05	0.11	0.01	0.06	0.17	0.18	0.11	0.13-0.14
7/10/11	Lower	0.21		0.45		0.77	0.81	0.77	0.26-0.41

Table 4.6: Comparison between EA gauging station data and the discharges calculated from ECM and aDv data. The gauging station is on the same channel as the true right tributary of the lower confluence and the main channel of the upper confluence (values in black text). The EA data are given as the range of values measured during the data collection period.

The data in Table 4.6 demonstrate that discharge data obtained using the trapezium method does have some uncertainty, with multiple cross-sections for the same channel giving discharge variations of up to 0.12m<sup>3</sup>/s. The comparison between the EA data and the local calculated discharges is more positive, however. The EA station data should be compared directly with only the main channel at the upper confluence and the true right tributary of the lower confluence (the values given in black text). To ease comparison, those values for which a direct comparison should not be made are in grey.

For the main channel of the upper confluence there is good agreement on all three occasions, although the 20<sup>th</sup> September dataset has values at the lower end of the range of gauging station discharges. This may be explained by small tributaries downstream of the confluence contributing more in the higher flow conditions. The true right tributary of the lower confluence has slightly higher calculated discharges than the gauging station data on all three occasions, with the differences highest on 8<sup>th</sup> April 2011. Again, however, part of this could be explained by small additional contributions to the discharge between the gauging station and the confluence itself.

Therefore, the similarities between the discharge data collected *in situ* and the EA gauging station data indicate that neither method is unreliable. This means that there can be confidence in the use of the gauging station data to determine the magnitude of floods through the reach, which will provide important boundary condition data when simulating flows in which bedload transport is active.

#### *4.5.2 Mean Flow Results*

This section presents the time-averaged three-dimensional aDv data for the upper and lower Moor House confluences. All three aDv datasets were analysed in depth for both their mean flow velocity and the characteristics of the flow turbulence (presented in Section 4.6). However, results are presented from only the lower confluence on 7<sup>th</sup> October 2011 and the upper confluence on 20<sup>th</sup> September 2011 (the two datasets obtained in medium discharges). This is because having analysed the low flow data from the upper confluence (23<sup>rd</sup> September 2011), flow velocities and water depths were found to be too low to provide any additional insight into the nature of the flow field at the upper confluence.

In presenting the mean flow data from the upper and lower confluences, this section places particular emphasis on identifying which of the major flow features from the classical river confluence model are found at these upland river confluences. From the review of river confluence research in Chapter 2, the focus will be on the following six flow features:

1. the shear/mixing layer and evidence for these two processes;
2. the flow separation zones on the downstream corners;
3. helical flow cells in the centre of the confluence, which resemble the back-to-back meander bends described by Ashmore and Parker (1983);
4. flow divergence downstream of the mixing zone which has the potential to develop into a zone of sediment deposition;
5. increases in velocity downstream as the total cross-sectional area is reduced; and
6. where the beds are discordant, flow in the lee of the step and the resultant upwelling at the downstream corner, as identified by Best and Roy (1991).

The discussion in Section 4.5.3 will consider which of these features are present or absent and possible explanations for this. In addition, it will highlight those features for which the mean flow data alone provide insufficient evidence and therefore will determine the focus of the analysis of flow turbulence in Section 4.6.

Figure 4.15 shows the direction and magnitude of the flow in the *xy*-plane for the lower confluence on 7<sup>th</sup> October 2011. Figure 4.16 meanwhile gives the same

information for the upper confluence during the medium discharge flow of 20<sup>th</sup> September 2011.

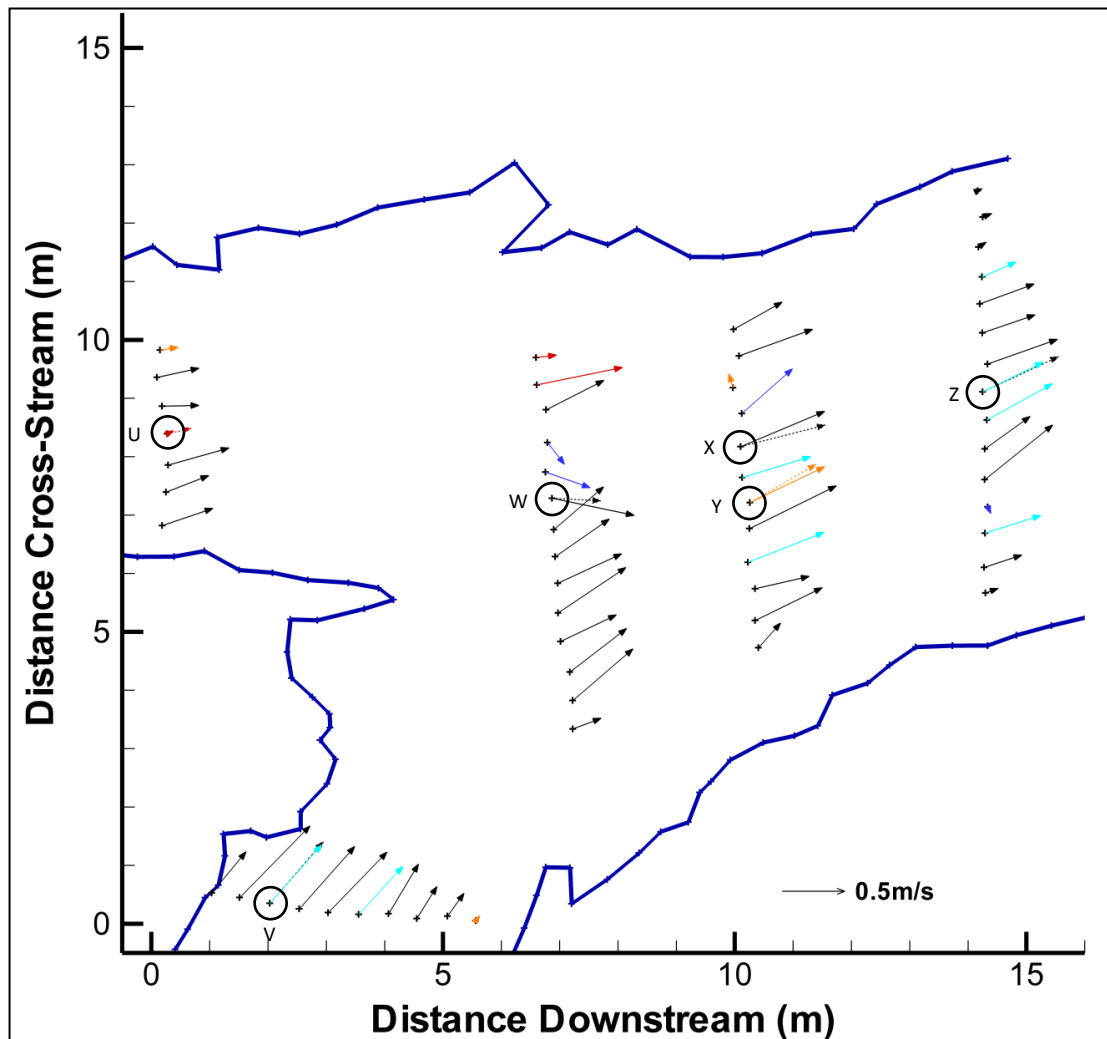


Figure 4.15: Flow directions and velocities at the lower confluence for the medium flow of 7<sup>th</sup> October 2011. Solid arrows give the 0.4d measurement and dashed arrows the velocity profile average. Flow towards the bed is highlighted in orange (>5°) or red (>10°), with flow towards the surface in light blue (>5°) or dark blue (>10°).

The horizontal flow in the lower confluence (Figure 4.15) shows a small amount of flow deflection for both tributaries as they enter the confluence, although the true right tributary clearly dominates. This dominance reflects the differences in tributary discharges calculated for the lower confluence on 7<sup>th</sup> October 2011 (given in Table 4.6). The true right tributary is characterised by deeper and faster flow on its true left bank, whilst the true left tributary has less cross-stream variation. Of the six major flow processes identified above, there is evidence of a flow separation zone on the true left downstream corner, with very slow velocities recorded in the area 14m downstream and



11m cross-stream. However, there is no obvious divergence of the thalweg flow near the confluence outlet or any significant change in thalweg velocities between cross-sections. Instead, the channel width increases, implying that the increase in discharge is largely accounted for by a greater cross-sectional area.

For most of the lower confluence cross-sections, there is little variability in the angle of the flow, although the major exception to this is the area surrounding Profile W. A comparison with Figure 4.7 suggests that this is in the part of the confluence where the flow from the true left tributary enters the main channel over a steep avalanche face, being routed around some large boulders in the process. In order to examine the potential presence of strong secondary flows, it will be necessary to investigate the variations in flow direction through the vertical velocity profiles, in particular Profiles W, X and Y.

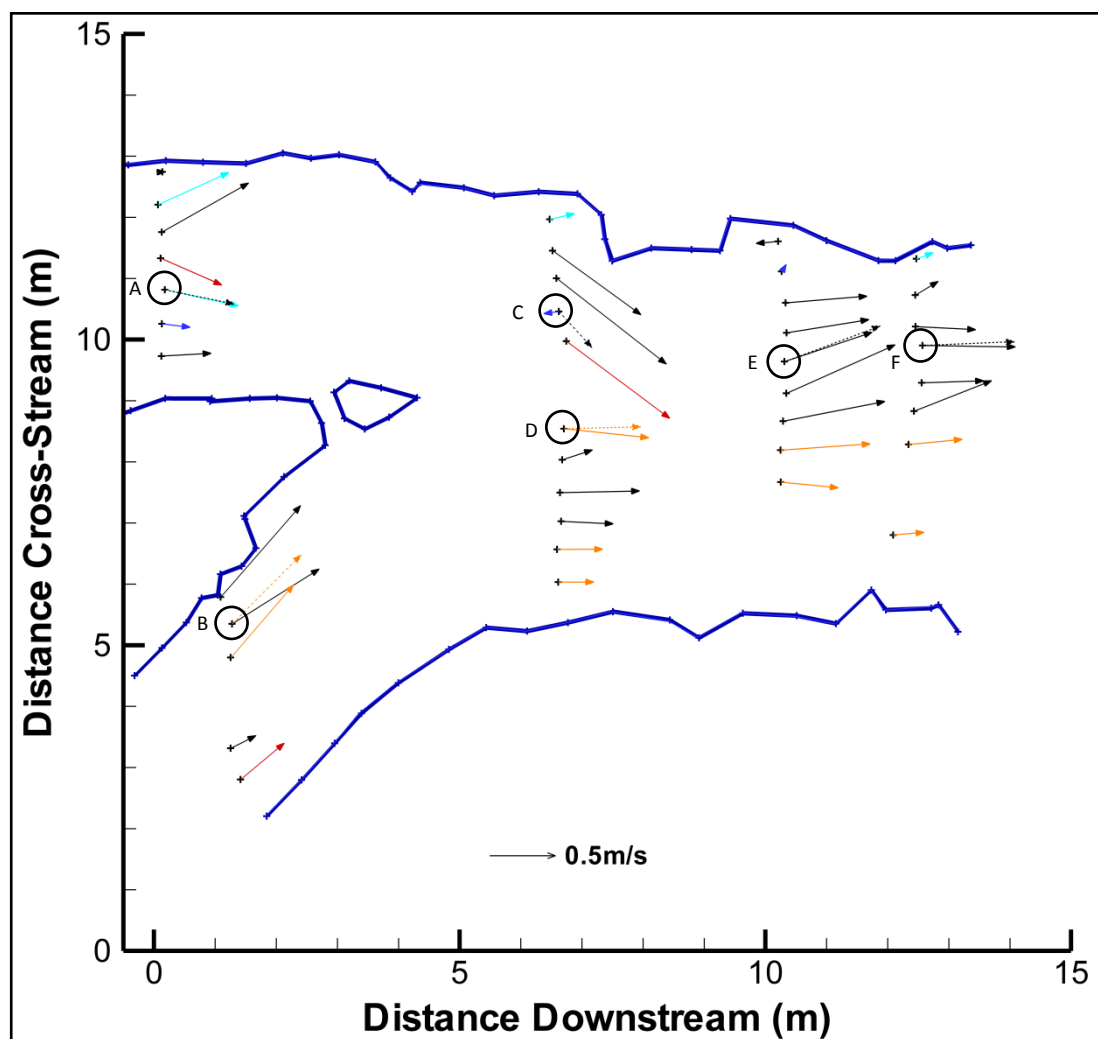


Figure 4.16: Flow directions and velocities for the upper confluence in a medium flow of 20<sup>th</sup> September 2011. This figure uses the same notation as in the previous figure.

In Figure 4.16 the true right inlet has faster flow on its deeper true left bank, whilst the true left inlet has a zone in the centre of the channel where the flow separates. On the DEM in Figure 4.8, this can be seen as a small area of higher topography in the middle of the true left channel, approximately 0.8m downstream of the inlet cross-section. As the true left tributary joins the main channel there is a clear increase in velocity, as the water flows through the narrow, deep constriction highlighted in Section 4.3.4. It is therefore in this zone that the maximum velocities are found, rather than further downstream in the main channel. A flow separation zone is visible on the downstream corner (at 10m downstream, 11m cross-stream), but there is no evidence of flow divergence in the downstream channel.

Figures 4.15 and 4.16 also show the vertical component of the flow using different coloured arrows. A minimum vertical angle of  $5^\circ$  was chosen to ensure that the results were not affected by any errors due to the probe being held slightly off-vertical on the wading rod, whilst particularly large vertical flow angles (greater than  $10^\circ$ ) are emphasised by darker colours. However, there are no clear patterns visible for either confluence, suggesting any patterns in the vertical velocity component are more subtle.

Figures 4.15 and 4.16 have provided evidence for some of the flow features set out at the beginning of this section. However, in order to determine whether the confluences have secondary flow structures consistent with the presence of helical flow cells or flow features related to bed discordance, data from vertical velocity profiles are required.

In Section 3.8.2, it was specified that at least one velocity profile should be taken at each cross-section, either in the thalweg or zone of deepest flow. Although data from a single profile would be insufficient to definitively identify the presence of, for example, back-to-back helical cells, they can indicate the presence of strong secondary flows which will be investigated further in the numerical modelling in Chapter 5.

For both of the aDv datasets presented here, measurements were taken from six vertical velocity profiles, one for each cross-section and an additional one obtained from one of the cross-sections in the centre of the confluence. Average horizontal velocities were determined from these profiles and were shown in Figures 4.15 and 4.16 as dashed arrows. Many of the averaged velocity values agree well with the single point measurement taken at  $0.4d$  above the bed, thus justifying the use of  $0.4d$  measurements as an estimate of depth-averaged flow velocity. However, there are some profiles (W

and X for the lower confluence and B and D for the upper confluence) where there is a clear difference in flow direction, which may indicate the presence of secondary flow.

In the vertical velocity profiles, substantial variations in flow direction with depth will indicate the presence of strong secondary flows. However, as the information was obtained from aDv data, it is also possible to assess the variability in flow direction through time. This enables the variability in flow direction between different depths to be assessed relative to the temporal variability within each dataset. If there is significant variability in the recorded flow angles at each depth, then the overall pattern of secondary flow is unlikely to be consistent through time. However, if there is very little overlap between the ranges of instantaneous flow direction for each dataset, then the evidence for some form of secondary flow is substantially stronger. As such, for each dataset of the velocity profiles at the lower and upper confluences, Figures 4.17 and 4.18 show the variability in the recorded flow directions in the form of radar plots. In all cases the flow angles are given relative to the depth-averaged flow direction (which is given a value of  $0^\circ$ ).

For the velocity profiles at the lower confluence in Figure 4.17, the main pattern is for flow in the downstream channel to be towards the true left at the bed and the true right at the surface. This is particularly evident at Profiles W and Y, with Profile X having a similar but weaker form. However, this pattern does not extend as far downstream as Profile Z, where the flow nearest the bed tends to move towards the true right bank. This suggests either that there are helical secondary circulation cells developing at this location in the confluence, or that flow from the true left tributary is flowing over the top of that from the true right tributary. In the tributaries, Profile U has substantial variability throughout much of the flow depth, which is likely to be linked to the very low flows near the bed that were identified in Figure 4.10u. This was caused by the presence of a submerged boulder just downstream of the measurement location. Profile V, meanwhile, has some evidence of flow at the bed moving towards the true right. This may be due to a weak helical circulation cell developing as a result of the curvature of the tributary as it enters the confluence (as is found in meander bends).

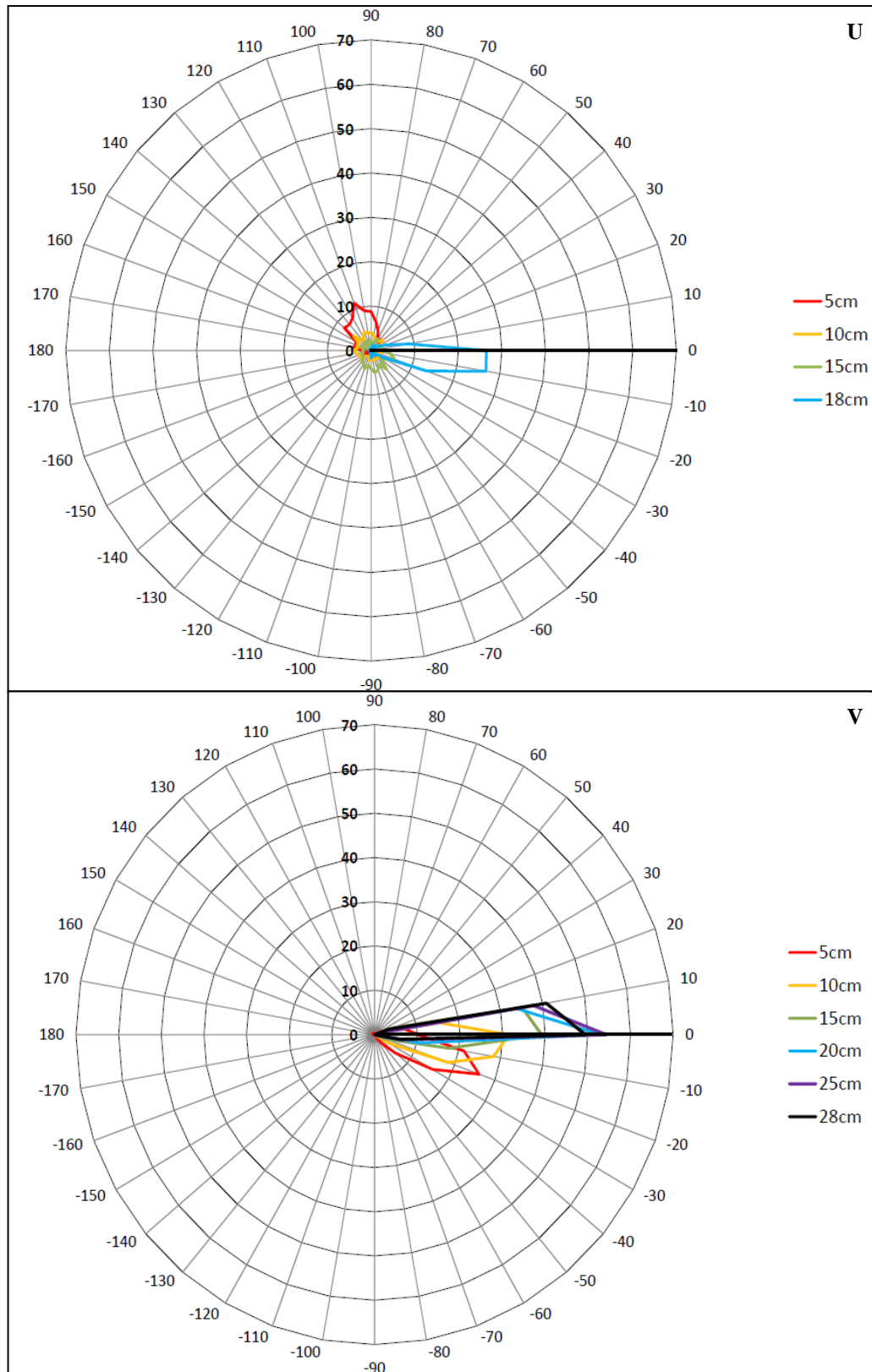


Figure 4.17: Radar plots showing deviations from the mean flow angle for each dataset (given as the elevation above the bed) of velocity profiles U and V at the lower confluence. The graph shows the percentage of the time series for which the flow is at a given angle (to the nearest 10°). The mean flow angle for each velocity profile is set at 0°. Figure continues on the next two pages.

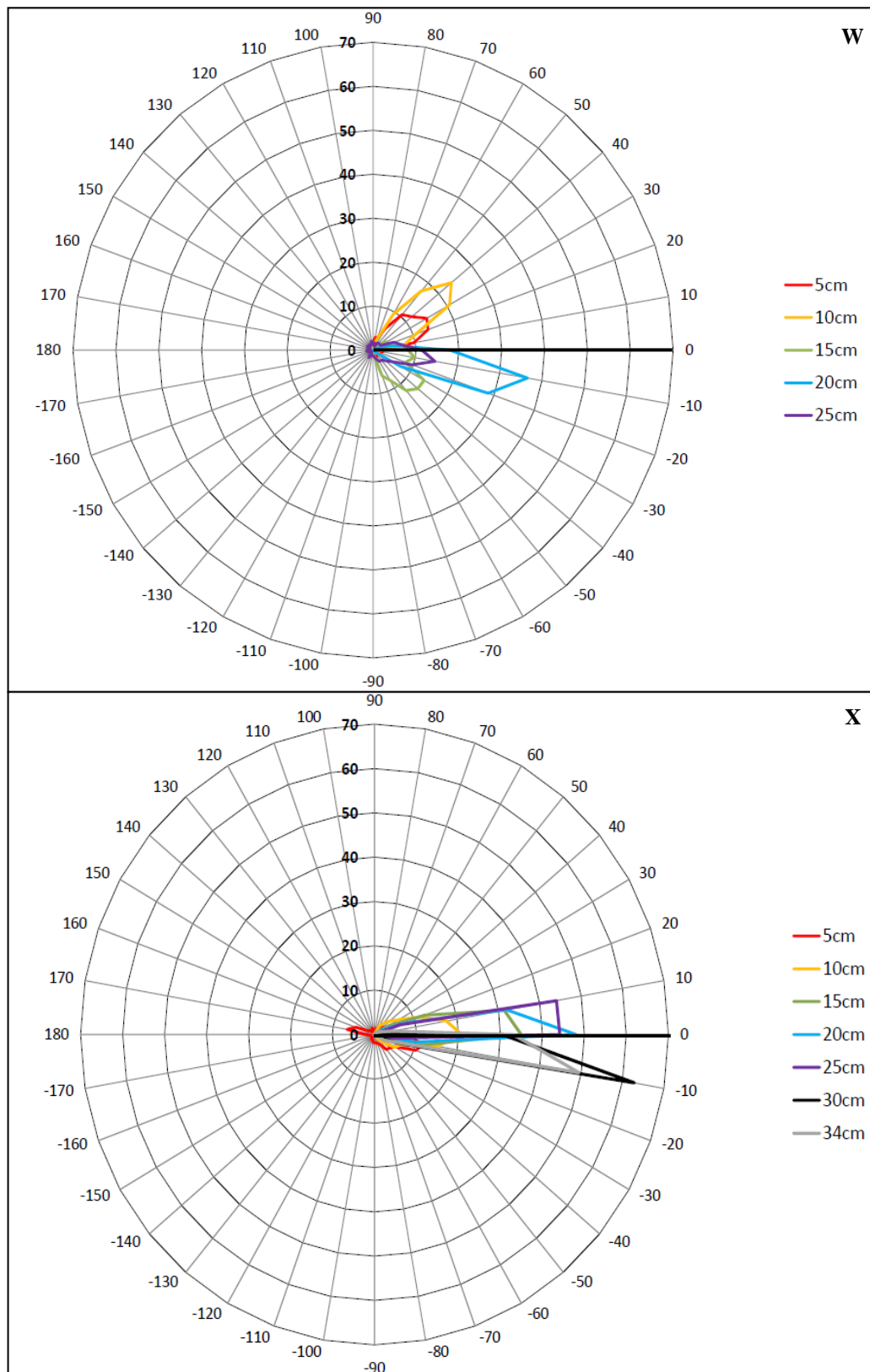


Figure 4.17 (continued): Radar plots for Profiles W and X at the lower confluence.

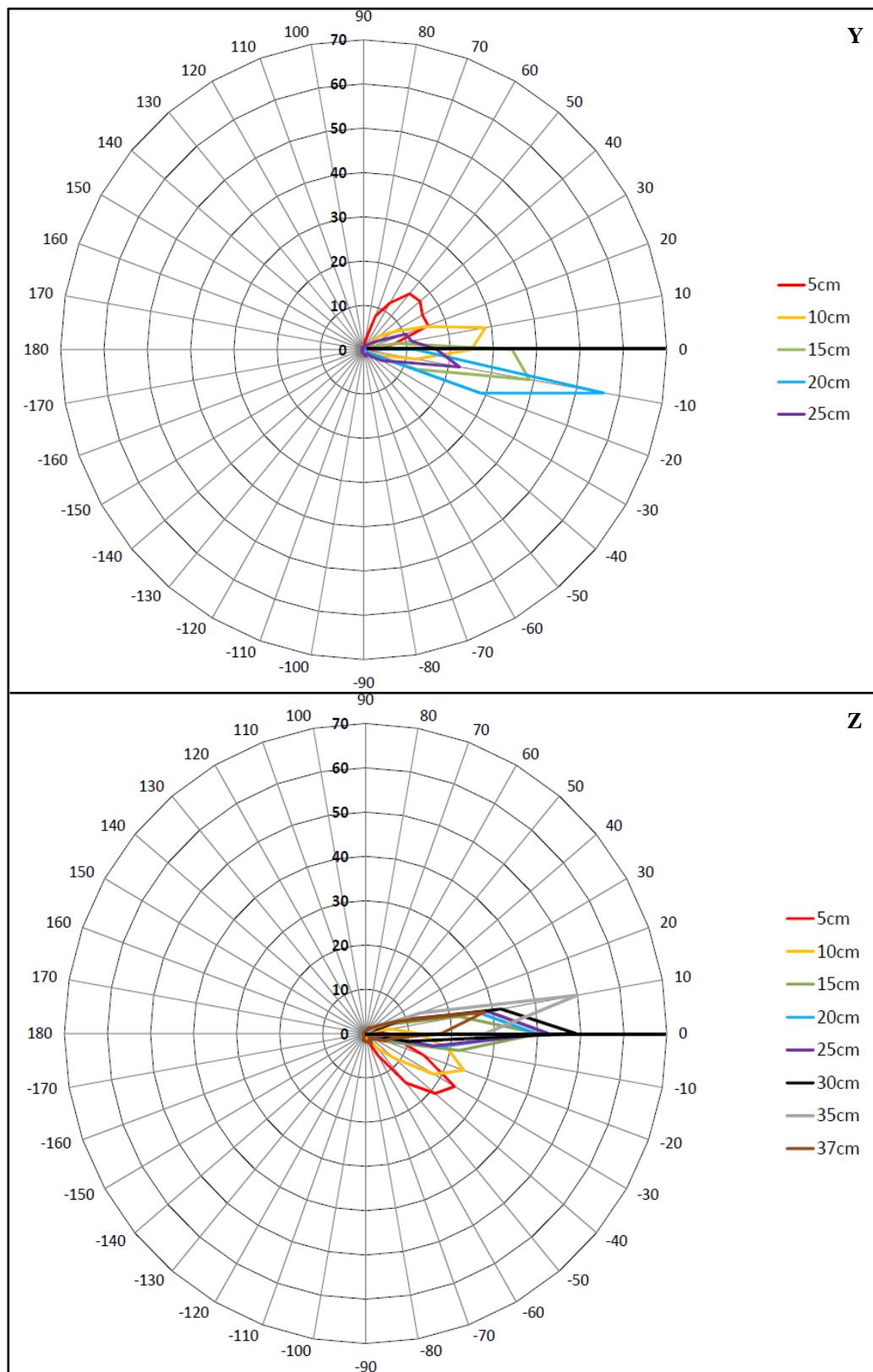


Figure 4.17 (continued): Radar plots for Profiles Y and Z at the lower confluence.

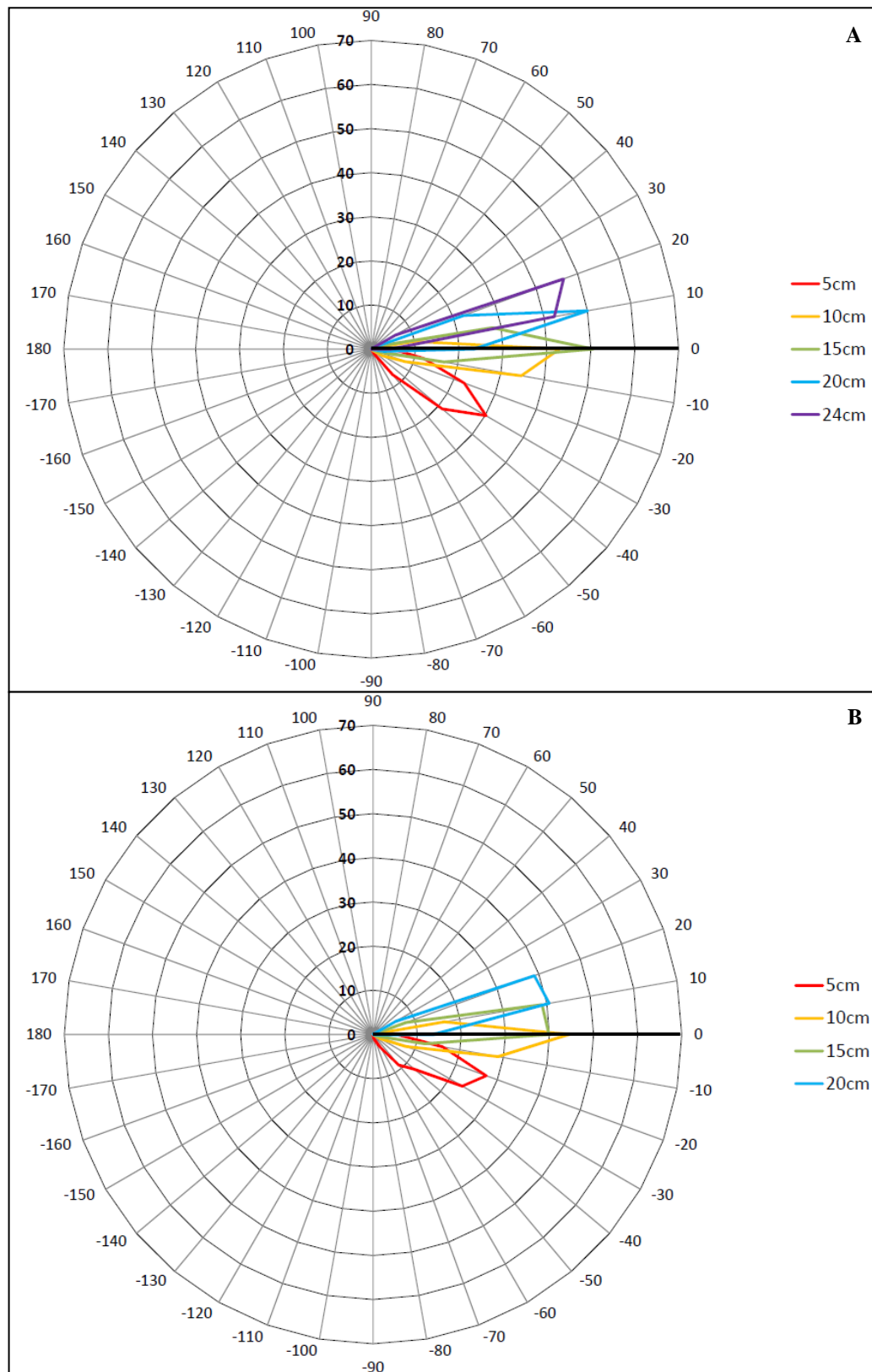


Figure 4.18: Radar plots for Profiles A and B at the upper confluence from the dataset of 20<sup>th</sup> September 2011. The figure uses the same notation as in Figure 4.17. Figure continues on the next two pages.



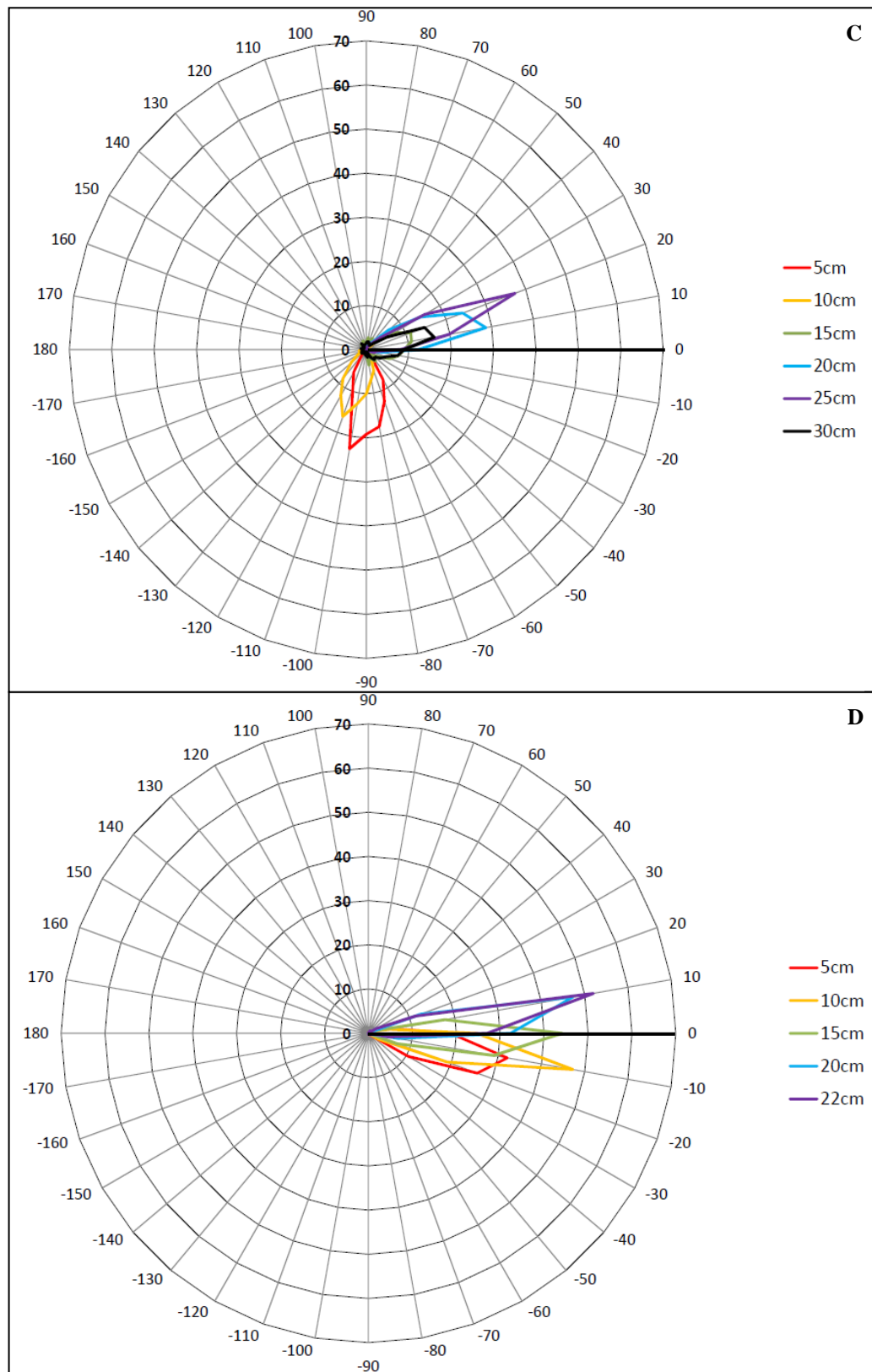


Figure 4.18 (continued): Radar plots for Profiles C and D at the upper confluence from the dataset of 20<sup>th</sup> September 2011.



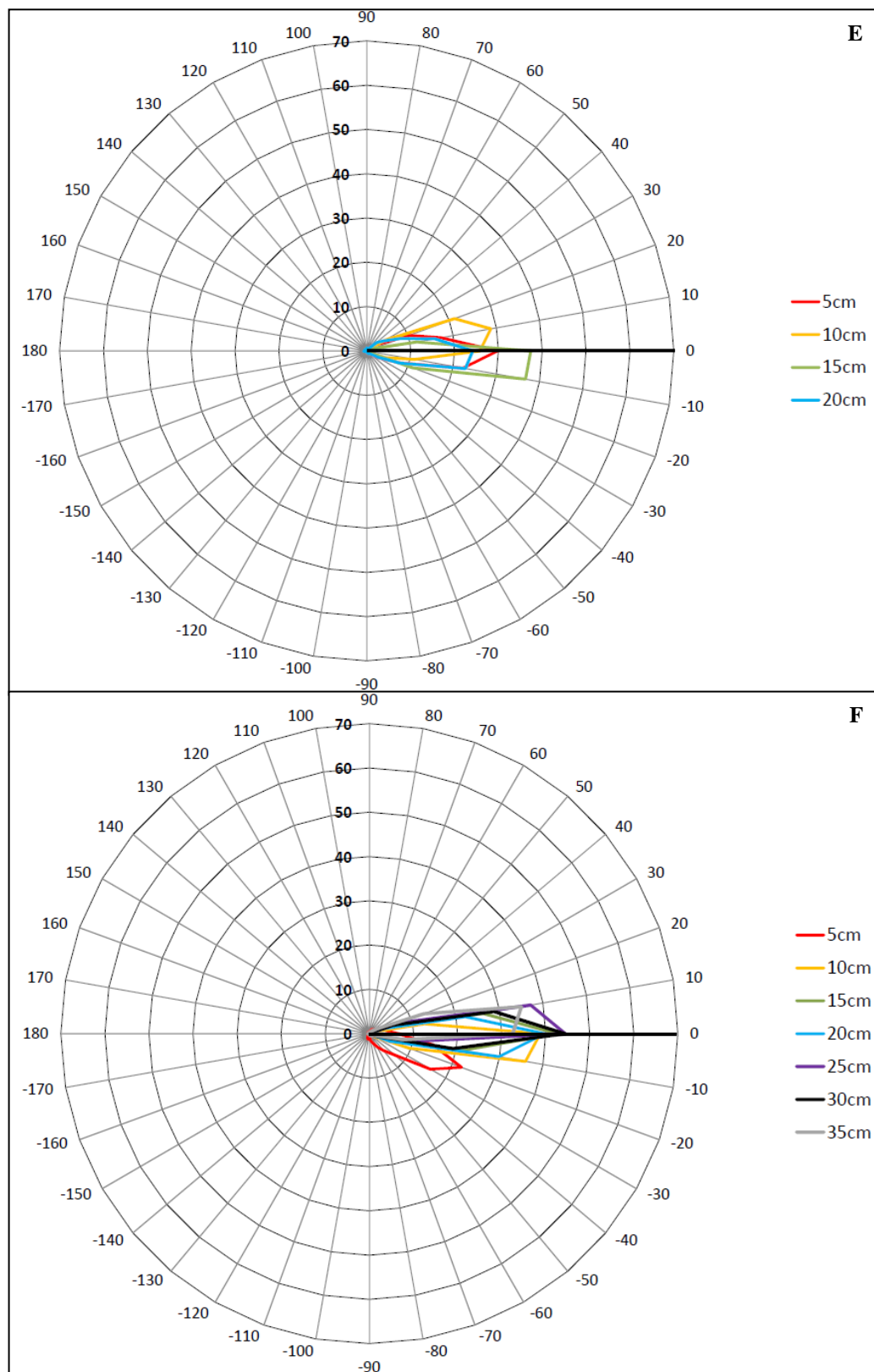


Figure 4.18 (continued): Radar plots for Profiles E and F at the upper confluence from the dataset of 20<sup>th</sup> September 2011.

For the velocity profiles at the upper confluence (Figure 4.18), the strongest evidence of secondary flow is in the tributaries, with both profiles A and B showing a tendency for flow to be towards the true left at the surface and the true right at the bed. In the case of Profile B, this is likely to be due to the curvature of the true right tributary and a weak helical cell developing as a result. For Profile A, there is no such curvature, but the flow is being deflected around an obstacle (visible just downstream of the inlet in the DEM in Figure 4.8). In the main channel, Profile D appears to have a similar, but weaker trend, which may imply a small amount of flow deflection as the true left tributary joins the main channel or that this zone of the channel is still being affected by the curvature of true right tributary further upstream. The remainder of the profiles show no clear evidence of variability in flow direction with depth, with the exception of Profile C, which, like Profile U, has particularly low flows near the bed (see Figure 4.9c).

#### *4.5.3 Discussion of the Mean Flow at the Moor House Confluences*

In Section 4.5.2, six key flow processes were identified from the classical model of river confluences. The mean flow data were then presented to determine whether these flow processes could be identified in the Moor House confluences. From the horizontal velocity data (Figure 4.15), there is clear evidence of a flow separation zone in the vicinity of the downstream corner of the lower confluence. A similar zone is visible at the upper confluence (Figure 4.16). Ashmore *et al.* (1992) suggested that the more gently curving banks of natural confluences are less likely to induce flow separation zones, but both Moor House confluences provide evidence against this assertion. Nevertheless, the evidence from Ashmore *et al.* (1992) suggests that the formation of these flow separation zones is likely to be due to the specific geometry of the Moor House confluences.

The classical model of river confluences also identifies the flow separation zone as an area of deposition within the confluence, potentially leading to a lateral bar developing (Best, 1986; Leite Ribeiro *et al.*, 2012). Reviewing the DEMs (Figures 4.7 and 4.8), however, shows that if anything, these flow separation zones are deeper areas within the confluence. This means they are unlikely to be zones of deposition and implies that the flow and morphology of the confluence may not be in equilibrium at these medium discharges.

As cross-sectional area reduces in the downstream channel, the flow velocity is expected to increase to satisfy mass continuity (Rhoads and Kenworthy, 1995). The reality at natural confluences, however, is that this is not always clearly present (Ashmore *et al.*, 1992; Wallis *et al.*, 2008; Szupiany *et al.*, 2009). The Moor House confluences have provided more evidence for this, with no clear increase in velocity in the downstream channel in either Figure 4.15 or 4.16. The lack of a substantial increase in flow velocity implies that the higher discharge is accounted for through an increase in cross-sectional area. This is supported by the DEMs in Figures 4.7 and 4.8, which show the downstream channel is deeper and wider than the tributaries.

Mosley (1976) identified the possibility of flow divergence downstream of the mixing zone, leading to the formation of a mid-channel bar. However, Parsons *et al.* (2008) implied that symmetry in the planform geometry is important if this is to occur in natural confluences. This would explain why flow divergence has not been identified as a key component of the flow field at either the Bayonne-Berthier or Kaskaskia-Copper Slough confluences (Biron *et al.*, 1993, 2002, 2004a; De Serres *et al.*, 1999; Bradbrook *et al.*, 2000a; Rhoads and Sukhodolov, 2001, 2008; Boyer *et al.*, 2006; Rhoads *et al.*, 2009; Constantinescu *et al.*, 2011). Likewise, from Figures 4.15 and 4.16 there is no evidence of flow divergence in the downstream channel of either Moor House confluence. However, at present there is insufficient information to determine whether asymmetry or another factor causes the lack of flow divergence.

In the centre of the confluence, the classical model of river confluences (as discussed in Section 1.2) implies that two helical flow cells will form, meaning the confluence resembles back-to-back meander bends (Ashmore and Parker, 1983). However, in the case of discordant beds, research has found the helical cells to be weaker, with water from the deeper tributary instead tending to flow in the lee of the step before upwelling at the downstream corner (Best and Roy, 1991).

As identified in Section 4.3.3, the lower confluence has a very clear discordance between the two tributary beds and the flow field would therefore be expected to resemble the second of the two options above. The results presented in Figure 4.17 suggest that this is the case, as the radar plots show flow which is moving towards the true left at the bed and towards the true right at the surface. It could be argued that this is, in fact, just one half of back-to-back helical cells and that a counter-rotating cell would be found further to the true left. However, there is no evidence for this in any of the other plots from the main channel. Furthermore, Profile W is located sufficiently

close to the step (Figure 4.15) to make the formation of a complete helical cell in this small area highly unlikely. Therefore, it is much more likely that the water from the true right tributary is flowing in the lee of the step at the lower confluence. However, there is no evidence for the upwelling at the downstream corner identified by Best and Roy (1991), suggesting that the flow field does not completely replicate that expected in the classical model.

It was noted in Section 4.3.4 that the upper confluence morphology is more complex than that at the lower confluence. Although the elevations between the two tributaries vary, they are not as consistent as for the lower confluence. Therefore, the upper confluence flow field would not be expected to fall easily into either the discordant or concordant categories of the classical model of river confluences. However, there is evidence of secondary flow circulation in Profiles A, B and D, with flow in all cases in the direction of the true left bank at the surface and true right at the bed. In the case of Profile B (in the true right tributary), this suggests a helical flow cell may develop due to the curvature of the channel, as would be expected in a meander bend. Profile A, meanwhile, is affected by the deflection of flow around an object downstream of the inlet, which seems to be sufficient to initiate a secondary flow cell.

In the centre of the upstream confluence, Profile D (Figure 4.18) has the characteristics of being the true right part of a back-to-back circulation cell. However, there is no evidence for a counter-rotating cell in the region of Profile C. Instead, the steep water surface slopes and constriction of the flow (as identified in Section 4.3.4) encourage very fast, downward flow with no clear secondary circulation cells. Therefore, Profile D may be caused by three different factors: flow deflection due to the water joining from the true left tributary, a continuation of the flow cell identified at Profile B or flow deflection as a result of the raised topography between the two tributary channels. The likelihood is that it is a combination of these three factors and therefore the flow field at the upper confluence exemplifies the complexity and variability of the underlying topography.

The final flow process set out at the beginning of Section 4.5.2 is the shear or mixing layer. As noted in Section 2.3, this can be an area of highly complex flow, with shear between the two tributary flows causing Kelvin-Helmholtz instabilities, the development of quasi-2D coherent flow structures, wake flow around the flow stagnation zone and weak jet flow (Rhoads and Sukhodolov, 2008; Constantinescu *et al.*, 2011). However, an analysis of mean flow alone is insufficient to determine whether

these flow structures are present in the centre of the confluence and if so, what form they take. Therefore, Section 4.6 will investigate the nature of the flow turbulence at the Moor House confluences.

Given the evidence from this section, it can be argued that neither Moor House confluence exemplifies the classic model of river confluences. In the case of flow divergence and the zone of maximum velocity, subsequent research has suggested that specific conditions are necessary for them to exist in natural confluences (Ashmore *et al.*, 1992; Parsons *et al.*, 2008; Wallis *et al.*, 2008; Szupiany *et al.*, 2009). Therefore, their absence in the Moor House confluences is unsurprising. In the case of flow in the lee of the step in a discordant confluence, there is evidence that the flow field replicates this at the lower confluence, but without the strong zone of upwelling at the downstream corner. The helical cells at the upper confluence, meanwhile, are incomplete and for Profile D the process causing its formation may be more complex than the classical model suggests. Both confluences show evidence of a flow separation zone near the downstream corner, but unlike the classical model neither shows evidence of the development of a lateral bar.

The reasons for this disagreement with the classical model are likely to be due to two major aspects of these upland confluences: the highly variable bed topography (and associated increase in roughness) and the steeper water surface slopes. Separating out the two causes is far from straightforward, as the flow and morphology are interdependent components of Leeder's (1983) flow 'trinity'. Furthermore, the influence of these two components will vary depending on the specific confluence. However, it is possible to come to some conclusions about the driving forces behind flow at these types of upland river confluences.

In the case of the lower confluence, the bed discordance and resultant steep water surface slope from the true left tributary into the main channel is the main feature. The major secondary flow is related to this, although the extent of the flow cell is more localised. Therefore, although the bed morphology helps form the flow cell, much like Parsons *et al.* (2007) found with the dunes on the Rio Parana, the high roughness at the bed may be responsible for disrupting the cell and reducing its persistence downstream. At the upper confluence, the morphology is more complex and the flow field reflects this. However, the ultimate cause of this topographic complexity may well be the water surface slope from the true left tributary into the main channel. At low and medium flows, the majority of water from the true left flows through a topographic constriction,

leading to a zone of faster flow and deeper topography. However, in high flows where the bed is active, this constriction will be insufficient to convey all of the water into the main channel. Therefore, the increased stream power of the true left tributary may well become more important and this could explain the interruption of the true right thalweg by the upstream corner bar (as identified in Section 4.3.4).

Therefore, the disagreements with the classical river confluence model found in this section are mostly due to the large variability in the bed topography relative to the water depths. However, some of this variability may well be driven by the steep water surface slopes and in particular, the differences in elevation between the two tributaries. The two processes are therefore interlinked and understanding the flow field at the Moor House confluences requires knowledge of the impacts of both factors.

## 4.6 Turbulence in the Three-Dimensional Flow Results

Section 4.5 has demonstrated that the mean flow field can be used to determine the presence or absence of a number of flow processes considered characteristic to river confluences. However, this is not possible for the shear or mixing zone (process 1 in Section 4.5.2), which is characterised more by the presence of turbulent flow structures in a variety of forms (Rhoads and Sukhodolov, 2008; Constantinescu *et al.*, 2011). This section will therefore examine the nature of the turbulent flow processes in the Moor House confluences.

The first method that will be used to investigating the strength of turbulent flow structures is to determine the spatial variability in turbulent kinetic energy (TKE) throughout the confluences. TKE ( $k$ ) is calculated from Equation 4.1:

$$k = \frac{1}{2} \rho (\overline{u'^2} + \overline{v'^2} + \overline{w'^2}) \quad (4.1)$$

where  $u'$ ,  $v'$  and  $w'$  are the instantaneous velocity fluctuations about the mean (in the downstream, cross-stream and vertical directions respectively) and  $\rho$  is the density of water. However, care must be taken when interpreting the TKE values, as noise in the flow signal will significantly increase the calculated value. Although any spikes greater than three standard deviations from the mean were removed and replaced with a value determined by linear interpolation (following the method of Rhoads and Sukhodolov

(2001)), this will not help those time series which are particularly badly affected by low signal-to-noise ratios.

Figure 4.19 shows the five velocity time series for Profile W (from Figures 4.10, 4.15 and 4.17), with their  $k$  values given in the figure caption. Whilst time series B, C and D appear to have few spikes in the data, time series A suffers from some noise and time series E is more badly affected. Time series A and E are the ones taken from nearest the bed and the surface respectively, which is unsurprising given the limitations of aDv methods identified in Section 3.8.2. Nevertheless, the random fluctuations in these two time series would appear to have artificially increased the turbulent kinetic energy values, in particular for time series E (212kJ). Therefore very high values of  $k$  should be treated with caution and ideally investigated in more detail.

The second method which will be used to establish the turbulence in the flow will be the Reynolds Stress (RS). Like TKE, RS is calculated from the instantaneous fluctuations about the mean, as given in Equation 4.2:

$$RS = -\frac{1}{2}\rho(\overline{u'w'}) \quad (4.2)$$

In this case, Reynolds Stress will be calculated for the downstream ( $u$ ) and vertical ( $w$ ) components. Reynolds Stress calculated from the downstream and vertical components provides a good indication of the frequency and strength of the sweep and ejection events which are important for the transport of sediment in rivers (Keylock *et al.*, 2012). Ejections are instances of slower than average downstream flow and higher than average vertical flow, whilst sweeps have higher downstream velocities and lower vertical velocities compared to the mean (Robert, 2003). Both ejections and sweeps will therefore have one of  $u'$  or  $w'$  positive and the other negative, meaning their product will be negative in both cases. All other fluctuations about the mean velocity will give positive values of  $(\overline{u'w'})$ . With reference to Equation 4.2, it can be seen that a high positive value of Reynolds Stress is therefore an indication of a high proportion of sweeps and ejections. Locations in the channel with high positive Reynolds Stress values are therefore potentially areas of higher particle transport.

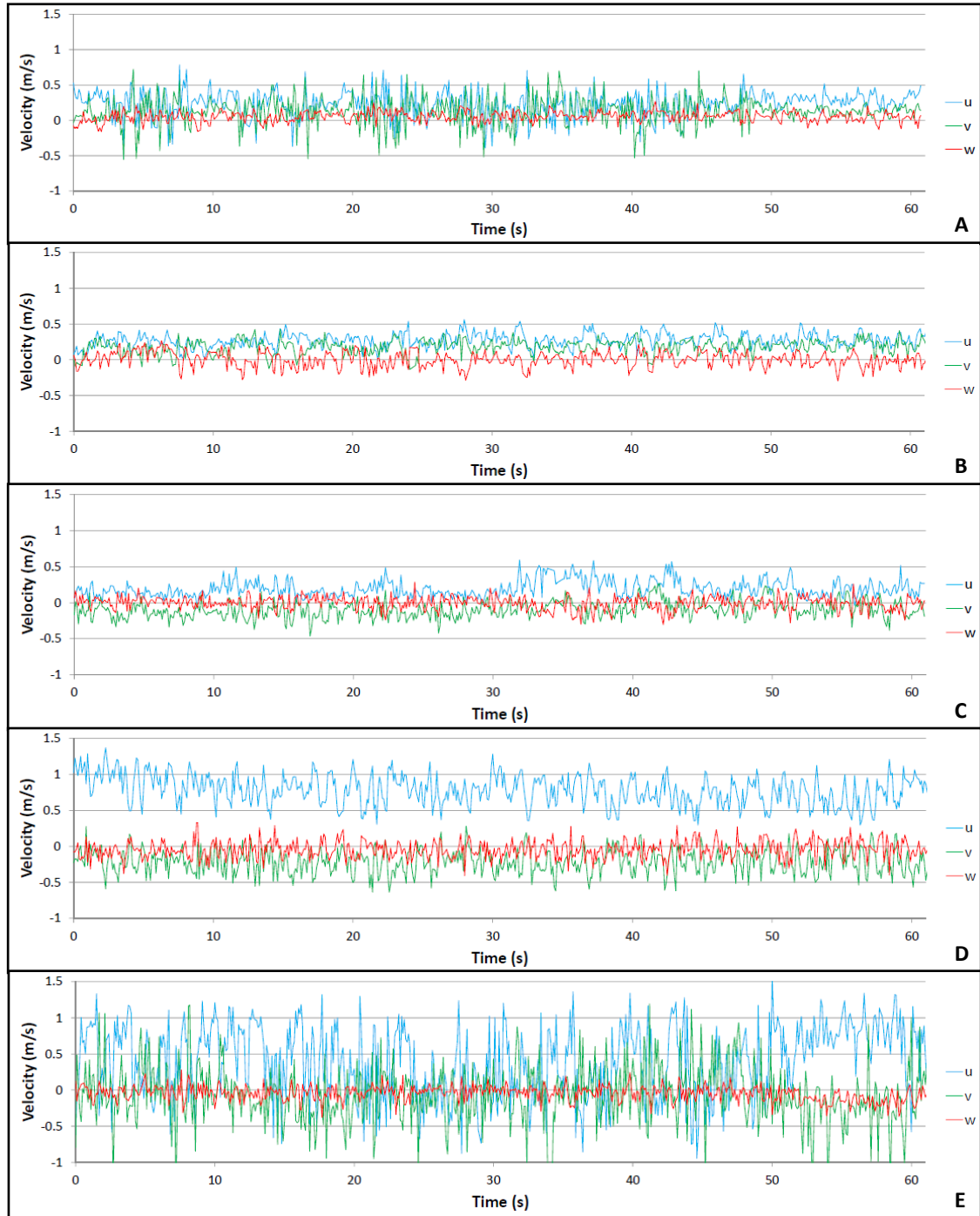


Figure 4.19: Velocity time series for Profile W at the lower confluence, measured at heights of (a) 0.05m, (b) 0.1m, (c) 0.15m, (d) 0.2m and (e) 0.25m above the bed. The values of  $k$  for plots (a) to (e) were 38.5J, 14.8J, 17.5J, 43.4J and 212.5J respectively.

However, TKE and RS can provide only an indication of the zones in the confluence which are characterised by high levels of turbulence. As noted in section 4.5.3, this turbulence can take variety of forms (Kelvin-Helmholtz instabilities, quasi-2D coherent flow structures, wake flow and weak jet flow). Spectral analysis can help to



determine whether the turbulence is dominated by particular frequencies and therefore can provide some insight into the cause of high values of TKE and RS. The power spectral density of a flow can be estimated by performing a fast Fourier transformation on the dataset (Singh *et al.*, 2010). This gives a log-log plot of the power spectral density against the frequency (similar to a magnitude-frequency plot). The work of Kolmogorov suggested that the turbulent energy should dissipate from lower to higher frequencies with a gradient of  $-5/3$  (MacVicar *et al.*, 2007; Singh *et al.*, 2010). Therefore, deviations from this  $-5/3$  gradient line can be used to ascertain whether there is an increase in the power of turbulent structures at particular frequencies.

At the higher frequency end of the spectral plots, significant deviations from the  $-5/3$  gradient line would indicate a major contribution to TKE coming from instrumentation noise (MacVicar *et al.*, 2007). Furthermore, by comparing the spectral plots for each velocity component, it is possible to determine whether turbulence is isotropic (with similar fluctuations in all three flow directions) or anisotropic (with turbulence dominating in one or two dimensions). Anisotropic turbulence would be indicated by a peak for one or two of the velocity components at a given frequency, with the power spectral density much lower in the other dimensions.

This section will therefore present the TKE and RS values obtained from each of the three-dimensional flow datasets, before selecting some of the profiles with higher  $k$  values for further investigation using spectral analysis. The final part of this section will discuss the results and the implications for understanding flow at the Moor House confluences.

#### 4.6.1 Turbulent Kinetic Energy in the Moor House Confluences

Figure 4.20 shows the TKE and RS values for each aDv measurement in the lower confluence, whilst Figure 4.21 provides the same data for the upper confluence on 20<sup>th</sup> September.

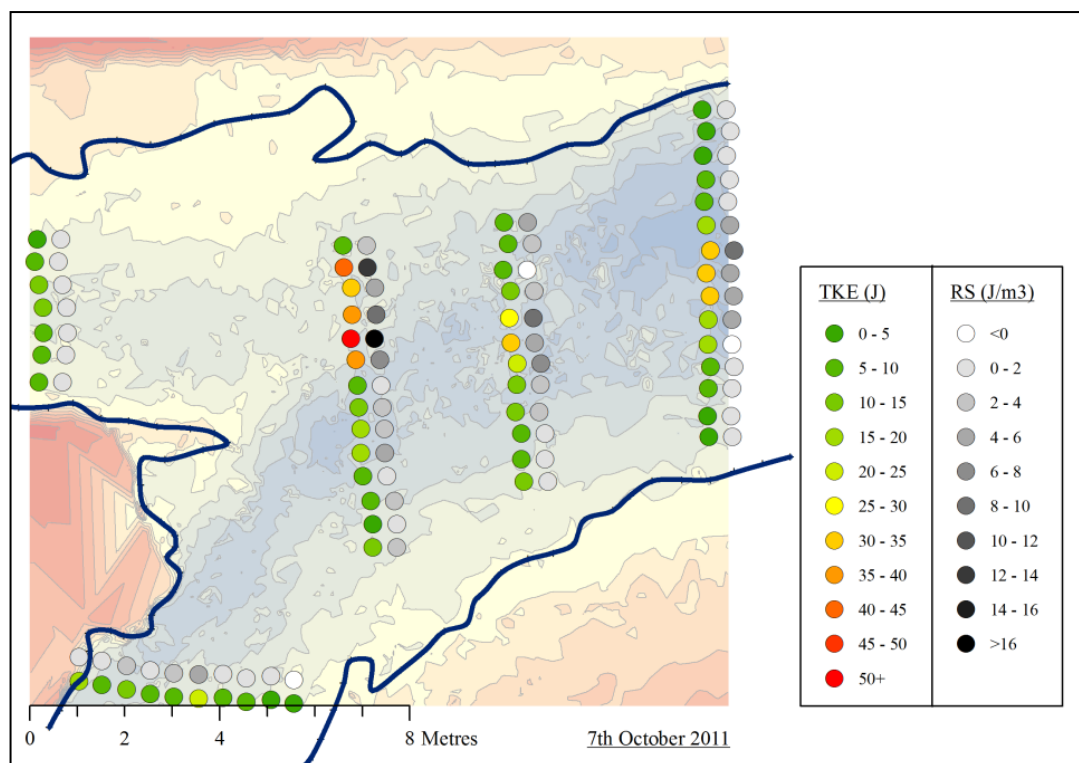


Figure 4.20: Turbulent kinetic energy (TKE) and Reynolds Stress (RS) values for the lower confluence. These values are taken from the 0.4d datasets obtained on 7<sup>th</sup> October 2011.

For the lower confluence, the highest TKE and RS values are found in the channel cross-section at 7m downstream, mostly towards the true left bank. This is in the region surrounding Profile W, which is the area where the true left tributary enters the main channel (see Figure 4.15). Other elevated values of TKE and RS are found in the centre of both the 10m cross-section and the outlet cross-section, in areas which are characterised by the meeting of flow from the two tributaries.

For the upper confluence during the medium discharge flow (20<sup>th</sup> September 2011), Figure 4.21 shows that high TKE values are found in the true right tributary, whilst an isolated higher value is seen in the true left tributary. However, these do not necessarily correspond with high values of RS. Elevated values of both TKE and RS are found in the centre of the 10m cross-section (in the vicinity of Profile E), which is located slightly downstream of where the two tributary flows join (see Figure 4.16).

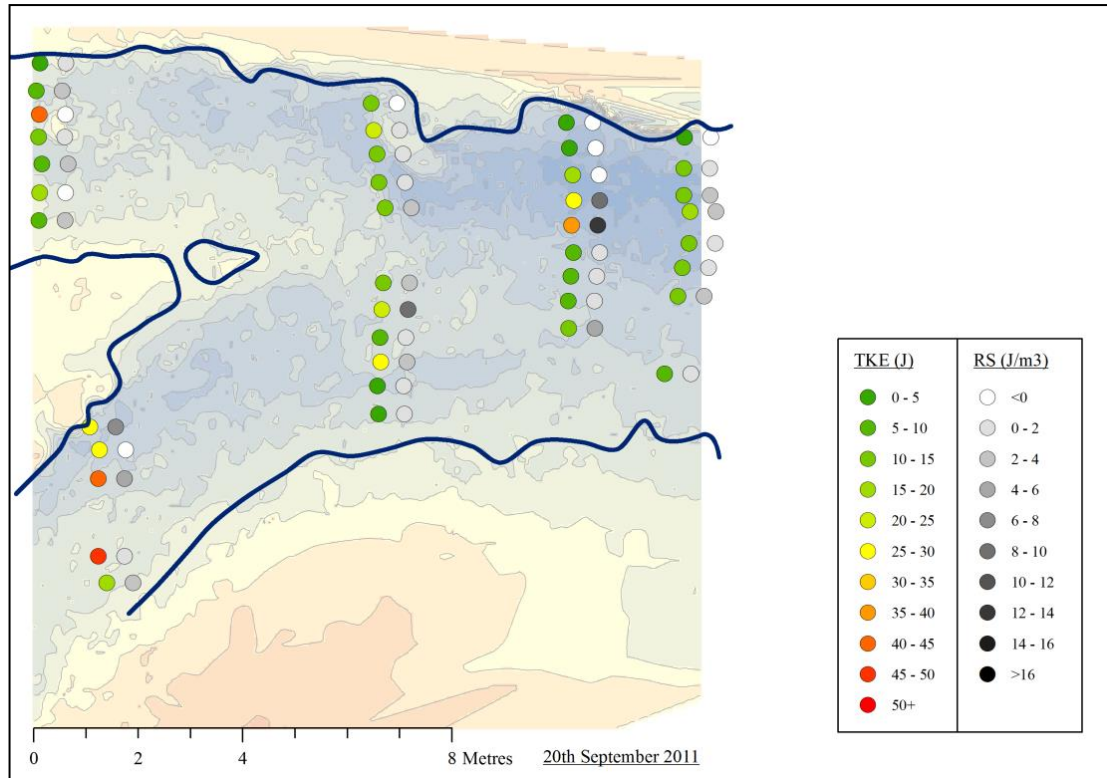


Figure 4.21: Turbulent kinetic energy (TKE) and Reynolds Stress (RS) values for the upper confluence on 20<sup>th</sup> September 2011. These values are taken from the 0.4d datasets.

#### 4.6.2 Spectral Analysis of the Flow Data

In Section 4.6.1, both Moor House confluences were shown to have elevated values of TKE and RS in the area where the two tributary flows join. However, as noted in Section 4.6, additional analysis is required to obtain an insight into what form this turbulence takes. Therefore this section presents spectral analysis plots from datasets within the more turbulent zones of both confluences. Spectral analysis plots can help to determine the extent of any anisotropy in the flow turbulence and whether high TKE values are the result of noise or particularly strong coherent flow structures at a given frequency.

Due to the high values of  $k$  in the area surrounding Profile W in the lower confluence, this velocity profile is selected for the spectral analysis plots. In addition, the same analysis is undertaken on aDv dataset 61, which is the 0.4d dataset with the highest TKE value. For the upper confluence, spectral plots are presented for Profile E and aDv dataset 49, which are both located in the zone of higher TKE and RS identified from Figure 4.21.

Figure 4.22 presents the spectral plots for the five datasets in Profile W, with an additional line plotted to show the  $-5/3$  gradient. In general, datasets B, C and D follow the  $-5/3$  gradient at the higher frequency end of the spectral plots for all three velocity components. For all three velocity components of dataset E, and the horizontal velocity components of dataset A, the higher frequency section of the graph has a much flatter gradient and thus deviates significantly from the  $-5/3$  line. This agrees with the velocity time series in Figure 4.19, where datasets A and E are both significantly affected by noise.

Looking in more detail at the spectral plots, there is a suggestion that there are higher power values for the horizontal velocity components in the 0.3-0.4Hz range, in particular in dataset D. However, this is inconsistent between datasets and otherwise there is very little to suggest the presence of anisotropic turbulence or the formation of quasi-2D coherent flow structures at a particular frequency.

Figure 4.23 gives the spectral plot for dataset 61 at the lower confluence and the corresponding velocity, TKE and RS time series. The TKE value is high, but not on the same scale as dataset E in Figures 4.19 and 4.22. The velocity time series in Figure 4.23 is correspondingly less spiky and the spectral plot appears to follow a  $-5/3$  gradient at frequencies above 2Hz. There is, however, a peak visible in the data at 1.5-2Hz, with the power spectral density slightly increasing to this peak for all three velocity components. This suggests that the dominant contributor to the high turbulent kinetic energy is fluctuations over timescales of less than 1s.

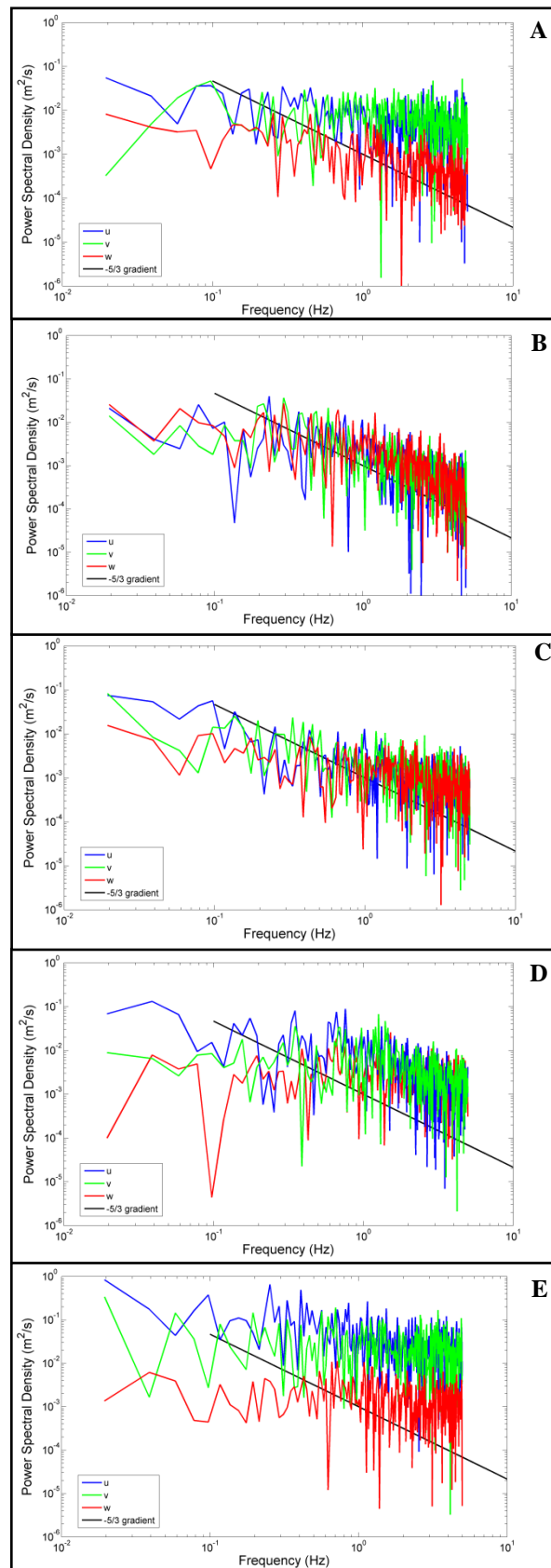


Figure 4.22: Spectral analysis plots for Profile W at the lower confluence. The spectral plots are for measurements at 0.05m (a), 0.1m (b), 0.15m (c), 0.2m (d) and 0.25m (e) above the bed. The  $-5/3$  gradient line is plotted for reference.

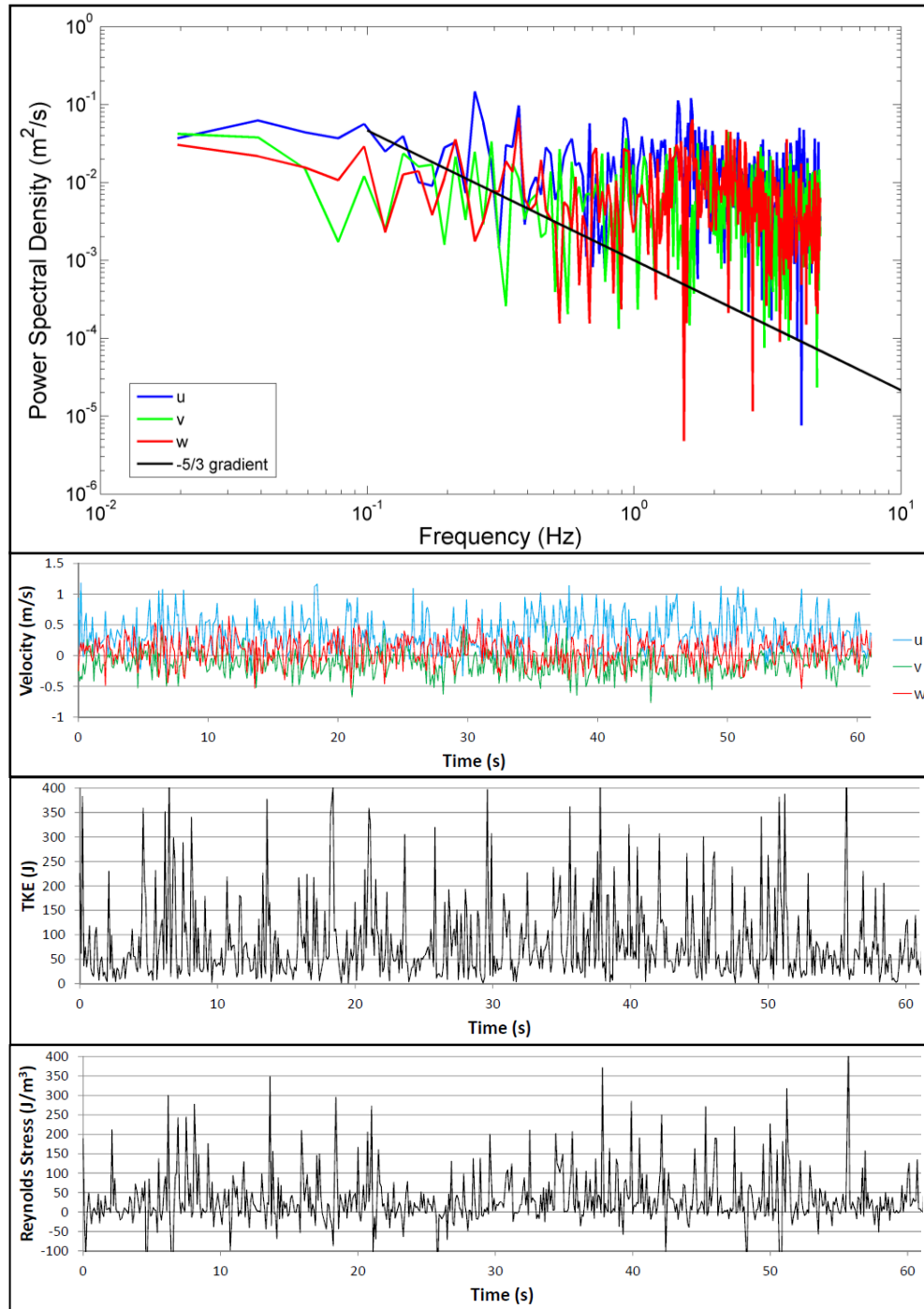


Figure 4.23: Spectral analysis plot for lower confluence aDv dataset 61 (*top*), the dataset with the highest calculated TKE in Figure 4.22 ( $k = 82.2\text{kJ}$ ). The velocity, TKE and Reynolds Stress time series are given for reference.

Figure 4.24 presents the spectral plots for Profile E, with a  $-5/3$  gradient plotted for reference.

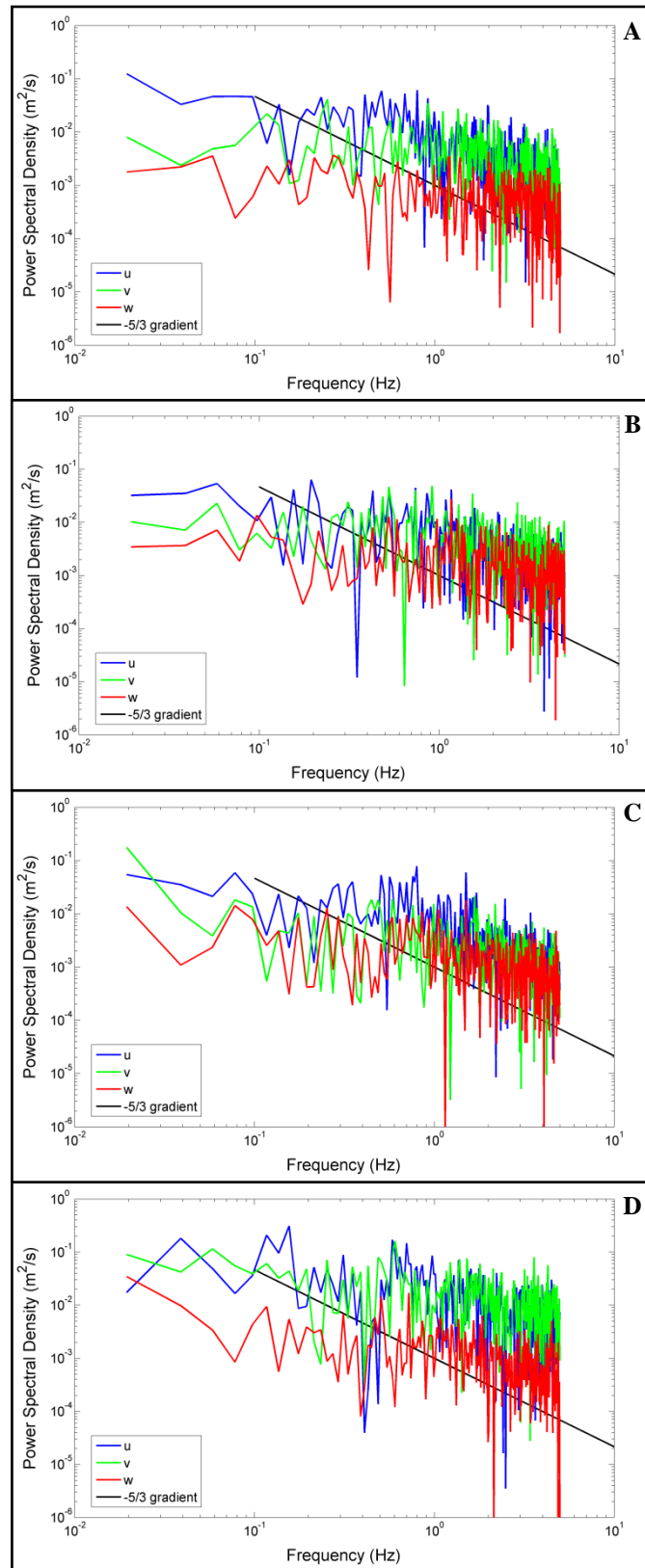


Figure 4.24: Spectral analysis plots for Profile E at the upper confluence. The spectral plots are for measurements at 0.05m (a), 0.1m (b), 0.15m (c) and 0.2m (d) above the bed, with the -5/3 gradient line plotted for reference. The TKE values for these four datasets are 32.4J, 35.0J, 31.0J and 91.9J respectively.

In Figure 4.24, datasets B and C follow the  $-5/3$  gradient at the higher frequency end of the spectral plots for all three velocity components. Dataset D, meanwhile, has similarities with Figure 4.22e, with the higher frequency part of the graph seeing a flatter gradient, possibly due to occasional spikes in the velocity time series. Both datasets A and D from Figure 4.24 have lower power spectral density values for the vertical velocity component, which might indicate the presence of quasi-2D flow structures. Figure 4.24c, meanwhile, has a possible peak in the 0.5-1.0Hz range, especially for the downstream velocity. However, there is no evidence that any of these patterns are consistent throughout the velocity profile and therefore any turbulent structures are likely to be more localised.

The spectral plot for dataset 49 and the time series for velocity, TKE and RS are given in Figure 4.25. The time series shows a clearly turbulent flow, but with very few visible spikes in the data. The spectral plot largely follows the  $-5/3$  line, but unlike in Figure 4.23 there is not a clear peak in the power spectral density values. However, much like in Figure 4.23, any differences between the velocity components are negligible, thus providing little evidence for anisotropic turbulent flow structures.



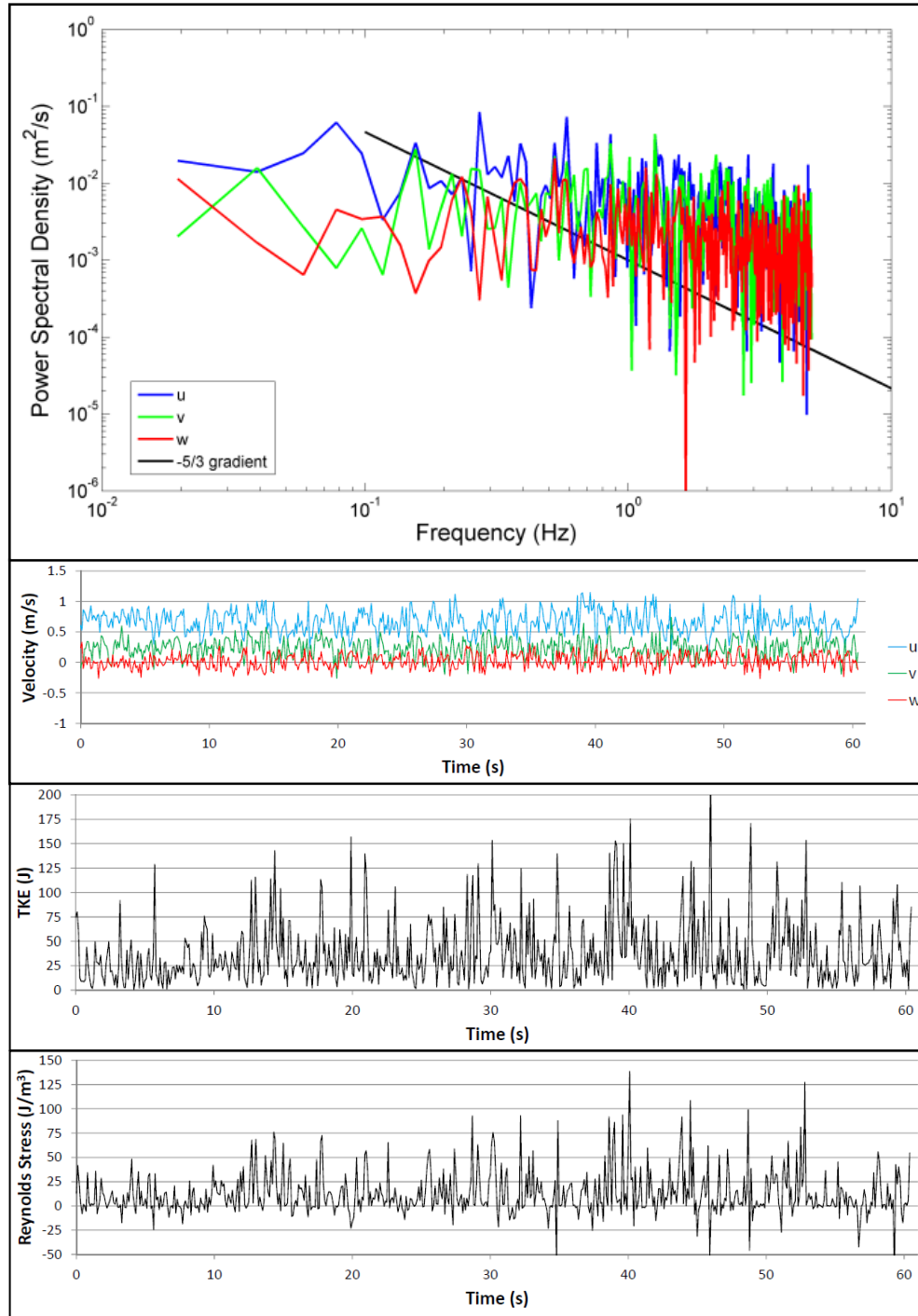


Figure 4.25: Spectral analysis plot for upper confluence aDv dataset 49 (*top*), the dataset with the highest calculated TKE in the downstream channel ( $k = 37.0\text{kJ}$ ). The velocity, TKE and Reynolds Stress time series are given for reference.

#### 4.6.3 Discussion of Flow Turbulence

From the TKE values in Figures 4.20 and 4.21, it is possible to identify the location of the most turbulent parts of the confluence. Although care must be taken when interpreting the highest values of TKE (in case poor signal-to-noise ratios are the

cause), both the lower and upper confluences show a clear pattern of higher TKE and RS values where the two flows meet. For TKE, values of  $k$  rise from a background level of 5-10J to approximately 30J in these zones. This can be compared to the variations in  $k$  with depth by looking at the values calculated for Profiles W (given in the caption to Figure 4.19) and E (Figure 4.24). For ease of reference, these values are reproduced in graphical form in Figure 4.26.

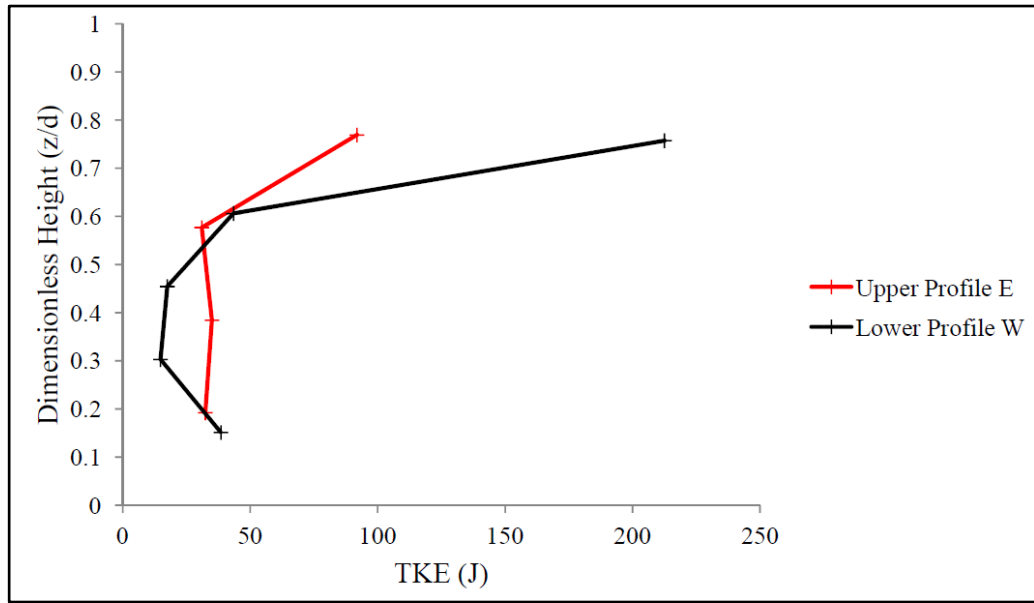


Figure 4.26: Plots of TKE with depth for velocity profiles W and E. Elevations above the bed are normalised to the channel depth.

The increase in TKE in the mixing zone can be seen to be of a similar magnitude to the rise near the bed for Profile W, but substantially less than the increases found near the water surface for both profiles. However, as noted in the discussion of Figure 4.19e, a substantial part of this increase in TKE near the surface may be due to spikes in the data as a result of the aDv being affected by the presence of air bubbles in the sampling volume.

Therefore, the higher TKE and RS values where the two flows meet demonstrate that mixing of the tributaries is still a cause of increased turbulence at upland river confluences. However, this zone of higher turbulence is relatively localised; although it persists further downstream, it weakens quickly. This suggests that the bed roughness may well play a role in disrupting the development of the turbulent structures or generating other, smaller scale eddies (as the increase in  $k$  towards the bed in Profile W implies).

In addition to the increased turbulence where the flows meet, at the lower confluence there are high values of TKE and RS to the true left of this central zone in the cross-section at 7m downstream. The velocity time series in Figure 4.23 demonstrates that this is not due to an excessively spiky dataset, whilst the spectral plot shows a small peak at around 1.5-2Hz. This may be interpreted as being due to the presence of small boulders on the top of the avalanche face, which cause the development of small-scale isotropic turbulence that dissipates quickly. These boulders can be seen to be disturbing the flow in the photograph in Figure 4.1.

By contrast, the spectral plot of dataset 49 from the upper confluence (Figure 4.25) does not show the same peak that is found in Figure 4.23. This can be explained by the fact that this dataset was taken from within the centre of the main channel, away from any large clusters of boulders. However, there is little evidence of a peak elsewhere, which suggests that the meeting of the two flows does not produce turbulent structures at a characteristic frequency as would be expected of Kelvin-Helmholtz instabilities in a shear layer. Therefore, although the mixing of the flows does lead to increased turbulence, it is clearly more localised and shows no evidence of being characterised by large-scale coherent flow structures. This is different to lowland river confluences, which in the past have been found to have quasi-2D (horizontal) coherent flow cells in this zone (*e.g.* Babarutsi and Chu, 1998; Rhoads and Sukhodolov, 2004).

For the velocity profiles, datasets A and E in Profile W (Figure 4.22) provide good examples of spectral plots where noise plays a role in artificially elevating the TKE value. Otherwise, the spectral plots in both Profiles W and E (Figure 4.24) have very few deviations from the  $-5/3$  gradient line. This further supports the conclusion that there are no clear coherent anisotropic turbulent structures which develop in the confluence mixing zone.

In the case of the Moor House confluences, therefore, it is argued that the tributaries meet at a turbulent mixing layer which does not extend for a considerable distance either cross-stream or downstream. Instead, it is proposed that at lower flows the high topographic variability of the cobble bed plays a dual role, encouraging the development of small-scale turbulent structures whilst also causing the damping of larger-scale turbulent structures. This ensures any coherent flow structures are relatively short-lived. Outside of the mixing zone, any turbulence is therefore mostly small-scale, isotropic and largely controlled by small vortices related to the presence of large roughness elements.

## **4.7 Discussion of Flow at the Moor House Confluences**

The topographic, roughness and flow data collected from the Moor House confluences can be considered to have satisfied the requirement in Section 1.6 for a high-quality field dataset from an upland river confluence. The stable nature of the confluence morphology made it possible to obtain DEM data with high point densities, Wolman counts on all except one of the bars adjacent to the confluence and three separate spatially-distributed three-dimensional aDv datasets. In all cases, the data quality satisfied the criteria set out in Section 3.8.

From Sections 4.3, 4.5 and 4.6, it is notable that neither the topography nor the flow field fits particularly well with the classical model of river confluences presented in Section 1.2. Of the six major flow processes highlighted at the beginning of Section 4.5, only four have been shown to be present in some form. There is no evidence of flow divergence downstream of the centre of the confluence, nor of significant flow acceleration.

Of those which are present, the flow at the lower confluence as a result of the bed discordance fits quite well with that suggested by Best and Roy (1991), although there is not the clear zone of upwelling at the downstream corner. The flow separation zones, meanwhile, are present but also characterised by deeper water, which contradicts the assumption that these are zones of deposition (Best, 1986; Leite Ribeiro *et al.*, 2012). Whilst there is some evidence of helical secondary circulation cells at the upper confluence, they are not in the strong, back-to-back form identified by Mosley (1976). Finally, as set out in Section 4.6, although the mixing of the tributaries results in an increase in turbulence in the centre of the channel, there is no evidence of this being coherent, anisotropic or persistent downstream. Instead, the turbulence is characterised by small-scale, isotropic structures which are disrupted by the rough bed topography.

The reason for the poor fit with the classical model is largely due to the significant influence of topography on the flow field. This forces the flow and disrupts the formation of any large-scale turbulent structures. The water surface slope seems to have less impact, although it should be stressed that this conclusion only holds at the low and medium discharges in which data were collected. There is evidence that the flow field and confluence morphology are not in equilibrium and so further investigations would be necessary to understand the processes operating in the higher, channel-forming discharges. Chapter 5 will develop numerical methods to simulate

these flows, while the second half of this chapter will investigate the topography, roughness and flow processes at river confluences with much steeper water surface slopes.

## **4.8 Borgne d'Arolla Field Site Conditions and Data Collection**

As noted in Section 1.6, the field site on the Borgne d'Arolla was chosen to provide examples of river confluences with very steep water surface slopes, dynamic topography and active bedload transport. The nature of the flow on the Borgne d'Arolla braid plain, and the role played by the purging of the sediment traps was explained in Section 1.6.2. In baseflow conditions, this results in steep, fast, supercritical flow, which can cause evolution of the morphology of the bed and banks over periods as short as a few hours. Similar conditions were experienced in the river confluences considered by Ashmore and Parker (1983) and Ashmore *et al.* (1992), with individual confluences experiencing significant change over a period of hours. As such, the criteria for data quality set out in Section 3.8 accounted for the likely limits on the available time for data collection.

The purge flows, meanwhile, can result in significant reorganisation of the braid plain, with a completely new channel pattern forming. This is demonstrated by the panoramic photographs of the braid plain in Figures 4.27 and 4.28. Figure 4.27 shows the differences in flow routing between two different purges on 24<sup>th</sup> August 2011, with some noticeable changes to the channel pattern. Figure 4.28, meanwhile, shows the braid plain before and after a large meltwater and rainstorm induced flood on the evening of 26<sup>th</sup> August 2011, highlighting the changes that occurred on the floodplain in these high discharge events.

Therefore, the confluences of the Borgne d'Arolla braid plain provide examples of much more topographically dynamic and steeper confluences than those found at Moor House National Nature Reserve. Consequently, the selection of appropriate confluences for data collection is a far more complicated process which has to be done *in situ* on a day-to-day basis. The next section sets out this selection process and the confluences ultimately chosen for further analysis.



Figure 4.27: Merged photographs of the Borgne d'Arolla braid plain on 24<sup>th</sup> August 2011, showing the purges at 11:10am (a) and 1:40pm (b) local time. The braid plain is approximately 50m wide at this location.





Figure 4.28: Merged photographs of the Arolla braid plain on 25<sup>th</sup> August 2011 (a) and 28<sup>th</sup> August 2011 (b), before and after a large flood. Both sets of photographs are taken at low discharges, with clear differences in flow routing. The blue and red circles highlight a large tree trunk deposited on the braid plain by the flood and a zone where the vegetation has been eroded due to the high flows.

#### *4.8.1 Data Collection Process*

In the criteria of Section 1.6, it was stipulated that there should be at least two examples of confluences with very steep water surface slopes, with the Arolla field site chosen specifically to satisfy this. In addition, in Section 3.8.2 it was determined that an attempt would be made to obtain three-dimensional aDv data to establish whether such an approach was feasible in these highly turbulent flows. As noted above, the dynamic nature of the Borgne d'Arolla braid plain means that the most appropriate confluence sites cannot be pre-defined and must be selected on each individual day of the field work, with the best of these chosen for further analysis.

A good dataset was considered to be one in which the topographic, flow and particle transport data were collected to the quality standards required in Section 3.8. In addition, however, the confluence in question should not undergo any significant (*i.e.* visible) evolution in morphology or change in discharge during the course of the data collection. In some cases, it was known at the time of data collection that the dataset was incomplete or interrupted, for example when the collection of data was disrupted by a purge event. Therefore, it was resolved that data collection would continue until three good datasets were obtained, of which the best two would be selected for further analysis. This would ensure that the criteria in Section 1.6 were satisfied even if one of the apparently 'good' datasets was found to have flaws during post-processing. The selection of two good quality datasets would therefore correspond to the two confluence sites studied at Moor House National Nature Reserve. These two confluence datasets would, however, be supplemented by an additional dataset which used the aDv to get three-dimensional flow data in these highly turbulent, supercritical flows.

Table 4.7 shows the complete set of confluence datasets from the Borgne d'Arolla field site, along with notes taken in the field on the quality of the individual datasets. In total, nine confluence datasets were collected during the field experiments.



	DEM Data	Flow Data	Particle Data	Roughness	Notes/Limitations
<b>A</b>	High resolution	ECM. Five inlet measurements only.	Seven individual particle tracks.	None	Longer time spent on topographic data collection resulted in substantial change in morphology for the particle experiments.
<b>B</b>	Bank outline	ECM. Measurements only in channel centre to estimate discharge ratio.	Moor House method attempted (seed and resurvey).	2 Wolman counts with associated photos.	Data collection interrupted by purges three times during the day. Particles hard to see in turbid water and almost all had exited the confluence by the survey the next day.
<b>C</b>	Breaks of slope	ECM. Inlets only, 0.2m spacing.	None	Wolman count in left tributary, plus photos.	Attempted to obtain flow and particle data during a purge, but insufficient time to get both datasets.
<b>D</b>	Breaks of slope	ECM. Inlets only, 0.1m spacing.	Individual particle tracks, for two different grain sizes.	Photos only	First purge interrupted DEM and flow data collection. Second purge resulted in some particle tracks not being surveyed <i>in situ</i> .
<b>E</b>	Breaks of slope	aDv. 17 points located throughout the confluence.	None	Photos	Purge arrival was shortly after data collection. Considered to be the good aDv dataset required in Section 4.8.1.
<b>F</b>	Breaks of slope	aDv. Purge flow for inlet data but back to low flow for outlets.	None	Photos	Attempted to obtain flow data during a purge. As for Confluence C, insufficient time before the return of baseflow conditions.
<b>G</b>	Breaks of slope	ECM. Inlets at 0.2m spacing, plus five outlet data points.	Individual tracers and pebble patch outlines.	Photos	Data considered 'good' from the criteria in Section 4.8.1.
<b>H</b>	Breaks of slope	ECM. Inlets at 0.2, spacing, plus three outlet points.	Individual tracers and pebble patch outlines.	Photos	Data considered 'good' from the criteria in Section 4.8.1.
<b>I</b>	Breaks of slope	ECM. Inlets at 0.2m spacing, 4 outlet points and some aDv datasets.	Individual tracers and pebble patch outlines	Photos	Data considered 'good' from the criteria in Section 4.8.1.

Table 4.7: Summary of data collected for each of the nine Arolla confluences (A to I).

Confluences B and D were significantly affected by changes to the flow conditions during the measurement period due to the arrival of a purge and therefore did not satisfy the requirement for a constant discharge during data collection. Data from Confluences C and F, meanwhile, were taken during a purge, but this approach was found to be unfeasible due to the limited time available before baseflow conditions returned. Confluence A suffered similar problems to Confluences B and D, but it was noticeable changes to the confluence morphology rather than the discharge which resulted in rejection. Therefore, none of these five confluences were considered of sufficient quality to be used for further analysis.

Confluences G, H and I, however, were considered to satisfy the data quality requirements in Section 3.8. The individual topographic, flow and particle tracking data satisfied the quality criteria set out in Section 3.8 and none of the confluences experienced significant changes in confluence morphology and flow discharge during the course of data collection. In addition, Confluence E met the requirement for a complete three-dimensional velocity dataset and so would be used to assess the performance of the aDv.

Having obtained these four confluence datasets, three were selected for further analysis. Of these four, the Confluence I dataset was discarded, as further analysis found a small disparity between the alignment of the inlet flow data and the topographic domain. Therefore, Confluences E, G and H were selected for further analysis. Photographs of these three confluences are given in Figure 4.29.

Although only Confluences E, G and H were selected for in-depth analysis of the flow data, it was decided to use all of the available GSD and roughness data collected during the field work. This was done to enable a better range of characteristic grain size values to be determined for the braid plain surface.



Figure 4.29: Photographs of the three confluences to be analysed in this section: E (*top*), G (*middle*) and H (*bottom*). The photograph of Confluence E was taken shortly after the end of data collection, during which time a small purge event had commenced.

#### 4.8.2 Characteristics of the Flow at the Arolla Confluences

The channel and flow characteristics of the three confluences to be investigated in this part of the chapter are given in Table 4.8.

		E	G	H
Channel Width	TL tributary	0.9m	1.2m	1.3m
	TR tributary	0.7m	2.2m	1.3m
	Main Channel	1.3m	2.3m	1.7m
Channel Depth	TL tributary	0.08m	0.12m	0.12m
	TR tributary	0.1m	0.11m	0.16m
	Main Channel	0.2m	0.18m	0.2m
Cross-sectional area	TL tributary	0.04m <sup>2</sup>	0.11m <sup>2</sup>	0.13m <sup>2</sup>
	TR tributary	0.08m <sup>2</sup>	0.18m <sup>2</sup>	0.16m <sup>2</sup>
	Main Channel	0.12m <sup>2</sup>	0.34m <sup>2</sup>	0.2m <sup>2</sup>
Froude Number		0.52-1.23	0.86-1.26	0.81-1.07

Table 4.8: Flow and channel characteristics of the three Arolla confluences (E, G and H) to be studied in depth. Widths and areas are taken from the cross-sections selected as confluence inlets and outlets.

A comparison with the equivalent table for Moor House (Table 4.1) shows that the Arolla confluences are significantly narrower, with lower maximum water depths and thus much lower cross-sectional areas. In addition, whereas the flows at Moor House are subcritical, the Froude numbers calculated for the Arolla confluences show that the flow is either supercritical or close to critical. There is therefore a significant difference in the flow regimes of the two sites, satisfying Criterion 1 of Section 1.6.

## 4.9 Topographic Data at the Arolla Confluences

As noted in Section 4.1, the data analysed in this chapter were collected for two principal purposes: to provide greater insight into the processes operating on upland river confluences and to obtain boundary condition and input data for the numerical modelling experiments. In the case of the Arolla confluences, their dynamic nature means that the numerical modelling becomes a very important tool for understanding the flow and bedload transport processes. Therefore, the primary concern for the Arolla datasets is to provide data of sufficient quality to enable further experiments to be conducted using the numerical models.

However, in addition to assessing the quality of the topographic data for this purpose, this section will use the data to ascertain whether any of the major morphological features predicted by the classical river confluence model are present. From the review in Chapter 2, these morphological features are considered to be the scour hole (and associated avalanche faces), bed discordance between the channels, and lateral or mid-channel depositional bars.

#### *4.9.1 Data Quality*

Unlike at Moor House National Nature Reserve, the base station did not necessarily reoccupy the same point when collecting topographic data from the Arolla confluences. As the braid plain was constantly reorganising itself on a daily (and sometimes hourly) basis, the optimal location for the base station varied depending on the confluence being studied. Therefore, although quality control points were set up for the first confluence datasets, on subsequent days it was usually not possible to have a direct line of site to at least three of the points (the minimum number required to place the two datasets on the same grid whilst still having an independent test point). Quality control points could not be placed on the braid plain itself, as they would be lost in this constant reorganisation.

As a result of this, an alternative method to verify the individual point quality had to be found. The quality of point data collected using the Leica Total Station has already been demonstrated to be satisfactory in the quality control tests conducted in Section 4.3 (which included all dGPS and Total Station datasets collected at Moor House). However, it was deemed preferable that this range of error values be confirmed for the Arolla datasets.

In Table 4.2 it was demonstrated that the horizontal component tended to be the source of the majority of the error. Therefore, it was decided that a comparison would be made between distances recorded using the Total Station and the tape measure used to determine the locations for the inlet flow data measurements. When the tape measure was stretched out to mark the confluence inlets, two known points on the tape were recorded. A comparison could thus be made between the horizontal distance measured on the tape and that calculated between the two Total Station points. The results of this comparison for five of the confluences are presented in Table 4.9.

Confluence	Distances Measured (m)	
	Tape Measure	Total Station
C	1.90	1.75
C	0.60	0.51
D	4.00	3.94
D	5.00	4.99
G	7.00	7.05
H	2.00	1.94
J	7.00	6.98

Table 4.9: Differences between the horizontal distances recorded by tape measure and their equivalents calculated from the Leica Total Station data.

The mean difference and Root Mean Squared Error (RMSE) of these results were calculated as 0.063m and 0.076m respectively. This is slightly higher than the mean errors recorded in Table 4.2, largely due to the high errors recorded at Confluence C. With one exception, the Total Station distances underestimate the tape measurements, so part of the error (in particular for Confluence C) may be explained by the tape not being completely straight, horizontal and taut.

The criteria in Section 3.8.1 set a minimum point density of 4pts/m<sup>2</sup>, which Lane *et al.* (1994) found to be the minimum required to obtain a good representation of the morphology in these fluvial environments. Figures 4.30, 4.31 and 4.32 show the point density plots for Confluences E, G and H respectively. As for the equivalent plots for the Moor House confluences, the value of each cell gives the number of data points that were located within 0.564m of the cell, which is equivalent to a 1m<sup>2</sup> circle being centred over the cell.

The point density values are highest in Confluence E, which can be explained by it being the smallest of the three. Confluence G, meanwhile, has the lowest point densities of the three confluences, although again that may be linked to size, as it has the largest inundated area of the three confluences. In all three cases, however, the in-channel point densities exceed the minimum required in the criteria in Section 3.8.1.



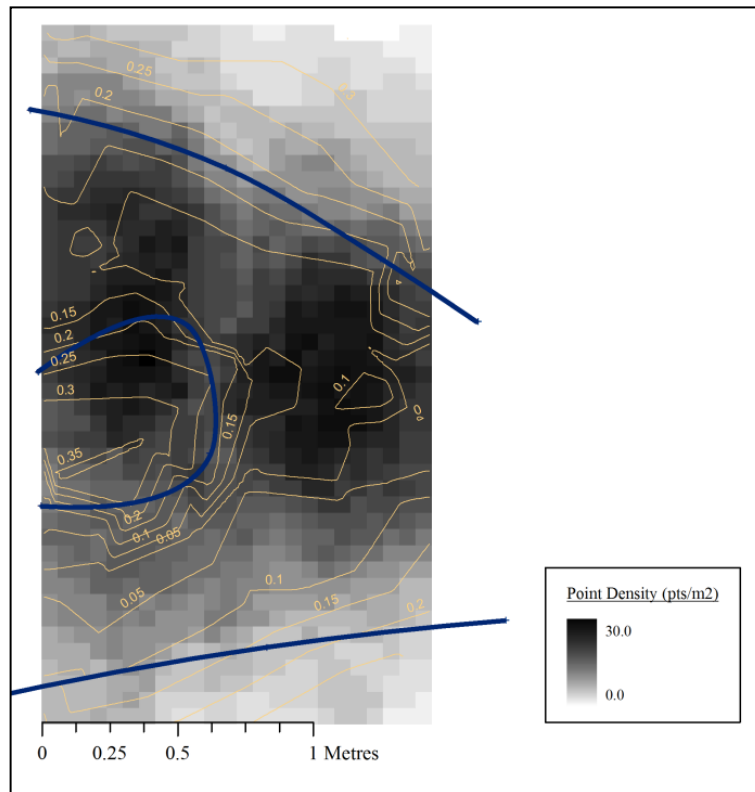


Figure 4.30: Point densities for the DEM of Confluence E. The dark blue line indicates the water edge.

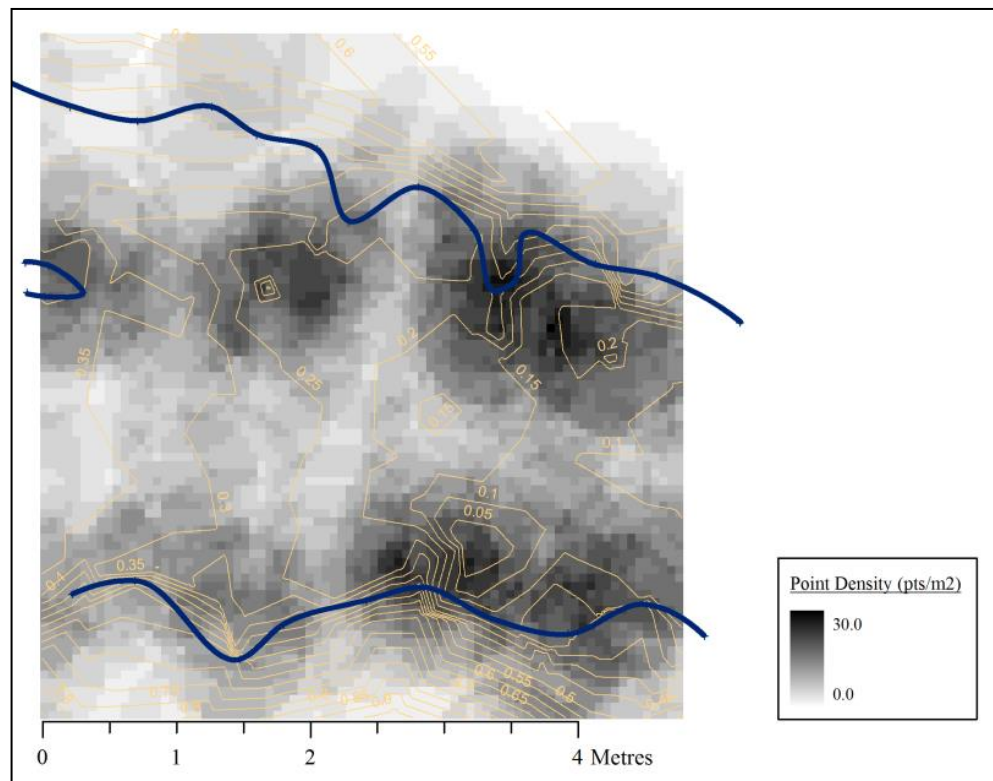


Figure 4.31: Point densities for the DEM of Confluence G, with the blue line showing the water edge.

In all three confluences, the highest point densities are found in the channel, although not necessarily in the centre of the channel. All three confluences have zones of higher point density at the upstream corner, but whilst Confluences E and H tend towards higher point densities in the middle of the channel, it is noticeable that Confluence G prioritises zones on the edge of the channel. This demonstrates the focus in Section 3.8.1 on a representative point distribution, with the points clustering around the areas of the confluence with the most variable topography.

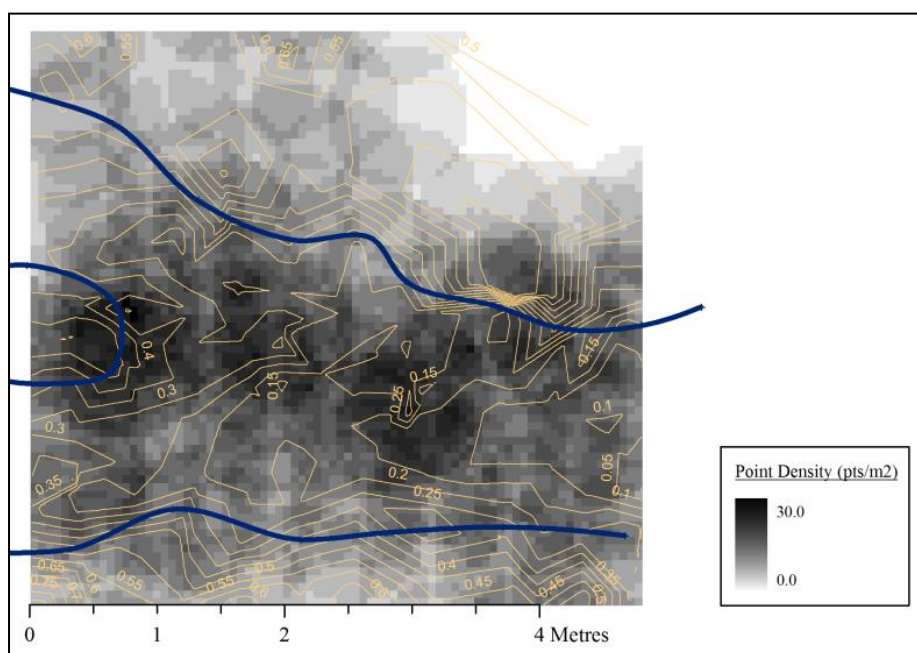


Figure 4.32: Point densities for the DEM of Confluence H. The dark blue line marks the water edge.

#### 4.9.2 Topographic Data

The Digital Elevation Models (DEMs) for Confluences E, G and H are given in Figures 4.33, 4.34 and 4.35. As for the Moor House confluences, the point data were converted to a TIN using Delaunay triangulation and then to a raster by linear interpolation. A comparison between the point density plots in the previous section and these DEMs shows that the areas of higher point density are indeed largely associated with specific topographic highs or lows. For Confluence G in particular, the areas of high point density are linked to (i) a boulder in the channel centre at 1.5m downstream, (ii) a pebble cluster and associated leeward depression at 3m downstream on the true right and (iii) a pebble cluster 3.5m downstream on the true left.



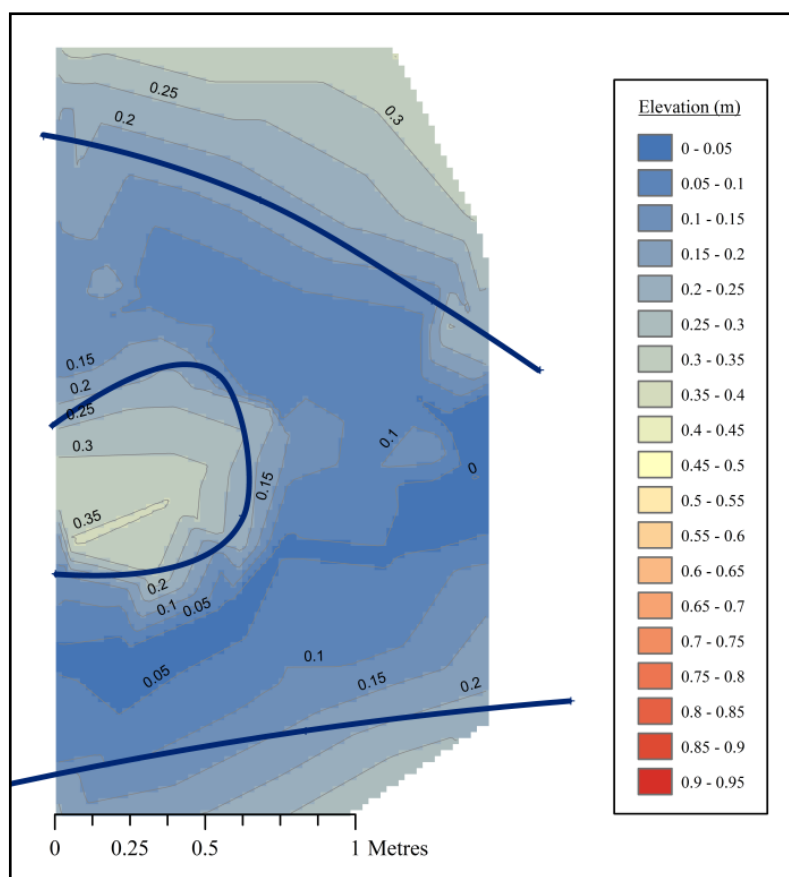


Figure 4.33: The DEM for Confluence E, with the dark blue line showing the water edge. The colour scaling is the same for all three DEMs presented in this section to enable comparisons.

From the DEM in Figure 4.33, Confluence E can be seen to have a very well-defined bank between the two tributaries, which is in fact a large boulder at the downstream end of the bar (as shown in Figure 4.29). The true right tributary has a slightly deeper thalweg than the true left, but there is no clearly defined step into the main channel from the true left tributary, as would be expected of a discordant confluence. In addition, there is no evidence of depositional bars within the channel or a scour hole where the two flows join.

Confluence G (Figure 4.34) is a confluence with a junction angle very close to  $0^\circ$ . It has very clear banks on the true left and true right, which, given the high range of elevations in the confluence, means these banks are relatively steep. This contrasts with the very low profile of the bar which separates the two tributary flows. As noted above, large rocks or pebble clusters are visible on the bed of the channel, demonstrating that the level of detail in the channel representation is good. However, as with Confluence E, there is little evidence of the three major morphological features set out above. Instead,

the most distinct feature is the topographic hollow in the lee of a patch of large cobbles on the true right bank.

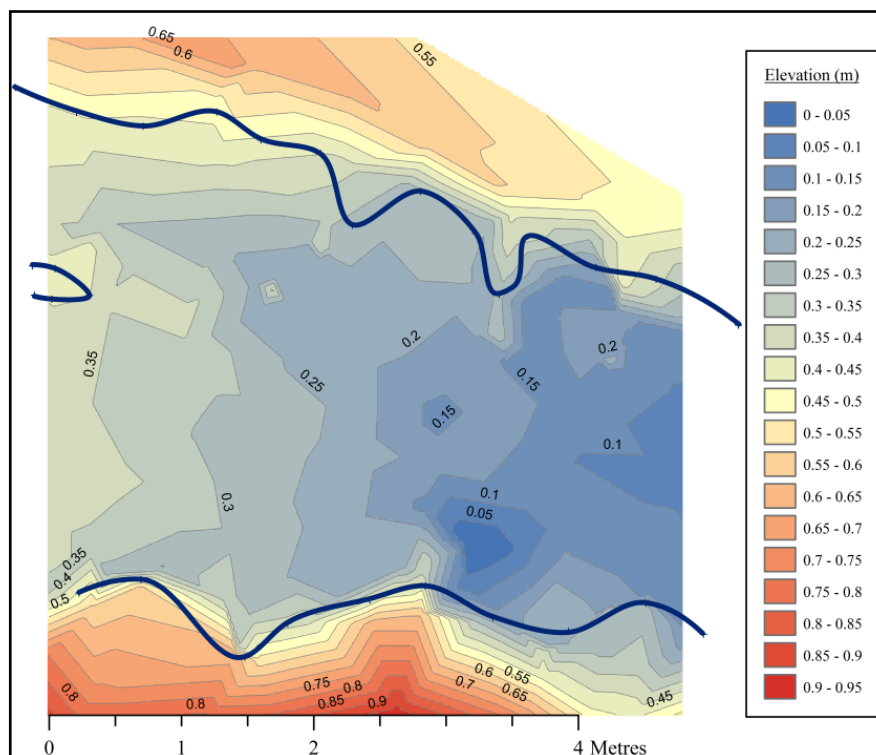


Figure 4.34: The DEM for Confluence G, with the blue line marking the water edge.

The DEM of Confluence H in Figure 4.35 again shows banks that are well-defined and steep. The junction angle is approximately  $30^\circ$ , although the bar between the tributaries is still less elevated than the banks on either side. Within the channel, there is sufficient detail to see features such as a boulder in the centre of the channel at approximately 3m downstream. The topography within the channel has very few clear patterns and there is no evidence of a scour hole, depositional bars or the morphological features considered to be typical by the classic model of river confluences.

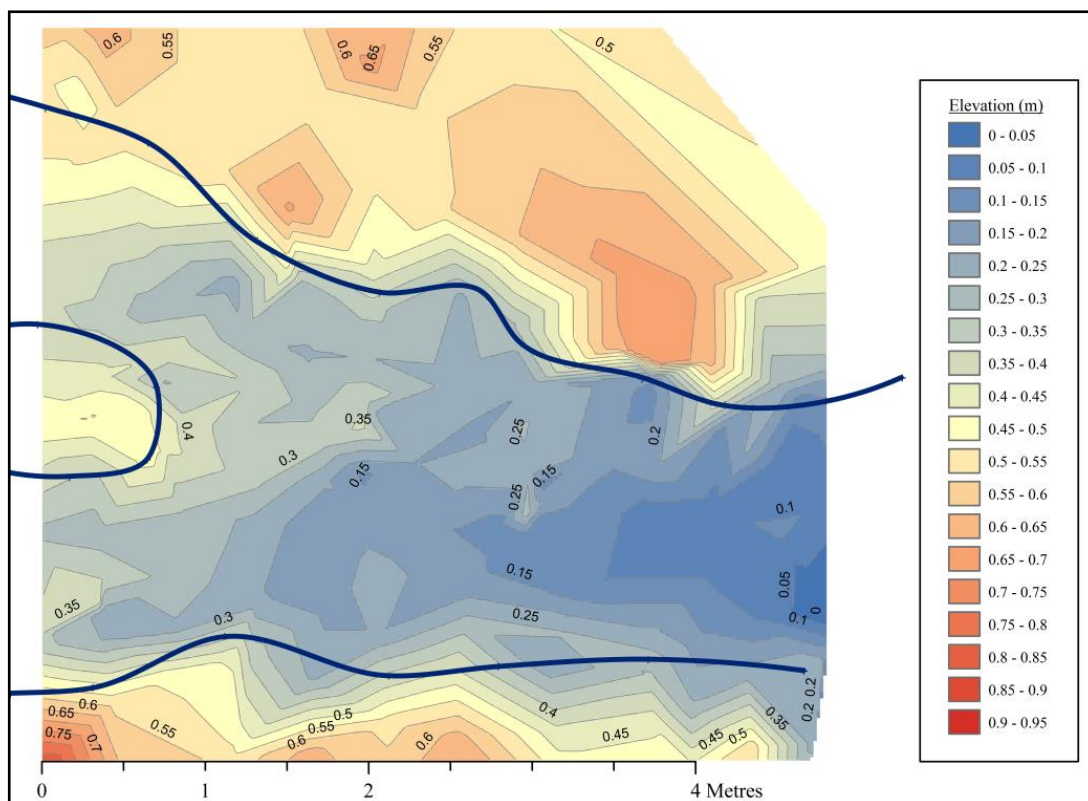


Figure 4.35: The DEM for Confluence H, with the water edge given by the blue line.

#### 4.9.3 Discussion of Topographic Data

The topographic data presented in this section satisfy the quality criteria set out in Section 3.8.1. Although the mean difference and RMSE of the individual point errors are above the 0.05m threshold, this value is significantly affected by the large underestimation (0.15m and 0.09m) of distances at Confluence C. This suggests that the tape measure at Confluence C was not completely taut and therefore that these values are anomalous. As such, the individual point data quality is not considered a cause for concern, as without these anomalous values the mean individual point error would be 0.04m (which is within the range required in Section 3.8.1). The point densities, meanwhile, satisfy the minimum requirements set out in Section 3.8.1, with the inundated areas above the 4pts/m<sup>2</sup> threshold. In terms of point distribution, the qualitative evidence is positive and suggests that the sampling strategy ensured the topographic features most likely to impact on the flow were included (such as the small boulders in the channels of Confluences G and H).

The Arolla confluences show very few of the major morphological features from the classical river confluence model (as identified by Best (1986)). In none of the confluences were scour holes or depositional bars visible, whilst the only evidence of discordant beds was a slightly deeper true right thalweg in Confluence E. Instead, the major morphological features within these confluences are associated with large boulders or pebble clusters and depressions in the lee of these. This contrasts with the work of Ashmore *et al.* (1992) in similar conditions, which identified a scour hole in one of their two confluences. However, this may be partly explained by the confluences in this study having lower junction angles than those used by Ashmore *et al.* (1992). Other possible reasons for this disparity with the classical model are that the steep water surface slope results in different flow processes to those which are believed to form these morphological features or that the dynamic nature of the braid plain means that the flow and morphology are rarely in equilibrium. Determining the process responsible, however, would require substantial data on the three-dimensional flow field, most likely from three-dimensional numerical modelling of the flow.

#### **4.10 Grain Size Distribution and Roughness Data**

The results from Section 4.4 demonstrated that attempting to characterise the roughness of a channel bed is problematic, as there is no definitive method available to calculate roughness height. With the many different methods for estimating roughness, a range of equally valid values can be found. Furthermore, characterising a complex river bed with just one value is very much a simplification, meaning that in reality the aim is usually to obtain a best estimate that is of the correct order of magnitude.

In Section 4.4 it was demonstrated that methods of obtaining a roughness height from a characteristic grain size tended to produce lower values than methods which used velocity profiles. In addition, for the characteristic grain size approaches, it was found that the photosieving and Wolman count methods produced similar GSD data. For the Arolla confluences, the shallow nature of the flow made the velocity profile method much less viable, in particular when attempting to take velocity measurements at low elevations above a mobile bed or close to a variable water surface. Therefore, the use of characteristic grain size methods to determine roughness was considered the only feasible option.

This section begins by presenting a comparison between the Wolman Count and photosieving methods. In Section 4.4 these methods were found to give very similar results, so the comparison is designed to determine whether this is still the case on this specific site. Having done this, the results from the photosieving analysis are presented for Confluences E, G and H and values for roughness height calculated from the characteristic grain sizes.

#### *4.10.1 Comparison of Wolman Counts and Photosieving*

GSD data were obtained using both the Carbonneau *et al.* (2004) photosieving method and a standard Wolman count for Confluences B and C. For Confluence C, a 1m<sup>2</sup> quadrat was sampled every 0.1m to give 121 data points for the Wolman count. At Confluence B, however, the channel width was too narrow for a 1m<sup>2</sup> quadrat and so the sampling site was split into two 0.5m<sup>2</sup> quadrats (of 36 data points), with one in each tributary. As some large particles were counted multiple times in the field, the actual numbers of pebbles included in the subsequent analysis were 28, 34 and 114 for the Confluence B True Left, Confluence B True Right and Confluence C datasets respectively.

Figure 4.36 shows the comparison between the GSDs obtained for the three Wolman count datasets and those obtained from analysing the photos using the Carbonneau *et al.* (2004) method. Of the three sites, the closest match is for the true left tributary of Confluence B. For the other two sites there is greater variation between the results from the two methods, although the broad pattern is still clear.

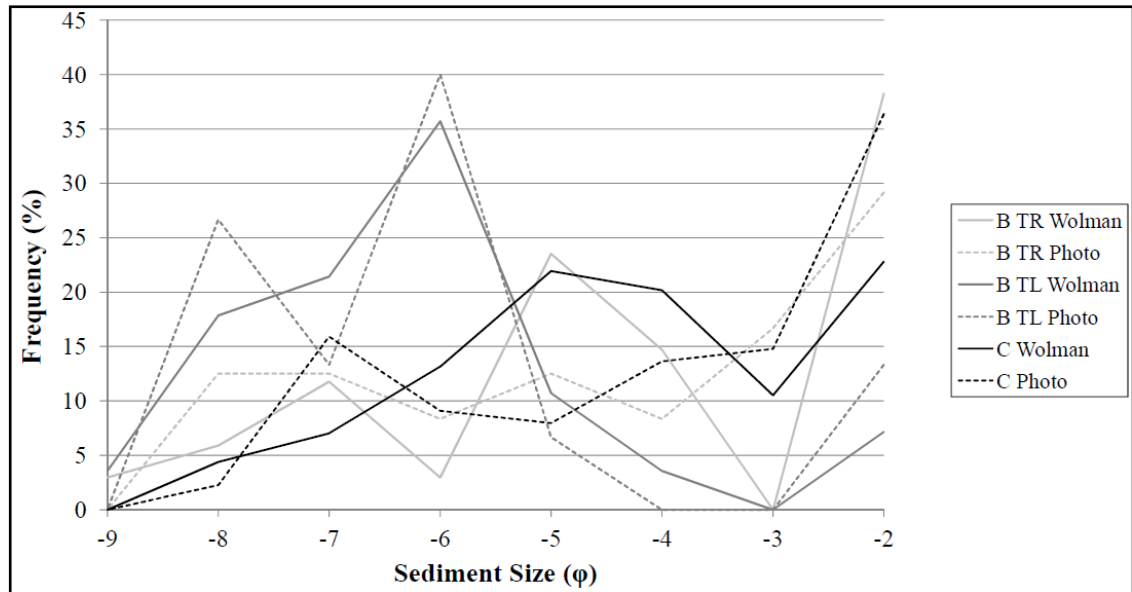


Figure 4.36: Grain Size Distributions for three sites on the Borgne d'Arolla braid plain, calculated from both a field Wolman count and photosieving. Frequencies are for the number of pebbles finer than the given grain size. The legend shows the confluence (*i.e.* B or C) and, in the case of Confluence B, the tributary (true left, TL, or true right, TR).

A comparison of the characteristic grain size measurements for the two different methods is given in Table 4.10, along with calculated RMSE values. As with the qualitative assessment of the GSDs from Figure 4.36, the true left tributary dataset from Confluence B performs the best, with the RMSE value less than half that of the other two datasets.

	Confluence C TL		Confluence B TL		Confluence B TR	
	Photo	Wolman Count	Photo	Wolman Count	Photo	Wolman Count
<b>D<sub>25</sub></b>	0	4.8	36.4	35.2	2.5	3.3
<b>D<sub>50</sub></b>	8.2	14.6	53.9	57.6	13.2	14.4
<b>D<sub>75</sub></b>	41.2	31.7	120.7	117.3	48.4	31
<b>D<sub>84</sub></b>	69.7	52.8	160.2	166.9	93.7	89.0
<b>RMSE</b>	10.5		4.2		9.0	

Table 4.10: Comparison of the characteristic grain sizes (in mm) obtained using the Wolman count and photosieving ('Photo') methods for three sites on the Borgne d'Arolla. In the Wolman counts, the minimum sediment size measured was 2mm.

#### 4.10.2 Calculating Roughness Heights from Grain Size Distributions

For the three Arolla confluences studied in detail, GSDs were determined by photosieving. The D<sub>50</sub> and D<sub>84</sub> values which were found from these GSD data are presented in Table 4.11.

	<b>GSD Percentile</b>	<b>Grain Size (mm)</b>
<b>Confluence E (True Left)</b>	D <sub>50</sub>	5.1
	D <sub>84</sub>	72.0
<b>Confluence E (True Right)</b>	D <sub>50</sub>	14.0
	D <sub>84</sub>	57.0
<b>Confluence G (Middle Bar)*</b>	D <sub>50</sub>	11.4
	D <sub>84</sub>	47.8
<b>Confluence H (True Right)</b>	D <sub>50</sub>	16.5
	D <sub>84</sub>	102.8
<b>Confluence H (Middle)</b>	D <sub>50</sub>	16.7
	D <sub>84</sub>	34.8
<b>Confluence H (True Left)*</b>	D <sub>50</sub>	34.4
	D <sub>84</sub>	92.2

Table 4.11: D<sub>50</sub> and D<sub>84</sub> values for the four confluences analysed in this chapter. All grain sizes are calculated using the photosieving method. Sites marked with asterisks (\*) had deeper water that restricted the view on multiple occasions.

The results from Table 4.11 demonstrate the significant variability that is found within individual confluences. In addition, for Confluence H the true right and middle datasets have similar median grain sizes but D<sub>84</sub> values that differ by a factor of 3. Therefore, finding a characteristic grain size from just one dataset is likely to have a significant level of uncertainty. In order to estimate the roughness height, average D<sub>50</sub> and D<sub>84</sub> values were obtained for each of the three confluences. By averaging the values, the effect of some of the large-scale variability is removed. Table 4.12 shows the roughness heights calculated from the averaged grain size data. Although there is variability between confluences, there are also substantial differences between methods, which reflects the inconsistency in the relationship between the D<sub>50</sub> and D<sub>84</sub> values displayed in Table 4.11.

	<b>Method</b>	<b>k<sub>s</sub> (mm)</b>	<b>z<sub>0</sub> (mm)</b>
<b>Confluence E</b>	0.1D <sub>84</sub>		6.5
	3.5D <sub>84</sub>	225.8	7.5
	6.8D <sub>50</sub>	65.3	2.2
<b>Confluence G</b>	0.1D <sub>84</sub>		4.8
	3.5D <sub>84</sub>	167.7	5.6
	6.8D <sub>50</sub>	77.5	2.6
<b>Confluence H</b>	0.1D <sub>84</sub>		7.7
	3.5D <sub>84</sub>	268.1	8.9
	6.8D <sub>50</sub>	153	5.1

Table 4.12: Roughness heights calculated from the characteristic grain sizes given in Table 4.11.

#### 4.10.3 Discussion of Roughness Data

Following similar tests in Section 4.4, the comparison between the Wolman count and Carbonneau *et al.* (2004) photosieving methods was conducted in order to verify that, on the Borgne d'Arolla braid plain, photosieving provides an acceptable alternative to *in situ* Wolman counts. The qualitative and quantitative analysis in Figure 4.36 and Table 4.10 suggests that the broad pattern of the GSD is replicated by the photosieving, although there are some disparities. The biggest differences between characteristic grain sizes (Table 4.10) tend to be at the coarser end of the GSD, with the photosieving method, in general, over-predicting the characteristic grain size values given by the Wolman count. A possible explanation for this is sampler bias, whereby the sampler subconsciously attempts to avoid measuring the same very large particle four or five times. The possibility of similar bias is reduced in the Carbonneau *et al.* (2004) photosieving method because the particle to be measured is marked very clearly and precisely by the crosshairs. In addition, some of the error may be due to the relatively large proportion of fines (glacial flour) found on the Borgne d'Arolla braid plain. As noted in Section 3.8.3, photosieving becomes more difficult when many particles are of a similar size to the pixels. However, this would only be expected to have a small effect at the finer end of the GSD.

There is significant variability in the characteristic grain size measurements, both within and between confluences. This demonstrates the poorly sorted nature of the bed, with the surface of the braid plain made up of cobble-sized clasts and patches of deposited glacial flour. The GSD can therefore vary considerably depending on the extent to which deposition of fines has occurred on that particular patch.

It is unsurprising, given the variability in the GSDs, that there are differences between confluences for the calculated roughness heights. However, the variability between methods in Table 4.12 also demonstrates that each of these approaches provides only an estimate of roughness height. In Section 4.4.3, it was noted that it is not straightforward to get a representative value of the roughness height that applies throughout a gravel-bed river. For the Borgne d'Arolla confluences, these problems are further complicated because the bed is almost constantly in motion and therefore any friction force would be expected to be lower than that implied by the calculated roughness height. Therefore, whilst values for the roughness height have been found



and these values agree on the appropriate order of magnitude, the uncertainty inherent within these types of data means that providing a more precise value is difficult.

## **4.11 Flow Data**

This section presents the flow data from Confluences E, G and H. As with Section 4.9, the primary concern of flow data collected on the Borgne d'Arolla braid plain is to provide reliable input and validation data for further investigations using numerical modelling. Because the flow data are largely one-dimensional, it is not possible to conduct the same in-depth analysis as in Section 4.5, where the results were examined for evidence of each of the flow processes highlighted in the classical river confluence model (Mosley, 1976; Ashmore and Parker, 1983; Best, 1986; Best and Roy, 1991). However, the data can still be assessed for the error in the channel discharges calculated from flow velocity measurements (which are required as boundary conditions in the numerical models), the length of time series required to reach stationarity, the viability of obtaining aDv data in these highly turbulent, supercritical confluences and any insights that these three-dimensional aDv data can provide.

This section therefore begins by addressing the issues of stationarity and aDv data quality using the flow data obtained from Confluence E. The aDv data are found to be particularly affected by white noise in these environments, although some datasets are sufficiently unaffected to be able to test for stationarity. The mean flow data and calculated discharges are then presented from Confluences G and H, before the results are discussed.

### *4.11.1 Flow Data Quality and Stationarity Tests*

Figure 4.37 shows an example of aDv data taken from Arolla Confluence I. In spite of the data being obtained from a fast-flowing section of the confluence, the mean velocities from these data are 0.06m/s, -0.07m/s and -0.01m/s in the downstream, cross-stream and vertical directions. Furthermore, it can be seen from Figure 4.37 that the dataset is very spiky, especially for the horizontal components of the flow. It is unrealistic to expect flow in a steep natural river to have such large variations in velocity with such low mean values. Therefore, it is argued that this aDv dataset has been substantially affected by white noise. The most likely reason for this is that the

interaction between the highly turbulent white water at the surface and the rough bed results in large concentrations of air bubbles passing through the sampling volume. As noted in Section 3.8.2, a susceptibility to flows with large proportions of air bubbles present is one of the major limitations of aDv instruments.

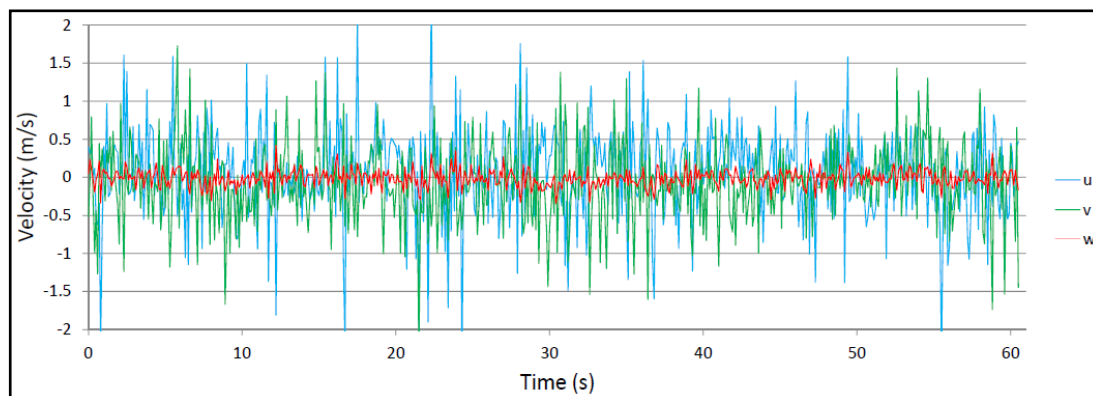


Figure 4.37: Velocity time series for an example aDv dataset from Confluence I.

Although the white noise in Figure 4.37 was not present to such a large extent in every dataset, the number of datasets affected meant that any quantities derived from the data (*e.g.* discharge) would be subject to considerable error. Indeed, during the course of the field experiments it was found that to obtain datasets less affected by white noise often required a process of trial and error in the positioning of the probe. This could result in the data being collected a significant distance away from the intended measurement location. Therefore, using the Electromagnetic Current Meter (ECM) was considered the best way of reducing the uncertainty in both the values and location of the data collected. As noted in Section 3.8.2, the ECM has the disadvantage that only one-dimensional flow data can be obtained and that it is an intrusive method which may affect the flow. However, it is known to be less sensitive to the presence of air bubbles (Rodriguez *et al.*, 1999), which will be a major advantage in these environments. In addition, the ECM has two other advantages at these steeply-sloping, dynamic, shallow and highly turbulent confluences. Firstly, the fact that the measuring volume is immediately above the probe (rather than 5cm below) is helpful as it reduces the potential for interference in the signal from the active bed. Secondly, the smaller distance between the probe and measuring volume enables data to be collected in much shallower water.

When using the ECM, it is also necessary to be able to perform some form of check on the data quality. The ECM calculates only the mean velocity and the standard

deviation, so the data quality cannot be assessed in as much depth as for the aDv data. However, in order to identify potentially anomalous data, it was determined that any result where the standard deviation exceeded 0.1m/s (equivalent to 10% of the mean velocity in most cases) would be repeated to check the results. For comparison, the standard deviations for the data in Figure 4.37 are 0.596m/s, 0.517m/s and 0.11m/s for the downstream, cross-stream and vertical velocities respectively (which is the equivalent of up to 10x the mean values).

Although the quality of the aDv data was found to be inconsistent, two datasets which were less affected by white noise were used to check the length of time required to ensure stationarity in the results. The results were checked visually to ensure that the dataset was not affected by white noise before being used for the assessment. Figure 4.38 shows four of the aDv datasets obtained at Confluence E. There is a visible difference between datasets 4 and 14 on the one hand and datasets 8 and 10 on the other. Dataset 10 has large fluctuations in the horizontal velocity components throughout, whilst in the case of dataset 8, the plot becomes substantially spikier after 17s. The latter demonstrates that the inconsistencies in the aDv data are temporal as well as spatial.

As a result of the visual tests, datasets 4 and 14 were used to determine the measurement time required to ensure stationarity in the velocity data. Therefore, Figure 4.39 plots the length of time series against mean velocity for these two datasets, while Figure 4.40 gives the standard deviation.

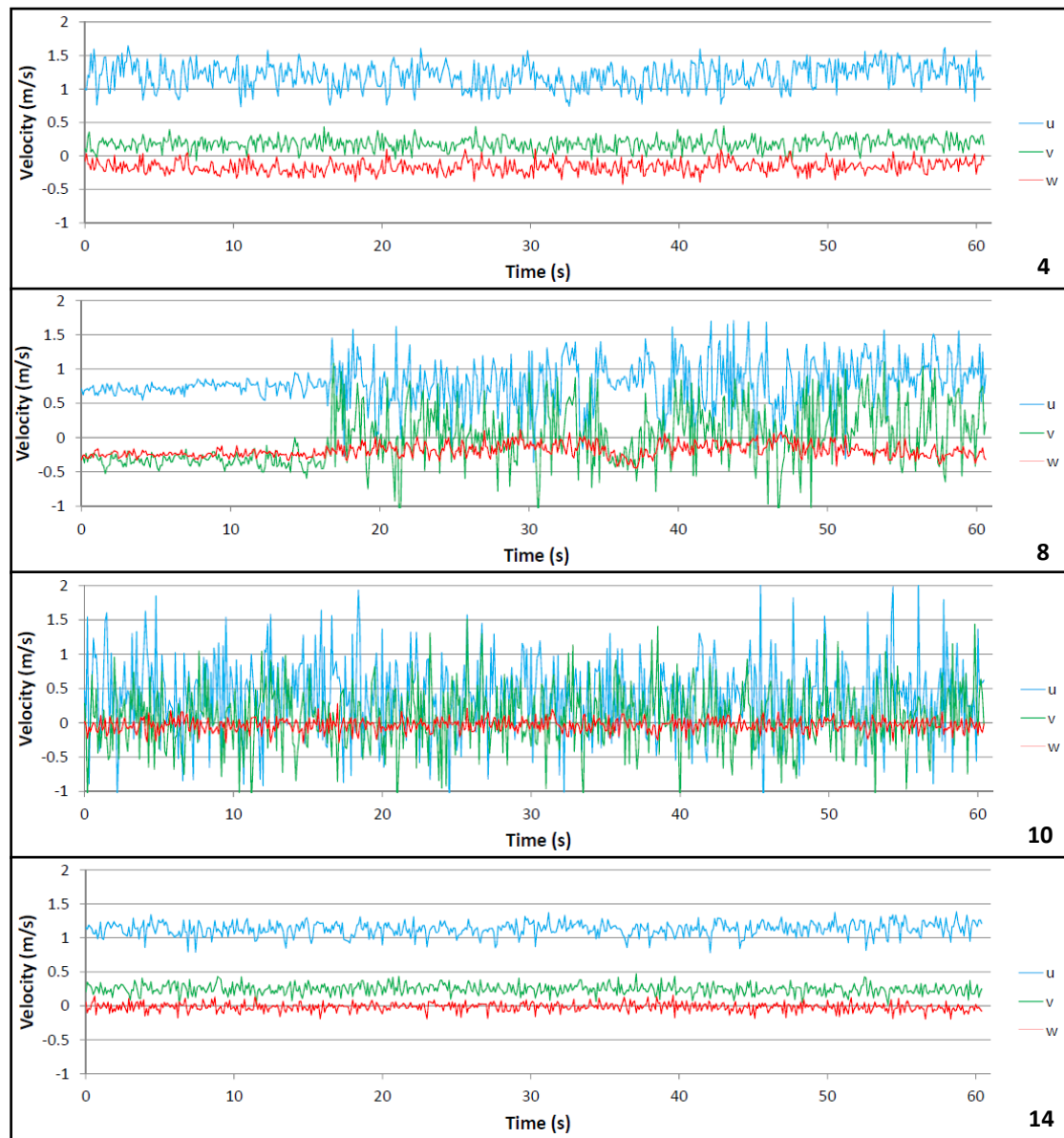


Figure 4.38: Velocity time series for four of the aDv datasets from Confluence E.

In Figure 4.39, datasets 4 and 14 both converge on a mean velocity quickly, sometimes in as little as 15s. Similar patterns are seen in the plots of standard deviation in Figure 4.40, with the values being constant after 25s in all cases. With the data stationary by 15-25s (depending on the dataset and velocity component), a time series length of 30s can be considered adequate to ensure stationarity has been reached when measuring flow at the Arolla confluences. Indeed, there is some evidence to support the 20s measurement periods of Roy and Bergeron (1990).

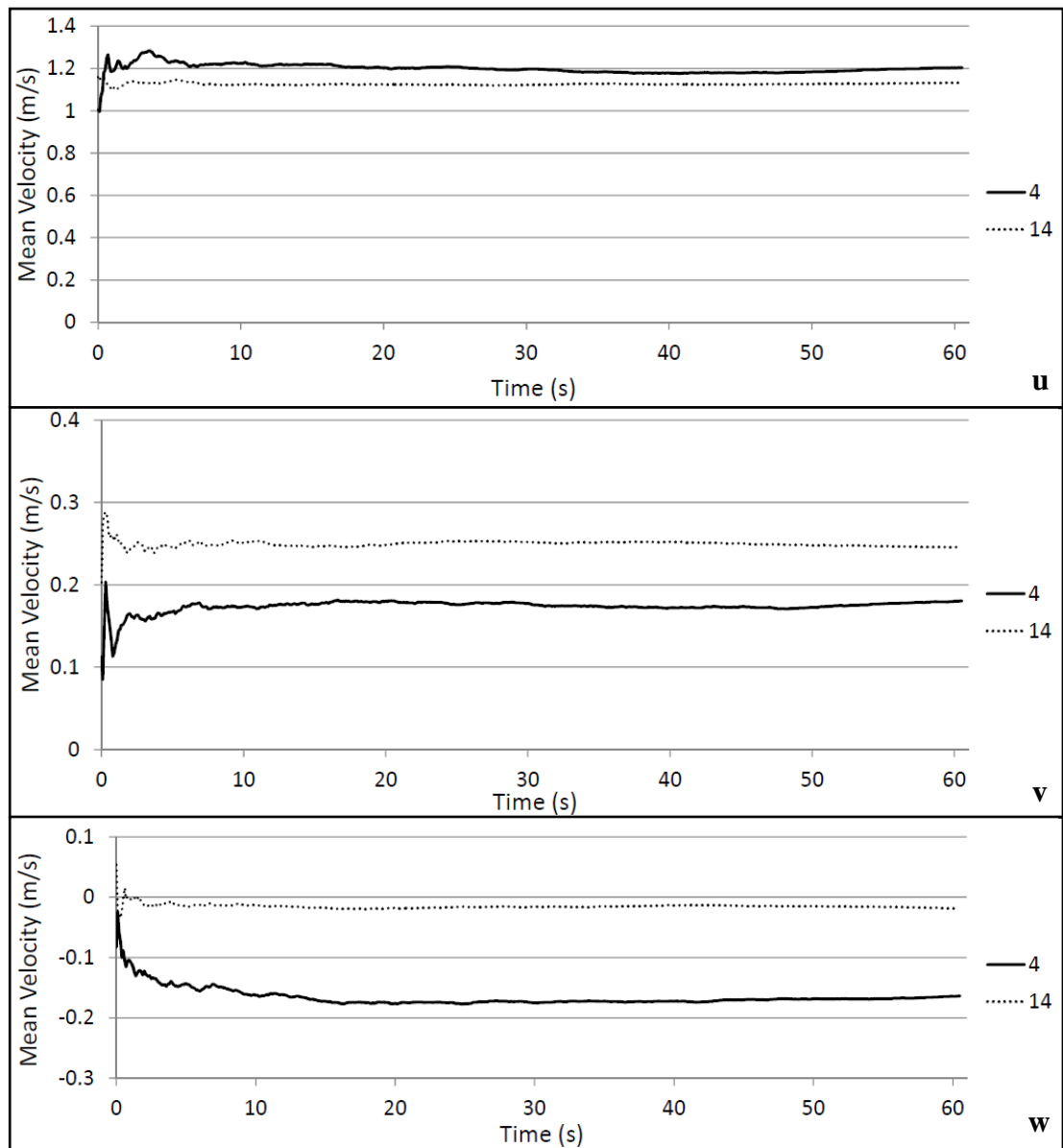


Figure 4.39: Stationarity plots of mean velocity against length of time series for datasets 4 and 14.

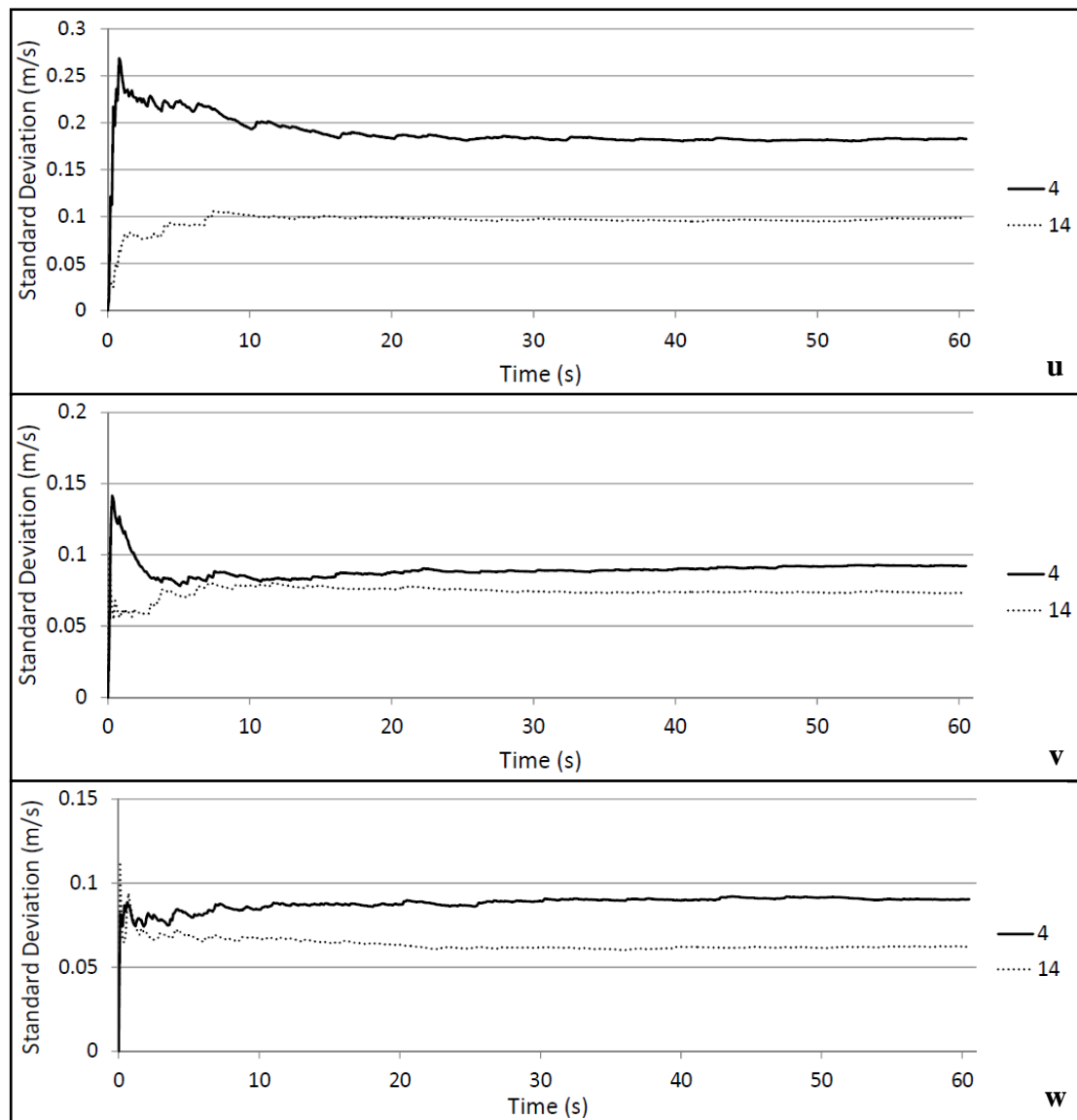


Figure 4.40: Stationarity plots of standard deviation against length of time series for datasets 4 and 14.

#### 4.11.2 Mean Flow Data

The mean flow readings were obtained by taking measurements at  $0.4d$  above the bed, where  $d$  is the water depth. The results in Section 4.5 demonstrated that in most cases this provides a reasonable estimate of the depth-averaged flow velocity. Figures 4.41 and 4.42 show the flow velocities and directions for Confluences G and H, along with the discharges calculated using the trapezium rule. Flow velocity data were obtained using the ECM and therefore the flow directions had to be determined from the visible surface flow directions (as recorded by the Leica Total Station).

The inlet data point locations were set at 0.2m intervals along a fixed tape measure, as required in Section 3.8.2. This scales to a  $y/w_c$  ratio of 0.09-0.15, depending on the tributary channel width. Outlet flow velocities were also recorded, but as these are not required for boundary conditions in the numerical model (and therefore did not have a specified spacing in Section 3.8.2), these were spaced at approximately 0.5m ( $y/w_c = 0.2-0.33$ ) and the exact point locations were surveyed using the Leica Total Station.

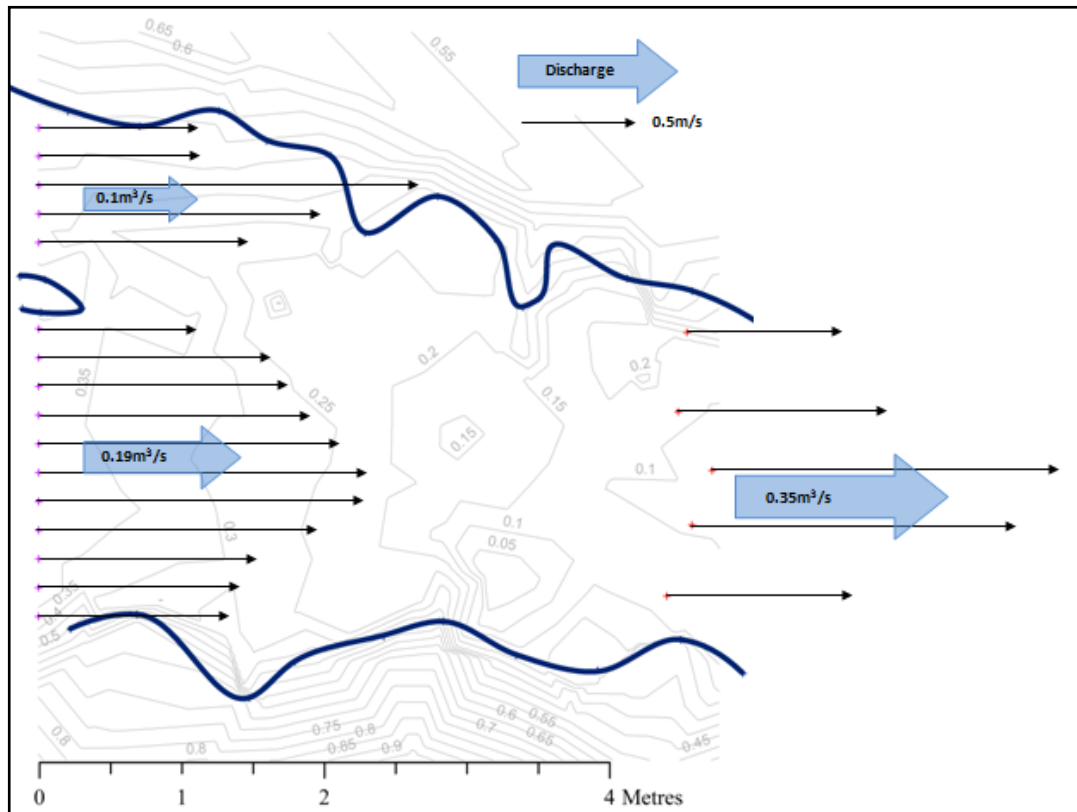


Figure 4.41: Flow velocities and calculated discharges for the inlets and outlets of Confluence G.

In both confluences, flow velocities are high ( $>1\text{m/s}$  in many cases), with values tending to increase towards the centre of the channel. For these two confluences, surface flow directions within a tributary or the main channel were recorded as being consistent, although that only held as far as could be seen by eye for the surface velocities. The lack of three-dimensional flow data, however, makes it impossible to discern any other flow structures.

As discharge data were calculated for the two tributaries and the downstream channel at both confluences, the differences between the results can be used to quantify the uncertainty in these values. These errors will be caused by a combination of the

uncertainty in the velocity data, the representativeness of the  $0.4d$  value for the depth-averaged velocity and the assumptions of the trapezium rule. For Confluence G the sum of the tributary discharges is  $0.06\text{m}^3/\text{s}$  lower than the calculated outlet discharge, giving an error of 17%. For Confluence H, meanwhile, the combined discharge of the tributaries is  $0.03\text{m}^3/\text{s}$  higher, which is equivalent to 13% of the main channel discharge.

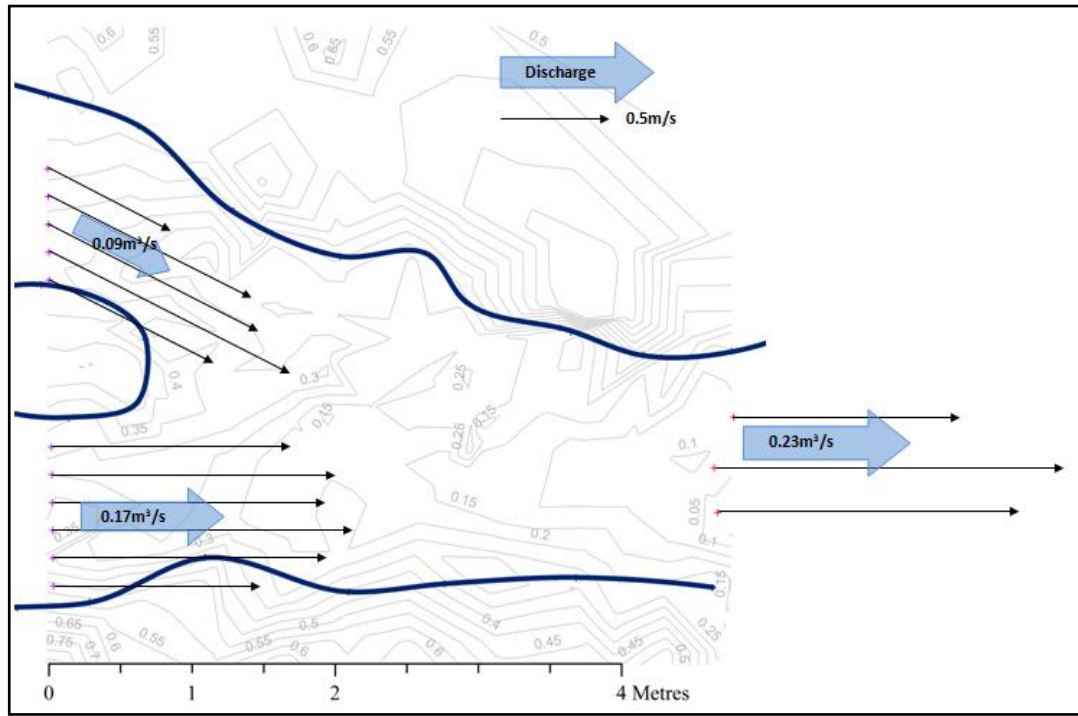


Figure 4.42: Flow velocities and calculated discharges for the inlets and outlets of Confluence H. Discharge arrow areas and velocity arrow lengths are proportional to those in Figure 4.41 for ease of comparison.

#### 4.11.3 Discussion of Flow Data

The first priority of the flow measurements presented in this section was to ensure that there was sufficient boundary condition data for the numerical modelling experiments to be conducted in Chapter 5. In addition, it is important to quantify the likely errors in these data, as such errors can have a substantial effect on how well the numerical model reproduces the flow at these confluences.

In Section 4.11.1, three examples were given of aDv datasets that had the appearance of being substantially affected by white noise. It was noted that this was not consistently found to be a problem in all datasets, but varied spatially and, in the case of dataset 8 at Confluence E, temporally. The frequency with which these problems were



encountered was sufficient to raise considerable doubts about the accuracy of any discharges derived from the flow data, which would be a concern for subsequent numerical modelling. Therefore, it was argued that it using the ECM was necessary in order to have more confidence in the discharge data.

Although there were problems with the reliability of the aDv data in this environment, there were a number of datasets unaffected by noise. Two of these datasets from Confluence E were used to test the period of time required to ensure stationarity in the flow data. In the absence of instantaneous ECM data, this provides the best method available for assessing the potential error due to the measurement period. The data in Figures 4.39 and 4.40 suggest that stationarity was reached after 15-25s, meaning that the 30s measurement periods used were sufficient.

The velocity data were used to determine discharges for each channel at Confluences G and H. By comparing these discharges it was found that the total errors were 17% and 13% for Confluences G and H respectively, which are similar in magnitude to those in Table 4.6 for the Moor House confluences.

The mean flow data show the high downstream velocities which characterise the Arolla confluences. The highest velocities tend to be found in the centre of the channel, although even at the channel margins the velocities are higher than most values recorded at the Moor House confluences. In terms of flow direction, less solid conclusions can be drawn due to the methods used, but the evidence presented here suggests that these confluences are in fact relatively straightforward, with most flow in the channel following a similar direction.

## **4.12 Comparison of the Arolla and Moor House Confluences**

The selection of the Borgne d'Arolla braid plain was designed to provide a more dynamic and steeper set of confluences to study, which would complement the more stable confluences of Moor House National Nature Reserve. The data presented from the Arolla field experiments have satisfied the quality criteria set out in Section 3.8, although due to the nature of the site, it was not possible to obtain topographic and flow data at the same spatial density as for the Moor House confluences. Nevertheless, in satisfying the criteria in Section 3.8, it can be used to provide boundary condition and input data for the numerical modelling process, which was considered the primary aim of this set of field experiments. Therefore, although the immediate conclusions which

can be drawn from the data are fewer and more uncertain than for the Moor House confluences, there are sufficient data presented in this section to be able to set up numerical modelling experiments. From these experiments it should be possible to obtain a better understanding of the flow processes in operation at these steep, dynamic river confluences.

The data presented from the Arolla confluences have demonstrated that the morphology has very few features consistent with those identified in the classical model of river confluences (Mosley, 1976; Ashmore and Parker, 1983; Best, 1986; Best and Roy, 1991). Scour holes and avalanche faces are not present, with bed topography largely dominated by features associated with large clasts deposited in the channel. This is similar to the Moor House confluences, which are not characterised by these morphological features except in the case of the bed discordance at the lower confluence.

The GSD at the Arolla confluences is more variable than at the Moor House confluences, which reflects the much more poorly sorted bed. Although the range of characteristic particle sizes is similar between the two sites, there is a less obvious peak grain size in Figure 4.36 compared to the plot for Moor House in Figure 4.11. Furthermore, for the Arolla plot in Figure 4.36, there is, for most sites, a greater proportion of fines compared to the Moor House GSDs. This greater proportion of fines is largely responsible for the generally lower roughness height values calculated for the Arolla confluences (Table 4.12) compared to those found for the Moor House confluences. However, as was noted in Section 4.10, it is arguable that in the case where the bed is constantly in motion these roughness heights may well be an overestimate, as the actual drag force acting on the flow would be reduced.

The fast, supercritical flow at the Arolla confluences (Table 4.8) provides a clear contrast to the slower, subcritical flow of the Moor House confluences (Table 4.1), thus satisfying Criterion 1 from Section 1.6. The use of the one-dimensional ECM (for reasons of data quality) means that it is difficult to draw further conclusions about the characteristics of the flow at the Arolla confluences, or indeed to make comparisons with the Moor House data. This demonstrates the limitations of field methods and therefore the importance of the opportunities provided by numerical modelling. The reliability of the flow data presented in both Sections 4.5 and 4.11 is therefore important, as it provides boundary conditions, inlet data and validation data for the numerical models. In both cases, the quality of the data is sufficient to provide dependable inlet

and outlet velocities, although the three-dimensional Moor House data are naturally more detailed regarding the flow in the centre of the confluence and secondary flow circulation.

Therefore, although the field data presented from Moor House National Nature Reserve have helped to meet the second research aim in Section 1.5, more experiments are required in order to fully understand the flow processes operating at steep, upland river confluences and the resultant effect on particle transport and morphological evolution. In the case of the Moor House confluences, this would be experiments in the higher discharge flows which result in changes to the channel morphology. For the Arolla confluences, more detail is required on the three-dimensional flow field within the confluence. In both cases, it is highly problematic to do this using field experiments, as these conditions are inherently dynamic and therefore place considerable time and methodological constraints on data collection. Therefore, the most feasible option is to take advantage of the progress in three-dimensional flow modelling. The development of numerical modelling methods capable of representing the flow at upland river confluences is therefore considered a priority.

### **4.13 Conclusions**

This chapter has presented topographic, roughness and flow data from two different, upland field sites. The first, at Moor House National Nature Reserve, is characterised by stable topography, more gently sloping water surfaces and subcritical flow. The second, from the Borgne d'Arolla braid plain, is highly dynamic, constantly evolving and has very steep water surface slopes with flow that is predominantly supercritical. However, there are key similarities between the sites, with both providing examples of shallow confluences with sloping water surfaces and bed material which is largely dominated by gravels and cobbles (particle sizes of  $-3\phi$  to  $-9\phi$ ).

With the upper and lower confluence sites having been introduced in Section 1.6.1, Section 4.2 provided further information on the weather conditions and flow regime of the Moor House confluences. These data demonstrated that the long-term discharge record is dominated by low flow periods interspersed with occasional flashy floods.

Section 4.3 introduced the topographic data for the Moor House confluences and assessed the dataset quality. The lower confluence at Moor House was shown to be a

discordant junction, with a very well-defined step from the true left tributary into the main channel. However, there was no evidence of a scour hole or the presence of depositional bars. The upper confluence, meanwhile, had a more complex morphology, with the more elevated true left tributary flowing through a deep constriction into the main channel. The true right thalweg, meanwhile, was interrupted by the extension of the upstream corner bar, so that at the time the flows met, it was in fact the true right tributary which had the higher elevation. The irregular nature of the topography at both confluences can be attributed to their steeper nature and the fact that the channel bed is made up of a range of larger clasts. These factors are characteristic of upland confluences and crucially are very different from the lowland confluences on which much of the classical model has been based. This is likely to have important implications for the sediment transport at such confluences, which will be addressed in detail in Chapters 6 and 7.

Section 4.4 presented the GSD data from three sites on each of the Moor House confluences, with a comparison made between the results obtained using a Wolman count and the Carbonneau *et al.* (2004) photosieving method. Both methods were shown to give similar GSD results. These results were then used to calculate roughness heights for the channel, which were compared to those calculated from the velocity profile data for each confluence. Although the roughness heights were of a similar order of magnitude, it was found that the velocity profile data gave higher values for the roughness height. However, the two methods agreed that the roughness height was greater at the lower confluence. Nevertheless, it was resolved that any numerical modelling would test for the sensitivity to the roughness height value.

The mean flow data for Moor House showed that with the exception of the lower confluence dataset on 8<sup>th</sup> April 2011, the discharges calculated from the velocity data for the appropriate channels were within  $0.04\text{m}^3/\text{s}$  of those given by the EA gauging station. This provided confidence in the discharges determined from both the velocity measurements and the gauging station data, with the latter important for providing the boundary conditions in high flow simulations of the confluences. The mean flow data were investigated for evidence of the presence of six major flow processes identified from the classical model of river confluences. Although both the upper and lower confluences were found to have a flow separation zone, this was not linked to a zone of deposition, suggesting that the flow may not be in equilibrium with the confluence morphology. There was no evidence of flow divergence in the main channel that might

lead to the development of a mid-channel bar, nor substantial increases in velocity in the main channel.

From the velocity profile data at the lower confluence, evidence was uncovered of water from the true right tributary flowing in the lee of the step from the true left tributary. However, there was no evidence of a zone of upwelling on the downstream corner, as Best and Roy (1991) found in their laboratory experiments. For the upper confluence, there was evidence of possible helical secondary flow cells, but not in the back-to-back counter-rotating form of Mosley (1976). Instead, they were largely linked to either the curvature of the true right tributary or the deflection of flow around topographic obstacles.

Of the six flow processes identified, the shear/mixing layer could not be identified and investigated with mean flow data alone. Therefore, Section 4.6 examined the turbulence in the Moor House flow data, by calculating turbulent kinetic energy (TKE) and Reynolds Stress (RS). Elevated levels of TKE and RS were found in both confluences where the two flows mixed, although this zone was not particularly persistent in any direction. In order to determine the nature of this increased turbulence, spectral density plots were produced from the velocity data in this zone of higher TKE and RS values. These plots demonstrated that any peaks in the power spectral density were small and were not consistent throughout the flow depth. There was also no clear difference between the different velocity components at any given frequency. As noted in the discussion of the flow data in Section 4.7, this implied that the turbulence was largely small-scale and isotropic, rather than being characterised by large-scale quasi-2D coherent flow structures.

With Section 4.8 the focus switched to the steeper and more dynamic confluences of the Borgne d'Arolla braid plain. A summary of the data collected at all nine confluences was set out, along with a justification for the choice of three confluences to be analysed further. One of these, Confluence E, was selected because it included a full dataset of three-dimensional flow data obtained using the aDv. The other two (Confluences G and H), meanwhile, were selected because they were considered to be the best of those datasets which satisfied all of the data quality criteria in Section 3.8. In addition, all three datasets were unaffected by any noticeable changes to discharge or confluence morphology during the data collection period.

Section 4.9 presented the topographic data from the Arolla confluences, including an analysis of the individual point data quality and the point density

distribution. Having excluded the anomalous data from Confluence C, the mean error in the individual point data was found to be on a par with that at Moor House and lower than that required in the criteria of Section 3.8.1. Point densities were also found to be within the acceptable range, although average point densities were found to be lower for the confluences with larger inundated areas. The Digital Elevation Models themselves showed very little evidence of the morphological features expected in the classical model of river confluences (*e.g.* Best, 1986). It was suggested that this may be evidence that, as at Moor House, the morphology is not in equilibrium with the flow.

Section 4.10 presented GSD and roughness data from the Arolla confluences. The nature of the flow meant it was not possible to obtain roughness heights from velocity profile data, so instead the values were calculated from characteristic grain sizes. Although there was agreement between the Wolman and photosieving methods on the shape of the GSD, there was much more variability than for the Moor House confluences. This reflected the more poorly sorted nature of the bed and the difficulties associated with recording particles finer than the pixel size using the Carbonneau *et al.* (2004) photosieving method. Roughness heights were calculated from the GSD data and found to be lower than those at the Moor House confluences, although it was noted that on a mobile bed the roughness heights may overestimate the friction effect.

In Section 4.11, the flow data from the Arolla confluences were presented. Many of the aDv datasets were found to be badly affected by white noise, although two of the unaffected datasets from Confluence E were used to conduct stationarity tests. From these tests, a time series of 30s was found to be sufficient to obtain mean flow velocity data that were stationary. The ECM data for Confluences G and H were used to calculate discharges at the inlets and outlet, with the differences used as an indication of the error (17% and 13% for Confluences G and H respectively). These errors should be accounted for when drawing conclusions from any subsequent numerical modelling. The flow field itself showed higher velocities in the centre of the channel, and maximum velocities which were approximately double those at Moor House. However, because of the one-dimensional nature of the measurements, it was not possible to draw any more conclusions on the nature of the flow field.

As such, in the discussion comparing the Moor House and Arolla datasets (Section 4.12) it was argued that there was a need for more information on the flow at upland river confluences. It was suggested that as obtaining more detail from the field experiments is far from straightforward, the most feasible option was to take advantage

of recent advances in numerical modelling. Therefore, developing a three-dimensional flow modelling approach which can be applied to these steep, upland river confluences is the subject of Chapter 5.

**The Dynamics of Upland River Confluences**  
**Volume 2**

Matthew James Tancock

**Department of Geography**  
**Durham University**

Thesis submitted for the degree of Doctor of Philosophy

2014



## Table of Contents

<b>Chapter 5: Free Surface Modelling of Flow at Upland River Confluences.....</b>	<b>205</b>
5.1 Introduction.....	205
5.2 Description of the Height of Liquid (HOL) Free Surface Model .....	206
5.3 Testing the HOL Model .....	209
5.3.1 Model Verification .....	209
5.3.2 Model Validation.....	210
5.3.3 Errors Associated with Geolocation.....	211
5.4 Model Verification Using Arolla Confluence E .....	212
5.5 Model Calibration and Sensitivity Tests.....	216
5.5.1 Results from the Model Calibration and Sensitivity Tests .....	218
5.5.2 Discussion of Model Calibration and Sensitivity Testing.....	222
5.6 Model Validation Using Straight, Gravel-Bed Channels .....	223
5.6.1 Validation Using the Upper Confluence Inlets .....	224
5.6.2 Validation Using the Lower Confluence Inlets .....	229
5.6.3 Discussion of Model Validation in Straight, Gravel-Bed Channels.....	234
5.7 Model Validation Using the Moor House Confluences.....	234
5.7.1 Model Setup.....	235
5.7.2 Results from Modelling the Upper Moor House Confluence .....	235
5.7.3 Results from Modelling the Lower Moor House Confluence .....	241
5.7.4 Discussion of the Moor House Confluence Validation Tests .....	246
5.8 Model Validation Using the Arolla Datasets .....	247
5.8.1 Validation Using Confluence G .....	248
5.8.2 Validation Using Confluence H .....	252
5.8.3 Discussion of the Arolla Confluence Validation Tests .....	257
5.9 Discussion of Overall HOL Model Performance.....	258
5.10 Interpreting the Flow Dynamics at the Moor House Confluences .....	259
5.10.1 Flow Dynamics at the Upper Confluence .....	259
5.10.2 Flow Dynamics at the Lower Confluence .....	265
5.10.3 Discussion of the Low Flow Dynamics of the Moor House Confluences .....	269
5.11 HOL Scenario Modelling at the Moor House Confluences.....	271
5.11.1 High Discharges at the Upper Confluence .....	272
5.11.2 High Discharges at the Lower Confluence.....	281
5.11.3 Discussion of High Discharge Flows at the Moor House Confluences .....	290
5.12 Interpreting the Flow Dynamics at the Arolla Confluences .....	294
5.12.1 Flow Dynamics at Confluence G .....	294
5.12.2 Flow Dynamics at Confluence H .....	299

5.12.3	Discussion of the Flow Dynamics at the Arolla Confluences.....	304
5.13	Discussion of Flow at Upland River Confluences.....	307
5.14	Conclusions.....	309
<b>Chapter 6:</b>	<b>Bedload Transport at Upland River Confluences .....</b>	<b>312</b>
6.1	Introduction.....	312
6.2	Particle Tracking at Moor House Nature Reserve .....	313
6.2.1	Particle Tracking Experiment Design at Moor House .....	314
6.2.2	Data Quality and Recovery Rates.....	317
6.2.3	Particle Survey Dates .....	317
6.2.4	Particle Tracks at the Upper Confluence.....	318
6.2.5	Upper Confluence Particle Densities and Near-Bed Streamlines .....	324
6.2.6	Particle Tracks at the Lower Confluence .....	329
6.2.7	Lower Confluence Particle Densities and Near-Bed Streamlines.....	333
6.2.8	Discussion of Particle Tracks at the Moor House Confluences .....	336
6.3	Grain Size and Roundness Effects on Bedload Transport.....	338
6.3.1	Results from the Particle Size and Roundness Experiments.....	338
6.3.2	Discussion of Particle Size and Roundness Effects on Bedload Transport.....	344
6.4	Particle Tracking at the Borgne d’Arolla Confluences.....	345
6.4.1	Particle Tracking Experiment Design on the Borgne d’Arolla .....	345
6.4.2	Results from the Particle Tracking Experiments at Confluence G.....	347
6.4.3	Results from the Particle Tracking Experiments at Confluence H.....	349
6.4.4	Discussion of Arolla Particle Trajectory Data.....	350
6.5	Comparison of the Moor House and Arolla Confluences.....	352
6.6	Conclusions.....	354
<b>Chapter 7:</b>	<b>Discrete Particle Modelling of Upland River Confluences .....</b>	<b>356</b>
7.1	Introduction.....	356
7.2	Modelling Bedload Transport in Natural Rivers .....	357
7.2.1	Eulerian Sediment Transport Models.....	358
7.2.2	Discrete Particle Models.....	361
7.2.3	Modelling Saltation Using DPMs .....	362
7.2.4	Uncertainty in the DPMs .....	364
7.2.5	Discussion of Bedload Transport Models .....	365
7.3	Model Development and Implementation .....	365
7.3.1	Model Physics .....	366
7.3.2	Flow Turbulence.....	368
7.3.3	Particle Initiation .....	369
7.3.4	Particle Density and Values for the Friction and Drag Co-efficients....	371
7.3.5	The GLUE Methodology.....	373
7.3.6	Number of Parameter Sets and Time Step Variables .....	376

7.4	Model Calibration and Evaluation Using the Arolla Confluences .....	379
7.4.1	Model Calibration Using the Confluence G Particle Patches .....	379
7.4.2	Model Evaluation Using the Borgne d'Arolla Data .....	384
7.4.3	Discussion of the Arolla Confluence Results .....	390
7.5	Modelling Bedload Transport at the Moor House Confluences .....	392
7.5.1	First Simulations of the Upper and Lower Confluences .....	392
7.5.2	Second Simulations of the Upper and Lower Confluences .....	397
7.5.3	Discussion of the Model Results from the Moor House Confluences .....	403
7.6	Conclusions .....	406
<b>Chapter 8:</b>	<b>Conclusions .....</b>	<b>408</b>
8.1	Introduction .....	408
8.2	Evaluation of the Research Objectives .....	409
8.2.1	Research Objective 1: To obtain and to present high quality field data on the morphology, flow field and particle transport at a range of upland river confluences .....	409
8.2.2	Research Objective 2: To develop the application of numerical approaches to improve the understanding of steep river confluence flow dynamics .....	411
8.2.3	Research Objective 3: To use the topographic and flow data obtained as part of Objective 1 to test the performance of the numerical flow model developed in Objective 2 .....	412
8.2.4	Research Objective 4: To create a sediment transport and morphology model which uses the three-dimensional flow modelling developed in Objective 2 to determine the major processes driving particle movement in upland river confluences .....	413
8.2.5	Research Objective 5: To use the particle tracking data collected as part of Objective 1 to test the sediment transport model developed in Objective 4 .....	415
8.3	The Dynamics of Upland River Confluences .....	416
8.4	Further Research .....	421
8.4.1	Field Experiments .....	421
8.4.2	Numerical Modelling .....	423
8.4.3	River Confluence Dynamics .....	423
8.5	Conclusions .....	424
<b>Reference List</b>	<b>.....</b>	<b>425</b>

## List of Figures

Figure 5.1:	Model output showing the pressure distribution of a steeply sloped flume (bed slope = 0.1) modelled without an explicit treatment of the free surface. ....	207
Figure 5.2:	Digital Elevation Models (DEMs) for Arolla Confluence E, using a 2cm grid, 4cm grid and 8cm grid. ....	213
Figure 5.3:	Graphs showing the change in water surface elevation through time for three locations in Confluence E: in the true left, true right and downstream channels. ....	215
Figure 5.4:	An example of the position of the model cross-section used for comparison with the field data. ....	217
Figure 5.5:	Modelled water surface elevations for the six test runs at the true left tributary of the upper confluence. ....	219
Figure 5.6:	Contour plots of downstream flow velocity for each of the test runs at the upper confluence true left tributary. ....	220
Figure 5.7:	Velocity profiles for each of the upper confluence true left tributary test runs. ....	222
Figure 5.8:	Modelled and measured water surface elevations for the inlets at the upper Moor House confluence. ....	224
Figure 5.9:	Contour plots showing the modelled and measured flow velocities for the upper confluence tributaries. ....	225
Figure 5.10:	Modelled and measured velocity profiles for the upper confluence true left and true right tributaries. ....	226
Figure 5.11:	Modelled and measured velocities for the upper confluence tributaries, with error bars giving the potential geolocation errors. ...	228
Figure 5.12:	Modelled and measured water surface elevations for the inlets at the lower Moor House confluence. ....	229
Figure 5.13:	Contour plots showing the modelled and measured (filled circles) flow velocities for the lower confluence tributaries. ....	230
Figure 5.14:	Modelled and measured velocity profiles for the lower confluence true left and true right tributaries. ....	231
Figure 5.15:	Modelled and measured velocities plotted for the lower confluence tributaries, with error bars showing the potential geolocation errors. ....	233
Figure 5.16:	Three-dimensional view of modelled and measured water surface elevations for the upper Moor House confluence. ....	236
Figure 5.17:	Modelled water surface extent compared to the measured water edge from 20 <sup>th</sup> September 2011 and modelled minus measured water surface elevations for the upper confluence. ....	237

Figure 5.18: Comparison of modelled and measured water surface elevations at the upper confluence, with points within 2m of the outlet marked in red. ....	238
Figure 5.19: Depth-averaged modelled flow velocities for the upper confluence at Moor House Nature Reserve. ....	239
Figure 5.20: Modelled and measured downstream and cross-stream velocities for the upper confluence at Moor House Nature Reserve. ....	240
Figure 5.21: Three-dimensional view of modelled and measured water surface elevations for the lower Moor House confluence. ....	241
Figure 5.22: Two-dimensional plot of modelled water extent at the lower confluence compared to the measured water edge from 7 <sup>th</sup> October 2011 and a diagram showing the difference between modelled and measured water surface elevations. ....	242
Figure 5.23: Modelled and measured water surface elevations for the lower confluence, with the points located within 2m of the outlet marked in red. ....	243
Figure 5.24: Depth-averaged modelled flow velocities for the lower confluence at Moor House Nature Reserve. ....	244
Figure 5.25: Modelled and measured downstream and cross-stream velocities for the lower confluence, with RMA regression lines, 1:1 lines and error bars showing the range of values in the adjacent model cells. ....	245
Figure 5.26: Modelled and measured water surface elevations for Confluence G on the Borgne d’Arolla braid plain, shown in three-dimensional form. ....	249
Figure 5.27: Confluence G modelled water extent and a comparison of modelled and measured water surface elevations. ....	250
Figure 5.28: Plot showing modelled and measured water surface elevations for Confluence G. ....	251
Figure 5.29: Contour plot showing modelled downstream velocity at the outlet of Confluence G. ....	251
Figure 5.30: Modelled and measured downstream velocities for Confluence G, plotted with the RMA regression line and errors bars. ....	252
Figure 5.31: Three-dimensional modelled and measured water surface elevations for Confluence H on the Borgne d’Arolla braid plain. ....	253
Figure 5.32: Two-dimensional plot of modelled water extent at Confluence H compared to the surveyed water edge and a diagram showing the difference between modelled and measured water surface elevations. ....	254
Figure 5.33: Modelled and measured water surface elevations for Confluence H. ....	255
Figure 5.34: Modelled downstream flow velocities at Confluence H with measured velocities superimposed for comparison. ....	256

Figure 5.35: Modelled and measured downstream flow velocities at Confluence H plotted with geolocation error bars. ....	256
Figure 5.36: Contour and vector plots for three cross-sections through the centre of the upper Moor House confluence. ....	261
Figure 5.37: Helicity plots for three cross-sections through the centre of the upper Moor House confluence. ....	262
Figure 5.38: Plot of helicity index with distance downstream at the upper Moor House confluence. ....	263
Figure 5.39: Turbulent kinetic energy and bed shear stress from the modelled data of the upper confluence. ....	264
Figure 5.40: Contour and vector plots for three cross-sections in the middle of the lower confluence. ....	266
Figure 5.41: Helicity plots for three cross-sections at the lower Moor House confluence. ....	267
Figure 5.42: Plot of helicity index with distance downstream at the lower Moor House confluence. ....	268
Figure 5.43: Turbulent kinetic energy and bed shear stress plots using the modelled data from the lower confluence. ....	269
Figure 5.44: Three-dimensional view of the modelled water surface elevations for high flows at the upper Moor House confluence. ....	273
Figure 5.45: Depth-averaged flow velocities for the true-left dominated and true right dominated floods at the upper confluence. ....	274
Figure 5.46: Contour and vector plots for the three cross-sections at the upper confluence, derived from the model output of UpperRun007. ....	275
Figure 5.47: Helicity plots for three cross-sections at the upper Moor House confluence, taken from the output data of UpperRun007. ....	276
Figure 5.48: Contour and vector plots for the three upper confluence cross-sections, taken from the model output of UpperRun008. ....	277
Figure 5.49: Helicity plots for the upper Moor House confluence, derived from the model output of UpperRun008. ....	278
Figure 5.50: Variations in helicity index with distance downstream for UpperRun007 and UpperRun008. ....	279
Figure 5.51: Calculated TKE for UpperRun007 and UpperRun008. ....	280
Figure 5.52: Calculated bed shear stress for UpperRun007 and UpperRun008. ....	281
Figure 5.53: Modelled water surface elevations for the lower confluence in floods dominated by the true right tributary (LowerRun005) and the true left tributary (LowerRun007). ....	282
Figure 5.54: Depth-averaged flow velocities for the lower confluence in high discharges dominated by the true right and true left tributaries. ....	283
Figure 5.55: Contour and vector plots for the three lower confluence cross-sections, taken from the model output of LowerRun005. ....	284

Figure 5.56: Helicity plots for the lower Moor House confluence, derived from LowerRun005. ....	285
Figure 5.57: Contour and vector plots for the three cross-sections at the lower confluence, derived from the model output of LowerRun007. ....	286
Figure 5.58: Helicity plots for the three lower confluence cross-sections, using the model output from LowerRun007. ....	287
Figure 5.59: Helicity index plot for LowerRun005 (true right tributary dominant) and LowerRun007 (true left tributary dominant) at the lower Moor House confluence. ....	288
Figure 5.60: Modelled TKE for LowerRun005 and LowerRun007. ....	289
Figure 5.61: Bed shear stress calculations for the true right and true left dominated flows at the lower confluence. ....	290
Figure 5.62: Plan view of the depth-averaged flow velocities from the model of Confluence G. ....	294
Figure 5.63: Contour and vector plots for three cross-sections in Confluence G, with downstream velocity given by the contours. Local deviations from the depth-averaged cross-stream and vertical velocities are shown by the vectors. ....	295
Figure 5.64: Helicity plots for the three Confluence G cross-sections. ....	296
Figure 5.65: Turbulent kinetic energy and bed shear stress plots using the modelled data from Confluence G. ....	297
Figure 5.66: Variations in helicity index in Confluence G and a plot of turbulent kinetic energy, bed shear stress and water surface elevation against distance downstream. ....	298
Figure 5.67: Depth-averaged flow velocities for Confluence H calculated from the model output. ....	300
Figure 5.68: Contour and vector plots for three cross-sections in the centre of Confluence H. ....	301
Figure 5.69: Helicity plots for the three Confluence H cross-sections. ....	302
Figure 5.70: Calculated TKE and bed shear stress for the Confluence H model data. ....	303
Figure 5.71: Graph showing helicity index plotted against distance downstream for Confluence H, alongside equivalent plots for turbulent kinetic energy, bed shear stress and water surface elevation. ....	304
Figure 6.1: Grain size distributions for the tracer and bed particles at the Moor House confluences. ....	314
Figure 6.2: Photograph of the upper confluence at the beginning of the second particle tracking experiment. ....	316
Figure 6.3: Discharge data from the EA gauging station, with the dates of particle surveys marked by dashed lines. ....	318

Figure 6.4:	Particle positions for the first experiment at the upper confluence. ...	319
Figure 6.5:	Particle positions for the second upper confluence experiment. ....	322
Figure 6.6:	Near-bed (25mm) streamlines from UpperRun007 (true left tributary dominant) superimposed on the particle densities from Experiment 1 at the upper confluence. ....	325
Figure 6.7:	Near-bed streamlines from UpperRun008 and particle densities from Experiment 1 at the upper confluence. ....	326
Figure 6.8:	Near-bed streamlines from UpperRun007 superimposed on particle densities calculated from the results of Experiment 2 at the upper confluence. ....	327
Figure 6.9:	Near-bed streamlines from UpperRun008 and particle densities from Experiment 2 at the upper confluence. ....	328
Figure 6.10:	Particle positions for the second experiment at the lower confluence. ....	330
Figure 6.11:	Near-bed streamlines from LowerRun005 (flow predominantly from the true right tributary) superimposed on the particle densities from Experiment 2 at the lower confluence. ....	334
Figure 6.12:	Near-bed streamlines from LowerRun007 and particle densities from Experiment 2 at the lower confluence. ....	335
Figure 6.13:	Particle density plots for the rounded and angular particles during Experiment 2 at the upper confluence. ....	338
Figure 6.14:	Tracer grain size distributions in each patch for the zones marked in Figure 6.4e (from Experiment 1 at the upper confluence). ....	340
Figure 6.15:	Bar charts showing the grain size distributions for each patch in the second upper confluence experiment. ....	342
Figure 6.16:	Photograph of Arolla Confluence B during a purge, showing the difference in turbidity between the purge flow in the true left tributary and the low flow in the true right tributary. ....	346
Figure 6.17:	Results from particle tracking experiments for Confluence G using individual particle tracks and pebble patches. ....	348
Figure 6.18:	Results from particle tracking experiments using individual particle tracks and pebble patches at Confluence H. ....	350
Figure 7.1:	Diagram showing the major forces acting on a particle placed on a flat surface. ....	358
Figure 7.2:	Diagram showing the tracer particle at rest in the pocket between two bed particles. ....	370
Figure 7.3:	Plot of the vertical distribution of drag co-efficients for a sphere. ....	373
Figure 7.4:	Dotty plots showing the distribution of NSE values for the sliding friction co-efficient in a preliminary version of the model. ....	378



Figure 7.5:	Plot showing the change in the number of behavioural simulations with the number of time steps. ....	378
Figure 7.6:	Plot showing the spread of particle paths for the true right patch of Confluence G. ....	380
Figure 7.7:	Dotty plots for simulations of the true right patch of Confluence G, with the red line showing the threshold for a parameter set to be considered behavioural. ....	381
Figure 7.8:	Plot showing the spread of particle paths for the true left patch of Confluence G. ....	382
Figure 7.9:	Dotty plots for simulations of the true left patch of Confluence G, with the red line showing the threshold for a parameter set to be considered behavioural. ....	383
Figure 7.10:	Modelled and measured particle trajectories for the true right patch of Confluence H. ....	384
Figure 7.11:	Dotty plots for simulations of the true right patch of Confluence H, with the threshold to be considered behavioural given by the red line. ....	385
Figure 7.12:	Plot showing the modelled and measured (orange polygon) spread of particle paths for the true left patch of Confluence H. ....	386
Figure 7.13:	Dotty plots for simulations of the true left patch of Confluence H. ...	387
Figure 7.14:	Plot showing the spread of particle paths for the additional tests in the true left and true right tributaries of Confluence G, with the observed individual particle tracks given by the black lines. ....	389
Figure 7.15:	Plot showing the particle paths for the additional tests in both tributaries at Confluence H, with the observed individual particle tracks given in black. ....	390
Figure 7.16:	Plot showing the spread of particle paths for patches seeded in the true left and true right halves of the lower Moor House confluence tributaries, using the flow data from LowerRun005. ....	393
Figure 7.17:	Plot showing the percentage chance of particle initiation and the spread of particle paths for patches seeded in the true left and true right halves of the lower Moor House confluence tributaries, using the flow data from LowerRun007. ....	394
Figure 7.18:	Plot showing the spread of particle paths for patches seeded in the true left and true right halves of the upper Moor House confluence tributaries, using the flow data from UpperRun007. ....	395
Figure 7.19:	Plot showing the likelihood of particle initiation and the spread of particle paths for patches seeded in the true left and true right halves of the upper Moor House confluence tributaries, using the flow data from UpperRun008. ....	396
Figure 7.20:	Three-dimensional water surface plot and the depth-averaged flow velocities for LowerRun008. ....	399

Figure 7.21: Plot showing the spread of particle paths for patches seeded in the true left and true right halves of the lower Moor House confluence tributaries, using the flow data from LowerRun008. ....	400
Figure 7.22: Three-dimensional view of the water surface and plan view of the depth-averaged flow velocities for UpperRun009. ....	401
Figure 7.23: Plot showing the spread of particle paths for patches seeded in the true left and true right halves of the upper Moor House confluence tributaries, using the flow data from UpperRun009. ....	402
Figure 7.24: Photographs showing the upper confluence before and after the very large flood ( $26\text{m}^3/\text{s}$ ) of 22 <sup>nd</sup> June 2012. ....	404
Figure 8.1: Schematic diagrams of flow and sediment dynamics at upland river confluences. ....	418

## List of Tables

Table 5.1:	Model runtimes (in hours) for each of the models to be discussed in this chapter. ....	208
Table 5.2:	Calculated Grid Convergence Index (GCI) values for the medium and finest resolution grids at Confluence E. ....	216
Table 5.3:	Details of the model sensitivity tests using the true left tributary of the upper confluence. ....	218
Table 5.4:	Mean absolute and normalised difference values for the modelled water surface elevations at the true left tributary of the upper confluence. ....	219
Table 5.5:	Mean absolute differences for the modelled flow velocities in the true left tributary of the upper confluence. ....	222
Table 5.6:	Discharges for the true left (TL) and true right (TR) inlets in the upper and lower confluence scenario models. ....	272
Table 6.1:	Summary of research previously conducted into bedload dynamics at river confluences. ....	312
Table 6.2:	Mean positions and standard deviations (in metres) for the angular and the rounded particles in each of the four surveys of Experiment 2 at the upper confluence. ....	339
Table 6.3:	Distribution of tracer particle sizes in each patch at the end of the first experiment at the upper confluence. ....	340
Table 6.4:	Tracer particle sizes for each patch during the second experiment at the upper confluence. ....	343
Table 6.5:	The tracer particle size results from Table 6.4 converted into percentages for ease of comparison. ....	343
Table 7.1:	The mass, volume and calculated density for five randomly-selected tracer particles. ....	371
Table 7.2:	Table showing the results from tests to determine the static friction co-efficient.....	372
Table 7.3:	The range of parameter values used in the particle tracking model. All values are dimensionless unless stated.....	375

# Chapter 5:

## Free Surface Modelling of Flow at Upland River Confluences

### 5.1 Introduction

In Chapter 4, topographic, roughness and flow data were presented from river confluences at two sites. All of the confluences studied at these two different sites were upland confluences with sloping water surfaces and gravel or cobble beds. At Moor House Nature Reserve, the greater stability of the confluence planform allowed a high quality dataset to be collected to improve understanding of the flow processes operating at these sloping river confluences. The confluences on the Borgne d'Arolla, meanwhile, were steeper and more dynamic. This meant that although it was more challenging to obtain data before the confluence morphology had changed, it did allow for information on individual particle tracks to be collected for flow velocities which had been measured *in situ*. The particle transport data for both confluences will be presented in Chapter 6, but in order to be able to interpret these data and draw firmer conclusions, it is first necessary to understand the flow field at these confluences.

For both field datasets presented in Chapter 4, there is an opportunity to obtain a more complete understanding of the flow field using numerical modelling. In the case of the Arolla datasets, the highly turbulent flow reduced the reliability of the three-dimensional acoustic Doppler velocimeter (aDv) data, meaning that only one-dimensional flow data were collected. Therefore, at the Arolla confluences, numerical simulations of the flow through the confluences may provide more information on the three-dimensional aspects of the flow field. For the Moor House confluences, meanwhile, numerical modelling will allow the flow field to be investigated at discharges higher than those recorded in the field (*i.e.* those which initiate particle transport).

As discussed in Section 3.2, Computation Fluid Dynamics (CFD) provides the most appropriate form of numerical modelling for understanding the processes in river confluences, due to the complex three-dimensional nature of the flow. However, the traditional use of a rigid lid treatment of the free surface (described in Section 3.4.10) is

less appropriate when the water surface becomes very steep. Therefore, this chapter applies a Height-of-Liquid (HOL) model to the Moor House and Arolla confluences and assesses its performance. As far as the author is aware, this form of modelling is a new application to natural river confluences and therefore this process has involved considerable testing of the model under a range of conditions.

This chapter will therefore begin with a description of the HOL model and a demonstration of the reasons why it is necessary to use an explicit treatment of the free surface in these circumstances. This is followed by an explanation of the testing procedure before the results are presented. The results from the model verification tests are presented first, before model calibration and sensitivity analysis is undertaken in Section 5.5. The model validation tests are then conducted in three parts. The first tests assess the model performance on straight, gravel-bed channels using the inflow cross-sections from the Moor House confluences. The second set of tests then compare the results from models of both Moor House confluences with the data from Section 4.5, before the final validation tests use the flow data from Confluences G and H on the Borgne d'Arolla (Section 4.11). The results from the tests are then discussed, before the model is used to investigate the flow field at the Moor House and Arolla confluences in more detail in Sections 5.10, 5.11 and 5.12. Finally, from these results, Section 5.13 discusses the flow dynamics of upland river confluences.

## 5.2 Description of the Height of Liquid (HOL) Free Surface Model

When modelling flow in steeply-sloping natural rivers, variability in the free surface becomes an important boundary condition in the model because of its impact on conservation of mass and momentum. In addition, the free surface is important to understanding the sediment transport process, as water surface slopes are known to influence the distribution of bed shear stress (Chanson, 2000).

As explained in detail in Section 3.4.10, previous research using numerical modelling of river confluences (*e.g.* Bradbrook *et al.*, 1998, 2001) has accounted for the conservation of mass using a porosity value in the uppermost layer of cells (Figure 3.4c). However, such an approach still requires a rigid lid boundary to be specified in advance. Although this is feasible where the water surface is planar with minimal fluctuations, it is less applicable when the water surface varies considerably (Rodriguez *et al.*, 2004) and needs to be approximated *a priori*. Figure 5.1 shows that in a simple,

sloped flume the standard rigid-lid approach gives a physically unrealistic pressure distribution. The theoretical water surface is given by the 0Pa isobar, but in the case of the flume in Figure 5.1 this gives a water depth of 0.04m at the inlet and 0.2m at the outlet. Such large disparities cannot be accounted for by using a porosity value in the top layer of cells and therefore in steeply-sloping river confluences an explicit treatment of the free surface becomes necessary.

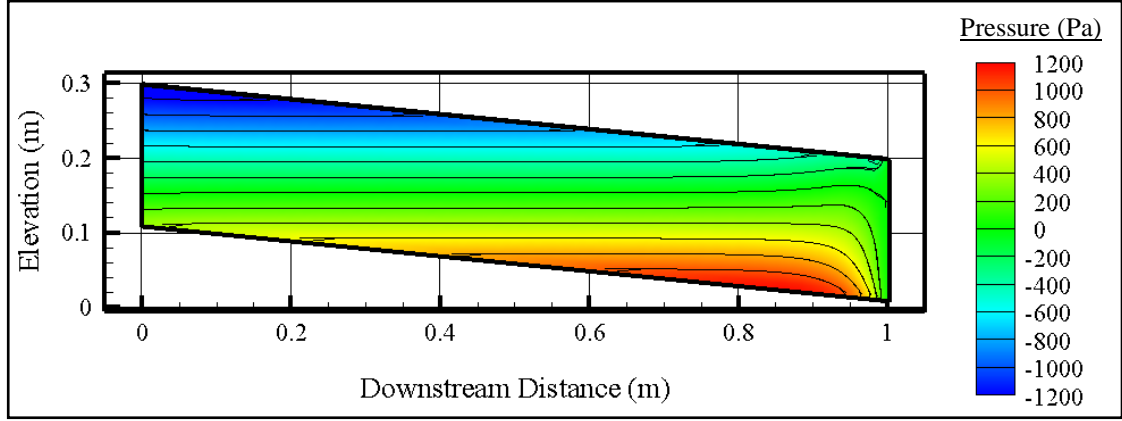


Figure 5.1: Model output showing the pressure distribution of a steeply sloped flume (bed slope = 0.1) modelled without an explicit treatment of the free surface (flow is from left to right). The hydrostatic pressure distribution dominates, with the implied free surface location (at 0Pa) unrealistic.

The Height-of-Liquid (HOL) model is a built-in component of the PHOENICS code which is designed to model the free surface, providing there is a single boundary between the two phases in the water column (CHAM, 2013). The HOL method calculates an additional variable for each cell (VFOL), which is the fraction of the cell volume that is liquid. The value of VFOL therefore varies from 0 to 1, with cells full of water having a VFOL value of 1. This is calculated by determining the mass balance changes between time steps for a given water column:

$$m_{l,t} = m_{l,t-1} + \Delta m_l \quad (5.1)$$

where  $m_l$  is the mass of liquid in a cell column and the subscripts  $t$  and  $t-1$  refer to the current and previous time steps respectively. The change in mass for a given time step ( $\Delta m$ ) is calculated from (Ben Haj *et al.*, 2002):

$$\Delta m_l = \sum_{in} A_i \Delta t \Phi_i \rho_L \mathbf{u}_i \mathbf{n}_i + \sum_{out} A_i \Delta t \Phi_i \rho_L \mathbf{u}_i \mathbf{n}_i \quad (5.2)$$

where  $A_i$  is the cross-sectional area of the cell,  $\Delta t$  is the length of time step,  $\rho_L$  is the density of the liquid,  $\Phi_i$  is the upwind value of the volume of fluid (VFOL) variable,  $\mathbf{u}_i$  is the velocity in the direction  $i$  and  $\mathbf{n}_i$  is the surface normal vector of the face  $i$ .

In preliminary testing of the HOL method, it was found that steady-state models experienced numerical instabilities, meaning that the models had to be run in time-dependent mode (as noted in Section 3.7). The convergence criterion developed in this chapter meant that models were run until the point at which changes in the water surface elevation between time steps were negligible. In effect, therefore, the aim was to run the time-dependent model until it had reached a steady state. In implementing this method, it was found that a time step of approximately 0.001s was needed to ensure numerical stability, which implied there was a substantial computational cost to this approach. Table 5.1 shows this computational time for each of the simulations for which results are presented in this chapter.

	Model Simulation	Grid Resolution	Time (hours)
Moor House Simulations	Upper TL Inlet	8x8x4cm	448
	Upper TR Inlet	8x8x4cm	474
	Lower TL Inlet	8x8x4cm	404
	Lower TR Inlet	8x8x4cm	1582
	Upper	16x16x8cm	237
	Lower	16x16x8cm	165
	Upper 007	16x16x8cm	598
	Upper 008	16x16x8cm	408
	Lower 005	16x16x8cm	340
	Lower 007	16x16x8cm	484
Arolla Simulations	Confluence E coarse	8x8x8cm	7
	Confluence E fine	4x4x4cm	93
	Confluence E finest	2x2x2cm	1083
	Confluence G	4x4x2cm	2082
	Confluence H	4x4x2cm	1821

Table 5.1: Model runtimes (in hours) for each of the models to be discussed in this chapter. Simulations were run on Intel Core i7 processors (2.93GHz) with 16GB RAM. For the upper true left tributary simulations the figure quoted is for the longest of the six runs.

As can be seen in Table 5.1, as a result of being run in time-dependent mode, model runtimes approached three months in some cases. However, this was considered justifiable on the grounds that the rigid lid approach (as demonstrated by Figure 5.1) would not necessarily give physically realistic flow fields in steep river confluences where the water surface slope cannot be well-specified in advance. This is important not only to improve the understanding of the flow field but also for correctly determining the bed shear stress and thus the sediment transport dynamics. Understanding the sediment transport at steep river confluences is a key objective of this thesis (Section 1.5) and therefore it is imperative that flow modelling is able to account for the impact of water surface variations.

### 5.3 Testing the HOL Model

As noted in Section 3.5, model verification and validation are essential components when developing and applying numerical models. PHOENICS has already been demonstrated to give reliable representations of flow through river confluences in a series of studies (Bradbrook *et al.*, 1998, 2001; Biron *et al.*, 2002, 2004a; Sandbach *et al.*, 2012). Therefore, the introduction of the HOL method means that this aspect of the model, in particular, needs to undergo careful testing. It was highlighted in the previous section, however, that the simulations have a high computational cost. This means that the strategy for testing the model needs to be carefully considered, to ensure the model has undergone as thorough an examination as possible. The following sections set out this strategy, with model verification covered in Section 5.3.1 and model validation in Section 5.3.2. Section 5.3.3, meanwhile, will address the issue of errors in the geolocation of individual point measurements, which has consequences for the interpretation of the results throughout this chapter.

#### 5.3.1 Model Verification

In Section 3.5, model verification was split into code verification and solution verification. As PHOENICS is a commercially-available code, it is verification of the individual solutions which is the major concern in this chapter. This includes determining whether iterative convergence, grid convergence and time step convergence are achieved.



However, undertaking these tests is not straightforward as a result of the highly variable bed topography and the use of the HOL method to determine the water surface elevation. As Lane *et al.* (1999a) note, the complex nature of gravel-bed rivers reduces the likelihood that a grid independent solution can be achieved. After all, in changing the size of the grid, the irregular topography will be resampled and the values at each grid cell altered. Furthermore, as discussed in Section 5.2, steady-state HOL simulations are numerically unstable. This means it is necessary to use a time-dependent model so that the simulation will converge to a solution. The consequence of this is that iterative convergence is more complex than in standard steady-state models, as it is inextricably linked to the time step and the convergence of the solution through time. Therefore, the model verification tests need to take this into consideration.

Given the computational requirements of the HOL method (Table 5.1), it is unfeasible to run further simulations at double the grid resolution in order to determine the Grid Convergence Index (GCI). Doubling the grid resolution would require at least an eightfold increase in CPU time to solve, which for the longest simulations would amount to approximately 2 years. As such, the grid independence tests were conducted for one natural river confluence (Arolla Confluence E) to provide an indication of the likely error as a result of the grid resolution.

In order to test the convergence of the solution through iterations and time steps, the water surface elevation was plotted against time for three different locations within the confluence. The model can be considered to have converged iteratively once an increase in the number of time steps results in no significant change to the modelled water surface elevation. For all subsequent simulations using the HOL method, the models were run until they had reached this state.

### 5.3.2 Model Validation

In the case of model validation, the field data presented throughout Chapter 4 were used to test the extent to which the simulations represent the processes operating at natural river confluences. There is a large amount of data from both the Moor House and Arolla confluences, so a three-part validation strategy was implemented.

In the first phase of the validation tests, the model results were compared to the measured water surface elevations and flow data at the Moor House inlets. These tests were conducted to determine whether the HOL model could reliably simulate single-

thread gravel-bed rivers (as the HOL model has yet to be tested for natural open channel flows). Having confirmed this, it would then be legitimate to move onto validating the model using the more complex flow fields of sloping river confluences.

The second phase of validation primarily made use of the three-dimensional velocity data and detailed water edge surveys obtained at the Moor House confluences. The model results were compared to the water surface elevation, water edge and flow velocity data.

The final phase of validation investigated the performance of the HOL model when simulating the much steeper Arolla confluences. As for the Moor House confluences, these tests used the available water surface elevation data and outlet velocity data for comparison with the numerical simulations.

Having undertaken this tripartite model validation strategy, the performance of the HOL model has been tested under a range of conditions. As such, greater confidence can be placed in the model results and the HOL method used for further investigations into the nature of the flow at steep, upland river confluences.

### 5.3.3 *Errors Associated with Geolocation*

When validating numerical models using field data, it is necessary to ensure that the modelled and measured values being compared are geolocated, and, in the case of velocities, that the orientations are correct. For water surface elevation, the major source of error is likely to be due to the linear interpolation between the water edge points, which cannot account for variations in the centre of the channel.

In the case of flow velocity data, comparing individual point data with model cell-centre values introduces additional uncertainty to these comparisons. It has already been observed in Section 4.3.1 that the mean error in surveyed point locations is of the order of 0.05m. In addition to this, there will be errors associated with the location of the flow velocity measurements due to the position of the tape measure, the position of the instrument on its frame and the actual location of the measured water volume relative to the instrument. Therefore, the actual location of the  $0.4d$  (where  $d$  is water depth) velocity measurements is subject to considerable error.

Although this error can be minimised as much as possible by ensuring good practice in the collection of field data, it is still likely that the actual location of the point data could vary by more than 0.05m from the recorded location. An example of the

uncertainty in the field location can be seen graphically in Figure 4.15, where the locations of the tributary inlet data deviate from what was, in the field, a straight line marked by a tape measure stretched across the channel.

Throughout this chapter, where field point data have been taken at  $0.4d$ , the points have been plotted at the location which is 40% of the distance between the DEM bed and measured water surface. This method was chosen instead of using the distance from the bed as measured in the field, because the depth measured by the ruler will be greater than that averaged over a cell of the DEM. The method chosen was considered to be the best way to ensure a like-with-like comparison between modelled and measured estimates of depth-averaged flow velocity. For the velocity profile data, meanwhile, it is distance below the measured water surface elevation which is used, as the local variation in water surface elevation will be much smaller than the topographic fluctuations (which will be more irregular due to the presence of large clasts). The water surface elevation raster is therefore considered a more reliable baseline than the DEM. However, given the uncertainty in these comparisons, in this chapter plots of modelled and measured flow velocity will also give an indication of potential error due to uncertainty in geolocation.

In the case of the Moor House confluences, the standard grid size for simulations of the full confluences was 0.16m in the horizontal directions and 0.08m in the vertical direction. Potential geolocation errors of more than 0.05m therefore mean that it is feasible for the uncertainty to be of the order of one cell's width in each direction. As such, the error bars reported in this chapter show the range of values in a 3x3x3 cell block around the recorded measurement point. For the Arolla confluences G and H, meanwhile, cell sizes were 0.04m in the horizontal directions and 0.02m in the vertical direction. In this case the uncertainty could arguably extend to multiple cells in each direction, although as with the Moor House comparisons, the error bars show the range of values in the 3x3x3 block of cells surrounding the measurement point.

## **5.4 Model Verification Using Arolla Confluence E**

The aDv data from Confluence E on the Borgne d'Arolla braid plain (presented in Section 4.11) were found to be too badly affected by noise from the highly turbulent and supercritical flow to be able to draw firm conclusions regarding the nature of the

flow at the confluence. However, the confluence itself was the smallest of those investigated on the Borgne d'Arolla braid plain and as such, had a higher point density than the other Arolla confluences. Therefore, due to its size and the higher quality of the topographic data, it was considered ideal for model verification tests and in particular the grid independence tests.

As discussed in Section 3.5, the aim of model verification is to ensure the numerical accuracy of the simulation, not its representation of the real-world system (Oberkampf and Trucano, 2008). Therefore, providing the boundary conditions are the same for all simulations, the accuracy of the boundary condition data is not a key concern. As a result, the inlet discharges were set assuming a uniform inlet velocity of 0.6m/s, which was considered a realistic value given the results from the more reliable aDv datasets. This gave inlet discharges of 0.42m<sup>3</sup>/s and 0.34m<sup>3</sup>/s for the true left and true right tributary inlets respectively. Figure 5.2 shows the three Digital Elevation Models for the iterative and grid convergence tests.

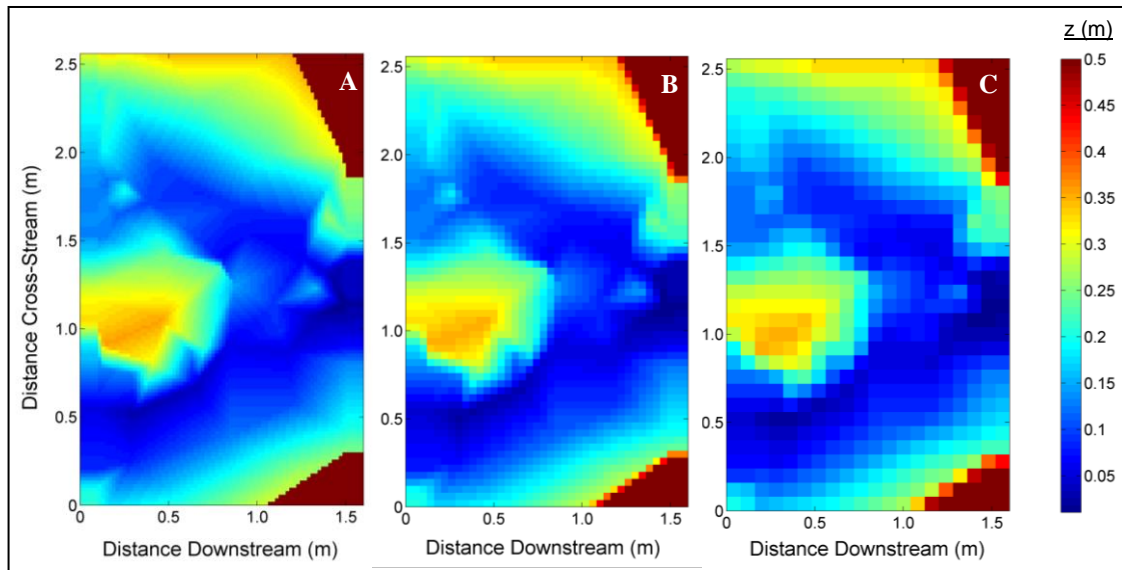


Figure 5.2: Digital Elevation Models (DEMs) for Arolla Confluence E, using a 2cm grid (a), 4cm grid (b) and 8cm grid (c). The model DEM had a 0.4m run-in zone and a 0.72m run-out zone to reduce the effects of the inlets and outlets on the flow field. Run-in and run-out zones had a zero bed slope, with the lengths determined using the findings from Figure 5.4 (and equivalents), scaled to channel width.

In order to test iterative convergence, a location in each of the channel centres was chosen arbitrarily and the water surface elevation of this point plotted through time. Figure 5.3 gives the results for the simulations at the three different grid resolutions. For the two finer resolution simulations (Figures 5.3b and 5.3c), the initial spikes in water

surface elevations are due to minor instabilities in the wetting process which resolve themselves with time.

The results in Figure 5.3 demonstrate that the simulation time required to achieve convergence on a solution is dependent on the grid resolution. With the coarsest grid (Figure 5.3a), the model has converged by 15s of model time. For the medium grid resolution (Figure 5.3b) convergence is not achieved until 80s, whilst for the finest grid (Figure 5.3c) it takes 150s. This has implications for any attempts to achieve grid independence, as not only will a halving of the grid cell size result in an eightfold increase in computational time, there is also the likelihood of a doubling of the number of time steps required to reach convergence. This will be a consequence of the relaxation required to ensure numerical stability, and therefore it would be difficult to increase the model speed in these circumstances. However, Figure 5.3 does show that the water surface elevations are converging to the same values regardless of grid resolution, which suggests that the simulation is grid independent, at least for the predicted water surface elevation.

In order to assess the uncertainty due to grid resolution, the Grid Convergence Index (GCI) was calculated for the Confluence E simulations using the methods set out in Section 3.5.3. In the first instance, the water surface elevation data were used to calculate a value for  $p_o$ , the observed order of convergence. The median value of  $p_o$  was found, as this was less likely to be affected by large anomalies. For confluence E this was calculated as 1.17. Having a calculated value for  $p_o$  meant that the factor of safety ( $F_s$ ) can be reduced from 3 to 1.25 (Roache, 1998). However, in this case the value of  $p_o$  is such that evaluating Equation 3.18 using either  $F_s = 3$  and  $p_o = 2$  or  $F_s = 1.25$  and  $p_o = 1.17$  will yield the same GCI. Table 5.2 gives the GCI calculations for both the medium and finest grids for the seven major variables.

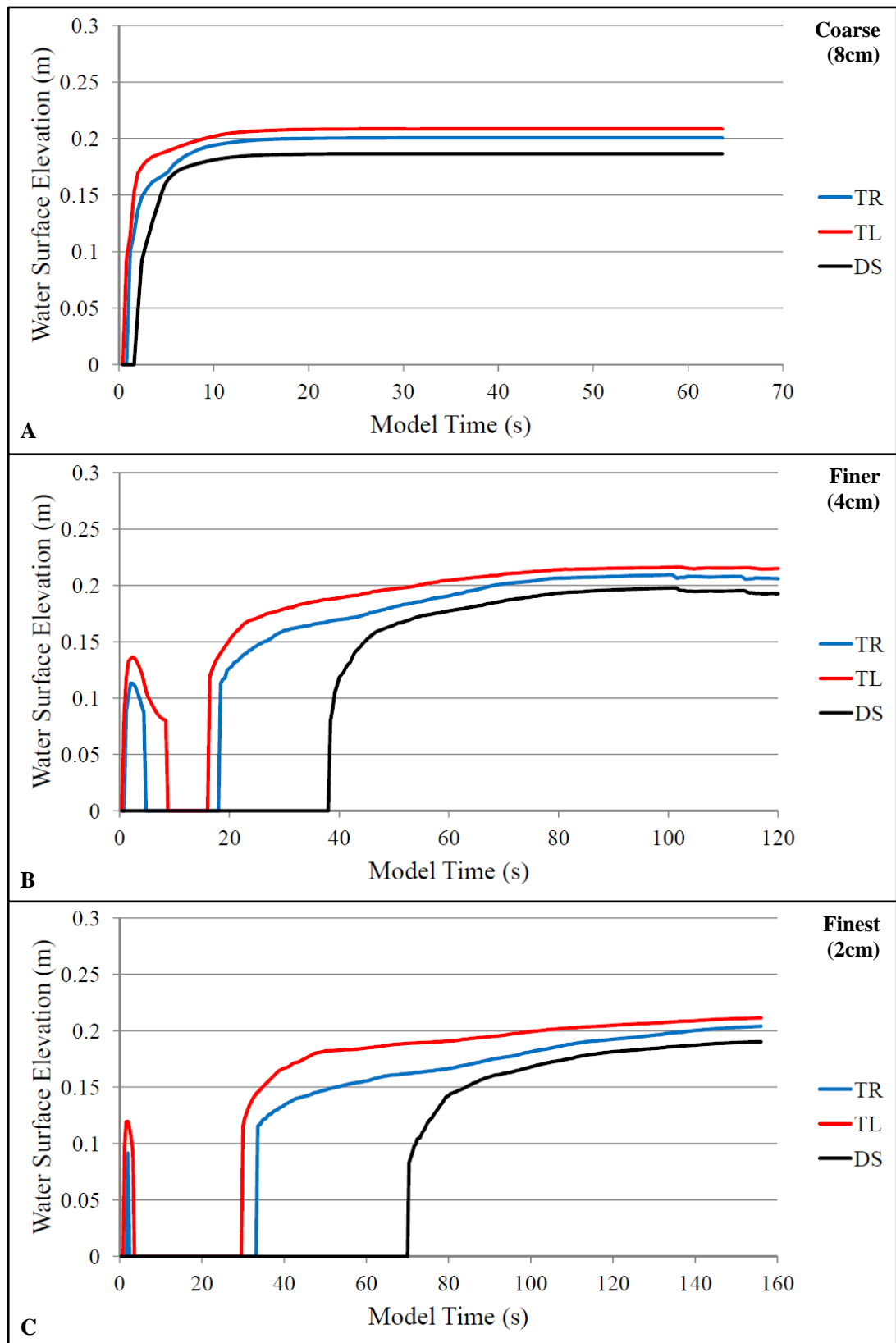


Figure 5.3: Graphs showing the change in water surface elevation through time for three locations in Confluence E: in the true left (TL), true right (TR) and downstream (DS) channels. Plots (a), (b) and (c) show the results from the 2cm, 4cm and 8cm grid resolution simulations respectively.

Variable	Median GCI12 (%)	Median GCI23 (%)
Pressure	10.8	23.5
U Velocity	6.6	8.2
V Velocity	8.8	22.5
W Velocity	44.4	92.2
EP	62.6	183.4
TKE	46.2	119.3
WSE	1.0	2.3

Table 5.2: Calculated Grid Convergence Index (GCI) values for the medium (GCI23) and finest (GCI12) resolution grids at Confluence E. TKE is turbulent kinetic energy ( $k$ ), EP is the dissipation rate ( $\epsilon$ ) and WSE is the water surface elevation.

In discussing the values in Table 5.2, it should be acknowledged that in gravel-bed rivers, the errors values may be misleading and unduly pessimistic. This is because irregular topography will mean a change in grid resolution alters the DEM and thus the topographic forcing of the flow. Nevertheless, it can still be used to indicate where there is greater uncertainty in the output parameters.

From Table 5.2, grid resolution errors are lower for the finest resolution grid, in many cases by approximately half. For both grids, the smallest errors are seen in water surface elevation, with downstream ( $u$ ) velocity, cross-stream ( $v$ ) velocity and pressure the next best performing. Meanwhile, the errors in vertical velocity, turbulent kinetic energy and dissipation rate are much more significant, at 45-65% for the finest grid. These results are not surprising, as the changes in topography would be expected to have a greater relative effect on the vertical velocity (where values tend to be lower) and the turbulence model parameters (which are derived from other variables). Nevertheless, as a result of the shallow flows at upland confluences and the higher GCI values for vertical velocity, the decision was taken to use preferentially finer grid spacing in the  $z$ -direction (as shown in Table 5.1).

## 5.5 Model Calibration and Sensitivity Tests

In Section 5.3.2, the strategy for validation of the HOL model was set out. Before conducting the validation tests, however, it was necessary to calibrate the model and determine the sensitivity of the HOL model to parameters such as wall roughness and the method of representing the bed topography. For this purpose, the flow and water surface elevation data from the true left tributary at the upper Moor House confluence

were used to test the variability in model results. The topography from the inlet cross-section was represented as a flume, with the same topographic cross-section repeated for each cell downstream. In this section, results are presented from six different test runs, with the most appropriate model setup determined from these experiments.

When testing using the model inlets, the field data will be affected by the flow and topography upstream and downstream of the cross-section in a way that cannot realistically be represented in the model. However, the results should provide an indication of whether the model is capable of replicating the water surface elevation and velocity distributions seen in a natural river channel. Ideally, the inlet would be represented by a cross-section of infinite length in the downstream direction. As this is not feasible, however, part of the testing in this section will assess the impact of varying the length of the domain in the downstream direction.

In testing the model in this way, it is necessary to determine a cross-section from the model domain to compare with the field data. Rather than picking an arbitrary location, it was decided to use the modelled water surface slope to select the most appropriate model cross-section. As Figure 5.4 shows, the water surface slope from one cell to the next is particularly affected by the presence of the inlet and outlet, but in the middle tends to stabilise. In this central section, where the elevation change from one cell to the next is at a minimum, is considered to be the most appropriate model cross-section for comparison purposes.

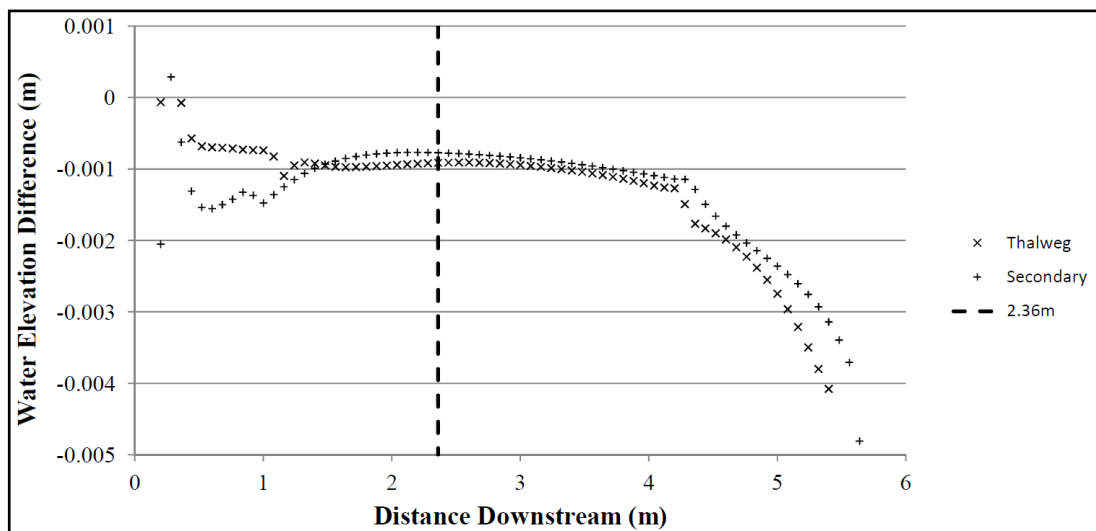


Figure 5.4: An example of the position of the model cross-section used for comparison with the field data. The cross-section is selected by finding where the difference in water elevation between consecutive downstream cells (taken from the sum of the disparities at two separate locations) is closest to 0. The first and last 20 cells are excluded due to the impact of the inlet and outlet.



Therefore, for each simulation of the confluence inlets, the downstream variations in water surface slope were plotted for two locations. One of these locations was the thalweg, while the secondary location was the deepest point in the other half of the channel cross-section. The first and last 20 cells were excluded to remove the effect of the inlet and outlet, with cross-section chosen at the point where the combined slope for the two datasets reached a minimum. The dashed line in Figure 5.4 shows the cross-section selected on this basis.

Table 5.3 shows the details of each of the test runs for the true left tributary of the upper Moor House confluence. The three parameters that were varied were the domain length, roughness height and the method used to represent the bed topography.

Simulation	Domain Length	Treatment of the Bed Topography
TestRun001	6m	Topography rounded to the nearest whole cell, roughness height as determined in Section 4.4.1.
TestRun002	6m	Topography rounded to the nearest whole cell, roughness height half that in TestRun001.
TestRun003	6m	Sub-grid cell topography represented by volume porosity, roughness height as for TestRun001.
TestRun004	6m	Sub-grid cell topography represented by volume and face porosities, roughness height as for TestRun001.
TestRun005	12m	Sub-grid cell topography represented by volume porosity, roughness height as for TestRun001.
TestRun006	12m	Sub-grid cell topography represented by volume and face porosities, roughness height as for TestRun001.

Table 5.3: Details of the model sensitivity tests using the true left tributary of the upper confluence. The six model runs assess the sensitivity of the model to domain length, porosity treatment and roughness height.

### 5.5.1 Results from the Model Calibration and Sensitivity Tests

Figure 5.5 shows the measured water surface elevation for the cross-section along with each of the simulated water surfaces. The mean absolute and normalised differences between the modelled and measured water surfaces for each run are given in Table 5.4.

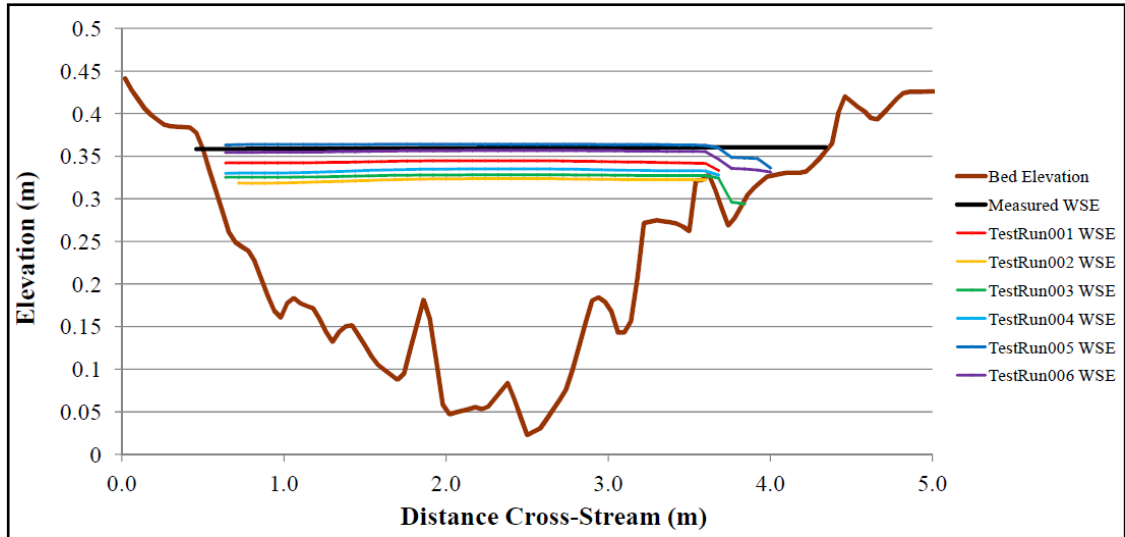


Figure 5.5: Modelled water surface elevations for the six test runs at the true left tributary of the upper confluence. The measured water surface is provided for comparison.

	Mean Difference (m)	Normalised Difference (%)
<b>TestRun001</b>	$0.0165 \pm 0.002$	9.5
<b>TestRun002</b>	$0.0386 \pm 0.006$	22.3
<b>TestRun003</b>	$0.0334 \pm 0.006$	19.3
<b>TestRun004</b>	$0.0265 \pm 0.002$	15.3
<b>TestRun005</b>	$0.0052 \pm 0.004$	3.0
<b>TestRun006</b>	$0.0062 \pm 0.007$	3.6

Table 5.4: Mean absolute and normalised difference values for the modelled water surface elevations at the true left tributary of the upper confluence. Normalised differences are given as a percentage of the mean measured water depth (0.173m).

The contour plots in Figure 5.6 present the measured and modelled velocity results, while a comparison of the vertical velocity profiles is given in Figure 5.7. In Figure 5.6, the field data are marked by filled circles which use the same colour axis as for the contour plots. For ease of reference between plots, where the model visibly (qualitatively) over-predicts the measured data, these circles are marked with a plus sign. For clear under-predictions by the model the circles have a minus sign inside.

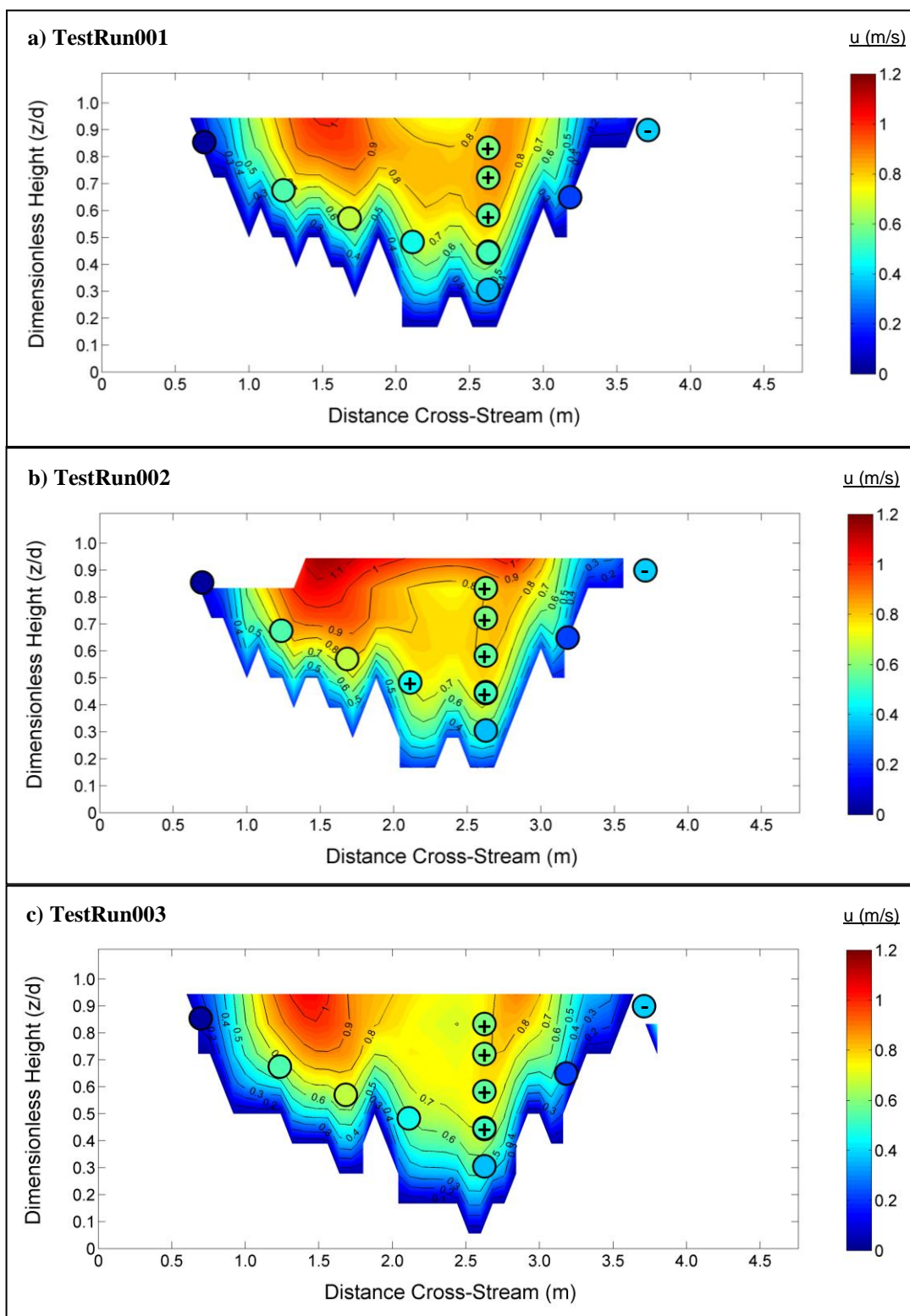


Figure 5.6: Contour plots of downstream flow velocity for each of the test runs at the upper confluence true left tributary. The field measurements are plotted in the circles, with the positions for the depth-averaged field data located at 40% of the depth (using DEM bed surface and measured water level). The velocity profile data are plotted using distance from the measured water surface. Locations where the model over-predicts the field data are marked with '+' signs, whilst under-prediction is signified by '-' signs. Figure continues on the next page.

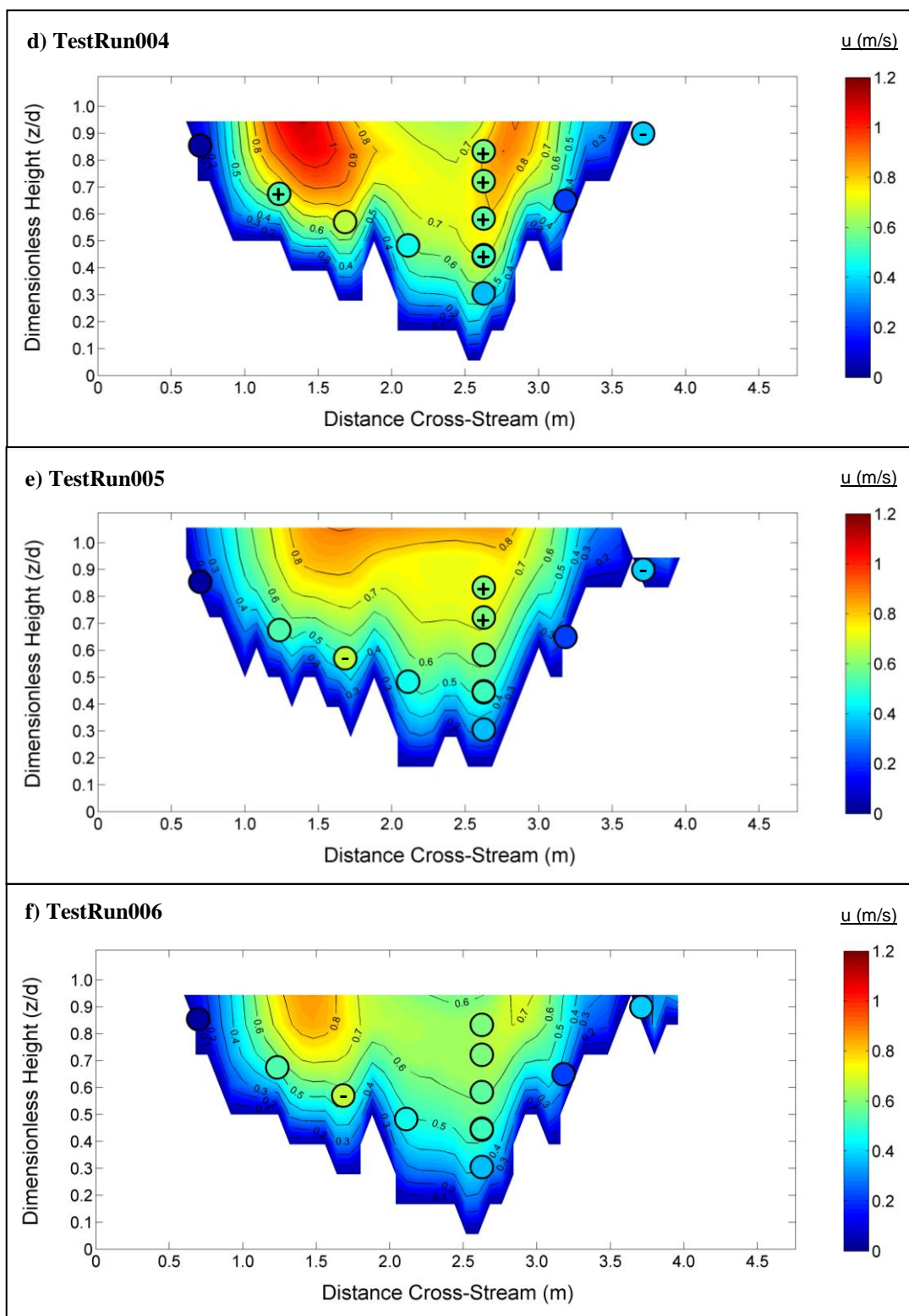


Figure 5.6 (continued): Contour plots of downstream flow velocity for test runs 004 to 006.

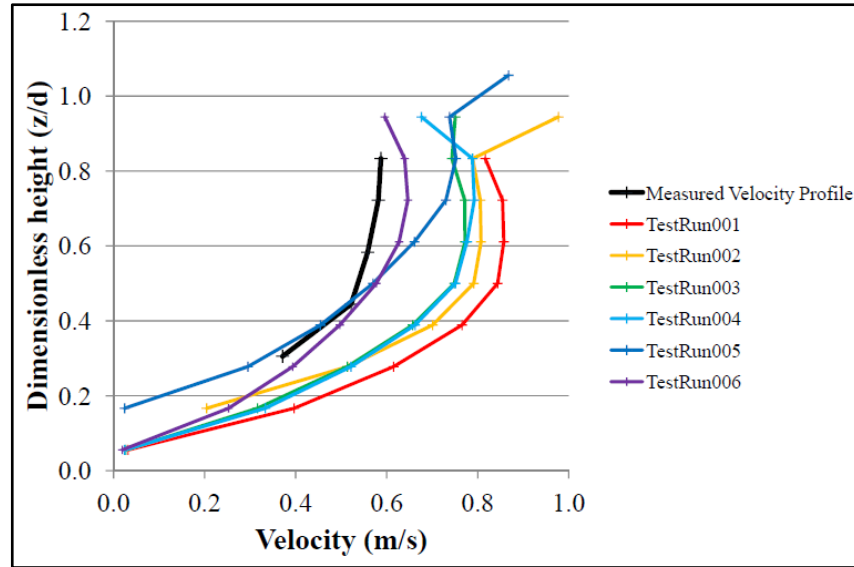


Figure 5.7: Velocity profiles for each of the upper confluence true left tributary test runs. Model data are taken from the centres of cells that are at least partially filled with water (which in one case results in a  $z/d$  value greater than 1).

Figures 5.6 and 5.7 show that TestRun005 and TestRun006 give much closer representations of the measured field data, a finding which is supported by the mean absolute differences given in Table 5.5.

	Mean Difference (m/s)
<b>TestRun001</b>	$0.166 \pm 0.124$
<b>TestRun002</b>	$0.207 \pm 0.088$
<b>TestRun003</b>	$0.172 \pm 0.076$
<b>TestRun004</b>	$0.187 \pm 0.079$
<b>TestRun005</b>	$0.084 \pm 0.065$
<b>TestRun006</b>	$0.073 \pm 0.063$

Table 5.5: Mean absolute differences for the modelled flow velocities in the true left tributary of the upper confluence.

### 5.5.2 Discussion of Model Calibration and Sensitivity Testing

The results presented in this section demonstrate how important the treatment of the water surface is to the prediction of flow velocities in natural channels. A comparison of Figures 5.5 and 5.7 shows that even minor variations in the modelled water surface will have a large impact on the predicted flow velocity profiles.

The greatest impact on the modelled water surface elevation and flow velocity is the length of the domain. This can be seen clearly in Figures 5.5, 5.6 and 5.7, with runs 005 and 006 giving noticeably different water surface elevations and velocity profiles.

The mean absolute error (MAE) values in Tables 5.4 and 5.5 support this conclusion, with runs 005 and 006 matching the field data better than the rest. This is due to the effect of the downstream boundary on the flow field, with the impact reduced as the domain is lengthened. Changing the bed roughness (as shown by runs 001 and 002) has a small impact on both the predicted water surface and flow velocities, with the water slightly shallower and faster in the lower roughness case (as would be expected). However, the results in Tables 5.4 and 5.5 show the sensitivity to roughness to be much lower than for domain length. This agrees with the argument of Lane *et al.* (1999a) that roughness has a lesser impact on the flow in three-dimensional models than two-dimensional models. Meanwhile, the effect on the model output of using the nearest whole cell, the volume porosity only or the volume and face porosities is negligible.

For subsequent simulations, it was therefore decided to use domain lengths of 2.5-3 times the channel width (the equivalent of the 12m domain length in this section). Given the limited sensitivity of the model to roughness height, it was decided that for the Moor House confluences there was no need to deviate from the calculated roughness values from Section 4.4.1 (0.019m and 0.026m for the upper and lower confluences respectively). For representing the sub-grid scale topography, meanwhile, all four porosity parameters were used.

## 5.6 Model Validation Using Straight, Gravel-Bed Channels

Having determined the most appropriate model setup in the previous section, the first part of the model validation strategy (as set out in Section 5.3.2) was conducted using the inlets from the upper and lower Moor House confluences. In the case of the true right inlets at both confluences, the domain was set up to reflect the 45° flow angle relative to the cross-section. As a result, in this case the model output was compared to the measured cross-stream velocity, as well as the water surface elevations and downstream flow velocities used for the true left inlets. This section will address the upper and lower confluences separately (Sections 5.6.1 and 5.6.2 respectively), before discussing the results in Section 5.6.3. It should be noted, however, that in the previous section the model has effectively been calibrated using the true left inlet of the upper confluence. Therefore, although the results are provided for comparison in this section, they should not be considered an independent test of model performance.

## 5.6.1 Validation Using the Upper Confluence Inlets

Figure 5.8 shows the modelled and measured water surface elevations for the true left and true right inlets of the upper Moor House confluences.

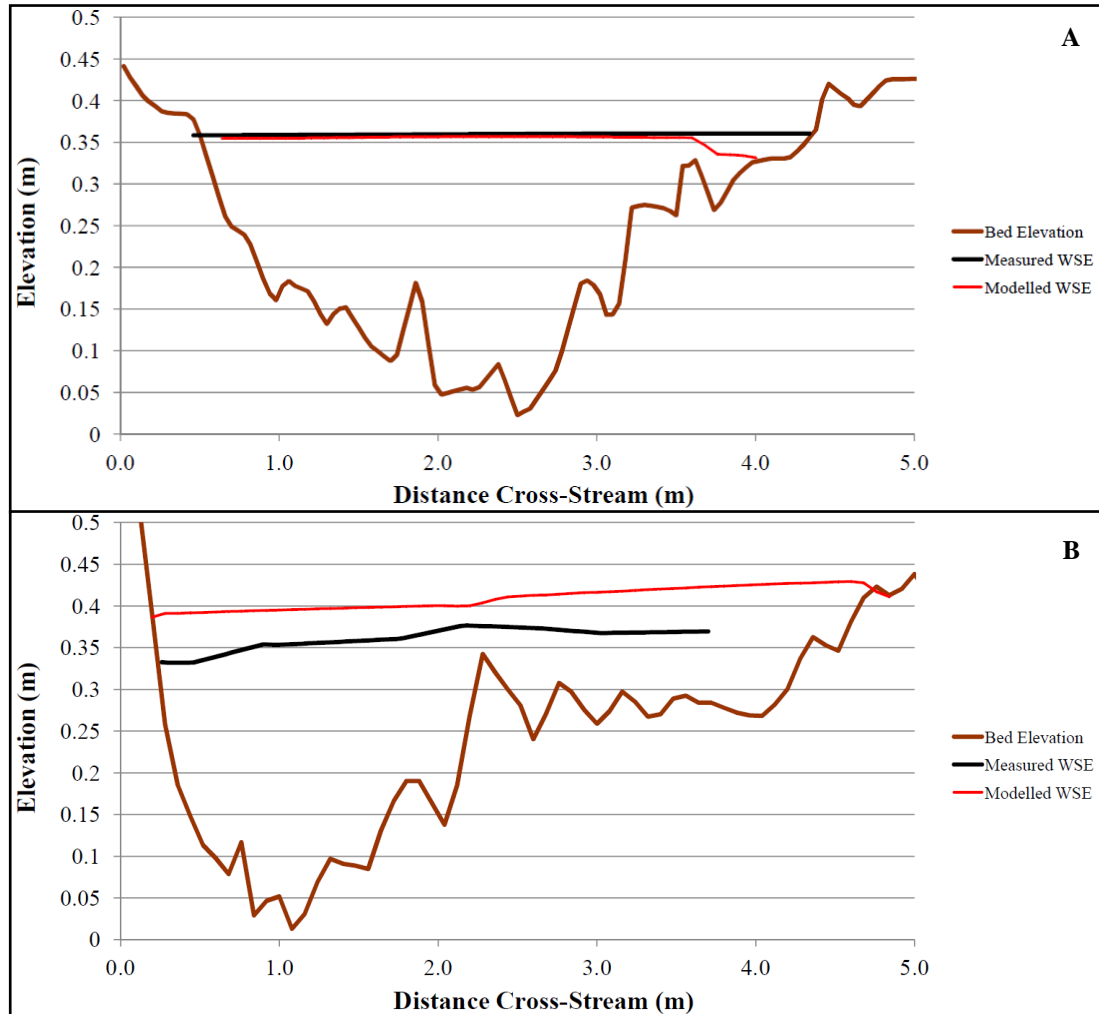


Figure 5.8: Modelled and measured water surface elevations for the inlets at the upper Moor House confluence. The true left tributary (mean difference of  $0.0062\text{m} \pm 0.007$ ) is plotted in (a) while the true right tributary (mean absolute difference of  $0.044\text{m} \pm 0.009$ ) is given in (b).

In Figure 5.8, the close match between modelled and measured water surface elevations from TestRun006 is clearly shown. For the true right inlet, however, the model over-predicts the measured water surface elevation by  $0.044\text{m} \pm 0.009$ .

A comparison between the modelled and measured flow velocities is given in Figure 5.9 for the inlet as a whole, whilst Figure 5.10 plots modelled and measured flows in the velocity profile data.



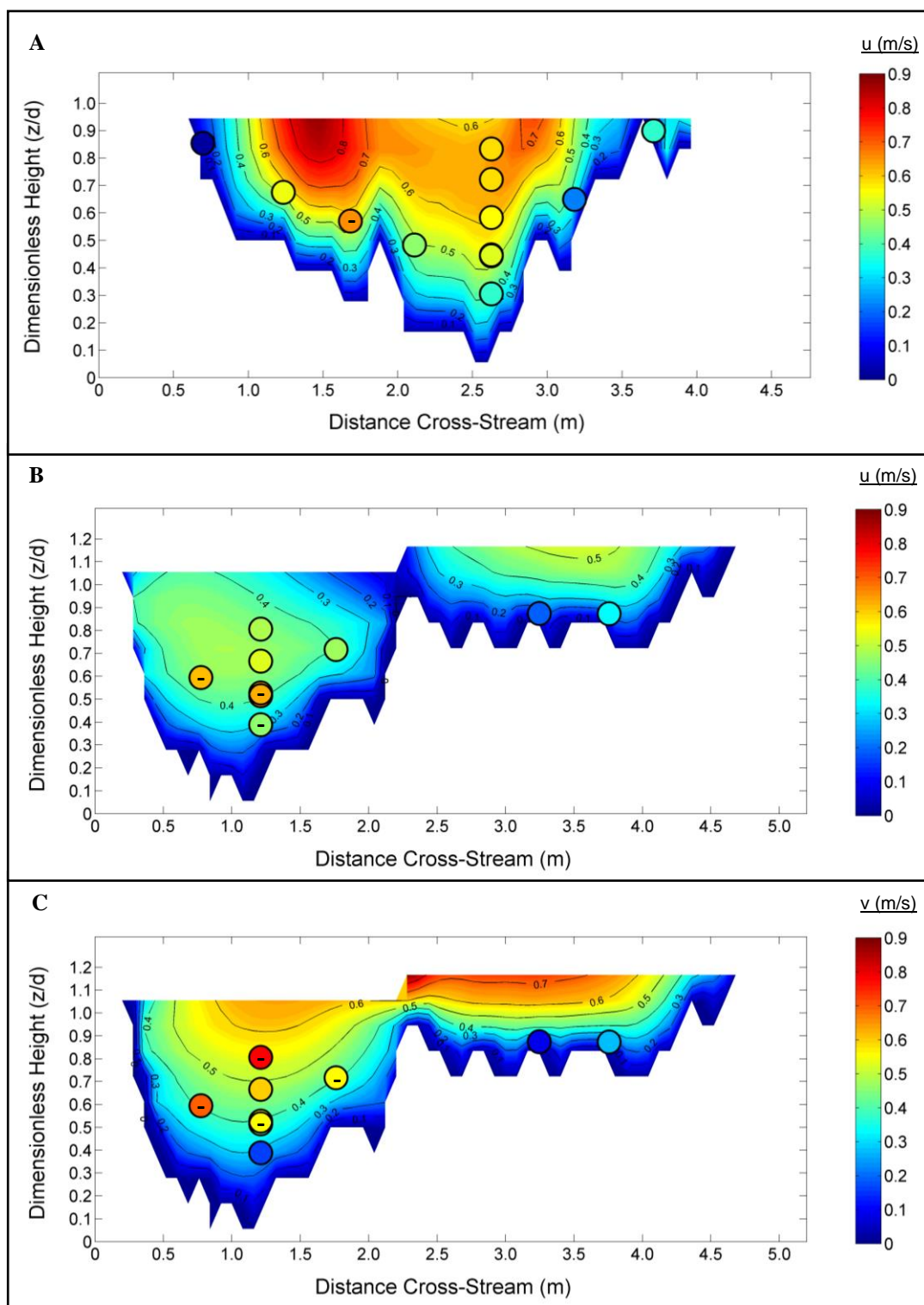


Figure 5.9: Contour plots showing the modelled and measured (filled circles) flow velocities for the upper confluence tributaries. Over- and under-predictions by the model are denoted by '+' and '-' signs. Downstream velocity for the true left tributary is in (a), with the downstream and cross-stream velocities for the true right tributary in (b) and (c) respectively. Mean absolute differences are  $0.073\text{m/s} \pm 0.063$  (a),  $0.161\text{m/s} \pm 0.088$  (b) and  $0.162\text{m/s} \pm 0.08$  (c), compared to mean velocities of  $0.4\text{m/s}$  (a),  $0.45\text{m/s}$  (b) and  $0.41\text{m/s}$  (c).



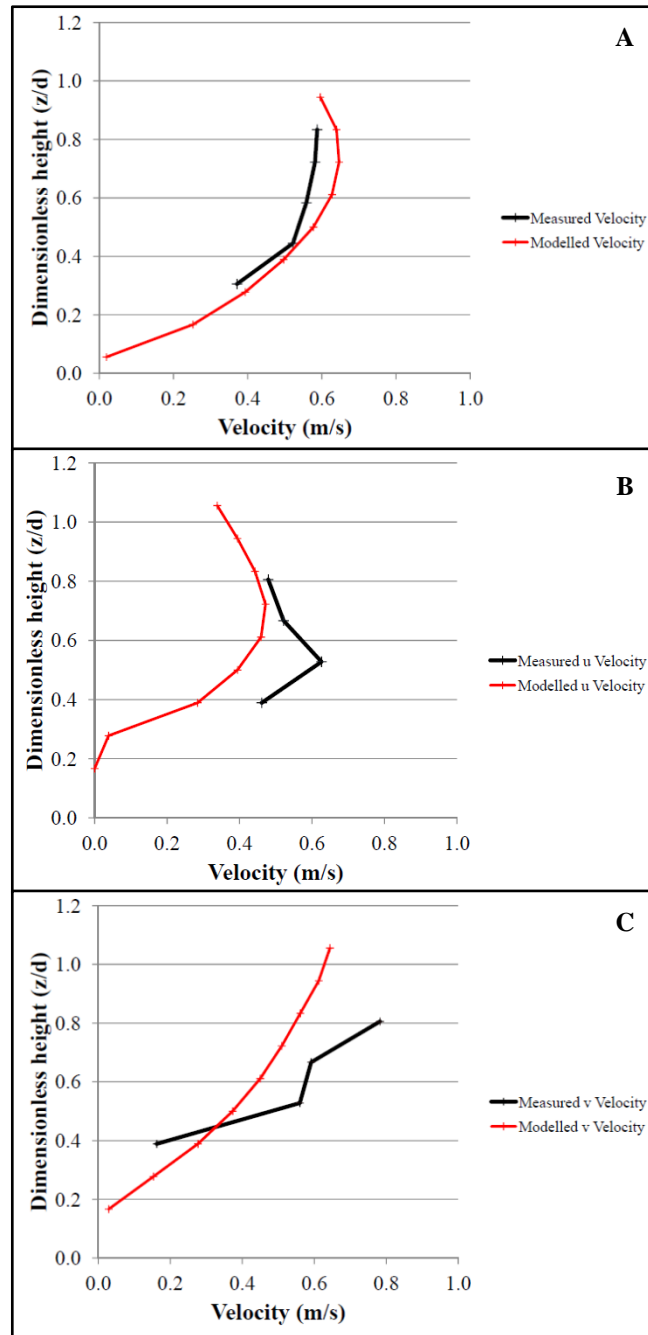


Figure 5.10: Modelled and measured velocity profiles for the upper confluence true left tributary (a) and true right tributary (b and c). Downstream velocity is plotted in (a) and (b), cross-stream velocity in (c).

As with the water surface elevations, the performance of the model for the true right inlet is not as good as that for the true left, largely due to the model predicting lower velocities in the thalweg (as identified by the minus signs in Figure 5.9). This is unsurprising, as an over-prediction of the water surface elevation requires a lower average flow velocity to satisfy mass conservation. The result is MAE values that are approximately double those for the true left inlet. Figure 5.10 reflects this for the

velocity profiles, with the shape of the profiles well represented, but a general tendency to underestimate the velocity. However, the good representation of the shape of the velocity profiles is particularly important, as it will allow reliable estimates of bed shear stress to be determined from the model outputs. This will enable conclusions to be drawn about the sediment dynamics, which will be investigated in detail in Chapters 6 and 7.

Although there are disparities in the modelled and measured flow velocities, it was explained in Section 5.3.3 that geolocation errors need to be accounted for when making comparisons. As such, Figure 5.11 compares the modelled and measured flow velocities, with error bars showing the range of velocity values from the adjacent cells (a 3x3 cell box around the measurement point). The regression lines, meanwhile, are calculated using the Reduced Major Axis (RMA) regression method (Kermack and Haldane, 1950; Sokal and Rohlf, 1995), which is considered a more appropriate method when there are known errors in the measured value. For this research, the RMA regression lines were determined using the software of Bohonak and van der Linde (2004).

The Pearson's correlation ( $p_c$ ) values in Figure 5.11 show a generally strong agreement between the modelled and measured data, while the  $R^2$  values point to a good fit to the RMA regression lines. The regression lines themselves, however, reflect the tendency for the true right tributary flow velocities to be underestimated by the model. The error bars show that the actual disparities could be much lower, although the under-prediction of higher velocities in the true right tributary is still evident.

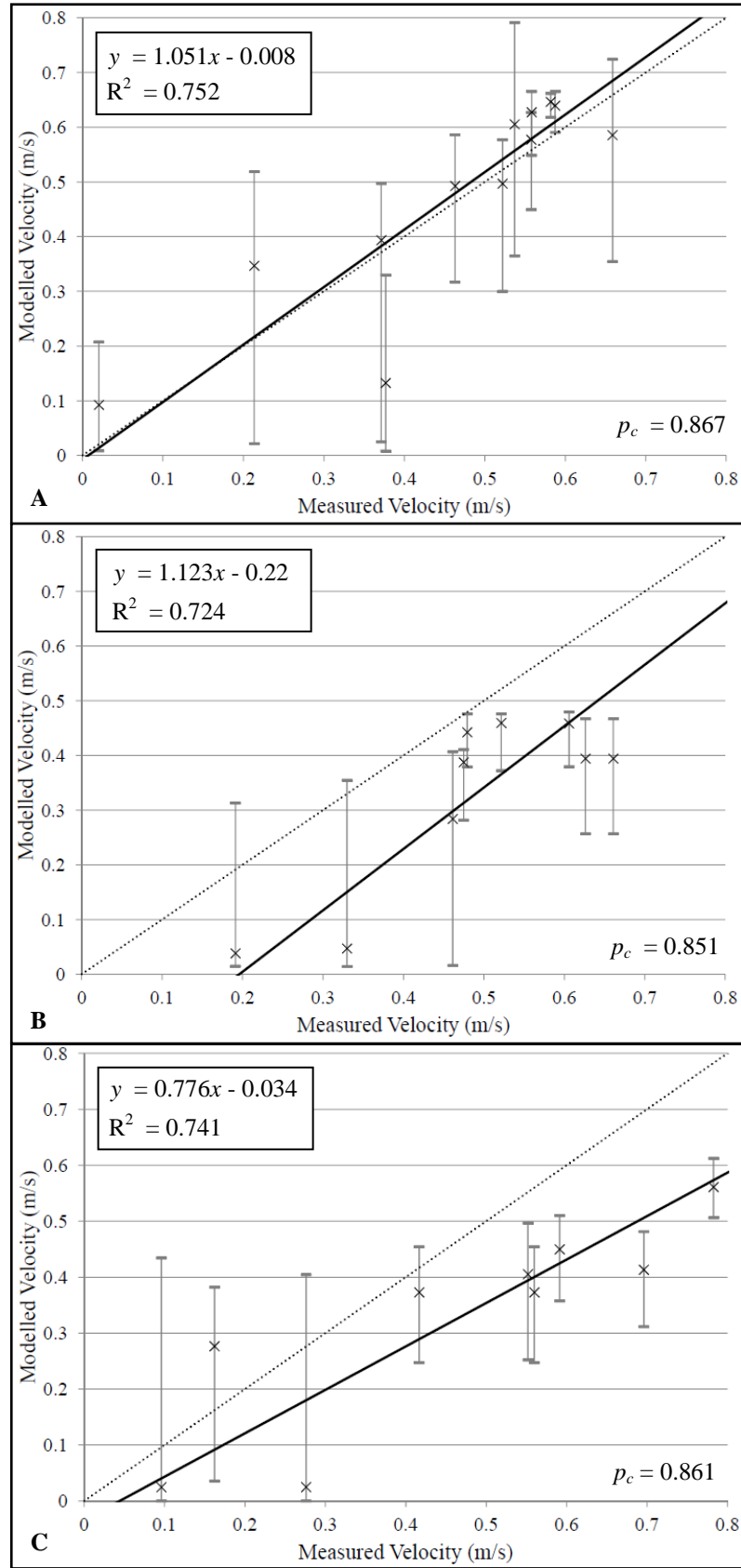


Figure 5.11: Modelled and measured velocities for the upper confluence tributaries, with error bars giving the potential geolocation errors. Pearson's correlation ( $p_c$ ) is marked on the graphs. Plots are for the true left tributary (a, downstream velocity) and true right tributary (downstream velocity in (b) and cross-stream velocity in (c)). The equation and  $R^2$  values from RMA regression are given in the boxes.

### 5.6.2 Validation Using the Lower Confluence Inlets

Figure 5.12 presents the measured and modelled water surface elevations for both inlets at the lower Moor House confluence.

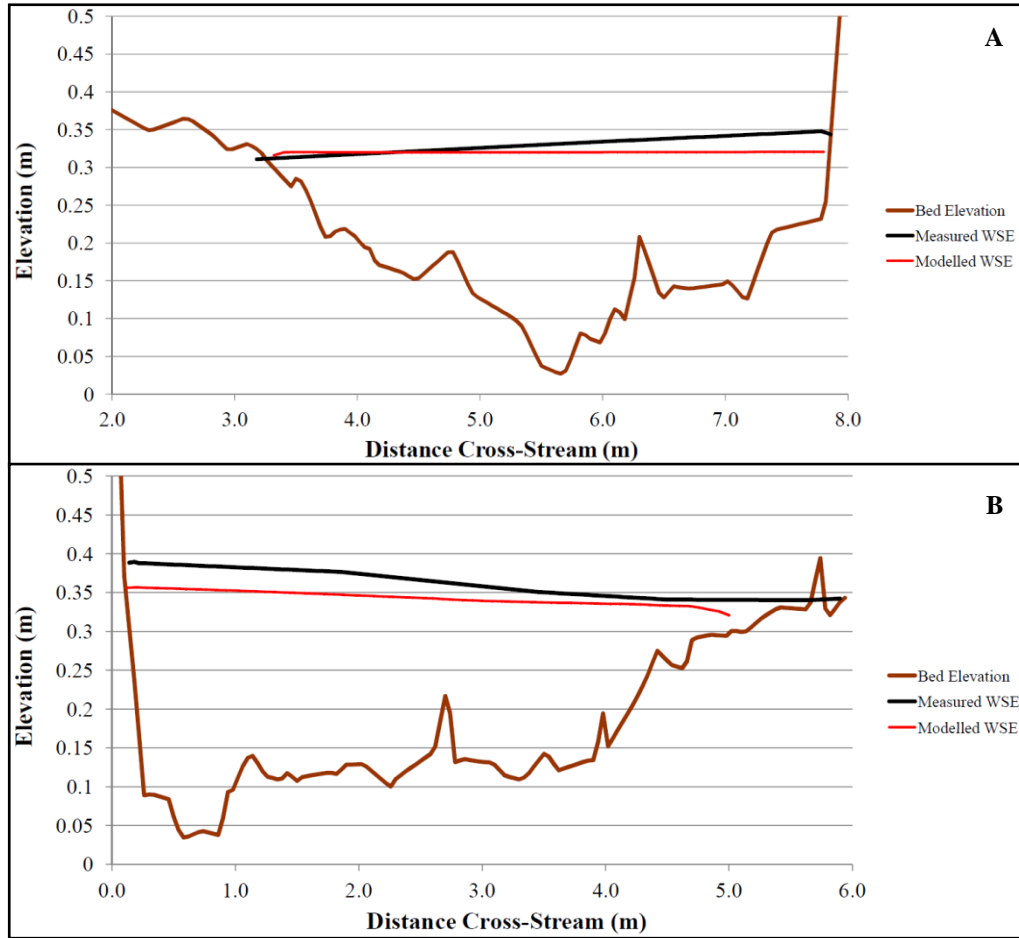


Figure 5.12: Modelled and measured water surface elevations for the inlets at the lower Moor House confluence. The true left tributary (mean absolute error of  $0.012\text{m} \pm 0.008$ ) is plotted in (a), while the true right tributary (mean absolute error of  $0.021\text{m} \pm 0.009$ ) is given in (b).

In Figure 5.12, the modelled water surface of the true left inlet is very close to that measured in the field, with a MAE of just  $0.012\text{m} \pm 0.008$ . The water surface elevation at the true right inlet, meanwhile, is slightly under-predicted by the model, although the MAE of  $0.023\text{m} \pm 0.009$  shows that this disparity is not particularly large.

Figures 5.13 and 5.14 show the modelled and measured flow velocities for the inlet cross-sections and velocity profiles. Figure 5.13 also highlights those locations where there are substantial disparities between modelled and measured values.

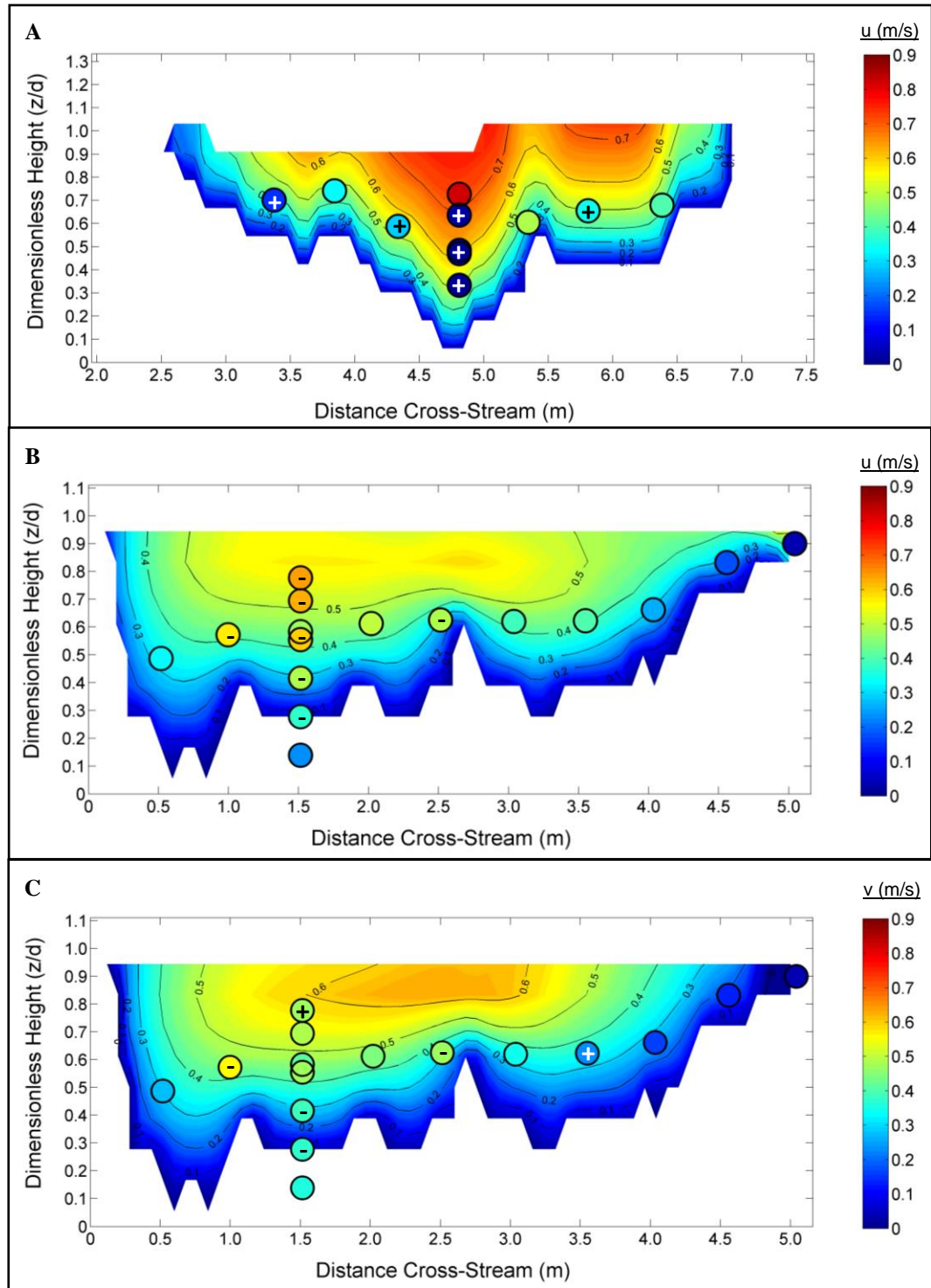


Figure 5.13: Contour plots showing the modelled and measured (filled circles) flow velocities for the lower confluence tributaries. The downstream velocity for the true left tributary is given in (a), with the downstream and cross-stream velocities for the true right tributary in (b) and (c) respectively. Model over-prediction is represented by a '+' and under-prediction by a '-'. Mean absolute errors are  $0.313\text{m/s} \pm 0.226$  (a),  $0.108\text{m/s} \pm 0.1$  (b) and  $0.111\text{m/s} \pm 0.099$  (c). Excluding the three anomalous field measurements in (a) reduces the mean difference to  $0.169\text{m/s} \pm 0.072$ . Mean flow velocities are  $0.29\text{m/s}$  (a),  $0.36\text{m/s}$  (b) and  $0.31\text{m/s}$  (c).

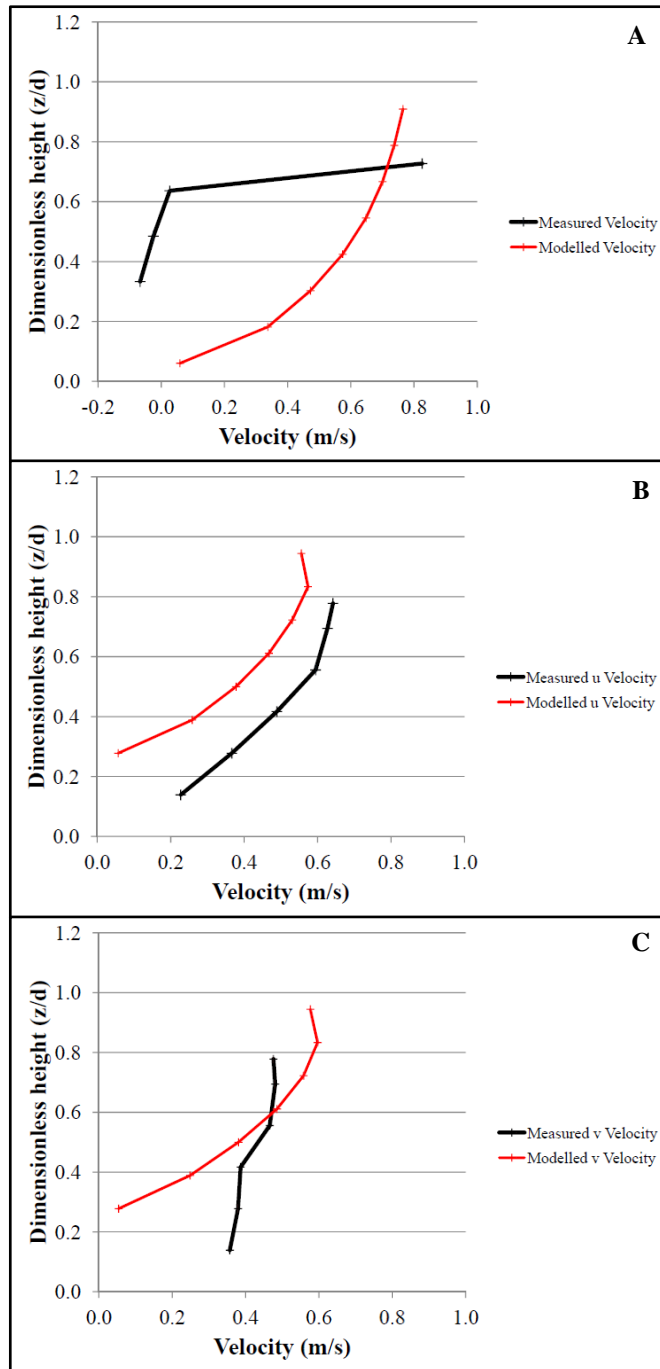


Figure 5.14: Modelled and measured velocity profiles for the lower confluence true left tributary (a) and true right tributary (b and c). Downstream velocity is plotted in (a) and (b), cross-stream velocity in (c).

The results from Figures 5.13 and 5.14 show that the major discrepancy between the recorded flow velocities and those predicted by the model is for the velocity profile at the true left inlet. Although the data point nearest the surface is not too different from the modelled velocities in the vicinity, the three points below it have substantially lower velocities than predicted by the model. This is due to the velocity profile being affected by the presence of a large boulder submerged just downstream of the cross-section,

which disrupts the flow in the field and explains the substantial differences between the modelled and measured velocities. Indeed, were these three anomalous points to be excluded from the calculations, the MAE would drop from  $0.314\text{m/s} \pm 0.226$  to  $0.169\text{m/s} \pm 0.072$ , which is much more in line with the values from the true right inlet.

The true right inlet flow velocities, whilst showing some differences between the modelled and measured values, are largely consistent between the two datasets. The velocity profiles in Figure 5.14 show a tendency to under-predict the downstream velocities by 0.1-0.2m/s, but this is not replicated in the cross-stream velocities. The results from the true right inlet in Figure 5.13 do, however, have one measured data point which is below the bed surface in the model. This is most likely due to the DEM not representing a small hollow in the bed (possibly between bed particles) and demonstrates the arguments made in Section 5.3.3 about the uncertainty associated with the geolocation of measured flow velocity data.

Figure 5.15 plots the modelled and measured flow velocities for the lower confluence inlets with the maximum and minimum values from the surrounding cells. For the true left inlet, the red circles highlight those measurements affected by the presence of a submerged boulder. As a result of these points, the Pearson's correlation and fit to the RMA regression line are poor, with the regression line demonstrating a substantial over-prediction by the model at low velocities. For the true right inlet, the correlation and  $R^2$  values are higher, although the agreement is not as strong as for the upper confluence. The error bars, however, show that geolocation errors may account for a significant proportion of the disparities.

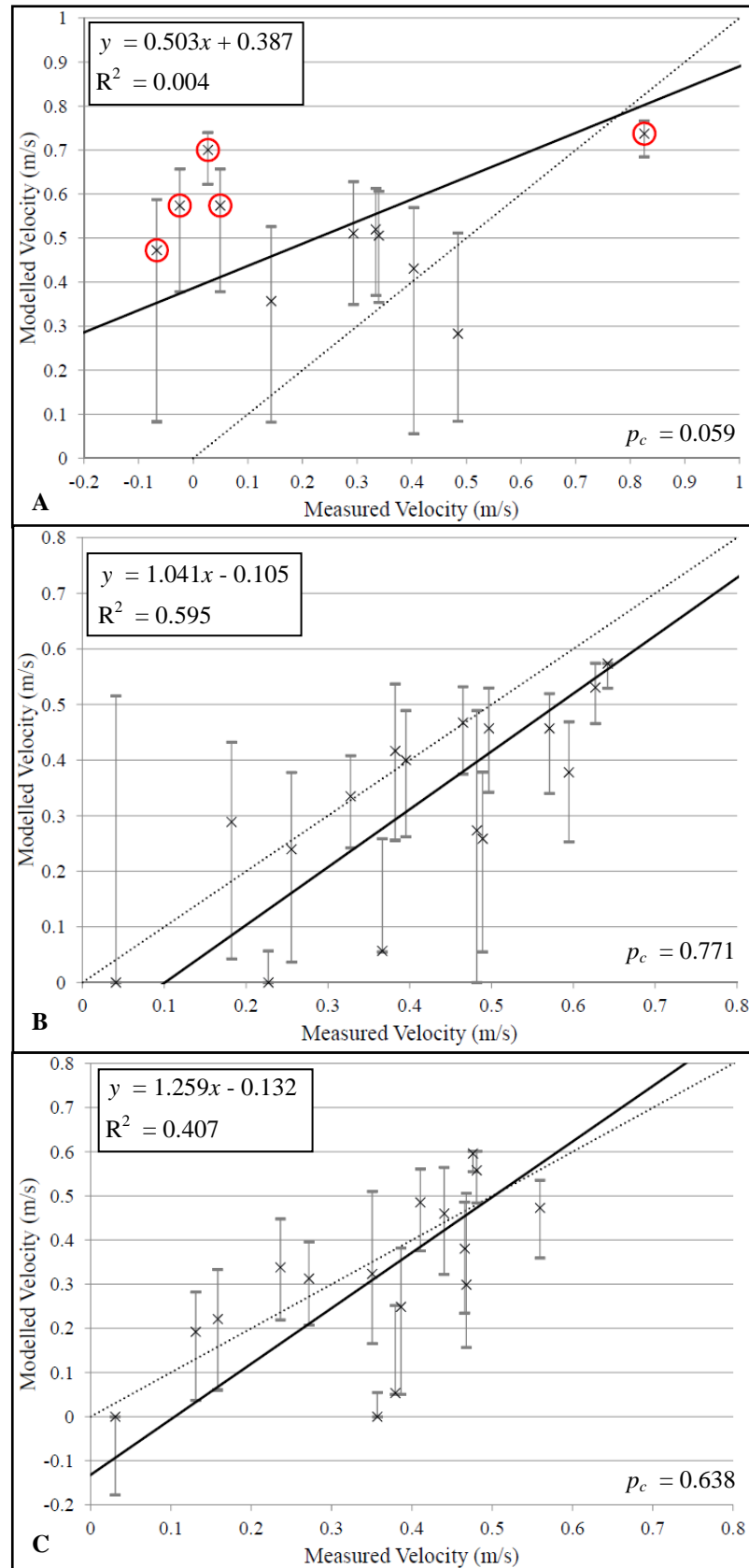


Figure 5.15: Modelled and measured velocities plotted for the lower confluence tributaries, with error bars showing the potential geolocation errors. The equation and  $R^2$  values for the RMA regression (solid black) lines are given in the boxes. Plots are for the lower confluence true left tributary (a, downstream velocity) and true right tributary (downstream velocity in (b) and cross-stream velocity in (c)).



### *5.6.3 Discussion of Model Validation in Straight, Gravel-Bed Channels*

In this section, the HOL model has been tested using the inlet cross-sections from the Moor House confluences. The upper true left inlet was included for comparison, but should essentially be treated as having been calibrated to the field data. Therefore, analysis of the validity of the model should refer mainly to the remaining three datasets.

The results from these three validation datasets are encouraging. Differences between the modelled and measured water surfaces are of the order of a few centimetres at most (equating to less than 10% of the flow depths for all tributaries except the upper true right inlet) and water levels are not consistently over- or under-predicted. Errors on this scale are of the same order of magnitude or less than the potential errors reported for the topographic data (Section 4.3.1), which suggests that the disparities between the field data and the model are just as likely to be due to uncertainty in the field data. In terms of flow velocities, the biggest anomaly between modelled and measured data is in the velocity profile at the lower true left inlet, although as explained above, this is skewed by anomalies in the measured velocity profile. Other disparities between the modelled and measured flow data are likely to be due to a combination of geolocation errors and the inability of the model to replicate the intricacies of the sub-grid scale topography (*e.g.* grain organisation).

Therefore, the results from this section provide evidence that the HOL model, within a CFD framework and in conjunction with the Mass Flux Scaling Algorithm (MFSA), can represent the flow and water surface elevation on idealised, straight channels. The next stage in validating the model is to test it using data from stable upland river confluences, as found at Moor House Nature Reserve.

## **5.7 Model Validation Using the Moor House Confluences**

Having demonstrated the good performance of the HOL model at representing flow through straight, gravel-bed channels, this section will determine how well the model can reproduce the water surface elevations and flow velocities from the river confluences of Moor House Nature Reserve.

### 5.7.1 Model Setup

It was found in Section 5.5 that areas in the vicinity of the inlet and outlet will have a flow field that is affected by the presence of these boundaries. Therefore, in setting up the model simulations, cells were added to the upstream and downstream ends of the model to give the domain run-in and run-out areas. However, the desire for long run-in and run-out sections to allow the flow field to resolve itself had to be balanced with the computational cost of adding a large number of extra cells. Because the results from the previous sections showed a much greater water surface slope towards the outlet (see Figure 5.4), more cells were added to the downstream end of the domain than the upstream end. Therefore, the run-in areas for both confluences were 6 cells (0.96m) long and the run-out areas were 34 cells (5.44m) long.

For the upper confluence, the roughness height was set to 0.018m, while for the lower confluence it was set to 0.029m. These are the values calculated from the velocity profile data in Section 4.4.1. The model inlets were set up with a uniform flow velocity across the channel cross-section (essentially as a discharge input) to ensure model stability. At the outlet, ideally the pressure distribution would be a known boundary condition. However, at present it is not realistically possible to specify the dynamic pressure distribution *a priori*. As such, the pressure was set to zero in all models to avoid any artificial effects caused by inaccurately specifying the pressure distribution. This will cause the flow field to become like a waterfall near the outlet, hence the need for a longer run-out area.

### 5.7.2 Results from Modelling the Upper Moor House Confluence

Figure 5.16 shows the measured and modelled water surface elevations for the upper confluence in three dimensions. The ability to produce these comparative diagrams is a consequence of using a free-surface model; rigid-lid approaches determine the water surface elevation *a priori*, usually as a flat, horizontal surface in studies of natural rivers. In addition, Figure 5.17a plots the modelled water extent to enable comparisons with the measured water outline, while Figure 5.17b shows the elevation differences between the measured and modelled water surfaces. In both Figures 5.16 and 5.17, three key features from the water surface are highlighted. These are the disparity in modelled and measured water elevations near the outlet (*i*), the good

representation of the complexity in the water surface where the true left tributary joins the main channel (ii) and the close agreement between water surface elevations and channel widths in the tributaries (iii).

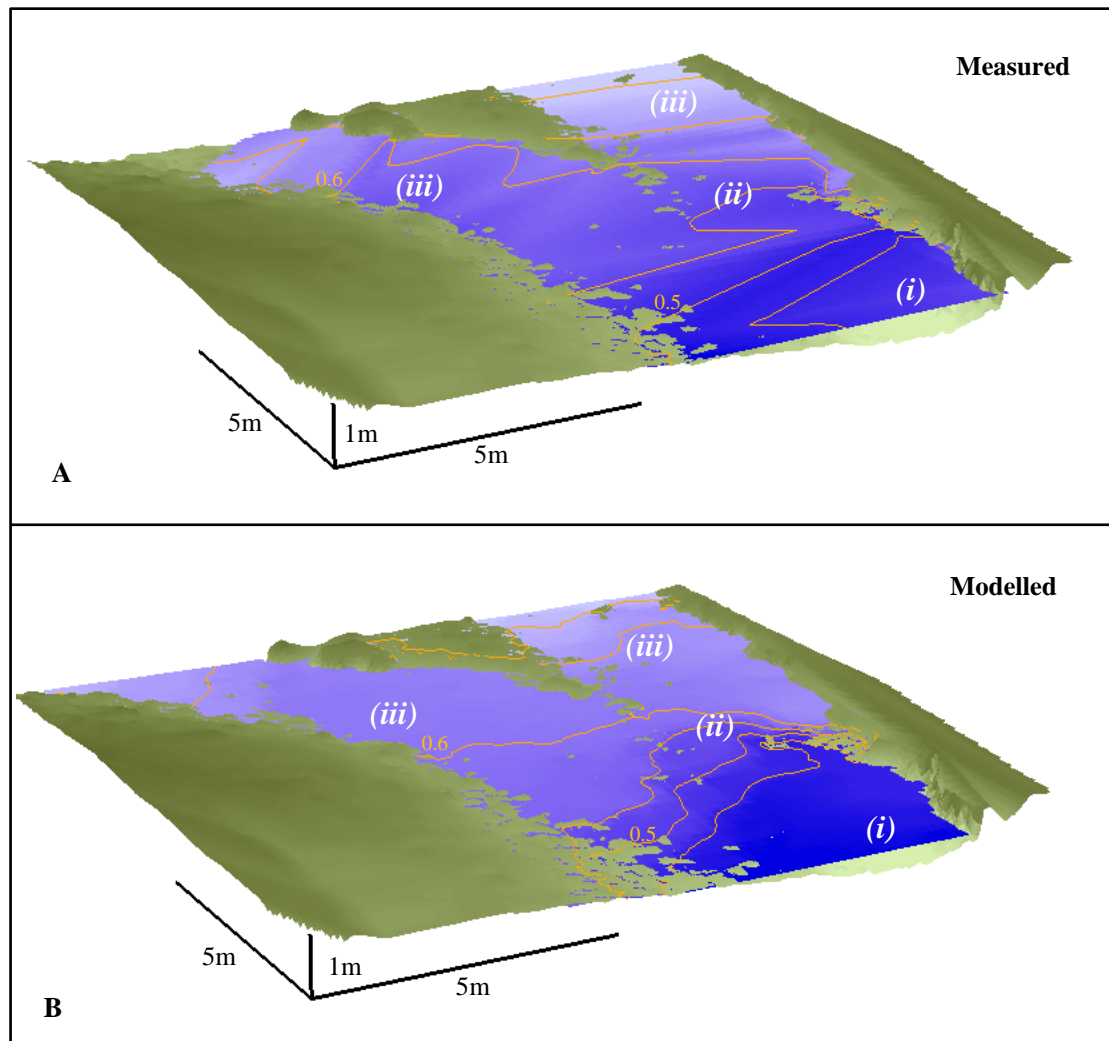


Figure 5.16: Three-dimensional view of modelled and measured water surface elevations for the upper Moor House confluence. Flow is from top left to bottom right of picture.

In Figure 5.17b an additional feature is marked, which is where the model predicts a higher water surface near the downstream corner (iv). This is linked to flow over a block of peat attached to this corner, which can be seen in Figure 4.1b to be a zone where the water surface fluctuates substantially. Part of this error is therefore likely to be due to the interpolation between water edge points not picking up these in-channel water surface undulations.

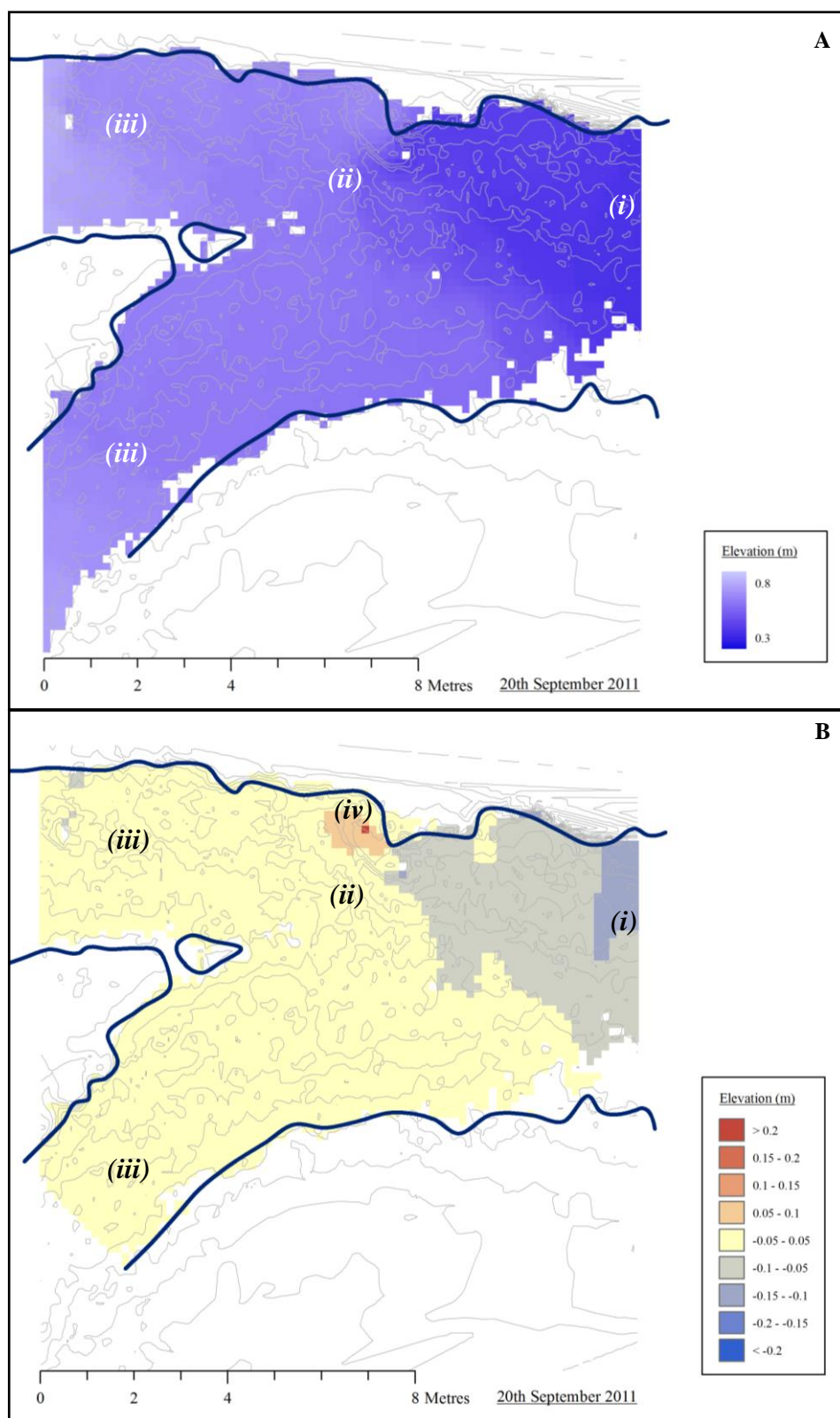


Figure 5.17: Modelled water surface extent compared to the measured water edge (navy blue line) from 20<sup>th</sup> September 2011 (a) and modelled minus measured water surface elevations (b) for the upper confluence.

Figures 5.16 and 5.17 show that the two datasets are qualitatively very similar, with the biggest disparity near to the outlet where the modelled water surface level

drops and the channel narrows (*i*). A plot of the modelled and measured water surface elevations in Figure 5.18 also shows a very close match between the two water surfaces, with the biggest differences for points within 2m of the outlet (marked in red). The MAE of the modelled data is low at  $0.031\text{m} \pm 0.028$  and there is a strong correlation (0.9) between the two sets of data.

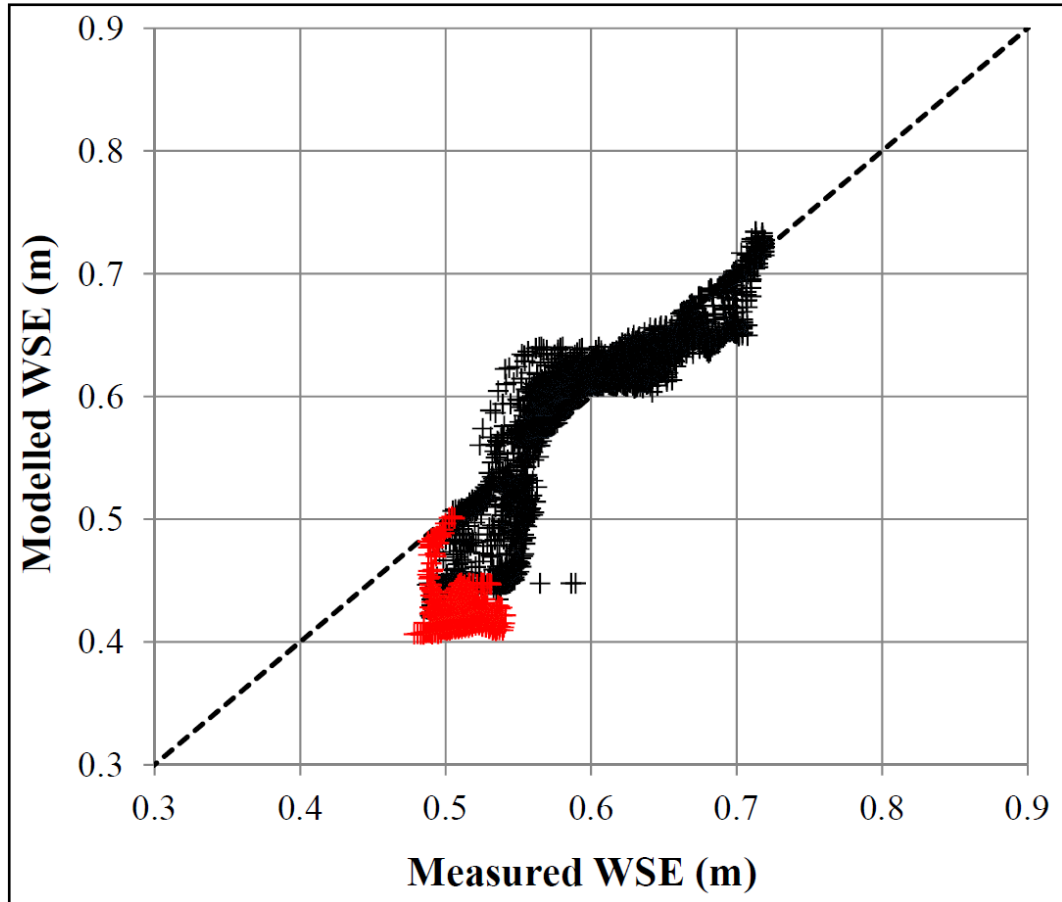


Figure 5.18: Comparison of modelled and measured water surface elevations at the upper confluence, with points within 2m of the outlet marked in red. Pearson's correlation and mean absolute difference are 0.896 ( $p$ -value  $< 0.0001$ ) and  $0.031\text{m} \pm 0.028$  respectively.

Figure 5.19 gives the plan view of the modelled depth-averaged velocities. This can be compared to the field data in Figure 4.16. Qualitatively there is a good match between the two datasets, with the flow acceleration at the exit of the true left tributary (*i*), the flow divergence around an obstacle near the true left inlet (*ii*) and the position of the zone of fastest flow in the main channel (*iii*) all replicated. In addition to this, the model replicates a zone of slower flow near the true left bank (*iv*) and the faster flow on the outside of the bend in the true right tributary (*v*). However, there are some disagreements with the measured data in Figure 4.16, most notably where the model

shows slower flow rather than flow recirculation in (iv) and where modelled flow directions in the centre of the main channel are too far towards the true left (vi).

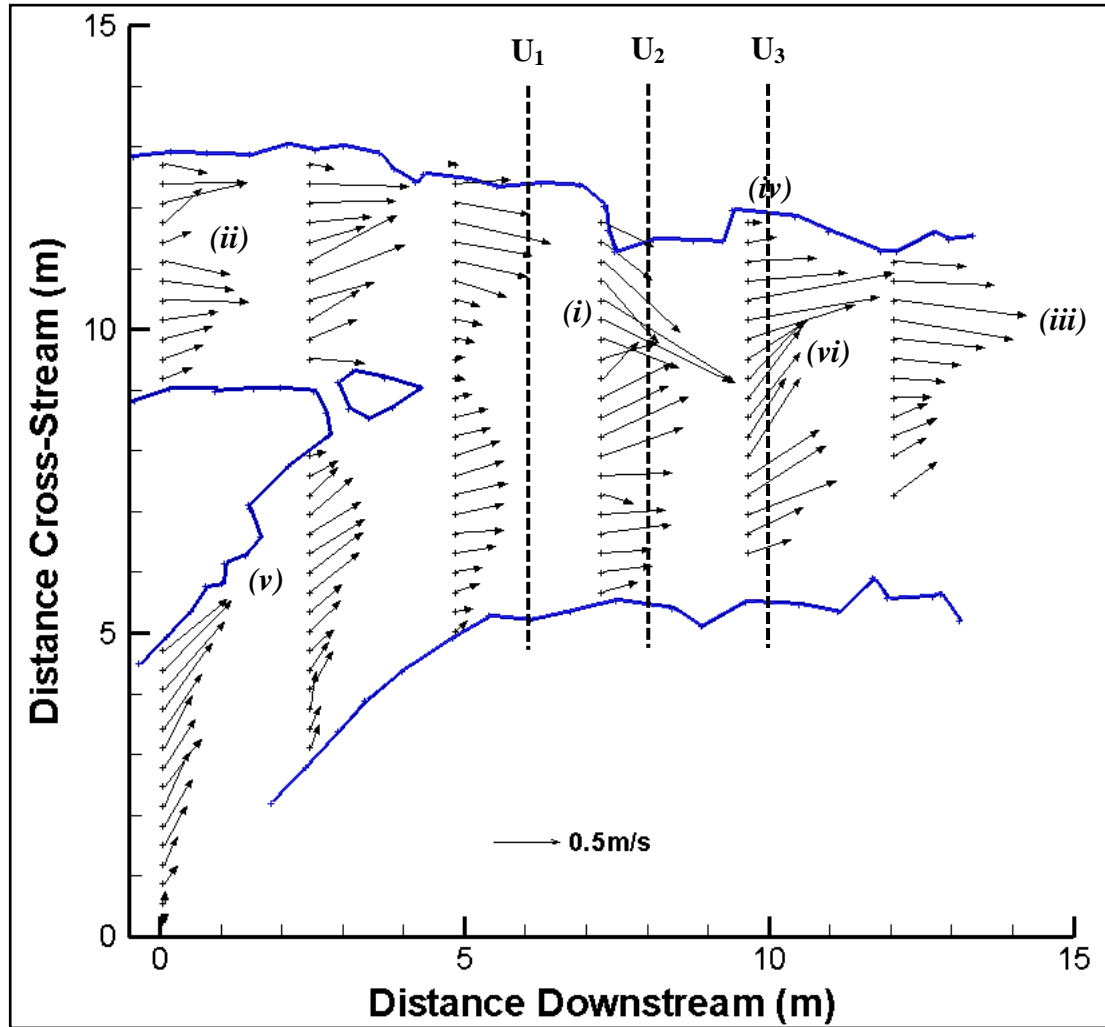


Figure 5.19: Depth-averaged modelled flow velocities for the upper confluence at Moor House Nature Reserve. Depth averages were calculated using the full vertical velocity profile, weighting the values where a cell was partially filled with water. The dashed lines give the names and locations of the cross-sections referred to later in the chapter.

In spite of this good qualitative agreement, the comparison between modelled and measured velocities in Figure 5.20 is poor. For the downstream velocity, the MAE of  $0.265\text{m/s} \pm 0.224$  is 54% of the mean downstream velocity ( $0.495\text{m/s}$ ), while for the cross-stream velocity, the MAE of  $0.144\text{m/s} \pm 0.167$  is 84% of the mean absolute cross-stream velocity ( $0.172\text{m/s}$ ). In both cases, the RMA regression lines are close to the 1:1 line, but the fit is poor (especially for the downstream velocity in Figure 5.20a). This is reflected in the Pearson's correlation values, with no correlation for the downstream velocity and a clear (but not strong) positive correlation for the cross-stream velocity. However, part of this poor agreement can be attributed to the geolocation errors

highlighted in Section 5.3.3, along with the model's inability to fully represent the detail of the sub-grid scale roughness and its effect on the near-bed flow. Figure 5.20 also shows, as error bars, the range of modelled values from the adjacent cells to the one used for comparison (as a 3x3x3 cell box). In most cases, this demonstrates considerable uncertainty and can explain a large part of the apparent disparity between the results from the qualitative and quantitative comparisons.

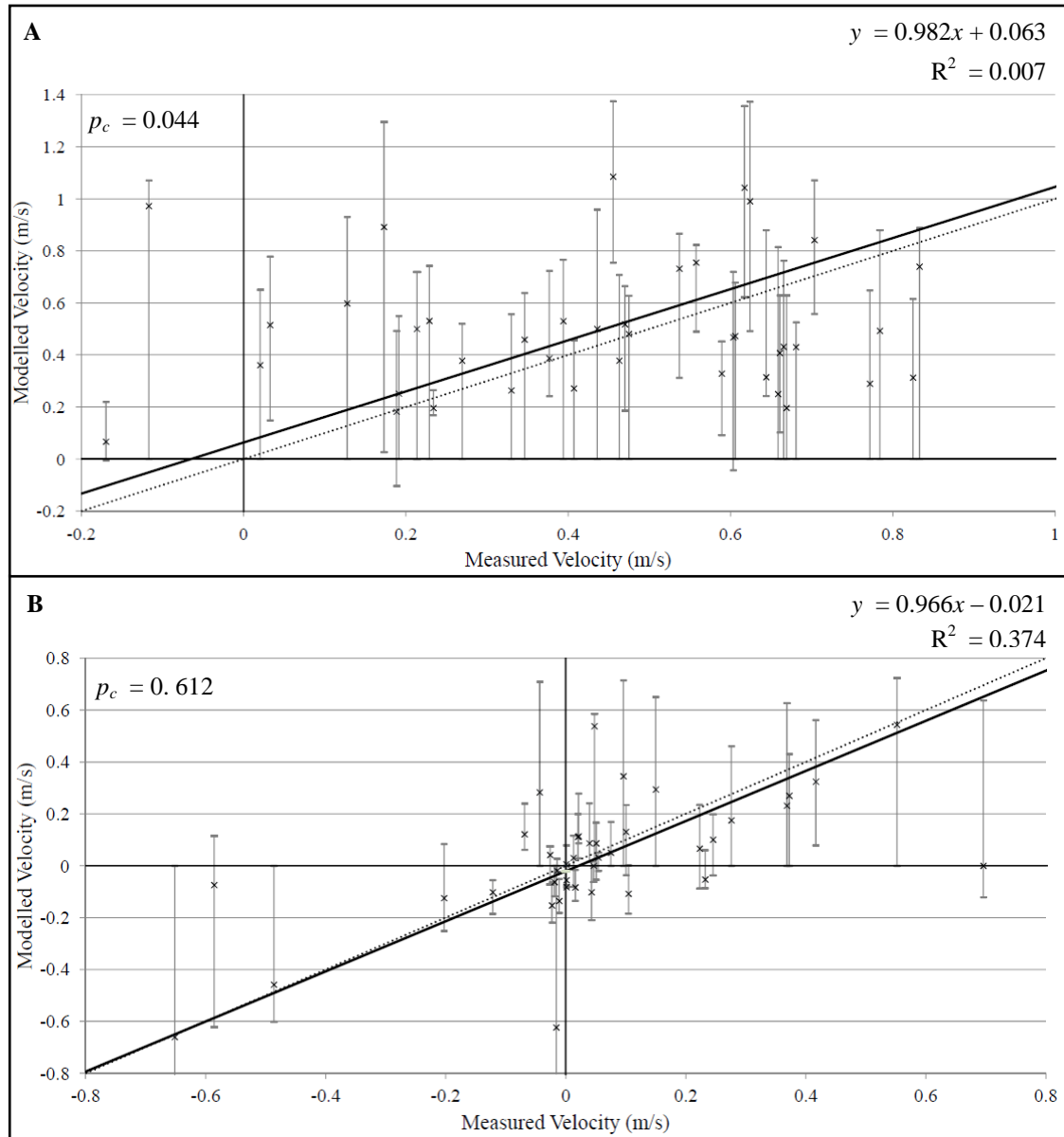


Figure 5.20: Modelled and measured downstream (a) and cross-stream (b) velocities for the upper confluence at Moor House Nature Reserve. RMA regression lines are given as solid black lines, while the dashed line is the 1:1 line and the error bars (as described in the text) are given in grey. Mean absolute differences are  $0.265\text{m/s} \pm 0.224$  and  $0.144\text{m/s} \pm 0.167$  for downstream and cross-stream velocity (compared to mean velocities of  $0.495\text{m/s}$  and  $0.172\text{m/s}$ ). The  $p$ -values for the Pearson's correlations are  $0.3937$  for the downstream velocity and  $<0.0001$  for cross-stream velocity.

## 5.7.3 Results from Modelling the Lower Moor House Confluence

For the lower confluence, Figure 5.21 shows the measured and modelled three-dimensional water surface elevation plots whilst the two-dimensional view and DEM of difference are plotted in Figure 5.22. Again, the use of the HOL model allows comparisons between the water surfaces in a way that would not be possible with a rigid-lid approach.

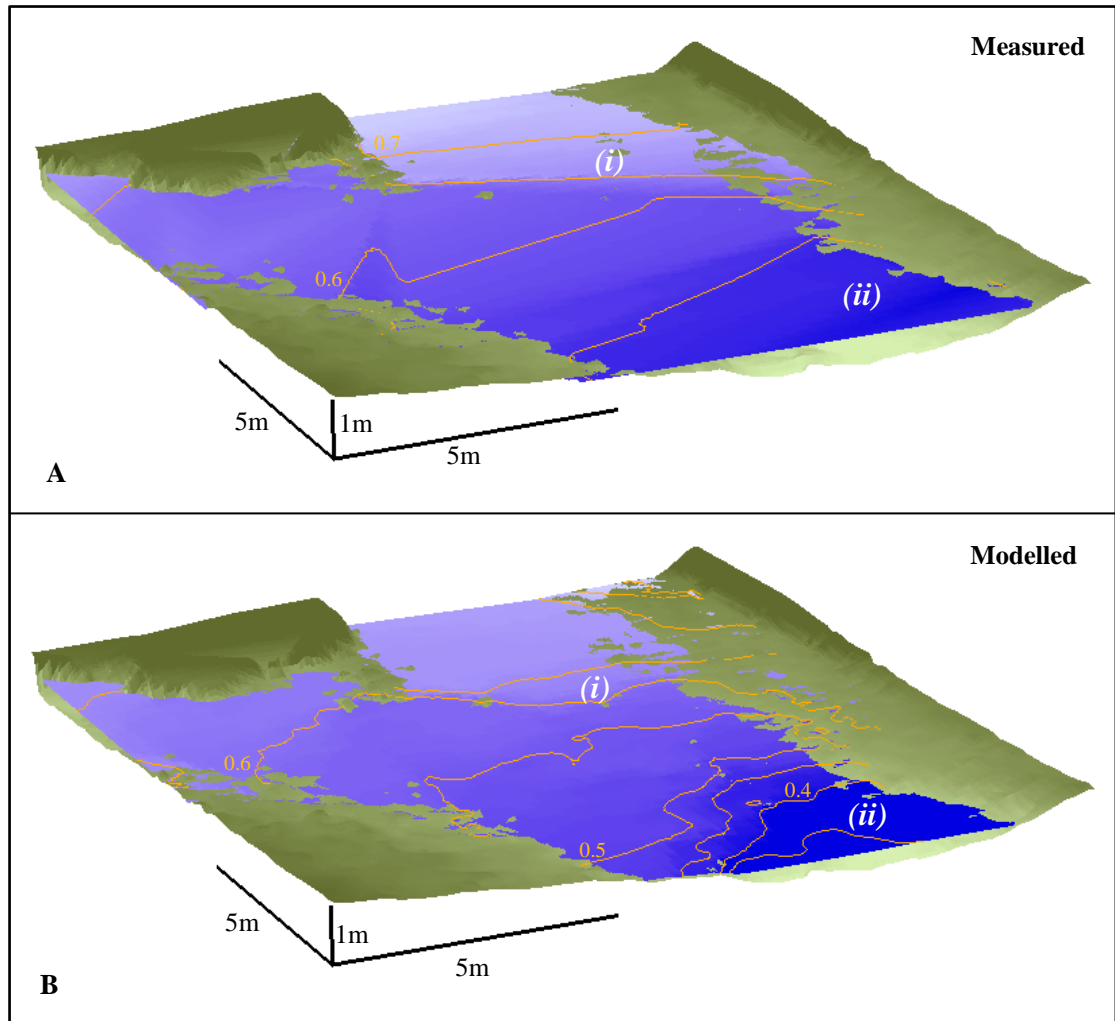


Figure 5.21: Three-dimensional view of modelled and measured water surface elevations for the lower Moor House confluence. Flow is from top left to bottom right of picture.

In both the modelled and measured plots in Figure 5.21, a distinct change in elevation can be seen at (i), where the water surface drops sharply as the true left tributary enters the main channel. This is located at the same point as the bed discordance highlighted previously in Figure 4.7. The main visible difference between the modelled and measured water surface elevations in Figure 5.21 is the lower



elevations near the confluence outlet (ii), which is more clearly shown in Figure 5.22b. However, Figure 5.22b also shows that this is the only major area of difference, with the rest of the confluence having a modelled water surface that is within 0.05m of the measured elevations, including the region around the true left tributary step (i).

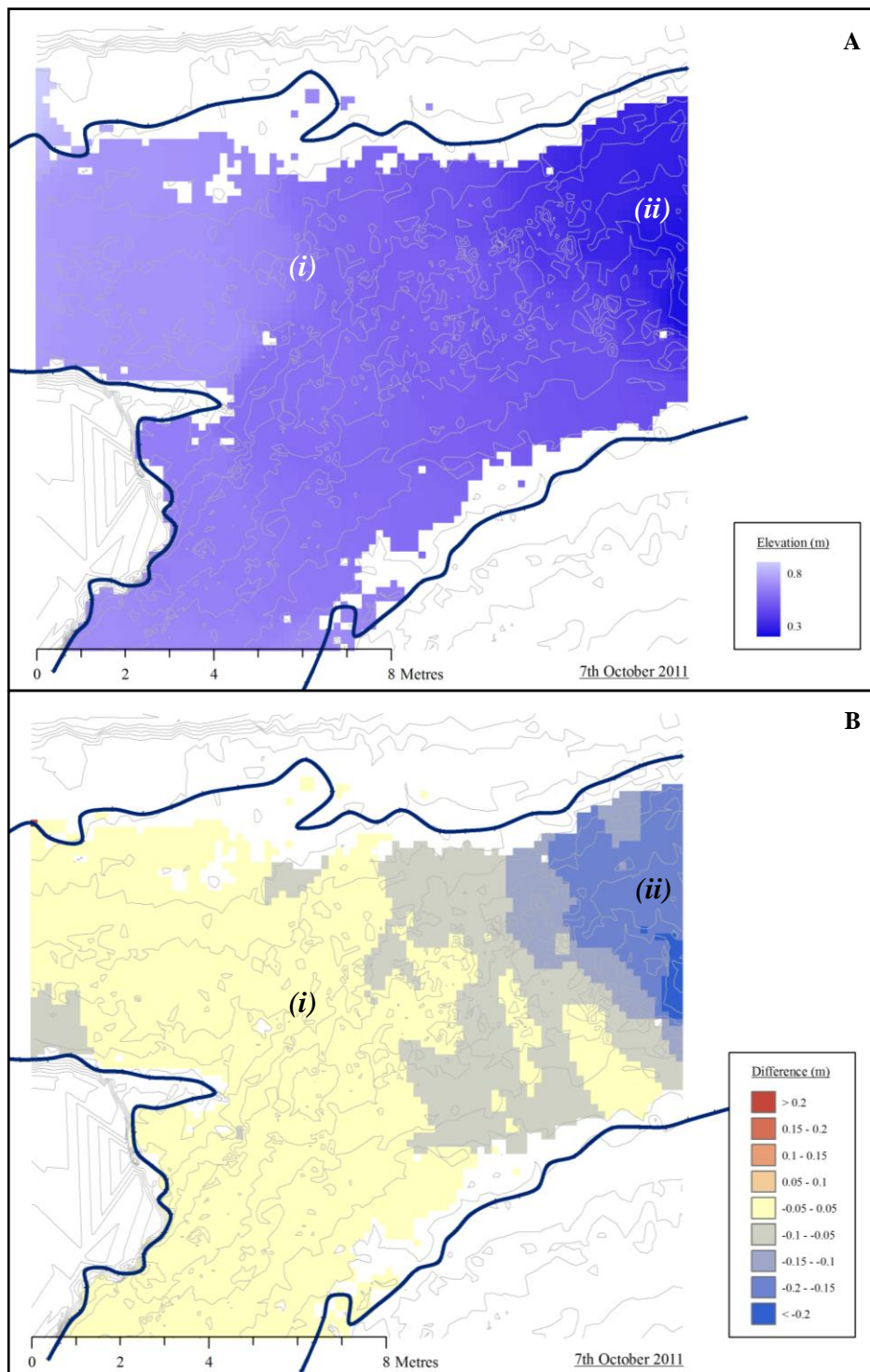


Figure 5.22: Two-dimensional plot of modelled water extent at the lower confluence compared to the measured water edge (navy blue line) from 7<sup>th</sup> October 2011 (a) and diagram showing the difference between modelled and measured water surface elevations (b).

A plot of the modelled and measured water surface elevations (Figure 5.23) shows that most disparities are under-predictions and highlights that the largest of these are located in the last 2m of the domain (marked in red). In spite of the effects of these points, the MAE value is still relatively low at  $0.051\text{m} \pm 0.044$ , whilst the Pearson's correlation is high at 0.93. Some of this error between modelled and measured water surfaces is likely to be due to the uncertainty in the measured water edge data and the interpolation between these points, although the effect of the outlet will still be the primary cause.

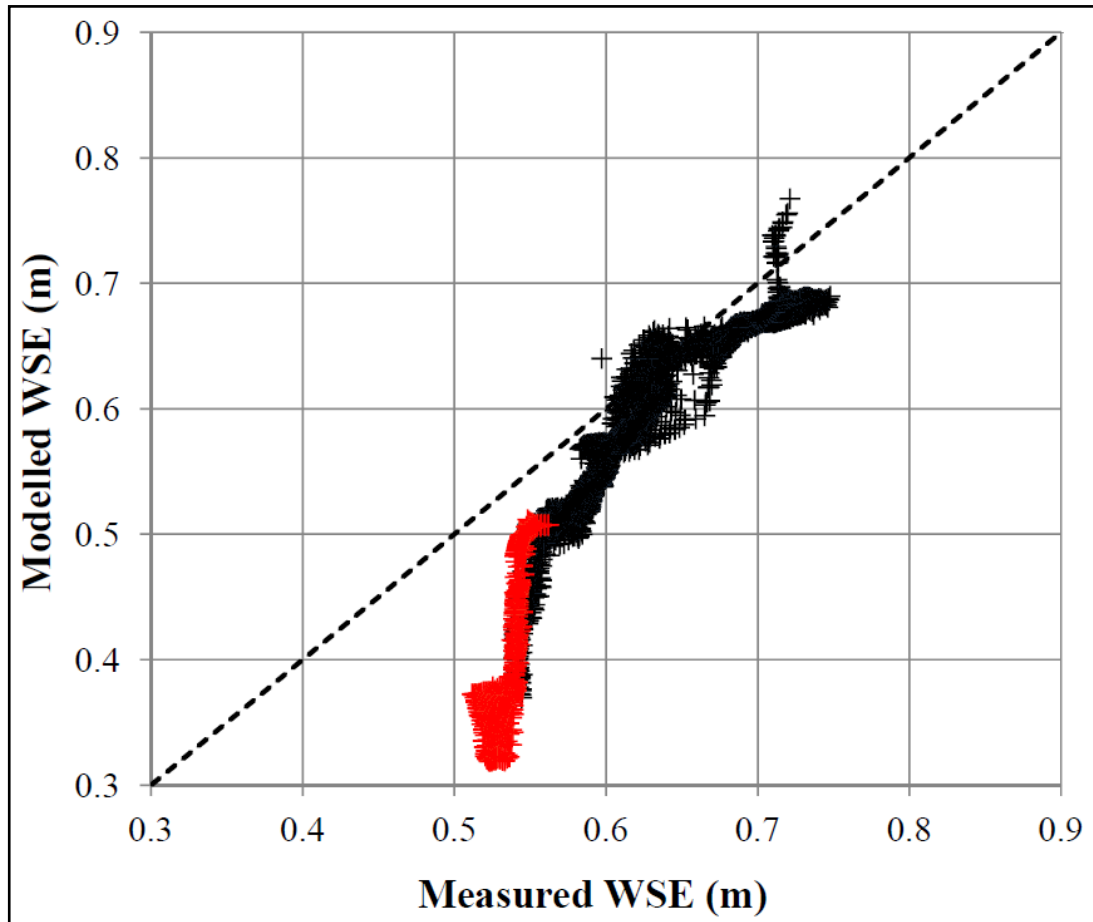


Figure 5.23: Modelled and measured water surface elevations for the lower confluence, with the points located within 2m of the outlet marked in red. The Pearson's correlation is calculated as 0.925 ( $p < 0.0001$ ), whilst the mean absolute difference is  $0.051\text{m} \pm 0.044$ .

For the flow field, Figure 5.24 gives a plan view of the modelled depth-averaged flow velocities. Five key features of the flow field are marked on Figure 5.24 (i-v), which can be compared qualitatively with Figure 4.15. At location (i), the area of lower or recirculating flow is being represented, while the generally lower velocities in the true left tributary are also clearly shown (ii). The faster flow around the true left

tributary step is replicated in (iii), as is the tendency for higher velocities near the left bank of the true right tributary (iv). For the zone of fastest flow in the main channel (v), the model prediction is reasonable, but a little further to the left than was shown in Figure 4.15.

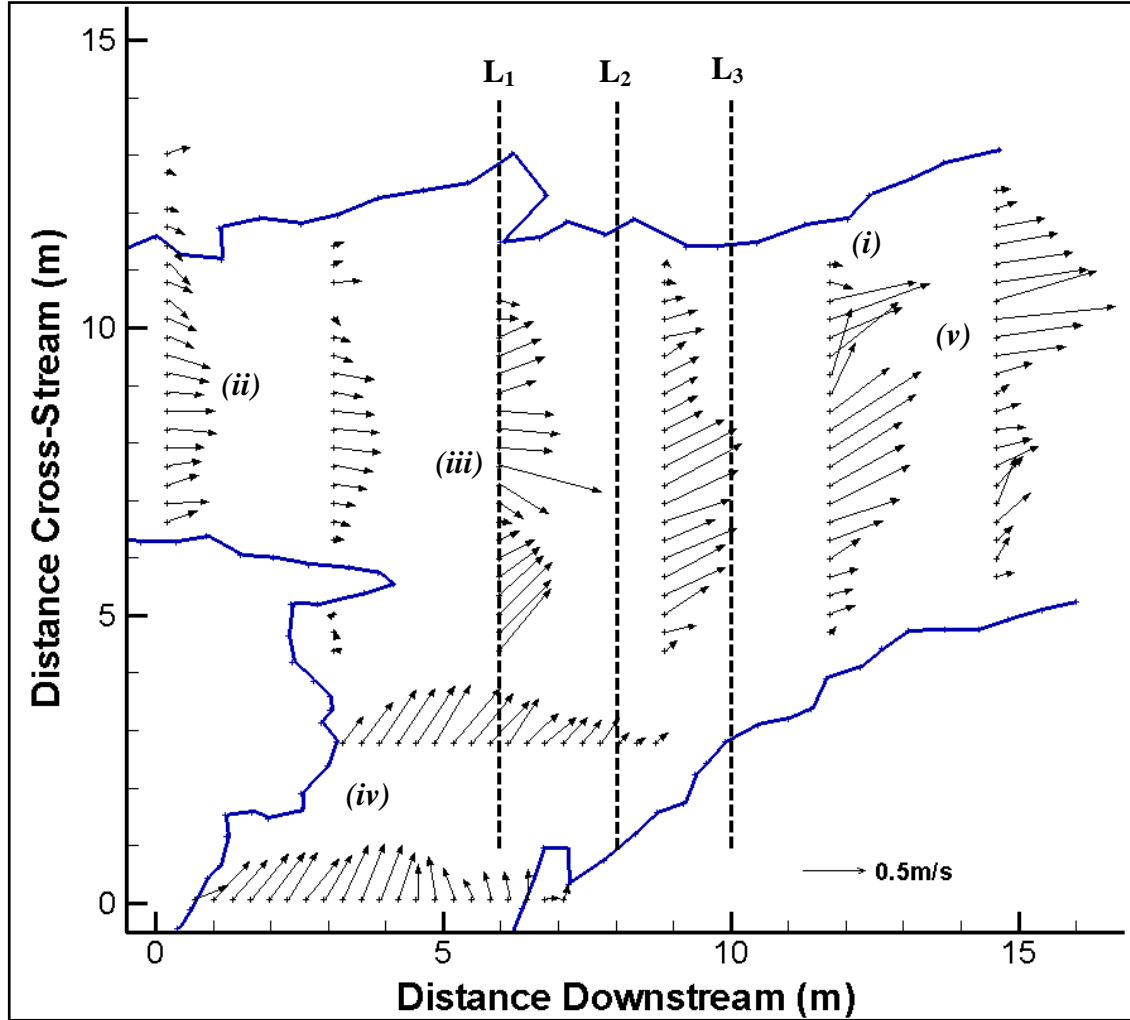


Figure 5.24: Depth-averaged modelled flow velocities for the lower confluence at Moor House Nature Reserve. The dashed lines show the cross-section locations used later in the chapter.

Although on a qualitative level the model appears to be very representative of the flow field, like the upper confluence there are greater differences in the quantitative comparisons. The MAE values for downstream and cross-stream velocity are  $0.208\text{m/s} \pm 0.166$  and  $0.126\text{m/s} \pm 0.106$ , which compare to average flow speeds of  $0.366\text{m/s}$  and  $0.211\text{m/s}$  respectively. The Pearson's values also show only a weak, positive correlation between the two datasets. The RMA regression lines in Figure 5.25 both have poor levels of fit, although the cross-stream velocity is marginally better and has a regression line very close to the 1:1 line. However, as with the upper confluence, the error bars,

which give the range of values in the 3x3x3 cell box surrounding the recorded measurement point, show a high level of uncertainty due to potential geolocation errors. In most cases these error bars are substantially wider than the MAE, which again suggests that the apparently poor quantitative analysis can be attributed in large part to this uncertainty.

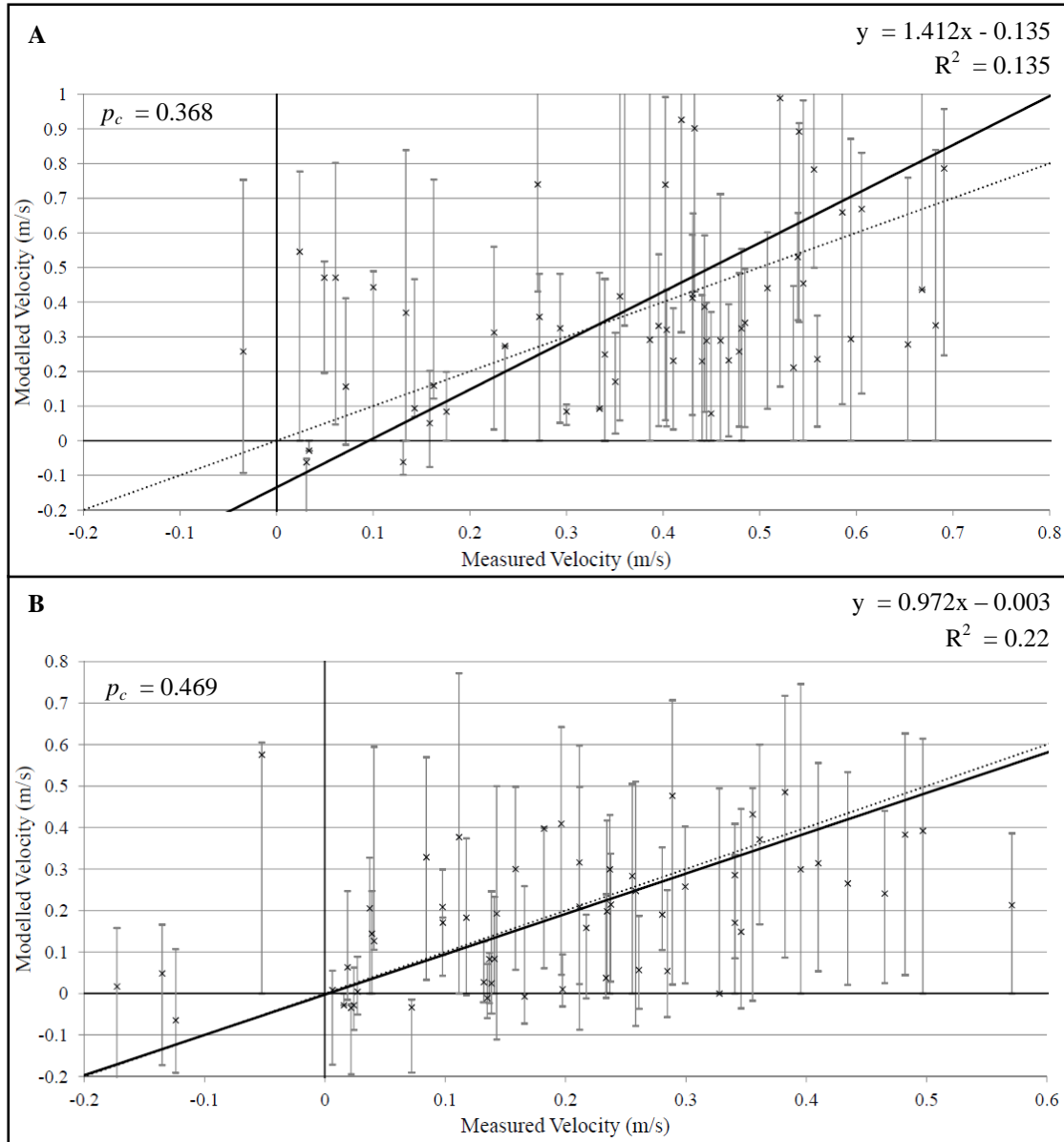


Figure 5.25: Modelled and measured downstream (a) and cross-stream (b) velocities for the lower confluence, with RMA regression (solid black) lines, 1:1 (dashed) lines and error bars (grey) showing the range of values in the adjacent model cells. For downstream velocity, mean absolute difference is  $0.208\text{m/s} \pm 0.166$  compared to an average velocity of  $0.366\text{m/s}$ . For cross-stream velocity, mean difference is  $0.126\text{m/s} \pm 0.106$  compared to a mean absolute velocity of  $0.211\text{m/s}$ . The  $p$ -values for the Pearson's correlations are 0.0022 (downstream velocity) and 0.0001 (cross-stream velocity).

#### 5.7.4 Discussion of the Moor House Confluence Validation Tests

The results from the second phase of model validation in this section are largely positive, but with some concerns over the agreement between the modelled and measured velocity values. This applies to both the upper and lower confluences, suggesting that the performance of the model is not dependent on the specific site (unlike errors at the lower true left inlet in Section 5.6).

The results in this section have demonstrated that there can be a lot of confidence in the use of the HOL model in these upland confluences for representing the water surface elevation. At the upper confluence, the comparison between the water surface elevations is good both qualitatively and quantitatively (Figures 5.16, 5.17 and 5.18), with the only disparities located near the model outlet (at *(i)* in Figure 5.17b) and around the peat block at *(iv)* in Figure 5.17b. For the lower confluence, the results are similar, with the model again replicating the measured surface well, in particular at the drop over the avalanche face from the true left tributary (*(i)* in Figures 5.16 and 5.17). The area of biggest disparity, meanwhile, is also that nearest the model outlet (at *(ii)* in Figure 5.22b).

It is argued that the disparity near the outlet in both confluences is unlikely to be due to a problem with the model itself, but rather a limitation of using a zero pressure outlet. Ideally, the run-out area at the downstream edge would be extended to substantially reduce the impact of the outlet, but this is not necessarily feasible given the additional computational cost incurred. Nevertheless, in spite of this limitation, the representation of the main features of the water surface is good. In addition, Figures 5.16 and 5.21 demonstrate that the model includes subtle variations in the water surface that the measured water surface does not show due to the data being interpolated between water edge points. The HOL model therefore shows much promise in improving the understanding of the effects of the free surface on confluence dynamics.

For both confluences, the qualitative assessments of the modelled flow velocities were encouraging. For the upper confluence, the data given in Figure 5.19 have very similar features to those highlighted for the field data in Figure 4.16. The zone of faster flow in the true right tributary is clear (*(v)*), as is its position in the downstream channel (*(iii)*). The model also represented the flow divergence around the peat block in the centre of the true left tributary (*(ii)*) and the rapid increase in flow velocity as water from this tributary enters the main channel (*(i)*). Areas of disagreement between the model and field

data are limited and largely due to disparities in the modelled flow directions in parts of the main channel (*iv* and *vi*). At the lower confluence, the modelled flow data in Figure 5.24 also have a number of clear similarities with the field data (Figure 4.15). The zone of fastest flow is seen to come from near the true left bank of the true right tributary (*iv*) and move across towards the true left bank of the main channel (*v*). Additionally, there is evidence of the model replicating the recirculation zone near the true left bank (*i*).

Given the encouraging results from this qualitative assessment, the poor correlation and MAE values appear somewhat contradictory. However, the error bars marked on Figures 5.20 and 5.25 provide an explanation for this discrepancy. With the uncertainty in the exact location of the velocity data in the field and the discretisation inherent in the model, the relevant velocities to be used in the comparisons are subject to considerable error. This geolocation error for individual point data is, in most cases, much greater than the MAE and is therefore likely to be an important cause of the poor quantitative agreement. In addition, it has already been demonstrated (Lane *et al.*, 2004) that in channels with rough beds, simulations of the flow can be very sensitive to the accuracy and precision of the topographic representation, in particular the sub-grid scale roughness. It is therefore argued that the grid-scale disparities in the quantitative flow comparisons should not be considered evidence that the HOL model is incapable of representing the key flow processes at upland river confluences.

As a result, this section has demonstrated that the HOL model is capable of replicating the water surface elevation and the major flow features of upland river confluences. However, when drawing conclusions from flow velocity values at the grid scale, it is imperative that the errors due to discretisation, geolocation and the sub-grid scale topographic effects are taken into account.

## **5.8 Model Validation Using the Arolla Datasets**

It was observed in Section 4.8 that the confluences on the Borgne d'Arolla braid plain are generally steeper, more turbulent and therefore more dynamic than those found at Moor House Nature Reserve. They therefore provide a challenging test of the HOL model and its ability to replicate the flow conditions where there are steep water surface slopes. Confluence E has already been used in the verification tests in Section 5.4, but was considered unsuitable for model validation due to the unreliability of the measured flow data. Therefore, this section will present the results from simulations of

Confluences G and H, for which the field results were given in Section 4.8. Although the data collected at the Arolla confluences were not as detailed as the Moor House datasets, the measured water surface elevation and outlet velocities provide sufficient information to assess the performance of the model in these situations.

The models were set up in the same way as for the Moor House simulations with uniform flow velocities at the inlet, a zero pressure outlet and run-in and run-out areas. For Confluences G and H, the run-in area was 18 cells (0.72m) long and the run-out area was 32 cells (1.28m) long. For Confluence E, the model roughness value was set at 0.004m, which was obtained by averaging the  $0.1D_{84}$  and  $6.5D_{50}$  methods from Table 4.11. This gave a value of 4.35mm, which was rounded to 0.004m. When calculating the roughness heights confluences G and H, values of 3.7mm and 6.4mm were obtained. However, given the lesser effect of roughness in three-dimensional flow models (Lane *et al.*, 1999a), the insensitivity of the model to roughness height demonstrated in Section 5.5 and the similarity of the values, it was considered more appropriate to have consistency in the values across all Arolla confluences in the first instance.

### 5.8.1 Validation Using Confluence G

Figure 5.26 presents the three-dimensional modelled and measured water surfaces at Confluence G, while Figure 5.27 shows the plan view of the modelled water extent and the differences between the datasets. Both figures highlight three key features of the flow: the water superelevation and depression around large obstacles (*i*), the overestimation of the water elevation near the inlet (*ii*) and the development of surface water waves (*iii*).

Figures 5.26 and 5.27 show that in general the modelled water surface is very similar to that measured *in situ*, although there is a tendency for the model to overestimate the elevation near the inlets (*ii*). Other disparities tend to be associated with modelled water surface fluctuations that the interpolation between measured water edge points would not have represented. Therefore, the close match between the modelled and measured water extents in Figure 5.27 may be a more reliable guide to overall model performance. The plot of modelled and measured water surfaces in Figure 5.28 shows a general pattern of overestimation by the model, although the MAE of  $0.037\text{m} \pm 0.028$  means that this is relatively small.

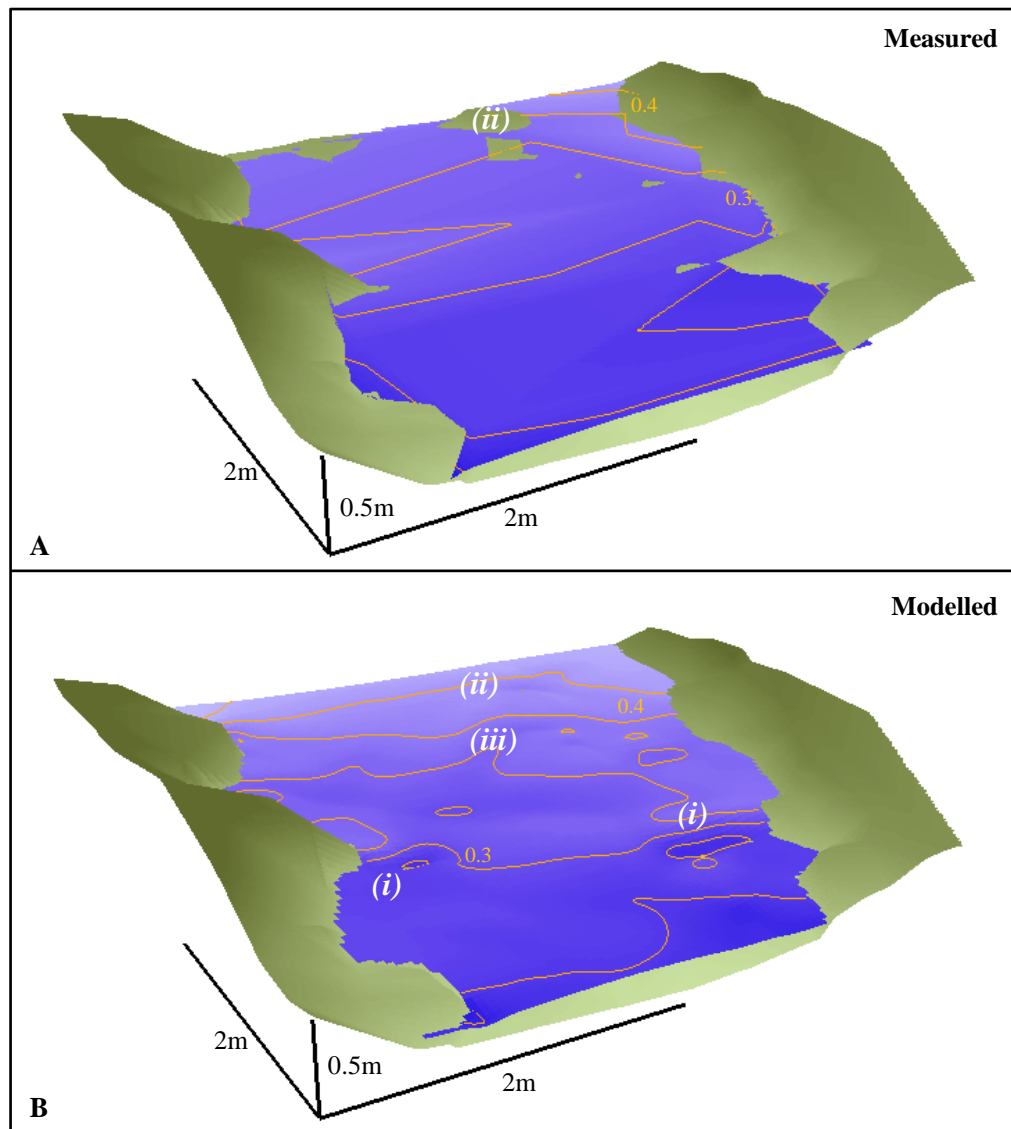


Figure 5.26: Modelled and measured water surface elevations for Confluence G on the Borgne d'Arolla braid plain, shown in three-dimensional form.

Figure 5.29 shows the contour plot of modelled flow velocities, with the velocity readings from the outlet (as presented originally in Figure 4.41) shown for comparison. The two datasets are then compared in Figure 5.30, with the RMA regression line given on the plot. Both plots show that three of the five points agree well, whilst the other two have been over-predicted by the model. The MAE of  $0.296\text{m/s} \pm 0.18$ , which equates to 27% of the mean velocity, indicates that the overall agreement is good. However, with only five data points the results of the statistical tests should be treated with caution.



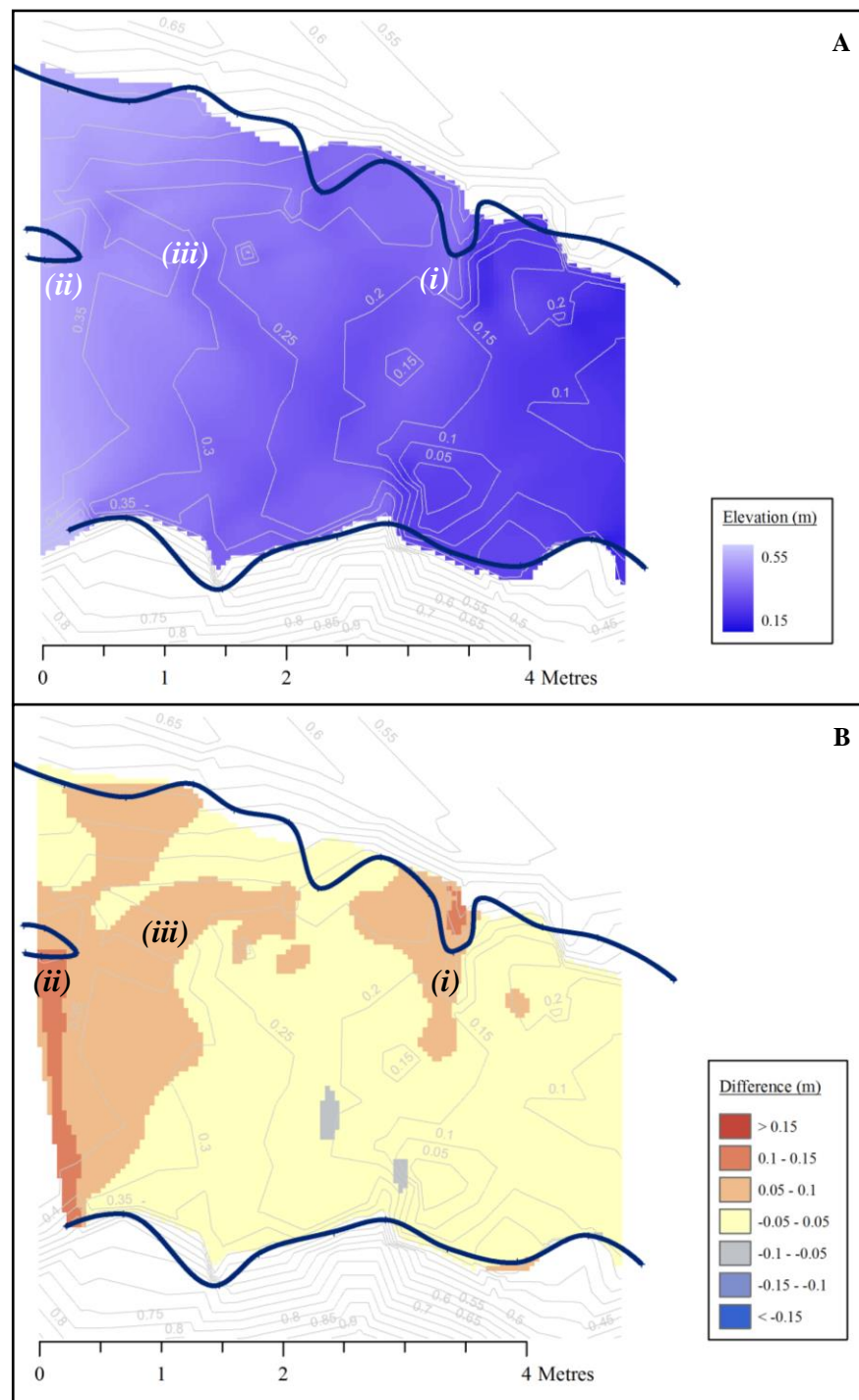


Figure 5.27: Confluence G modelled water extent (a) and comparison of modelled and measured water surface elevations (b). The water edge measured in the field is marked by the navy blue line.

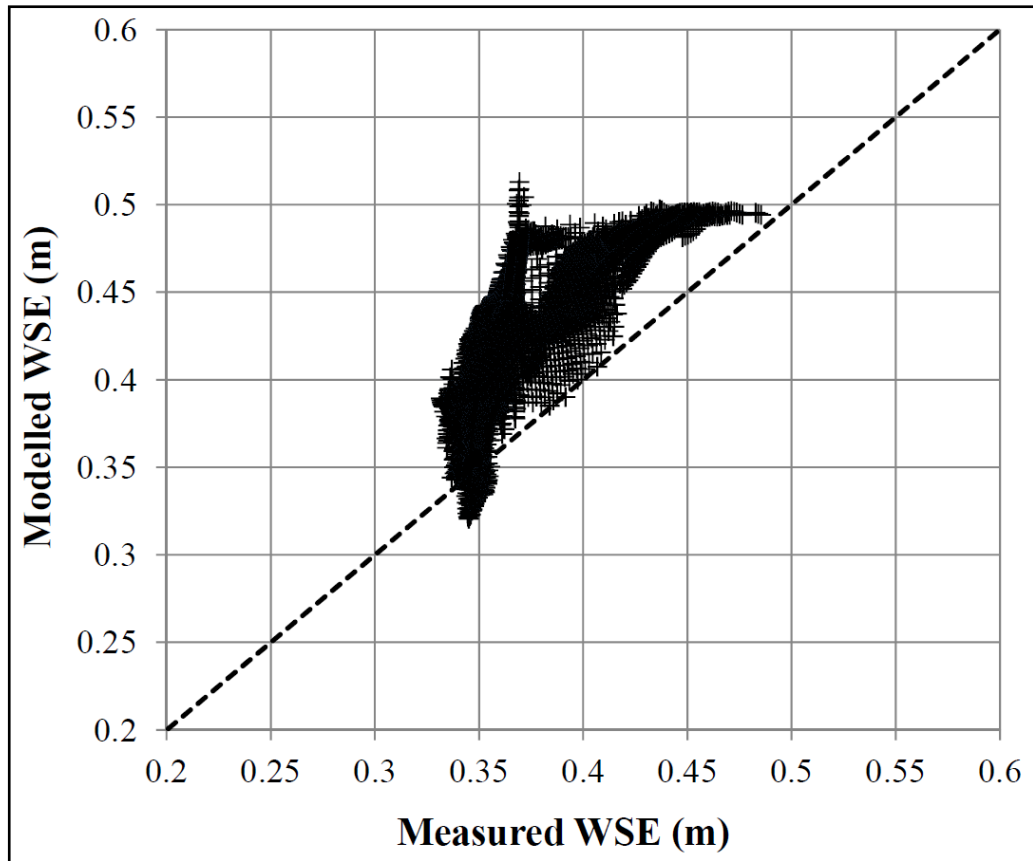


Figure 5.28: Plot showing modelled and measured water surface elevations for Confluence G. The Pearson's correlation is 0.89 and the mean absolute difference is  $0.037\text{m} \pm 0.028$ .

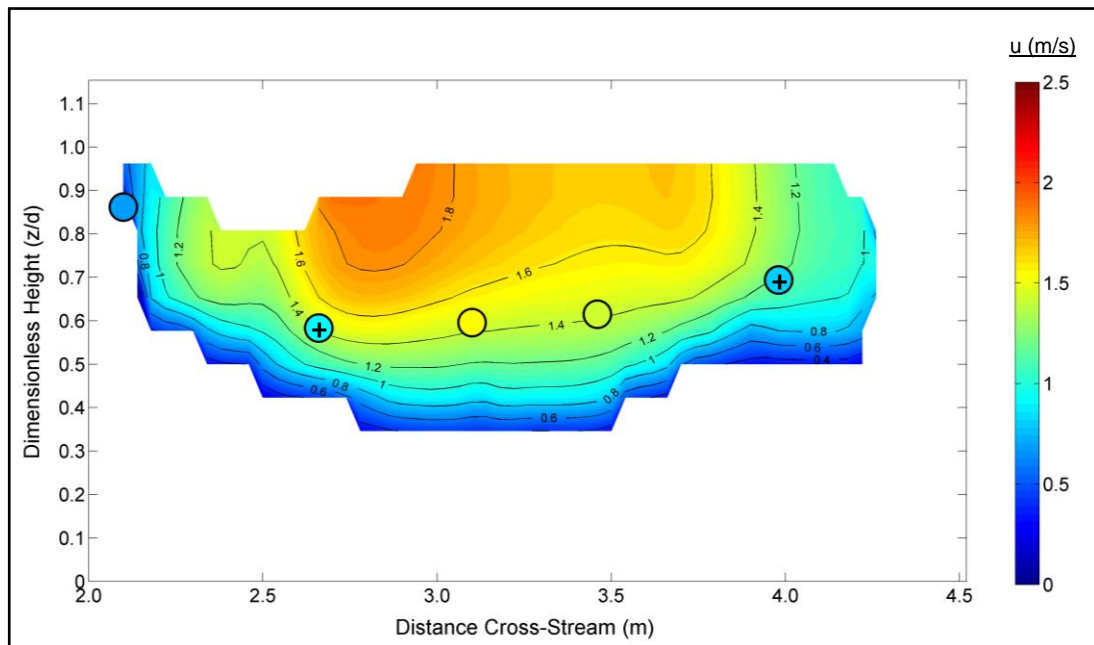


Figure 5.29: Contour plot showing modelled main channel velocity at the outlet of Confluence G. The filled circles give the measured velocities for comparison, with a '+' sign indicating an over-prediction by the model. The mean downstream velocity is  $1.08\text{m/s}$ , with mean absolute difference between modelled and measured values calculated as  $0.296\text{m/s} \pm 0.18$ .

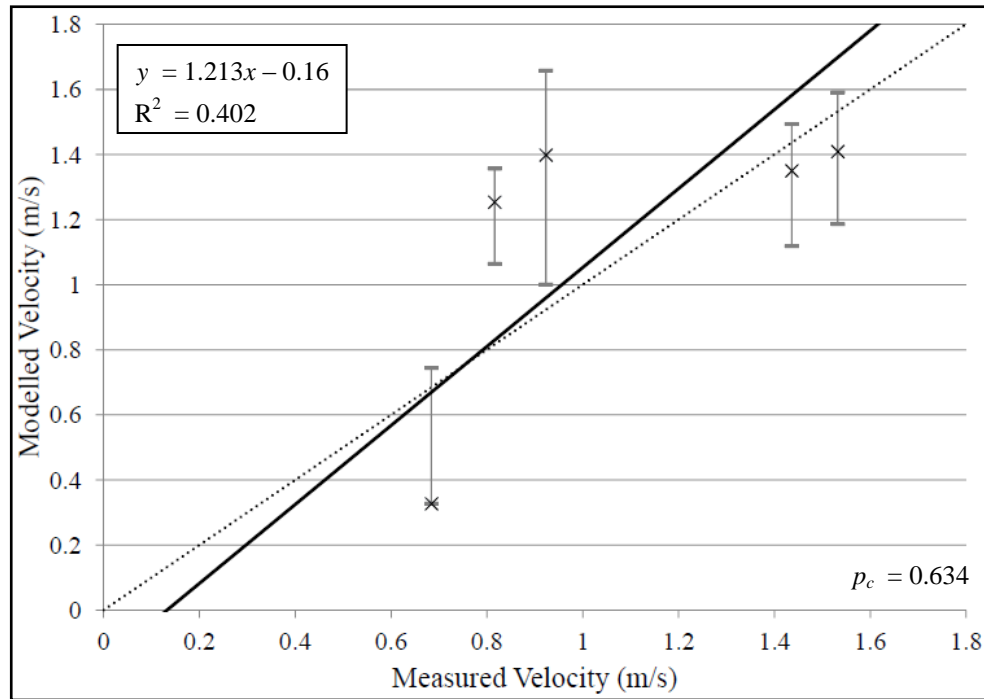


Figure 5.30: Modelled and measured main channel velocities for Confluence G, plotted with the RMA regression line and errors bars. Although the RMA regression line and Pearson's correlation have been calculated for reference, the values should be treated cautiously given that there are only five data points.

### 5.8.2 Validation Using Confluence H

For Confluence H, Figures 5.31 and 5.32 show the three-dimensional and two-dimensional plots of the differences between modelled and measured water surface elevations. In both diagrams the development of surface water waves can be clearly seen (i), as well as a tendency for higher modelled water elevations near the inlets (ii). In Figure 5.31, the model also shows water superelevation and depression around a large clast in the middle of the confluence (iii).

Figure 5.39b shows a general trend for overestimation of the measured water surface elevation, but a comparison with Figure 5.39a shows that these highs are associated with peaks in the surface waves. Therefore, some of the disparity may be linked to the interpolated water edge points not recording the variations in water surface elevation in the centre of the confluence. The photograph in Figure 4.29 shows that this confluence has particularly large surface water waves and so there will be greater uncertainty in the field data furthest from the banks.

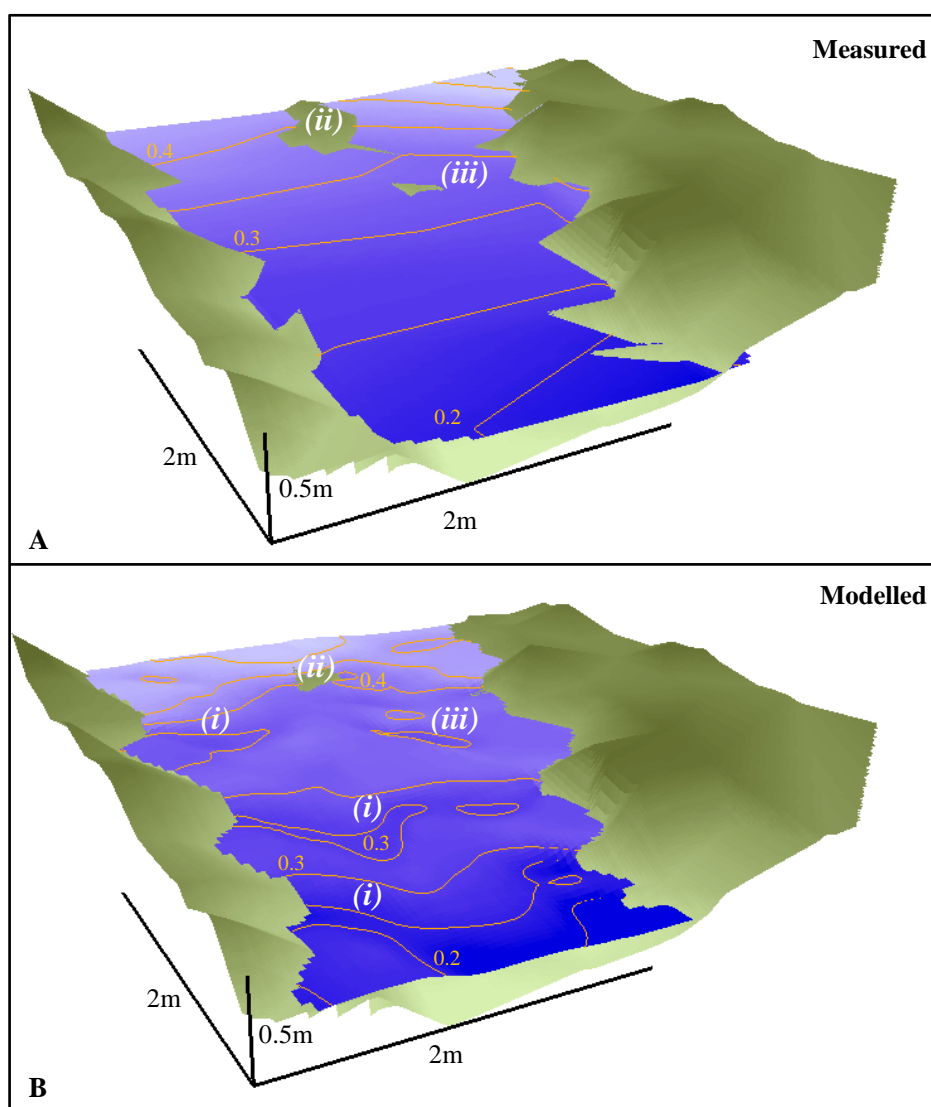


Figure 5.31: Three-dimensional modelled and measured water surface elevations for Confluence H on the Borgne d'Arolla braid plain.

The plot of modelled against measured water surface elevations in Figure 5.33 shows that the overestimation of the measured water surface is common throughout, although the MAE of  $0.048\text{m} \pm 0.025$  is relatively low. In addition, the high Pearson's correlation value (0.93) implies that slope of the water surface is being replicated.

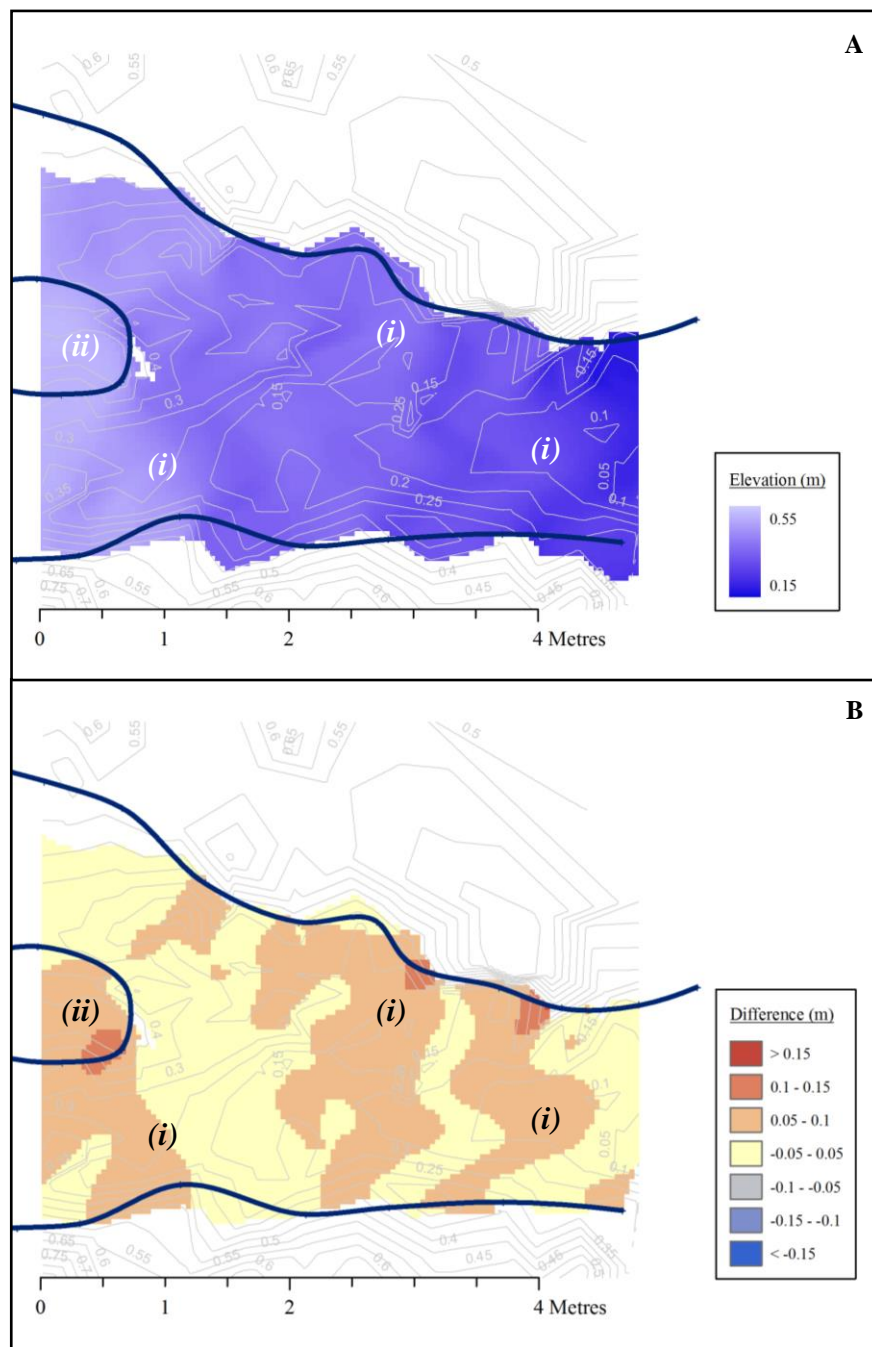


Figure 5.32: Two-dimensional plot of modelled water extent at Confluence H compared to the surveyed water edge (a) and diagram showing the difference between modelled and measured water surface elevations (b).

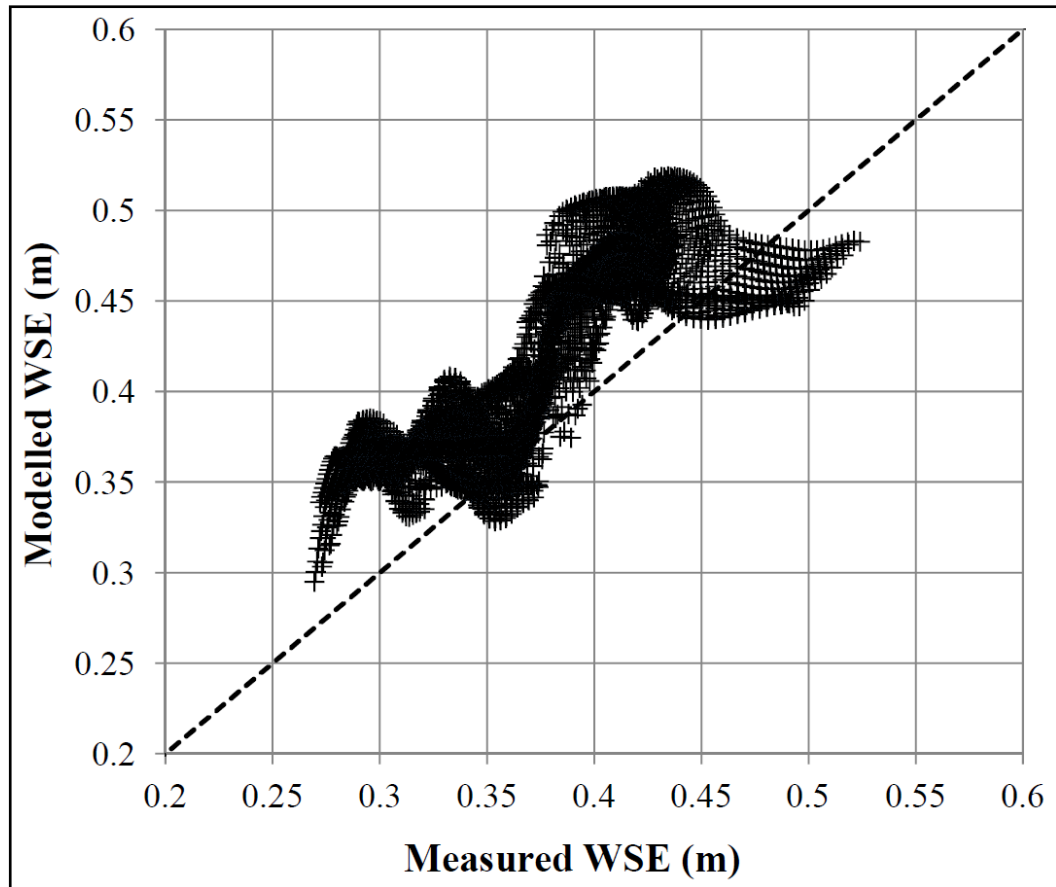


Figure 5.33: Modelled and measured water surface elevations for Confluence H. The mean absolute difference is  $0.048\text{m} \pm 0.025$ , while Pearson's correlation is 0.93.

Figures 5.34 and 5.35 compare the measured and modelled flow velocities at the confluence outlet. Two of the three points are marked as being overestimated by the model in Figure 5.34, but the MAE of  $0.311\text{m/s} \pm 0.254$  equates to just 24% of the mean downstream velocity. Similarly, in Figure 5.35, the tendency for the model to overestimate the measured velocities (confirmed by the RMA regression line) is balanced by the fact that the error bars for all three data points cross or get very close to the 1:1 line. The Pearson's correlation is lower than that for Confluence G, but still falls into the category of being neither a particular weak nor a strong positive correlation. There is therefore no evidence to suggest that the model is incapable of replicating the flow field at this confluence, although it is not possible to draw any stronger conclusions with only three data points.

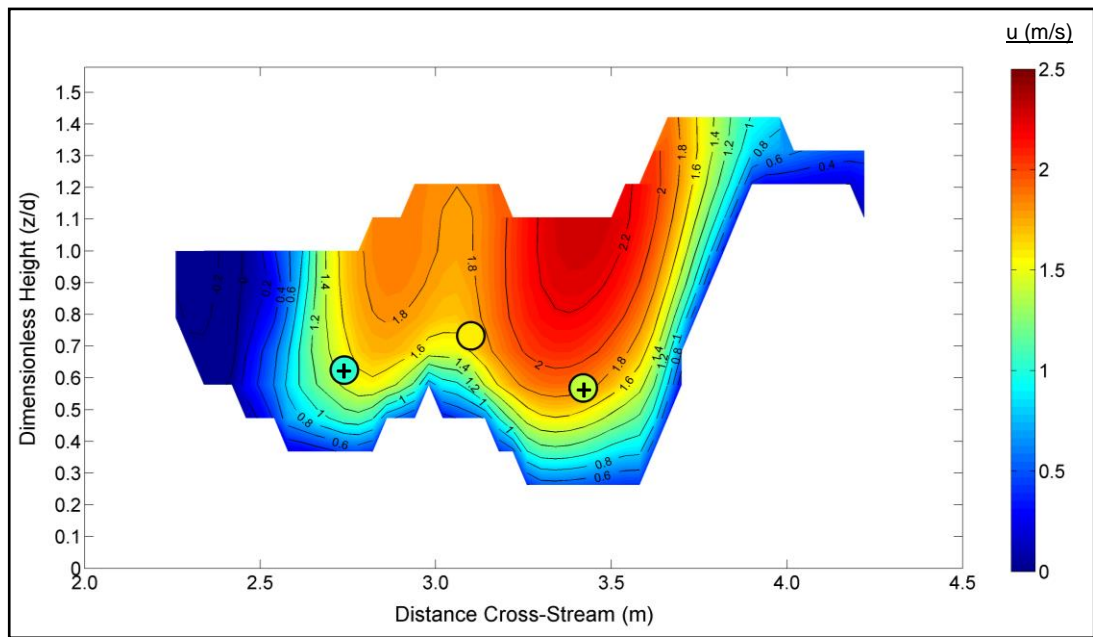


Figure 5.34: Modelled downstream flow velocities (contours) at Confluence H with measured velocities (filled circles) superimposed for comparison. A '+' sign denotes the model over-estimating the measured flow velocity. The mean absolute difference between the datasets is  $0.311\text{m/s} \pm 0.254$ , compared to a mean downstream velocity of  $1.32\text{m/s}$ .

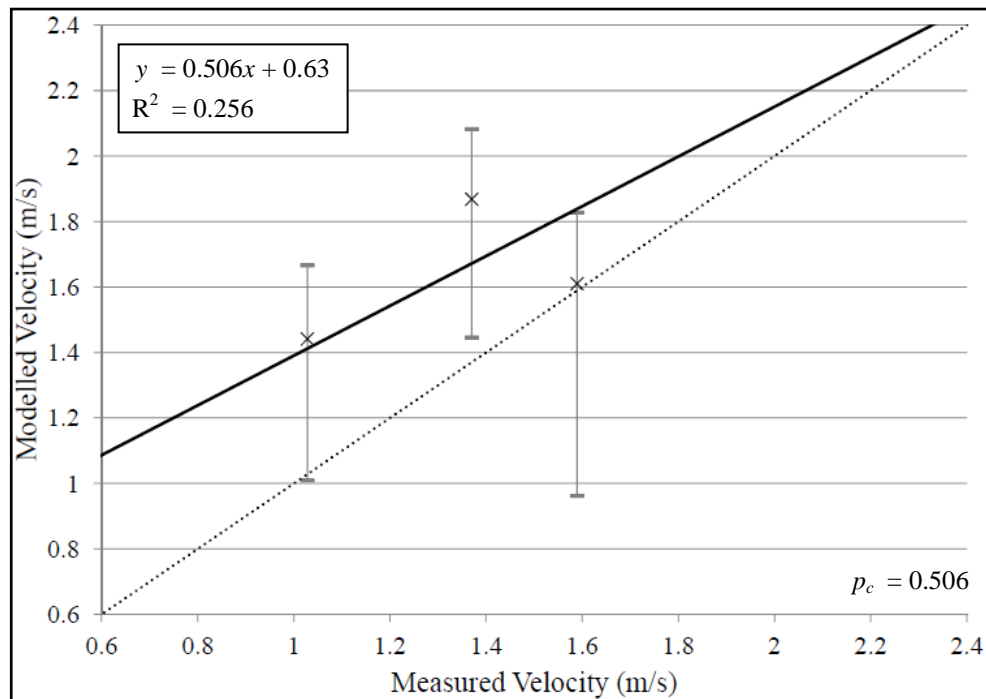


Figure 5.35: Modelled and measured downstream flow velocities at Confluence H plotted with geolocation error bars. As with Figure 5.30, the low number of data points means that the Pearson's correlation value and RMA regression line should be considered as only an indication of the likely trend.



### 5.8.3 Discussion of the Arolla Confluence Validation Tests

As with the Moor House confluences, the simulation of the water surface at both Arolla confluences is good. In Confluence G the main disparities between the modelled and measured values tend to be associated with the inlet (at (ii) in Figures 5.26 and 5.27), although Figure 5.28 suggests this pattern is replicated throughout the confluence. From Figure 5.26, however, it can be seen that the model replicates the fluctuations in water surface elevation (*i* and *iii*) that are evident from the photographs of the confluence (see Figure 4.29), but are not recorded in the measured water surface elevations.

At Confluence H, meanwhile, the disparity in predicted water surface elevation can be largely attributed to the surface water waves, which are clearly present in Figure 4.29. These standing waves are more prominent at Confluence H, which may be associated with the lower range of Froude numbers in Table 4.8 (0.81-1.07 compared to 0.86-1.26 for Confluence G). If much of the flow at Confluence H is indeed subcritical, then an estimate of the standing wave height is given by  $h_w/d \approx 1.312(1-Fr)$  (Chanson, 2000). Using the lower end of the range of Froude numbers in Table 4.8 (0.8-0.9) gives standing wave heights of approximately  $0.15d$ - $0.25d$ , or 0.03-0.05m, which is of the same order as the MAE values. Therefore, given the highly variable water surface at both confluences, it is arguable that the model may actually provide a better indication of the water surface elevation than that found by interpolating the water edge points.

A detailed comparison of the flow velocity predictions is more difficult due to the limited amount and one-dimensional nature of the flow data collected. However, the evidence presented in this section is positive, with both confluences getting MAE values that, relative to the mean downstream velocity, are substantially lower than those found at the Moor House confluences in Section 5.7. Furthermore, even when there are disparities in the modelled and measured values, in all cases the error bars cross or get close to the 1:1 line. This is a particularly good result as Figures 5.30 and 5.35 shows only the range of values in the adjacent cells (a 3x3x3 cell block around the data point), which allows for geolocation errors of the order of 4cm in the horizontal direction and 2cm in the vertical direction. Given the potential errors set out in Section 5.3.3, this is likely to be a conservative estimate of the uncertainty.

Therefore, the results from this third and final part of the model validation process suggest that the HOL model can provide a good representation of the processes



operating at these steeply-sloping river confluences. Indeed, it could be argued that when it comes to the water surface elevation, some of the disparities between modelled and measured data are in fact due to the model providing a better representation of the confluence processes than could be obtained from analysing the field data.

## **5.9 Discussion of Overall HOL Model Performance**

As a result of HOL method being largely untested on natural rivers, a three-part model validation strategy was set out in Section 5.3.2. The results from these tests have been presented and discussed in Sections 5.6, 5.7 and 5.8. In the tests on straight, idealised channels in Section 5.6, the model results were promising, with the biggest disagreements being at the lower true left inlet, where the presence of a submerged boulder downstream of the cross-section was not replicated in the model setup.

In the experiments on the Moor House confluences (Section 5.7), the overall performance of the model was good, apart from in the quantitative comparisons between the modelled and measured flow velocities. The apparent discrepancy between the good qualitative agreement and poor quantitative agreement was argued to be due to a combination of the geolocation errors and model discretisation resulting in significant uncertainty in the modelled and measured values to be compared. Therefore, at the broader, confluence scale the HOL model was shown to be representing the flow processes well, but at the scale of individual point measurements this uncertainty was leading to much greater error values.

In Section 5.8, the tests on the Arolla confluences demonstrated that the HOL method is capable of simulating the flow processes at much steeper confluences. In particular, the model was demonstrated to be particularly good at representing the water surface undulations that were visible in the photographs but not recorded in the measured water surface (which interpolated between data points on the channel edge). At these confluences there were fewer velocity data points for comparison, but the data that were available demonstrated that the differences between modelled and measured velocities were invariably smaller than the uncertainty due to geolocation.

Therefore, the overall conclusion to be drawn from the validation tests is that the HOL model has been found to be very good at representing the fluctuations in the water surface and the flow processes at the confluence scale. Meanwhile, in many cases, the disparities between the modelled and measured data (in particular the velocity data) can

be partly attributed to limitations in the field data. Although care should be taken when using the velocity data to understand processes at the smallest scales, the HOL model has been shown to be a potentially powerful tool for understanding the flow field at these steep river confluences.

## **5.10 Interpreting the Flow Dynamics at the Moor House Confluences**

Having successfully tested the HOL model under a range of different conditions, it can now be used to investigate further the flow dynamics in the Moor House and Arolla confluences. In this section, the HOL model output for the upper and lower confluences (introduced in Section 5.7) is used to examine the secondary circulation, turbulent kinetic energy and bed shear stress at lower discharges. This will provide a baseline for comparisons with the results to be presented in the following section, where the model will be used to test a range of higher discharge scenarios for the two Moor House confluences. The comparison between these different scenarios will further the understanding of how the flow dynamics changes at higher discharges, which will have implications for the nature of sediment dynamics. Finally, in Section 5.12, the HOL model will be applied to the much steeper confluences of the Borgne d'Arolla braid plain in order to investigate the impact of slope on the flow field at river junctions.

### *5.10.1 Flow Dynamics at the Upper Confluence*

Figure 5.36 shows the secondary circulation patterns for three equally spaced cross-sections in the middle of the upper confluence (as identified previously in Figure 5.19). The downstream velocity distribution is given by the contour plots, while the vectors show variations in cross-stream and vertical velocity from the depth-averaged values. Possible secondary circulation cells are marked by the white arrows, where thicker arrows denote stronger secondary flow. In order to explicitly evaluate the strength and extent of any helical cells, Figure 5.37 plots the local helicity ( $H$ ) values for the same cross-sections, which are calculated by multiplying the downstream velocity by the vorticity (Hunt and Hussain, 1991). This is given in Equation 5.3:

$$H = u \left( \frac{dw}{dy} - \frac{dv}{dz} \right) \quad (5.3)$$

where  $u$ ,  $v$  and  $w$  are the downstream, cross-stream and vertical velocities (in the  $x$ ,  $y$  and  $z$  directions respectively). The overall strength of the helicity in the cross-section is given by a helicity index, HI, which is calculated from Equation 5.4.

$$HI = c \frac{\sum |H|}{A} \quad (5.4)$$

where  $A$  is the cross-sectional area and  $c$  is a constant that accounts for the differences in model grid size. As the cells in the  $yz$ -plane for the Moor House confluences are 16 times larger than those for the Arolla confluences, the values of  $c$  were set to 1 and 0.0625 respectively. Using these values of  $c$  ensures that all values of HI used throughout this chapter can be compared directly.

Figures 5.36 and 5.37 show that the strongest helicity values are found in the true left tributary of the confluence where flow accelerates as a result of being constricted (*i*). However, this appears to be a localised phenomenon resulting from cross-stream and vertical velocity variations that are atypically high. Otherwise, any secondary circulation cells are weak, with the strongest being a single cell to the left of the 10m cross-section. In Figure 5.38, the helicity index is plotted against distance downstream. This again shows a spike in HI which corresponds to the flow constriction zone (at 8m downstream), with no evidence that helicity increases once the two high velocity cores from the tributaries have met (at approximately 9.5m downstream).

Figure 5.39 plots the turbulent kinetic energy (TKE) and shear stress as calculated from the model output. The TKE value is taken from the middle of the water column, to reduce the presence of anomalies caused by the proximity of the bed and water surface. For the same reason, the TKE values were not calculated unless the water column was at least three cells deep (with a cell considered to be sufficiently full of water if the VFOL variable was greater than 0.5). Due to the shallow nature of the flow at these discharges, however, there are large areas that are inundated but have no TKE data (marked on the plots in navy blue). It is for this reason that although Figure 5.39a

can be compared to the values of TKE calculated from the aDv data in Figure 4.21, no formal, quantitative validation of the model output was possible.

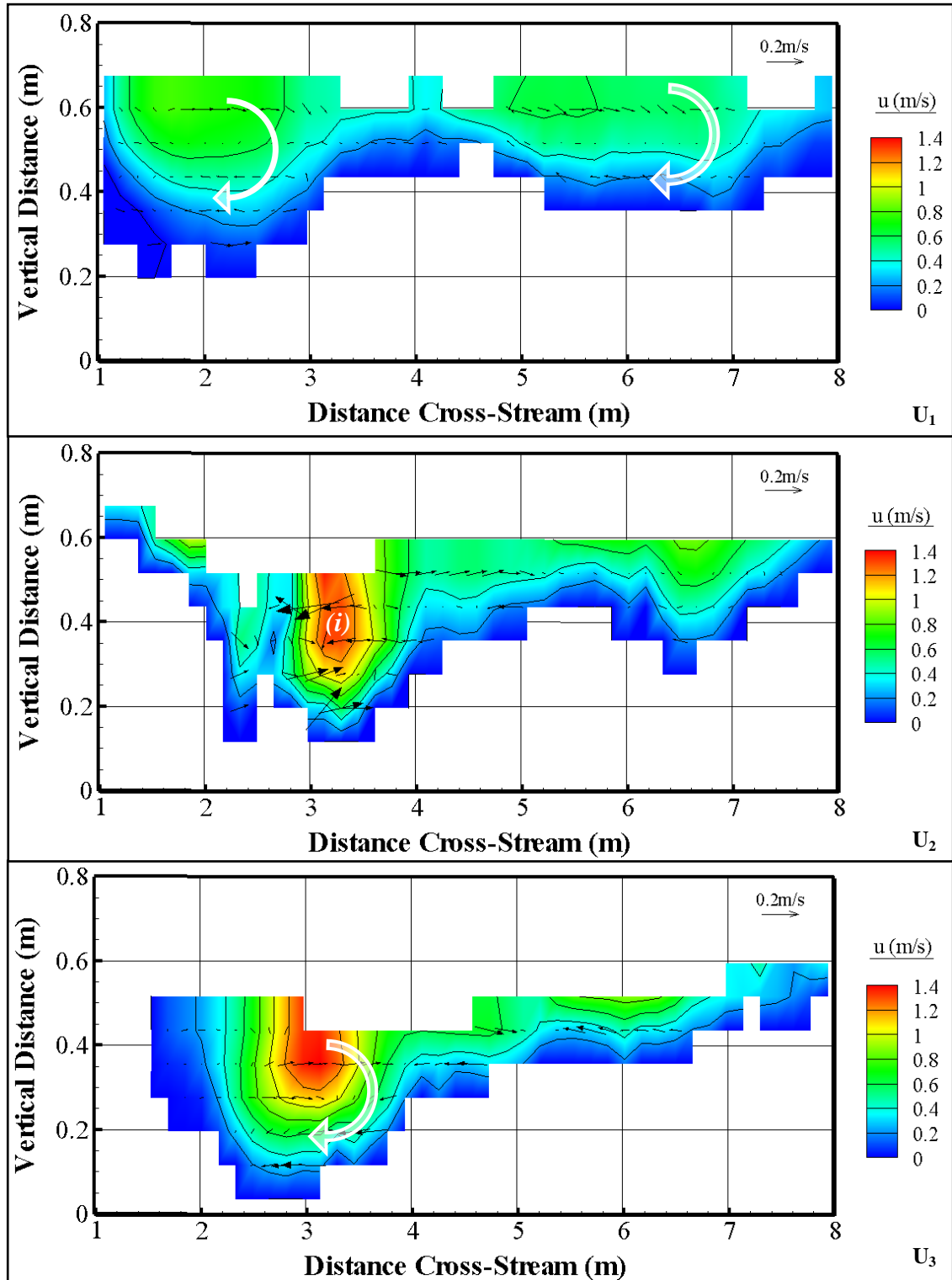


Figure 5.36: Contour and vector plots for three cross-sections through the centre of the upper Moor House confluence. The contours plot downstream velocity, while the vectors show cross-stream and vertical velocity deviations from the depth-averaged flow values. Arrowheads are scaled to the length of the arrow to enable better visualisation of the strength of the secondary circulation.

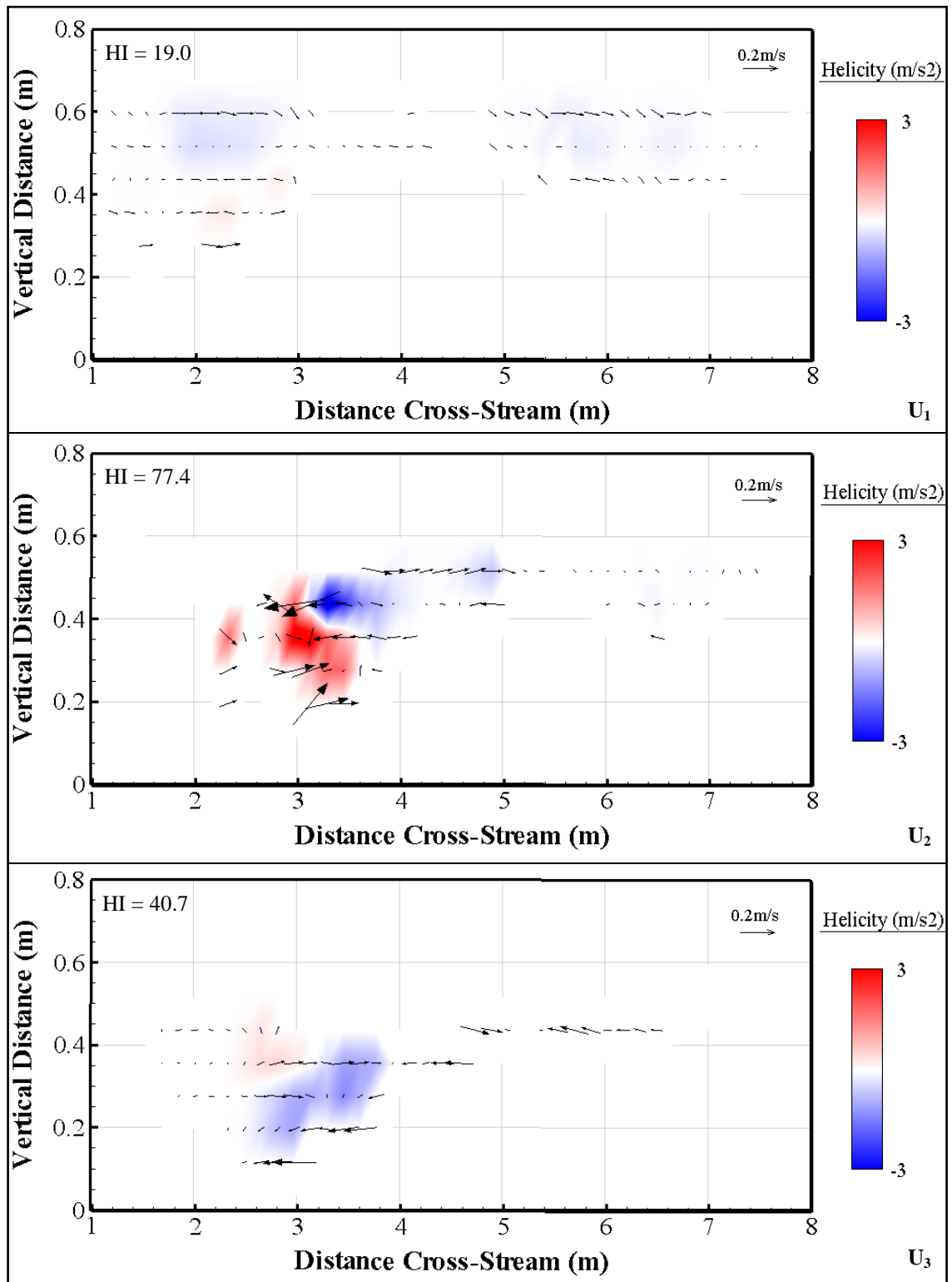


Figure 5.37: Helicity plots for three cross-sections through the centre of the upper Moor House confluence. The contours show helicity, with the vectors giving the cross-stream and vertical velocity deviations as in Figure 5.36. Positive helicity values (red) indicate anticlockwise secondary circulation.

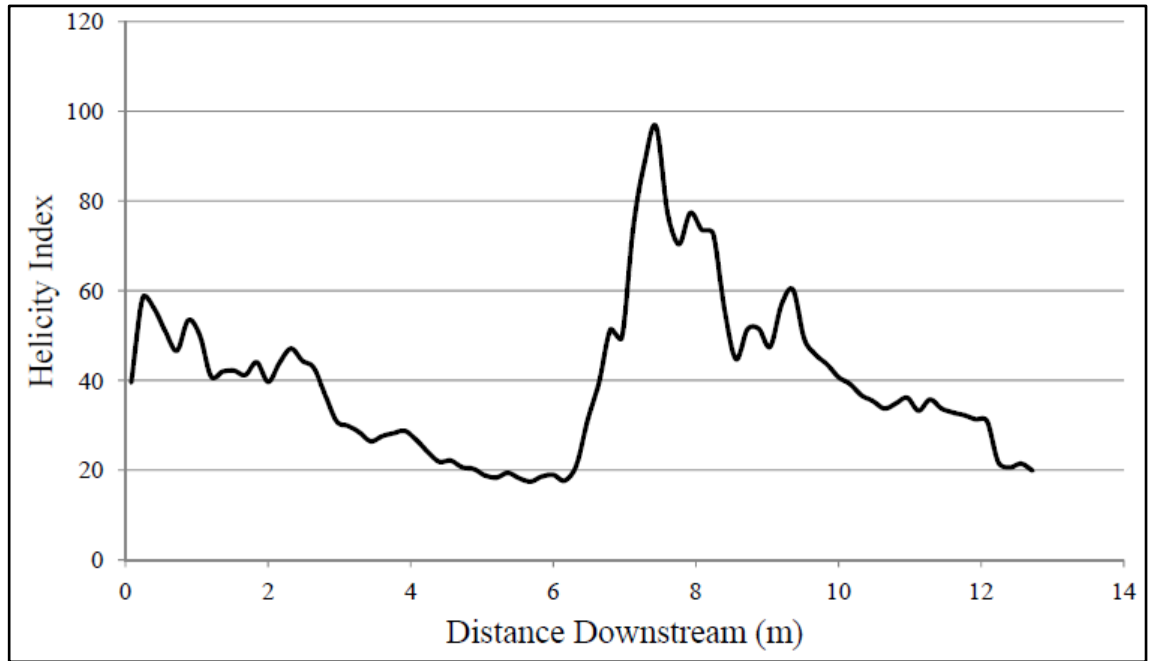


Figure 5.38: Plot of helicity index with distance downstream at the upper Moor House confluence.

Bed shear stress was calculated using Wilcock's (1996) method using multiple observations of  $u$  in a vertical water column. In a plot of the natural log of the depth against velocity, the gradient of a least-squares trend line will be equal to  $u^*/\kappa$ , where  $u^*$  is the shear velocity and  $\kappa$  is the von Karman constant (Wilcock, 1996). Having calculated  $u^*$ , the local bed shear stress ( $\tau_0$ ) can be found from (Wilcock, 1996):

$$u^* = \sqrt{\frac{\tau_0}{\rho}} \quad (5.5)$$

where  $\rho$  is the density of water. As for Figure 5.39, the parts of the confluence where the water is too shallow to be able to calculate the shear stress are marked in navy blue.

Both plots show elevated values to the left of centre in the main channel (i), although it is less clear for the bed shear stress. For TKE, the location of (i) corresponds to the area of higher turbulence identified in Figure 4.21.

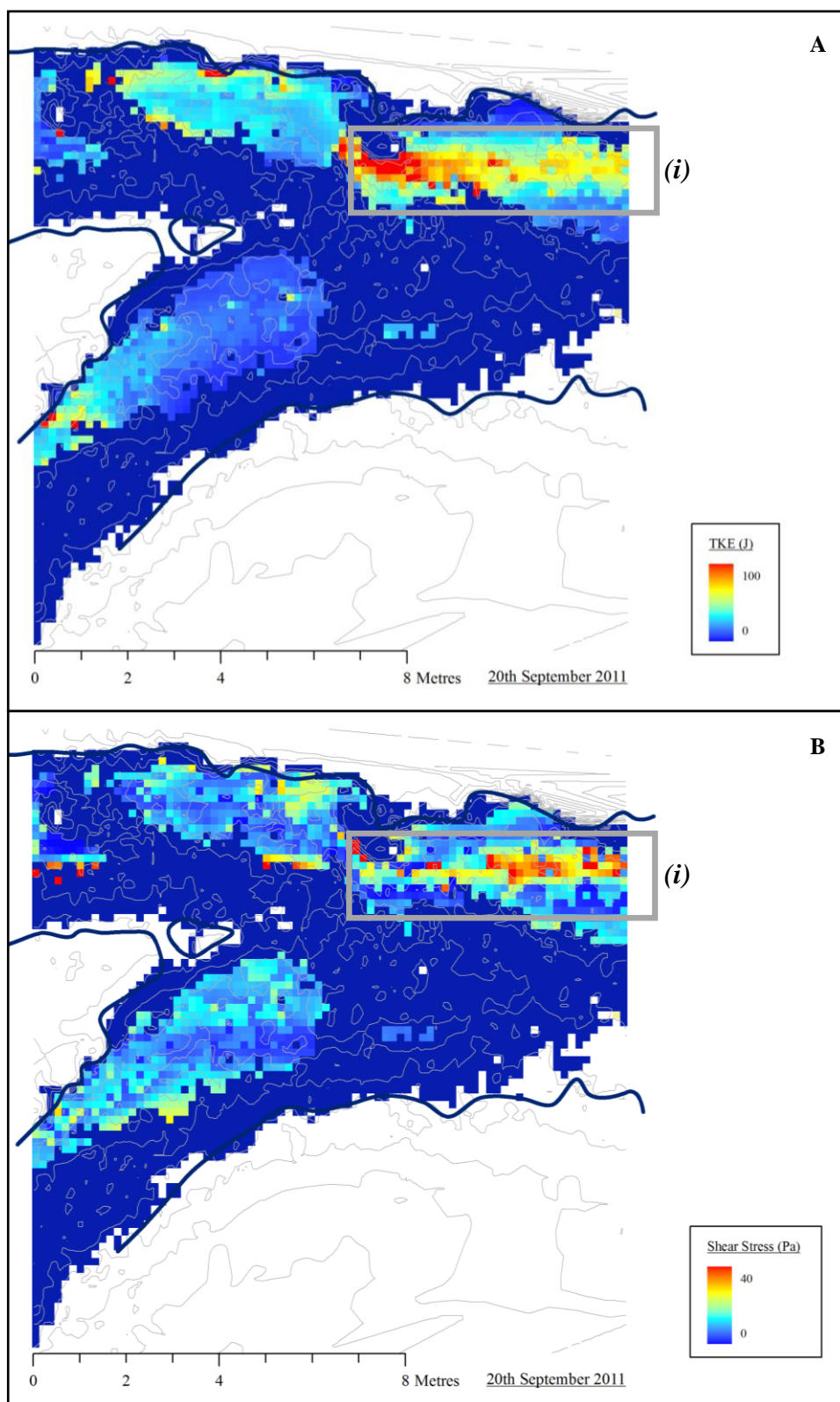


Figure 5.39: Turbulent kinetic energy (a) and bed shear stress (b) from the modelled data of the upper confluence. Cells which are water-covered but too shallow to give TKE and shear stress values are shown in navy blue.

### *5.10.2 Flow Dynamics at the Lower Confluence*

The secondary circulation patterns for the lower confluence are presented in Figure 5.40, with the corresponding helicity plots in Figure 5.41. The cross-section labels refer to the locations plotted previously on Figure 5.24. In addition, Figure 5.42 plots the variations in helicity index (in the  $yz$ -plane) with distance downstream.

In Figure 5.40, the two high velocity cores merge over the course of 4m (equating to approximately half of the channel width). In addition, there is a clearly defined secondary circulation cell in the true right half of the tributary, as marked by the white arrows. These cells, however, are largely evident from the differences in cross-stream velocity, with less clear evidence of strong upwelling and downwelling at the edges to complete the full circulation cell. The helicity plots in Figure 5.41 support these findings, with strong clockwise circulation cells in the true right of each cross-section. The strongest of these is at the 6m cross-section, although as the cell weakens downstream it expands to cover a greater area. The long profile plot of helicity index, meanwhile, shows this peak in HI at approximately 6m downstream is part of more general pattern of increases with distance downstream.



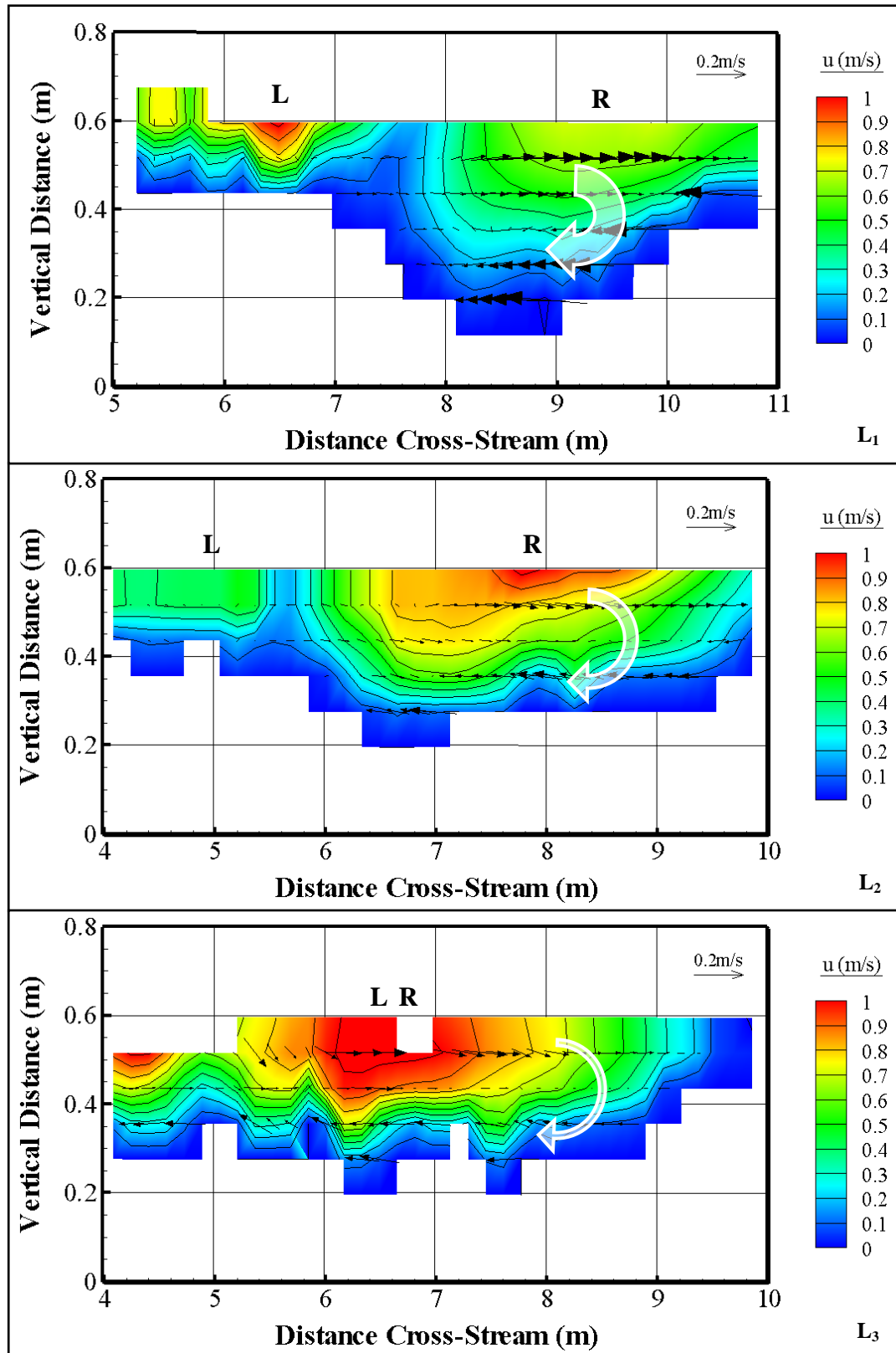


Figure 5.40: Contour and vector plots for three cross-sections in the middle of the lower confluence. The contours show downstream velocity, with the vectors giving deviations from the depth-averaged cross-stream and vertical velocity values. Arrowheads are scaled to the length of the arrow. The two high velocity cores from the tributaries are marked as 'L' (true left) and 'R' (true right).

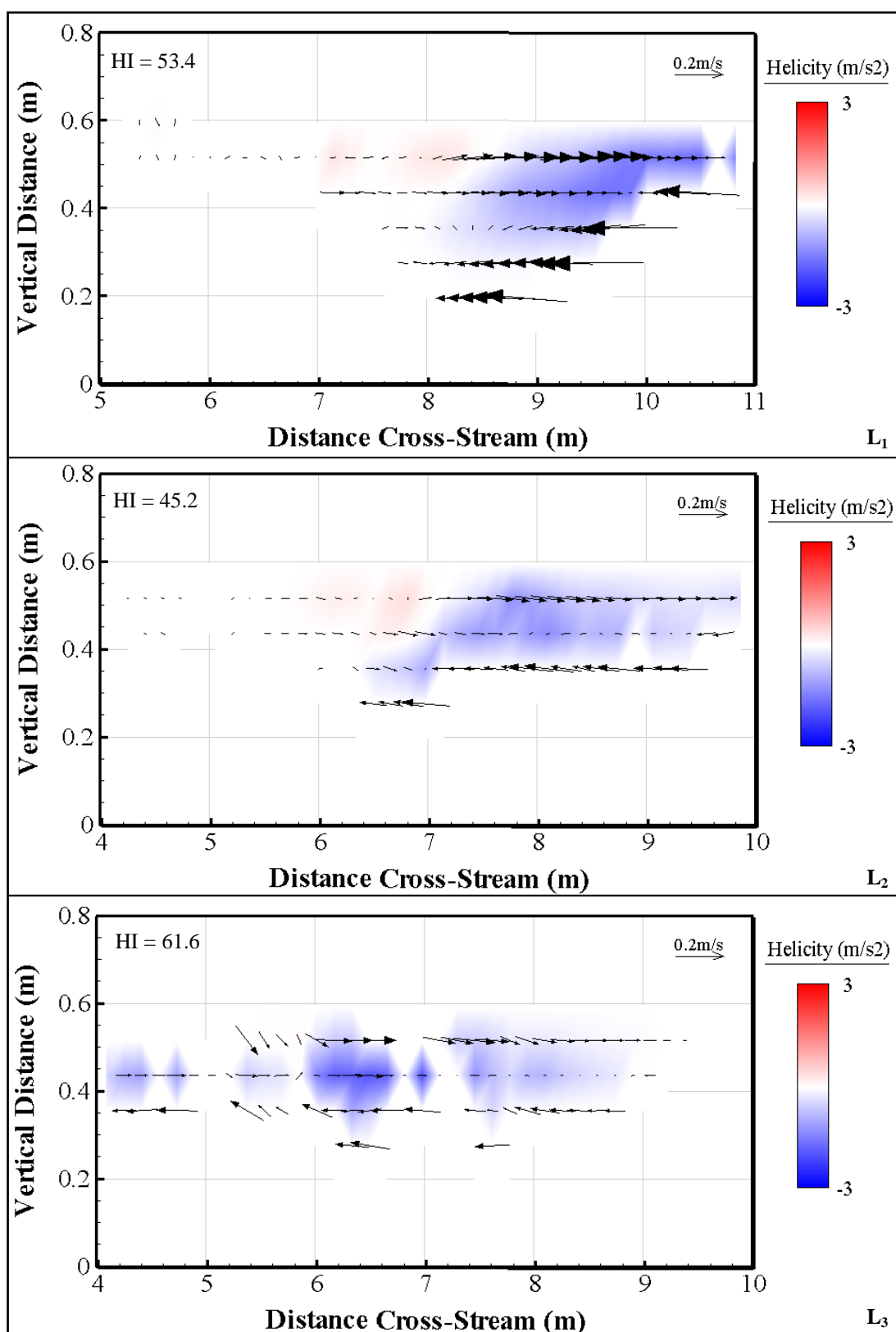


Figure 5.41: Helicity plots for three cross-sections at the lower Moor House confluence. The cross-stream and vertical velocity vectors are the same as in Figure 5.40. Positive helicity values (red) indicate anticlockwise secondary circulation.

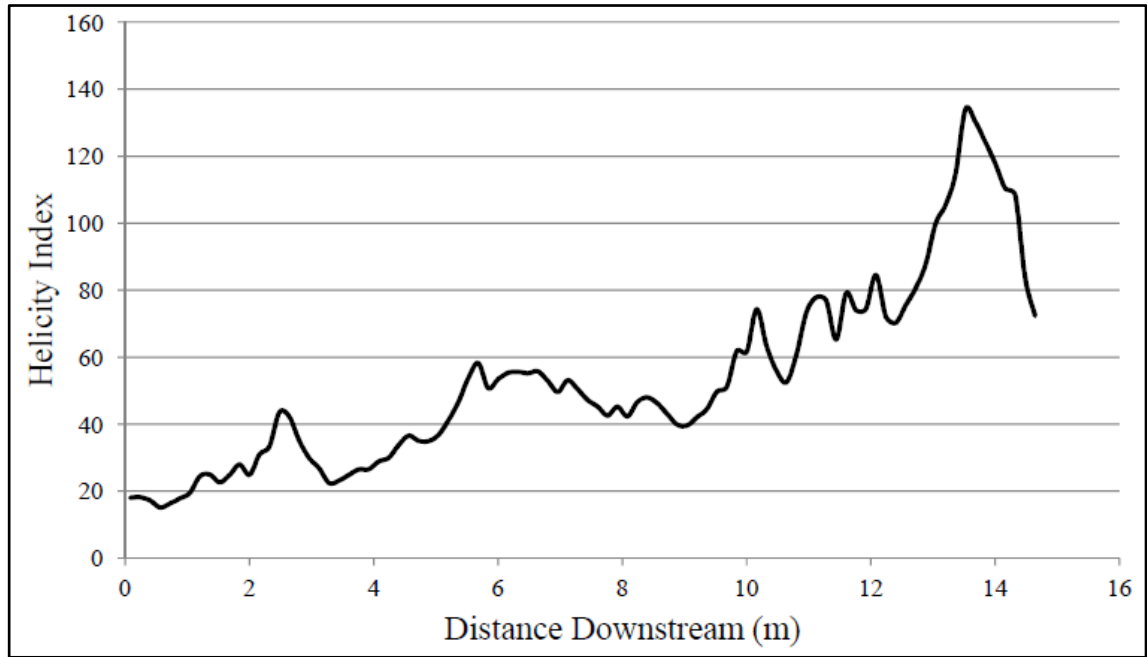


Figure 5.42: Plot of helicity index with distance downstream at the lower Moor House confluence.

The TKE and shear stress plots for the lower confluence are given in Figure 5.43. There are large parts of the confluence, in particular in the true left tributary, which are too shallow to be able to calculate the shear stress and TKE values. One such area is the region around the step from the true left tributary into the main channel (*i*), which from the field data in Figure 4.20 is the location of the highest TKE. In the absence of data for this, the model predicts an area of higher TKE and shear stress in the centre of the main channel (*ii*). This agrees with the data in Figure 4.20, although the field data suggest the location of this zone may be a little further towards the true right bank than given by the model.

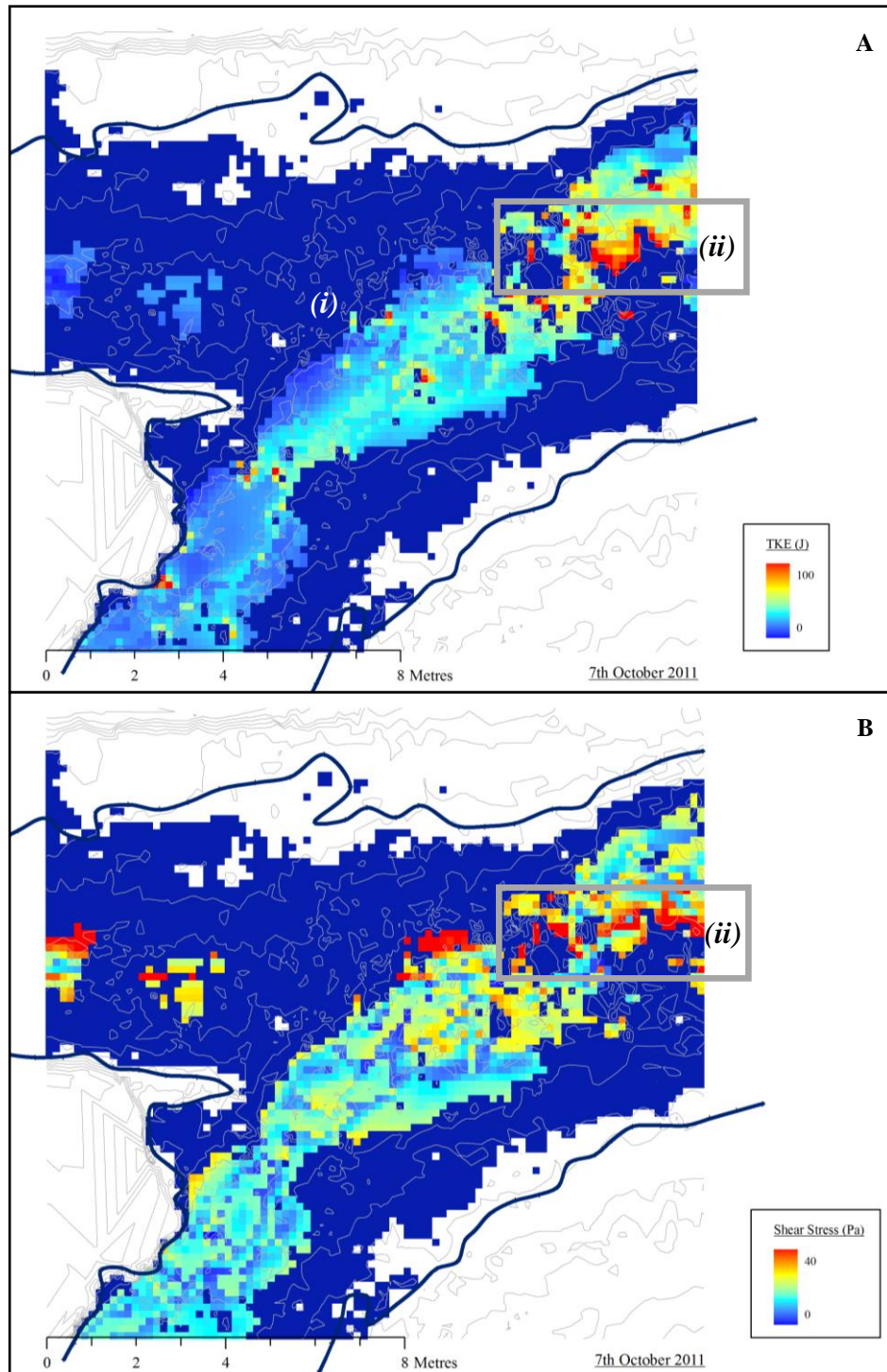


Figure 5.43: Turbulent kinetic energy (a) and bed shear stress (b) plots using the modelled data from the lower confluence. Navy blue cells are those which were water-covered but insufficiently deep to obtain data for TKE and shear stress.

### 5.10.3 Discussion of the Low Flow Dynamics of the Moor House Confluences

The use of the HOL method to simulate flow through the Moor House confluences has enabled more information to be obtained on the secondary flow,

turbulence and shear stress in these upland river confluences. This enables firmer conclusions to be drawn about the nature of the flow field than were possible from the point data collected in Sections 4.5 and 4.6.

At the upper confluence, the high velocity core that develops due to the flow constriction can be seen very clearly in Figure 5.36 (i), with the flow velocity rapidly increasing in this zone over a very short downstream distance. However, there is very little in the way of strong secondary flow cells (Figures 5.36 and 5.37), with the clearest difference in the water column observed as the high velocity core develops.

Furthermore, any secondary flow patterns appear to be very short-lived, with none persisting from one cross-section to the next (*i.e.* 0.3 channel widths). This is the same finding as for the vertical profiles in Section 4.5.2, where the data show that the strongest secondary circulation cells are found in the tributaries (rather than at the corresponding velocity profiles C, D and E), due to topographic forcing from either the channel curvature or the presence of in-channel obstacles (Figure 4.16). Figure 5.38 supports this conclusion, with values of HI generally decreasing downstream except for a large spike associated with strong secondary circulation in the flow constriction zone.

Figure 5.39 shows that there is a narrow zone of high TKE and shear stress that stretches from the exit of the flow constriction to the outlet (i). Elsewhere in the confluence, both TKE and shear stress are relatively low. This compares well with the TKE calculations from the field data presented in Figure 4.21, with elevated values towards the true left of the downstream channel. The zone of higher shear stress is associated with this zone of higher TKE, suggesting that any sediment transport at these discharges may be driven by small-scale turbulent structures.

At the lower confluence, Figure 5.40 provides a good example of two high velocity cores evolving into a single core with distance downstream. However, it is the secondary circulation and helicity in Figures 5.40 and 5.41 that are most notable, as they replicate almost exactly the process identified from the field data in profiles W, X and Y (Section 4.5.2). This circulation cell has flow towards the true right at the surface and towards the true left at the bed. Therefore, as Gaudet and Roy (1995) argue will happen at shallow, discordant river junctions, water from the shallower true left tributary is flowing over the top of water from the true right tributary. This results in a single secondary circulation cell extended across the whole of the true right tributary and supports the argument in Section 4.5.3 that it was unlikely to be the true left half of back-to-back helical cells.

However, Figure 5.42 indicates that the helicity patterns may be more complex. Increases in HI with distance downstream could indicate that the confluence is causing stronger helical cells to form. A comparison with the radar plots in Figure 4.17, though, suggests the reason is more subtle. In Figure 4.17, profiles V (true right tributary) and Z (furthest downstream) show evidence of anticlockwise secondary circulation, while the opposite is true for profiles W, X and Y (in the centre of the confluence). Therefore, the trends in Figure 5.41 could be caused by complex interactions between the clockwise secondary circulation caused by the bed discordance and anticlockwise helical cells caused by the curvature of the true right and downstream channels. The increase in HI with  $x$ , meanwhile, could be due to the true left tributary, which has much lower helicities, contributing less to the combined cross-sectional area of the channel (in the  $yz$ -plane) as distance downstream increases. Therefore, these data demonstrate the importance of both topographic forcing and the disparity in water surface elevations between the two tributaries in driving flow at these upland river confluences.

In Figure 5.43, it is difficult to draw particularly strong conclusions about the nature of the TKE and shear stress in the lower confluence, as a result of the limited data. However, from what can be seen in both diagrams, the centre of the downstream channel (*ii*) is the location of elevated values of TKE and shear stress. This zone is relatively limited in spatial extent, with a maximum width of approximately 1m (equating to 15% of the channel width), which agrees with the TKE data from Figure 4.20.

## **5.11 HOL Scenario Modelling at the Moor House Confluences**

Following on from the investigations into the flow dynamics at lower flows, this section tests the impact of different high discharges on the flow field at the Moor House confluences. The ability to conduct these experiments has important implications for understanding the sediment dynamics as, unlike the Arolla confluences, it is not straightforward to record flow data during the channel-forming discharges at Moor House. In conducting these tests, the aim was to use discharges close to bankfull, in order to replicate those flows which will initiate particle transport without introducing the added complication of simulating overbank flow. In addition, the simulations compared the flow fields for a true right dominated event with those dominated by flow from the true left.

Six hypothetical simulations were run using different input discharges for the upper confluence, with four different simulations used for the lower confluence. The details of these simulations are given in Table 5.6, with discharges for both the true left dominant and true right dominant cases incrementally increased until flow got close to breaching one of the banks. This section will present the results from two simulations for each confluence, in order to show the dynamics of the flow when each tributary dominates. The simulations to be presented were those which gave flows that were close to overtopping one of the banks in the model domain, although the irregular bank elevations means these cannot truly be considered to be ‘bankfull’ discharges. With reference to the gauging station data in Figure 4.2, the total discharges in these simulations (which range from 3.5m<sup>3</sup>/s to 6m<sup>3</sup>/s) can be seen to correspond to the high flows which pass through Trout Beck with a return period of 2-4 weeks.

Run Name	Discharges (cumecs)		Run Name	Discharges (cumecs)	
	TL	TR		TL	TR
LowerRun003	1	1.5	UpperRun003	1.5	1.5
LowerRun004	1.5	2	UpperRun004	2.5	1.5
LowerRun005	2	4	UpperRun005	2.5	1
LowerRun007	3	1.5	UpperRun006	4	1
			UpperRun007	4	1
			UpperRun008	1	2.5

Table 5.6: Discharges for the true left (TL) and true right (TR) inlets in the upper and lower confluence scenario models. UpperRun007 differs from UpperRun006 by having the true left inlet flow angled at 20° towards the true right bank (to account for the likely flow direction at bankfull discharges). The simulations which are not analysed in this section are in grey.

### 5.11.1 High Discharges at the Upper Confluence

For the upper confluence, the two simulations presented here are Upper Run007 and Upper Run008. Upper Run007 has a true right discharge of 1m<sup>3</sup>/s, while the true left discharge is 4m<sup>3</sup>/s. In addition, the true left inlet discharge was rotated 20° towards the true right, to better reflect the likely direction of flow in higher discharges (as can be seen looking upstream in Figure 4.1). Upper Run008, meanwhile, has a true left discharge of 1m<sup>3</sup>/s and a true right discharge of 2.5m<sup>3</sup>/s.

Figure 5.44 shows the three-dimensional view of the water surface for both simulations, while depth-averaged velocities are given in Figure 5.45. The secondary

circulation and helicity plots for UpperRun007 are in Figures 5.46 and 5.47, with the equivalents for UpperRun008 in Figures 5.48 and 5.49. Figure 5.50 then plots the downstream variations in HI for both scenarios. Finally, the modelled TKE plots for both simulations are in Figure 5.51, while the calculated bed shear stress is presented in Figure 5.52.

In Figure 5.44, there is a ridge visible in the water surface as water from the true left tributary flows over the upstream corner bar (i), but only when the true left tributary is dominant. In both cases, however, the largest fluctuation in the water surface is due to superelevation and depression as the water flows over the peat block attached to the downstream corner (ii).

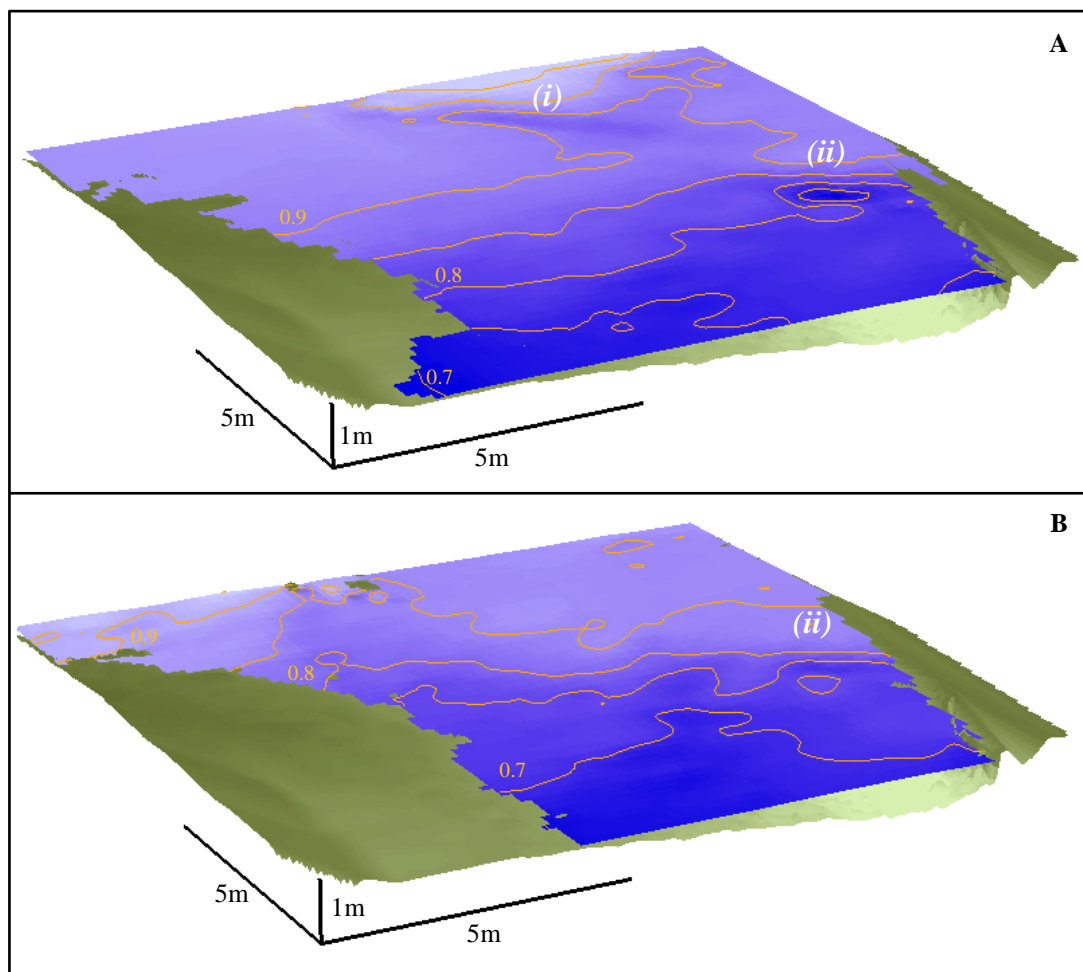


Figure 5.44: Three-dimensional view of the modelled water surface elevations for high flows at the upper Moor House confluence. Run007 (a) is a true left dominated flood and Run008 (b) is one dominated by flow from the true right.

In the plots of depth-averaged flow in Figure 5.45, the two high velocity cores are seen to be better-defined at the outlet when the true left tributary dominates (i). In addition, a dominant true left tributary changes the flow directions in the main channel



towards the true right bank (ii), making the confluence flow field look less like that of a meander bend.

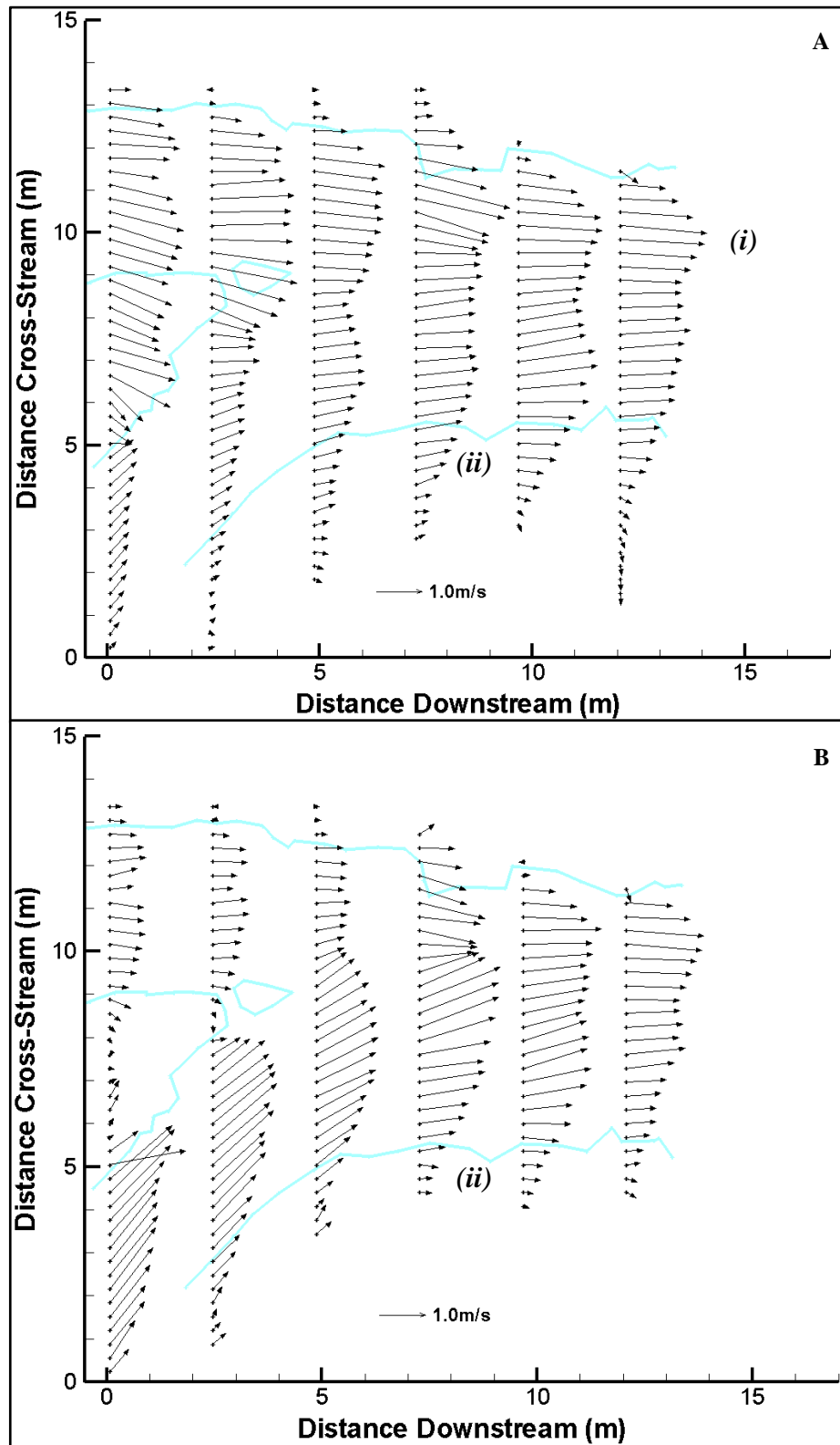


Figure 5.45: Depth-averaged flow velocities for the true-left dominated (a) and true right dominated (b) floods at the upper confluence. The measured water edge from 20<sup>th</sup> September 2011 is shown in light blue to provide a point of reference to previous figures.

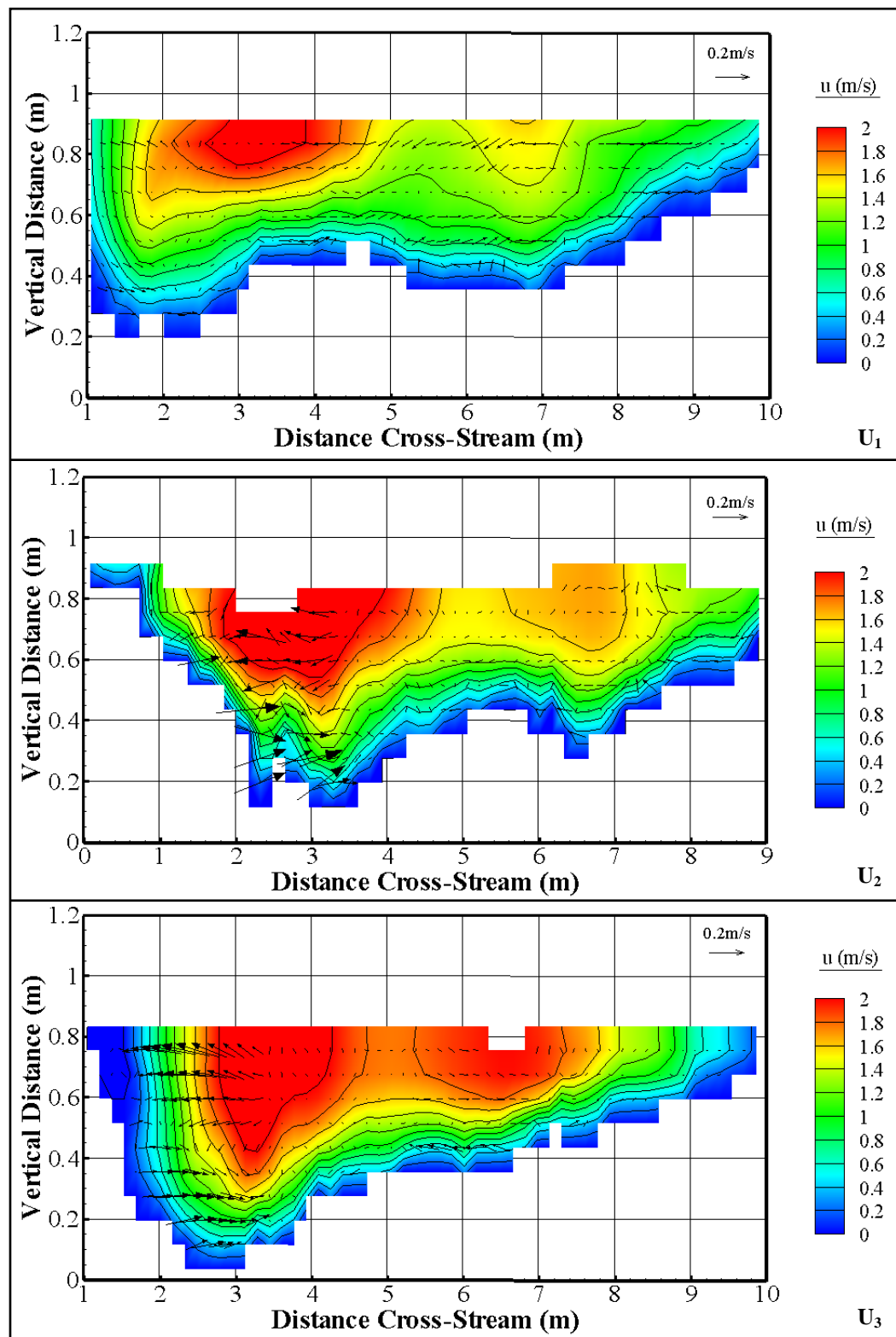


Figure 5.46: Contour and vector plots for the three cross-sections at the upper confluence, derived from the model output of UpperRun007.

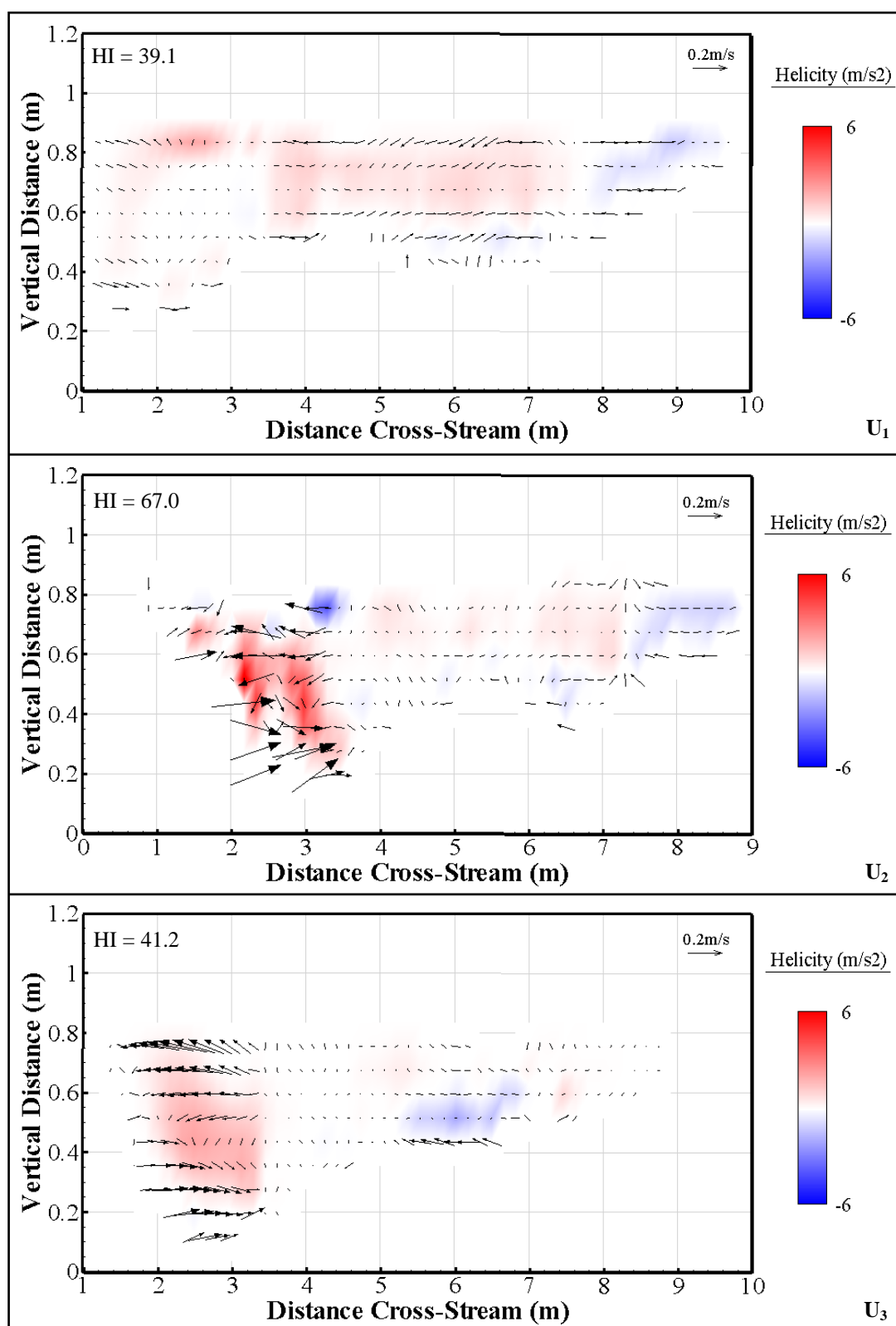


Figure 5.47: Helicity plots for three cross-sections at the upper Moor House confluence, taken from the output data of UpperRun007.

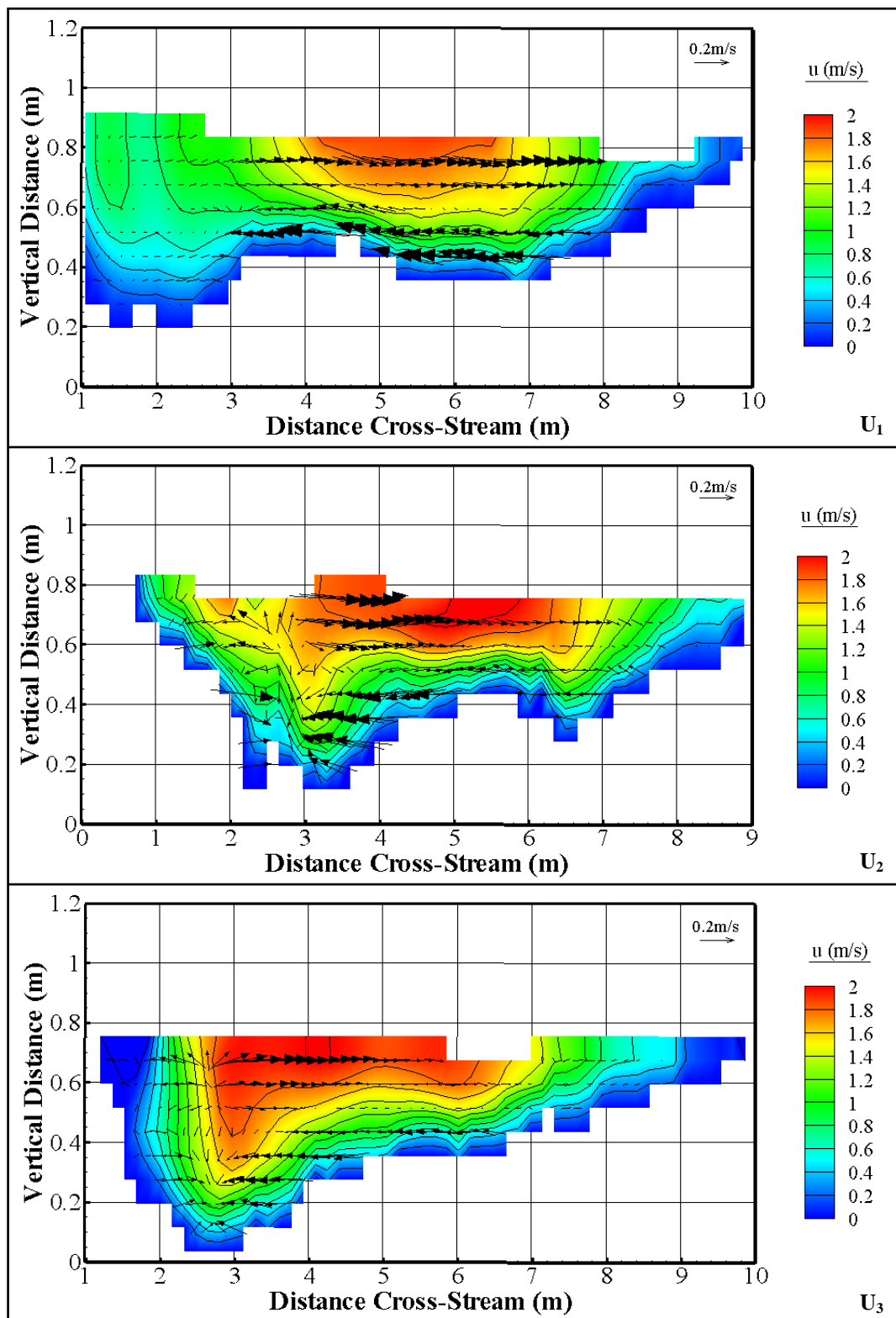


Figure 5.48: Contour and vector plots for the three upper confluence cross-sections, taken from the model output of UpperRun008.

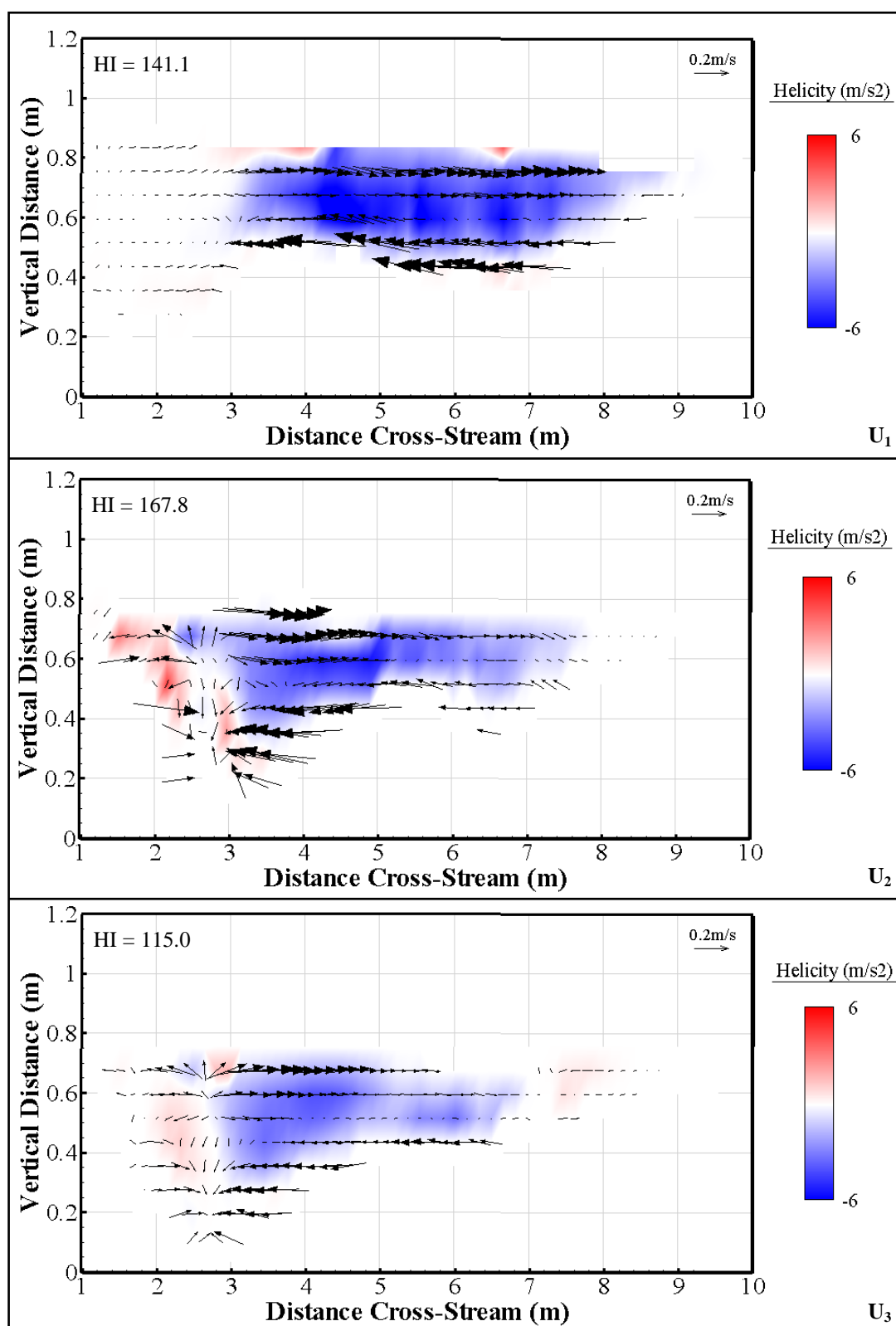


Figure 5.49: Helicity plots for the upper Moor House confluence, derived from the model output of UpperRun008.

The secondary circulation and helicity plots in Figures 5.44 to 5.47 show distinctly different patterns depending on the discharge ratio. When the true left tributary dominates (Figures 5.45 and 5.46), the two high velocity cores are distinct for longer, while the secondary circulation is generally localised and weaker. The strongest secondary flow is an anticlockwise cell associated with the constriction zone as the true left tributary enters the main channel. When the true right tributary dominates, however, there is a single high velocity core that is dominated by a strong clockwise secondary circulation cell. The effect of the flow constriction is still there, but much weaker and further towards the true left bank. Figure 5.50, meanwhile, shows HI peaks in the centre of the confluence for both scenarios, although values are lower throughout for Run007.

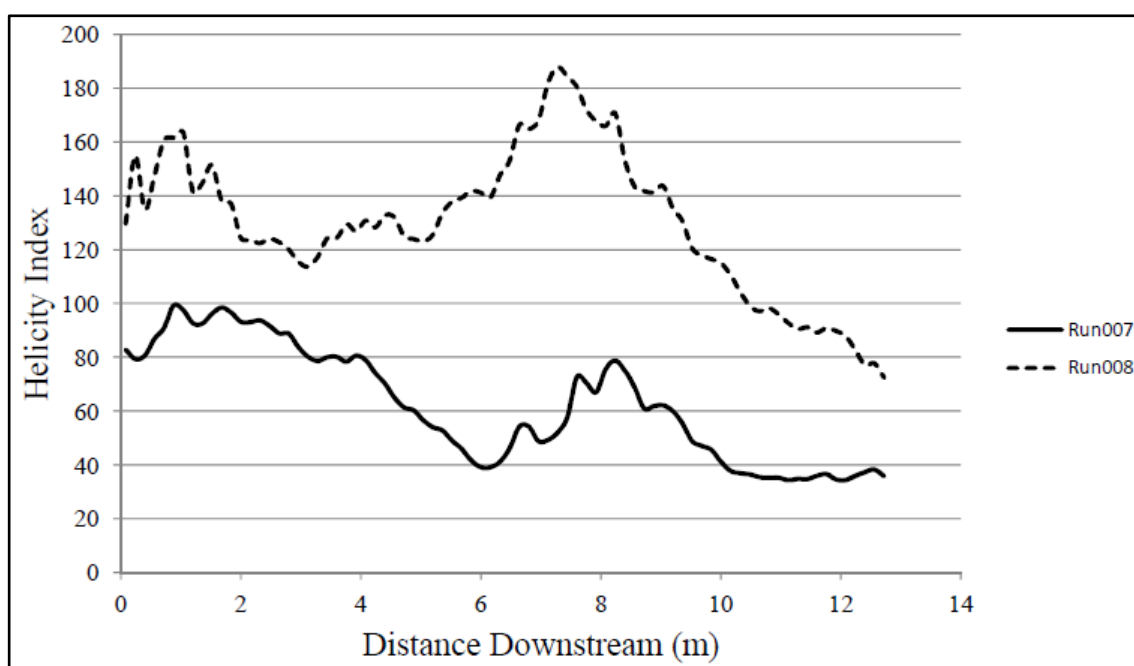


Figure 5.50: Variations in helicity index with distance downstream for UpperRun007 and UpperRun008.

The plots of TKE in Figure 5.51 show higher levels of turbulence in the true right tributary when it is dominant than *vice versa* (i). The highest TKE when the true left tributary dominates is over the upstream corner bar (ii), but in UpperRun008 this zone moves further downstream and to the right (iii), where the higher topography from the upstream bar cuts across the true right thalweg.

In Figure 5.52, the bed shear stress is seen to be higher in a dominant true right tributary than a dominant true left tributary (i), although the true left side of the upstream bar has higher values of  $\tau_0$  regardless of discharge (ii). In the case of the

dominant true left tributary in UpperRun007, bed shear stress in the true right tributary is seen to increase only once flow from the true left starts to interact with it (iii).

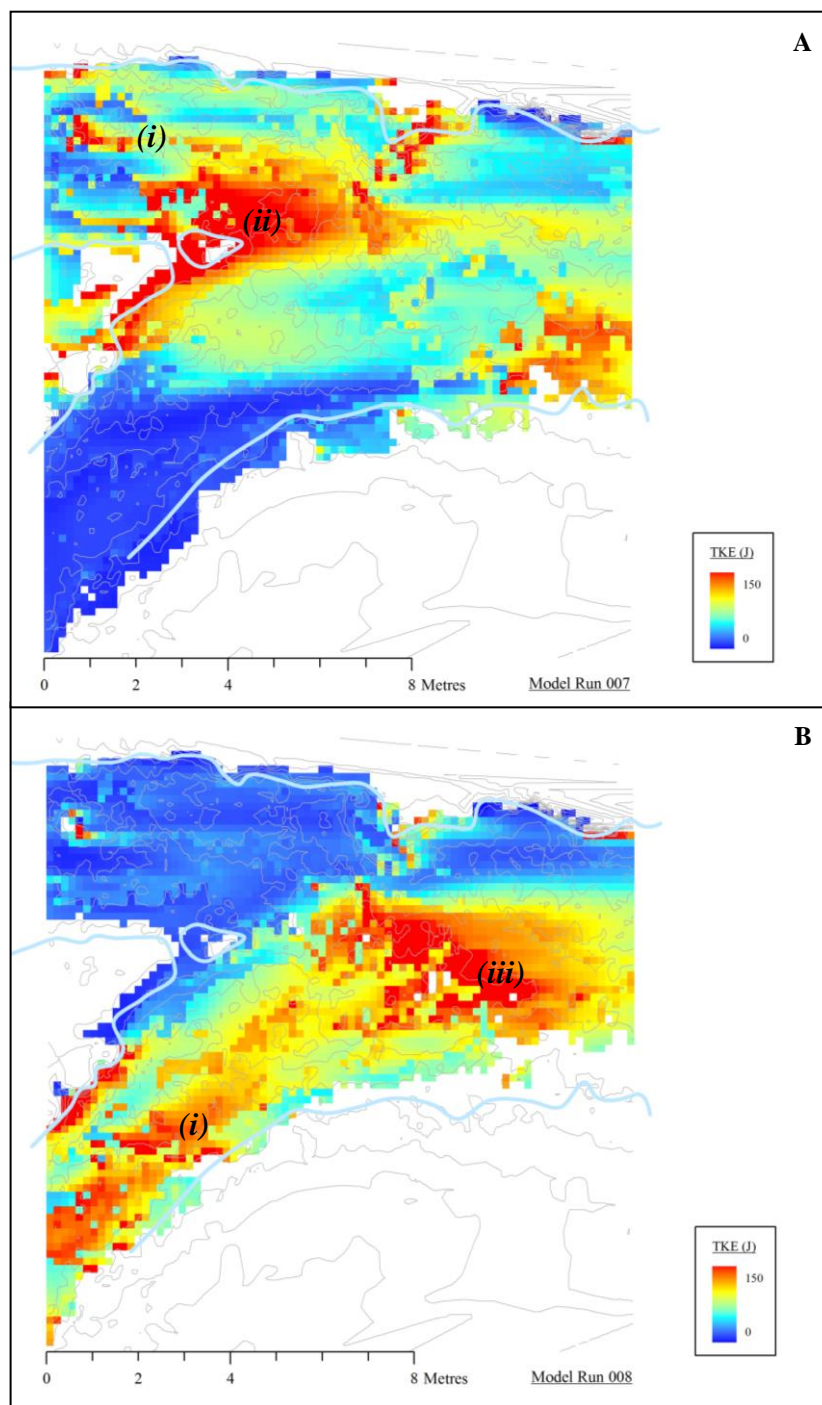


Figure 5.51: Calculated TKE for UpperRun007 (a) and UpperRun008 (b).



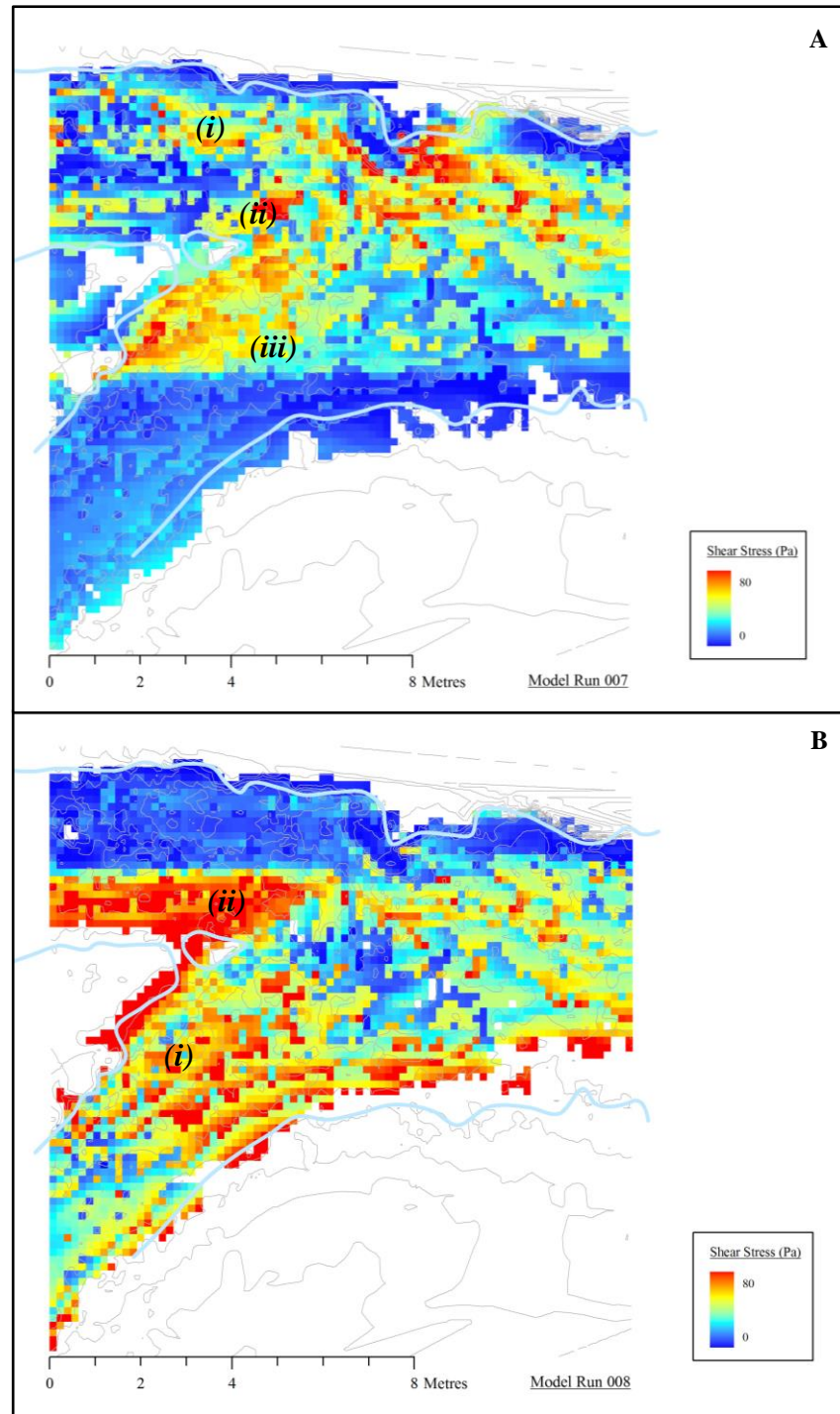


Figure 5.52: Calculated bed shear stress for UpperRun007 (a) and UpperRun008 (b).

### 5.11.2 High Discharges at the Lower Confluence

For the lower confluence, the two simulations presented in this section are Lower Run005 and Lower Run007, for which the discharges are given in Table 5.6. These are the flows which get close to overtopping the lowest part of the banks when



the true right and true left tributaries dominate respectively. Figure 5.53 shows the three-dimensional view of the water surface for both simulations. There are some minor fluctuations visible, but the surface is largely flat (i) and the channel widths are similar between the runs except near the outlet (ii).

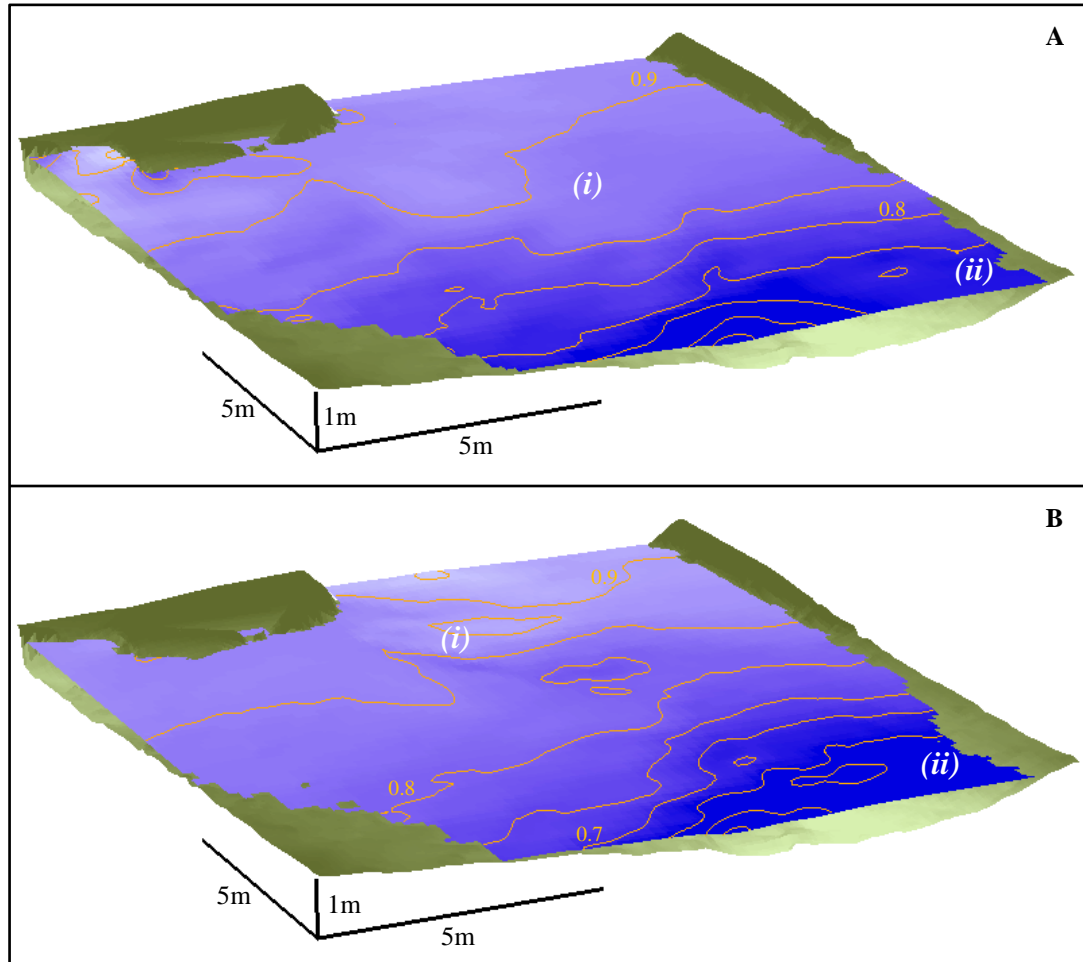


Figure 5.53: Modelled water surface elevations for the lower confluence in floods dominated by the true right tributary (LowerRun005, *a*) and the true left tributary (LowerRun007, *b*).

Figure 5.54 shows the depth-averaged velocities for both simulations. In both cases the dominant tributary is very clear (i), but this has very little impact on the zone of fastest flow in the downstream tributary (ii). The dominance of the tributaries, however, does affect the direction of the flow in the centre of the main channel (iii) with flow much further towards the true left when the true right tributary dominates.

The secondary flow and helicity plots for the two scenarios are given in Figures 5.55 to 5.58, with the long profile plot of HI in Figure 5.59.

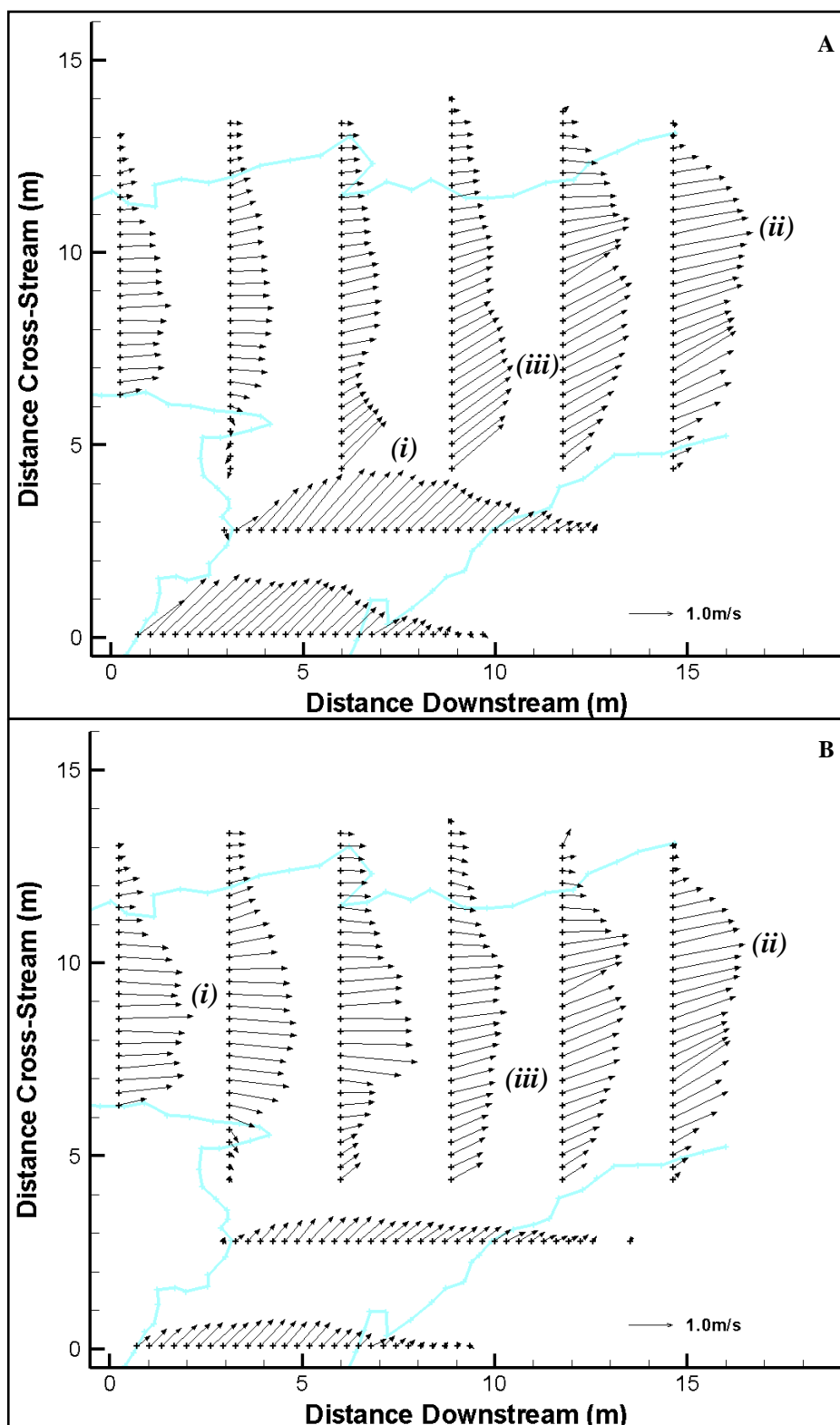


Figure 5.54: Depth-averaged flow velocities for the lower confluence in high discharges dominated by the true right (a) and true left (b) tributaries. The measured water edge from 7<sup>th</sup> October 2011 is marked in light blue for reference.

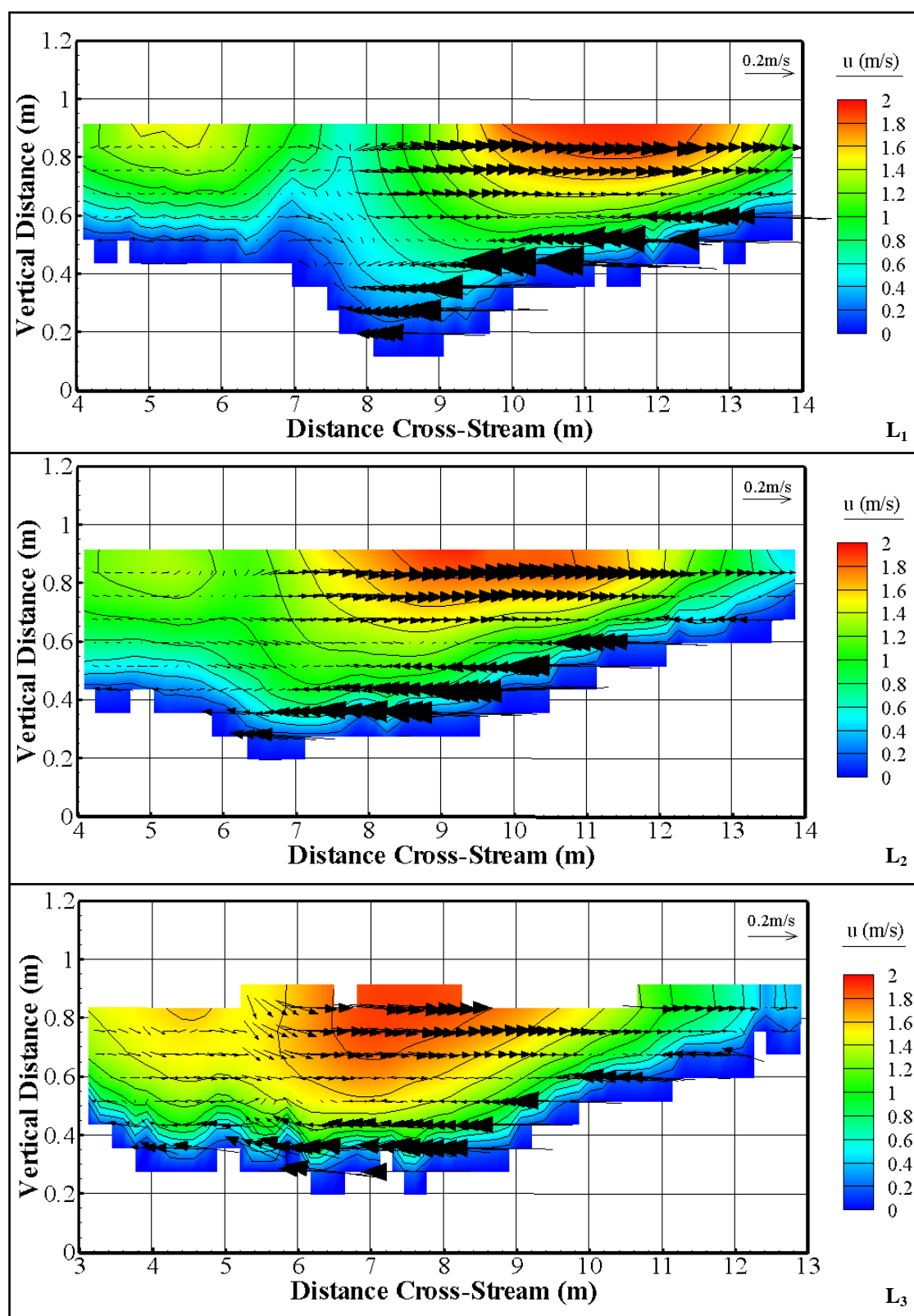


Figure 5.55: Contour and vector plots for the three lower confluence cross-sections, taken from the model output of LowerRun005.

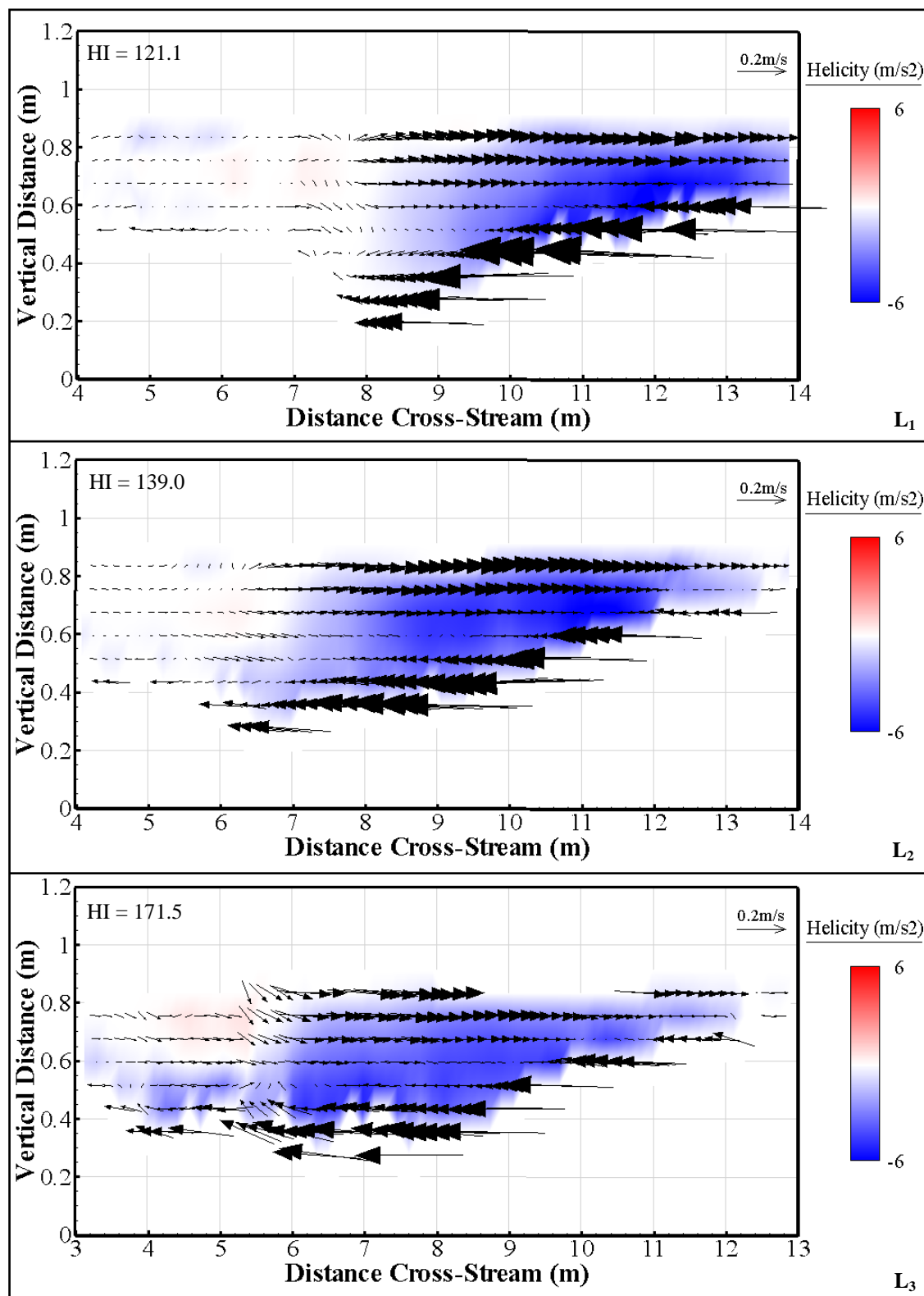


Figure 5.56: Helicity plots for the lower Moor House confluence, derived from LowerRun005.

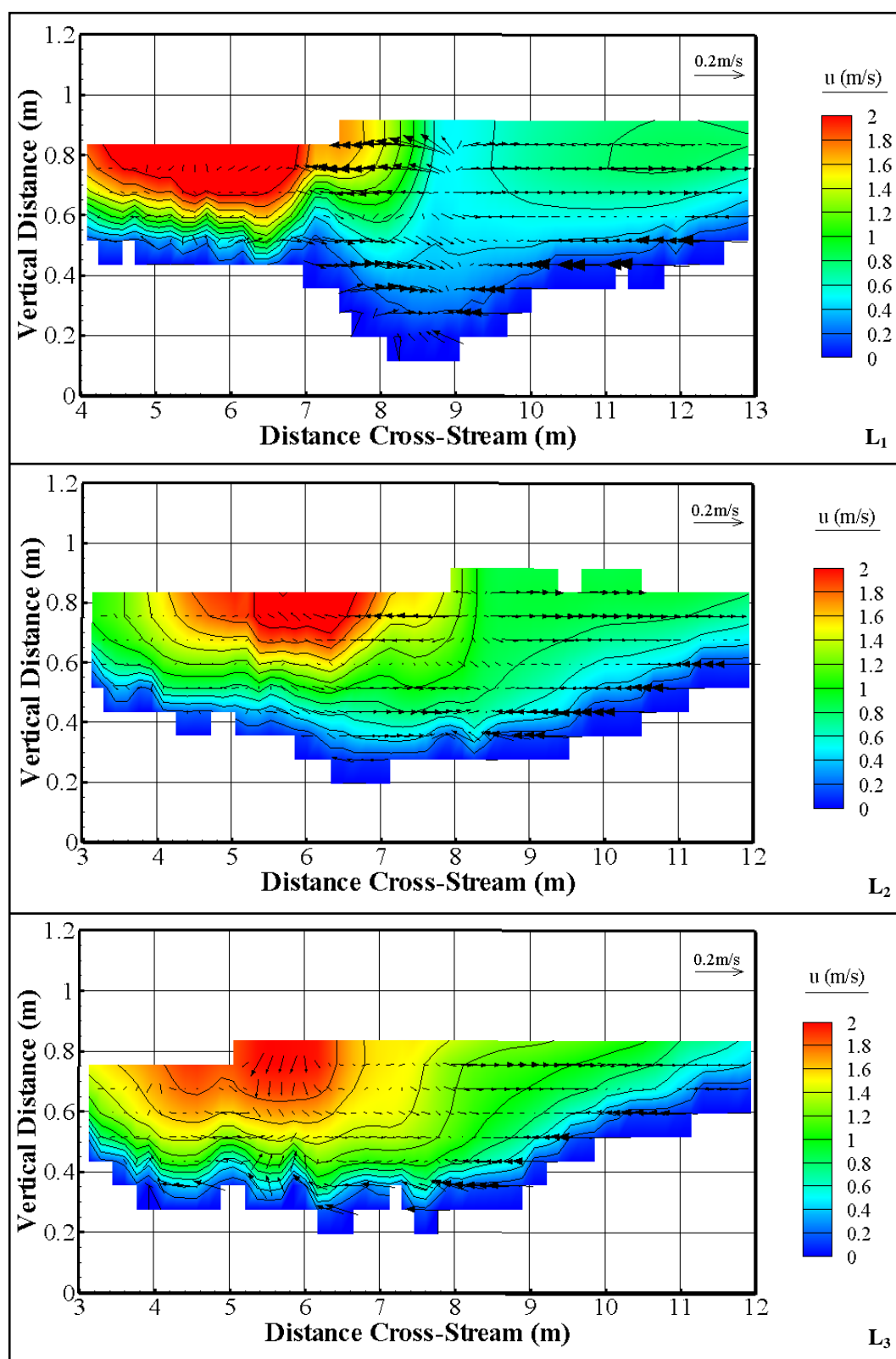


Figure 5.57: Contour and vector plots for the three cross-sections at the lower confluence, derived from the model output of LowerRun007.

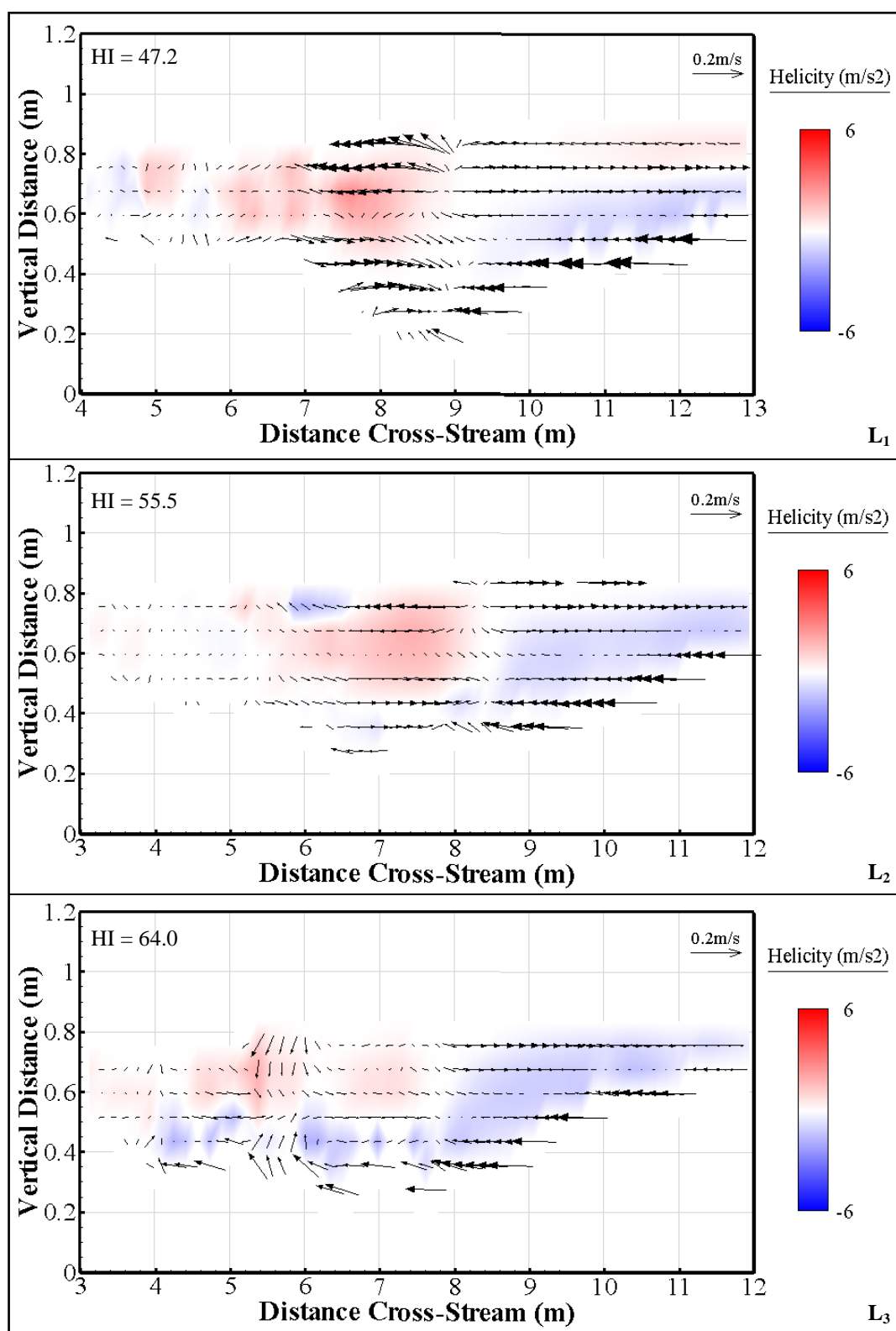


Figure 5.58: Helicity plots for the three lower confluence cross-sections, using the model output from LowerRun007.

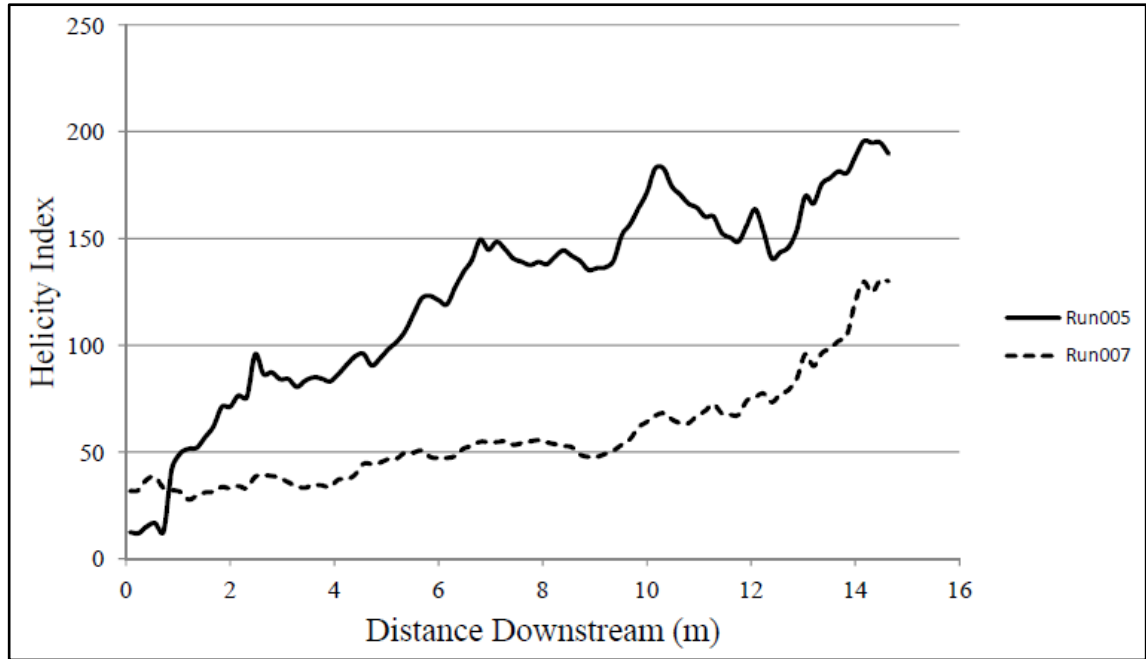


Figure 5.59: Helicity index plot for LowerRun005 (true right tributary dominant) and LowerRun007 (true left tributary dominant) at the lower Moor House confluence.

For the true right dominant case (Figures 5.55 and 5.56), there is a single, strong clockwise helical cell that dominates most of the channel width. In the true left dominant case (Figures 5.57 and 5.58), the helicity values are much weaker, although some clear patterns emerge. At the 6m cross-section, the flow from the true right tributary has anticlockwise helical flow, which weakens with distance downstream. Meanwhile, a clockwise helical cell is present in the true right half of the channel and remains weak but clearly present throughout. The secondary flow is therefore considerably more complex than at low flow or when the true right tributary dominates. In Figure 5.59, there is an increase in HI with distance downstream for both scenarios, matching the pattern in Figure 5.42. However, the localised peak as the true left tributary joins (at 6m downstream) is visible only for the true right dominant case, which corresponds to the differences found between Figures 5.56 and 5.58.

The modelled TKE is given in Figure 5.60, with its most notable feature the drop in turbulence in the lee of the step (*i*) when the true right tributary dominates. Otherwise, the TKE tends to be higher in the dominant tributary, although this zone of elevated values is less persistent if the true left tributary dominates (*ii*).

In the calculated bed shear stress plots in Figure 5.61, the shear stress in the true left tributary is high regardless of which tributary dominates (*i*). Additionally, in both



cases, the highest values of  $\tau_0$  tend to be found in a narrow zone in the centre of the main channel (ii), which corresponds to the zone of maximum velocity in Figure 5.54.

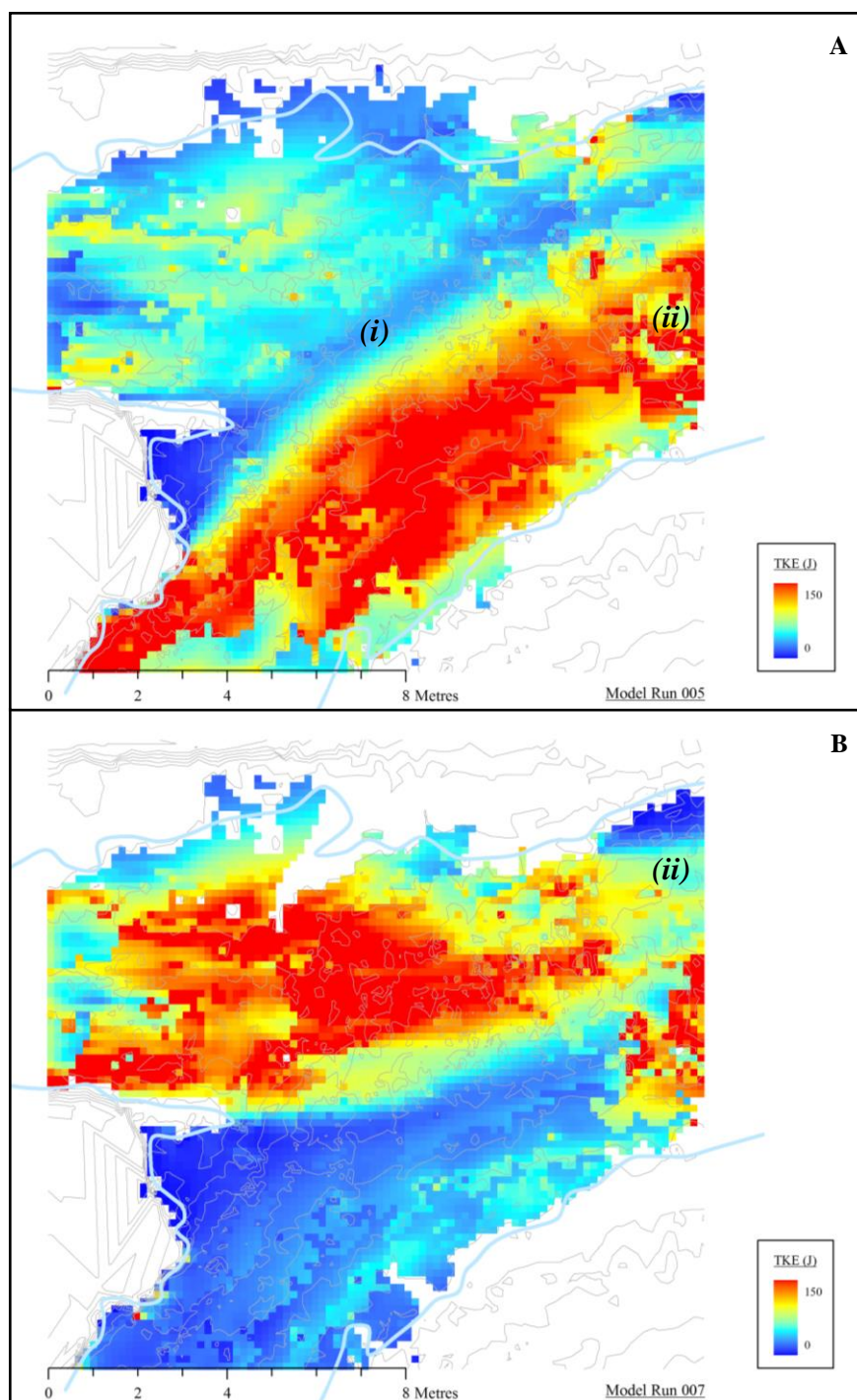


Figure 5.60: Modelled TKE for LowerRun005 (a) and LowerRun007 (b).



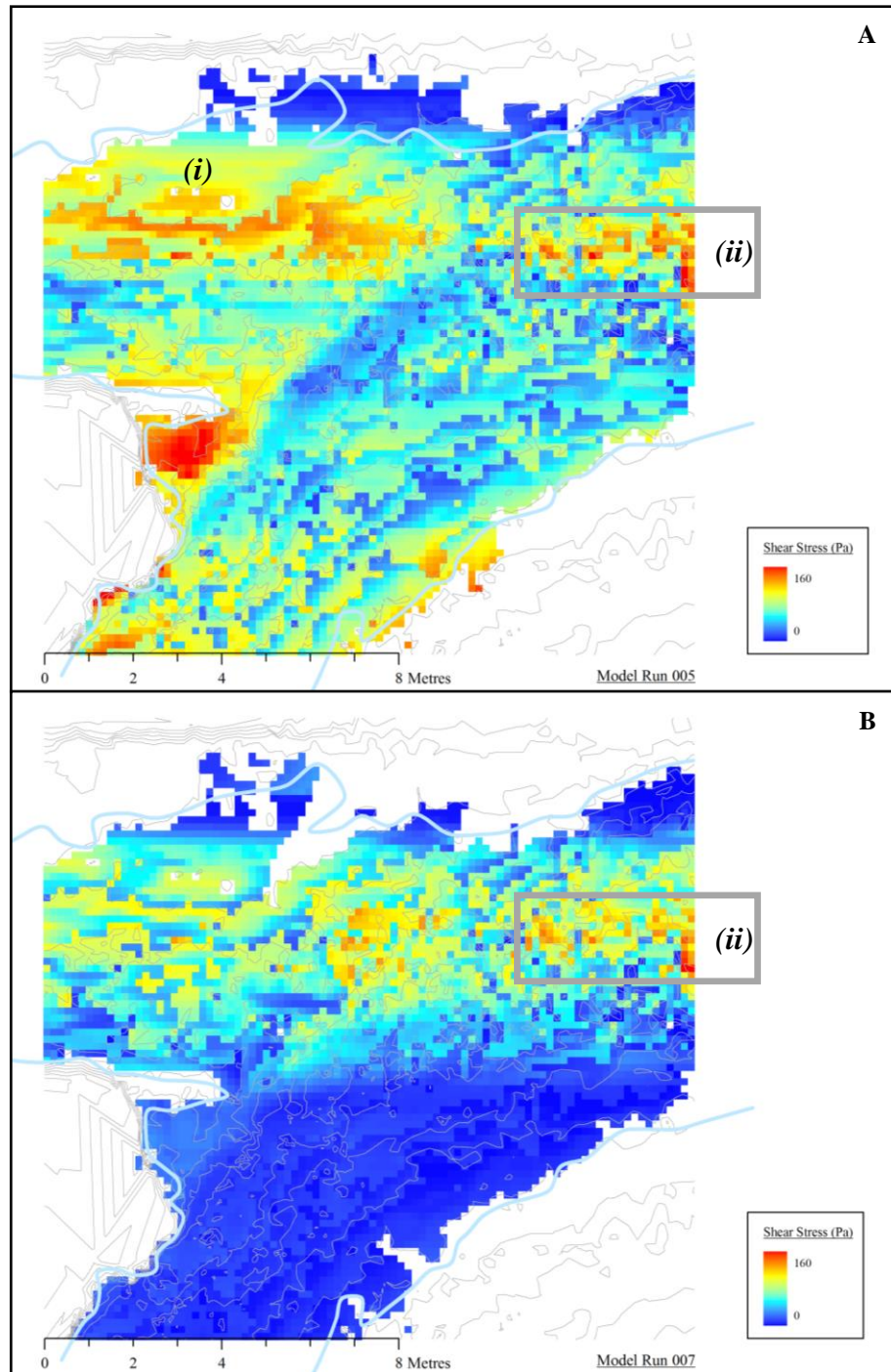


Figure 5.61: Bed shear stress calculations for the true right (a) and true left (b) dominated flows at the lower confluence. Note that due to the higher values of shear stress, the scale has been doubled from Figure 5.52.

### 5.11.3 Discussion of High Discharge Flows at the Moor House Confluences

The results from the scenario testing in this section have shown a number of differences in how the water surface and flow field respond to different discharge ratios

in high flows. However, there are also some patterns which emerge that seem to characterise flow at these more stable, upland confluences.

At the upper confluence, Figure 5.44 shows that the true left dominated simulation gives higher water surface elevations, although this is mostly explained by the higher overall discharge. The slope from true left tributary over the upstream corner bar and into the true right tributary is very clear in that case (*i*), but not when the discharge ratio is switched to favour the true right tributary. Both simulations show water surface variations over the peat block which is attached to the true left downstream corner (*ii*), suggesting its presence disrupts the confluence flow field regardless of discharge ratio. However, in general, the water surface is relatively flat.

For depth-averaged flow in Figure 5.45, when the true right tributary dominates the confluence looks more like a meander bend, with higher flow on the outside of the bend continuing into the main channel. However, in Figure 5.45a, these flow lines straighten (*ii*), leading to two separate high velocity cores persisting for longer (*i*).

For secondary circulation, in the case of a dominant true left tributary (Figures 5.46 and 5.47), the strongest helical cell is in the flow constriction zone at the exit of the true left tributary. As Figure 4.8 shows, this constriction is angled towards the true right bank (at 7m downstream), so the secondary circulation corresponds to flow that is being deflected in this direction. When the true right tributary dominates, it would be expected that the secondary flow would match that of a meander bend, with flow towards the outer bank at the surface. The evidence from the model is that the opposite occurs. The likely explanation for this is that it is a similar process to that identified at low flow for the lower confluence in Figure 5.40. With such a strong flow from the true right, water from the true left tributary has little option but to flow over top of the flow from the true right via the upstream corner bar. This would give the circulation patterns seen in Figure 5.49 and also accounts for the reduction in strength of the cell with distance downstream. The lower strength of the helical flow at the exit of the true left tributary ( $U_2$  in Figure 5.49) supports this hypothesis, as it implies that proportionally less of the flow from the true left tributary is entering the confluence via the flow constriction zone. This process would also help to explain why the peak in helicity index (from Figure 5.50) is slightly further upstream when the true right tributary dominates, as the main secondary flow is associated with the upstream corner bar rather than the flow constriction zone at its downstream edge.

In terms of the calculated TKE in Figure 5.51, when the true left tributary dominates the submerged upstream corner bar is the zone of highest TKE (*ii*). This then leads to an elevated zone of TKE in the main channel off the downstream edge of the submerged bar. When the true right tributary dominates it is the downstream extent of this bar which causes the highest TKE. The ridge of sediment from the bar cuts across the thalweg of the true right tributary, giving shallower water (*iii*) and suggesting that it is the bed interacting with the flow which results in the zones of higher turbulence.

For shear stress in Figure 5.52, values are typically higher in the more dominant tributary (*i*). However, there are some exceptions, with the true left edge of the submerged bar seeing higher shear stress values regardless of the respective discharges (*ii*). The true left tributary has generally lower values of  $\tau_0$ , which suggests that with the exception of particles situated on the submerged bar, sediment transport will not be as high from the true left channel as from the true right.

For the lower confluence, the three-dimensional water surface plots in Figure 5.50 again show very little variability in the water surface, with the possible exception of a ridge as the water flows over the step in Figure 5.53b (*i*). The water levels are slightly higher and the downstream channel slightly wider for the true right dominated case (*ii*), which is to be expected given the higher total discharge. However, the limited amount of water surface variability implies that high discharge events at both Moor House confluences will have different flow characteristics to those at the Arolla confluences (which Figures 5.26b and 5.31b show to have much greater water surface fluctuations).

In Figure 5.54, the depth-averaged flow velocities show a similar pattern to that for the upper confluence. A dominant true right tributary makes the confluence more similar to a meander bend, while a dominant true left tributary straightens the flow angles (*iii*). However, the effect is not as marked as for the upper confluence, with the flow angles always tending towards the true left bank of the main channel. In both cases a single high velocity core develops quickly in the main channel, regardless of the discharge ratio (*ii*).

With respect to secondary circulation, in the true right dominant case the single clockwise flow cell in Figures 5.55 and 5.56 appears to be an extension of the phenomenon recorded in the field (Figure 4.17) and in the low flow simulations (Figure 5.40), where the bed discordance routes water from the true left tributary over the top of that from the true right. The HI plot for this scenario in Figure 5.59 also has a similar

pattern to that for low flow conditions (Figure 5.42). For the true left dominant case, meanwhile, the clockwise flow cell at the 6m cross-section in Figures 5.57 and 5.58 is similar to that which would be expected in a meander bend and so may be due to the curvature of the tributary before it enters the confluence. As the two flows start to mix, the flow from the edge of the true left tributary will also provide a blocking force which helps to maintain this helical cell. However, further downstream the impact of the true left tributary is much greater, pushing the helical cell that is characteristic of the lower confluence at low flow towards the true right bank. The dominance of the true left tributary therefore seems to be largely negating the impact of the discordant bed in this scenario, which has the side-effect of reducing the overall strength of the helical flow cells (Figure 5.59).

The TKE plots in Figure 5.60 show the higher values are associated with the tributary which dominates. However, when the true right tributary dominates, there is evidence of a zone of much less turbulent water in the lee of the step (*i*). If the true left dominates, this feature is not present, at least in the centre of the water column from which the data in Figure 5.60 were taken. It is possible, therefore, that at locations closer to the bed there is still a sheltering effect. When the true left tributary is dominant, the higher TKE in the true left channel persists into the main channel before weakening, whereas a dominant true right tributary results in higher TKE values on the true right side of the confluence throughout the domain (*ii*). This may be due to the shallower water on the true right encouraging the constant generation of turbulence over the irregular bed, whereas water from the true left tributary flows over the step and into deeper water, where dissipation would be more likely. However, further experiments would be needed to test this hypothesis.

The shear stress patterns in Figure 5.61 show much variability, with higher flows from the true right giving higher bed shear stresses in the centre of the true left tributary than if the true left is dominant (*i*). In both cases, however, there is a region of elevated bed shear stress in the zone of maximum velocity (*ii*), implying that the impact of discharge ratio on sediment transport in the main channel is relatively limited. When the true left tributary dominates, meanwhile, the shear stress seems to increase slightly upon entering the main channel, rather than weakening. This may be due to shallower flows over the step into the main channel or could be associated with the known variations in flow direction through the water column in this part of the confluence (Figures 4.17 and 5.40). However, a higher resolution study using both field and

numerical experiments would be needed to obtain greater insight into the local processes operating in this part of the confluence.

## 5.12 Interpreting the Flow Dynamics at the Arolla Confluences

Having validated the model in Sections 5.6 to 5.8, one of the key advantages of using the HOL model to simulate the Arolla confluences is that more detail can be obtained on the flow dynamics than was possible from field data alone. This section will explore the two confluences in more detail before discussing the extent to which the flow field changes as the water surface slope increases.

### 5.12.1 Flow Dynamics at Confluence G

Figure 5.62 shows the modelled depth-averaged flow field for Confluence G, while Figures 5.63 and 5.64 show the secondary circulation and helicity values respectively at three equally-spaced cross-sections.

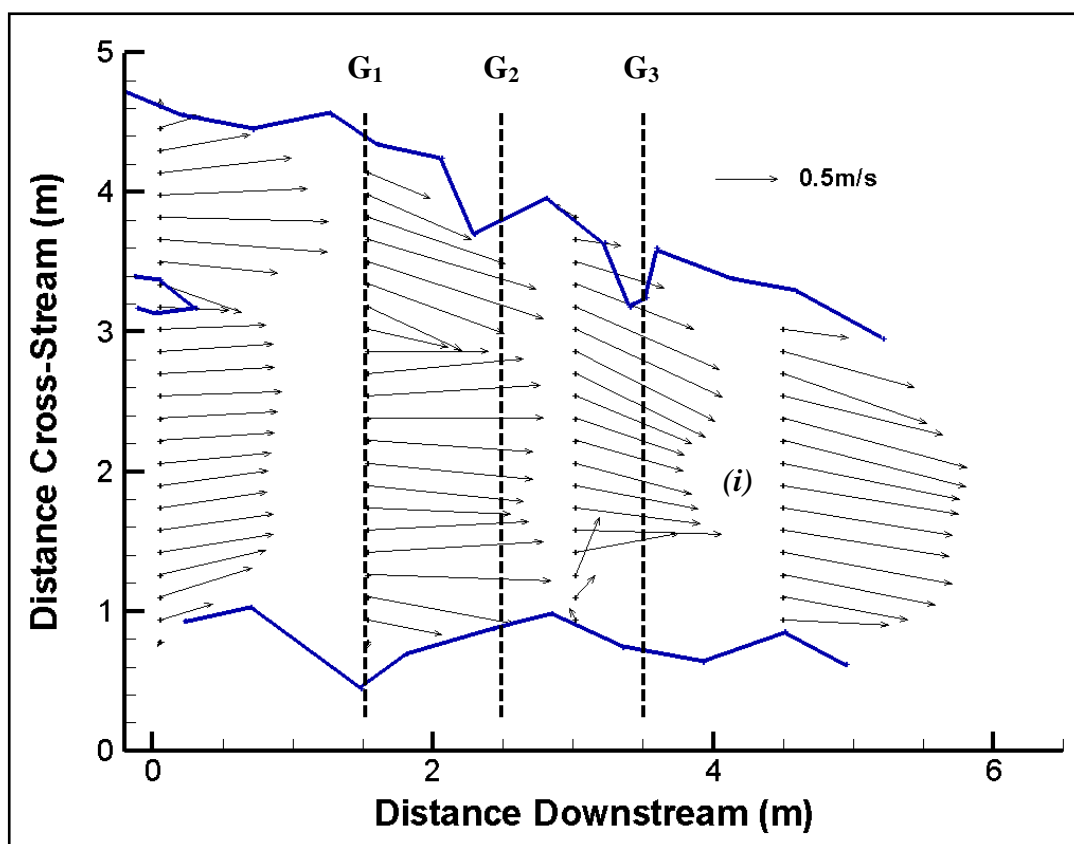


Figure 5.62: Plan view of the depth-averaged flow velocities from the model of Confluence G. The dashed lines show the locations of the cross-sections used to investigate helicity.

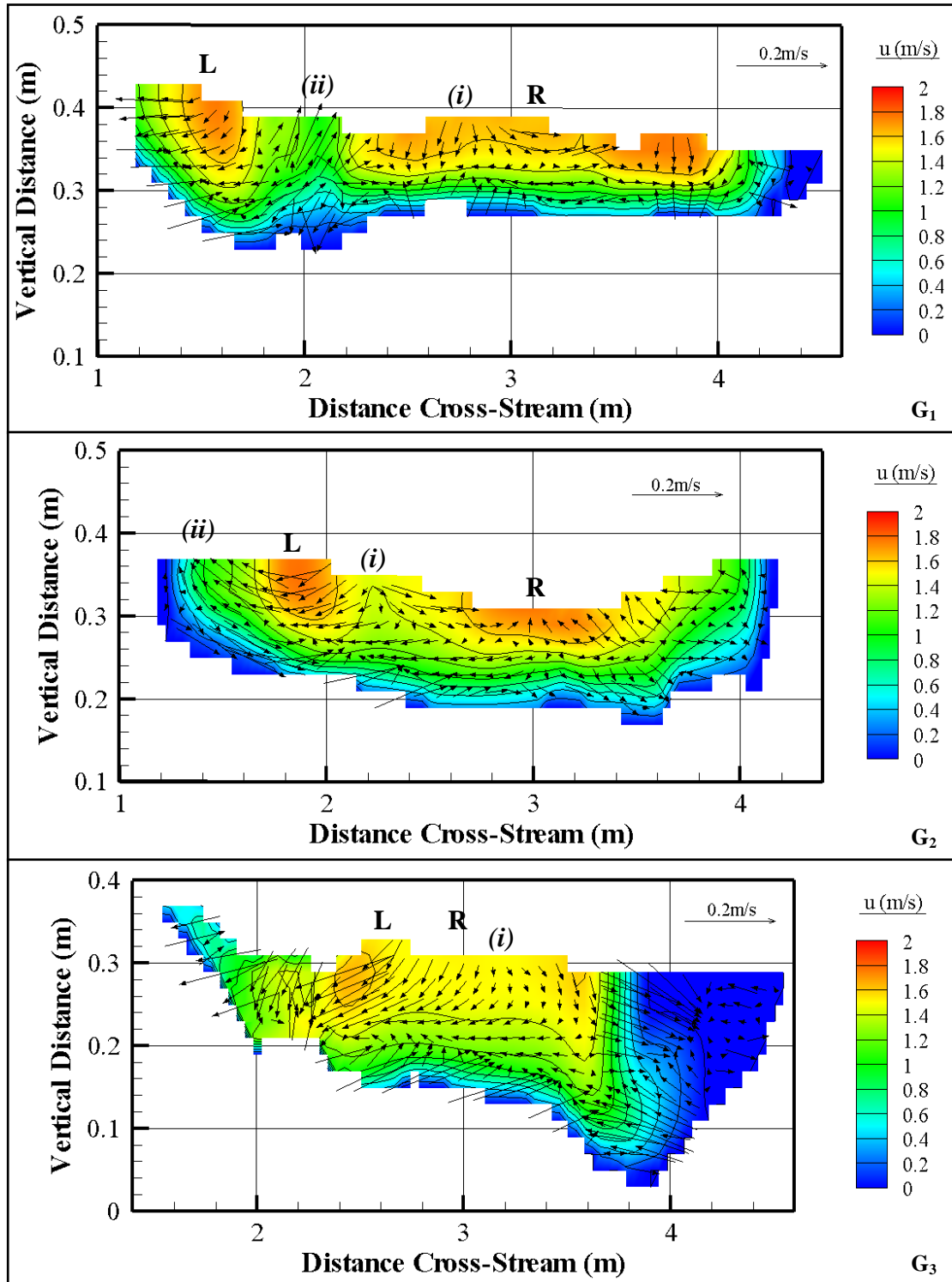


Figure 5.63: Contour and vector plots for three cross-sections in Confluence G, with downstream velocity given by the contours. Local deviations from the depth-averaged cross-stream and vertical velocities are shown by the vectors. For all Arolla confluence plots the arrowheads are kept constant in size due to the higher grid resolution. The high velocity cores from the true left and true right tributaries are denoted by 'L' and 'R' respectively.

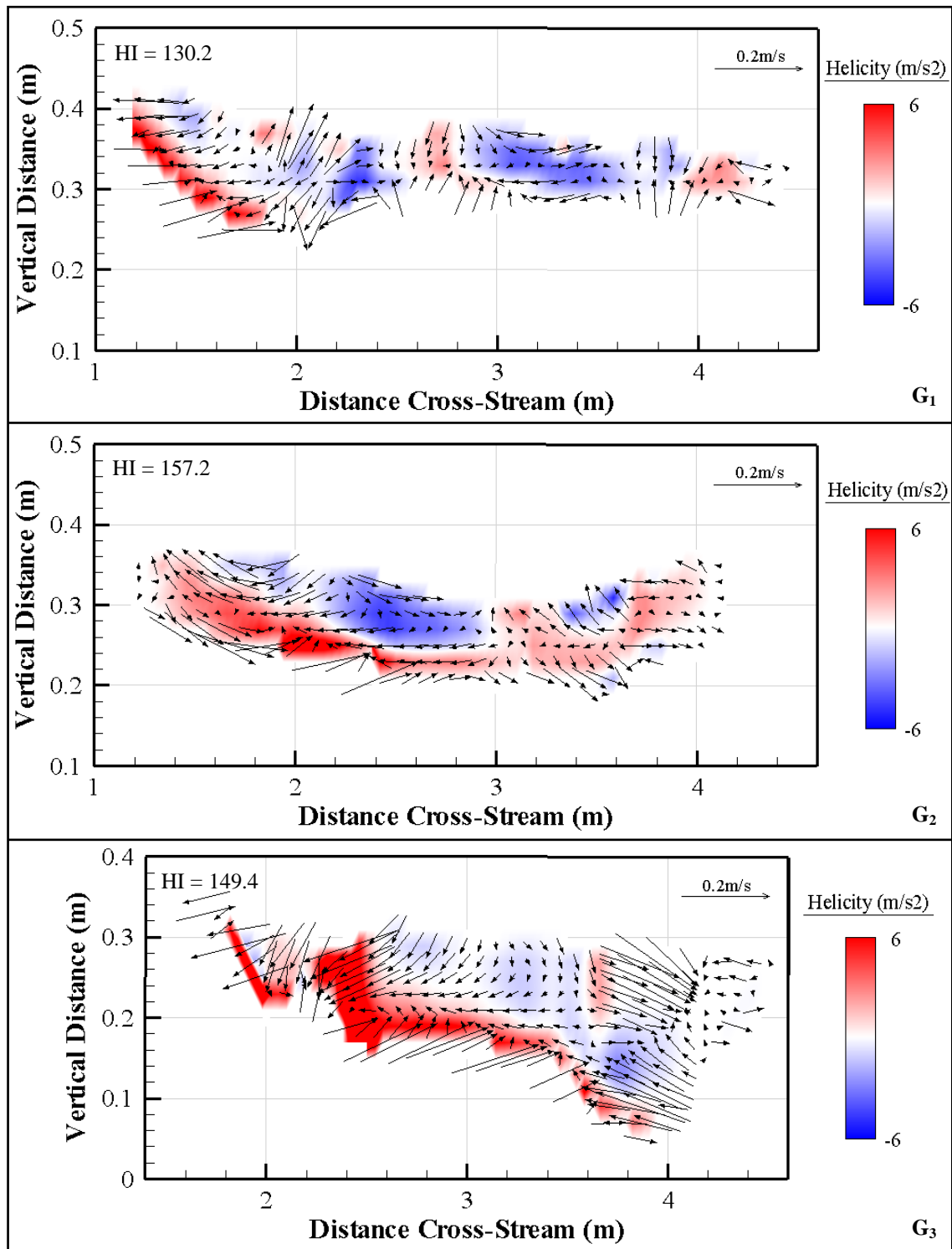


Figure 5.64: Helicity plots for the three Confluence G cross-sections.

Figure 5.65 shows the TKE and shear stress calculated from the model, while Figure 5.66 plots the variations in HI, TKE, shear stress and water surface elevation in the downstream direction.



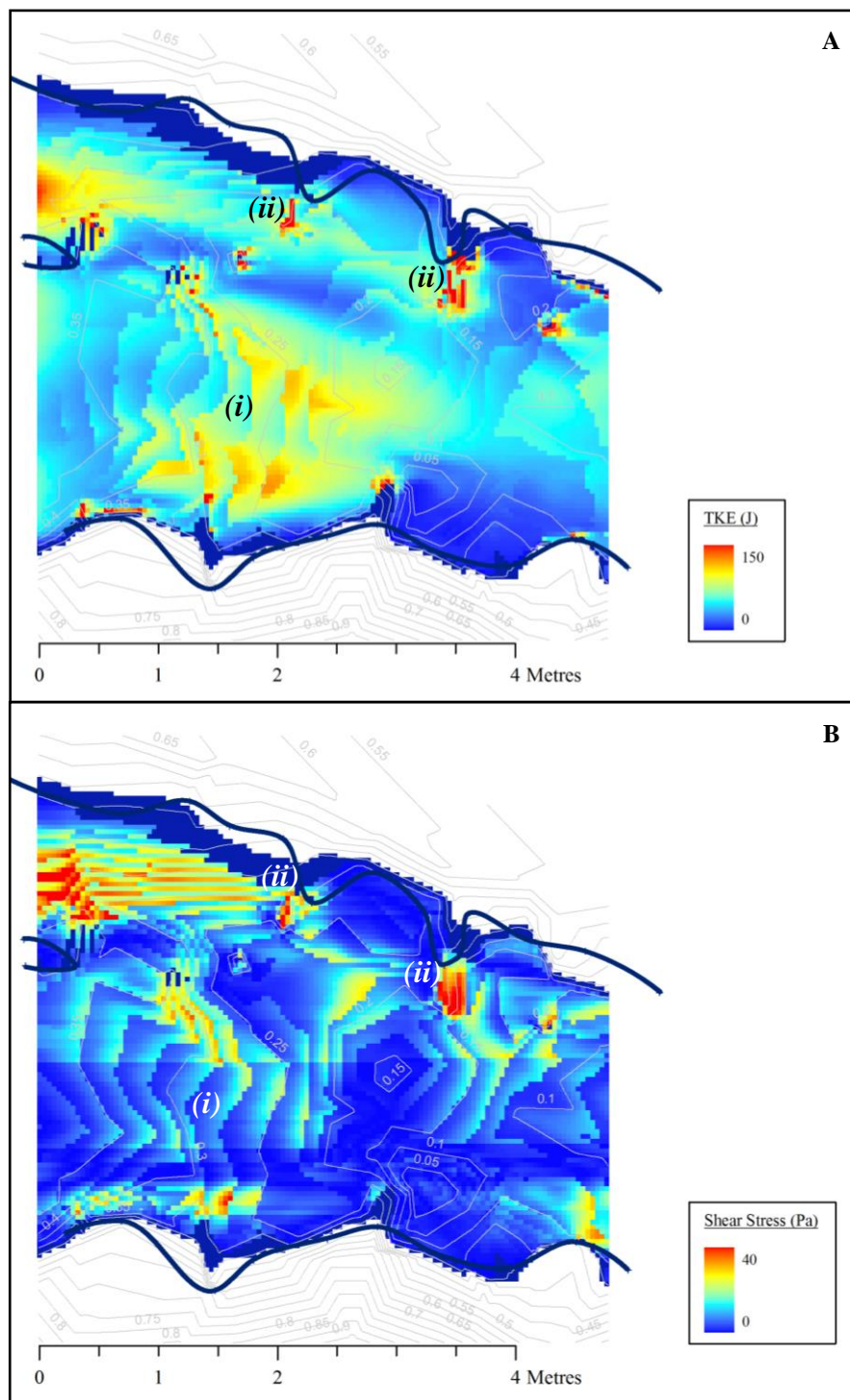


Figure 5.65: Turbulent kinetic energy (a) and bed shear stress (b) plots using the modelled data from Confluence G. Cells in navy blue have no data due to the shallow nature of the flow.



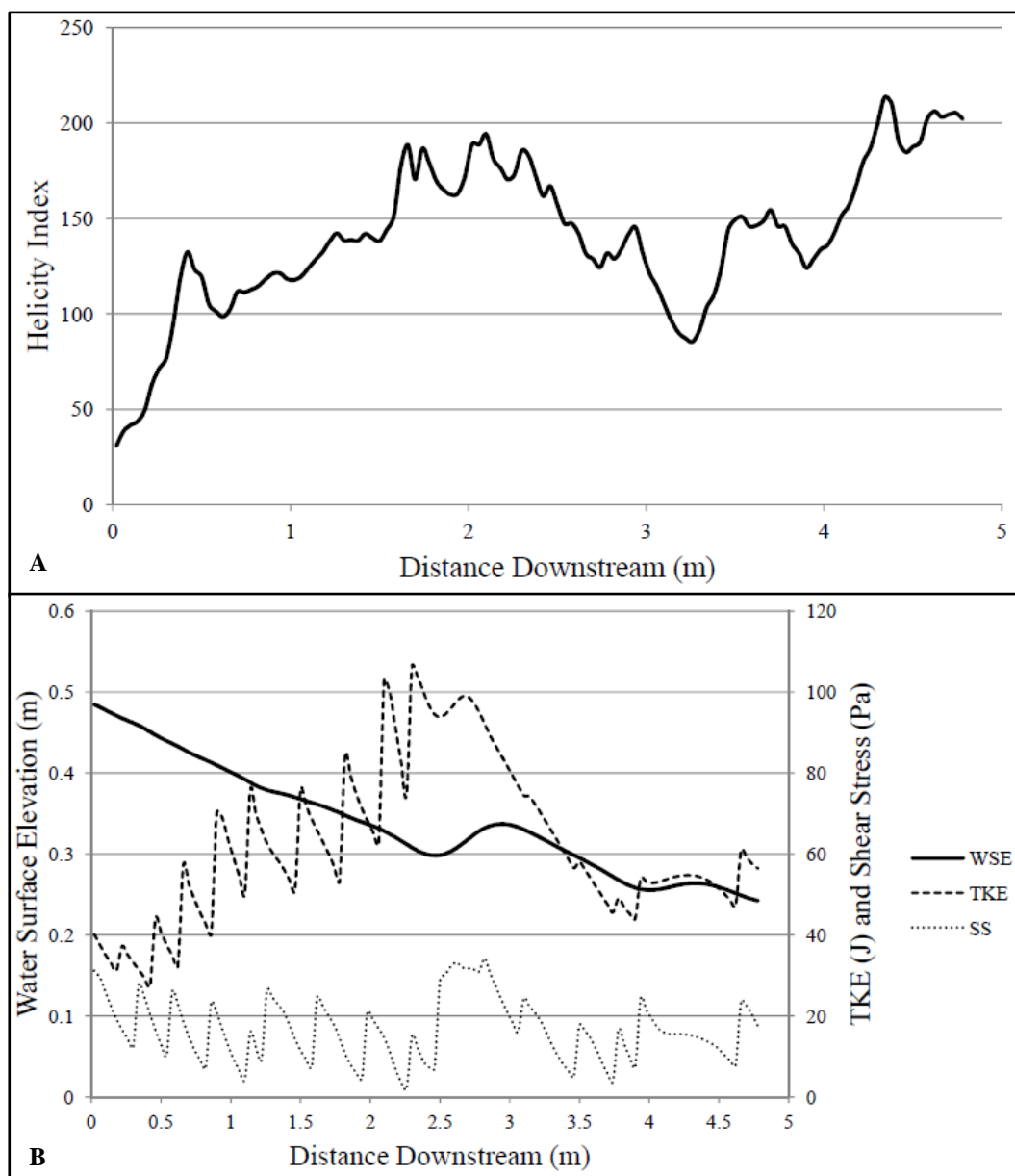


Figure 5.66: Variations in helicity index in Confluence G (a) and a plot of turbulent kinetic energy (TKE), bed shear stress (SS) and water surface elevation (WSE) against distance downstream (b). The values in (b) are taken from along a straight line drawn at 1.94m from the true right bank.

In Figure 5.62, the flow velocities are very similar across each cross-section, with a tendency for lower velocities nearer the bank (as found in Section 4.11.2). The two high velocity cores from the tributary merge within 1-2 channel widths (*i*), which is quick for a confluence with a junction angle close to  $0^\circ$ .

In Figure 5.63, the high velocity cores from the left and right tributaries are marked and like Figure 5.62 show a rapid transformation to a single core. Also highlighted are areas where higher water surface elevations are giving downwelling (*i*) and zones of upwelling that result in the subsequent relative increase in the water level

(ii) further downstream. The helicity plots in Figure 5.64 demonstrate the presence of lots of strong, localised helical cells, but there are no large-scale structures that extend over a substantial proportion of the channel. In the downstream direction, meanwhile, Figure 5.66a shows much variation in HI through the confluence but few obvious patterns. The exception is a sharp increase in the first 0.5m, which suggests the joining of the two tributary flows may help to increase the overall helicity.

In Figure 5.65, the TKE and bed shear stress patterns are dominated by two processes: the apparent pulsing of the values in the downstream direction (i) and the tendency for particularly high turbulence and bed shear stress around isolated topographic features or obstacles (ii). In order to try to explain the process at (i), Figure 5.66b takes a line through the centre of the true right and downstream channels (at 1.94m from the true right bank) to compare the fluctuations in TKE and bed shear stress against the water surface elevation. This shows that the small-scale variations are superimposed on top of a separate, larger variability. The second of these patterns shows peaks in both shear stress and TKE in water surface depressions and lower values under localised highs in the water surface. The small-scale, fluctuations, meanwhile, show no particular pattern and are therefore likely to be due to the method used to select the appropriate data from a discretised mesh.

### 5.12.2 Flow Dynamics at Confluence H

Figure 5.67 presents the modelled depth-averaged flow velocities for Confluence H. The vectors can be seen to primarily follow the downstream direction, with the two separate cores of higher velocity appearing to merge by the outlet (i). There is some deflection of the two tributary flows (ii), as shown by the dashed red lines, although this is quite limited until the divergence at the final cross-section.

The secondary flow and helicity in Confluence H is investigated further in Figures 5.68 and 5.69, while Figure 5.70 shows the calculated TKE and shear stress in Confluence H. Downstream variations in HI, TKE, bed shear stress and WSE are shown in Figure 5.71.

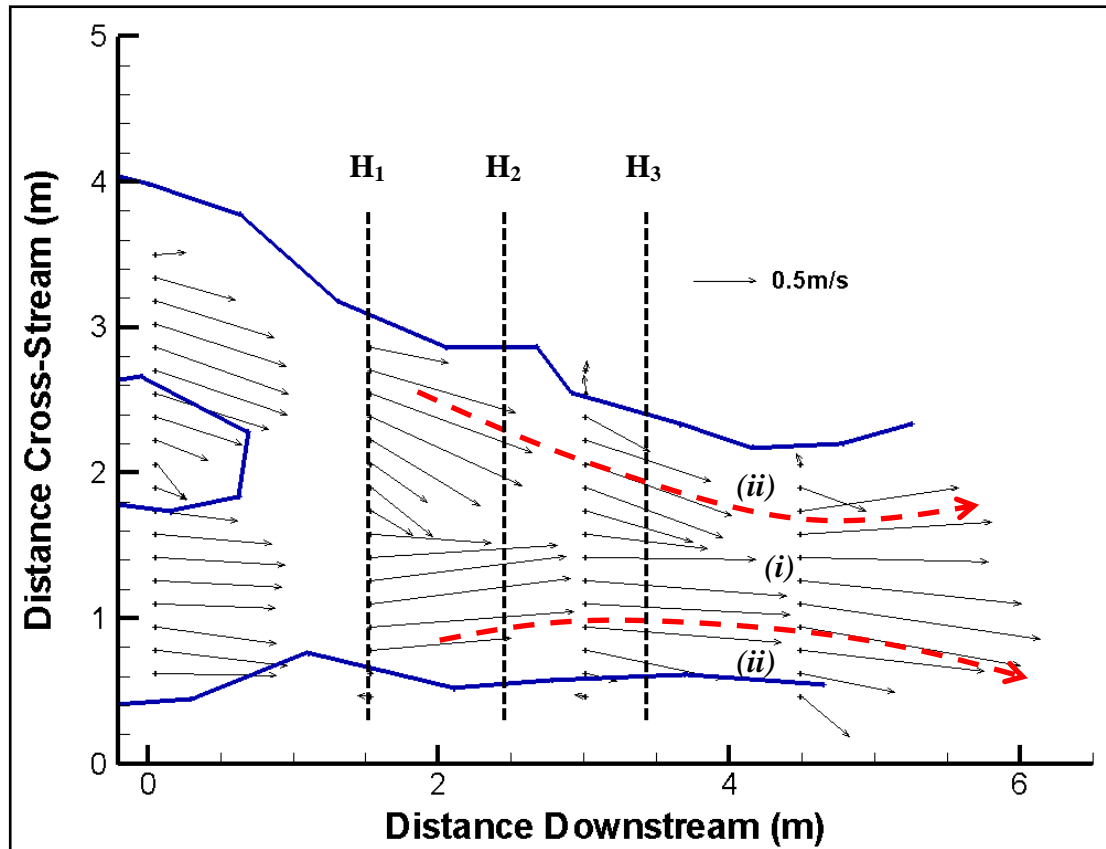


Figure 5.67: Depth-averaged flow velocities for Confluence H calculated from the model output. The dashed red line shows approximate flow lines for the two tributary flows and highlights the flow deflection at the downstream end of the confluence. The dashed black lines show the cross-section locations.

In Figure 5.68, the two high velocity cores can be seen to start merging into one, although the process is incomplete by the final cross-section. Secondary circulation cells are marked by white arrows, as well as the topographic highs that encourage downwelling (i) and upwelling that encourages a higher relative water surface further downstream (ii). The helicity plots in Figure 5.69 show that the cross-sections appear to be dominated by two separate anticlockwise helical cells which weaken and merge with distance downstream. However, in the true left tributary, there are anomalously high secondary velocities near the bed which may be largely responsible for the anticlockwise direction of the circulation cells. Figure 5.71a, meanwhile, shows a peak in HI at 1.5m downstream and a tendency for the values to rise after 3.5m. Like Confluence G, the former may be due to the two tributary flows meeting. For the latter, however, the increases in HI may be linked to the greater mutual flow deflection identified at (ii) in Figure 5.67.

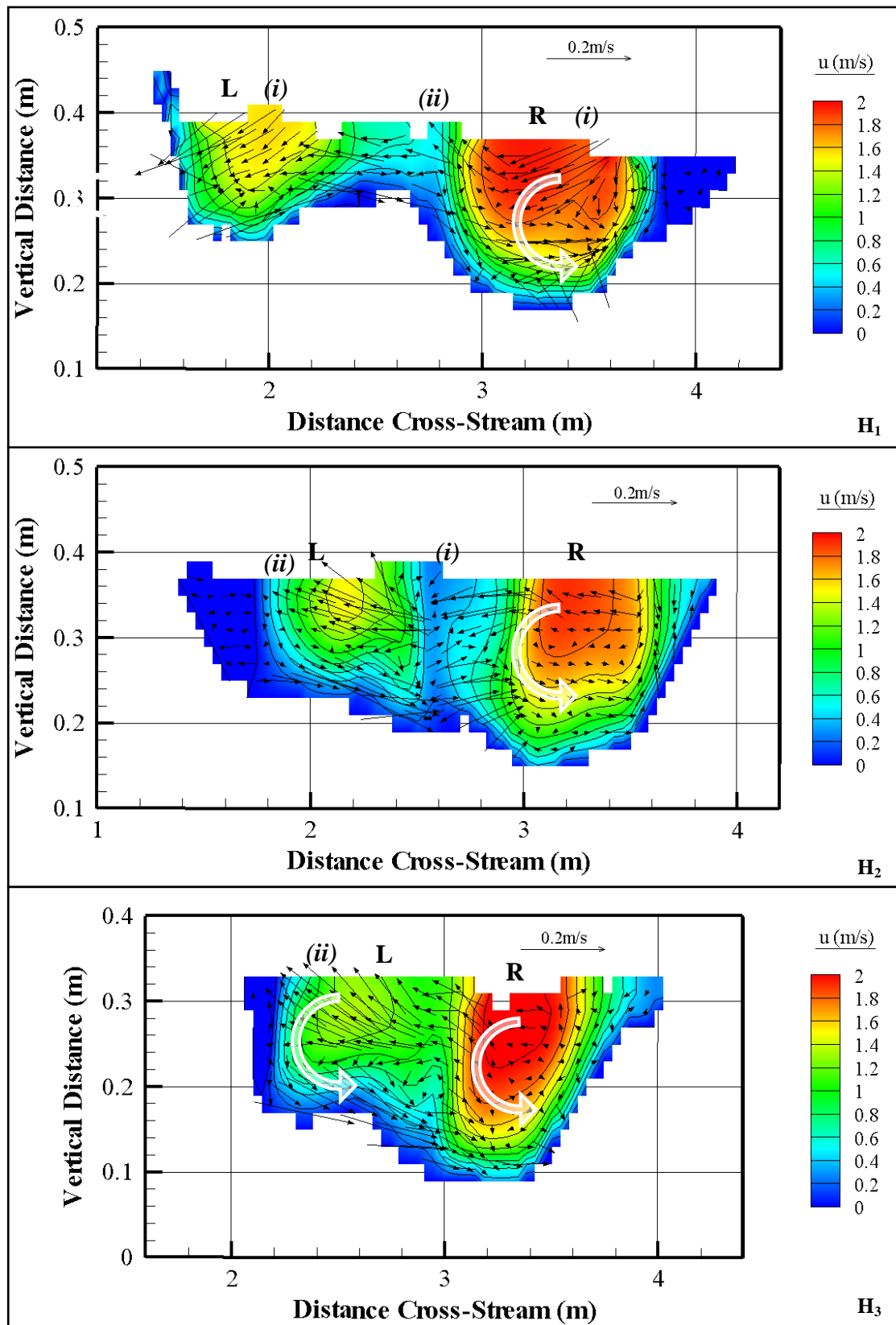


Figure 5.68: Contour and vector plots for three cross-sections in the centre of Confluence H. The plot style is the same as for Figure 5.63, with the addition of white circular arrows to highlight secondary flow cells.

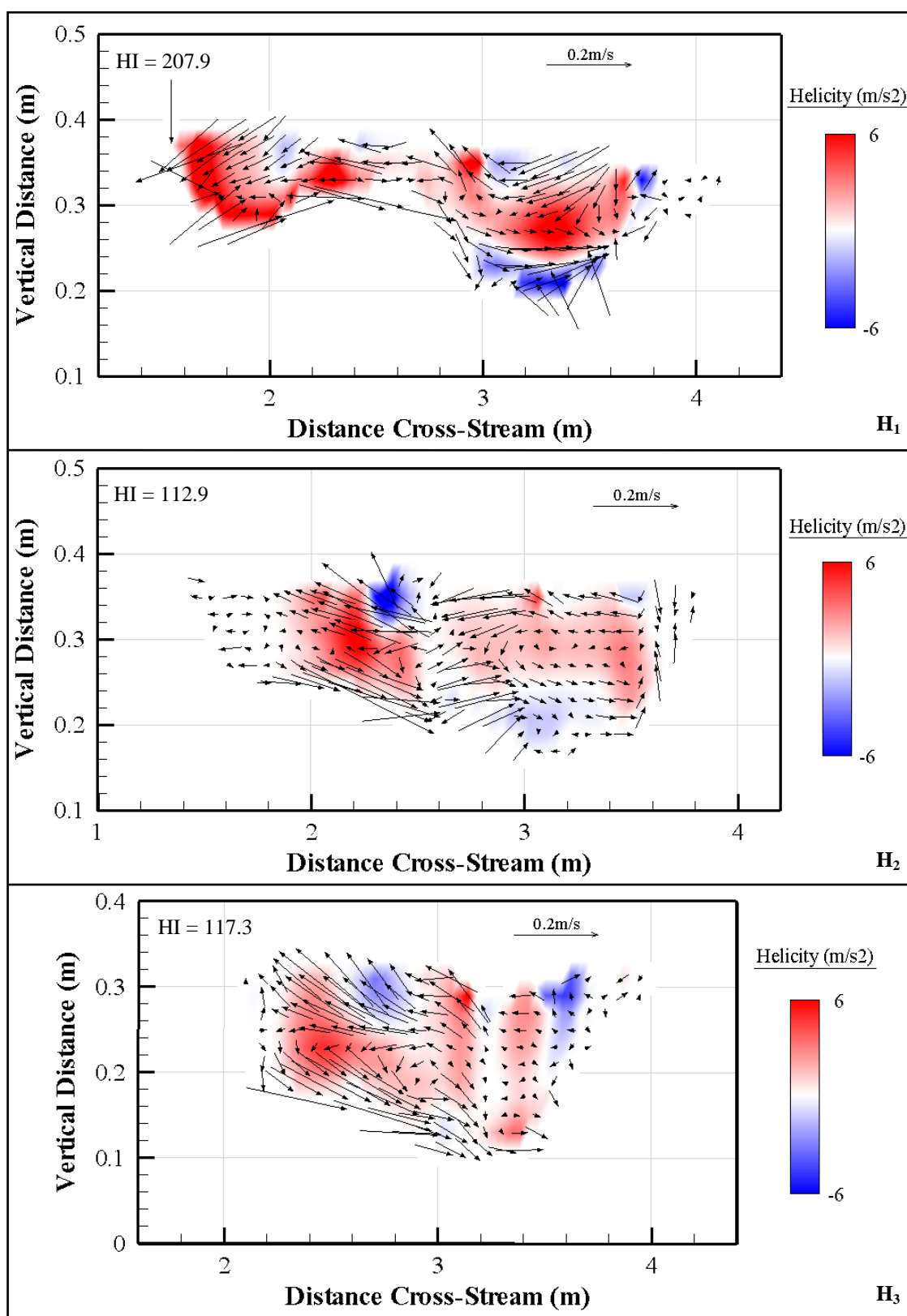


Figure 5.69: Helicity plots for the three Confluence H cross-sections.

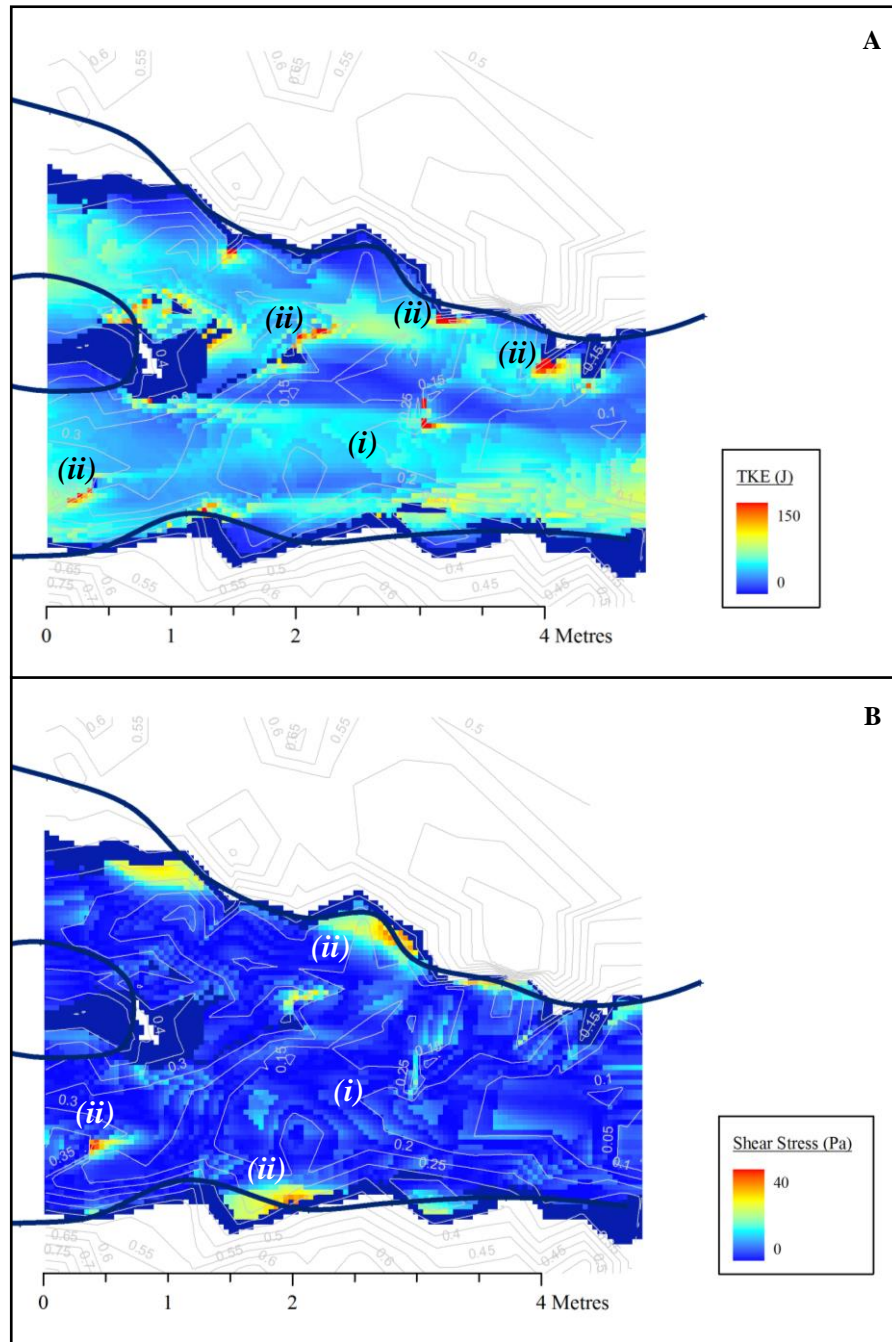


Figure 5.70: Calculated TKE (a) and bed shear stress (b) for the Confluence H model data. Navy blue cells are inundated but too shallow to calculate values.

Much like Figure 5.65, the two main features in Figure 5.70 are evidence of pulsing in the TKE and shear stress values (i) and isolated higher values due to large clasts (ii). Figure 5.71 therefore compares the TKE and bed shear stress with water surface elevation to investigate the role played by the water surface fluctuations.

As with Figure 5.66, there are variations on two different scales in Figure 5.71, with a tendency for peaks in TKE and shear stress to be associated with water surface

minima. However, the pattern is not as clear as for Figure 5.66, with the shorter-term variations more dominant.

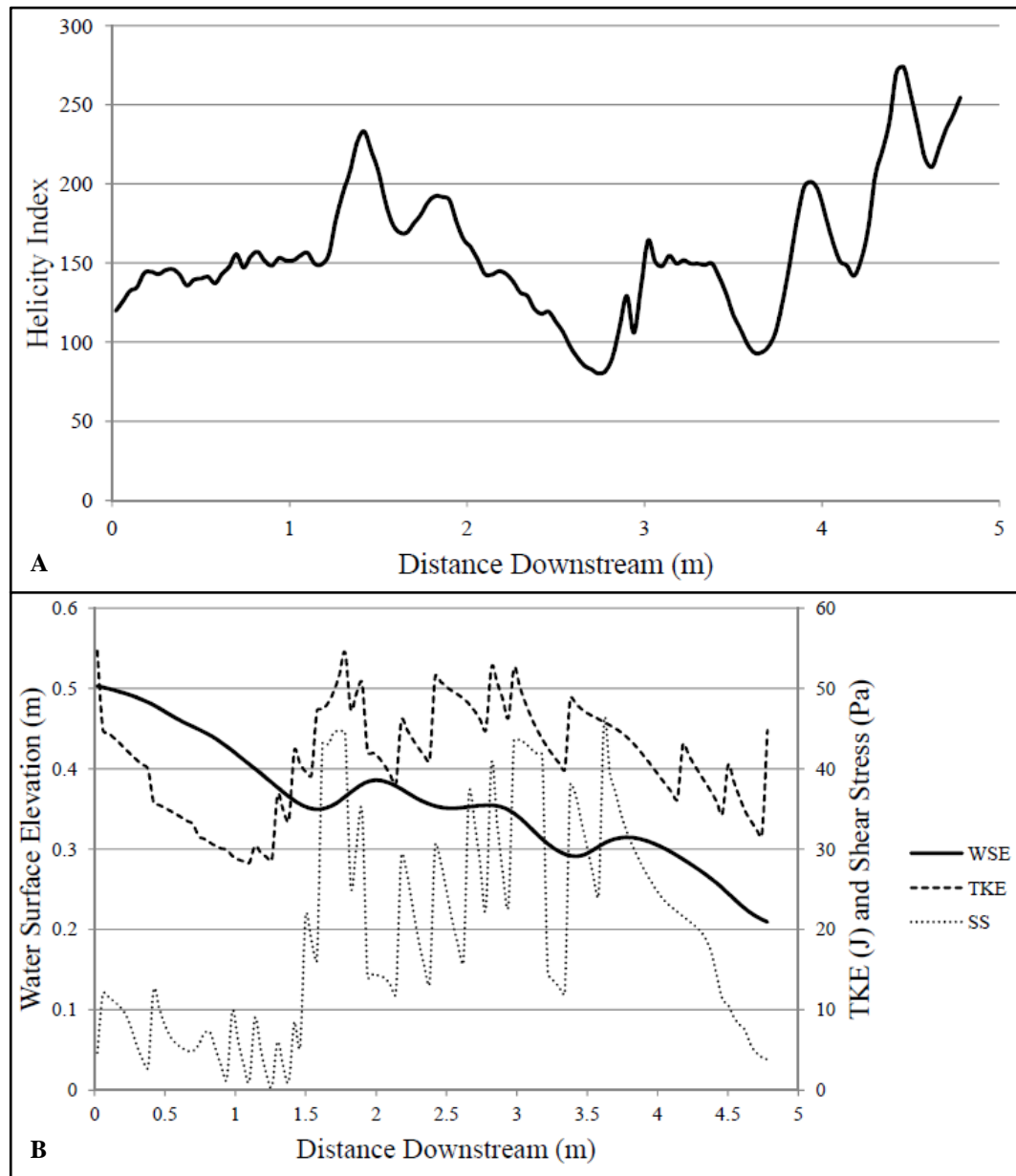


Figure 5.71: Graph showing helicity index plotted against distance downstream (a) for Confluence H, with the equivalent plots for turbulent kinetic energy (TKE), bed shear stress (SS) and water surface elevation (WSE) in (b). In diagram (b), the values are taken from along a straight line located 1.3m from the true right bank.

### 5.12.3 Discussion of the Flow Dynamics at the Arolla Confluences

By using the HOL model to simulate the Arolla confluences, it has been possible to obtain more information on the flow dynamics at these steeper confluences. This is particularly useful given the difficulties experienced in trying to obtain three-dimensional aDv data in the field.

At Confluence G, Figure 5.62 shows two cores of higher velocity combining into a single core within a very short distance downstream. For a junction angle close to  $0^\circ$  and similar flow velocities in both tributaries, two separate cores would be expected to persist for a much longer distance (Rhoads and Kenworthy, 1998). In Section 2.3.4, it was noted that faster mixing than expected required either strong secondary circulation cells or high levels of turbulence. Figures 5.63 and 5.64 show no evidence of strong secondary circulation extending across much of the channel width, so the high TKE in Figure 5.65 can be considered the most likely cause of rapid mixing. However, the results in Figure 5.63 suggest another process is affecting the mixing of the tributary flows. The major secondary flow is highlighted in Figure 5.63 as zones of higher water surface elevation that have downwelling (*i*) and zones of upwelling that lead to relative increases in water surface further downstream (*ii*). Therefore, the steep slopes at these confluences are encouraging greater fluctuations in the water surface which help to drive the high variability in cross-stream and vertical velocities. This explains the high helicity index, which is on a par with the highest values obtained from the Moor House confluence scenario tests, in spite of the absence of large circulation cells. Furthermore, the high variability in cross-stream and vertical velocities will encourage more rapid mixing and merging of the two high velocity cores.

The water surface variations also explain some of the variability in TKE and shear stress at Confluence G. Chanson (2000) found that such fluctuations would cause shear stress maxima under troughs and minima under wave crests because of the local water surface slope effects. Although Figure 5.66b has demonstrated that the clearest pattern of TKE and shear stress pulsing in Figure 5.65 is likely to be an artefact of the data collection method, there is still an underlying trend for TKE and shear stress peaks to coincide with localised water surface depressions.

Figures 5.63 and 5.65 suggest that topographic forcing and bed roughness play a lesser role than water surface slopes in driving the flow dynamics. The lack of helical flow cells can often be explained by higher levels of roughness disrupting the flow, for example the upper confluence in Section 5.10 or the impact of form roughness from sand dunes on confluence-diffuence units of the Rio Parana (Parsons *et al.*, 2007). However in Confluence G, the dynamic nature of the confluence means that the bed is often in motion and therefore the concept of a roughness height becomes much less clearly defined. In addition, the high shear stress values and their variability due to water surface fluctuations (Chanson, 2000) will ensure many topographic obstacles are



quickly eroded, thus reducing the impact of topographic forcing on the flow. This reinforces the view that in these steeply sloping confluences, understanding the flow and sediment dynamics requires a reliable representation of the water surface.

In Confluence H, the depth-averaged flow field in Figure 5.67 shows very little cross-stream flow, with most flow in a downstream direction. As the two tributary flows join, there is a small amount of deflection visible in the vectors (*ii*), but this is generally minor until the final cross-section. The secondary circulation in Figures 5.68 and 5.69, however, is much more complex, with evidence of a helical cell developing on the true right side of the channel. The results show little evidence for counter-rotating cells; if anything, a single cell persists across the entire channel width. However, it should be noted that the true left half of the channel has some anomalously high horizontal velocities near the bed which may be skewing the helicity values. Therefore, the potential presence of more traditional back-to-back helical cells in parts of the confluence should not be completely discounted.

There is also some evidence for the links between water surface variations and the variability in vertical velocity, although this effect becomes weaker as the secondary flow cells become clearer with distance downstream. It is interesting that in spite of the stronger secondary flow cells and the higher junction angle, the two high velocity cores take longer to merge than for Confluence G, suggesting water surface fluctuations are a major driver of mixing at these confluences. As for Confluence G, topographic forcing and bed roughness appears to have little effect on the flow field in Figure 5.68.

In Figure 5.69, there is evidence of elevated TKE in the areas where the downstream velocity is highest. Spikes in TKE, meanwhile, tend to be associated with the presence of topographic obstacles, especially near the banks (*ii*). In some cases these peaks can be seen to result in higher TKE in the lee of the obstacle for some distance, suggesting that the large particles encourage the generation of turbulence, which then dissipates with distance downstream. For the shear stress, there are high values near the channel edge (*ii*), which may be due to recirculating or shallow flow giving anomalous results in these areas. Meanwhile, in Figure 5.71b there is some evidence of the water surface driving TKE and shear stress fluctuations, but it is not as clear as for Confluence G.

Although this discussion has focused on the more dominant role played by the water surface slope at these steep confluences, Figures 5.66a and 5.71a suggest that the mutual deflection of the tributary flows can lead to stronger helicity. Both Figures 5.66a

and 5.71a show spikes in HI at the point where the two tributary flows meet, while in Figure 5.71a there is also evidence of the helicity index increasing as the two tributaries flows deflect one another (at (ii) in Figure 5.67). This demonstrates that while the flow at these confluences is very different from that in the classical river confluence model, there are still some aspects of the conceptual model which remain relevant in these environments.

### 5.13 Discussion of Flow at Upland River Confluences

Throughout the validation tests set out in Sections 5.6 to 5.8, the HOL model has given a significant improvement over the standard approaches to modelling the free surface. Although there are disparities between the modelled and measured results, in most cases these differences can be at least partly attributed to the uncertainty in the field measurements. The combination of errors in the flow data, errors in the topographic data and uncertainty due to geolocation often account for a substantial part of any discrepancies. Indeed, the model results can sometimes provide a more realistic representation of the confluences than the field data, with the water surface fluctuations at the Arolla confluences the most notable example. The model has therefore proved to be very useful in providing additional information on confluence flow dynamics that could not be obtained from the data in Chapter 4.

From these additional results, it is now possible to draw some conclusions into what drives the flow field at steeply sloping river confluences. In the classic river confluence model, the flow field is either dominated by mutual flow deflection and the back-to-back helical cells which result (Mosley, 1976; Ashmore and Parker, 1983; Best, 1986; Biron *et al.*, 2002) or the presence of bed discordance which encourages flow from the deeper tributary to pass in the lee of the step and give upwelling at the downstream corner (Best and Roy, 1991; Bradbrook *et al.*, 1998). In terms of the former, there is very little evidence of the double helical cell at any of the Moor House confluences, although some helical cells do exist in one of the two tributaries. At the lower Moor House confluence, the flow field does replicate many of the flow features of discordant junctions, with clear evidence that water from the true left tributary passes over the top of that from the true right (as Gaudet and Roy (1995) argue should happen when river levels are shallow). However, the confluence planform and bed topography ensure that in this case there is no clear zone of upwelling at the downstream corner.

At the upper confluence, the major flow structure of interest is the jet-like flow as described by Rhoads and Sukhodolov (2008). Water from the true left tributary is constricted into a fast, narrow zone as it enters the main channel, giving localised increases in TKE and shear stress (Figure 5.38(i)). Secondary flow cells are not well developed, most likely due to the complex topography and the effect of the high levels of roughness from the channel bed.

For the Arolla confluences, flow is in some senses simpler, with flow generally fast and in the downstream direction, but also surprisingly complex when investigated in more detail. The secondary flow can exhibit helical cells, but is also liable to be more locally dependent on the fluctuations in the water surface. This results in localised areas of upwelling and downwelling that affect the water surface further downstream. In addition to this, the calculated TKE and shear stress are seen to vary in response to peaks and troughs in the surface water waves. The effect of topographic forcing and bed roughness is substantially reduced, largely because the bed is often in motion and as a result most variations in the bed topography do not persist for a long time. The exception to this is in the case of particularly large obstacles, which can encourage localised highs in TKE that dissipate with distance downstream.

Therefore, the two different types of upland river confluence investigated in this chapter have very different characteristics. By comparing the confluences to the schematic diagrams in Figure 2.1, these differences can be highlighted relative to the classical model of river confluences. The Moor House confluences are more typical compared to these diagrams, with some evidence of flow separation zones, a clear zone of maximum velocity, avalanche faces (due to bed discordance) and upstream corner bars. Furthermore, the flow field at the discordant lower confluence is largely typical of junctions of that type, with water from the deeper tributary flowing under water from the shallower tributary. However, where differences do exist with the classical model, they are largely caused by topographic forcing and the high levels of bed roughness. This leads to weak secondary circulation cells and small-scale, localised increases in turbulence as the flows mix or large topographic obstacles are encountered. In addition to this, the results from Section 5.11 demonstrate that at higher flows, the discharge ratio can also have a substantial impact on the flow field.

The increase in steepness to the Arolla confluence, however, leads to a change whereby bed roughness and topographic forcing have a much lesser role. This is due to the dynamism of the confluences and the ease at which the bed is reworked. This might

be expected to remove some of the reasons for the incomplete agreement between the Moor House confluences and the classical model. However, there are very few of the features identified in Figure 2.1 that were clearly replicated in the Arolla confluences. This is because the steeper water surfaces and flow that is close to critical or supercritical results in substantial local variations in the water surface. These undulations become the primary drivers of the secondary flow and turbulence, which mean that whilst the steep slopes ensure an apparently straightforward depth-averaged flow field (dominated by movement in the downstream direction), the secondary flow becomes much more complex. The importance of the water slope to the flow field at these confluences has therefore demonstrated the major advantages that the HOL model provides for improving the understanding of the flow, and by extension the sediment dynamics, at these steep river confluences.

## **5.14 Conclusions**

This chapter has explained, implemented, tested and applied an explicit free surface Height-of-Liquid (HOL) model to the upland river confluences of Moor House Nature Reserve and the Borgne d'Arolla braid plain.

In Section 5.2, the issue with using a rigid-lid approach to model steep water surface slopes was demonstrated, before the HOL model was explained in detail. This was followed in Section 5.3 by the planned testing strategy, incorporating both model verification and validation. In addition, Section 5.3 highlighted some of the issues that are associated with attempting to validate a grid-based model with discrete point data. It was determined that, in particular for the flow velocity measurements, this uncertainty should be reported by showing the range of values in the adjacent model cells as error bars.

Section 5.4 presented model verification tests for Arolla Confluence E, which incorporated iterative and grid convergence tests. In the case of iterative convergence, the explicit free surface nature of the model meant that it would converge onto a solution through time steps, as the water filled the confluence from the inlets. It was demonstrated that an increase in grid resolution not only increased the computational time needed due to the increase in the number of calculations to be performed, but also increased the number of time steps required to achieve convergence. In the grid convergence tests, the finest grid was found to have errors approximately half that for

the medium resolution DEM, although the disparities were relatively small compared to the differences between variables. While errors for the pressure, downstream and cross-stream velocity were low, vertical velocity, turbulent kinetic energy and energy dissipation were all much higher. The high GCI values for vertical velocity encouraged the use of a finer grid resolution in the vertical direction instead of using a cubed mesh. Of all the GCI values, however, it is notable that the water surface elevation was by far the lowest, suggesting that the HOL model accomplishes its primary task of simulating the water surface elevation with very little uncertainty.

Having conducted the grid verification tests, in Section 5.5 the model was calibrated and assessed for its sensitivity to domain length, roughness height and topographic representation in simulations of the true left inlet of the upper Moor House confluence. These tests demonstrated that the biggest impact on model prediction was the domain length, with the model less sensitive to the roughness height and the exact form of the Mass Flux Scaling Algorithm (MFSA) used.

In Section 5.6, the HOL model was validated for the first time, using the inlets from both Moor House confluences. Although some variability was seen, the model generally performed well, with the biggest anomaly (at the lower true left inlet) explained by the presence of a boulder just downstream of the measured cross-section. This demonstrated the model could reliably represent flow through single-thread gravel-bed rivers.

Having performed the initial stage of model validation on simple channels in Section 5.6, the following section moved on to test the HOL model on the river confluences of Moor House Nature Reserve. Model performance was good, although the water surface elevation was underestimated near the outlet, largely due to the zero-pressure boundary conditions. In addition, the quantitative comparisons between modelled and measured velocities appeared poor due to the high levels of uncertainty caused by geolocation errors. Nevertheless, the model was able to replicate the majority of the flow features highlighted in Section 4.5.

Section 5.8 then used the much steeper confluences of the Borgne d'Arolla braid plain to determine whether the HOL model could cope when flow became supercritical. The model tended to over-predict the water surface elevation, particularly near the confluence inlet, but the modelled flow velocities at the outlet were close to those measured in the field.

Having conducted the validation tests and determined (in the discussion in Section 5.9) that the overall model performance was good, the model was then used to obtain more information on the secondary flow and turbulence at these confluences. For the Moor House confluences, this involved investigating the flow field for the low flow simulations (Section 5.10) and different high discharge scenarios (Section 5.11). This was followed by a presentation of similar results for the Arolla confluences in Section 5.12. In the final discussion (Section 5.13), the results from these three sections were compared. It was argued that the major difference as water surface slopes increase is a change from a flow field that is largely forced by the topography to one that has the water surface slope and surface water waves as a key driver.

Having applied the HOL model to explore in detail the flow processes operating at upland river confluences, the next step is to address the implications of these processes for sediment transport. Investigating the sediment dynamics of these confluences will therefore be the focus of the next two chapters.

# Chapter 6:

## Bedload Transport at Upland River Confluences

### 6.1 Introduction

In Section 1.5, the research question, aims and objectives highlighted the importance of understanding the links between the flow field, sediment transport and confluence morphology (Figures 1.1 and 1.3). In particular, it was noted that there has been less research on the upland river confluences which would be expected to make up a substantial proportion of the junctions in a given catchment. As such, in Section 1.6 the Moor House and Borgne d'Arolla field sites were chosen to provide examples of upland river confluences with steep water surface slopes. The Moor House confluences were chosen because of their relative stability, while the Arolla confluences were selected for their steeper water surface slopes, greater dynamism and active bedload transport.

In Chapter 2, the research conducted to date regarding the sediment dynamics at river confluences was reviewed. Table 6.1 gives a summary of those studies that have specifically addressed bedload dynamics in river confluences.

Study	Location	Findings
Best (1988)	River Ure and Widdale Beck confluence, North Yorkshire, UK	From the field and laboratory studies, concluded that particles are transported around the scour hole with greater segregation at higher junction angles.
Roy and Bergeron (1990)	Ruisseau du Sud catchment, Québec, Canada	Particles were found to travel through the confluence scour hole. Particle size did not affect the transport path, just the time taken.
Boyer <i>et al.</i> (2006)	Bayonne-Berthier junction, Québec, Canada	Found that the maximum bedload transport was found at the edge of the shear layer, where turbulence intensity varies sharply.

Table 6.1: Summary of research previously conducted into bedload dynamics at river confluences.

It can be seen from Table 6.1 that there has been very limited research into the bedload dynamics at river confluences. For the steep, upland river confluences of

interest to this study, it is bedload transport rather than suspended sediment that is of most interest. Although suspended sediment is transported through these upland confluences, the bed is characterised by gravel and cobble grains (Section 4.4), implying that it is the bedload transport processes which will drive the major changes to confluence morphology. It is for this reason, as well as the lack of recent studies into bedload transport at river confluences, that this chapter will focus on the bedload component of the sediment dynamics.

This chapter presents data from particle tracking experiments conducted at the Moor House and Arolla confluences for which the topographic, roughness and flow data were presented in Chapter 4. These data were collected for two reasons, firstly to provide more information on the sediment dynamics at upland river confluences (as required by Criterion 1 in Section 1.5) and secondly to provide validation data for a reduced-complexity particle transport model (Criterion 5 in Section 1.5). The Moor House particle tracking experiments will be addressed in Section 6.2 before the impact of grain size and roundness on the tracer particle trajectories is investigated in Section 6.3. The results from the particle tracking experiments at the Arolla confluences are then presented in Section 6.4. Although the research methodology has been set out in Section 3.8, both Sections 6.2 and 6.4 will set out the specifics of the experiment design for that field site. In addition to this, Section 6.2 will also include a brief discussion of data quality and recovery rates. The chapter will then move on to compare the results from the Moor House and Arolla experiments (in Section 6.5) before the concluding remarks in Section 6.6.

## **6.2 Particle Tracking at Moor House Nature Reserve**

The nature of the topography and flow at the Moor House confluences was set out in Chapter 4, whilst in Chapter 5 numerical modelling was used to provide an insight into the processes operating during higher discharge flows. This section will begin by setting out the methodology of the particle tracking experiments conducted at the Moor House confluences. The data quality and particle recovery rates will then be discussed, followed by information on the experiment survey dates. The results from the particle tracking experiments for each confluence will be presented next, followed by an analysis of how these particle tracks compare to the near-bed flow fields simulated in



the scenario testing in Section 5.11. The extent to which the particle dynamics reflect the flow processes and agree with previous studies will then be discussed.

### 6.2.1 Particle Tracking Experiment Design at Moor House

At each of the two Moor House confluences, two sets of particle tracking experiments were conducted. The first experiments from each confluence were used to help to improve the methodology for the second experiments and also to provide important information on the magnitude of the high discharge event required to initiate particle transport. The discharge information was particularly important for ensuring site visits were arranged after any event likely to have resulted in particle transport.

For each experiment, four patches of 200 painted particles were placed into the confluence, with two patches in each tributary. This compares favourably with the 900 particles in total used by Best (1988), the 200-350 used in each study reach by Hodge *et al.* (2011) and the 127 particles used by Roy and Bergeron (1990) for river confluence studies, while each experiment matches the total of 800 used by Cray (2010) in his research into bedload transport in Trout Beck. It is also well in excess of the criteria in Section 3.8.4 that all patches be made up of at least 100 clasts. Figure 6.1 shows the Grain Size Distribution (GSD) of the tracer particles compared to that measured at the Moor House confluences. The tracer data were obtained before seeding the particles for the second experiment at the upper confluence, while the bed GSD was found by combining the results from the six patches in Section 4.4.

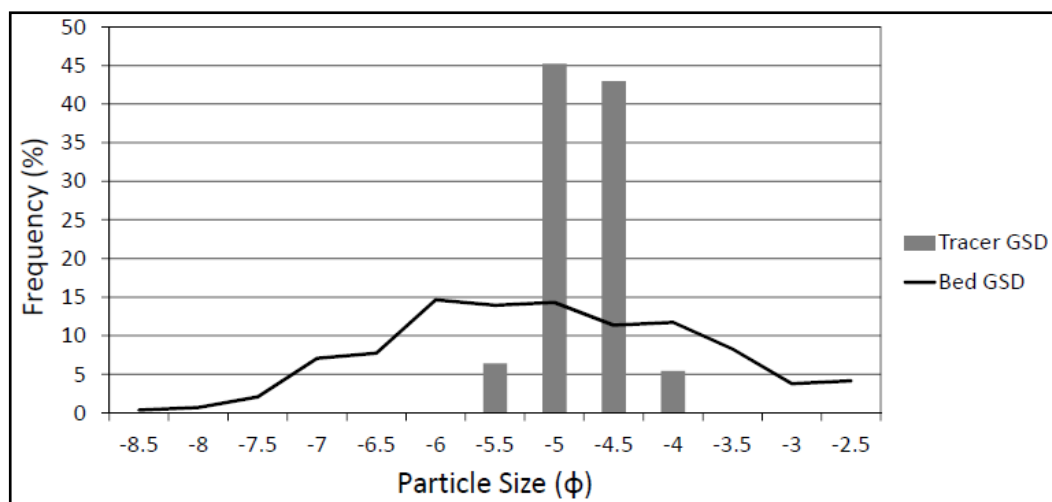


Figure 6.1: Grain size distributions for the tracer and bed particles at the Moor House confluences.

Figure 6.1 indicates that the tracer particles are slightly smaller than the modal bed particle size of  $-6\phi$  (64mm), but lie within the range of particle sizes that have frequencies exceeding 10%. A comparison with Table 4.4 shows that the distribution of tracer particles also falls within the range of  $D_{50}$  values found for the individual particle counts on each bar (23-54mm).

Each particle patch was painted a different, bright colour so that they could be distinguished at the bottom of the river (see Figure 6.2). The decision was taken to not use magnetic PIT tags (*e.g.* Lamarre and Roy, 2008a, 2008b) for three reasons. Firstly, both Lamarre and Roy (2008a) and Cray (2010) found that the minimum realistic size for drilling clasts was 40-45mm, which would be a major limitation given the median grain size in the confluences. Secondly, the interest from these studies was in the movement and dispersal of the patch as a whole, rather than in being able to track individual particles through the reach. As such, a larger number of untagged particles was considered preferable to a smaller number of clasts tagged with unique identifiers. Finally, the high recovery rates found by Cray (2010) in his experiments on Trout Beck (80-90% after a small flood and 60% after the largest flood) suggest that for transport over short distances magnetic tags may not be necessary.

The outline of each patch was surveyed on the day of seeding, with surveys on subsequent days recording the positions of any particles which had moved beyond the initial patch. These surveys were conducted using either dGPS or a Leica Total Station, with the data ultimately transformed onto the same arbitrary grid used for the DEMs in Section 4.3. The only time it was not possible to obtain data was between mid-December 2011 and late February 2012, as the site at Moor House became inaccessible due to deep snow or sheet ice on the access track.

Following the first set of experiments on both confluences, it was found that the paint on the particles discoloured through time, making it increasingly difficult to distinguish between them. Therefore, for the second experiment at each confluence the method of painting the particles was changed slightly. This involved painting patterns onto the particles (in the form of different coloured stripes and spots), which was found to be very effective. In addition to this, preliminary analysis of the first experiments was used to determine the most appropriate particle seeding positions for the second set of experiments.

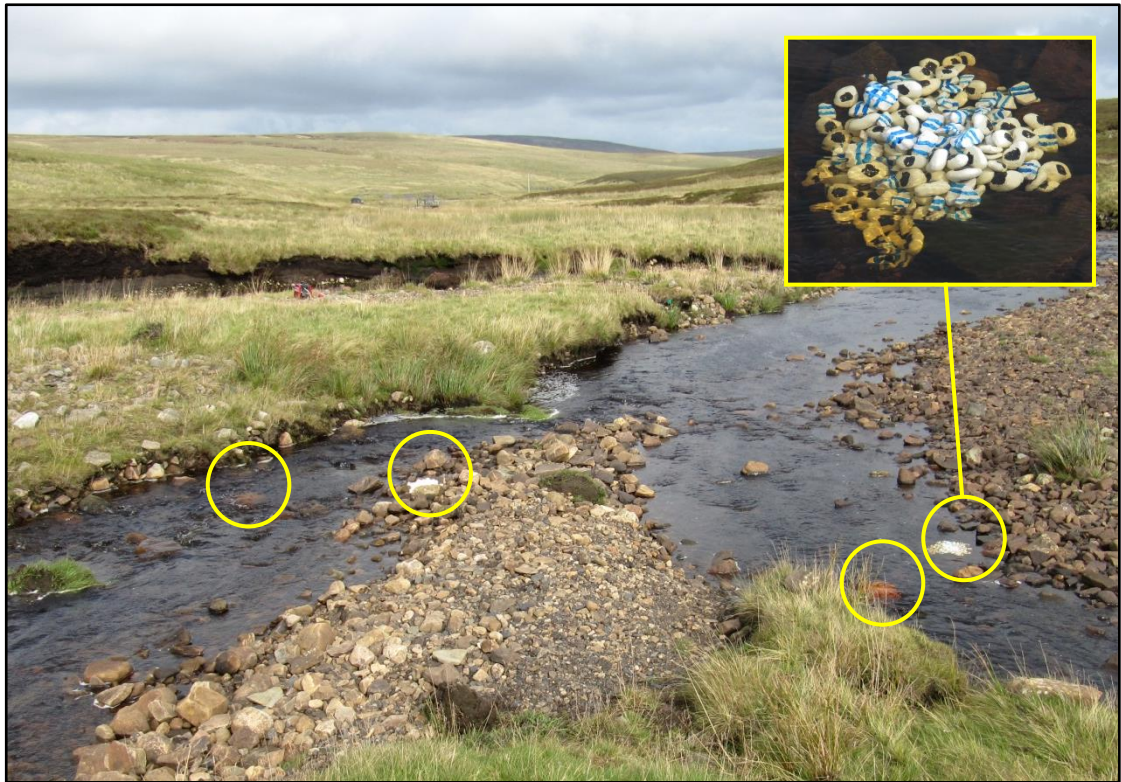


Figure 6.2: Photograph of the upper confluence at the beginning of the second particle tracking experiment. The inset shows the patch in the true right tributary that contains a mixture of angular (blue striped) and rounded (black spotted) pebbles.

To satisfy the criteria set out in Section 3.8.4, the second experiment for the upper confluence was also used to determine the effect of grain size and roundness on the transport of individual particles. In this experiment, the patch nearest the true right bank was made up of 100 smoother, rounded pebbles and 100 of the standard, more angular tracers used in the rest of the study. On the Powers (1953) scale (as given in MacLeod (2002)), the ‘rounded’ tracers would fall into the well rounded and highly spherical classification, compared to the standard tracers which are angular or sub-angular and of low sphericity. The smoother particles were of a more uniform size distribution than the standard tracers (75% <32mm and 25% <23mm). The inset of Figure 6.2 shows the two separate pebble types mixed together into a single patch on the day of seeding. In addition, a Wolman count was conducted alongside each survey of the particle positions. This involved dividing the channel into zones, with the GSD determined for the tracer particles in these zones.

### *6.2.2 Data Quality and Recovery Rates*

The individual point data quality from the dGPS and Total Station surveys has already been examined in Section 4.3, as the mean individual point errors included data from tracer particle surveys. Therefore, it is known that the mean error in recorded particle positions will be approximately 0.05m.

Recovery rates for the particle tracking experiments at the Moor House confluences varied between individual patches, as particles in faster moving patches tended to lose their paint or exit the confluence more quickly. However, recovery rates in excess of 50% were common, with maxima in the range of 75%. Higher recovery rates were recorded for the rounded pebbles in the second upper confluence, largely because they stood out from the bed particles (even without their paint). This made it easier to identify particles that were mostly buried or had only small amounts of paint left on them.

### *6.2.3 Particle Survey Dates*

Figure 6.3 shows the flow hydrograph for Trout Beck (taken from the EA gauging station data presented previously as Figure 4.2), with the seeding and survey dates marked. Figure 6.3 does not include days in which site visits were arranged but no survey was conducted because of a visible lack of movement.

There were a number of constraints which had to be accounted for when determining survey dates. Firstly, the site had to be accessible, which was not the case for the three months from December 2011 to February 2012. This meant it was not possible to obtain data after any of the smaller floods throughout December 2011 or the large ( $16\text{m}^3/\text{s}$ ) flood of 20<sup>th</sup> January 2012. Secondly, to be able to see to the river bed in all locations required sufficiently low flow (defined as discharges of below  $0.3\text{m}^3/\text{s}$  at the EA gauging station). The attempted survey of 23<sup>rd</sup> June 2011 had to be redone on 28<sup>th</sup> June 2011 for this reason. Thirdly, bright weather conditions made it easier to see to the bottom of the channel and so where a choice existed, site visits were arranged when visibility would be better. Finally, there were logistical constraints which had to be accounted for such as the availability of the appropriate equipment and field assistants. Given all of these constraints, surveys were arranged as soon as possible after every high flow event (considered to be flows in excess of  $5\text{m}^3/\text{s}$ ). The main exception to this

was following the survey of 1<sup>st</sup> March 2012, at which point it was realised that a flood far greater than any to that point would be required to give substantial movement of the remaining particles at the lower confluence.

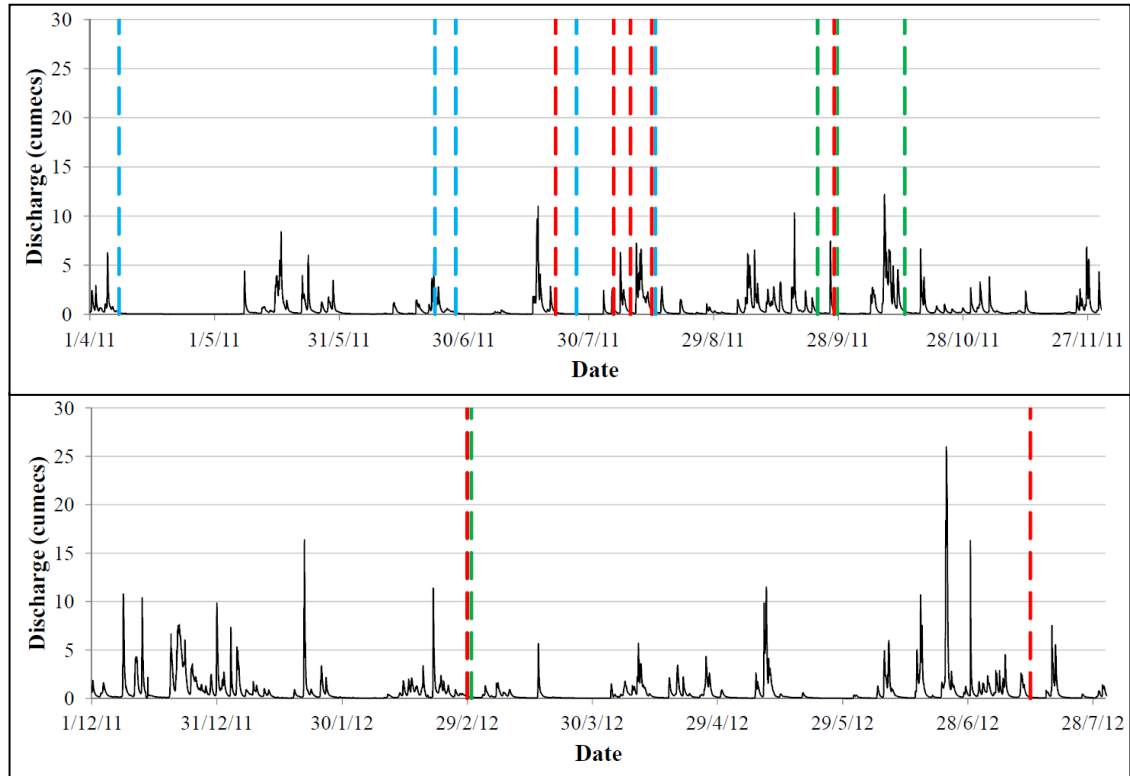


Figure 6.3: Discharge data from the EA gauging station, with the dates of particle surveys marked by dashed lines. For the upper confluence, the survey dates for the first experiment are marked by blue lines and for the second experiment by green lines. The red lines show survey dates for the second experiment at the lower confluence.

#### 6.2.4 Particle Tracks at the Upper Confluence

Figures 6.4 and 6.5 show the first and second particle tracking experiments for the upper confluence. In the first experiment, particles in the true left patches take much longer to move downstream than those in the true right, with only one particle found to have made it into the main channel from the true left tributary. The patches in the true right tributary, meanwhile, are transported much more quickly and tend to be pushed further to the true right, where they are deposited above the low flow waterline.



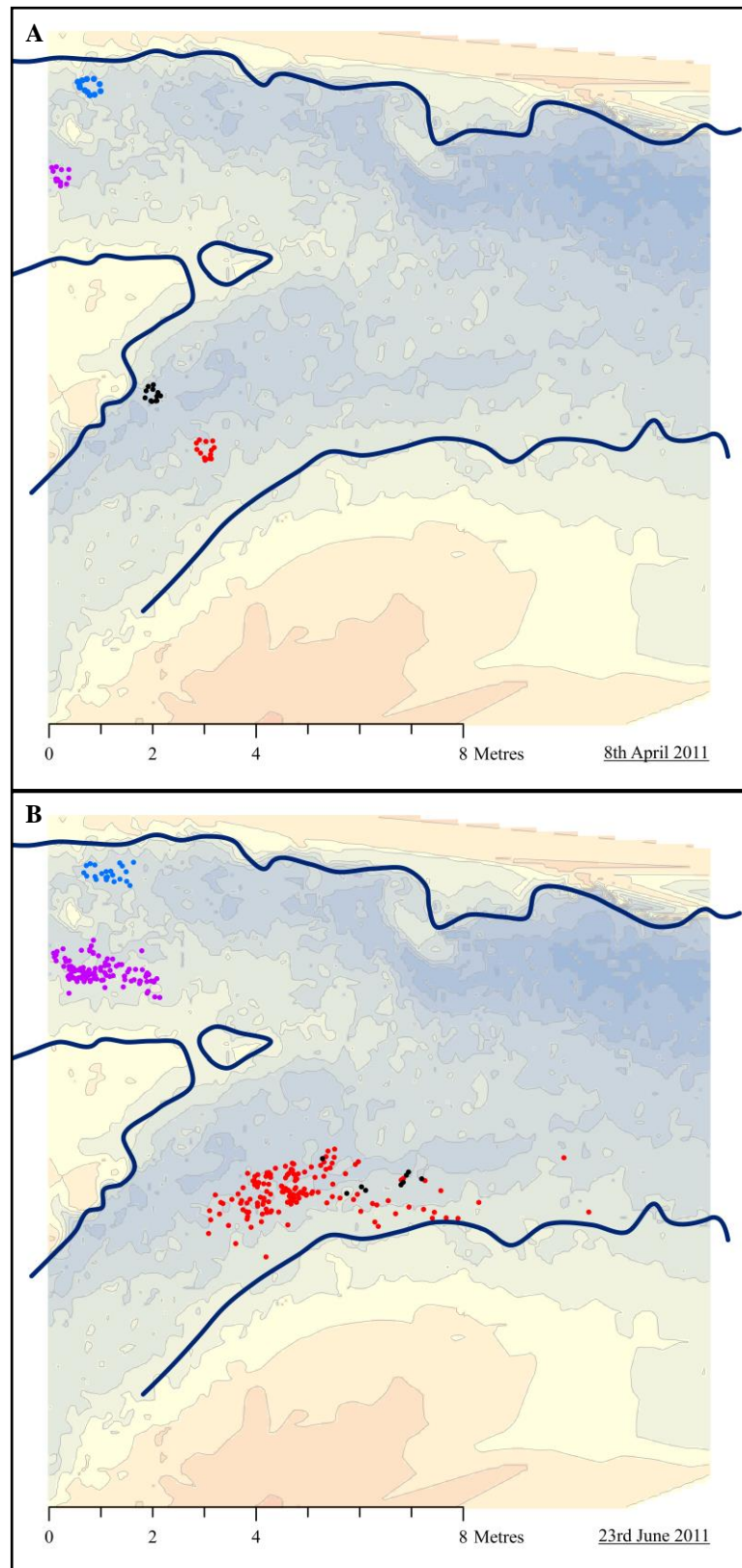


Figure 6.4: Particle positions at the time of seeding on 8<sup>th</sup> April 2011 (*a*) and on 23<sup>rd</sup> June 2011 (*b*) for the first experiment at the upper confluence. The water edge on 20<sup>th</sup> September 2011 is shown for reference. The small number of black dots in (*b*) is due to the water being too deep to see to the channel bed. The confluence was therefore resurveyed on 28<sup>th</sup> June 2011. The bed elevation is given by the background colour, using the same colour scale as Figure 4.8. Figure continues on the next two pages.

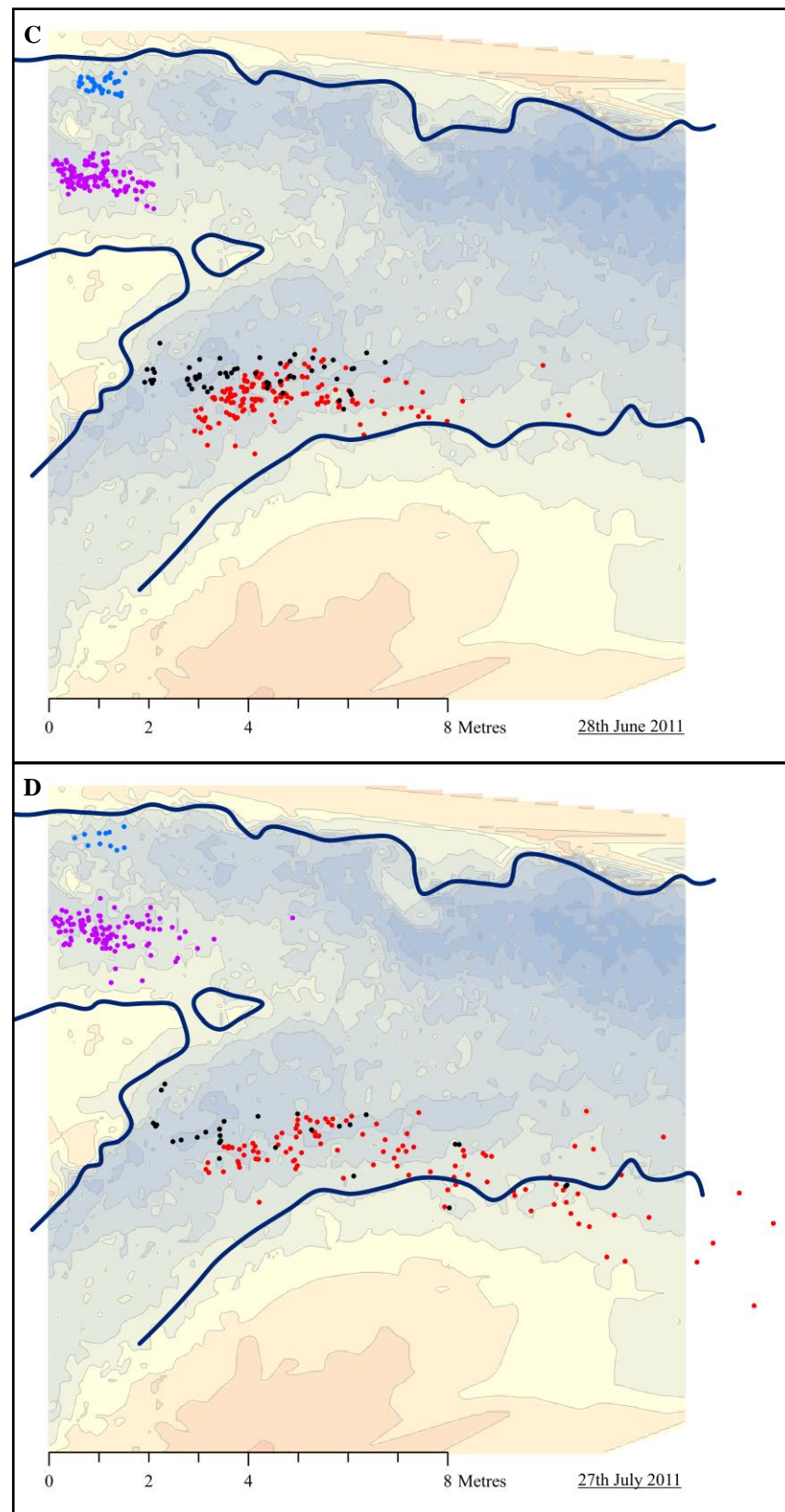


Figure 6.4 (continued): Particle positions on 28<sup>th</sup> June 2011 (c) and 27<sup>th</sup> July 2011 (d) for the first experiment at the upper confluence.

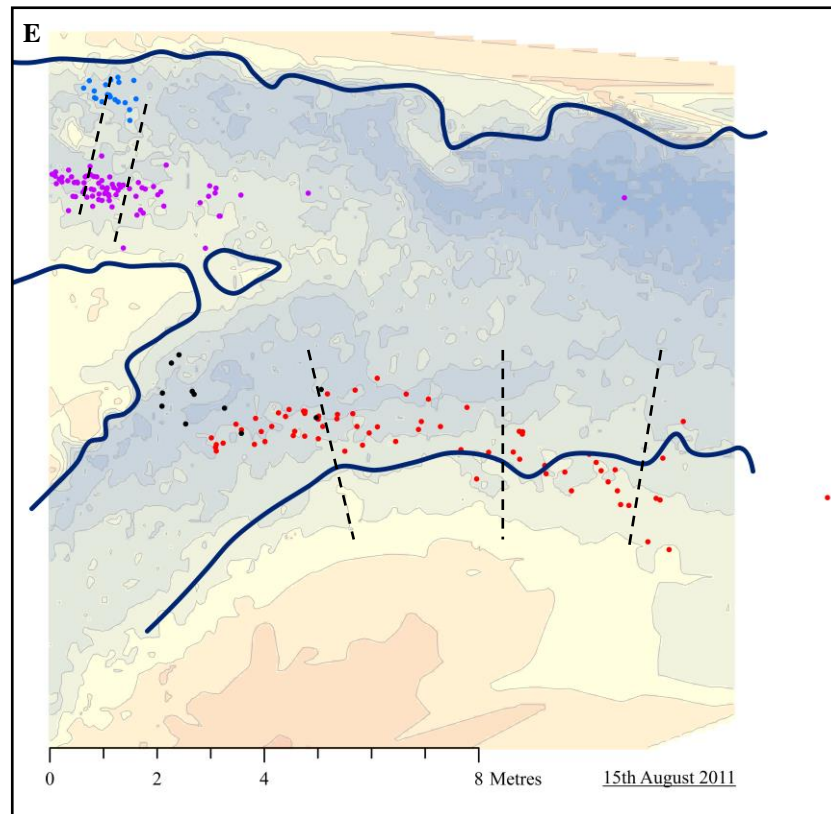


Figure 6.4 (continued): Final particle positions (on 15<sup>th</sup> August 2011) for the first experiment at the upper confluence (e). Dashed lines delineate the zones used to investigate the effect of particle size on distance transported downstream (discussed in Section 6.3).

In the second experiment at the upper confluence (Figure 6.5), the patches in the true right tributary follow similar trajectories to those in the first experiment, being mostly deposited on the true right bank. Although the two patches were placed in opposite halves of the tributary, there is considerable mixing of the pebbles and both patches ultimately travel along the same relatively narrow particle path. The rounded pebbles (denoted by the purple ‘+’ icons) in the furthest true right patch do not follow a clearly different trajectory to the more angular pebbles, although this will be assessed quantitatively in the next section.

In the true left tributary, both patches were placed further downstream as a result of the slower movement in this tributary in the first experiment. In addition, one of the patches was placed on the bar that separates the two tributaries at low flow (represented by orange spots in Figure 6.5). The patch seeded on the bar is shown in Figure 6.5 to have a much greater spread than any of the other patches. Indeed, many of these particles get very close to those which originated in the true right tributary, demonstrating considerable cross-stream movement. The other patch in the true left



tributary (represented by blue spots) moves very little until the final survey on 1<sup>st</sup> March 2012, when only two pebbles were recovered. From the limited data available on 14<sup>th</sup> October 2011, the initial direction of movement is slightly towards the true right.

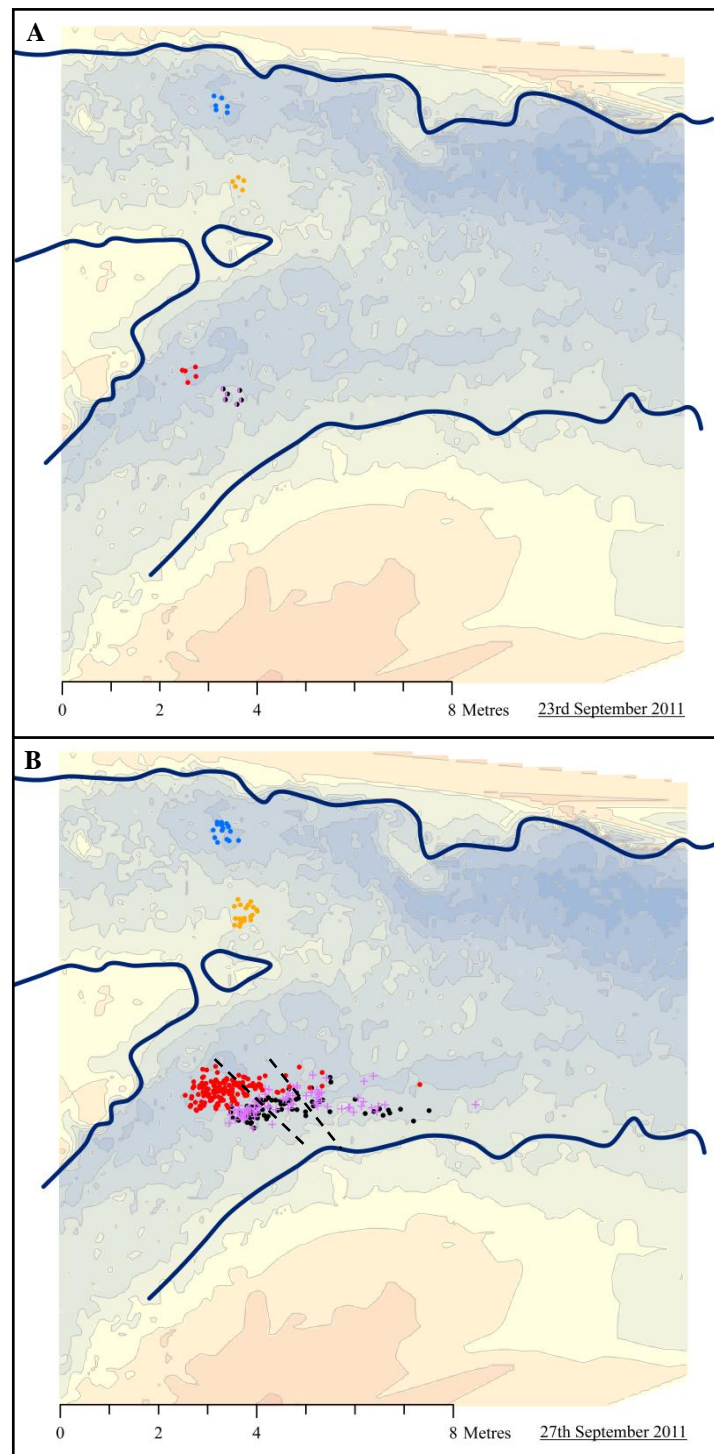


Figure 6.5: Particle positions at the time of seeding on 23<sup>rd</sup> September 2011 (a) and on 27<sup>th</sup> September 2011 (b) for the second upper confluence experiment. The water edge on 20<sup>th</sup> September 2011 is shown for reference. As in Figure 6.4e, dashed lines mark the zones used to assess the effect of particle size on distance transported. Figure continues on the next page.

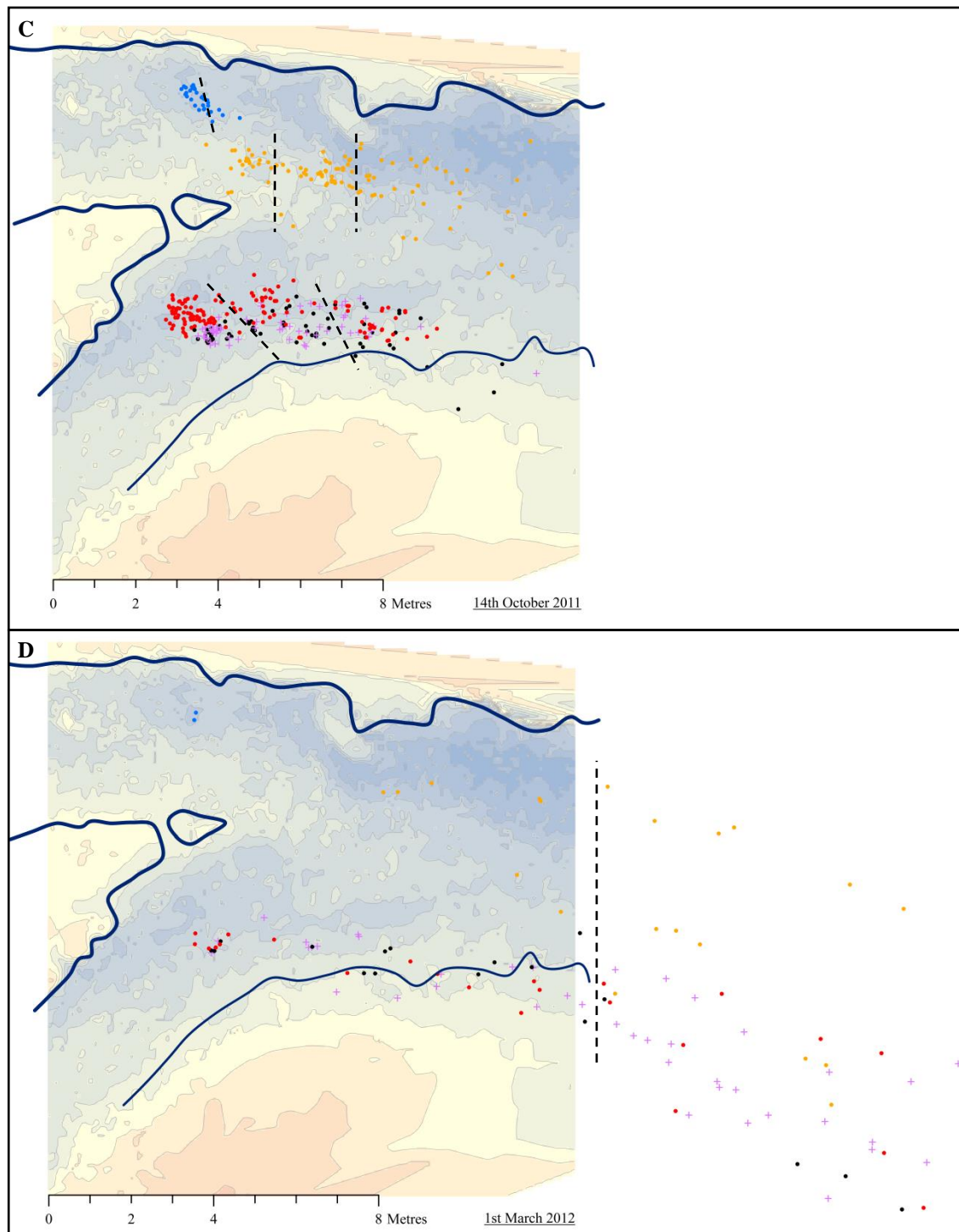


Figure 6.5 (continued): Particle positions on 14<sup>th</sup> October 2011 (c) and 1<sup>st</sup> March 2012 (d) for the second upper confluence experiment. Dashed lines delineate the zones of particle transport used in Section 6.3.

### *6.2.5 Upper Confluence Particle Densities and Near-Bed Streamlines*

In Section 5.11, the HOL model was used to investigate the flow field through the Moor House confluences during floods with different discharge ratios. This section compares the particle trajectories from the upper confluence experiments with near-bed streamlines derived from those HOL model results. The near-bed streamlines were calculated using the horizontal flow velocities at 25mm above the bed, which was chosen to be representative of the median tracer size (47% of the tracers in Figure 6.1 are smaller than 23mm). These streamlines are compared to particle density plots of all the surveyed particle positions for each experiment. The plots also give the measured  $D_{50}$  and  $D_{84}$  particle sizes for the bar adjacent to each tributary (the data from Section 4.4), as well as an indication of the water surface slope in each tributary (calculated from the modelled water surface elevations).

Figures 6.6 and 6.7 show the particle density plots for the first experiment at the upper confluence, with the streamlines from UpperRun007 (dominated by flow from the true left tributary) in Figure 6.6 and the UpperRun008 streamlines in Figure 6.7. Figures 6.8 and 6.9 show the same data but for the second particle tracking experiment.

For the particles seeded in the true right tributary, the tendency for the tracers to be transported towards the true right bank is explained by the near-bed streamlines. In both model scenarios, there is substantial deflection of the streamlines towards the true right bank. However, Figures 6.6a and 6.8a show that for UpperRun007 this deflection does not occur in the vicinity of the patches seeded near the true left bank of that tributary. This implies that the discharge ratio in this case ( $4\text{m}^3/\text{s}$  in the true left tributary compared to  $1\text{m}^3/\text{s}$  in the true right) may be unrealistically high.

For the true left tributary, there is generally less movement of the particles, except for the wide dispersal of the patch located on the upstream corner bar in the second experiment (Figures 6.8b and 6.9b). This also reflects the near-bed streamlines, which show that flow over the bar into the true right tributary and flow down the true left tributary into the main channel are both possible.

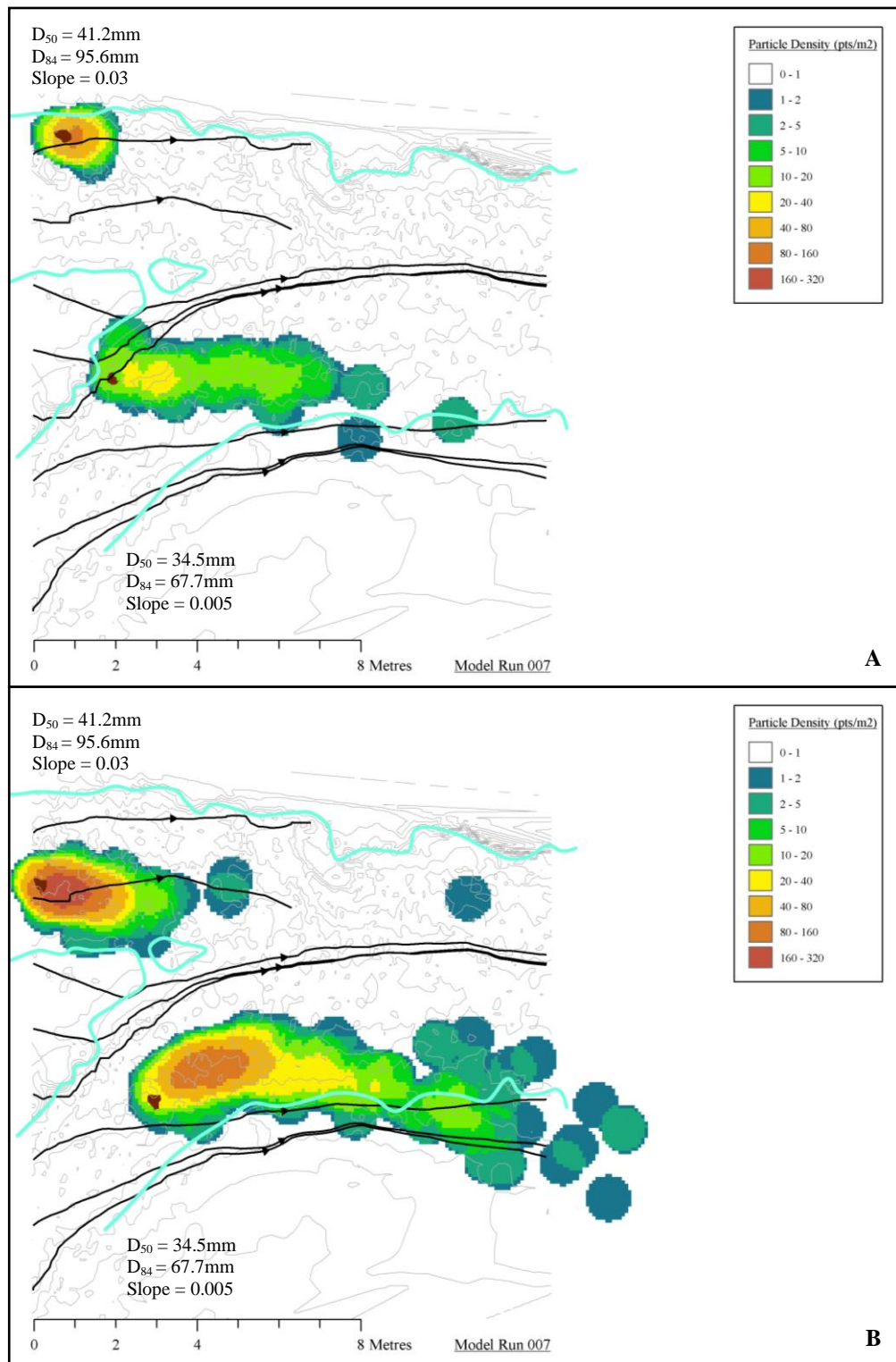


Figure 6.6: Near-bed (25mm) streamlines from UpperRun007 (true left tributary dominant) superimposed on the particle densities from Experiment 1 at the upper confluence. The true left patches in each tributary are given in (a), with the true right patches in (b). The dark brown polygons mark the outlines of the original seeding points. The streamlines nearest the true left bank finish in the centre of the channel as a result of entering zones of shallow and slow flow.



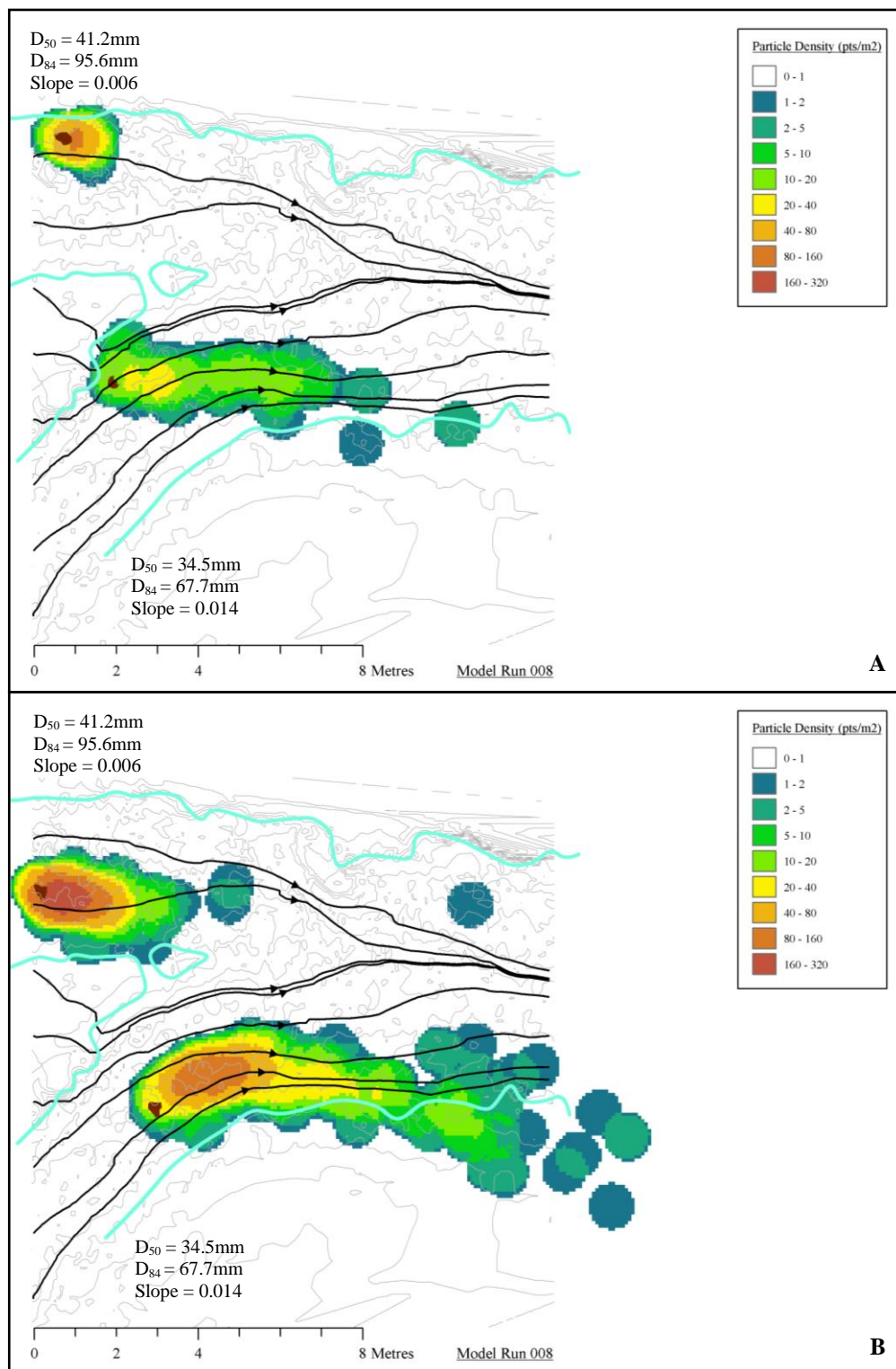


Figure 6.7: Near-bed streamlines from UpperRun008 and particle densities from Experiment 1 at the upper confluence. Notation is the same as for Figure 6.6.

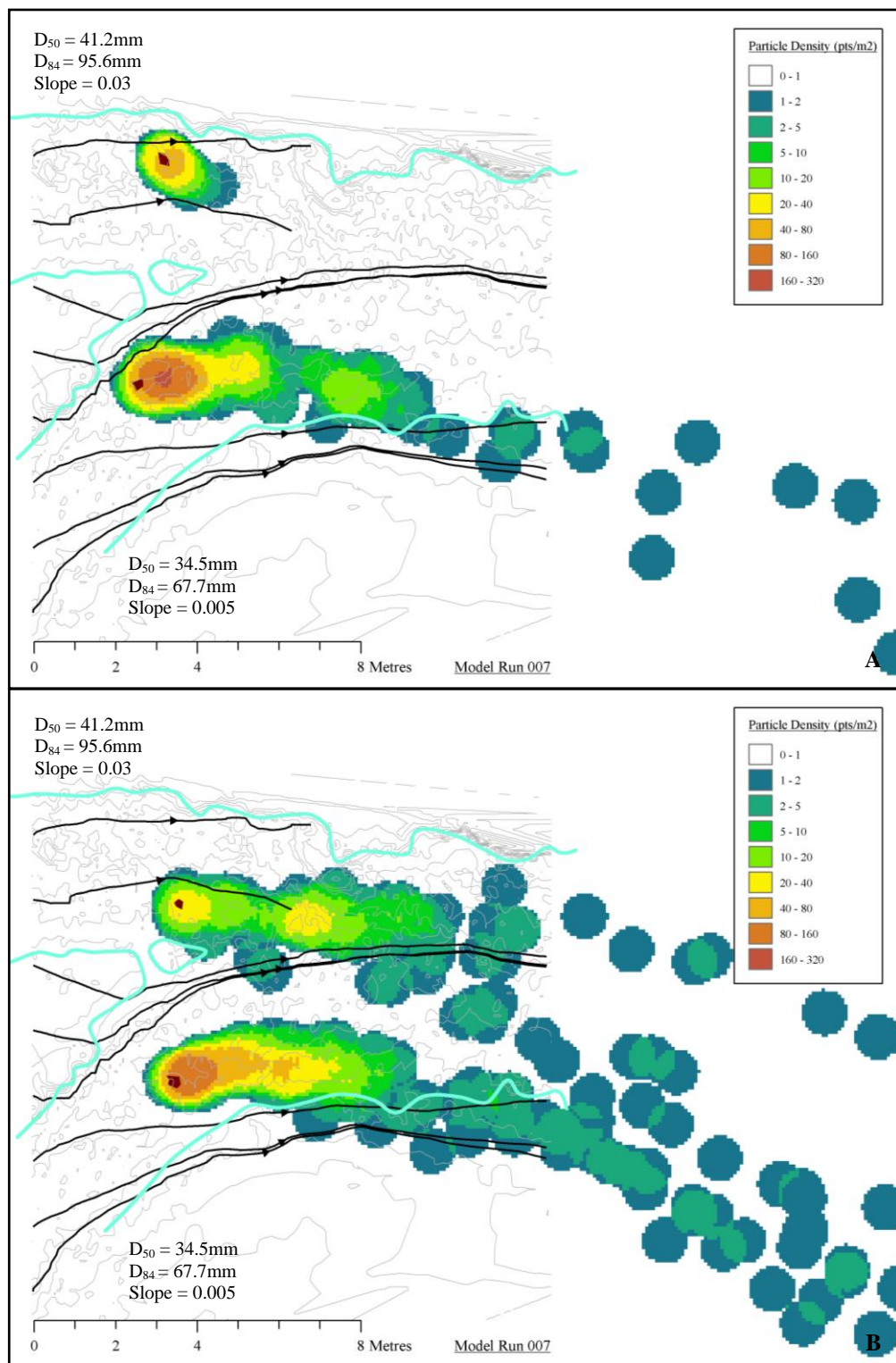


Figure 6.8: Near-bed streamlines from UpperRun007 superimposed on particle densities calculated from the results of Experiment 2 at the upper confluence. Notation is the same as for Figure 6.6.

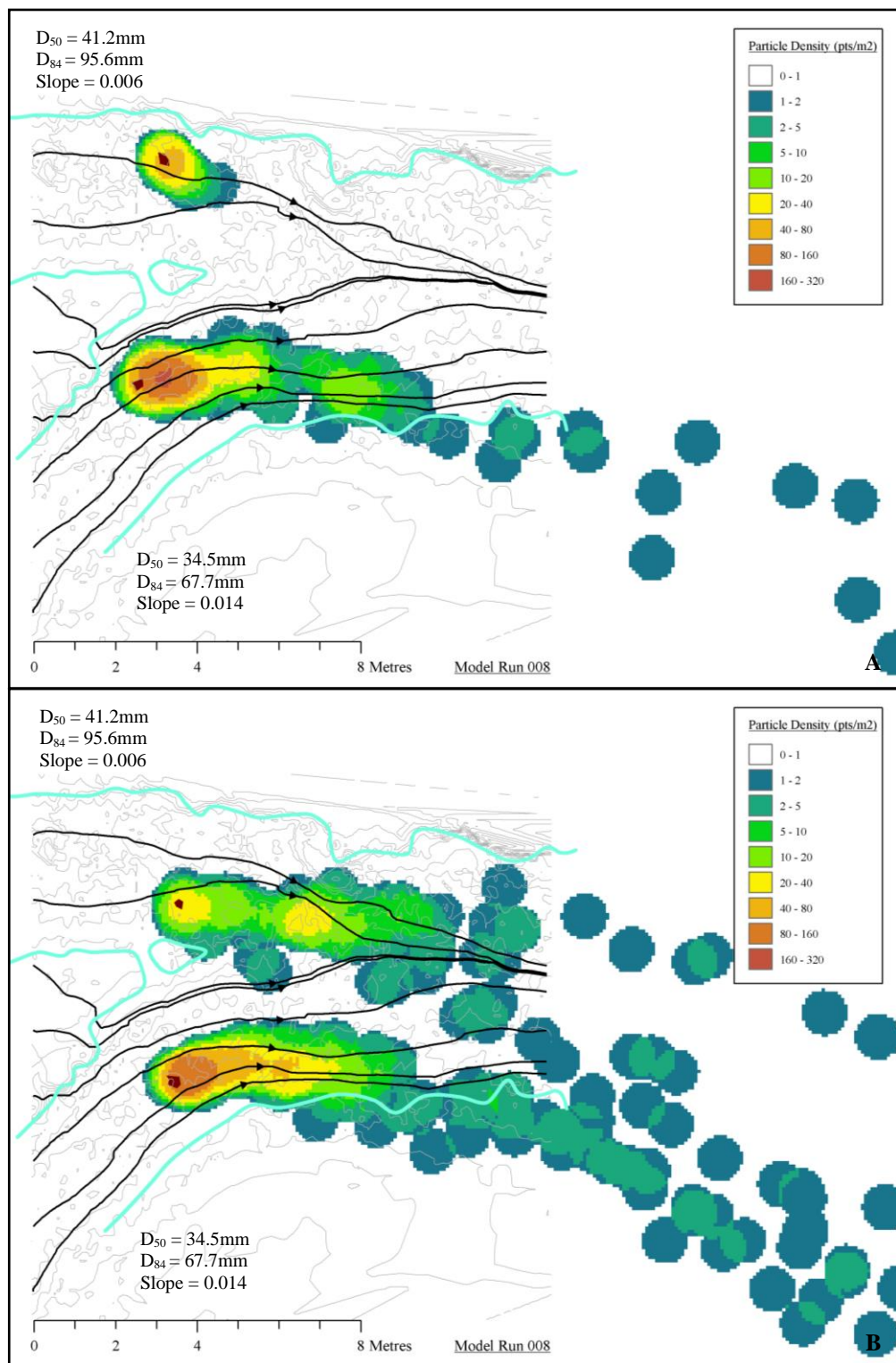


Figure 6.9: Near-bed streamlines from UpperRun008 and particle densities from Experiment 2 at the upper confluence. Notation is the same as for Figure 6.6.

### *6.2.6 Particle Tracks at the Lower Confluence*

Figure 6.10 shows the particle tracks for the second experiment at the lower confluence. The results from the first set of experiments are not presented here, as the particles in the true right tributary were transported too quickly to obtain useful data. The result of this first set of experiments was, however, very important for determining the optimal seeding location for the particles in the second experiment and the necessary frequency of surveys in the period shortly after seeding.

Figure 6.3 shows that the pebbles in the true right are transported far more quickly than those in the true left, with none of the true left particles making it into the main channel by the penultimate survey of 1<sup>st</sup> March 2012. It took an exceptionally large flood of 26m<sup>3</sup>/s on 22<sup>nd</sup> June 2012 to transport the majority of the true left tributary particles out of the confluence, although their exact route once in the main channel cannot be determined. The particle tracks of the two patches in the true right tributary, however, are visible from the data. Particles from both patches follow similar trajectories, starting off in narrow bands in the true right half of the channel before merging and spreading out further downstream.



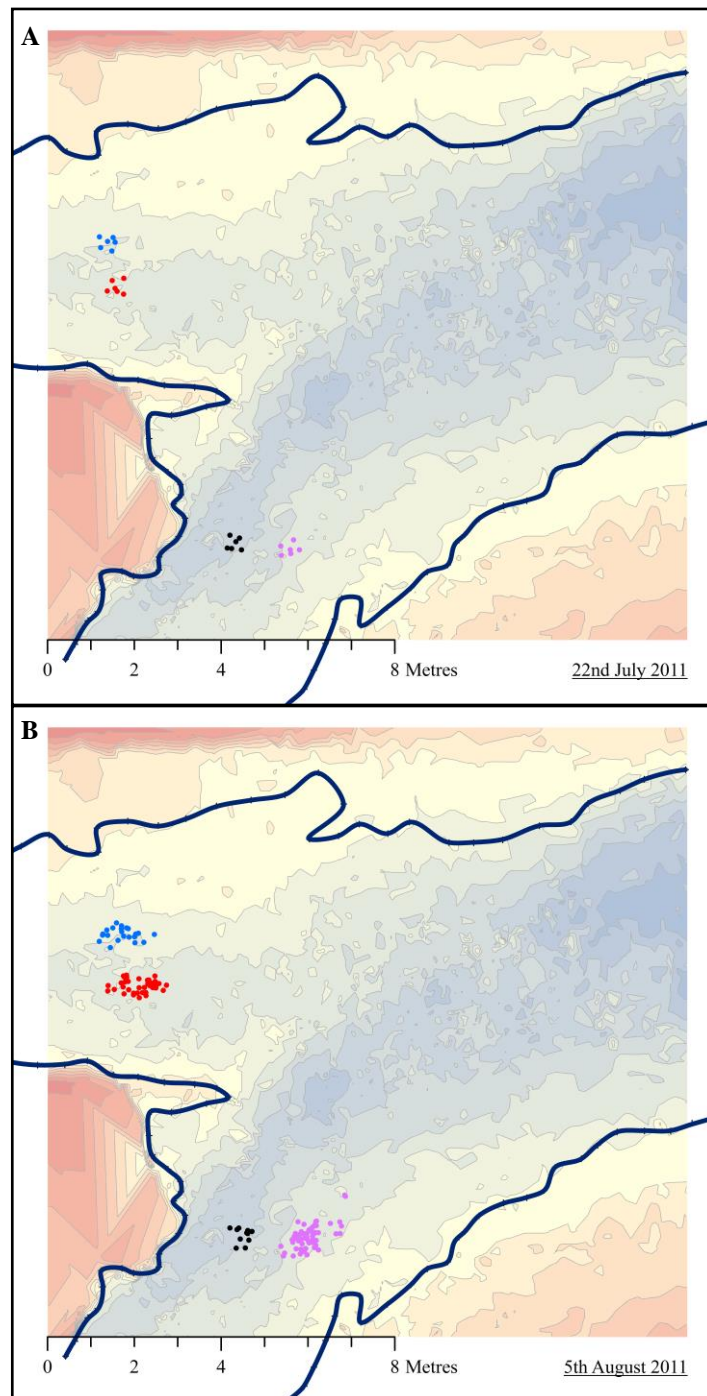


Figure 6.10: Particle positions at the time of seeding on 22<sup>nd</sup> July 2011 (a) and on 5<sup>th</sup> August 2011 (b) for the second experiment at the lower confluence. The water edge on 7<sup>th</sup> October 2011 is shown for reference. The elevation of the bed is given by the background colour, using the same scale as in Figure 4.7. Figure continues on the next three pages.

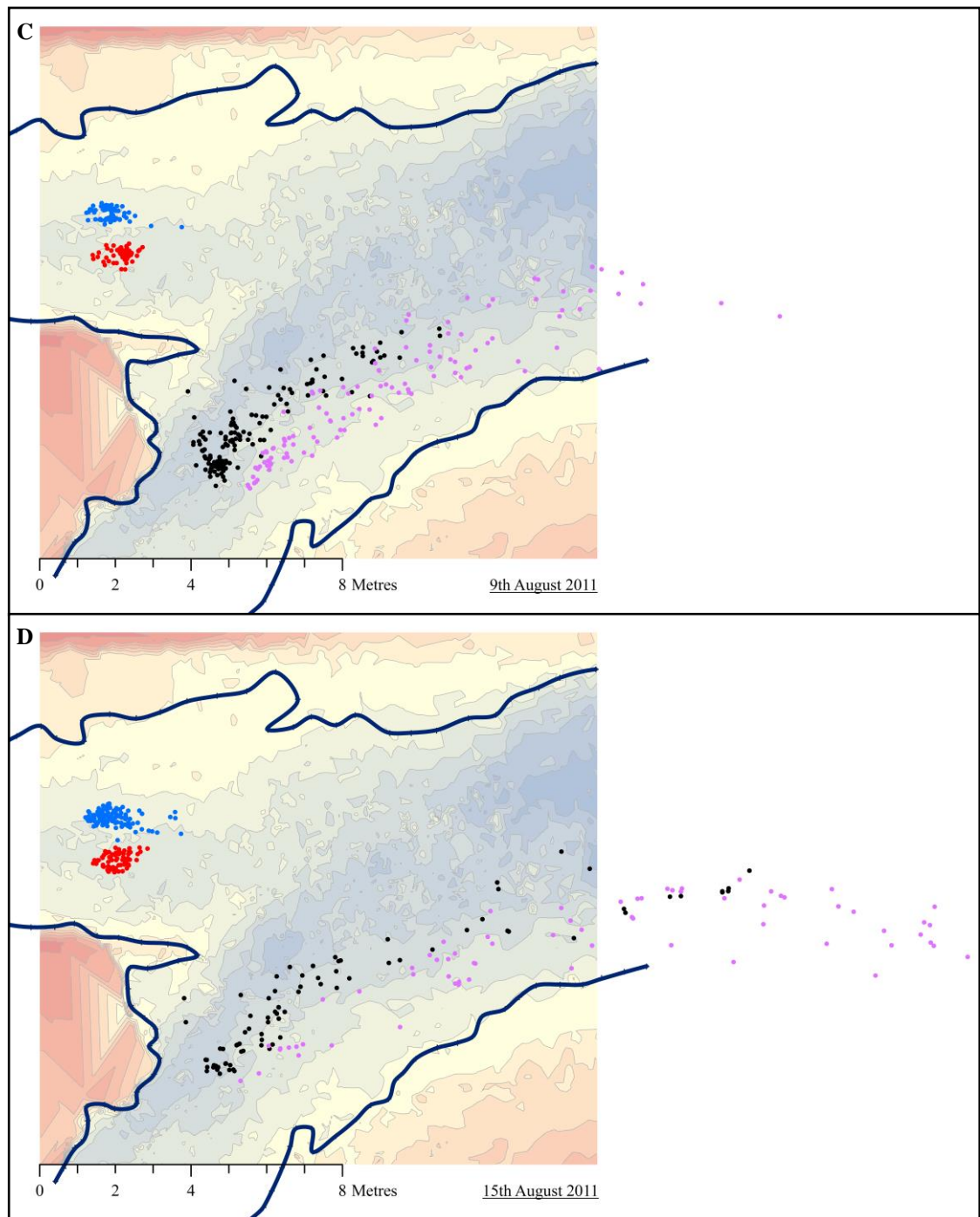


Figure 6.10 (continued): Particle positions on 9<sup>th</sup> August 2011 (c) and 15<sup>th</sup> August 2011 (d) for the second experiment at the lower confluence.

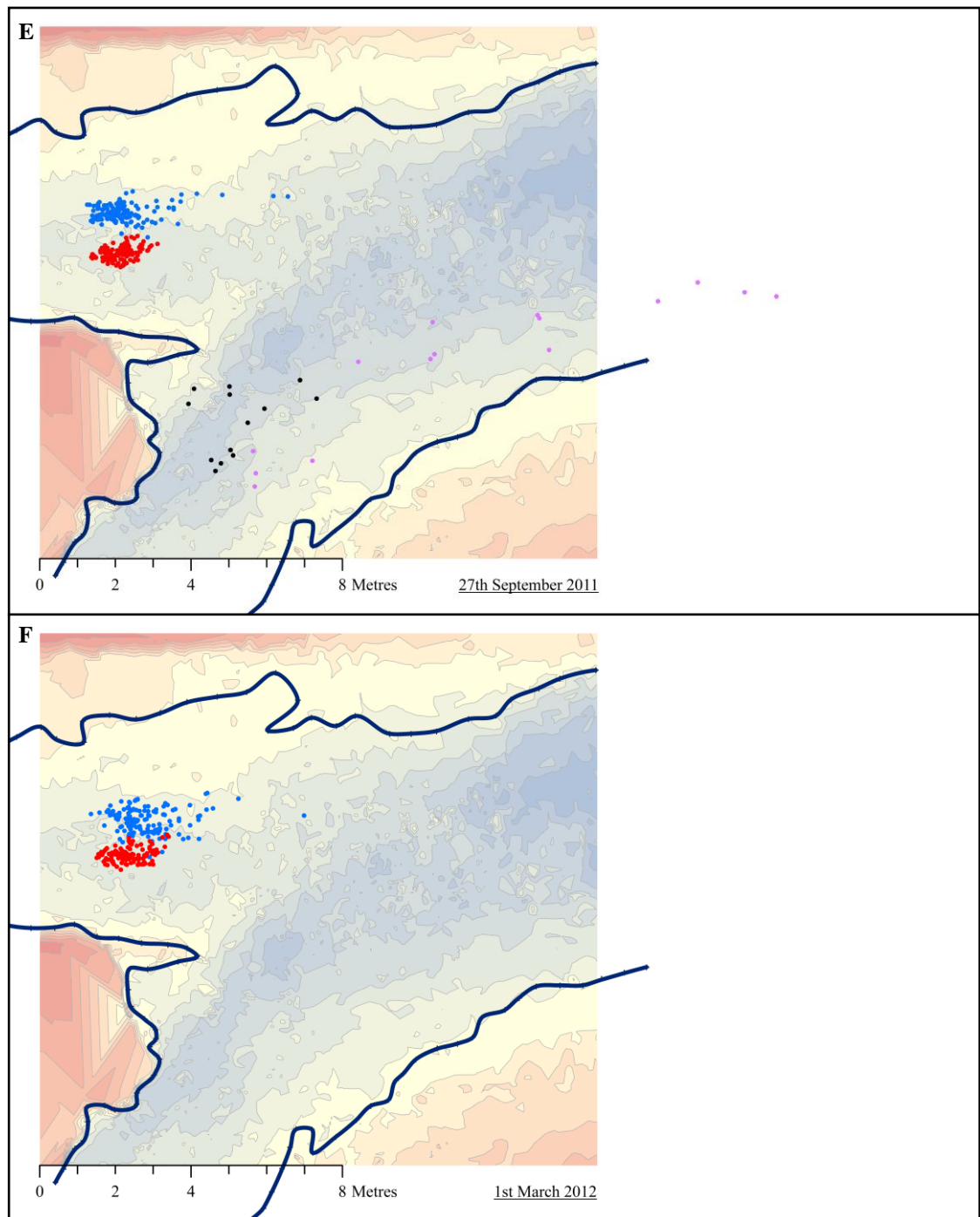


Figure 6.10 (continued): Particle positions on 27<sup>th</sup> September 2011 (e) and 1<sup>st</sup> March 2012 (f) for the second experiment at the lower confluence.

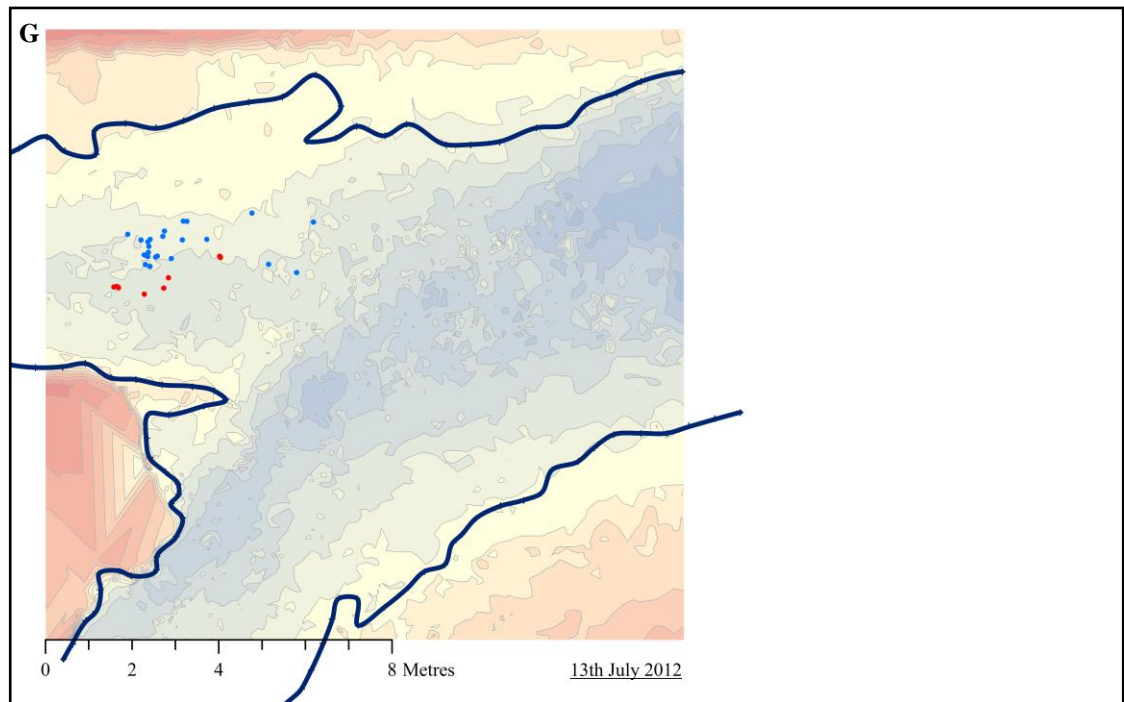


Figure 6.10 (continued): Final particle positions on 13<sup>th</sup> July 2012 (g) for the second experiment at the lower confluence.

#### 6.2.7 Lower Confluence Particle Densities and Near-Bed Streamlines

The calculated particle densities for each patch in the second experiment at the lower confluence are given in Figures 6.11 and 6.12. In Figure 6.11, the density plots are given with the near-bed flow lines for LowerRun005 (flow from the true right tributary dominant), while Figure 6.12 shows the streamlines for LowerRun007.

A comparison of Figures 6.11 and 6.12 shows that the particle trajectories follow the streamlines for LowerRun005 more closely, especially for the patch seeded near to the true left bank of the true right tributary. This would suggest that high discharges in this confluence tend to be dominated by flow from the true right tributary, which is consistent with the slower particle movement in the true left tributary. However, the differences between the near-bed streamlines for the two runs are relatively small, with much less variability than at the upper confluence.



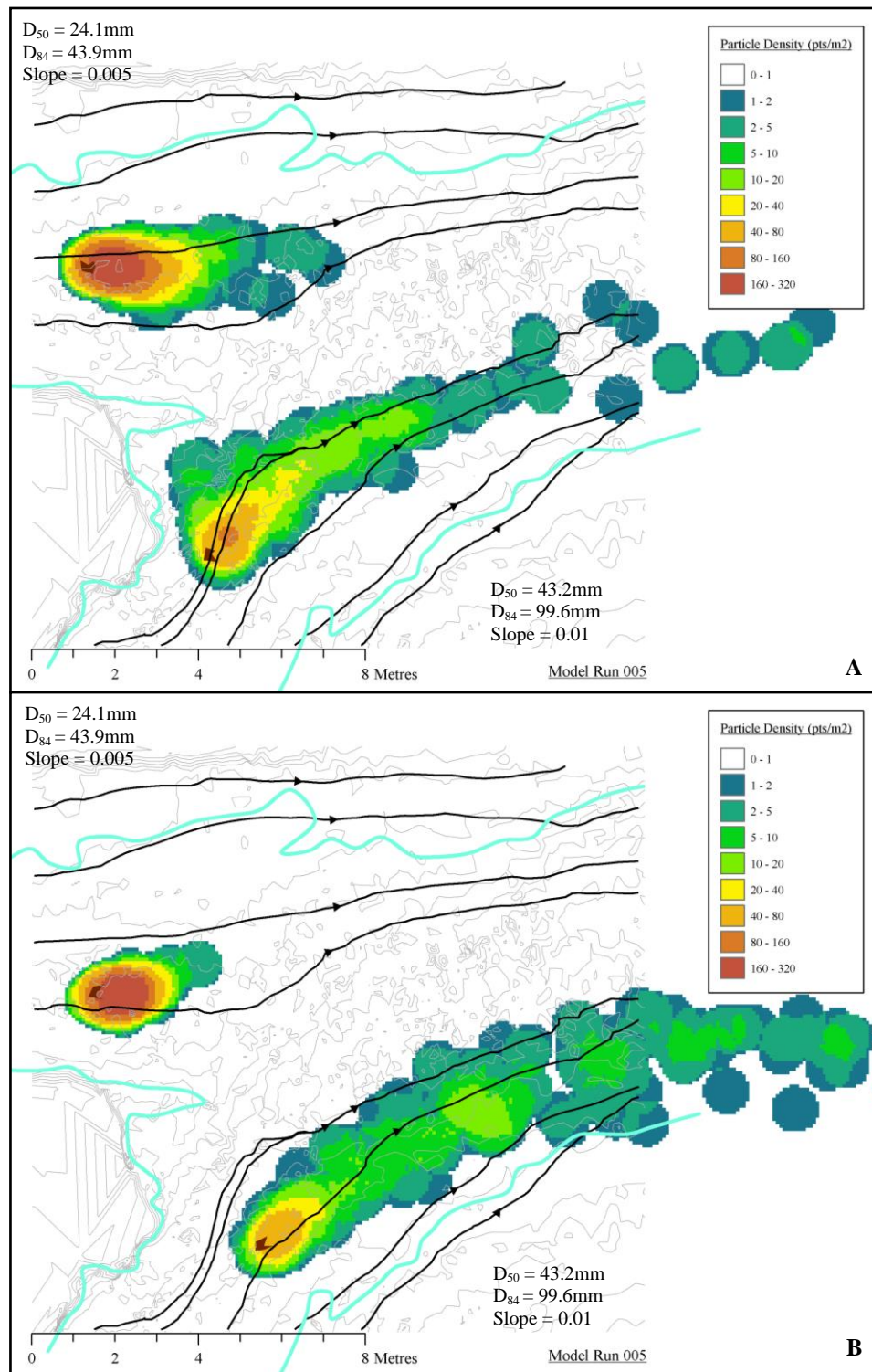


Figure 6.11: Near-bed streamlines from LowerRun005 (flow predominantly from the true right tributary) superimposed on the particle densities from Experiment 2 at the lower confluence. Notation is the same as for Figure 6.6.

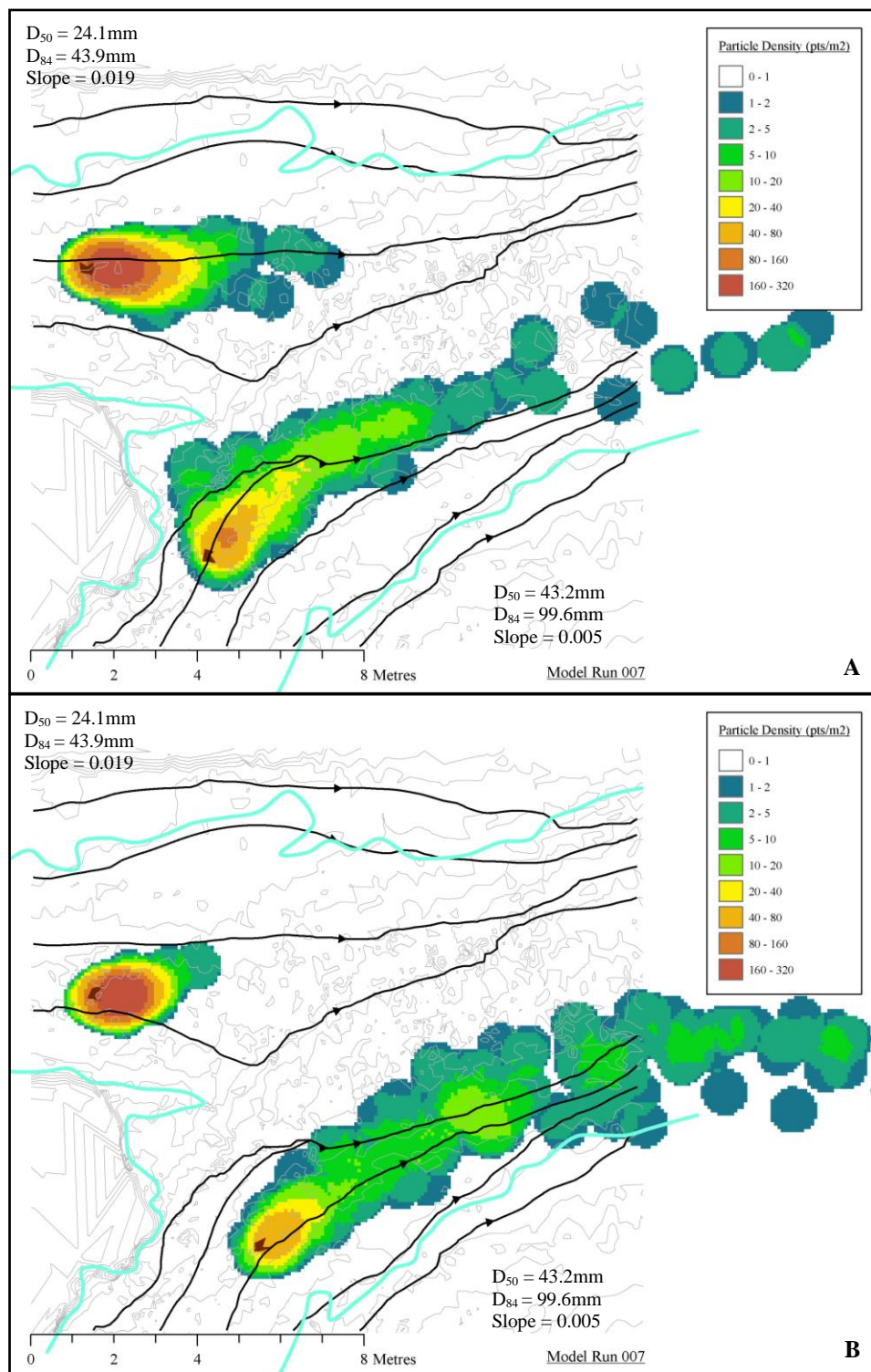


Figure 6.12: Near-bed streamlines from LowerRun007 and particle densities from Experiment 2 at the lower confluence. Notation is the same as for Figure 6.6.

### *6.2.8 Discussion of Particle Tracks at the Moor House Confluences*

For both experiments at the upper confluence (Figures 6.4 and 6.5) the particles in the true right tributary move significantly towards the true right, being deposited well above the low flow waterline. This is unsurprising given the near-bed streamlines in Figures 6.6 to 6.9, with a tendency for flow towards the true right bank regardless of the discharge ratio. However, the results in Figures 6.6 and 6.8, where the streamlines are taken from UpperRun007, suggest that a discharge ratio of 4 (in favour of the true left tributary) is higher than that usually experienced at this confluence. The near-bed streamlines from UpperRun007 are either deflected slightly too far towards the true right bank or not enough to account for the recorded particle movement. A comparison with the shear stress plots in Figure 5.52, meanwhile, shows higher values of shear stress can be found in the area of seeding even with a dominant true left tributary. Therefore, there is evidence that providing the true left tributary is not substantially more dominant than the true right, the flow conditions will enable particle initiation and transport towards the true right bank.

The patches placed in the true left tributary (two in the first experiment and one in the second) do not move as quickly. Again, this can be linked to the shear stress plots in Figure 5.52, with the bed shear stress found in general to be lower in the true left tributary. This implies that a higher discharge is required to move the particles in the true left tributary than in the true right. However, once particle transport has been initiated, the evidence from Figure 6.5 is that movement through the confluence is quick. The particles in the blue patch in Figure 6.5 do not move very far until the series of high flows between December 2011 and February 2012, after which they had almost completely disappeared.

The patch seeded on the upstream corner bar is different from the other particle trajectories as there is a much greater dispersion of the particles. Pebbles in this patch reached both banks of the main channel, although the streamlines in Figures 6.8 and 6.9 do not, by themselves, explain such a wide dispersal. However, the near-bed flow over this bar is highly variable, suggesting that the interactions between the discharge ratio, flow field and bed topography are more complex than in other areas of the confluence. Figure 5.52, meanwhile, shows that the seeding location is a zone of higher bed shear stress in both simulations. It can therefore be surmised that the particles seeded in this location will be entrained in most high flows, with the direction of transport dependent

on the dominance of the tributaries at that time. If flood peaks from the two channels do not coincide, then the tributary dominance will change throughout the flood, giving the potential for significant dispersal of the particles as seen in Figure 6.5c.

For the particle tracks at the lower confluence (Figure 6.10), the most notable difference between tracks from the true left and true right tributaries is the much slower movement of particles seeded in the true left tributary. By comparing Figures 6.3 and 6.10 it can be seen that it took a very large flood to move the majority of particles into the downstream channel. Although there is no evidence of particles being deposited in the downstream channel from the true left tributary, this is most likely due to the particles being transported straight through the confluence in these very high discharges.

The comparisons with the near-bed streamlines in Figures 6.11 and 6.12 show that the particle trajectories match the near-bed flow from LowerRun005 more closely (in particular for those seeded in the true right tributary). This would suggest that high-discharge events tend to be dominated by flow from the true right tributary, thus explaining the much slower movement of the particles seeded in the true left tributary. However, it should be noted that unlike at the upper confluence, the discharge ratio seems to have less effect on the near-bed streamlines (probably due to the bed discordance having a greater effect). Therefore, any flood passing through the confluence is likely to result in similar particle trajectories. The limited movement in the true left tributary is therefore the strongest evidence that these floods tend to be dominated by flow from the true right.

Both confluences at Moor House demonstrate that the highly complex nature of the topography and flow field at upland river confluences results in particle tracks which do not follow the classical routing identified in the laboratory by Mosley (1976). Although the particle tracks in the true right tributaries of both confluences appear to show deflection around the centre of the confluence, particles placed in the centre of the upper confluence were not confined to any particular route. Indeed, the data in this section are more similar to the results of Roy and Bergeron (1990), with particles capable of being transported through the centre of the confluence. Therefore, the bedload transport at these upland confluences is likely to be driven by a combination of factors: the underlying bed morphology, the high levels of bed roughness, the localised effect on the flow field and the variability in this flow field as junction angles and discharge ratios vary during floods.



### 6.3 Grain Size and Roundness Effects on Bedload Transport

#### 6.3.1 Results from the Particle Size and Roundness Experiments

The final survey of Experiment 1 and all surveys from Experiment 2 at the upper confluence were used to test the effect of grain size on particle transport, while Experiment 2 was also used to assess the impact of particle roundness. For the latter, Figure 6.13 shows the spread of the angular and rounded pebbles during Experiment 2.

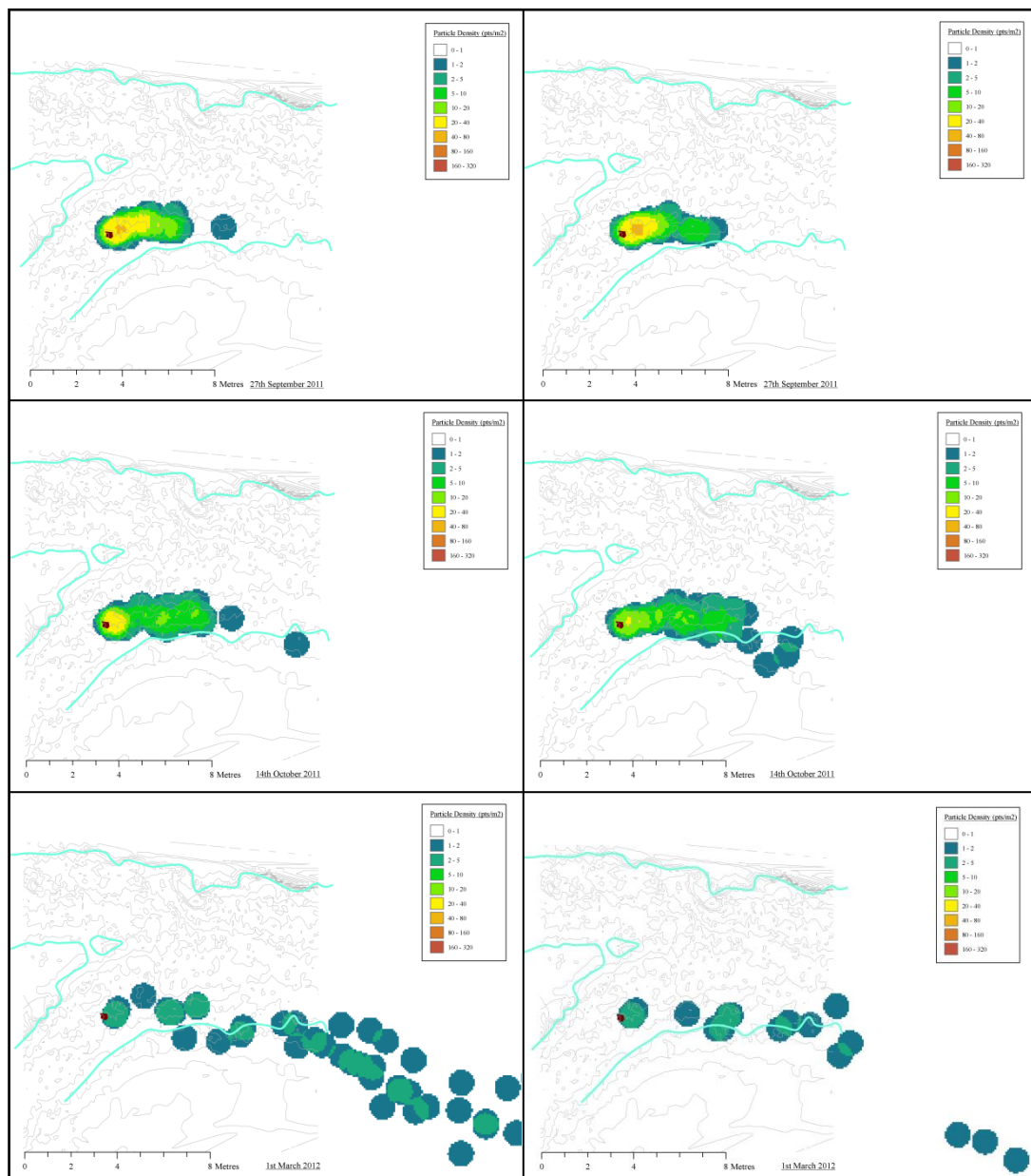


Figure 6.13: Particle density plots for the rounded (*left*) and angular (*right*) particles during Experiment 2 at the upper confluence. The initial seeding point is given by the dark brown polygon.

In Figure 6.13, although the angular particles follow a similar trajectory to the rounded ones, they appear to be transported through the confluence more quickly. To confirm this, Table 6.2 compares the mean particle positions on each survey date.

Date	Angular Particles			Rounded Particles		
	RR	x	y	RR	x	y
23/9/11		3.514	5.871		3.514	5.871
27/9/11	73	$4.662 \pm 0.969$	$6.123 \pm 0.195$	84	$4.678 \pm 0.975$	$6.207 \pm 0.225$
14/10/11	63	$5.923 \pm 1.922$	$6.019 \pm 0.45$	64	$5.374 \pm 1.664$	$6.109 \pm 0.316$
1/3/12	18	$11.439 \pm 5.986$	$4.451 \pm 2.345$	44	$13.52 \pm 5.662$	$3.962 \pm 1.908$

Table 6.2: Mean positions and standard deviations (in metres) for the angular and the rounded particles in each of the four surveys of Experiment 2 at the upper confluence. Distances are given from the lower left corner. The recovery rates from each patch (as a percentage) are given in the RR column.

In terms of distance moved downstream (x), there is little difference between the two pebble types on 27<sup>th</sup> September 2011, whilst on 14<sup>th</sup> October 2011 the angular particles have moved slightly further. The opposite is true of the final survey (1<sup>st</sup> March 2012), although the recovery rate for the rounded particles was much higher. Therefore, this change in pattern may be accounted for by some angular particles having been transported out of the confluence and therefore no longer contributing to the average position. Indeed, if the 18 remaining angular particles are assumed to be the slowest moving of that patch, then they should arguably be compared with the 18 rounded pebbles positioned furthest upstream, for which the mean  $x = 7.775\text{m} \pm 2.779$ . This is significantly less than the mean position for the angular particles. For the cross-stream average particle position there is less variability throughout, with the greatest disparity (0.5m) found at the final survey. By this point, the spread of the particles in the downstream direction will also affect the cross-stream distance (due to the angle of the main channel).

For the grain size analyses conducted at the upper confluence, different zones were defined based on the spread of the particles for the individual patches on each separate day. This was done to ensure the zones had similar numbers of individual particles for comparison. Figure 6.14 shows the Grain Size Distributions (GSDs) for each patch in the final survey of the first upper confluence experiment, split into these zones. Table 6.3, meanwhile, shows these data compared to the total GSD of the recovered particles in each patch.

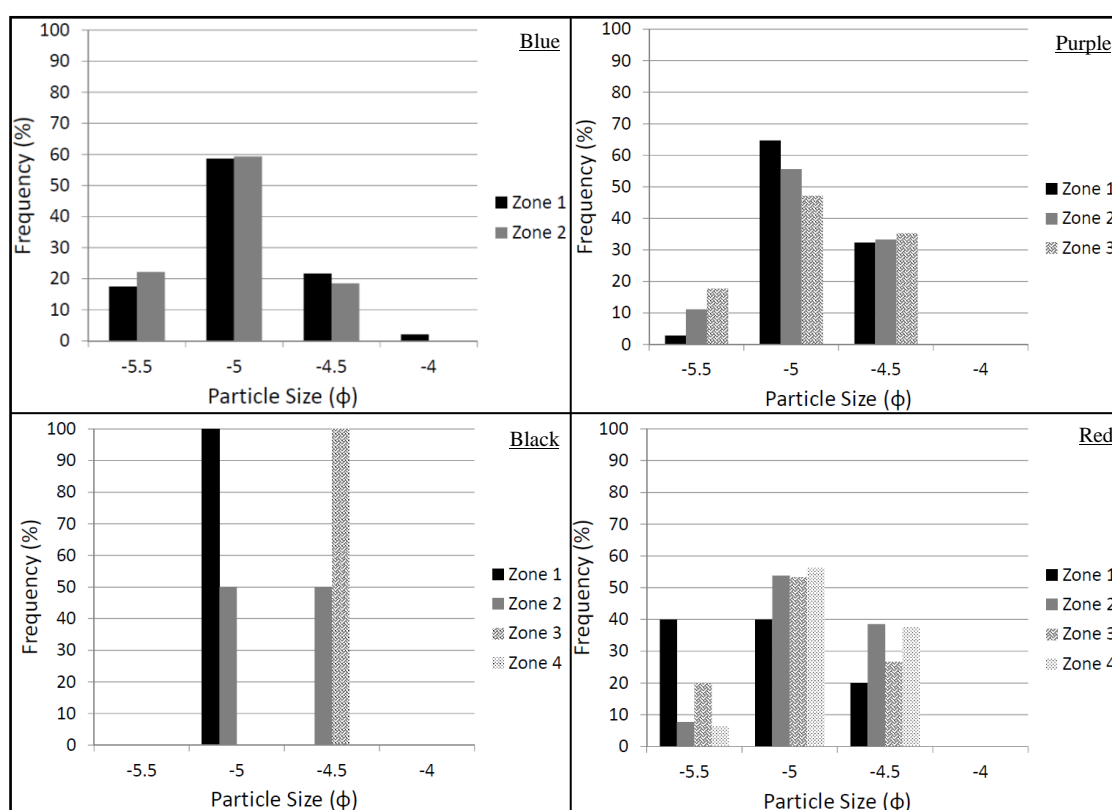


Figure 6.14: Tracer grain size distributions in each patch for the zones marked in Figure 6.4e (from Experiment 1 at the upper confluence). The named colours in the top right corner of each plot refer to the colour of the icon in Figure 6.4, while zone 1 is that located furthest upstream.

	Size (mm)	Zone					Percentage				
		Total	1	2	3	4	Total	1	2	3	4
Blue	45	31	25	6			18.2	17.5	22.2		
	32	100	84	16			58.8	58.7	59.3		
	23	36	31	5			21.2	21.7	18.5		
	16	3	3	0			1.8	2.1	0		
Purple	45	9	1	5	3		9.4	2.9	11.1	17.7	
	32	55	22	25	8		57.3	64.7	55.6	47.1	
	23	32	11	15	6		33.3	32.4	33.3	35.3	
	16	0	0	0	0		0	0	0	0	
Black	45	0	0	0	0	0	0	0	0	0	0
	32	4	3	1	0	0	66.7	100	50	0	0
	23	2	0	1	1	0	33.3	0	50	100	0
	16	0	0	0	0	0	0	0	0	0	0
Red	45	10	4	2	3	1	14.9	40	7.7	20	6.3
	32	35	4	14	8	9	52.2	40	53.8	53.3	56.2
	23	22	2	10	4	6	32.8	20	38.5	26.7	37.5
	16	0	0	0	0	0	0	0	0	0	0

Table 6.3: Distribution of tracer particle sizes in each patch at the end of the first experiment at the upper confluence.

With the exception of the patch denoted by black dots in Figure 6.4 (where numbers are too small to offer reliable conclusions), the percentages of each grain size within a zone are very similar to each other and to the overall GSD for that patch. To confirm this, chi-squared tests were conducted to determine whether there was a statistically significant difference between the GSDs in each zone for a given patch. Because of the low numbers of particles in the  $-4\phi$  and  $-5.5\phi$  bands, in all tests the results were combined into two particle size categories ( $\geq -4.5\phi$  and  $\leq -5\phi$ ). These tests showed no statistical difference for the blue, purple and red patches, with too few particles in the black patch to conduct the test.

For the second experiment at the upper confluence, grain size distributions were obtained before seeding and then for each subsequent survey. Figure 6.15 gives the results from these tests in bar chart form, with the number and percentage of particles in each zone given in Tables 6.4 and 6.5 respectively. In general, the rounded particles have percentages broadly similar to the initial distribution throughout. Very few pebbles are measured in the blue patch, but the results from Zone 2 on 14<sup>th</sup> October 2011 are consistent with the initial values. The orange particle patch has a general increase in the larger particle sizes both with distance downstream on 14<sup>th</sup> October 2011 and through the experiment. For both the red and black patches, there are deviations from the original values throughout the experiment, but there is no clear pattern to any of these deviations.

Chi-squared tests were conducted in the same way as for Experiment 1, with the red patch in the first survey and the blue and black patches in the final survey having too few particles to perform the test. In Tables 6.4 and 6.5, those patches with a statistically significant difference on a given survey date are highlighted in yellow. Although there are statistically significant differences in a number of cases, these are not consistently indicating that smaller or larger particles are travelling further.

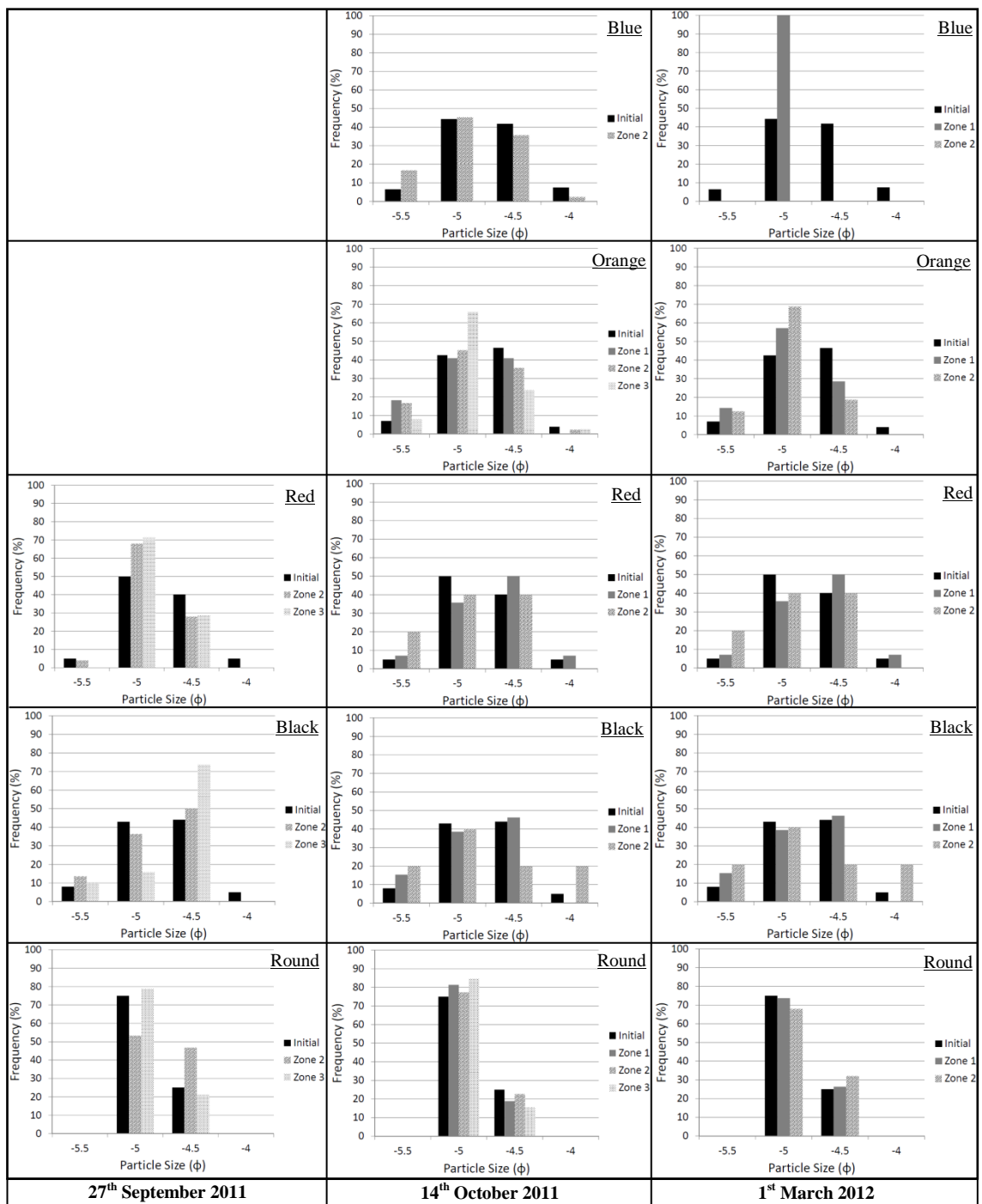


Figure 6.15: Bar charts showing the grain size distributions for each patch in the second upper confluence experiment. The named colours in the top right corner of each plot refer to those used to denote the angular particle patches in Figure 6.5. Zone 1 is located furthest upstream and the survey on 27th September 2011 did not measure particles in this zone to avoid disturbing those clasts yet to move.

	Size (mm)	Initial	27/9/11		14/10/11			1/3/12	
			2	3	1	2	3	1	2
Blue	45	13				1		0	0
	32	89				6		2	0
	23	84				6		0	0
	16	15				0		0	0
Orange	45	14			4	7	3	1	2
	32	85			9	19	25	4	11
	23	93			9	15	9	2	3
	16	8			0	1	1	0	0
Red	45	10	1	0	6	2	1	1	2
	32	101	17	5	37	23	18	5	4
	23	81	7	2	35	13	8	7	4
	16	10	0	0	2	0	1	1	0
Black	45	8	3	2	2	2	3	2	1
	32	43	8	3	14	8	6	5	2
	23	44	11	14	4	15	10	6	1
	16	5	0	0	0	0	0	0	1
Rounded	45	0	0	0	0	0	0	0	0
	32	75	8	26	26	17	11	14	17
	23	25	7	7	6	5	2	5	8
	16	0	0	0	0	0	0	0	0

Table 6.4: Tracer particle sizes for each patch during the second experiment at the upper confluence.

	Size (mm)	Initial	27/9/11		14/10/11			1/3/12	
			2	3	1	2	3	1	2
Blue	45	6.5				7.7		0	0
	32	44.3				46.2		100	0
	23	41.8				46.2		0	0
	16	7.5				0		0	0
Orange	45	7.0			18.2	16.7	7.9	14.3	12.5
	32	42.5			40.9	45.2	65.8	57.1	68.75
	23	46.5			40.9	35.7	23.7	28.6	18.75
	16	4.0			0	2.4	2.6	0	0
Red	45	5.0	4	0	7.5	5.3	3.6	7.1	20
	32	50.0	68	71.4	46.25	60.5	64.3	35.7	40
	23	40.1	28	28.6	43.75	34.2	28.6	50	40
	16	5.0	0	0	2.5	0	3.6	7.1	0
Black	45	8.0	13.6	10.5	10	8	15.8	15.4	20
	32	43.0	36.4	15.8	70	32	31.6	38.5	40
	23	44.0	50	73.7	20	60	52.6	46.2	20
	16	5.0	0	0	0	0	0	0	20
Rounded	45	0	0	0	0	0	0	0	0
	32	75.0	53.3	78.8	81.3	77.3	84.6	73.7	68
	23	25.0	46.7	21.2	18.8	22.7	15.4	26.3	32
	16	0	0	0	0	0	0	0	0

Table 6.5: The tracer particle size results from Table 6.4 converted into percentages for ease of comparison.

### *6.3.2 Discussion of Particle Size and Roundness Effects on Bedload Transport*

The particle tracking experiments at Moor House have demonstrated very little bias in the surveyed particle positions as a consequence of variability in grain size and roundness. For particle roundness, Figure 6.13 and Table 6.2 show very little cross-stream variation in the average angular and rounded particle positions. However, for distance transported downstream, the data in Table 6.2 are more complex. Rounded particles appear to move more slowly at first, before being further downstream on average by 1<sup>st</sup> March 2012. This last dataset, though, will have been affected by recovery rates, with very few angular particles found within the confluence on that date (as shown in Table 6.2). Therefore, it is considered more likely that this disparity is due to a greater number of angular particles having been transported out of the confluence by the time of the final survey. This would imply that, in general, the angular particles are transported more quickly through the confluence, although along very similar paths to the rounded particles. The most likely explanation for this is that the rounded particles have lower skin friction and therefore require a higher critical shear stress to initiate transport. However, further research would be required to determine whether skin friction plays a critical role in particle entrainment at these scales.

With respect to grain size, the results from the first experiment suggest that there is largely equal mobility in the particle movement, at least for this range of particle sizes. The second experiment (Tables 6.4 and 6.5) shows a similar pattern for the rounded particles, with only Zone 2 on 27<sup>th</sup> September 2011 showing large disparities. However, there is more variation for the angular particles, with the only consistent pattern being an increase in the larger particles recovered from the orange patch as time and transport distance increases. From Figure 6.5, though, it can be seen that particles in the orange patch were deposited in some of the deepest parts of the confluence, where visibility is lower and larger particles stand out more easily. Therefore, this increase in particle size may be partially due to larger particles being easier to recover.

As a result, it is argued that there is no conclusive evidence of particle size and roundness having a significant effect on the particle trajectories. There is some evidence that grain size and roundness may affect transport speed, but this may be partly due to the effect of particle size on recovery rate. Therefore, the results presented here reflect those found by Roy and Bergeron (1990), with particle paths unaffected by clast size. Furthermore, the similarity between the tracer particle sizes and median grain size for

the Moor House confluences suggests that the results presented here are likely to give a realistic representation of the bedload transport processes operating in these confluences.

## 6.4 Particle Tracking at the Borgne d'Arolla Confluences

A description of the field site and flow conditions on the Borgne d'Arolla braid plain was given in Chapter 4, along with the topographic and flow data from Confluences E, G and H. As with similar sites used by Ashmore and Parker (1983) and Ashmore *et al.* (1992), the Borgne d'Arolla braid plain is highly dynamic, with morphological change occurring over hourly timescales. As such, it was possible to conduct particle tests for discharges measured *in situ*, although the dynamism did reduce the time available for collecting detailed topographic and flow data. Therefore, in Section 5.12 the HOL model was used to obtain a much greater insight into the three-dimensional flow field at these confluences.

This section presents the particle tracking experiments conducted on Confluences G and H. The first part of the section will set out the methodology of the Borgne d'Arolla experiments, before the results themselves are presented. This will be followed by a discussion which assesses the extent to which the results agree with previous studies and whether the particle dynamics reflect the flow processes operating at these upland confluences, as investigated previously in Section 5.12.

### 6.4.1 Particle Tracking Experiment Design on the Borgne d'Arolla

In Section 1.6 it was determined that at least some of the confluences studied should provide data on individual particle tracks in real time. Due to the high flow velocities and active bed on the Borgne d'Arolla braid plain, it was possible to get individual particle tracks at these confluences, providing the particles were visible in the highly turbid water. Figure 6.16 shows the difference in turbidity between the tributaries at Confluence B, where a very clear tributary from the hillslope met the much more turbid water flowing through the braid plain (the photograph is taken during a small purge). In laboratory tests, suspended sediment concentrations of 5.44g/l and 0.98g/l were calculated from purge and low flow water samples respectively. Even for the low flow conditions, therefore, the suspended sediment concentrations are high (as a



comparison with the data in the review by Turowski *et al.* (2010) shows). This high water turbidity makes it difficult to locate particles on the bed, as can be seen in Figure 6.16 where tracer particles are visible only in the true right tributary.

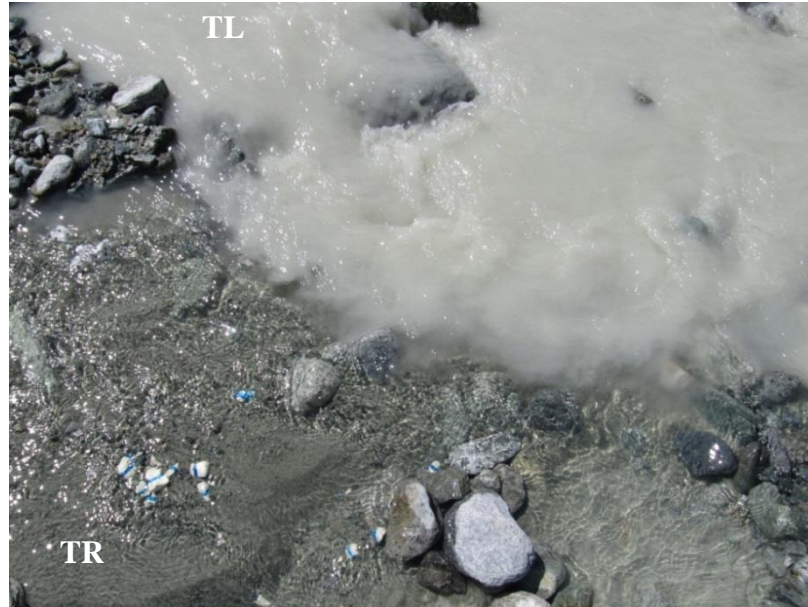


Figure 6.16: Photograph of Arolla Confluence B during a purge, showing the difference in turbidity between the purge flow in the true left tributary (TL) and the low flow in the true right tributary (TR). The photograph here shows an area of approximately  $1\text{m}^2$ .

Therefore, each set of experiments was set up with a sufficiently large and bright particle placed at a series of known starting points. In most cases this approximated to 0.2m spacing across the inlets. The tracer particle size was determined *in situ* based on the depth and visibility of the water. To aid the subsequent surveying of the particle trajectories, the experiments were recorded using the video function of a Canon PowerShot SX200 IS 12.1 megapixel digital camera. The particle trajectory was then plotted with reference to these videos using the Leica Total Station. In addition to the individual particle tracking experiments, patches of particles were released into the flow at a single point in each tributary to assess the spread of particles (using similar painted tracer particles to those used in the Moor House experiments). The outer limits of the particle trajectories were plotted using the Leica Total Station, again with the assistance of video footage.

#### 6.4.2 Results from the Particle Tracking Experiments at Confluence G

Figure 6.17 shows the results from the individual particle tracks and particle patch experiments for Confluence G. Figure 6.17b also shows the 25mm streamlines determined from the HOL model output in Section 5.12.

For the individual particle experiments, larger particle sizes were required in the true left tributary because initial attempts with smaller particles were thwarted by the very low visibility. This may explain the shorter distances travelled by particles seeded in that tributary. Those particles which do travel a considerable distance into the main channel tend to stay to the true left of centre, although two particles got stuck in the lee of a small boulder located 1.7m downstream.

The particles seeded in the true right tributary were, in general, transported further than those in the true left tributary. These particles tend to move through the confluence maintaining a line closer to the true right bank, regardless of starting position.

The polygons in Figure 6.17b connect the surveyed Total Station points from the particle patch experiments. The video footage was used to determine the cross-stream extents of the particle cloud as it was transported downstream and therefore these polygons represent the range of particle trajectories that were observed within each patch. The particle patch experiments for Confluence G reflect the individual transport paths, with particles in both patches being steered towards their own banks. This means the transport paths from the two tributary patches do not cross. Whilst the patches remain nearer their respective banks, however, the particles are also routed around large rocks and pebble clusters which stick out into the channel from the banks. In the case of the true left patch, this results in a narrow range of transport paths.

The true right particle patch in Confluence G largely follows the near-bed streamlines, with the flow being deflected towards the true right bank near the confluence outlet. The similarities are less clear for the true left patch, however, with the flow field predicting initial movement in the downstream direction whereas the particles move towards the true right.

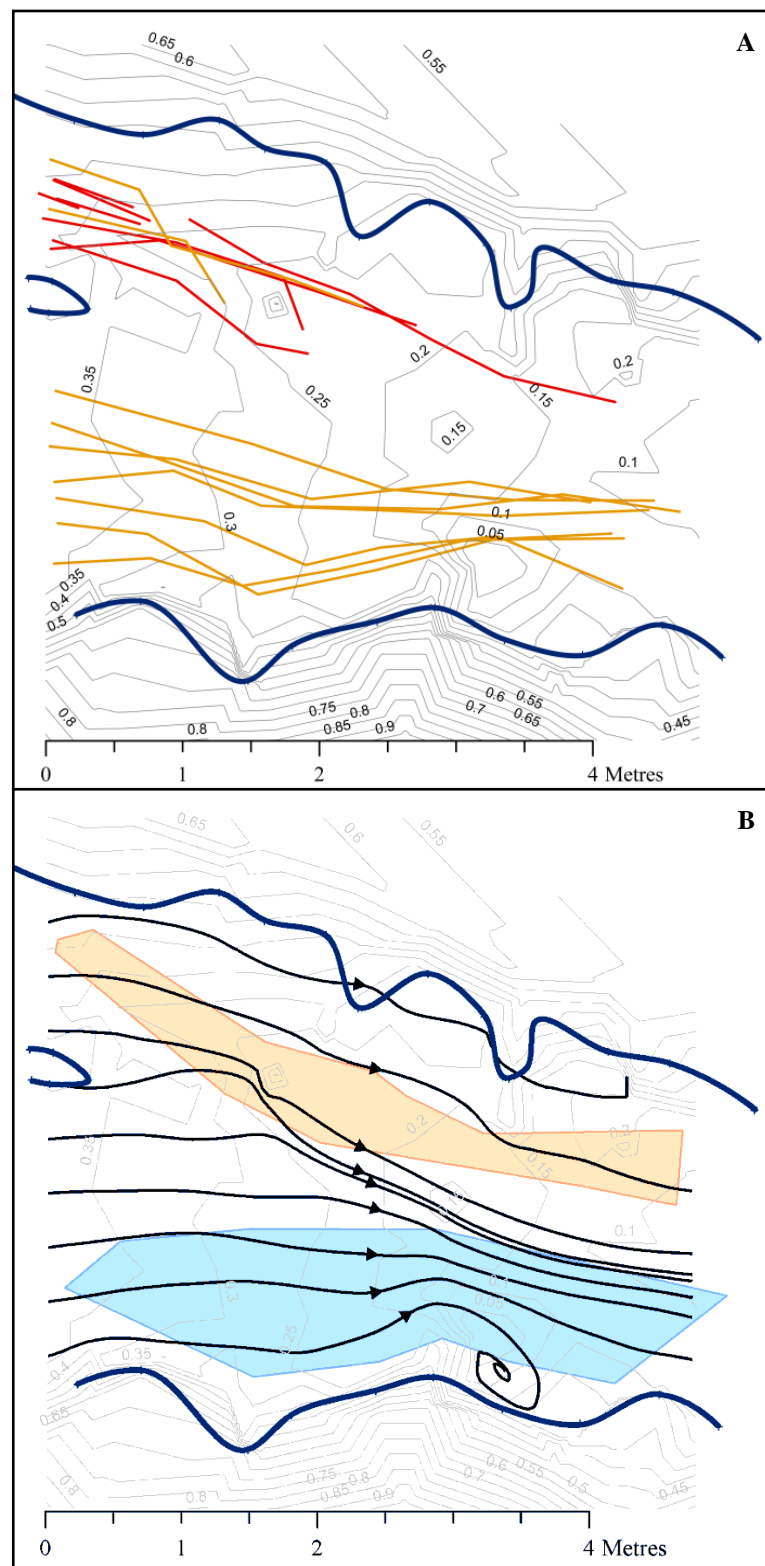


Figure 6.17: Results from particle tracking experiments for Confluence G using individual particle tracks (a) and pebble patches (b). The streamlines in (b) were calculated from the flow at 25mm above the bed in the HOL model results (Section 5.12). Individual particle sizes are given by the colour of the lines, with red particles <128mm and orange particles <64mm. Larger particles were used where visibility was particularly poor.

### *6.4.3 Results from the Particle Tracking Experiments at Confluence H*

Figure 6.18 shows the results from the individual particle tracking and patch experiments at Confluence H, with the near-bed streamlines also given in Figure 6.18b. In this case, through-water visibility was sufficient to enable all individual tracer particles to be less than 64mm in size. Particles in both tributaries of Confluence H reach the confluence outlet, although in the true right tributary it is much more dependent on initial starting position. With one exception, the particles starting in the true left tributary stay close to the true left bank. The difference in routing was found to be dependent on whether the particle passed to the left or right of a small boulder located in the centre of the channel, approximately 2m from the inlets. Meanwhile, those particles seeded in the true right tributary which are transported through the confluence tend to follow trajectories near the centre of the main channel.

The particle patch experiments show a greater spread of particle trajectories in the true left tributary. Particles in the true left patch can travel across the confluence towards the true right bank, whereas those starting in the true right tributary tend to follow paths in the deeper parts of the channel to the right of centre. The results from the patch in the true left tributary mirror the individual particle tracks, suggesting that this too is related to the presence of a small boulder in the middle of the channel.

The comparison between the streamlines and the particle patch outlines in Figure 6.18b show that the two do not clearly follow the same paths, although the differences are not substantial. The streamlines in the true left tributary also show the effect of the small boulder in the centre of the channel, with flow lines deviating around it. Furthermore, the fact that the streamlines from opposite tributaries meet in the centre of the downstream channel helps to explain the early mixing of particles from the two tributaries. However, the inconsistencies between the particle patch outlines and streamlines suggest that other forces are affecting the bedload transport in this confluence.

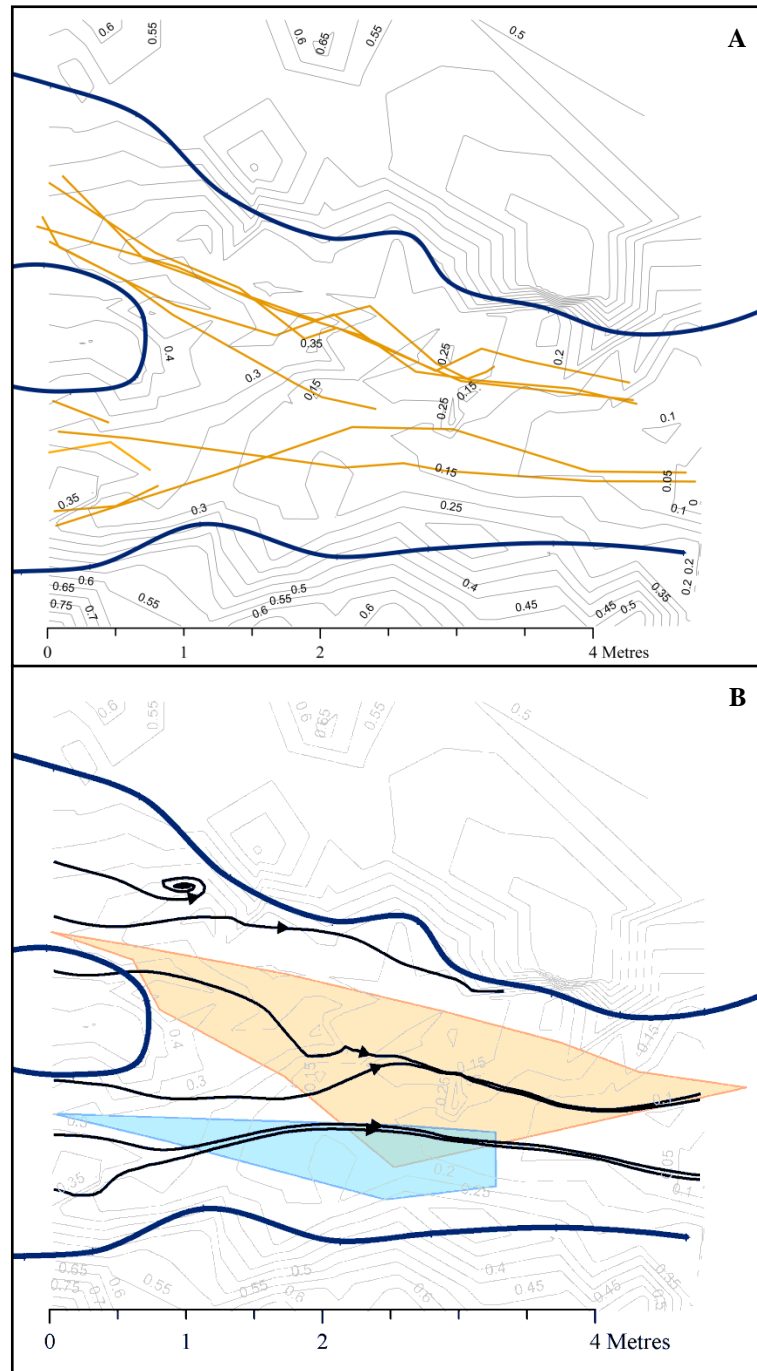


Figure 6.18: Results from particle tracking experiments using individual particle tracks (a) and pebble patches (b) at Confluence H. The shaded areas in (b) show the outer limits of all particle paths within the patch. All particles were <64mm in diameter and the streamlines in (b) show the modelled flow at 25mm above the bed.

#### 6.4.4 Discussion of Arolla Particle Trajectory Data

Both confluences on the Borgne d'Arolla braid plain show similar patterns between the results of the individual particle tracks and the particle patch experiments. However, these particle tracks are not always explained by the near-bed streamlines

derived from the HOL model output. There is a close relationship between the streamlines and particle trajectories in the true right tributary of Confluence G (Figure 6.17b), but for other tributaries the similarities are not as clear. The particle patch results also show localised differences between patches in which most particles follow a similar trajectory (the true left patch in Confluence G) and others where there is much more dispersion (the true left patch in Confluence H).

As such, the results presented in this section suggest that the near-bed flow is not the only factor driving sediment transport. Section 5.12 demonstrated that the confluences on the Borgne d'Arolla braid plain are characterised by complex secondary flow structures and high levels of turbulence. It is therefore likely that this encourages greater variability in the trajectories of particles seeded in the same location. Furthermore, the steep slopes of the channel bed (both cross-stream and downstream) are likely to help to drive the bedload in directions that may not be consistent with the near-bed flow lines. However, one of the biggest factors in the variability of bedload transport will be the presence of large clasts or pebble clusters within the channel. The true left patch in Confluence H (Figure 6.18b) is a particularly good example of this, with particles capable of following a wide range of particle trajectories depending on their routing around a small in-channel boulder. The true left patch in Confluence G shows a similar process but with a different outcome, as pebble clusters near the channel banks encourage most particles to follow a narrow path nearer the centre of the channel. Therefore, the results in this section suggest that the bedload in these steep upland confluences is driven by a combination of the near-bed flow field and localised variations in the channel bed topography.

At the confluence scale, however, there are broader patterns visible in the bedload transport which seem to fit relatively well with the classical model of river confluences. In the classical model, particles from separate tributaries are understood to be routed around the scour hole and mix much further downstream (Mosley, 1976; Best, 1986). Although the Arolla confluences have no clearly defined scour holes (as noted in Section 4.9), in almost all cases there is a tendency for the particle trajectories to be deflected away from the centre of the confluence. This directs particles from the two tributaries away from each other and prevents widespread mixing. The exception to this (at Confluence H) requires an increased junction angle and the presence of a large clast which can occasionally route particles into the centre of the channel. Although the majority of particles do not mix into a single zone further downstream, this may be

attributable to the lower junction angles, which according to the classical model of river confluences should result in weaker secondary circulation cells and therefore longer distances being required to give full mixing of the flow (Mosley, 1976; Ashmore and Parker, 1983; Bradbrook *et al.*, 2001). It is notable that the greater separation between particle patch trajectories at Confluence G also corresponds to a lack of channel-scale secondary flow cells in Figures 5.63 and 5.64.

Therefore, in these highly dynamic systems where the bed is active, the particle transport may become more like that envisaged by the classical model. This may be due to the steeper slopes and consequently higher stream powers ensuring that irregularities in the channel planform and topography are rapidly modified rather than providing large obstacles which affect the flow field throughout the confluence. As such, the much steeper nature of the Arolla confluences appears to negate some of the topographic effects on the flow and thus the bedload transport.

## 6.5 Comparison of the Moor House and Arolla Confluences

From the results presented in this chapter, it has been found that the Moor House confluences show more episodic particle movement, whereas at the Arolla confluences particle transport is active, even during low flow conditions. The steeper water surface slopes and more dynamic channel topography on the Borgne d'Arolla braid plain result in bedload transport processes that are profoundly different from those at the Moor House confluences.

At the Moor House confluences, the more stable banks and channel bed have an important and lasting effect on the flow field. The near-bed streamlines during floods reflect the interactions between this channel-scale topographic forcing of the flow and the discharge ratio. As such, if the simulated tributary discharges are representative of floods in these confluences, the near-bed streamlines derived from the HOL model output tend to match the particle trajectories. In the case of particles placed on the upstream corner bar at the upper confluence, the widespread dispersal of the particles can be explained by the seeding location. Given that the flood peaks from the two tributaries may not pass through the confluence at the same time, the discharge ratio can change throughout a flood. This will give substantial variability in the near-bed streamlines, in particular in the centre of the confluence where the two tributaries meet.

Therefore, particles entrained at the beginning of the flood may follow very different trajectories to those which move later on.

At the Arolla confluences, any topographic effect on the flow and bedload transport is more localised, mostly limited to large clasts and pebble clusters which cannot be easily eroded. However, in the remainder of the channel, the bed is highly active and will therefore be more likely to respond to the flow field than to force it. As such, at the confluence scale there is a tendency for the bedload to be routed away from the centre of the confluence, most likely due to the mutual deflection of the tributary flows. This makes the bedload transport process more similar to the classical model of river confluences than at the Moor House confluences. As particle transport occurs during low flows, any significant variations in this pattern will tend to be caused by the routing of particles around large obstacles rather than changes to the discharge ratio during floods. Meanwhile, smaller scale variability will be encouraged by the high levels of turbulence and the more complex secondary flow that was identified in Section 5.12.

The key differences in sediment dynamics between the Moor House and Arolla confluences can therefore be summarised as follows. The Arolla confluences have an active bed layer that will result in particles being transported through the confluence in a matter of seconds. The cross-stream variability in particle paths is relatively small, unless a large clast is placed in such a way that it diverts particles to one side or the other. The particle tracks do not necessarily follow the modelled near-bed flow directions exactly, but in the absence of large obstacles the variability is more localised, which is most probably due to small-scale differences in secondary flow, turbulence and bed slope. The Moor House confluences, on the other hand, experience episodic particle transport, with several large floods required to carry the particles through the confluence. Under the right conditions, the particle patches are capable of much greater cross-stream dispersal, although if the modelled discharge ratio is representative of the high-flow conditions, the particle paths tend to reflect the near-bed streamlines. A complex interaction between the discharge ratio during floods and topographic forcing of the flow by the relatively stable beds is therefore considered to be the key factor driving the bedload particle paths.

As a result, understanding the complexity of the particle transport at the Moor House confluences will require further investigations into the movement of particles during high flow events. As these data cannot be obtained in the field, it is necessary to



develop numerical modelling methods which enable the bedload dynamics to be investigated under a range of different flow conditions.

## **6.6 Conclusions**

This chapter has presented particle tracking data from the Moor House and Arolla field sites. The context to these experiments was provided in Chapter 4, in which the topographic, roughness and flow data were presented, and in Chapter 5, which used the HOL model to investigate the flow field at these confluences in more detail. This chapter therefore presented particle tracking data from two upland field sites known to have contrasting characteristics. The confluences of Moor House Nature Reserve are stable, with sloping water surfaces but subcritical flow. The confluences on the Borgne d'Arolla braid plain, meanwhile, are steeper, more dynamic and have flow which is for the most part supercritical. It is the implications of this contrast for the bedload dynamics which has been investigated in this chapter.

In Section 6.2, the results from the particle tracking experiments at Moor House were presented. The data were assessed for quality and found to satisfy the criteria in Section 3.8.4. The results showed particle movement which was episodic and variable between tributaries, with some patches moving very little until a large flood had passed through the confluences. It was also shown that there was substantial spread in some of the particle patches, in particular those located close to the centre of the upper confluence. This implies that in the centre of this confluence the flow field can be highly variable depending on the particular flow conditions. Therefore, understanding the interactions between flow, morphology and particle transport at these stable, upland confluences is far from straightforward. However, if the discharge ratio were simulated correctly, the modelled near-bed streamlines would be very similar to the particle trajectories.

The experiments in Section 6.3 investigated the impact of particle size and roundness on bedload transport at the Moor House confluences. It was found that, for the range of tracer particle sizes used in this study, the impact on particle transport was relatively minor. Although there were some zones where the particle distributions were statistically different to the initial Grain Size Distribution, the differences did not follow a consistent pattern. There is some evidence that angular particles were transported

more quickly than those that are more rounded, but the transport path was similar regardless of shape.

The results from the particle tracking experiments at the Borgne d'Arolla confluence were presented in Section 6.4. The section began by discussing the design of the experiments, which was found to be important for ensuring that reliable data could be obtained in the highly turbid waters of the Borgne d'Arolla. At the confluence scale, the main pattern was for the particle tracks at these confluences to be deflected away from the centre of the downstream channel. The particles were rarely found to travel across the confluence, with the exceptions being due to flow routing around particularly large clasts. As a result, it was argued that particle paths in these highly dynamic confluences better reflected the classical model of river confluences.

Section 6.5 compared the datasets from Section 6.2 and 6.4, noting that the greater complexity at the Moor House confluences was due to the complex interactions between the stable bed topography and the variable discharge ratios. At the Arolla confluences, meanwhile, the greater similarity to the classical model of river confluences was linked to the more active bed responding rapidly to the flow field. However, it was noted that in order to better understand the more complex particle transport processes at the Moor House confluences, it is necessary to develop a particle transport model which can use the high-discharge flow data from the simulations in Section 5.11. The development of a reduced-complexity particle model is therefore the focus of the following chapter.

# Chapter 7:

## Discrete Particle Modelling of Upland River Confluences

### 7.1 Introduction

The bedload transport data presented in Chapter 6 gave some useful insights into sediment processes at upland river confluences. However, in order to understand the interactions between the flow field and sediment transport, it is necessary to obtain data that link specific flow conditions to known particle trajectories. Although this information was acquired on the highly dynamic Borgne d'Arolla braid plain, it was not possible to obtain such data for the Moor House confluences, where bedload transport was much more episodic. Therefore, in order to truly understand the underlying processes it is necessary to be able to model the particle movement and to examine how this changes in different flow conditions. As such, in Section 1.5, two of the research objectives (4 and 5) set out the need to develop and to test (using the field data from Chapter 6) a sediment transport model which uses the three-dimensional flow model results from Chapter 5.

The summary in Table 6.1 showed that there has been limited research into bedload transport through natural river confluences, in particular at the steeply sloping confluences of interest in this thesis. The results from Chapter 6 are therefore highly valuable as they will enable thorough testing of the particle model at two different types of upland river confluence. In addition, it was shown from the experiments in Chapter 6 that particle patches seeded in these confluences exhibit substantial dispersal when transported downstream (*e.g.* Figure 6.5). Given that particles seeded in the same location can follow different paths, there may be limited benefit to employing highly complex modelling of individual trajectories. Instead, a more practical approach would be to develop a reduced-complexity model that is based on the fundamental physics, but disregards those factors which have a negligible impact at the geomorphological scale.

Therefore, this chapter begins by examining the current state of research into modelling bedload transport in natural rivers using Eulerian sediment transport models and Lagrangian discrete particle models (DPMs). In the case of DPMs, many of the

terms in the governing equations have empirical co-efficients which will be subject to some uncertainty. This uncertainty has implications for the modelling approach used in this chapter and is therefore also discussed. Section 7.3 presents a reduced-complexity DPM, with an explanation of its physical basis and the model setup. Due to the potential error in the empirical co-efficients, the GLUE methodology of Beven and Binley (1992) is introduced and its adaptation to the modelling in this chapter explained. In addition, Section 7.3 explains the steps taken to reduce the computational requirements of this type of analysis by rewriting the code to enable the parallel execution of the model on Graphics Processing Units (GPUs). In Section 7.4, the results from the calibration and testing of the model on the Arolla datasets are then presented, followed by its application to the Moor House confluences in Section 7.5. In each of these sections the implications of the results are discussed, from which the conclusions in Section 7.6 are drawn.

## **7.2 Modelling Bedload Transport in Natural Rivers**

Moreno and Bombardelli (2012) suggest that, in theory, the most complex possible modelling approach for particle transport would involve using a Computational Fluid Dynamics (CFD) solver to obtain the flow field around individual particles, before using this information to update the particle positions. Having done this, the computational mesh would be redefined and the process repeated for the next time step. Although the developments in Chapter 5 mean that there are CFD data available for the natural river confluences being studied, there are numerical stability issues associated with the re-meshing process (see Section 3.4.7) and substantial computational costs when running reach-scale models at grain-scale resolutions.

As a result, there are two main approaches that have been used to model bedload transport: Eulerian sediment transport models of different levels of complexity and Lagrangian discrete particle models (DPMs). More complex Eulerian models such as Delft3D and BASEMENT usually couple the two-dimensional shallow water equations with a range of models to calculate the flux of suspended sediment and bedload (Lesser *et al.*, 2004; Vetsch *et al.*, 2013; Deltares, 2013). Reduced-complexity Eulerian models, meanwhile, do not accurately represent the flow physics and may use more simplified methods to determine the sediment transport, but they have been demonstrated to be capable of reproducing major geomorphological processes in braided (Murray and

Paola, 1994, 1997; Thomas and Nicholas, 2002; Nicholas *et al.*, 2006; Lane, 2006) and single-thread (Nicholas, 2009, 2010; Nicholas *et al.*, 2012) channels.

By contrast, DPMs simulate the movement of individual particles (rather than volumes of sediment) based on the forces acting upon them. The forces resolved by these models (Figure 7.1) include the submerged gravity force, drag force, lift force (sometimes incorporating the Magnus spin force), Basset history force, added mass force and fluid acceleration force (Nino and Garcia, 1994). In addition, these models account for the collisions between individual particles.

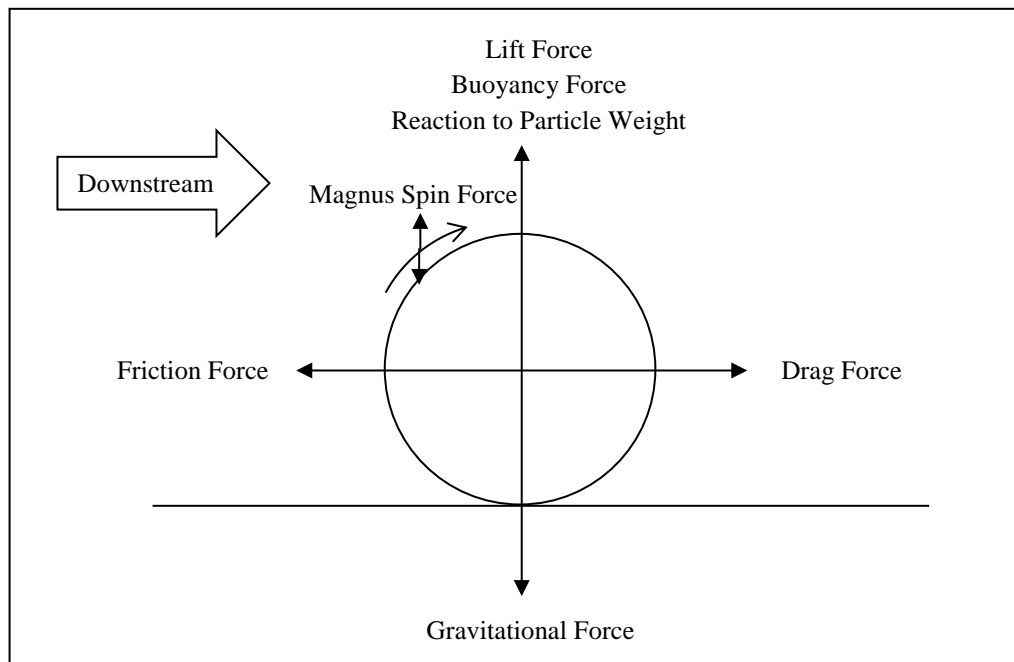


Figure 7.1: Diagram showing the major forces acting on a particle placed on a flat surface. The Basset history force, added mass force and fluid acceleration force are not shown.

This section will therefore summarise the principles behind these different modelling approaches and provide examples of their use. In many cases DPMs have been used to investigate the saltation process in detail and so this is addressed in a separate section. The uncertainty in these DPMs and the implications for the particle modelling approach to be used in this chapter will then be explored.

### 7.2.1 Eulerian Sediment Transport Models

The more complex Eulerian sediment transport models that are currently available have been applied to investigate the flow and sediment dynamics of a range of geomorphological features. Examples include meander bends (*e.g.* Darby *et al.*, 2002),

river spits (*e.g.* Dan *et al.*, 2011), river mouth bars (*e.g.* Edmonds and Sliggerland, 2007; Nardin and Fagherazzi, 2012; Siviglia *et al.*, 2013), river bifurcations (*e.g.* Sloff and Mosselman, 2012; Siviglia *et al.*, 2013), fringing coral reefs (*e.g.* Storlazzi *et al.*, 2011) and the near-shore region (*e.g.* Ruggiero *et al.*, 2009).

Although there are a number of different Eulerian sediment transport models available, in general they can be seen to share a number of key characteristics. Firstly, they tend to solve the flow field using a form of the two-dimensional shallow water equations, although in some cases a form of three-dimensional approach is used (*e.g.* Delft3D (Lesser *et al.*, 2004) and TELEMAC (Villaret *et al.*, 2013)). As part of this, there are often in-built modules to account for the effects of secondary flow, turbulence and wave processes (*e.g.* Lesser *et al.*, 2004). Secondly, the sediment transport will invariably be split into suspended sediment and bedload transport, with the suspended component modelled using the advection-diffusion equations (Villaret *et al.*, 2013; Deltares, 2013; Vetsch *et al.*, 2013). Thirdly, the modelling of the bedload will have methods to account for multiple sediment sizes, multiple layers of bed material and processes such as armouring (Lesser *et al.*, 2004; Villaret *et al.*, 2013). Finally, the flow, sediment transport and bed morphology components will be coupled at each time step, with the computational mesh updated where necessary to account for the sediment fluxes (Darby *et al.*, 2002; Lesser *et al.*, 2004; Deltares, 2013; Vetsch *et al.*, 2013, Villaret *et al.*, 2013).

Therefore, these more complex Eulerian models include a wide range of features in order to model sediment transport and thus morphological change in a physically realistic manner. However, one key limitation of these methods is that changes in the flow field and geomorphology occur over fundamentally different timescales. In some models (*e.g.* Delft3D), this is addressed by introducing a parameter which effectively speeds up the morphological change in the model (Lesser *et al.*, 2004; Deltares, 2013), although such an approach may not be ideal. There is also the potential for substantial computational costs in some applications. It is therefore unsurprising that reduced-complexity Eulerian models have also been popular for modelling the interactions between flow, sediment transport and morphological change.

Since Murray and Paola (1994) first demonstrated the potential of reduced-complexity models for replicating natural channel evolution, there has been increasing interest in the use of these models to simulate sediment transport. This is partly due to the fact that physically realistic and computationally efficient models of the evolution of

channel morphology are yet to be developed (Nicholas, 2010). Examples of the use of these reduced-complexity models are for simulating braiding (Murray and Paola, 1994, 1997; Thomas and Nicholas, 2002; Nicholas *et al.*, 2006), sinuous single-thread channels (Nicholas, 2009), alternate bars in a straight river channel (Nicholas, 2010) and flow velocities around mid-channel bars in very large rivers (Nicholas *et al.*, 2012).

The principle of reduced-complexity models is that through using a simplified version of the flow physics, the model can imitate the complexity of morphological change in natural rivers using a series of simpler local rules (Nicholas *et al.*, 2006; van de Wiel *et al.*, 2007). These simpler rules are used to determine the flow routing, from which the shear stress can be calculated using the flow depth and bed slope (Coulthard and van de Wiel, 2007). The shear stress calculations are used to model the sediment erosion, transport and deposition, enabling the cell elevations (and thus the morphology) to be changed ahead of the next time step (Coulthard, 2001). In some cases (*e.g.* the CAESAR model), simulation of the sediment transport can be highly sophisticated, accounting for multiple grain sizes and bed layers (Coulthard, 2001; van de Wiel *et al.*, 2007; Coulthard *et al.*, 2007).

The key advantage of these types of model is their computational efficiency. By using a simple approach to obtain the flow field and sediment transport, the model can be run for much longer periods of time (100-10,000 years) over large areas (10-100km) in order to assess the long-term river evolution (Thomas and Nicholas, 2002; Coulthard *et al.*, 2007; Nicholas and Quine, 2007; Nicholas *et al.*, 2012). Given the model runtimes in Table 5.1, such applications are clearly unfeasible using CFD models.

Although reduced-complexity models have been demonstrated to be very good at replicating the patterns seen in natural rivers, there are some key limitations. Firstly, the flow routing tends neither to conserve momentum nor to replicate the effects of turbulence and pressure gradient forces (van de Wiel *et al.*, 2007; Nicholas, 2009). Secondly, there are difficulties associated with modelling secondary flow and lateral sediment transport, which can play an important role in channel migration (Murray and Paola, 1994, 1997; Coulthard *et al.*, 2007; Van de Wiel *et al.*, 2007). Thirdly, it has been argued that such approaches can correctly reproduce the patterns of geomorphological evolution, but for the wrong reasons (Lane, 2006). Finally, attempts such as those by Nicholas (2009, 2010) and Nicholas *et al.* (2012) to introduce a more complex solution of the flow often compromise the key advantage of computational efficiency.

These issues with reduced-complexity models are well-known and generally accepted by those that use them (*e.g.* Coulthard *et al.*, 2007). However, given the complexity of the flow field at the upland confluences being studied in this thesis, it is inappropriate to simplify the fluid dynamics in this way. Furthermore, given that Objective 4 in Section 1.5 focuses on simulating the bedload transport *process* in upland river confluences, all of the Eulerian sediment transport models discussed in this section are considered unsuitable for this research. As Siviglia *et al.* (2013) note, such applications are designed for situations where there is morphological evolution over the medium term. Therefore, models that simulate the movement of individual particles are likely to be more appropriate.

### 7.2.2 Discrete Particle Models

Discrete Particle Models (also called Discrete Element Models) involve the tracking of individual particles and the detection of collisions between those particles (Cleary and Prakash, 2004). To avoid confusion with the Digital Elevation Models presented in Chapter 4, the abbreviation DPM will be used throughout to refer to all models of this type. DPMs have been used in a range of geomorphological applications, such as in landslides (Campbell *et al.*, 1995), the soil compaction process (Ransing *et al.*, 2004) and the movement of particles in the nearshore region (Drake and Calantoni, 2001; Calantoni *et al.*, 2004). A fuller summary of the applications of DPMs is given by Richards *et al.* (2004), but for the purpose of this research it is studies of bedload particle transport that are of interest.

In fluvial geomorphology, DPMs are generally used to simulate the entrainment of particles from an active bed layer that can be created within the model by dropping particles from above (McEwan and Heald, 2001). The equations of motion are evaluated at each time step and then algorithms developed to detect any collisions that have occurred due to the particle movement. The resultant momentum change from these collisions is then resolved for each affected particle before proceeding to the next time step. Original versions of DPMs assumed that all particles were spherical because of the complexity of using irregularly-shaped particles (Hodge *et al.*, 2007), although recent advances have extended these models to account for non-spherical forms (*e.g.* Calantoni *et al.*, 2004; Latham and Munjiza, 2004).



One of the major problems with DPMs is their long runtimes, which is due to the time required to detect particle collisions. The computational time increases substantially as the number of particles increases (Cleary and Prakash, 2004; Latham and Munjiza, 2004; Richards *et al.*, 2004; Heald *et al.*, 2004) and a realistic limit is considered to be tens of thousands of particles (Drake and Calantoni, 2001). This means that it is invariably not possible to simulate real processes, because of the much larger domain sizes and longer time periods required (Heald *et al.*, 2004; Latham and Munjiza, 2004). As such, these approaches are not yet suitable for modelling bedload transport in natural river confluences.

### *7.2.3 Modelling Saltation Using DPMs*

There has been substantial interest in modelling the saltation process, as it is considered to be the dominant method for transporting bedload (Nino and Garcia, 1994). DPMs are used for this purpose, but until recently they have tended to deal with the motion of single particles, thus removing the high computational cost associated with modelling the collision process. Instead, the main focus has been on determining the relative importance of different forces on the modelled particle trajectories.

One of the earliest attempts to model saltation in this way is that of Wiberg and Smith (1985), who developed a model which accounted for the drag, lift, added mass, gravitational and buoyancy forces acting on a single particle. The model also allowed for particle collisions with the bed, using a co-efficient of restitution to account for the loss of kinetic energy (Wiberg and Smith, 1985). In the decades since, a large amount of research has been conducted in an attempt to evaluate the impact of different forces on the saltation process, with particular focus on the Magnus spin force and Basset history force.

Although some studies exclude the Magnus spin force on the grounds that its effect is negligible or that it is difficult to determine the angular momentum of the particle (Nino and Garcia, 1994; McEwan *et al.*, 1999; Hardy, 2005; Wang *et al.*, 2009), others have included it and found that it plays a minor, but significant, role in particle saltation. Lee and Hsu (1994) found a 12% increase in saltation length and height when the Magnus spin force was included, with Nino and Garcia (1998) finding similar results with their model. More recently, the work by Lukerchenko *et al.* (2009) showed that the relative importance of the Magnus spin force to the overall force balance

increased towards the end of the trajectory. Therefore, there is substantial evidence that the Magnus spin force is important to particle saltation, even if its inclusion in DPMs is far from straightforward.

The Basset history force has also been the subject of much research in recent years, even though again some models exclude it (Lee and Hsu, 1994; Kelsey, 1996; McEwan *et al.*, 1999; Hardy, 2005). The Basset force is generally agreed to be necessary to accurately represent the height and length of the saltation hops, with its greatest influence as the particle approaches the bed (Nino and Garcia, 1994, 1998; Lukerchenko *et al.*, 2009). The importance of the Basset force is, however, linked to particle size, with Lukerchenko *et al.* (2012) finding that the Basset term only accounted for more than 10% of the total force on the particle if the particle diameter was smaller than 11mm. The inclusion of the Basset term in the equations of motion, though, comes with a high computational cost due to the need to store the particle acceleration data for all previous time steps (Lukerchenko *et al.*, 2012).

Other recent developments in the modelling of particle saltation have been in the representation of the bed, the flow and inter-particle collisions. In terms of bed representation, three-dimensional approaches have become more commonplace since they were first implemented by Sekine and Kikkawa (1992). Hardy (2005, 2006b) meanwhile, used the Mass Flux Scaling Algorithm (MFSA) to represent a gravel-bed channel within a CFD model framework, thus allowing saltation to be modelled using the three-dimensional flow data rather than assuming a logarithmic velocity profile.

Early models of particle saltation did not include inter-particle collisions (*e.g.* Nino and Garcia, 1994), but more recent research has attempted to determine their impact on the saltation process. Wang *et al.* (2009) established that in three-dimensional models the saltation heights could increase by 20-80% due to the collision process. Moreno and Bombardelli (2012), meanwhile, found that including collisions resulted in greater cross-stream diffusion of the particle trajectories, especially at lower bed shear stresses.

Due to the research reviewed in this section, the understanding of the saltation process has substantially increased. However, computational considerations have meant that these types of models have yet to be applied at the geomorphological scale (Kelsey, 1996; Hardy, 2005). Therefore, if this type of modelling is to be used to investigate the bedload transport processes at upland river confluences, inevitably some simplifications will be required.

#### 7.2.4 Uncertainty in the DPMs

As with most modelling techniques in fluvial geomorphology, the results from DPMs are subject to some uncertainty. Mountain rivers, in particular, are considered to be difficult to model, with significant disparities possible between model results and field data (Ancey *et al.*, 2008). In part, this is due to the difficulties in obtaining validation data at the appropriate scale (Cleary and Prakash, 2004; Heald *et al.*, 2004). However, it is also due to uncertainty over the appropriate values for the drag, lift and added mass co-efficients, which are discussed in turn below. In addition, if particle collisions are modelled there is a wide range of potential values for the co-efficient of restitution (*e.g.* McEwan *et al.*, 1999; Drake and Calantoni, 2001) and the assumption of spherical particles may lead to errors because the interlocking between stationary particles will not be represented (McEwan and Heald, 2001).

The drag force has been widely used in DPMs, but there is still some uncertainty regarding the most appropriate value for the co-efficient, especially in unsteady flows (Nino and Garcia, 1994). In particular, the flume experiments of Schmeeckle *et al.* (2007) found higher drag co-efficients than are normally stated, both for a sphere (0.76) and natural particles (0.91). The same is true for the added mass co-efficient, with some evidence that the actual value should be higher than the 0.5 normally used for a sphere (Nino and Garcia, 1994).

Compared to the drag term, there is much less understood about the lift force and its co-efficient (Nino and Garcia, 1994; Schmeeckle and Nelson, 2003). Schmeeckle *et al.* (2007) found little correlation between the lift force and flow velocity, thus bringing into question the validity of calculations made using this method. Unsurprisingly, there has therefore been some difficulty in calculating an appropriate value for the lift co-efficient (Bridge and Bennett, 1992). Generally, a lift co-efficient of 0.2 tends to be used because it is the value Wiberg and Smith (1985) calculated by re-analysing the data of Chepil (1961). However, there is clearly a wide range of potential values and little evidence to support the continued use of this one value.

There is therefore substantial evidence that if DPMs are to be used to determine the bedload transport in upland river confluences, there will be a number of sources of uncertainty in the model output. As a result, the modelling approach used should ideally account for this in some way.

### *7.2.5 Discussion of Bedload Transport Models*

There is little doubt that DPMs are a powerful tool for understanding the bedload transport process. However, it is also clear from the literature that there are some important issues with the method. Firstly, the complexity of such methods restricts their applicability to reach-scale bedload transport processes, especially if the entire active layer is being modelled. Secondly, attempts to represent the force balance as accurately as possible are somewhat undermined when extrapolated to larger scales because of the uncertainty in the co-efficients used. Finally, as was demonstrated in Chapter 6, the movement of bedload in natural rivers is also highly variable, meaning that models which produce just one particle trajectory will not truly represent the nature of bedload transport.

One solution to this problem would be to return to the Eulerian models described in Section 7.2.1. These have proved themselves to be very good at replicating the geomorphological patterns in many fluvial environments. However, they are designed for applications at much larger spatial and temporal scales than an individual river confluence, thus limiting the conclusions that can be drawn with respect to the bedload transport process.

As such, it is proposed that a modelling approach be developed which uses a less complex form of the DPM method. This will use a simplified version of the force calculations in the DPMs, but also allows uncertainty in the model parameters to be accounted for. The reduced-complexity DPM developed in the following section uses the uncertainty in the model parameters to give an indication of the probability that individual particle trajectories will be followed.

## **7.3 Model Development and Implementation**

This section explains the development of a reduced-complexity DPM, starting with the underlying physics of the model and the justification for excluding some of the forces. The methods used to account for flow turbulence and particle initiation are then discussed, followed by the presentation of results from experiments to determine the particle density, friction co-efficient and spatially-distributed drag co-efficients. The application of the GLUE methodology of Beven and Binley (1992) is then discussed, including the steps taken to reduce computational runtimes by running the simulations

in parallel on Graphics Processing Units (GPUs). Finally, preliminary tests are conducted to determine the appropriate values for the time step variables and the initial number of randomly-generated parameter sets for the GLUE method.

### 7.3.1 Model Physics

The equations of motion for particle transport are fundamentally derived from Newton's Second Law, which states that the rate of change in momentum will be equal to the forces acting on the particle (Wiberg and Smith, 1985). Section 7.2.3 has already discussed the different forces acting on a saltating particle, of which some (*e.g.* the Magnus and Basset terms) are often excluded from particle models on the grounds that they are negligible (*e.g.* Nino and Garcia, 1994; Hardy, 2005). The same assumption is made here, with the Magnus and Basset terms excluded on the grounds that their effect will be minor at the scale of interest.

The reduced-complexity DPM developed in this chapter is based on the equation of Schmeeckle and Nelson (2003):

$$(m + C_m m_f) \frac{dV}{dt} - m_f (1 + C_m) \frac{DU}{DT} = (m_f - m)g + F_D + F_L \quad (7.1)$$

In Equation 7.1,  $V$  is the velocity of the particle and  $U$  is the velocity of the fluid, while  $m$  is the mass of the particle and  $m_f$  the equivalent mass of fluid for the particle volume.  $C_m$  is the added mass co-efficient (usually set to 0.5 for a sphere), while  $F_D$  and  $F_L$  are the drag and lift forces respectively. The first term on the right hand side of Equation 7.1 corresponds to the combined gravitational and buoyancy forces on the particle.

Schmeeckle and Nelson (2003) argue that the second term on the left-hand side of the equation (in grey) is both difficult to estimate and unlikely to result in significant errors if omitted. As such, given the reduced-complexity nature of the model, it was determined that this term would be excluded.

Wiberg and Smith (1985) give the formulae for the drag and lift terms as:

$$F_D = C_D \frac{\rho}{2} A_D |u_f - u_s| (u_f - u_s) \quad (7.2)$$

and:

$$F_L = \frac{\rho}{2} A_L C_L [(u_0^2)_T - (u_0^2)_B] \quad (7.3)$$

where  $C_D$  and  $C_L$  are the drag and lift co-efficients respectively,  $A_D$  and  $A_L$  are the effective cross-sectional areas and  $\rho$  is the density of the fluid. In Equation 7.2,  $u_f$  and  $u_s$  refer to the velocities of the fluid and the particle respectively, while in Equation 7.3  $u_0^2$  is the ambient flow velocity at the top (subscript  $T$ ) and bottom ( $B$ ) of the particle.

Much of the complexity associated with the models described in Section 7.2.3 is due to the inclusion of the saltation process. In particular, this means that the forces in the vertical direction have to be resolved and the collisions with the bed must be simulated. As such, the decision was taken to model the particles as being in contact with the bed at all times, effectively assuming that they are always sliding or rolling. This is not to say that saltation is considered an unimportant process in bedload transport. After all, the evidence from the experiments of Nino *et al.* (1994) show clearly the importance of saltation in the steep, gravel-bed channels of interest to this study. Instead, it is argued that given the uncertainty in so many of the model parameters (Section 7.2.4), it is possible to adequately represent the likely bedload particle trajectories through a river confluence without having to explicitly account for the saltation process. The reduction in computational time instead allows multiple simulations to be run to account for the potential error in the co-efficients.

As the particles are assumed to be in contact with the bed at all times, it is necessary to account for the friction. The standard formula for friction ( $F_R$ ) is given in Equation 7.4:

$$F_R = \mu R_N \quad (7.4)$$

where  $\mu$  is the co-efficient of friction and  $R_N$  is the force normal to the bed slope (*i.e.* the reaction to the mass of the particle). The co-efficient of friction will differ depending on whether the particle is stationary or moving and therefore two different co-efficients are included in the model. The values given to these co-efficients and the range of acceptable values to be used in the GLUE methodology are discussed further in Section 7.3.5.

By discretising the time component of Equation 7.1, the particle momentum at a given time step can be calculated from the particle momentum at the previous time step and the forces acting on the particle at the current time step. Rearranging Equation 7.1 in this way gives:

$$V_t = \frac{(m + C_m m_f) V_{t-1} + ((m_f - m)g + F_D + F_L + F_r) \Delta t}{(m + C_m m_f)} \quad (7.5)$$

where  $\Delta t$  is the length of time step and the subscripts  $t$  and  $t-1$  refer to the current and previous time steps respectively. Equation 7.5 is used to calculate the new particle velocities in both the downstream and cross-stream directions, which are then used to determine the particle position ahead of the next time step. By using Equation 7.5, the model therefore accounts for the seven of the forces in Figure 7.1 (the added mass, buoyancy, gravitational (and reaction), drag, lift and friction forces), while excluding the fluid acceleration, Magnus spin and Basset history forces.

### 7.3.2 Flow Turbulence

Flow turbulence is known to play an important role in sediment entrainment in natural rivers (Hardy, 2005), although many DPMs use a standard logarithmic velocity profile and make various assumptions about the nature of the turbulence (*e.g.* Nino and Garcia, 1998; Moreno and Bombardelli, 2012). For this research, the CFD model results from Chapter 5 provide more detailed data on the flow velocities and turbulence intensity. The turbulence modelling method of Hardy (2005) is therefore used to take advantage of the additional flow information provided by the CFD models. The  $\kappa$ - $\varepsilon$  RNG turbulence model used in these simulations gives a value for the turbulent kinetic energy (TKE),  $k$ , which is defined as follows:

$$k = \frac{1}{2} (\overline{u'^2} + \overline{v'^2} + \overline{w'^2}) \quad (7.6)$$

where  $u'$ ,  $v'$  and  $w'$  are the instantaneous fluctuations from the mean velocity components in the downstream, cross-stream and vertical directions respectively. The  $\kappa$ - $\varepsilon$  RNG model assumes that turbulence is isotropic and therefore:

$$\overline{u'^2} = \overline{v'^2} = \overline{w'^2} \quad (7.7)$$

Substituting these values into Equation 7.6 and rearranging gives:

$$\frac{2k}{3} = \overline{u'^2} \quad (7.8)$$

As shown in Equation 7.9, the term on the right hand side of Equation 7.8 is equivalent to the variance ( $\sigma^2$ ) of the instantaneous velocity values.

$$\sigma^2 = \frac{\sum(u - \bar{u})^2}{n} = \frac{\sum(u')^2}{n} = \overline{u'^2} \quad (7.9)$$

This implies that:

$$\sigma^2 = \frac{2k}{3} \quad (7.10)$$

and therefore the standard deviation ( $\sigma$ ) can be calculated from:

$$\sigma = \sqrt{\frac{2k}{3}} \quad (7.11)$$

Therefore, the value of  $k$  from the CFD model output is used to obtain the standard deviation ( $\sigma$ ) of the flow velocity. Instantaneous flow velocities are calculated by multiplying  $\sigma$  by normally-distributed random numbers, which are then used by the model to determine the drag and lift forces at each time step.

### 7.3.3 Particle Initiation

In order to represent the bedload transport process, it is necessary to be able to determine when a particle will be entrained. Most entrainment models in DPMs tend to assume that the particles will pivot around one another (Bridge and Bennett, 1992). However, in the model developed here this is simplified to assume that a particle is



entrained if it has managed to slide up the slope between the bottom of the traced particle and the top of the bed particles which surround it. This is explained diagrammatically in Figure 7.2.

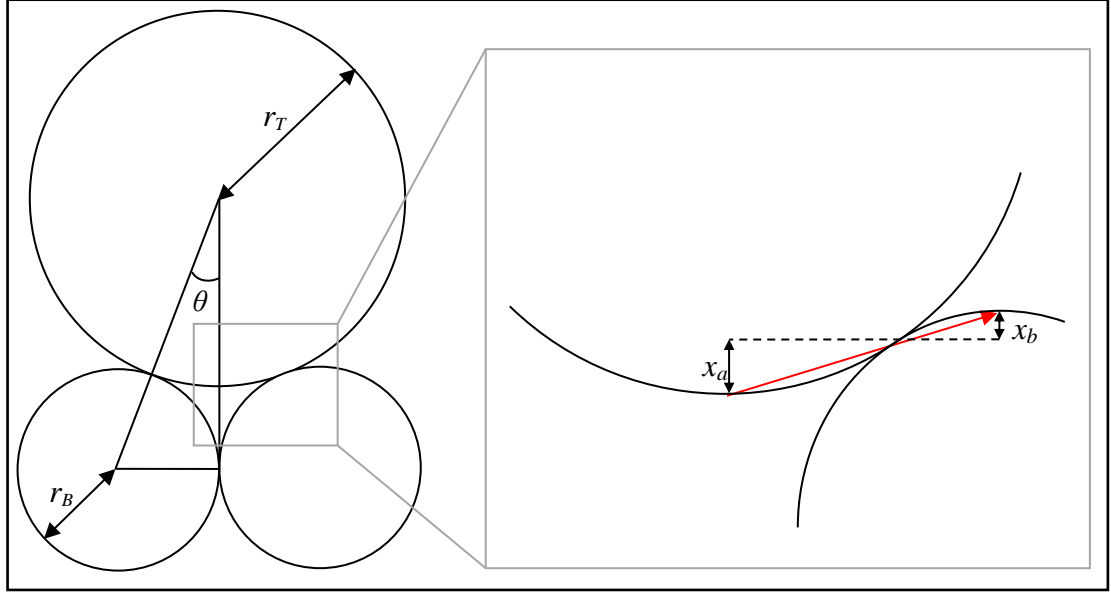


Figure 7.2: Diagram showing the tracer particle at rest in the pocket between two bed particles. The red arrow shows the slope which the particle must slide up to be entrained.

The angle,  $\theta$ , in Figure 7.2 can be determined using the radii of the bed and tracer particles ( $r_B$  and  $r_T$  respectively) as follows:

$$\sin \theta = \frac{r_B}{r_B + r_T} \quad (7.12)$$

The values  $x_a$  and  $x_b$  from Figure 7.2 are calculated by finding the adjacent of the right-angled triangle and subtracting it from the radius (which is equivalent to the hypotenuse). This gives  $x_a = r_T - (r_T \cos \theta)$  and  $x_b = r_B - (r_B \cos \theta)$ , with the slope from the bottom of the tracer particle to the top of the bed particle given by:

$$s = \frac{(x_a + x_b)}{r_B} \quad (7.13)$$

The model assumes that the slope is the same in all directions, and that the particle is considered to have escaped once the horizontal distance from its original starting position is greater than the radius of the bed particle. Additionally, the tracer

particle is assumed to be resting at an elevation below the height of the bed until it has escaped, which means that the model also accounts for the sheltering effect. Using this method, however, does have implications for the drag co-efficient, which are discussed in the following section.

#### 7.3.4 Particle Density and Values for the Friction and Drag Co-efficients

Using the model developed in this section requires a number of co-efficients and parameters to be determined before the model is run. These include the drag, lift and added mass co-efficients, as well as the particle density, friction co-efficient and bed particle size. With the exception of particle density, all of these parameters will be allowed to vary as part of the GLUE methodology (see Section 7.3.5) to give an indication of the uncertainty in the model results. Nevertheless, it is still necessary to determine the particle density and an initial estimate of the friction co-efficient *a priori*. In addition, because the model allows for spatially distributed values of the drag co-efficient, these had to be determined using preliminary CFD models.

The density of the particles was calculated from the mass and volume of five randomly selected tracer particles. A balance was used to find the mass and the volume was found using a measuring cylinder. The results are given in Table 7.1:

Particle Mass (g)	Volume (l)	Density (g/l)
133.7	0.05	2674
76.67	0.03	2556
26.61	0.01	2661
52.64	0.02	2632
37.63	0.015	2509

Table 7.1: The mass, volume and calculated density for five randomly-selected tracer particles.

The results from Table 7.1 give a mean density of 2,606g/l, which is equivalent to 2,606kg/m<sup>3</sup> and was rounded to 2,600kg/m<sup>3</sup>. This is very close to the value of 2650kg/m<sup>3</sup> for quartz particles, suggesting that the value calculated here is an acceptable estimate.

The static friction co-efficient can be found by testing the force required to initiate movement of a particle resting on a flat surface. Experiments were conducted by placing five different tracer particles on a horizontal rock surface (a paving slab) and pushing them using a force meter. The force was slowly increased until the particle

began to move, with the maximum value of the force recorded. The static co-efficient of friction is calculated by dividing the maximum force by the particle weight. The results of this are given in Table 7.2.

ID	Force required to overcome friction (N)					Particle Weight (N)	Friction co-efficient
	1	2	3	4	Average		
1	0.83	0.545	0.925	0.785	0.771	1.305	0.591
2	0.49	0.37	0.581	0.37	0.435	0.755	0.576
3	0.14	0.15	0.225	0.24	0.189	0.26	0.726
4	0.36	0.445	0.335	0.305	0.361	0.515	0.701
5	0.14	0.225	0.325	0.28	0.243	0.37	0.655

Table 7.2: Table showing the results from tests to determine the static friction co-efficient.

The results from Table 7.2 give an average static friction co-efficient of 0.65, which is similar to the value of 0.5 considered by Campbell *et al.* (1995) to be typical for rocks. This, however, can be considered an upper bound, as the widespread initiation of bed particles is likely to reduce the effective friction experienced by an individual particle. The sliding friction co-efficient is much harder to determine, not least because the contact between the tracer particle and the bed is essentially lubricated. The sliding friction co-efficient will therefore be substantially less than the static friction co-efficient. However, both friction co-efficients will be varied as part of the GLUE methodology and therefore a realistic range of values for each co-efficient is all that is required. Given the results in Table 7.2 and the discussion here, the range of potential values for the static and sliding friction co-efficients are set at 0-0.8 and 0-0.3 respectively. The sensitivity of the model to these values will be assessed in Section 7.4.

The initiation model described in Section 7.3.3 will result in the bed particles shielding the lower part of the tracer particle from the flow. Therefore, in this case the standard value of the drag co-efficient for a sphere (0.47) will be inaccurate. As such, CFD simulations were set up to resolve the flow around a sphere, using the Marjoribanks *et al.* (2012) method to determine the drag co-efficient at each vertical slab. This makes the assumption that a sphere is a series of cylinders of different radii stacked on top of one another. The results of the drag calculations for simulations at two different resolutions are given in Figure 7.3.

The negative values in Figure 7.3 are likely to be due to anomalies encountered as flow passes over the top of the sphere. As such, drag co-efficients of 0 are assigned at these points, although the low projected areas will lead to negligible drag forces in any

case. Near the centre of the sphere the value of  $C_D$  is approximately 1, which is the standard value for a cylinder, with the drag co-efficient decreasing nearer the poles.

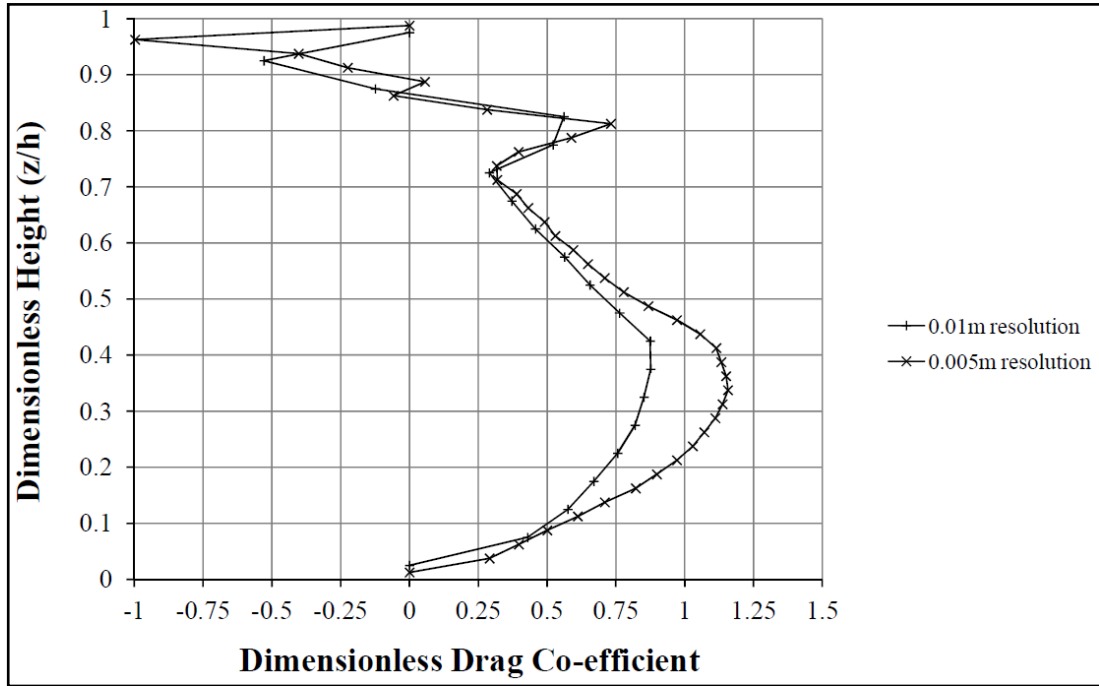


Figure 7.3: Plot of the vertical distribution of drag co-efficients for a sphere.

The distributed values of  $C_D$  for the higher resolution case were used in the model to calculate the drag force for each vertical slab. The sum of the drag forces for each segment is then used to determine the overall drag force on the particle.

### 7.3.5 The GLUE Methodology

Given the uncertainty in the model parameters discussed in Section 7.2.4, it seems inadvisable to arbitrarily select values for each co-efficient without assessing the sensitivity of the model to the outcome. One option would be to calibrate the model to find the optimal parameter set. However, it has been argued that in reality, the concept of a single, best-performing set of parameters is false (Beven and Binley, 1992; Beven, 2001). Furthermore, given the variability in particle trajectories shown in Chapter 6, it is arguably far more representative to allow the model to give a range of possible outcomes.

The GLUE methodology is a Monte Carlo technique that was formulated to account for the uncertainty in model parameter values and the equifinality in

environmental models that can result (Beven and Freer, 2001). Although originally designed for rainfall-runoff modelling, with minor changes the principles can be adapted to the modelling of bedload transport in natural rivers. A full description of the GLUE methodology is provided throughout the literature (Beven and Binley, 1992; Freer *et al.*, 1996; Beven, 2001, 2009), a summary of which is given below:

1. The first step is to choose an appropriate performance measure and determine the criteria for acceptance or rejection of individual parameter sets.
2. The range of potential values for each parameter must then be defined, along with a method of sampling from within this range.
3. The model is run for each parameter set and a value for the performance measure calculated.
4. All parameter sets which fail to reach the required level of performance are rejected, with the remainder defined as ‘behavioural’ and kept. It is important, however, to ensure that failures are not due to external factors such as errors in the input data (Beven, 2009).
5. The values of the performance measure are then used to weight subsequent predictions made by the model.
6. For each successive run of the model, the performance measure is used to remove non-behavioural parameter sets and update the weightings applied to the remainder.

There is inevitably a certain amount of subjectivity in this method, for example in the choice of performance measure and the range of parameter values allowed (Beven and Binley, 1992; Freer *et al.*, 1996). For the parameter values, the information in Sections 7.2.4 and 7.3.4 was used to determine an acceptable range, the details of which are given in Table 7.3. In the case of the drag co-efficient, the use of distributed values (as set out in Section 7.3.4) means that a single range of values was rejected in favour of a multiplier which changes all of the distributed values by the same percentage. Uniform random sampling was used to give the parameter values for an individual model run (following Freer *et al.*, 1996).

Parameter	Minimum Value	Maximum Value
Lift co-efficient	0	0.5
Drag co-efficient multiplier	0.5	1.5
Added mass co-efficient	0	1.0
Particle radius (m)	0.01	0.07
Bed particle radius (m)	0.001	0.02
Static friction co-efficient	0	0.8
Sliding friction co-efficient	0	0.3

Table 7.3: The range of parameter values used in the particle tracking model. All values are dimensionless unless stated.

For the choice of performance measure, it was decided to use the Nash-Sutcliffe efficiency (NSE) measure, which compares the sum of squared errors with the deviation of observed values from the mean (Nash and Sutcliffe, 1970). The equation for the NSE is given as follows:

$$NSE = 1 - \left( \frac{\sum (x_{mod} - x_{obs})^2}{\sum (x_{obs} - \bar{x})^2} \right) \quad (7.14)$$

where  $\bar{x}$  is the mean of the observed data,  $x_{obs}$  is the individual observed data value at a given time step or location and  $x_{mod}$  is the modelled value at that point.

Although originally designed for comparing modelled and observed discharge measurements through time (Nash and Sutcliffe, 1970), Equation 7.14 can be used for the particle tracking experiments. By interpolating between the surveyed points for the Arolla particle patch results given in Figures 6.17b and 6.18b, a centreline can be determined. The modelled particle tracks can then be compared to this centreline at intervals along the particle path (0.04m in this study, which is equivalent to one grid cell). The absolute distance between the modelled particle track and centreline at each data point is then used in the numerator of Equation 7.14. The denominator, meanwhile, uses the absolute distance from the mean location on the centreline.

In addition to the use of the particle patch centreline for obtaining the NSE values, the outer edges of the recorded particle patches can be used to determine the criterion for parameter sets to be rejected. It is argued that if a model were to give a particle path that was just outside these outer lines throughout, then it should be considered non-behavioural. Therefore, NSE values are calculated for both outer lines of each patch, with the lower of the two values used as the threshold for rejecting a parameter set.

The GLUE methodology was followed to give a range of behavioural parameter sets using the particle patches from Confluence G on the Borgne d'Arolla braid plain. However, because of the desire to obtain the range of potential particle paths, the NSE values were not used to weight the model output. Instead, the parameter sets are used to show the uncertainty in the model output and determine the likelihood of particle initiation from a given starting point. The model was then evaluated against the particle patch data from Confluence H. The NSE values were used to provide an indication of model performance, but because of concerns over the boundary conditions for one of the tests, it was decided that it would be inadvisable to reject the 'non-behavioural' parameter sets. In addition to the quantitative tests, the model output was compared qualitatively to the individual particle tracks for both Arolla confluences. Having conducted this testing, the model was applied to simulate particle paths at the Moor House confluences. The centre of each original pebble patch was used as the starting location, with simulations conducted using the flow model results presented in Section 5.11.

The major limitation for the GLUE methodology (along with most Monte Carlo techniques) is computational cost (Beven and Binley, 1992). However, recent developments in parallel computing were exploited to substantially reduce model runtimes. Standard Graphics Processing Units (GPUs) found in most computers have large numbers of cores which can be used to perform the same calculations simultaneously (NVIDIA, 2013). NVIDIA have developed the CUDA C programming language to enable programmers to take advantage of this capability. Although originally written in Matlab, the model was therefore rewritten in CUDA C to allow the model to run in parallel on any compatible GPU. For this research, the model was run on an NVS 5200M graphics card linked to a 2.9GHz Intel Core i7-3520M processor with 8GB RAM. This enabled a substantial speed-up in model runtimes, with a single model runtime of 0.025s in the CUDA C version comparing to a runtime of 4.6s using the original Matlab code.

### *7.3.6 Number of Parameter Sets and Time Step Variables*

In order to implement the GLUE-based methodology set out above, it is necessary to establish the initial number of parameter sets that will be used, as well as the time step length (to ensure model stability) and the number of time steps (to allow

all simulated particles to reach their destination). For the first of these, a simpler, preliminary version of the model was run for one million individual parameters sets. Dotty plots were then created using different percentages of these parameter sets to assess the effect on the spread of the point data. Figure 7.4 shows the plots for the sliding friction co-efficient (which showed the most distinct pattern) using 100,000, 200,000, 500,000 and all of the parameter sets. Given the very minor differences visible between the four plots in Figure 7.4, it was decided that 200,000 initial parameter sets were sufficient to represent the shape of the graphs.

For the length of time step, it was determined that a particle should move no further than one cell's length at each time step (similar to the Courant number condition for flow). Therefore, for the Arolla confluences the horizontal grid dimensions (0.04m) were divided by the maximum downstream flow velocity from the model output (2m/s) to give a time step length of 0.02s. The choice of the maximum number of time steps needs to balance the computational cost against the desire for all particles to have sufficient time to reach their destinations. As such, experiments were conducted using 10,000 parameter sets, with the number of time steps incrementally increased from 200 to 5,000. Figure 7.5 shows the number of behavioural parameter sets compared to the number of time steps and the net number of individual parameters sets that saw improved performances due to the increase in the number of time steps. From Figure 7.5 it can be seen that both values start to level off at around 2,000 time steps (equivalent to 40s of simulated time). Allowing for a safety margin, the number of time steps was set to 3,000 (60s of simulated time).

For the Moor House confluences, the maximum likely velocity of individual particles will vary depending on the flow dataset being used. Although the cell sizes are four times larger (0.16m), the maximum flow velocities can be at least double those at the Arolla confluences. Therefore the time step length was doubled to 0.04s. Given the larger domain, the number of time steps was also doubled to 6,000 (giving four minutes of simulated time).



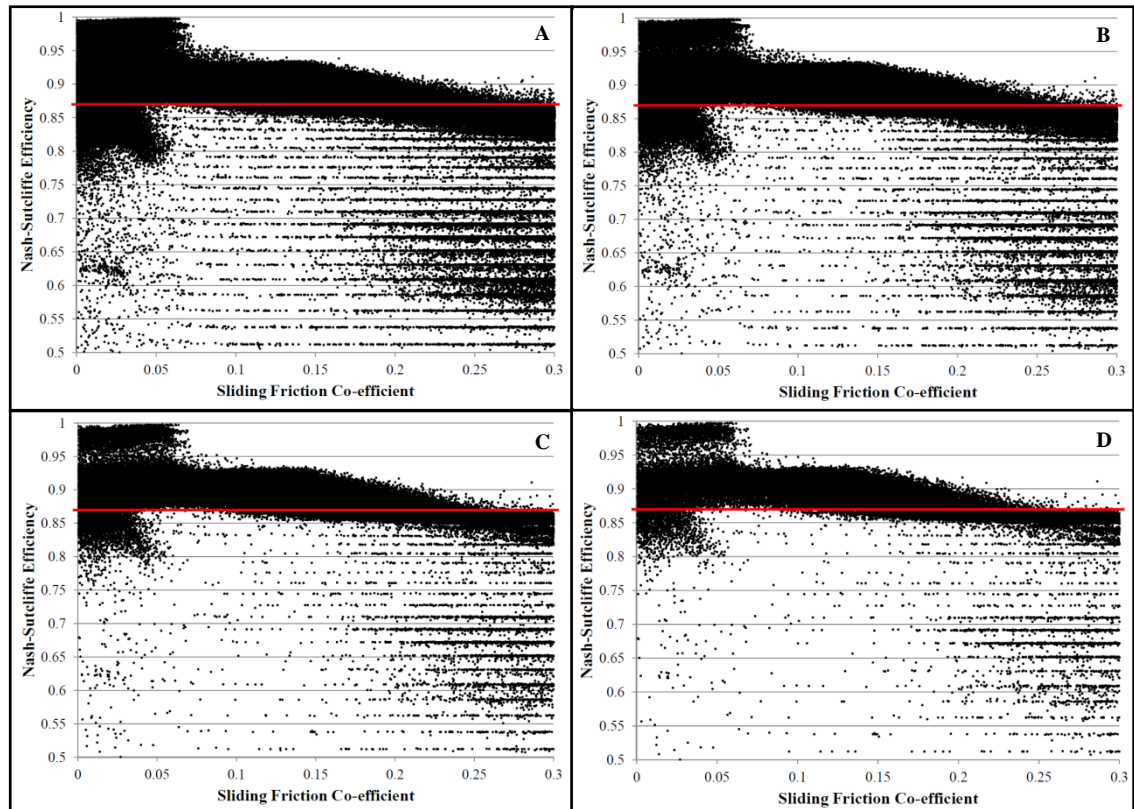


Figure 7.4: Dotty plots showing the distribution of NSE values for the sliding friction co-efficient in a preliminary version of the model. The model simulated the true right patch of Confluence G, with the threshold NSE value (0.87) given by the red line. Plots are for 1,000,000 (a), 500,000 (b), 200,000 (c) and 100,000 (d) simulations.

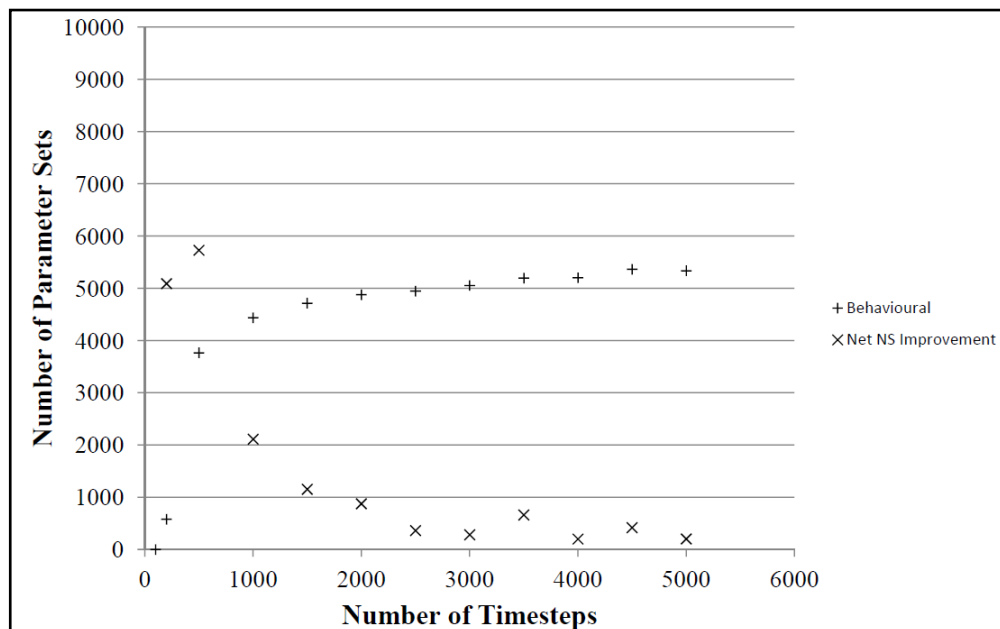


Figure 7.5: Plot showing the change in the number of behavioural simulations (out of a total of 10,000) with the number of time steps. The 'Net NS Improvement' is the number of individual parameter sets that performance worse with the increased number of time steps, subtracted from the number that perform better.

## 7.4 Model Calibration and Evaluation Using the Arolla Confluences

### 7.4.1 Model Calibration Using the Confluence G Particle Patches

Having used a uniform random number generator to obtain 200,000 initial parameter sets, the model was run using these inputs for the true right patch of Confluence G. The spread of the modelled particle tracks is given in Figure 7.6. Most particles follow close to the centre of the surveyed patch in the upstream part of the confluence, with some continuing to the outlet whilst others get caught in the topographic depression circled in red.

Of the initial parameter sets, 100,693 were found to be behavioural (50.3%). The sensitivity of the model to each parameter set is shown by the dotty plots in Figure 7.7, with the red line used to separate those considered behavioural from those which are not. The dotty plots show that the model is insensitive to most of the parameters, with the exception of the sliding friction co-efficient (Figure 7.7g). At higher values of the sliding friction co-efficient, the NSE values drop off and far fewer of the parameter sets exceed the threshold NSE value. This reflects the discussion in Section 5.13, where it was argued that in these confluences, the active nature of the bed can significantly reduce the effective roughness.

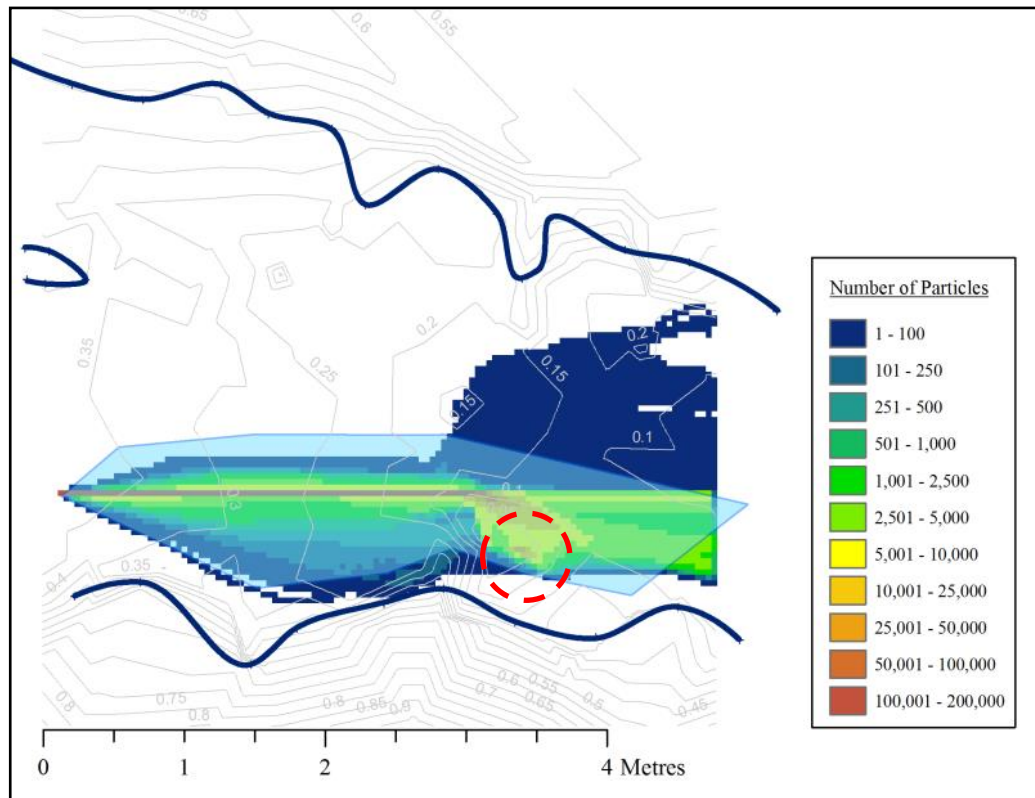


Figure 7.6: Plot showing the spread of particle paths for the true right patch of Confluence G. The outline of the patch measured in the field is given by the blue polygon. The red dashed circle shows the location of a topographic low.

The 100,693 behavioural parameter sets were then used to simulate the true left particle patch of the same confluence. The spread of the particles is shown in Figure 7.8, with the recorded patch from Figure 6.17b included for reference. Although there is some disagreement over the initial direction of particle movement, the main transport paths are similar further downstream.

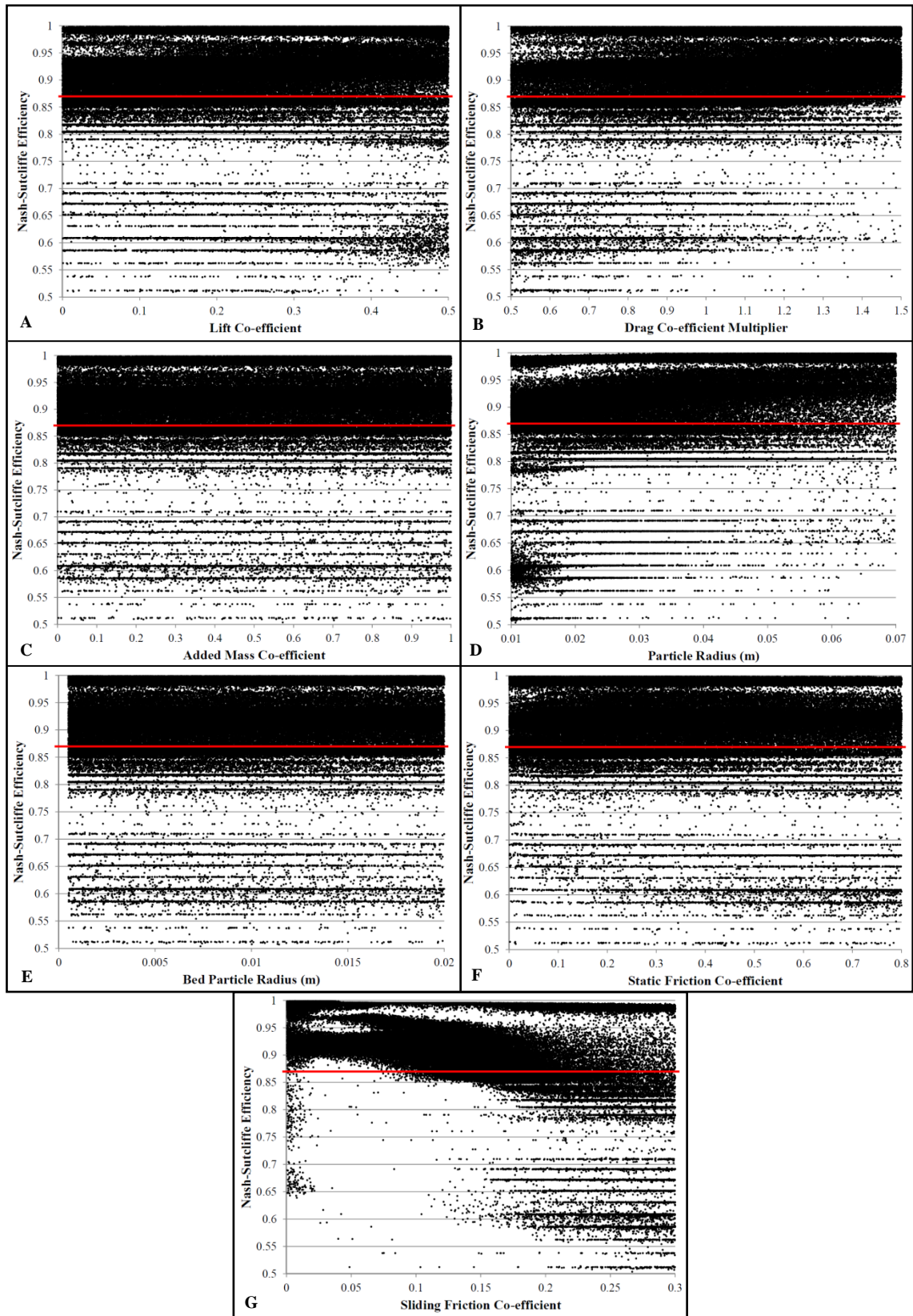


Figure 7.7: Dotty plots for simulations of the true right patch of Confluence G, with the red line showing the threshold for a parameter set to be considered behavioural. Plots (a) to (g) show the performance of the model compared to the value of each individual parameter.

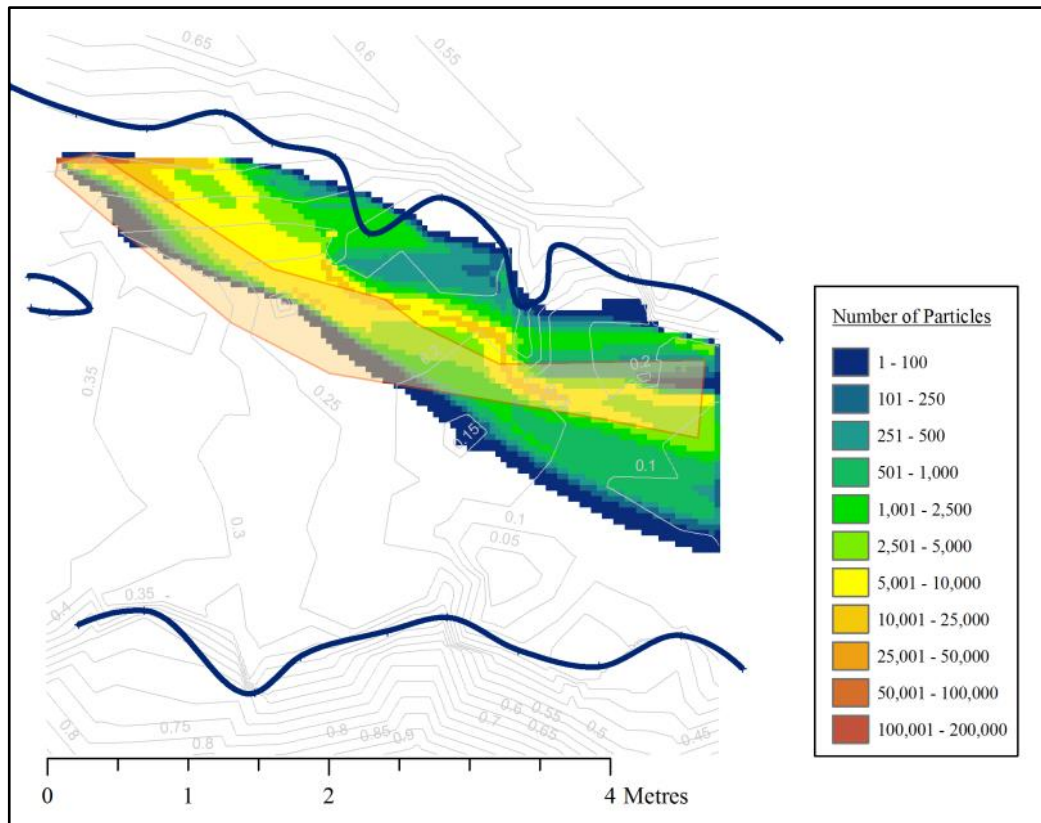


Figure 7.8: Plot showing the spread of particle paths for the true left patch of Confluence G. The orange polygon shows the patch dispersal recorded in the field.

The dotted plots in Figure 7.9 demonstrate once again that the sensitivity of the model to these parameters is low, with the exception of the sliding friction co-efficient. No parameter set is found to be behavioural if the sliding friction exceeds 0.15, which is substantially lower than the values found in Table 7.2. However, this is again likely to be explained by the bed being in motion.

Removing those considered non-behavioural after the true left patch simulations leaves 30,834 parameter sets. These are tested both quantitatively and qualitatively in the following section, using the rest of the particle data collected in Section 6.4.



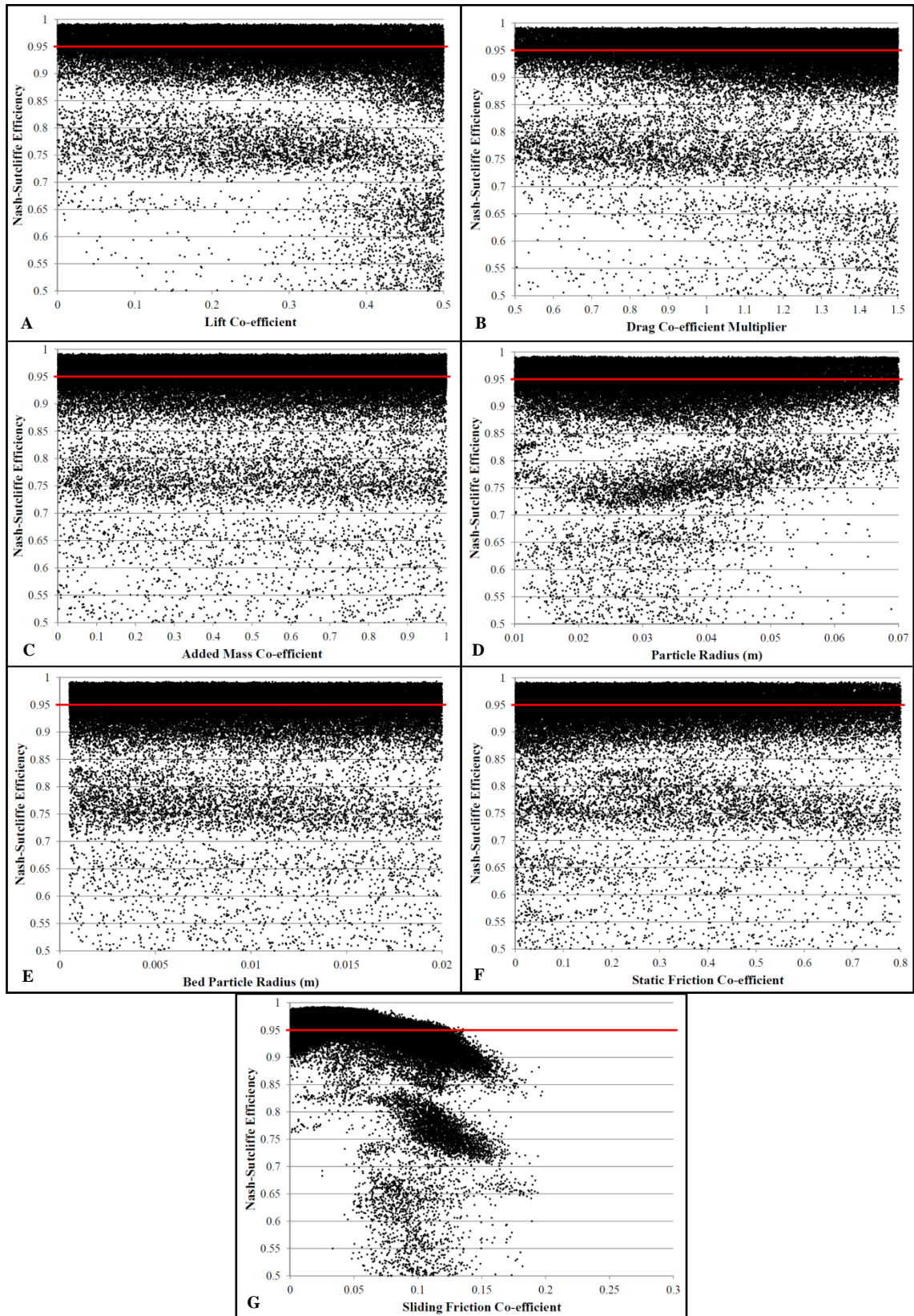


Figure 7.9: Dotty plots for simulations of the true left patch of Confluence G, with the red line showing the threshold for a parameter set to be considered behavioural (0.95). Plots (a) to (g) are for each of the seven parameters in Table 7.3.

## 7.4.2 Model Evaluation Using the Borgne d'Arolla Data

The particle patch experiments from Confluence H (Figure 6.18b) were used to quantitatively assess the performance of the model. Figure 7.10 shows the modelled particle paths for the true right patch, with the percentage value in Figure 7.10 giving the proportion of particles which have final positions more than 0.04m (one grid cell) from the starting location. The percentage values can therefore be considered to represent the modelled likelihood of particle initiation.

For the true right patch in Figure 7.10, the modelled particle paths agree well with the field measurements, with very little deviation outside of the blue polygon. This is backed up by the dotty plots in Figure 7.11, which show the vast majority of parameter sets performing close to or above the threshold derived from the outer limits of the measured particle paths. Of the 30,834 parameter sets, 24,025 simulations (77.9%) would be considered behavioural and 29,878 (96.9%) have NSE values above 0.9. It is noticeable from Figure 7.11, however, that higher sliding friction co-efficients are again associated with lower model performance.

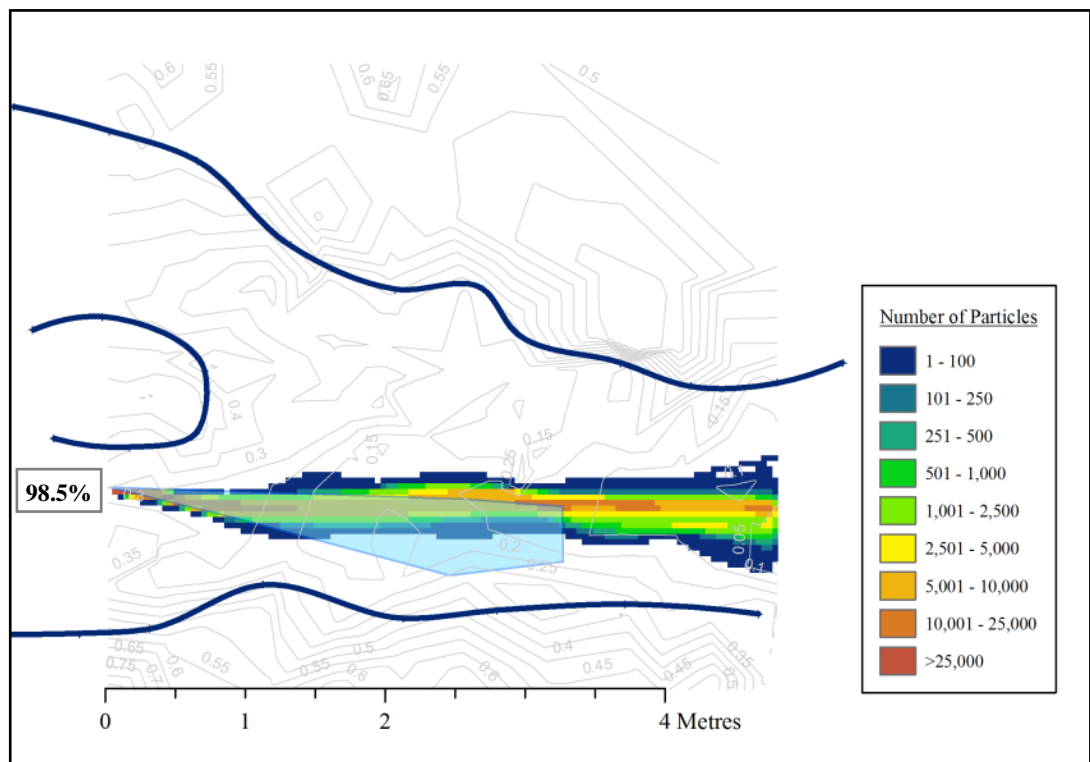


Figure 7.10: Modelled and measured particle trajectories for the true right patch of Confluence H. The patch outline measured in the field is given by the blue polygon. The percentage shows the likelihood of a tracer particle being initiated.

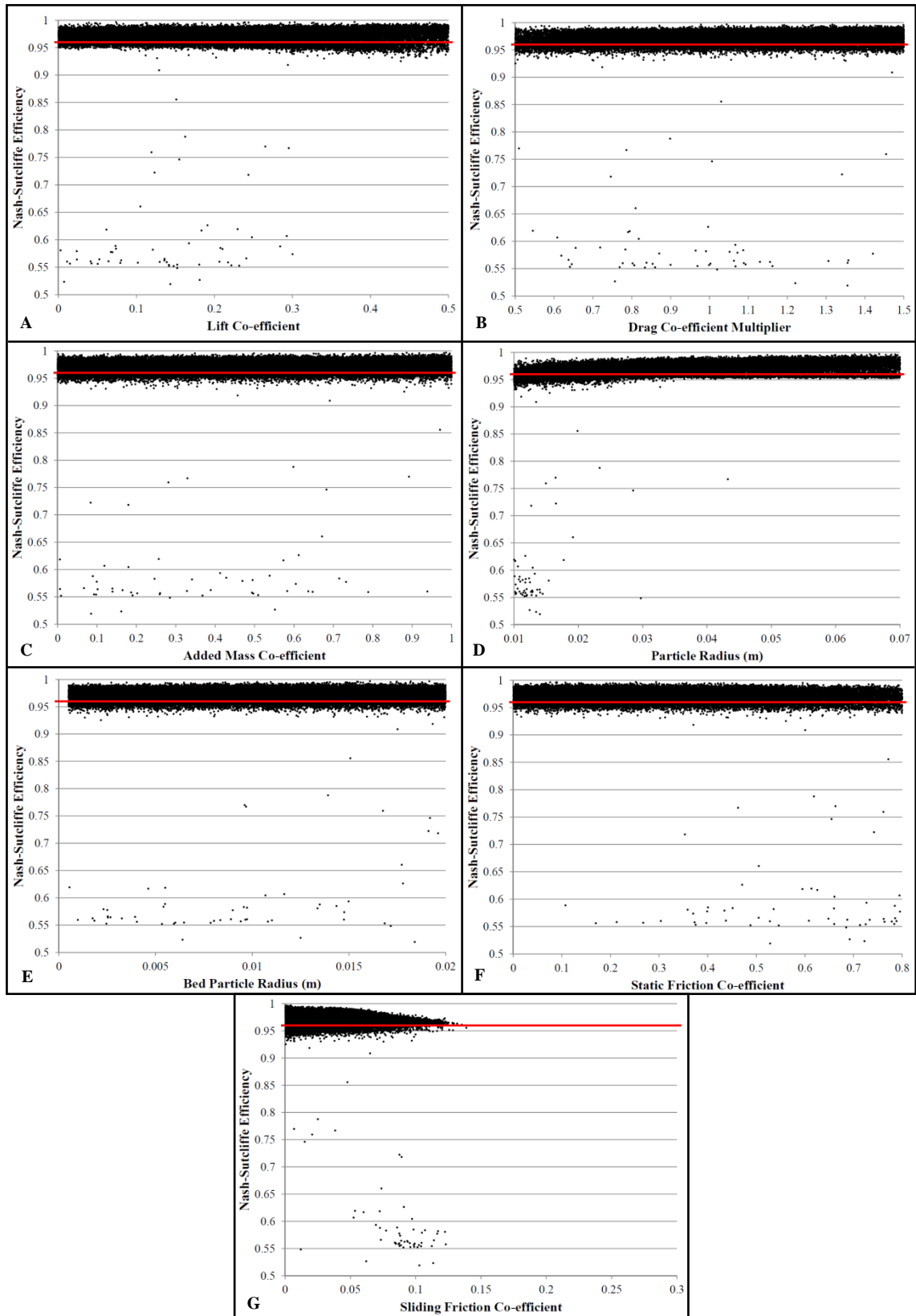


Figure 7.11: Dot plots for simulations of the true right patch of Confluence H, with the threshold to be considered behavioural (0.96) given by the red line. Plots (a) to (g) are for each of the seven parameters in Table 7.3.



For the true left patch of Confluence H, however, model performance is not as good (Figure 7.12). The vast majority of parameter sets simulate the particles being routed along the front of a ridge (marked at (i) in Figure 7.12) and into the depression marked by (ii). Although some particles do escape from this depression and continue downstream, the large disparity in the initial trajectories means that they are generally predicted to be transported further to the true left than was observed in the field. This meant that none of the parameter sets are considered behavioural, although the dotted plots in Figure 7.13 show that some do get close to the threshold. It is argued in this case, however, that the failure of the model is due to errors in the boundary conditions. In particular, the ridge highlighted in Figure 7.12(i) may have been eroded during the period between the collection of topographic and particle tracking data or it could be an artefact of the surveying method (and the inherent limitations on point density when working in steep, dynamic river confluences).

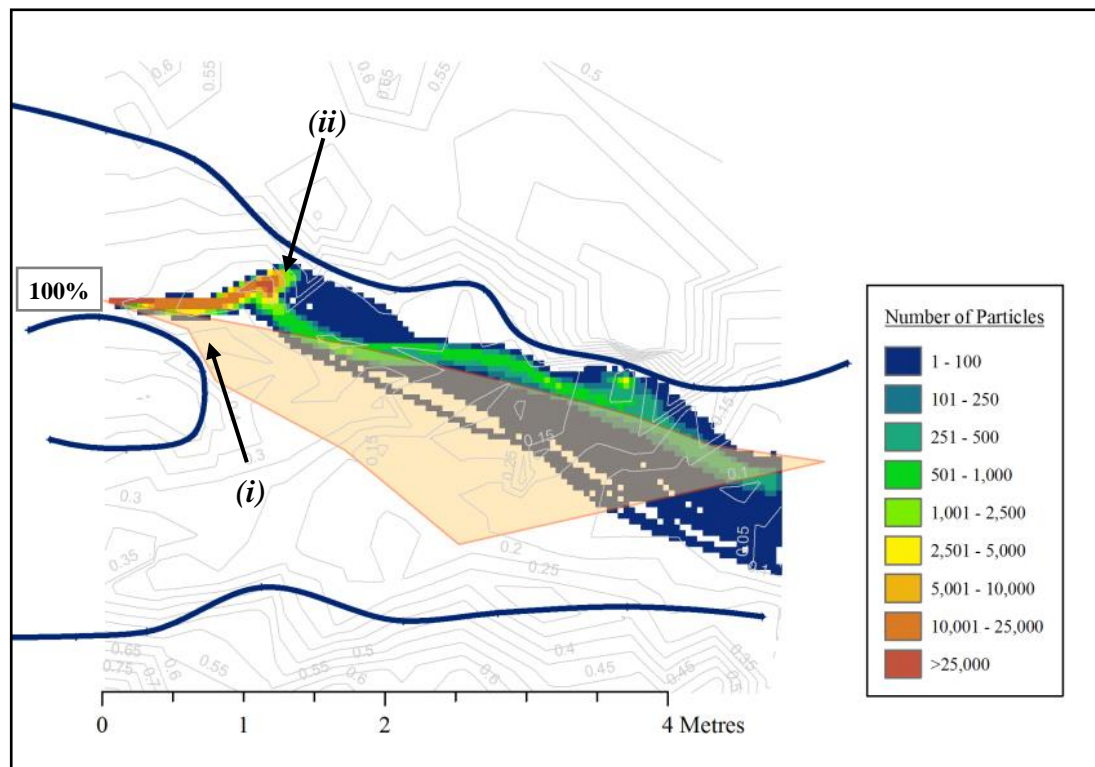


Figure 7.12: Plot showing the modelled and measured (orange polygon) spread of particle paths for the true left patch of Confluence H. The percentage figure shows that all particles were initiated.

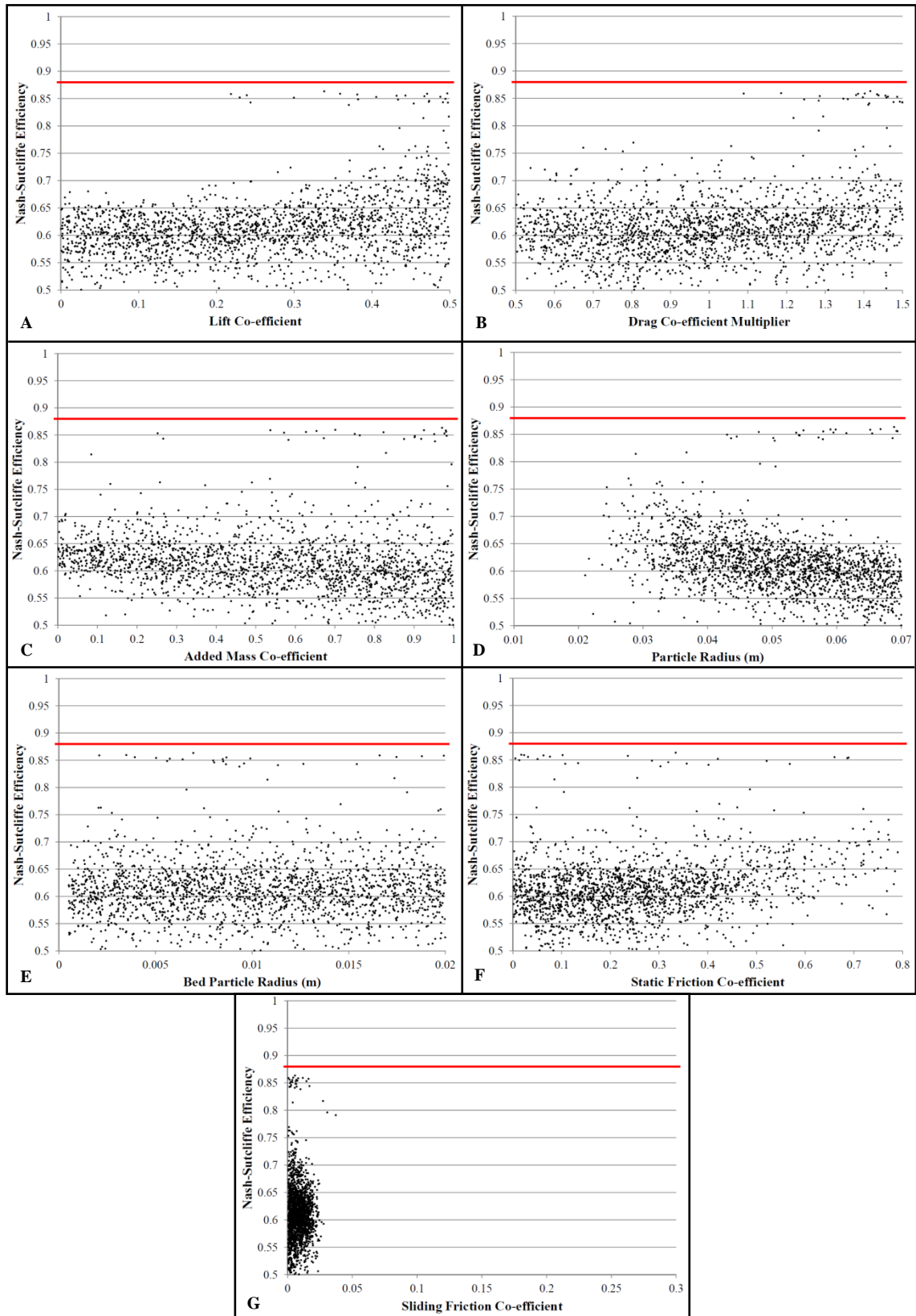


Figure 7.13: Dotty plots for simulations of the true left patch of Confluence H. The threshold for a parameter set to be considered behavioural is 0.88, which is marked in red on the plots. Plots (a) to (g) are for each of the seven parameters in Table 7.3.

In order to test the model qualitatively against the individual particle track data presented in Figures 6.17a and 6.18a, an additional seeding location was chosen for each tributary. This location was chosen so that it was in a different half of the tributary to the patch experiments.

Figure 7.14 shows the modelled spread of particles for both tributaries at Confluence G. In Figure 7.14a, the angle of the initial particle movement differs from that measured in the field, but the main zone of bedload transport (marked by the dashed red ellipse) is consistent in both cases. In Figure 7.14b, the observed particle trajectories are deflected towards the true right bank immediately on seeding. This is not reflected in the modelled paths, which predict that particles will start to move in that direction after approximately 2.5m.

For the additional tests at Confluence H (Figure 7.15), none of the particles in the true left tributary are initiated. This is due to this part of the confluence being dry in the flow model results (Figure 5.32a), which demonstrates that the particle model is correctly differentiating between the wet and dry cells from the model output. In the true right tributary, the model follows almost exactly the recorded particle path marked by (i). This provides further evidence that the predicted particle trajectories are reliable and can be used to draw conclusions regarding the sediment transport process at upland river confluences.

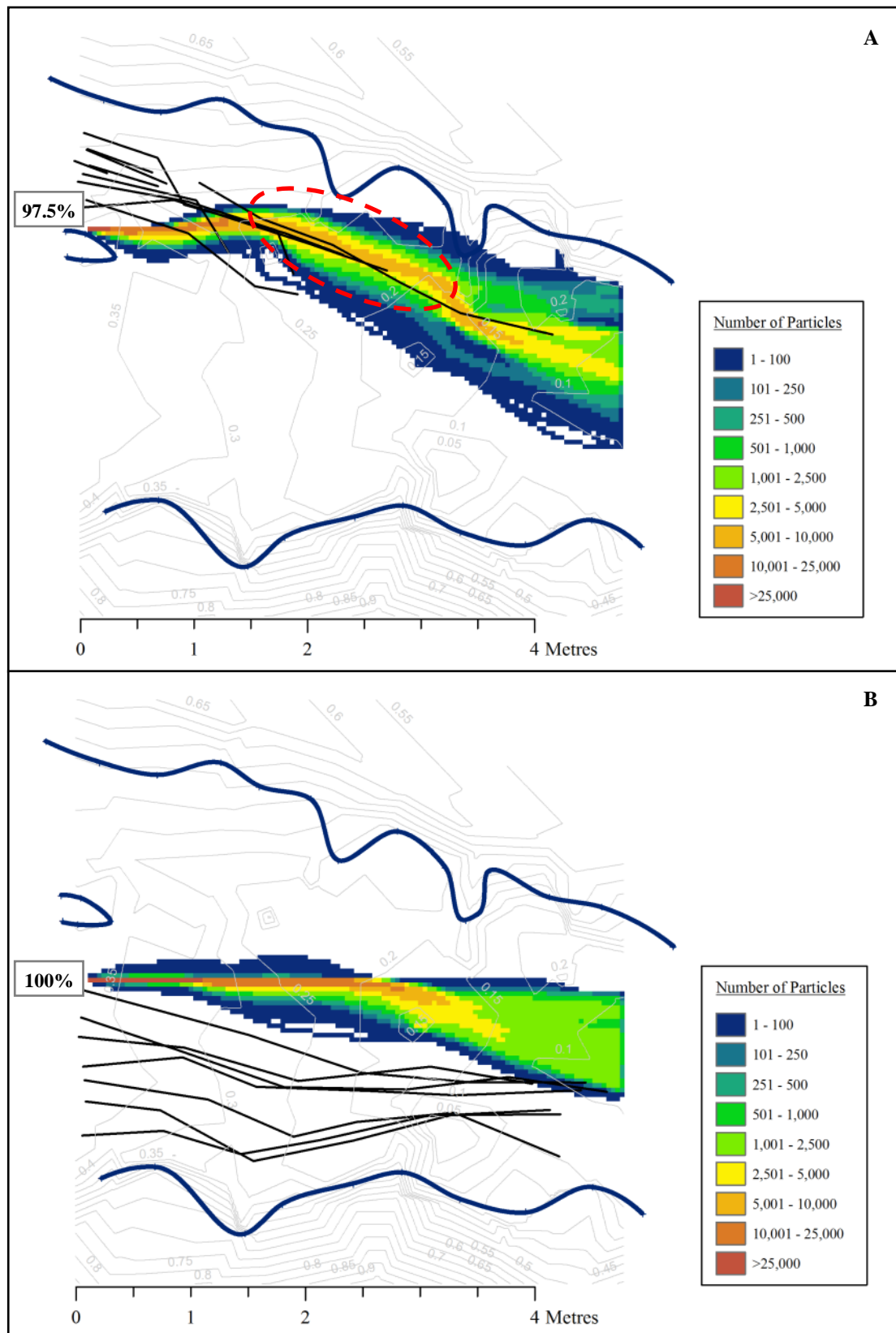


Figure 7.14: Plot showing the spread of particle paths for the additional tests in the true left (a) and true right (b) tributaries of Confluence G, with the observed individual particle tracks given by the black lines.

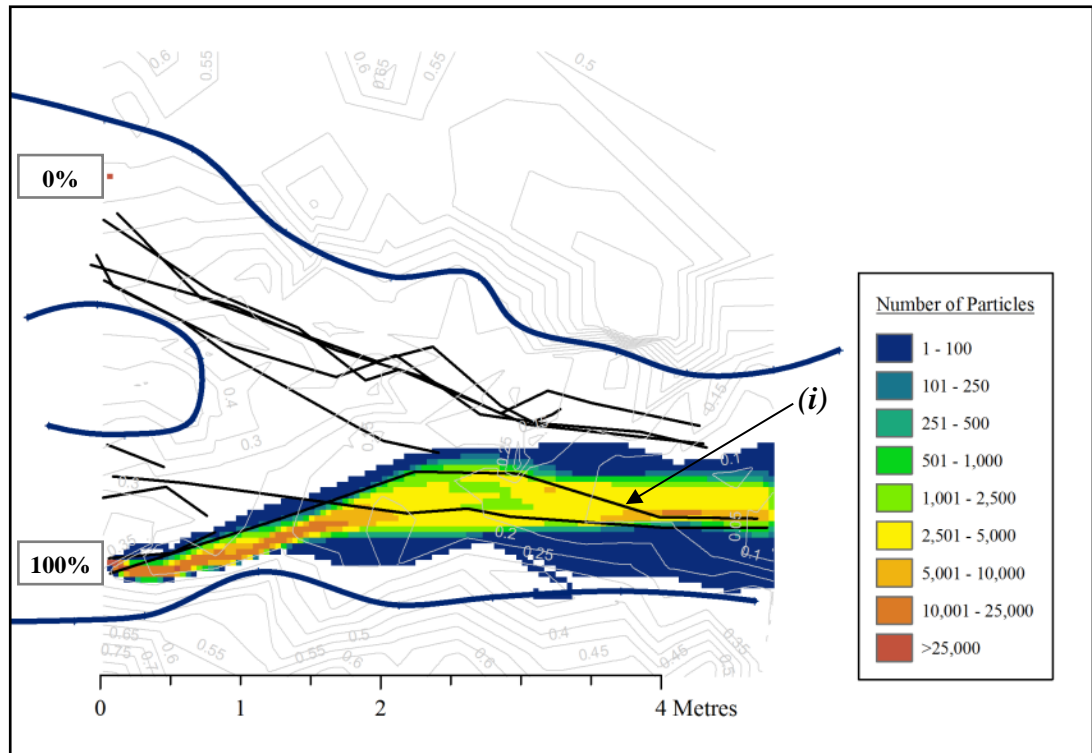


Figure 7.15: Plot showing the particle paths for the additional tests in both tributaries at Confluence H, with the observed individual particle tracks given in black.

#### 7.4.3 Discussion of the Arolla Confluence Results

By using the GLUE methodology to account for the uncertainty in the input parameters, the bedload transport model developed in this chapter is demonstrated to provide a good representation of both the measured particle trajectories in the Borgne d'Arolla confluences and their dispersal as they move downstream. In most cases, the uncertainty bounds in the model results match the spread of the particle patches from Section 6.4. This suggests that fundamentally the physical basis of the model is sufficient to represent the processes operating in these steep confluences.

The major disparity between the field data and model output is found in Figure 7.13, where none of the parameter sets are found to be behavioural. However, given the performance of the model in the other tests conducted in this section, this can be considered an anomaly. It is argued that the most likely reason for the poor performance in this case is an error in the underlying topography, in particular regarding the apparent ridge highlighted in Figure 7.12(i). This is probably due to the exact nature of this obstacle not being picked up in the Total Station survey. Alternatively, the channel bed

morphology may have changed in the time between the recording of the topographic data and the particle experiments being conducted.

Minor disparities in particle paths (in Figures 7.8, 7.14a and 7.14b), on the other hand, are found in the Confluence G tests and tend to be due to the initial direction of movement in the model differing to that recorded in the field. In all three cases, the field data suggest an initial direction of movement further towards the true right. It is argued that this is due to the assumption of flow in both tributaries being parallel to the downstream direction. The need to use Electromagnetic Current Meters (ECMs) to obtain the flow data meant that cross-stream flows were not recorded. Instead, they were estimated from the direction of flow at the surface. In the case of the true left tributary at Confluence G, the recorded particle tracks suggest that the flow direction is towards the true right. A change in the input flow direction to reflect this would also be expected to result in earlier deflection of the modelled particle paths in Figure 7.14b. This demonstrates the importance of tributary flow direction to the sediment dynamics at these steep river confluences.

Given the concerns over the boundary conditions in the tests in Figure 7.12, and the generally good performance of the model in all other tests in Section 7.4.2, it was deemed inadvisable to reject the parameter sets that failed to meet the threshold to be considered behavioural. After all, as Beven (2001) notes, if you test any model predictions in sufficient detail, eventually all parameter sets will be found to be ‘non-behavioural’ under some conditions. It was therefore considered more useful to be able to assess uncertainty in the modelling of the Moor House confluences using all 30,834 parameter sets than to eventually invalidate every parameter set by strictly adhering to the GLUE methodology.

By calibrating the model using the Borgne d’Arolla confluences but applying it to the Moor House confluences, it is necessary to address the issue of whether the calibrated parameter sets can be transferred between different sites. Such transferability issues may be particularly relevant when the bed material is substantially different. However, in this case the two sites have similar gravel and cobble beds, while the tracer particles are the same for both the calibration patches and the Moor House experiments. The major difference between the field sites is the steeper slopes at the Borgne d’Arolla confluences. However, as the effect of the slope will be reflected in the CFD output, it is considered that any uncertainty caused by the change in site is likely to be minor.

## **7.5 Modelling Bedload Transport at the Moor House Confluences**

### *7.5.1 First Simulations of the Upper and Lower Confluences*

Following the model calibration and evaluation procedure in Section 7.4, the bedload particle model developed in this chapter was applied to a range of high flow scenarios at the Moor House confluences. The bankfull discharge flow models from Section 5.11 were used to provide the input flow data, in order to assess the impact of different discharge ratios on bedload transport. The use of the model for this scenario testing will help to improve the understanding of the factors driving particle transport at the Moor House confluences, in particular where differences between the particle trajectories and near-bed streamlines were highlighted in Section 6.2.

For the lower confluence in Figures 7.16 and 7.17, the modelled particle paths do not correspond particularly well with the field data. This is especially the case for the true right tributary patches, which tend to be routed towards the centre of the confluence rather than towards the true right bank. The true left tributary results are better, broadly matching the range of particle trajectories when that tributary dominates (Figure 7.17) and being less likely to be entrained when it is not (Figure 7.16).

At the upper confluence (Figures 7.18 and 7.19), meanwhile, very few particles are entrained regardless of the dominance of the tributaries. If the true left tributary has a higher discharge (Figure 7.18), the particles seeded in that tributary tend to move through the confluence, but further to the true left than was found in the field. Furthermore, in the true left tributary in Figure 7.18a the model predicts greater movement than was recorded for the tracer particles. In all other cases, very few particles are predicted to be entrained and those that do tend to travel only very short distances.



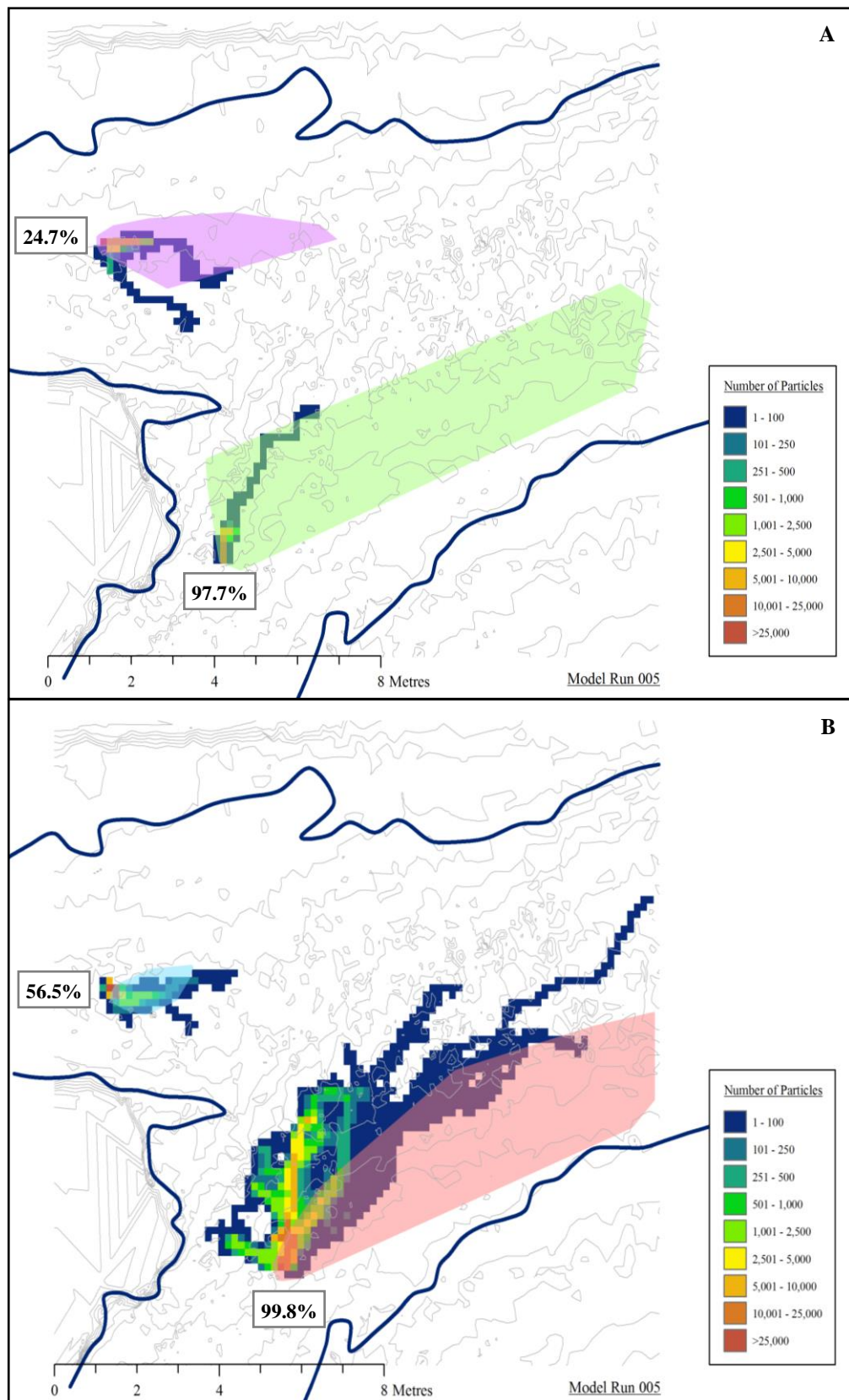


Figure 7.16: Plot showing the spread of particle paths for patches seeded in the true left (a) and true right (b) halves of the lower Moor House confluence tributaries, using the flow data from LowerRun005 (true right tributary dominant). The percentages are the modelled likelihood of particle initiation, while the polygons show the outer limits of the point data recorded in the field experiments.



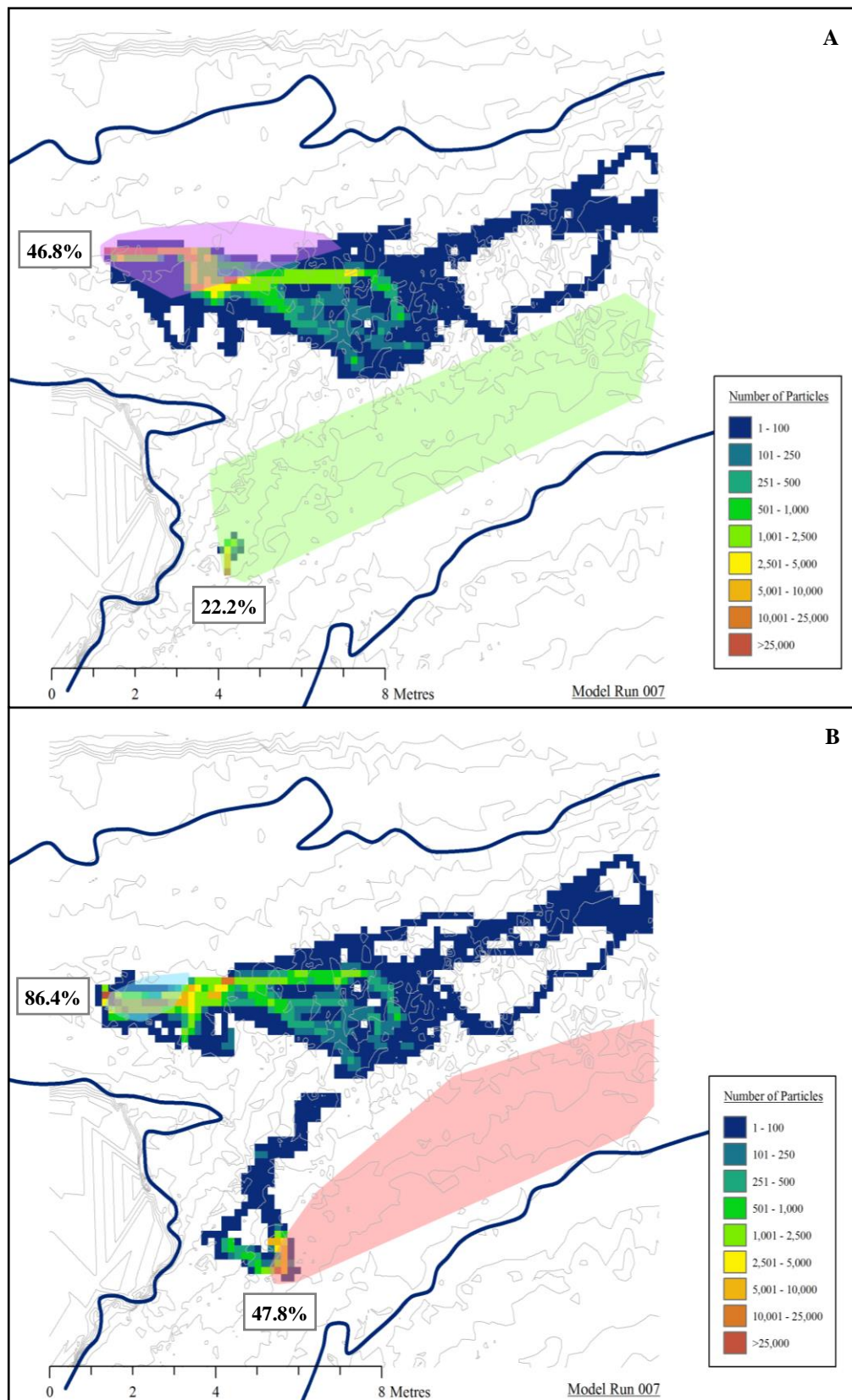


Figure 7.17: Plot showing the percentage chance of particle initiation and the spread of particle paths for patches seeded in the true left (a) and true right (b) halves of the lower Moor House confluence tributaries, using the flow data from LowerRun007 (true left tributary dominant). The polygons are the same as those in Figure 7.16.

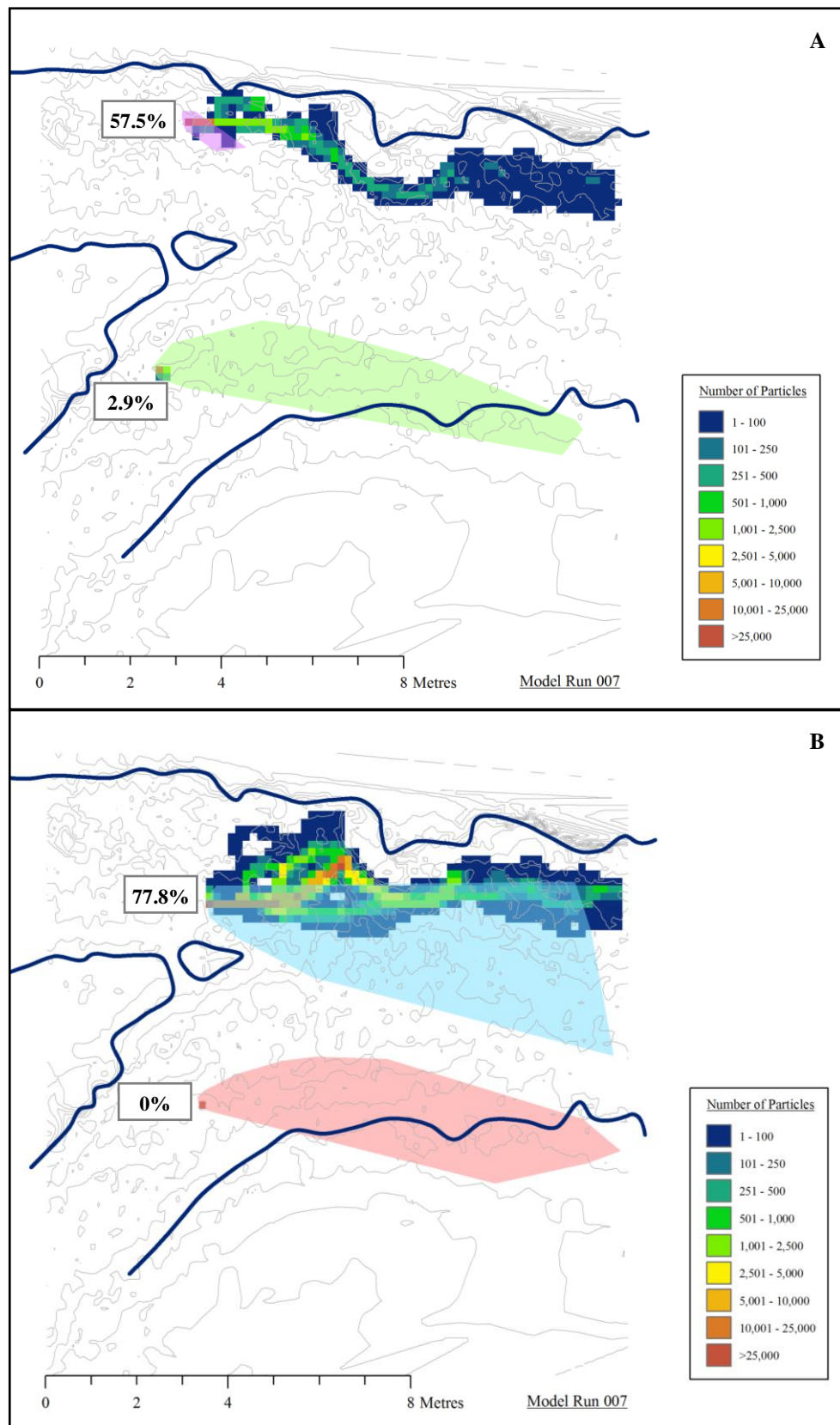


Figure 7.18: Plot showing the spread of particle paths for patches seeded in the true left (a) and true right (b) halves of the upper Moor House confluence tributaries, using the flow data from UpperRun007 (true left tributary dominant). The percentages are the modelled likelihood of particle initiation and the polygons show the extents of the point data from the second upper confluence field experiment.

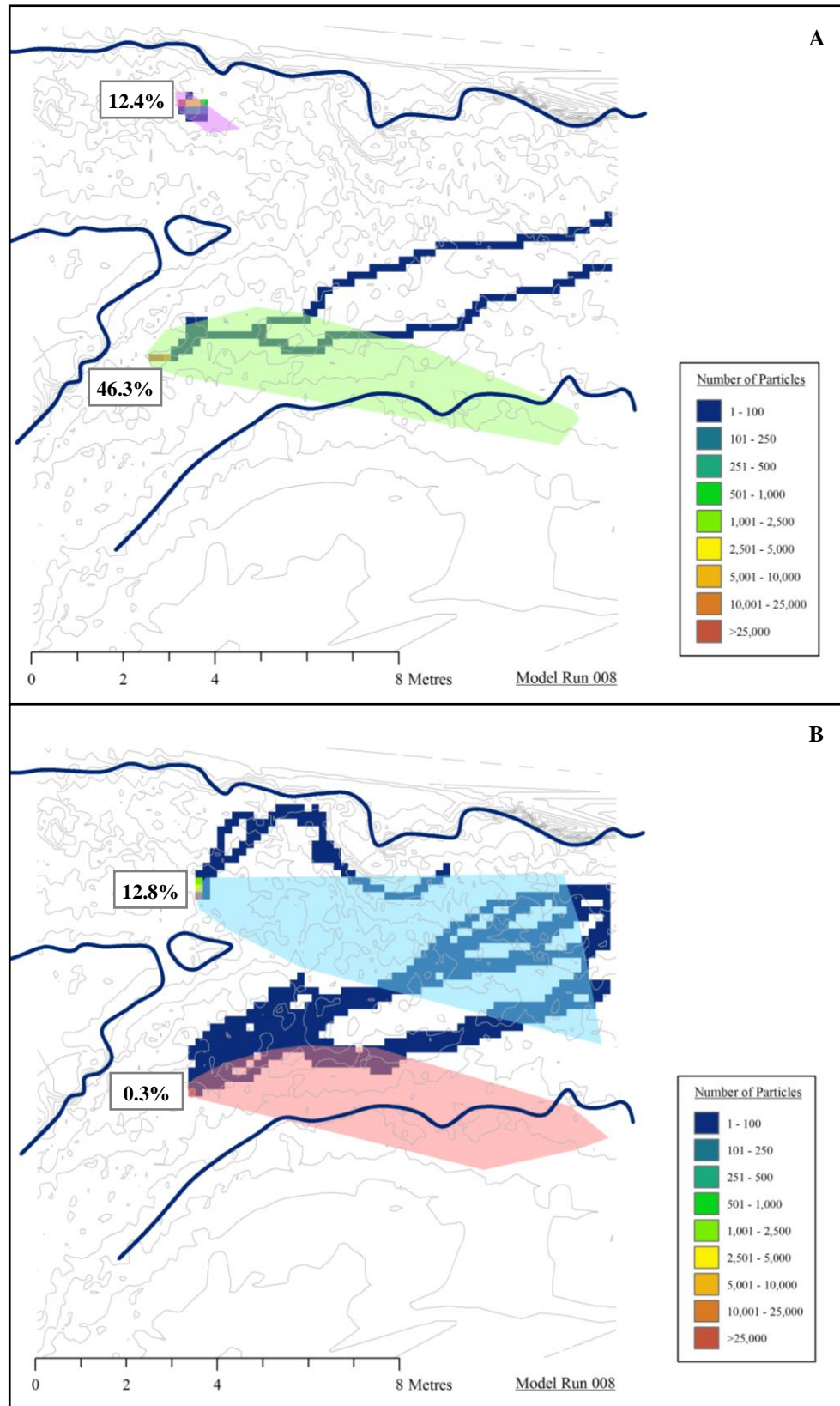


Figure 7.19: Plot showing the likelihood of particle initiation and the spread of particle paths for patches seeded in the true left (a) and true right (b) halves of the upper Moor House confluence tributaries, using the flow data from UpperRun008 (true right tributary dominant). The polygons show the same information as in Figure 7.18.

Therefore, the first impression given by the results in this section is that the particle model is performing poorly at these more stable confluences. However, the magnitude of the discharges recorded at the EA gauging station between tracer particle surveys (Figure 6.3) are generally much higher than those used for the flow model input data (Table 5.6). This suggests that the bankfull discharges simulated in Section 5.11 are insufficient to initiate particle movement on a large scale. Therefore, for each confluence an additional flow model was run using higher discharges than those in Table 5.6. These are presented in the following section.

### *7.5.2 Second Simulations of the Upper and Lower Confluences*

As a result of the findings in the previous section, two new flow simulations were run for the upper (UpperRun009) and lower (LowerRun008) confluences. The discharges were determined based on the original simulations in Section 5.11, the results of the particle tracking experiments in Section 6.2 and the model results from the previous section. At the lower confluence, the model predictions for the true left tributary when it is dominant are similar to the measured data. Therefore, the original discharge in this case was increased to  $4\text{m}^3/\text{s}$  from  $3\text{m}^3/\text{s}$ . However, comparing Figures 6.3 and 6.10 shows that most particle movement in the true right tributary occurs when discharges of  $5\text{--}10\text{m}^3/\text{s}$  have been recorded for that channel at the EA gauging station. Therefore, an inlet discharge of  $8\text{m}^3/\text{s}$  was used for the true right tributary.

At the upper confluence, the particle tracers in Figure 6.5 show a much greater tendency to move towards the true right bank. In addition, a comparison with Figure 6.3 shows that this movement is associated with total discharges for the confluence of  $8\text{--}16\text{m}^3/\text{s}$ . Therefore, to ensure the true left dominance, discharges of  $8\text{m}^3/\text{s}$  and  $6\text{m}^3/\text{s}$  were used for the true left and true right tributaries respectively. As with Run007 at the upper confluence, the inlet flow direction was angled at  $20^\circ$  towards the true right bank.

The results from LowerRun008 are given in Figure 7.20, with the subsequent particle model results in Figure 7.21. The water surface elevation can be seen to exceed the banks at (i) in Figure 7.20a, but any inaccuracies that result are thought unlikely to affect the flow in the regions of interest near the bed. The depth-averaged flow velocities in Figure 7.20b are particularly high at first in the true right tributary, but settle down to more realistic values at the second cross-section (at 3m cross-stream). This suggests that at these high discharges, it may be necessary to give the model a

longer run-in distance. However, as the particles are seeded 2-3m from the true left inlet, this is again considered unlikely to result in significant errors in the particle model results.

Using the new flow data in the particle model gives a much better representation of the particle dynamics. As in Figure 7.17, the movement of the patches in the true left tributary and the percentages of particles initiated match the field data very closely. However, unlike Figure 7.17, the movement of particles in the true right tributary is much more realistic, especially for the patch nearest the true right bank (Figure 7.21b). In Figure 7.21a, particles in the true right tributary get deposited after moving 3-4m, although some continue downstream in the expected direction. As for the Arolla confluences, this may be due to minor topographic variations at the sub-grid scale which cannot be represented at the modelled grid resolution.

Figure 7.22 presents the three-dimensional water surface elevation and depth-averaged flow velocity for UpperRun009. The simulated discharges give overbank flow at both (i) and (ii), with the latter seeing some sharp changes in water surface elevation as water flows over the upstream corner bar. The depth-averaged flow velocities in Figure 7.22b give a similar pattern to those in Figure 5.43a, albeit with higher velocity magnitudes. Using these flow velocities in the particle model again results in a better representation of the bedload transport (Figure 7.23). In the true right tributary, the simulated particle trajectories follow the same path as the tracer particles, although the deflection towards the true right seen near the outlet in the field data is not replicated. The particles in the true left tributary, meanwhile, give mixed results. Whilst the limited movement of those nearest the true left bank (Figure 7.23a) corresponds to the field data, the other patch in that tributary (Figure 7.23b) is still tending to move towards the true left bank before being deposited.



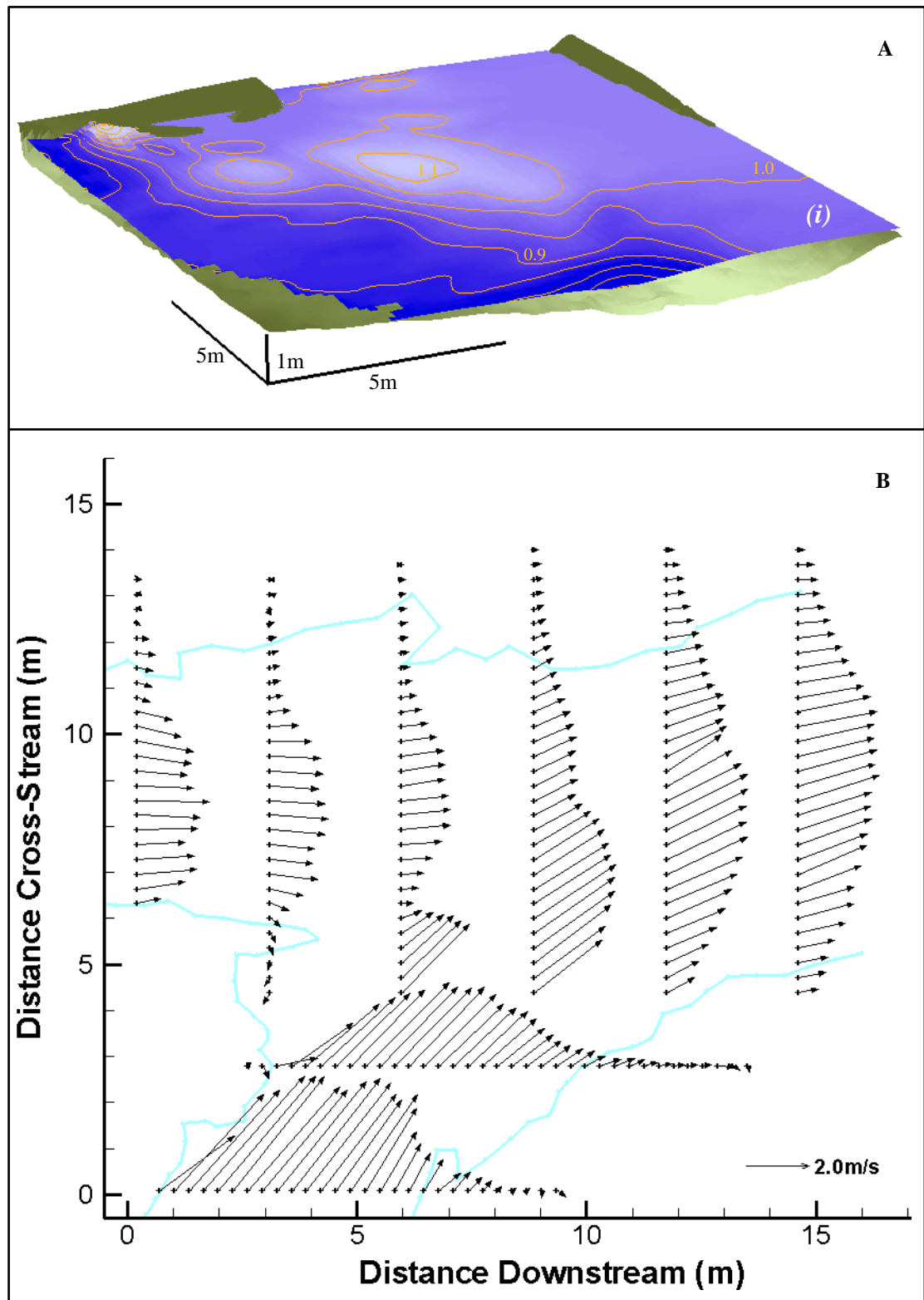


Figure 7.20: Three-dimensional water surface plot (a) and the depth-averaged flow velocities (b) for LowerRun008. The contours for the water surface are plotted at 5cm intervals.

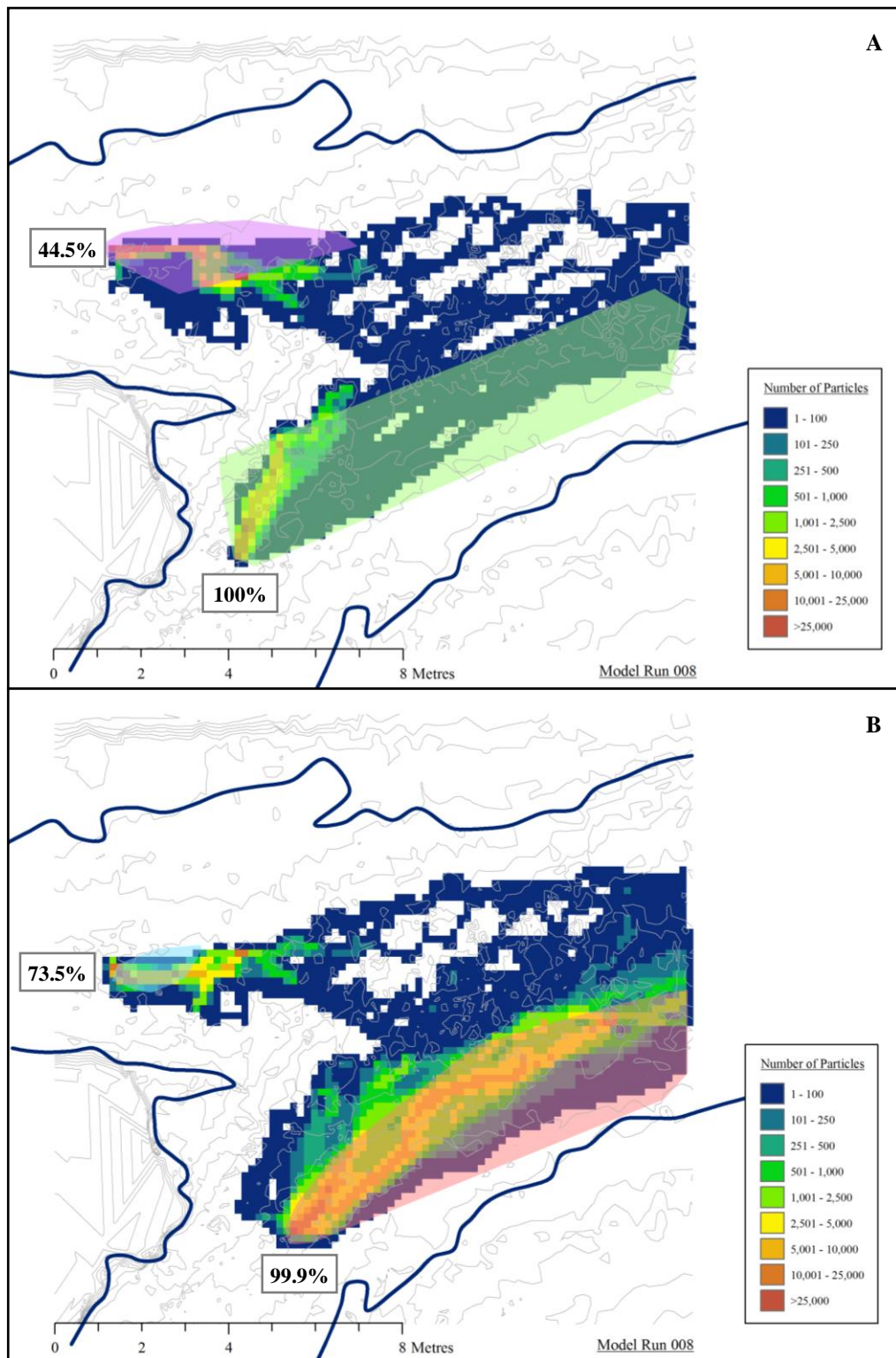


Figure 7.21: Plot showing the spread of particle paths for patches seeded in the true left (a) and true right (b) halves of the lower Moor House confluence tributaries, using the flow data from LowerRun008. The polygons and percentages give the same information as in Figure 7.16.

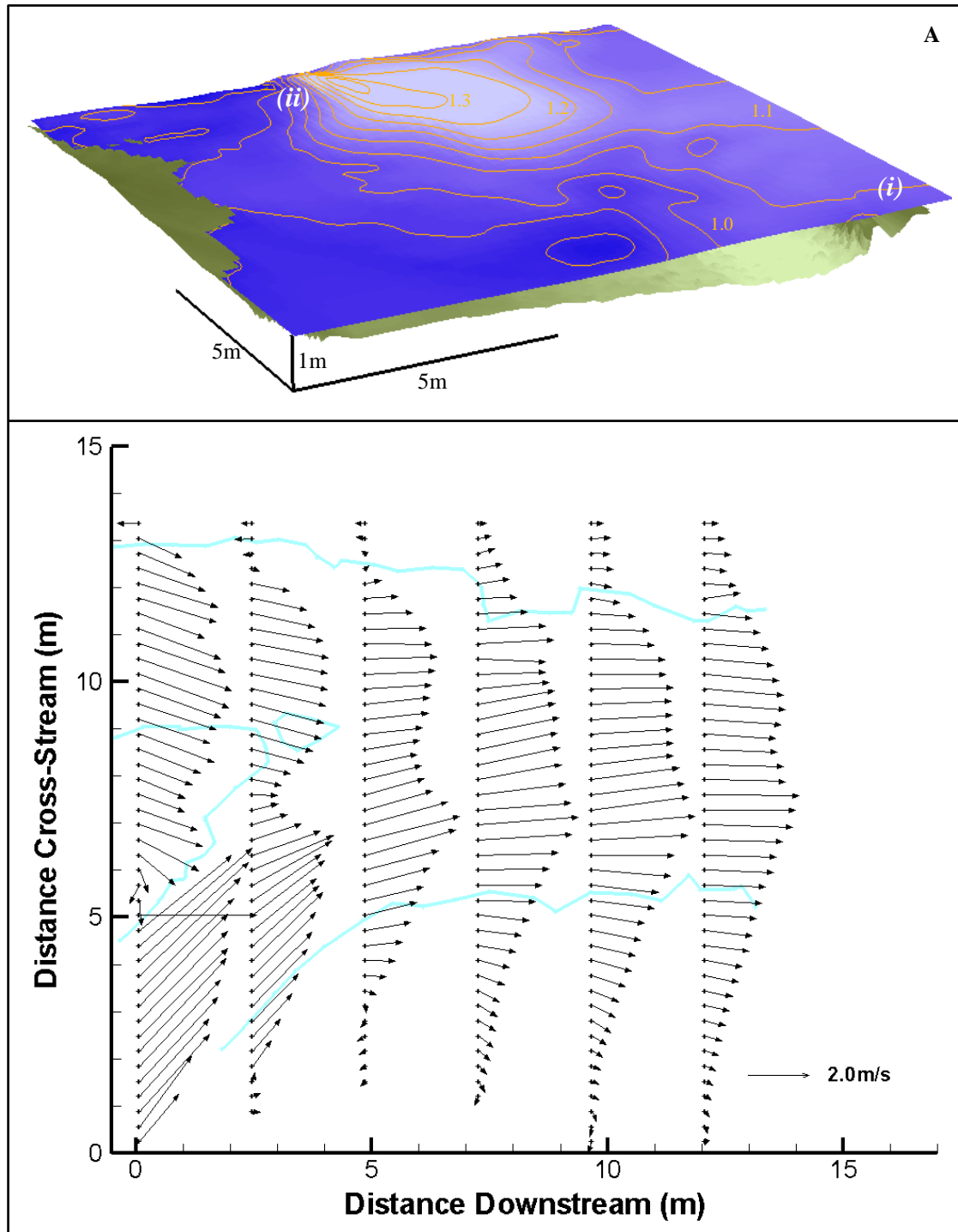


Figure 7.22: Three-dimensional view of the water surface (a) and plan view of the depth-averaged flow velocities (b) for UpperRun009.



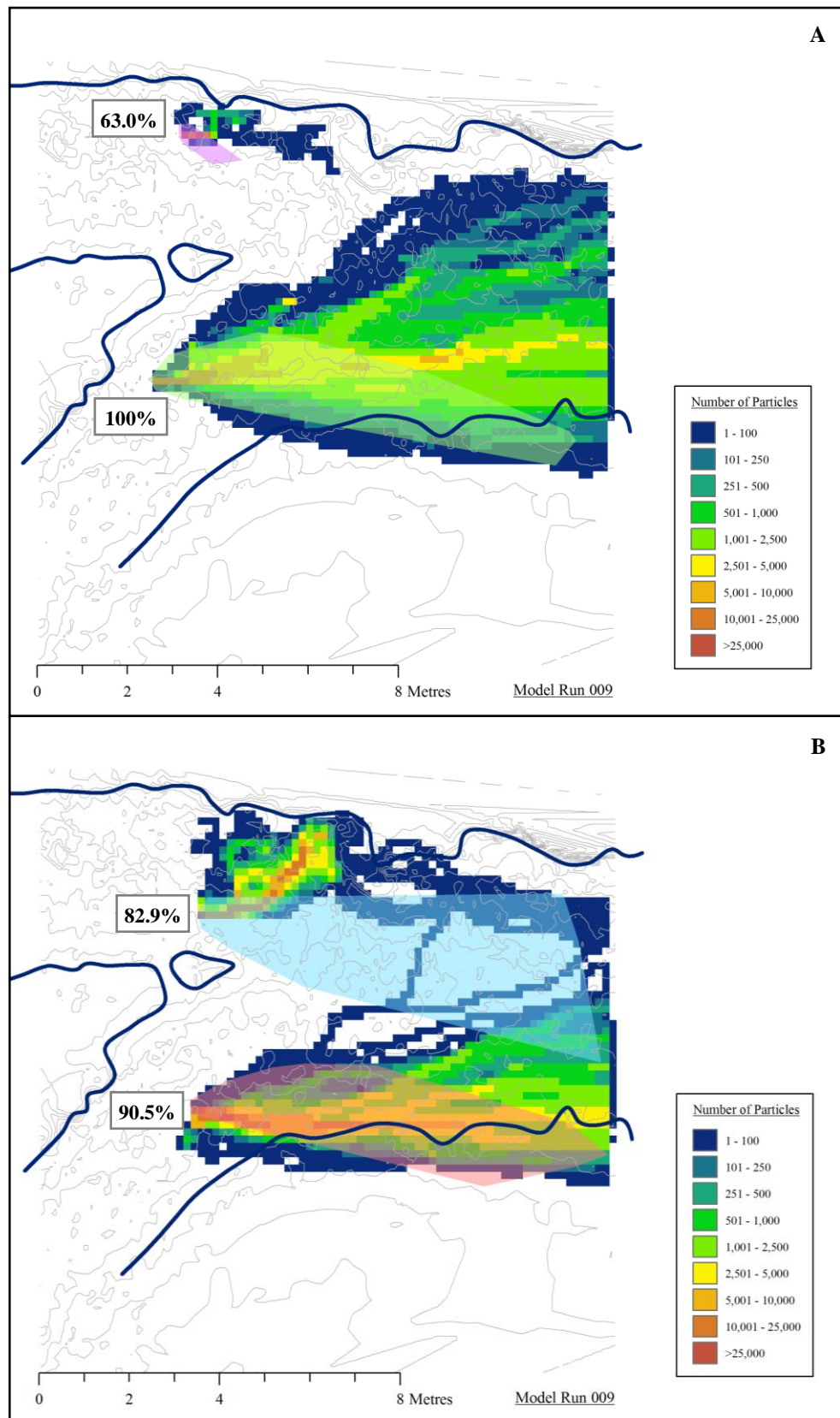


Figure 7.23: Plot showing the spread of particle paths for patches seeded in the true left (a) and true right (b) halves of the upper Moor House confluence tributaries, using the flow data from UpperRun009. The polygons and percentages give the same information as in Figure 7.18.

The photographic evidence in Figure 7.24 suggests a possible explanation for the disparity between the modelled and measured particle trajectories in the true left tributary of the upper confluence. These photographs show the upper confluence before and after the extremely large flood of 22<sup>nd</sup> June 2012, which had a peak discharge of  $26\text{m}^3/\text{s}$  at the EA gauging station. The flood can be seen to have eroded the upstream corner bar (dashed red circle) and eroded a new route for the true left tributary further upstream (solid black circle). In order to do both of these things, it is argued that the flow direction in this channel has to change considerably, by up to  $45^\circ$ . This is shown by the orange arrows in Figure 7.24, with the arrow in Figure 7.24b giving a hypothesised flow direction for the larger floods. Such a flow direction would explain the tendency for the measured particle trajectories to be further towards the true right bank than the model predicts.

### *7.5.3 Discussion of the Model Results from the Moor House Confluences*

The results from Section 7.5.1 suggested that although the particle model had performed well for the Arolla confluences, it was failing to replicate the processes in the more stable Moor House confluences. However, on closer inspection, the discharges simulated in Section 5.11 were found to be lower than those which resulted in significant particle movement (Figure 6.3). Therefore, additional flow simulations were run to see if higher discharges would result in the model predicting greater particle movement. The results from Section 7.5.2 showed that this is indeed the case, suggesting that not only is the reduced-complexity DPM developed in this chapter capable of replicating the particle trajectories, it is also able to indicate the threshold discharges required for particle entrainment.

The results for the lower confluence in Section 7.5.2 show very close agreement with the field data, with the exception of the patch in the true right tributary in Figure 7.21a. It is hypothesised that the failure of most particles in this patch to move downstream may be due to sub-grid scale topographic variations that the 0.16m resolution grid cells are unable to pick up. However, the overall performance of the model for this confluence is good, with the predicted likelihood of particle initiation much higher for the true right tributaries, and the modelled particle trajectories following the field data closely for three of the four patches.



Figure 7.24: Photographs showing the upper confluence before (a) and after (b) the very large flood ( $26\text{m}^3/\text{s}$ ) of 22<sup>nd</sup> June 2012. The orange arrows show the main flow direction in low flow conditions (a) and that for the biggest floods surmised from the morphological change seen in (b). Photographs were taken on 20<sup>th</sup> September 2011 (a) and 13<sup>th</sup> July 2012 (b).



At the upper confluence the percentage likelihood of particle initiation is again representative of the overall movement of the patch, with the lowest likelihood value for the patch nearest to the true left bank. For the particle trajectories, although the general direction is good for three of the four patches, the model generally predicts movement too far towards the true left bank. This is especially the case for the patch in the true left tributary in Figure 7.23b. However, it is argued that the photographs in Figure 7.24 demonstrate clear evidence that the  $20^\circ$  angle for the inlet velocities in the true left tributary underestimates the true flow direction at higher discharges. It is hypothesised, therefore, that using an inlet flow direction of  $45^\circ$  would deflect the particles further towards the true right bank.

In addition, this change in flow direction would help to explain the general lack of movement of the patch nearest the true left bank. As the seeding point is so close to the bank, a change in flow direction would result in this patch being sheltered from the main direction of flow by the true left bank, thus reducing the amount of particle movement in the highest flows. It also explains why the DEM in Figure 4.8 shows the thalweg in the true right tributary being interrupted by an extension of the upstream corner bar. If the flow direction changes at high discharges, particles on the upstream corner bar will be transported and deposited in that direction.

It has already been demonstrated in Chapter 6 that the Moor House confluences have very little in common with the classical conceptual model of river confluences presented in Section 1.2. However, the results from this section enable a much greater insight into why this is. Although the confluences show topographic forcing of the flow at lower discharges (see Section 4.5), at higher discharges the bed morphology will have a lower relative effect on the flow field. The same is true of the water surface slope, which will again be expected to have a less important role, particularly with respect to the processes at the bed which drive sediment transport.

The findings in this section are clear in that the biggest drivers of the bedload transport, and thus the sediment dynamics in general (given the gravel and cobble nature of the bed), are the flow direction and discharge ratio. This result is comparable to the findings in Section 5.11 regarding the factors affecting secondary flow at these confluences. In particular, the key factor is the main direction of flow in the tributaries when the discharges are sufficiently high to give widespread particle initiation. This is similar to the findings for the Arolla confluences in Section 7.4, where it is argued that the minor discrepancies between modelled and measured particle trajectories at

Confluence G are due to uncertainty in the flow direction at the inlets. Therefore, at these steep, upland river confluences with less well-defined banks, it is changes in flow direction with discharge that are the biggest influence on sediment transport and morphological change. Fundamentally, therefore, if we are to understand the sediment dynamics at steep upland river confluences, the first step should be to look at the flow processes upstream of the confluence.

## **7.6 Conclusions**

This chapter has presented a new reduced-complexity DPM and applied it to the confluences of the Borgne d'Arolla braid plain and Moor House Nature Reserve. In Section 7.2, the current state of research using Eulerian sediment transport models and DPMs was reviewed. It was found that in order to understand the bedload transport processes at the scale of natural river confluences, a reduced-complexity Lagrangian approach was required. Therefore, the model developed in this chapter would use a physical approach similar to that of the DPMs, but with various assumptions regarding the key forces and processes. In addition, it was argued that due to uncertainty in the co-efficients used in DPMs, the model should also be able to account for the corresponding uncertainty in the model output.

In Section 7.3, the reduced-complexity DPM was described in detail, which included the use of distributed values for the drag co-efficient found from CFD modelling of flow around a sphere. The Monte Carlo based GLUE methodology was explained, along with the manner in which the approach would be adapted for modelling particle trajectories. Because of the high computational cost of any Monte Carlo method, the model code was rewritten in CUDA C to enable it to be run in parallel on GPUs, thus giving a substantial decrease in overall model runtime. The results from the preliminary testing were also presented in this section, resulting in 200,000 initial parameter sets being used and total simulated times of 60s and 240s for the Arolla and Moor House confluences respectively.

In Section 7.4, the model was calibrated using the particle patch experiments of Confluence G on the Borgne d'Arolla. The non-behavioural parameter sets were removed to leave 30,834 parameter sets that were then used in subsequent model simulations. The model was tested on the remainder of the Arolla data, resulting in one incidence of a major discrepancy with the observed particle trajectories. This was

considered to be due to errors in the topographic data rather than a fundamental flaw in the model. Minor discrepancies in particle trajectories were usually due to differences in the initial direction of movement of the particle at Confluence G. It was argued that this was due to the assumption that all flow was at  $0^\circ$  to the downstream direction, whereas the individual particle tracks suggest flow from the true left tributary being angled slightly towards the true right bank.

Finally, the model was applied to the Moor House confluences in Section 7.5. These simulations used the modelled flows from Section 5.11, but the results from the particle model showed little agreement with the field data, except for the true left tributary of the lower confluence. It was found, however, that the discharges used in the higher flow simulations of Section 5.11 were lower than those which led to particle movement. An additional simulation was therefore run for each confluence, using the information from Figure 6.3 and Section 7.5.1 to determine the appropriate inlet discharges. The subsequent results from the particle model were much more representative of the field data, although at the upper confluence the model predicted particle trajectories too far towards the true left bank. From photographs taken before and after the large flood on 22<sup>nd</sup> June 2012, it was argued that the reason for this was a significant change in flow direction of the true left channel at higher discharges. Therefore given this finding and the results from Confluence G at the Borgne d'Arolla, it was concluded that to understand the sediment dynamics at steep, upland river confluences with less well-defined banks, the most important factor to consider is how the discharge ratios and flow directions change as a result of upstream processes.

# Chapter 8:

## Conclusions

### 8.1 Introduction

Chapter 1 showed that research into the dynamics of river confluences has largely focused on the flow field in lowland junctions. The sediment dynamics have received less attention, with the bedload transport work of Best (1988) and Roy and Bergeron (1990) the most relevant to this thesis. Meanwhile, even fewer studies have investigated upland river confluences with steep water surface slopes (Best, 1987, 1988; Ashmore *et al.*, 1992). Therefore, it was argued that if the understanding of the flow and sediment dynamics at river confluences was to be advanced, it would be necessary to explore the way in which the steeper water surface slopes of upland confluences affected their flow and sediment dynamics. This led to the overall question to be addressed in this thesis:

**What processes drive the dynamism of upland river confluences and how do these processes differ from those currently known to shape lowland river confluences?**

To respond to this question, the thesis had three aims:

- To improve our understanding of the feedback mechanisms operating between flow, sediment dynamics and morphology at steep river confluences.
- To investigate the flow processes at upland river confluences characterised by steep water surface slopes.
- To investigate the way in which the flow field drives the sediment transport and the resultant implications for morphological evolution in dynamic, upland river confluences.

In order to meet these aims, and thus answer the overall research question for the thesis, five principal objectives were addressed:

1. To obtain and to present high quality field data on the morphology, flow field and particle transport at a range of upland river confluences.
2. To develop the application of numerical approaches to improve the understanding of steep river confluence flow dynamics.
3. To use the topographic and flow data obtained as part of Objective 1 to test the performance of the numerical flow model developed in Objective 2.
4. To create a sediment transport model which uses the three-dimensional flow modelling developed in Objective 2 to determine the major processes driving particle movement in upland river confluences.
5. To use the particle tracking data collected as part of Objective 1 to test the sediment transport model developed in Objective 4.

This chapter will return to each of these objectives in turn, discussing how the thesis has satisfied the objective and the major findings applicable to each. The chapter will then consider the overall research question and present two new schematic diagrams to explain the processes operating at upland river confluences. The research presented in this thesis is then evaluated and suggestions made for further research.

## **8.2 Evaluation of the Research Objectives**

### *8.2.1 Research Objective 1: To obtain and to present high quality field data on the morphology, flow field and particle transport at a range of upland river confluences*

By selecting two confluences each from Moor House Nature Reserve and the Borgne d'Arolla braid plain, this thesis has obtained high quality data from four upland river confluences with different forms. At Moor House, the lower confluence resembled a classical discordant river junction, while the upper confluence bed morphology was more varied. The Borgne d'Arolla confluences differed from both of these by having steeper water surface slopes, unconsolidated banks, Froude numbers near unity and smaller junction angles (one was a  $0^{\circ}$  confluence and the other a  $30^{\circ}$  confluence). This meant there were different focuses for the respective field experiments, with higher-resolution topographic and flow data acquired from Moor House (*e.g.* Figures 4.5 and 4.6) and real-time particle tracking data obtained from the more dynamic Arolla



confluences (Figures 6.17 and 6.18). However, in spite of these differences, both sites share three key characteristics: (i) they are gravel or cobble bed, (ii) they have steeply sloping water surfaces (at a range of gradients) and (iii) they have some banks that are less well-defined. Furthermore, the data obtained from all four confluences satisfied the quality criteria set out in Section 3.8.

At both Moor House confluences, the flow field was found to be affected more by the bed and channel topography than the water surface slopes. This topographic effect occurred at the scale of individual particles, bed morphological features and the shape of the better-defined channel banks (Figures 4.15 and 4.16). The result was a complex flow field with inconsistent, weak and short-lived secondary circulation (Figures 4.17 and 4.18). The exception was near the avalanche face of the lower confluence, where Profiles W, X and Y in Figure 4.17 showed water from the true left tributary flowing over that from the true right, as is considered fairly typical of discordant junctions (*e.g.* Best and Roy, 1991; Biron *et al.*, 1993, 1996a; Bradbrook *et al.*, 2001). However, this strong secondary flow feature was still short-lived, persisting downstream for less than one channel's width. This is most likely due to the variable bed topography and higher roughness levels, both of which are known to affect the flow at shallow confluences (Roy and Bergeron, 1990; Rhoads and Kenworthy, 1995, 1998; De Serres *et al.*, 1999; Parsons *et al.*, 2007, 2008; Vermaas *et al.*, 2011).

The particle tracking experiments at the Moor House confluences (Section 6.2) provided evidence of considerable lateral dispersal from some seeding locations, in particular from the patch placed on the upstream corner bar of the upper confluence (Figure 6.5). In Sections 6.2.5 and 6.2.7, the tracer particle densities were compared with near-bed flow lines determined from the high discharge scenario modelling of the Moor House confluences (Section 5.11). The particle trajectories and modelled near-bed flow directions agreed for only some of the discharge ratio scenarios. Therefore this indicated that, as Rhoads *et al.* (2009) found for sand-bed confluences, the discharge ratio is important for bedload transport.

The Arolla confluences were found to exhibit major water surface undulations (Figure 4.29), but otherwise the field data suggested a less complex flow field than at the Moor House confluences, with the downstream flow component dominating and higher velocities away from the banks. The particle trajectories followed a similar pattern, although Figures 6.17 and 6.18 showed a small amount of curvature away from the centre of the confluence, thus implying some mutual deflection of the tributary

flows. At the more local scale, particle tracks were found to be affected by deviations around larger topographic obstacles, which were sometimes sufficient to route the particles towards the opposite bank (*e.g.* the true left patch in Figure 6.18b).

Therefore, the particle tracking experiments at both the Moor House and Arolla confluences showed the potential for bedload particles to cross the confluence, as found in the experiments of Roy and Bergeron (1990). However, while some particle dispersal was common, the crossing of particle paths was very much the exception. Instead, most patches tended to keep closer to their respective banks, meaning the results found here were not all that different from the segregated particle trajectories obtained by Best (1988) for the Widdale Beck confluence.

### 8.2.2 *Research Objective 2: To develop the application of numerical approaches to improve the understanding of steep river confluence flow dynamics*

In Section 3.7 it was noted that in confluences with steep water surface slopes, traditional rigid-lid or porosity-based approaches to simulating the free surface in Computational Fluid Dynamics (CFD) models were likely to be less appropriate. Therefore, in Chapter 5 the Height-of-Liquid (HOL) model from the PHOENICS code was adapted and applied to flow in the Moor House and Arolla confluences.

The advantages of adapting the HOL model in this way were demonstrated throughout Chapter 5. By using the HOL model, three-dimensional plots of the modelled water surface elevation can be obtained (*e.g.* Figures 5.21 and 5.31), which gives far more information on the spatial variability of the free surface than could be acquired from interpolating water edge points. However, it is through interrogating the model that the greatest improvement in understanding has been achieved. For the Moor House confluences, the HOL method was used to determine the effects of different discharge ratios on the water surface fluctuations, depth-averaged flow fields, secondary flow and the zones of higher TKE and shear stress (Section 5.11). At the Arolla confluences, meanwhile, use of the CFD model in this way provided significantly more detail on the flow field at these highly dynamic confluences than could be obtained from field experiments alone. In both cases, if the free surface had not been explicitly resolved using the HOL model, the confidence in the accuracy of the simulated flow field would have decreased as the water surface slopes increased.

### 8.2.3 *Research Objective 3: To use the topographic and flow data obtained as part of Objective 1 to test the performance of the numerical flow model developed in Objective 2*

Having collected a wide-ranging field dataset in Objective 1, the HOL model from Objective 2 could be thoroughly tested. This was important because whilst CFD modelling of river confluences has been undertaken in a number of studies (Bradbrook *et al.*, 1998, 2000a, 2000b, 2001; Lane *et al.*, 2000; Huang *et al.*, 2002; Biron *et al.*, 2004a; Constantinescu *et al.*, 2011; Sandbach *et al.*, 2012), to the author's knowledge this has not been extended to include explicit modelling of the free surface. Therefore, it was imperative that the performance of the model be assessed and its potential limitations found.

In the grid independence testing of Section 5.4, the greatest uncertainty due to the discretisation process was found in the vertical velocity and turbulence variables, with errors lower for pressure, the horizontal velocity components and the water surface elevation (Table 5.2). Obtaining grid convergence with gravel-bed rivers is known to be particularly problematic, as varying the grid resolution inherently changes the model boundary conditions (Lane *et al.*, 1999a). As such, these tests were important for quantifying the uncertainty in each of the modelled variables. Given the focus on implementing an explicit free surface model, it was therefore considered particularly encouraging that grid convergence errors were lowest for water surface elevation.

Model validation was undertaken using data from the Moor House and Arolla confluences. For water surface elevation the comparisons between modelled and observed data were good, with the greatest disparities due to the influence of the domain outlet at the Moor House confluences (Figures 5.17 and 5.22) and the presence of in-channel standing waves at the Arolla confluences (Figures 5.27 and 5.32). With respect to flow velocity, qualitatively the model was found to replicate most of the major flow features at the Moor House confluences (Figures 5.19 and 5.24). The poorer quantitative agreement (*e.g.* Figure 5.20), meanwhile, was argued to be due to a combination of geolocation errors and the model being unable to fully represent the detail and complexity of the flow around the large bed particles. The latter is of particular importance when flows are shallow.

In addition to the water surface elevation and velocity results, the HOL model was shown to be capable of replicating the key secondary and turbulent flow features

observed at the Moor House confluences. At the discordant lower confluence (Figure 5.40), water from the true right tributary is clearly flowing under that from the true left, as found in the aDv data (Figure 4.17). At the upper confluence, the model predicts a narrow zone of elevated TKE downstream of the flow constriction (at (i) in Figure 5.39a), which agrees well with the values in Figure 4.21.

Therefore, in testing the HOL model in Chapter 5 it was demonstrated that there can be some confidence in its ability to replicate the flow field, turbulence and water surface fluctuations at upland river confluences. In particular, it is argued that in these conditions, the HOL method has provided a much more physically realistic representation of the flow dynamics than would have been possible using a rigid lid approach (as shown in Figure 5.1), an approach which modifies the mesh (*e.g.* Huang *et al.*, 2002) or a porosity-based method (*e.g.* Bradbrook *et al.*, 1998). Although the mesh-modification and porosity approaches would be valid for flows with shallow water surface slopes, in steeper confluences both methods are susceptible to instability (Bradbrook *et al.*, 2000a, 2001). Therefore, the particular advantage of the HOL method is the scale of free surface variability it can accommodate.

#### 8.2.4 *Research Objective 4: To create a sediment transport model which uses the three-dimensional flow modelling developed in Objective 2 to determine the major processes driving particle movement in upland river confluences*

As a result of the developments in Chapter 5, it was possible to obtain three-dimensional flow fields for all of the steep confluences studied in this thesis. This has important implications for modelling sediment transport, as it provides sufficient detail to be able to resolve the forces acting on an individual particle. In Section 7.2, a number of different sediment modelling approaches were discussed. These included both more complex (*e.g.* Darby *et al.*, 2002; Dan *et al.*, 2011; Nardin and Fagherazzi, 2012) and reduced-complexity (*e.g.* Murray and Paola, 1994, 1997; Nicholas, 2009, 2010) Eulerian methods, as well as Discrete Particle Models (DPMs). DPMs were considered to be more applicable to this research as a result of the focus, in this objective, on understanding the processes driving bedload transport.

Research using DPMs has tended to focus on the effect of individual forces on particle saltation (*e.g.* Wiberg and Smith, 1985; Nino and Garcia, 1994, 1998;

Lukerchenko *et al.*, 2009) or on trying to represent the collisions in mass movements of particles (*e.g.* Latham and Munjiza, 2004; Cleary and Prakash, 2004). In both cases the forces are resolved in more detail than is needed when looking at reach-scale transport. Therefore, in Section 7.3 a reduced-complexity DPM was developed that was based on the underlying physics, but with some simplifications to reduce the computational cost. These included assuming all movement was along the bed (rather than trying to replicate the complex physics behind saltation), that the Magnus spin and Basset history forces would be negligible and that collisions between particles did not need to be modelled. The model code was written so that it could be executed in parallel on any compatible Graphics Processing Unit (GPU), enabling the Monte Carlo based GLUE methodology of Beven and Binley (1992) to be used to account for parameter uncertainty.

In adopting this approach, the model was able to give the probability that a particle starting from a particular point would be entrained, as well as the likely range of particle trajectories (*e.g.* Figure 7.21). Therefore the model gave far more information than a single modelled trajectory would have provided. Furthermore, using the GLUE framework meant that it was possible to determine whether disagreements between modelled and observed particle tracks were a function of uncertainty in the parameter set or due to more fundamental errors in the boundary conditions (such as the discharge ratio used in the original flow model).

After testing (see Section 8.2.5), the model was used to investigate the processes that have the most influence on sediment transport at the Moor House (Section 7.5) and Arolla (Section 7.4) confluences. In these experiments, it was found that successfully replicating the particle trajectories required an accurate representation of the discharges, discharge ratio and tributary flow directions. Of the river confluence bedload transport studies to date, Roy and Bergeron (1990) have already demonstrated the effect of stage, while Boyer *et al.* (2006) highlighted the importance of momentum ratio in a sand-bed confluence. Therefore, in this study it is the finding that bedload transport is strongly affected by the tributary flow directions during floods which is particularly novel. This effect has been evident at the Arolla and Moor House confluences because of the less well-defined banks at both sites. Such banks enable changes in the primary flow direction of the tributaries as water levels rise or the upstream channel morphology evolves.

### 8.2.5 *Research Objective 5: To use the particle tracking data collected as part of Objective 1 to test the sediment transport model developed in Objective 4*

Having developed a reduced-complexity DPM in Section 7.3, it was tested using the particle tracking field data from Chapter 6. This involved comparing the model output to data from the Arolla particle tracking experiments (for which the flow boundary conditions had been measured *in situ*). Having tested the model quantitatively in this way, it was then tested qualitatively by examining whether, under the right discharge conditions, it could replicate the observed particle movement at the Moor House confluences.

The testing of the model at the Arolla confluences showed that it replicated the direction and spread of the particle trajectories well, with one notable exception (Figure 7.12). In that case, it was argued that the failure was due to errors in the topographic boundary conditions rather than a fundamental flaw in the model. There were also minor discrepancies between the initial direction of the modelled and measured particle trajectories at Confluence G (Figures 7.8 and 7.14). In all three cases the modelled particles started off further to the true left than was observed. It was therefore suggested that the cause of this was the assumption of a  $0^\circ$  flow direction for the true left tributary, whereas the individual particle tracks in Figure 6.17a suggest an initial flow direction slightly towards the true right. However, the overall performance of the model was considered to be good, thus justifying the modelling approach used.

In applying the reduced-complexity DPM to the Moor House confluences, it was found that the model was capable of discriminating between discharges that led to widespread particle movement and those that did not. This is shown by comparing the plots in Section 7.5.1 for the bankfull discharge simulations with the higher discharge simulations in Section 7.5.2. This is particularly true of the lower confluence, where an increase in the true right tributary discharge gives a much better representation of the probability of initiation and the range of likely particle trajectories (Figure 7.21). The same is true for the upper confluence (Figure 7.23), although there is a tendency for the model to predict trajectories further to the true left. With reference to photographs in Figure 7.24, it was argued that the reason for this is a substantial change in the flow direction of the true left tributary as discharge increases.

### 8.3 The Dynamics of Upland River Confluences

The aim of this section is to use the results summarised in Section 8.2 to develop a conceptual model of the interactions between flow and sediment transport in upland river confluences.

At upland confluences, the bed topography has been demonstrated to play a key role in the flow dynamics. This has been shown to have an effect at lowland confluences, for example where the beds are discordant (*e.g.* Gaudet and Roy, 1995; Biron *et al.*, 1996a; Rhoads and Sukhodolov, 2001) or the flow interacts with large bedforms (*e.g.* Parsons *et al.*, 2007, 2008; Lane *et al.*, 2008; Sandbach *et al.*, 2012). However, at upland confluences the effect is found at a range of scales, from local scale routing around large rocks and pebble clusters to the larger-scale impacts of submerged bars and the channel banks. In addition, the flow modelling in Chapter 5 showed that at steeper confluences, water surface undulations become more important. Instead of local topographic variations driving the secondary circulation (Figure 5.40), standing waves lead to small-scale and short-lived secondary flow patterns (Figures 5.63 and 5.68). At steeper confluences, the water surface fluctuations also appear to drive variations in bed shear stress and TKE (Figures 5.66 and 5.71).

Generally, research in upland confluences (*e.g.* Best, 1987, 1988; Ashmore *et al.*, 1992) has not identified the water surface slope to be of such importance. From laboratory and numerical experiments, Huang *et al.* (2002) found that the junction angle affected water surface depression in the flow separation zone, but did not investigate the implications of this for natural confluences.

For bedload transport, the classical model of river confluences implies that secondary flow and shear layer turbulence are important for sediment dynamics (Mosley, 1976; Best, 1988). This may indeed be the case in lowland or idealised laboratory confluences. However, the comparison between observed and modelled particle tracks in Chapter 7 has led to a clear conclusion: bedload transport at upland confluences is affected by the changes in tributary flow direction as water levels rise over the less well-defined banks. At lowland confluences there may be slight variations in sediment transport paths as the discharge ratio changes (Boyer *et al.*, 2006), but the high banks restrict the opportunity for substantial changes in tributary flow direction. By contrast, where the banks are low and unconsolidated, there is the potential for large changes in junction angle and frequent, substantial reworking of the bed (as shown in

Figure 7.24). It is this process, therefore, that will differentiate upland river confluences from their lowland counterparts.

As a result of these findings, the schematic diagrams in Figure 2.1 have been redrawn to account for the differences at upland river confluences. As this thesis has shown that the steeper Arolla confluences behave differently to the more stable Moor House confluences, Figure 8.1 is split into two parts: upland river confluences with shallower water surface slopes (Figure 8.1a) and steeper upland river confluences (Figure 8.1b). The differences between Figures 2.1 and 8.1 are discussed below.

In both parts of Figure 8.1, the important link between the scour hole and the helical flow cells has been removed. This is because at the upland confluences studied in this thesis, there is little evidence to suggest that scour holes or strong back-to-back helical secondary flow cells are present. This is not to say such features do not exist at steep river confluences; Ashmore *et al.* (1992), for instance, found evidence for both on the Sunwapta River. Rather, it emphasises that they are much rarer than the classical model implies. Unlike large lowland confluences, this is not believed to be primarily due to high width-to-depth ratios (Parsons *et al.*, 2007, 2008). The ratios for the Moor House (15-25 depending on discharge) and Arolla (approximately 10) confluences are similar to those at confluences where helical cells have been identified previously (*e.g.* Ashmore *et al.*, 1992; Rhoads and Sukhodolov, 2001). Instead, it is the high relative roughness heights (Figure 8.1a) and highly variable water surface elevations (Figure 8.1b) which are considered the main causes at shallower and steeper upland confluences respectively. It should be noted, however, that in these environments a higher width-to-depth ratio will increase relative roughness heights and will therefore play some role in disrupting the helical cells.

In Figure 8.1a, the turbulent mixing layer and flow separation zones are less pervasive than in Figure 2.1. This is because small-scale turbulent fluctuations caused by interactions with the bed will tend to dominate, while the presence of flow recirculation will be very dependent on local variations in the better-defined parts of the bank. In Figure 8.1b, meanwhile, it is the variability of the free surface that is thought to have a much greater control on other aspects of the flow dynamics.



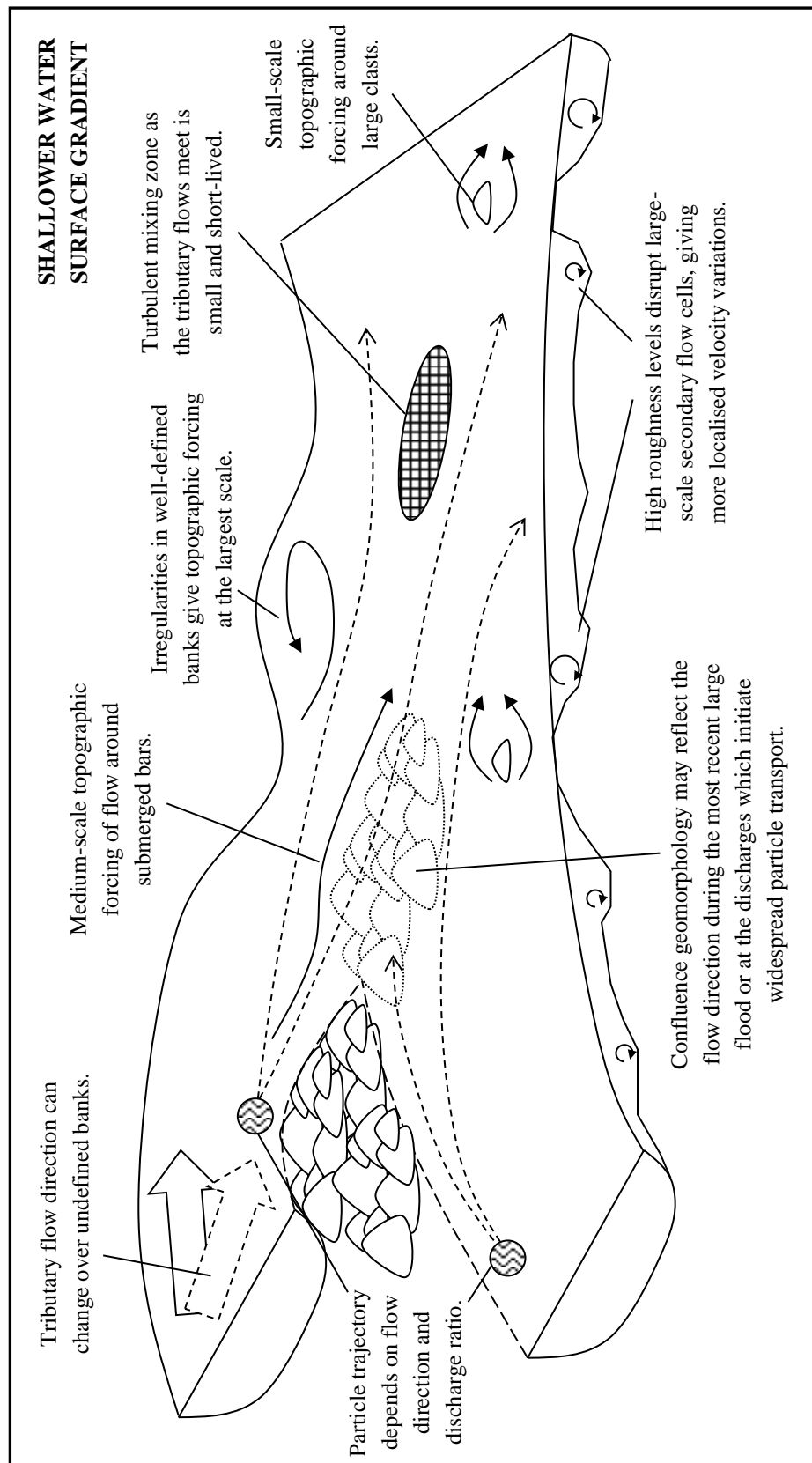


Figure 8.1a: Schematic diagram of flow and sediment dynamics at an upland river confluence with shallower water surface gradients. Well-defined banks are given by solid lines and poorly-defined banks by dashed lines. Arrows with solid lines show the flow direction, while those with dashed lines give particle trajectories. Submerged topographic features are given by dotted lines.

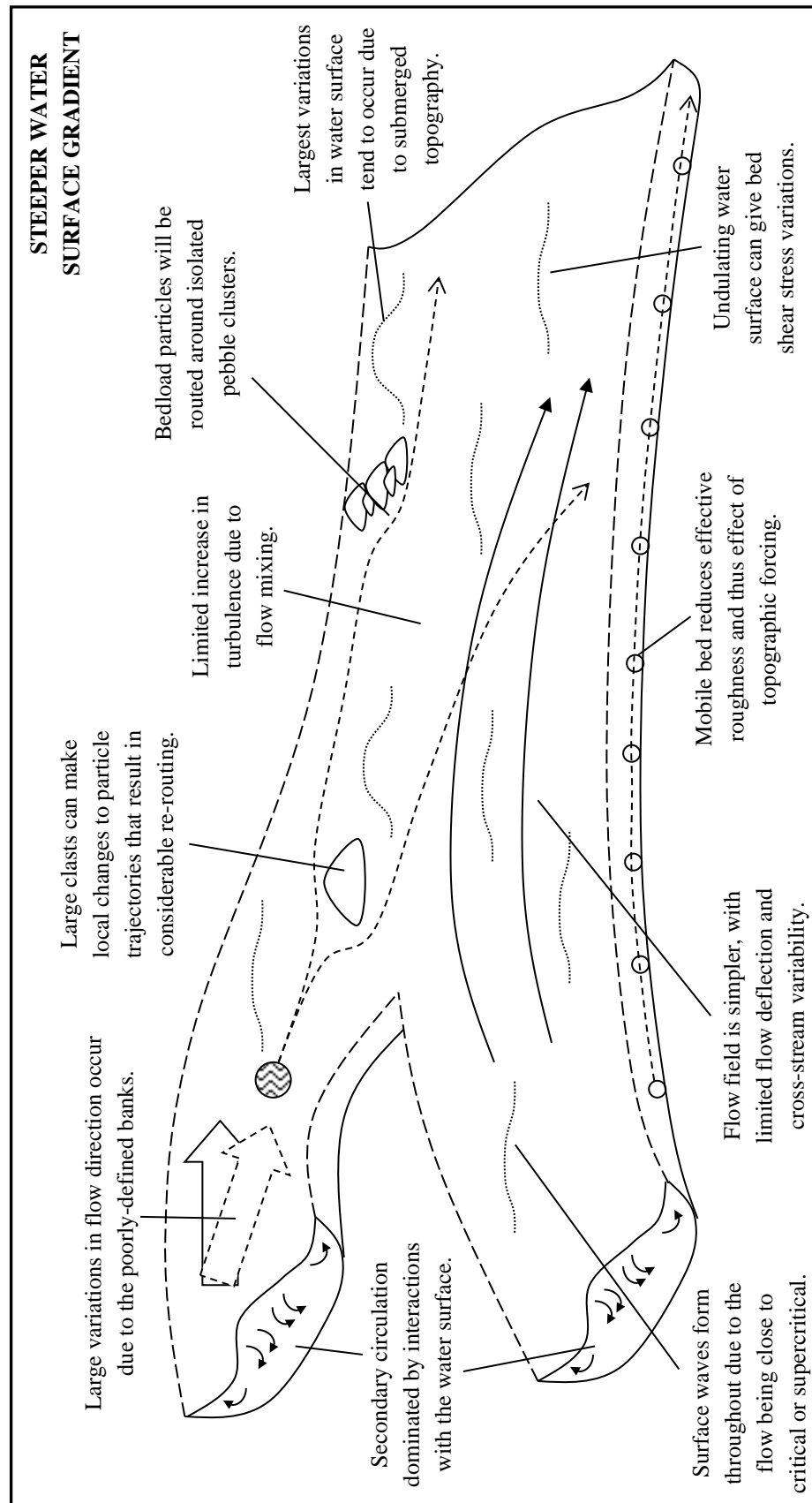


Figure 8.1b: Schematic diagram of flow and sediment dynamics at an upland river confluence with steeper water surface gradients. The diagram uses the same format as for the previous figure, but with water surface waves within the channel shown by dotted lines.

In terms of the geomorphology and sediment dynamics, the classical features of river confluences such as mid-channel bars and avalanche faces are not present in Figure 8.1a. Instead, the geomorphology will depend on the complex interactions between the nature of the banks (whether they are well- or poorly-defined) and the direction of flow during the most common or most recent high discharge event. In Figure 8.1b, meanwhile, it is the variability in the tributary flow direction over the unconsolidated banks and deviations around topographic obstacles that are highlighted as being most important for sediment dynamics. The lack of fixed morphological features in Figure 8.1b is a consequence of that, as the dynamic nature of the confluences rarely gives the opportunity for a consistent, stable morphology to develop. Morphological features will instead tend to be short-lived, unstable and dependent on the nature of the flow field at that confluence in the preceding minutes and hours.

Therefore, in focusing on upland river confluences, this thesis has demonstrated that the processes driving flow and sediment dynamics are much more variable than previously thought. The dynamics of upland river junctions are different to those at their lowland counterparts in a number of ways, with fluctuations in the water surface playing a much more prominent role as the valley gradient increases. Fundamentally, however, it is becoming harder to fit all river confluences into the classical model. It is perhaps this, above all other factors, which gives river confluences their unruly and untidy reputation (Ettema, 2008).

Given the much greater variability in the dynamics of upland river confluences that this thesis has highlighted, there are also important implications regarding the development of these findings to river confluences in general. Perhaps the most significant of these is the more reliable basis that numerical modelling methods can provide when developing and testing future hypotheses. Whereas laboratory studies are, by definition, idealised and field studies are usually subject to logistical constraints, numerical modelling has the advantage that it can be applied to a wide range of scenarios. This includes both the ability to simulate the rarer, high discharge events which reshape the confluence morphology and the opportunity to obtain high-resolution, spatially-distributed flow data for a specific set of conditions. Therefore, whilst there is still an important role to be played by field and laboratory studies, numerical modelling methods may offer the best opportunity for increasing the understanding of river confluences and specifically the way in which the many different morphologies can affect the flow and sediment dynamics.

## 8.4 Further Research

There are a number of ways in which the methods used in this thesis could be developed or the findings from it investigated in more detail. Therefore, this section evaluates the work in this thesis and suggests potential avenues for further research, focusing in turn on the field experiments, the numerical modelling and river confluence dynamics.

### 8.4.1 Field Experiments

In terms of the field methodology used in this thesis, there are three main areas for potential future developments. These are related to the topographic data, the flow measurements and the particle tracking experiments.

For the topographic data, the results from this thesis could be expanded in two ways. Firstly, at the Moor House confluences it was not feasible to resurvey the confluence morphology after each flood in the 18-month data collection period. In most cases the bed topography did not visibly alter between floods, but Figure 7.24 showed that the very large flood of 22<sup>nd</sup> June 2013 resulted in a dramatic change to the upper confluence morphology. Therefore, a longer-term study could look at the evolution of the confluence in different flood events through repeat dGPS surveys, using a similar approach to that of Brasington *et al.* (2000) for the River Feshie. At the Arolla confluences, meanwhile, the major limitation of the topographic data is in their detail. This was due to the difficulties associated with obtaining representative elevation data from a mobile bed and the time constraints of working in such highly dynamic systems. In the absence of a fast, non-intrusive surveying technique for turbid rivers, further research could make use of the speed and resolution of terrestrial LiDAR (*e.g.* Hodge *et al.*, 2009) for the channel banks, leaving more time available for the in-channel Total Station or dGPS survey.

With respect to the flow data, the two major areas in which improvements could be made are in the detail of the Moor House confluence measurements and by going beyond one-dimensional flow data at the Arolla confluences. Although the spatial coverage at both Moor House confluences is better than that specified in Section 3.8.2, it is still only at-a-point data. Therefore, further research could expand this by using multiple devices attached to a frame (*e.g.* Rhoads and Sukhodolov, 2004) or by using

aDcp approaches (*e.g.* Rhoads and Sukhodolov, 2001; Kostachuk *et al.*, 2005; Parsons *et al.*, 2006a, 2006b). Section 3.8.2 has already highlighted the problems of using aDcp in shallow water, but it might be possible to obtain these data in much higher discharges. At the Arolla confluences, air bubbles in the flow limited use of the aDv (Rodriguez *et al.*, 1999). However, using two-dimensional ECMs (*e.g.* De Serres *et al.*, 1999; MacVicar *et al.*, 2007) would be a significant advantage in future studies, as the horizontal flow direction would not need to be estimated. This limitation was most problematic in Section 7.4, where it was argued that some of the disagreements between modelled and observed particle trajectories were linked to the uncertainty in the inlet flow directions.

For the particle tracking experiments, there are a number of opportunities for expanding the research conducted in this thesis. From the results at Moor House, two additional areas for further investigations can be identified. Firstly, the possibility of investigating morphological change at these confluences (as noted above) could be linked to longer-term particle experiments using larger clasts. The monitoring of larger particles over longer timescales would enable and encourage the use of PIT tags to maximise recovery rates (Lamarre and Roy, 2008a, 2008b). Secondly, the results from the true left tributary of the lower confluence could be investigated in more detail. The data in Figure 6.10 show a similar pattern to that described by Best (1988), who found that particles from Widdale Beck could be tracked only as far as the avalanche face. Best (1988) suggested that possible causes were particle burial in the avalanche face or rapid transport in the main channel. As the research presented here has been unable to definitively identify the process responsible, further experiments with the targeted use of PIT tags may well prove more effective.

At the Arolla confluences, the major limitations in this study were the difficulties in seeing tracer particles in the highly turbid water and the need to survey particle tracks *a posteriori* with the help of video footage. For the latter, a series of geo-referenced video cameras mounted to a frame over the confluence could improve the accuracy of the recorded tracks, although the post-processing required would be complex. Overcoming the former, meanwhile, is a much bigger methodological challenge, as there is not yet a reliable way of obtaining real-time particle tracks when visibility is low. As river beds are usually invisible during channel-modifying flows, this is clearly an area in which much further research could be conducted.

### 8.4.2 Numerical Modelling

This thesis has made use of numerical modelling of both the flow (using the HOL model within a CFD framework) and individual particle transport (using a new, reduced-complexity DPM). Both methods have been developed to some extent within this thesis and while they have both proved to be potentially powerful tools, there are a number of possible areas for improvement.

For the HOL model, the biggest problem is in obtaining an appropriate balance between the desire for higher resolution grids and the associated non-linear increase in computational cost (Table 5.1 and Figure 5.3). Therefore, the next step should be to investigate if runtimes can be reduced, possibly by finding a way to get numerically stable steady-state solutions. In addition, grid sizes could be reduced if a reliable treatment of the pressure distribution at the outlet can be developed, as there would be no need for long run-out areas in the model.

For the reduced-complexity DPM, further work could focus on the deposition and re-entrainment process, as at present the model does not deposit slow-moving particles. Additional research could also investigate why the particle model underperforms in certain locations of the confluences, by running a much wider range of scenarios for the flow models before executing the particle model with these new data. A longer-term goal would be to develop a coupled flow and sediment transport model that can update the topography at each time step to reflect the particle movement.

### 8.4.3 River Confluence Dynamics

By investigating four different confluences in detail, the research conducted in this thesis has highlighted the potential role played by the water surface in driving the flow dynamics of steeper confluences. It has been known for some time that the dynamics of river confluences are affected by junction angle (Mosley 1976, Ashmore and Parker, 1983), planform symmetry (Ashmore and Parker, 1983; Ashmore *et al.*, 1992), discharge ratio (Rhoads and Kenworthy, 1995; Bradbrook *et al.*, 2001) and bed discordance (Best and Roy, 1991; Biron *et al.*, 1993). However, there has been much less focus on how these factors interact with increasing water surface slopes. This thesis can be considered a first step in increasing the understanding of these confluences, but stronger conclusions would require more evidence from a range of steep confluences.

In the first instance, this further research could focus on extending the early laboratory experiments of Mosley (1976) to incorporate a much more detailed treatment of the interactions between water surface slope and junction angle, symmetry and discharge ratio. However, greater improvements to understanding are likely to be obtained by undertaking a much more widespread cataloguing of the prevalence of flow and morphological features at upland confluences. If this were extended to cover all of the confluences present in a small catchment, it would provide a much clearer insight into the relative importance of the junction angle, symmetry, discharge ratio and amount of bed discordance on the dynamics of natural river confluences. Specifically, by accounting for the full range of confluence sizes, width-to-depth ratios and water surface slopes, it would be possible to investigate how commonly the flow features of large (*e.g.* Parsons *et al.*, 2007, 2008; Lane *et al.*, 2008; Laraque *et al.*, 2009; Sandbach *et al.*, 2012), lowland (*e.g.* Bradbrook *et al.*, 2000a; Rhoads and Sukhodolov, 2001, 2004, 2008; Constantinescu *et al.*, 2011, 2012) and upland (this thesis; Best, 1987, 1988; Ashmore *et al.*, 1992) confluences are found in all natural river junctions.

## **8.5 Conclusions**

This chapter has addressed each of the objectives of this thesis in turn and summarised how the research presented herein has aimed to achieve them (Section 8.2). This has enabled the overall research question of the thesis to be answered in Section 8.3, showing how the understanding of the dynamics of upland river confluences has been improved by this study. However, as explained in Section 8.4, there is still much that could be learnt through further investigations in these complex environments.

# References

- Abba, A., A. C. Cercignani and L. Valdetaro (2003) Analysis of subgrid scale models. *Computers and Mathematics with Applications*, 46, 521-535.
- Ancey, C., A. C. Davison, T. Boehm, M. Jodeau and P. Frey (2008) Entrainment and motion of coarse particles in a shallow water stream down a steep slope. *Journal of Fluid Mechanics*, 595, 83-114.
- Anderson, J. D. (1995) *Computational Fluid Dynamics*. New York: McGraw-Hill.
- Apsley, D. (2007) CFD calculation of turbulent flow with arbitrary wall roughness. *Flow Turbulence and Combustion*, 78, 153-175.
- Ashmore, P. and J. T. Gardner (2008) Unconfined Confluences in Braided Rivers. In: *River Confluences, Tributaries and the Fluvial Network*, eds. S. P. Rice, B. L. Rhoads and A. G. Roy. Chichester: John Wiley and Sons.
- Ashmore, P. and G. Parker (1983) Confluence scour in coarse braided streams. *Water Resources Research*, 19, 392-402.
- Ashmore, P. E., R. I. Ferguson, K. L. Prestegard, P. J. Ashworth and C. Paola (1992) Secondary flow in anabranch confluences of a braided, gravel-bed stream. *Earth Surface Processes and Landforms*, 17, 299-311.
- Ashworth, P. J. and R. I. Ferguson (1986) Interrelationships of channel processes, changes and sediments in a proglacial braided river. *Geografiska Annaler Series A - Physical Geography*, 68, 361-371.
- Babarutsi, S. and V. H. Chu (1998) Modelling transverse mixing layer in shallow open-channel flows. *Journal of Hydraulic Engineering-Asce*, 124, 718-727.
- Bates, P. D. and M. G. Anderson (1993) A 2-Dimensional Finite-Element Model for River Flow Inundation. *Proceedings of the Royal Society of London Series A - Mathematical Physical and Engineering Sciences*, 440, 481-491.
- Ben Haj, M., Z. Hafsia, H. Chaker and K. Maalel (2002) Two-dimensional free surface modelling for a non-dimensional dam-break problem. In: *Ninth International PHOENICS User Conference*. Moscow, Russia.
- Benda, L., C. Veldhuisen and J. Black (2003) Debris flows as agents of morphological heterogeneity at low-order confluences, Olympic Mountains, Washington. *Geological Society of America Bulletin*, 115, 1110-1121.
- Bertoldi, W., L. Zanoni and M. Tubino (2010) Assessment of morphological changes induced by flow and flood pulses in a gravel bed braided river: The Tagliamento River (Italy). *Geomorphology*, 114, 348-360.
- Best, J. L. (1986) The Morphology of River Channel Confluences. *Progress in Physical Geography*, 10, 157-174.
- (1987) Flow dynamics at river channel confluences: implications for sediment transport and bed morphology. In: *Recent Developments in Fluvial Sedimentology*, 27-35. SEPM (Society for Sedimentary Geology).



- (1988) Sediment Transport and Bed Morphology at River Channel Confluences. *Sedimentology*, 35, 481-498.
- Best, J. L. and I. Reid (1984) Separation zone at open-channel junctions. *Journal of Hydraulic Engineering-Asce*, 110, 1588-1594.
- Best, J. L. and B. L. Rhoads (2008) Sediment Transport, Bed Morphology and the Sedimentology of River Channel Confluences. In: *River Confluences, Tributaries and the Fluvial Network*, eds. S. P. Rice, B. L. Rhoads and A. G. Roy. Chichester: John Wiley and Sons.
- Best, J. L. and A. G. Roy (1991) Mixing-Layer Distortion at the Confluence of Channels of Different Depth. *Nature*, 350, 411-413.
- Beven, K. (2009) *Environmental Modelling: An Uncertain Future?* London: Routledge.
- Beven, K. and A. Binley (1992) The future of distributed models - model calibration and uncertainty prediction. *Hydrological Processes*, 6, 279-298.
- Beven, K. and J. Freer (2001) Equifinality, data assimilation, and uncertainty estimation in mechanistic modelling of complex environmental systems using the GLUE methodology. *Journal of Hydrology*, 249, 11-29.
- Beven, K. J. (2001) *Rainfall-Runoff Modelling: The Primer*. Chichester: J. Wiley and Sons.
- Biron, P., J. L. Best and A. G. Roy (1996a) Effects of bed discordance on flow dynamics at open channel confluences. *Journal of Hydraulic Engineering-Asce*, 122, 676-682.
- Biron, P., A. G. Roy and J. L. Best (1996b) Turbulent flow structure at concordant and discordant open-channel confluences. *Experiments in Fluids*, 21, 437-446.
- Biron, P. and S. N. Lane (2008) Modelling Hydraulics and Sediment Transport at River Confluences. In: *River Confluences, Tributaries and the Fluvial Network*, eds. S. P. Rice, B. L. Rhoads and A. G. Roy. Chichester: John Wiley and Sons.
- Biron, P., A. G. Roy, J. L. Best and C. J. Boyer (1993) Bed Morphology and Sedimentology at the Confluence of Unequal Depth Channels. *Geomorphology*, 8, 115-129.
- Biron, P. M., T. W. Haltigin, R. J. Hardy and M. F. Lapointe (2007) Assessing different methods of generating a three-dimensional numerical model mesh for a complex stream bed topography. *International Journal of Computational Fluid Dynamics*, 21, 37-47.
- Biron, P. M., S. N. Lane, A. G. Roy, K. F. Bradbrook and K. S. Richards (1998) Sensitivity of bed shear stress estimated from vertical velocity profiles: The problem of sampling resolution. *Earth Surface Processes and Landforms*, 23, 133-139.
- Biron, P. M., A. S. Ramamurthy and S. Han (2004a) Three-dimensional numerical modeling of mixing at river confluences. *Journal of Hydraulic Engineering-Asce*, 130, 243-253.
- Biron, P. M., A. Richer, A. D. Kirkbride, A. G. Roy and S. Han (2002) Spatial patterns of water surface topography at a river confluence. *Earth Surface Processes and Landforms*, 27, 913-928.

- Biron, P. M., C. Robson, M. F. Lapointe and S. J. Gaskin (2004b) Comparing different methods of bed shear stress estimates in simple and complex flow fields. *Earth Surface Processes and Landforms*, 29, 1403-1415.
- Bohonak, A.J. and K. van der Linde (2004) RMA: Software for Reduced Major Axis regression, Java version. <<http://www.kimvdlinde.com/professional/rma.html>>.
- Bouchez, J., E. Lajeunesse, J. Gaillardet, C. France-Lanord, P. Dutra-Maia and L. Maurice (2010) Turbulent mixing in the Amazon River: The isotopic memory of confluences. *Earth and Planetary Science Letters*, 290, 37-43.
- Boyer, C., A. G. Roy and J. L. Best (2006) Dynamics of a river channel confluence with discordant beds: Flow turbulence, bed load sediment transport, and bed morphology. *Journal of Geophysical Research-Earth Surface*, 111.
- Bradbrook, K. F., P. M. Biron, S. N. Lane, K. S. Richards and A. G. Roy (1998) Investigation of controls on secondary circulation in a simple confluence geometry using a three-dimensional numerical model. *Hydrological Processes*, 12, 1371-1396.
- Bradbrook, K. F., S. N. Lane and K. S. Richards (2000a) Numerical simulation of three-dimensional, time-averaged flow structure at river channel confluences. *Water Resources Research*, 36, 2731-2746.
- Bradbrook, K. F., S. N. Lane, K. S. Richards, P. M. Biron and A. G. Roy (2000b) Large Eddy Simulation of periodic flow characteristics at river channel confluences. *Journal of Hydraulic Research*, 38, 207-215.
- (2001) Role of bed discordance at asymmetrical river confluences. *Journal of Hydraulic Engineering-Asce*, 127, 351-368.
- Brasington, J., B. T. Rumsby and R. A. McVey (2000) Monitoring and modelling morphological change in a braided gravel-bed river using high resolution GPS-based survey. *Earth Surface Processes and Landforms*, 25, 973-990.
- Bridge, J. S. and S. J. Bennett (1992) A model for the entrainment and transport of sediment grains of mixed sizes, shapes, and densities. *Water Resources Research*, 28, 337-363.
- Bridge, J. S. and S. L. Gabel (1992) Flow and sediment dynamics in a low sinuosity, braided river - Calamus River, Nebraska Sandhills. *Sedimentology*, 39, 125-142.
- Bryan, R. B. and N. J. Kuhn (2002) Hydraulic conditions in experimental rill confluences and scour in erodible soils. *Water Resources Research*, 38.
- Buffin-Belanger, T. and A. G. Roy (2005) 1 min in the life of a river: selecting the optimal record length for the measurement of turbulence in fluvial boundary layers. *Geomorphology*, 68, 77-94.
- Butler, J. B., S. N. Lane, J. H. Chandler and E. Porfiri (2002) Through-water close range digital photogrammetry in flume and field environments. *Photogrammetric Record*, 17, 419-439.
- Calantoni, J., K. T. Holland and T. G. Drake (2004) Modelling sheet-flow sediment transport in wave-bottom boundary layers using discrete-element modelling. *Philosophical Transactions of the Royal Society of London Series A - Mathematical Physical and Engineering Sciences*, 362, 1987-2001.

- Campbell, C. S., P. W. Cleary and M. Hopkins (1995) Large-scale landslide simulations - global deformation, velocities and basal friction. *Journal of Geophysical Research-Solid Earth*, 100, 8267-8283.
- Carbonneau, P. E., S. N. Lane and N. E. Bergeron (2004) Catchment-scale mapping of surface grain size in gravel bed rivers using airborne digital imagery. *Water Resources Research*, 40.
- Casas, M. A., S. N. Lane, R. J. Hardy, G. Benito and P. J. Whiting (2010) Reconstruction of subgrid-scale topographic variability and its effect upon the spatial structure of three-dimensional river flow. *Water Resources Research*, 46.
- Celik, I. B., U. Ghia, P. J. Roache and C. J. Freitas (2008) Procedure for estimation and reporting of uncertainty due to discretization in CFD applications. *Journal of Fluids Engineering-Transactions of the Asme*, 130.
- CHAM (2013) POLIS, the PHOENICS On-Line Information System, viewed 23<sup>rd</sup> October 2013, <[http://www.cham.co.uk/phoenics/d\\_polis/polis.htm](http://www.cham.co.uk/phoenics/d_polis/polis.htm)>.
- Chanson, H. (2000) Boundary shear stress measurements in undular flows: Application to standing wave bed forms. *Water Resources Research*, 36, 3063-3076.
- Chen, H. C. and V. C. Patel (1988) Near-wall turbulence models for complex flows including separation. *AIAA Journal*, 26, 641-648.
- Chepil, W. S. (1961) The Use of Spheres to Measure Lift and Drag on Wind-Eroded Soil Grains. *Soil Science Society Proceedings*, 25, 343-345.
- Cleary, P. W. and M. Prakash (2004) Discrete-element modelling and smoothed particle hydrodynamics: potential in the environmental sciences. *Philosophical Transactions of the Royal Society A - Mathematical Physical and Engineering Sciences*, 362, 2003-2030.
- Clifford, N. J., K. S. Richards, R. A. Brown and S. N. Lane (1995) Scales of variation of suspended sediment concentration and turbidity in a glacial meltwater stream. *Geografiska Annaler Series A - Physical Geography*, 77A, 45-65.
- Clifford, N. J., K. S. Richards and A. Robert (1992) The influence of microform bed roughness elements on flow and sediment transport in gravel bed rivers – comment. *Earth Surface Processes and Landforms*, 17, 529-534.
- Constantinescu, G., S. Miyawaki, B. Rhoads and A. Sukhodolov (2012) Numerical analysis of the effect of momentum ratio on the dynamics and sediment-entrainment capacity of coherent flow structures at a stream confluence. *Journal of Geophysical Research-Earth Surface*, 117.
- Constantinescu, G., S. Miyawaki, B. Rhoads, A. Sukhodolov and G. Kirkil (2011) Structure of turbulent flow at a river confluence with momentum and velocity ratios close to 1: Insight provided by an eddy-resolving numerical simulation. *Water Resources Research*, 47.
- Coulthard, T. J. (2001) Landscape evolution models: a software review. *Hydrological Processes*, 15, 165-173.
- Coulthard, T. J., D. M. Hicks and M. J. Van De Wiel (2007) Cellular modelling of river catchments and reaches: Advantages, limitations and prospects. *Geomorphology*, 90, 192-207.

- Coulthard, T. J. and M. J. Van De Wiel (2007) Quantifying fluvial non linearity and finding self organized criticality? Insights from simulations of river basin evolution. *Geomorphology*, 91, 216-235.
- Craft, T. J., A. V. Gerasimov, H. Iacovides and B. E. Launder (2002) Progress in the generalization of wall-function treatments. *International Journal of Heat and Fluid Flow*, 23, 148-160.
- Cray, A. I. (2010) *The Dynamics of Coarse Sediment Transfer in an Upland Bedrock River*. MSc Thesis, Durham University.
- Creutin, J. D., M. Muste, A. A. Bradley, S. C. Kim and A. Kruger (2003) River gauging using PIV techniques: a proof of concept experiment on the Iowa River. *Journal of Hydrology*, 277, 182-194.
- Curtis, K. E., C. E. Renshaw, F. J. Magilligan and W. B. Dade (2010) Temporal and spatial scales of geomorphic adjustments to reduced competency following flow regulation in bedload-dominated systems. *Geomorphology*, 118, 105-117.
- Dan, S., D.-J. R. Walstra, M. J. F. Stive and N. Panin (2011) Processes controlling the development of a river mouth spit. *Marine Geology*, 280, 116-129.
- Darby, S. E., A. M. Alabyan and M. J. Van de Wiel (2002) Numerical simulation of bank erosion and channel migration in meandering rivers. *Water Resources Research*, 38.
- De Serres, B. and A. G. Roy (1990) Flow direction and branching geometry at junctions in dendritic river networks. *Professional Geographer*, 42, 194-201.
- De Serres, B., A. G. Roy, P. M. Biron and J. L. Best (1999) Three-dimensional structure of flow at a confluence of river channels with discordant beds. *Geomorphology*, 26, 313-335.
- Deltares (2013) Delft3D-FLOW User Manual, viewed 24<sup>th</sup> September 2013, <<http://oss.deltares.nl/web/delft3d/manuals>>.
- Didden, N. (1987) Performance evaluation of a shipboard 115-kHz Acoustic doppler Current Profiler. *Continental Shelf Research*, 7, 1231-1243.
- Drake, T. G. and J. Calantoni (2001) Discrete particle model for sheet flow sediment transport in the nearshore. *Journal of Geophysical Research-Oceans*, 106, 19859-19868.
- Dugdale, S. J., P. E. Carbonneau and D. Campbell (2010) Aerial photosieving of exposed gravel bars for the rapid calibration of airborne grain size maps. *Earth Surface Processes and Landforms*, 35, 627-639.
- Edmonds, D. A. and R. L. Slingerland (2007) Mechanics of river mouth bar formation: Implications for the morphodynamics of delta distributary networks. *Journal of Geophysical Research-Earth Surface*, 112.
- Elgar, S., B. Raubenheimer and R. T. Guza (2001) Current meter performance in the surf zone. *Journal of Atmospheric and Oceanic Technology*, 18, 1735-1746.
- (2005) Quality control of acoustic Doppler velocimeter data in the surfzone. *Measurement Science and Technology*, 16, 1889-1893.

- Ettema, R. (2008) Management of Confluences. In: *River Confluences, Tributaries and the Fluvial Network*, eds. S. P. Rice, B. L. Rhoads and A. G. Roy. Chichester: John Wiley and Sons.
- Ferguson, R. I. and T. Hoey (2008) Effects of Tributaries on Main-Channel Geomorphology. In: *River Confluences, Tributaries and the Fluvial Network*, eds. S. P. Rice, B. L. Rhoads and A. G. Roy. Chichester: John Wiley and Sons.
- Ferguson, R. I., D. R. Parsons, S. N. Lane and R. J. Hardy (2003) Flow in meander bends with recirculation at the inner bank. *Water Resources Research*, 39, 13.
- Ferguson, R. I. and S. J. Wathen (1998) Tracer-pebble movement along a concave river profile: Virtual velocity in relation to grain size and shear stress. *Water Resources Research*, 34, 2031-2038.
- Fernandes, C. C., J. Podos and J. G. Lundberg (2004) Amazonian ecology: Tributaries enhance the diversity of electric fishes. *Science*, 305, 1960-1962.
- Ferziger, J. H. and M. Peric (1999) *Computational Methods for Fluid Dynamics*. London: Springer-Verlag.
- Fischer-Antze, T., N. R. B. Olsen and D. Gutknecht (2008) Three-dimensional CFD modeling of morphological bed changes in the Danube River. *Water Resources Research*, 44.
- Freer, J., K. Beven and B. Ambroise (1996) Bayesian estimation of uncertainty in runoff prediction and the value of data: An application of the GLUE approach. *Water Resources Research*, 32, 2161-2173.
- Gascon, C. and M. L. Smith (2004) Ecology - Where rivers meet. *Science*, 305, 1922-1923.
- Gaudet, J. M. and A. G. Roy (1995) Effect of Bed Morphology on Flow Mixing Length at River Confluences. *Nature*, 373, 138-139.
- Graham, D. J., S. P. Rice and I. Reid (2005a) Comment: Photographic techniques for characterizing streambed particle sizes. *Transactions of the American Fisheries Society*, 134, 1599-1603.
- (2005b) A transferable method for the automated grain sizing of river gravels. *Water Resources Research*, 41.
- Hardy, R. J. (2005) Modelling granular sediment transport over water-worked gravels. *Earth Surface Processes and Landforms*, 30, 1069-1076.
- (2006a) Fluvial geomorphology. *Progress in Physical Geography*, 30, 553-567.
- (2006b) Modeling granular sediment transport over water worked gravels within a CFD framework. *River Flow 2006, Vols 1 and 2*, 913-918.
- (2008) Geomorphology Fluid Flow Modelling: Can Fluvial Flow Only Be Modelled Using a Three-Dimensional Approach? *Geography Compass*, 2, 215-234.
- Hardy, R. J., and S. N. Lane (2004) The numerical simulation of time dependent flow structures over water worked gravel. In: *River Flow 2004*, eds. M. Greco, A. Carravetta and R. Della Morte, 235-243.

- Hardy, R. J., S. N. Lane, R. I. Ferguson and D. R. Parsons (2003) Assessing the credibility of a series of computational fluid dynamic simulations of open channel flow. *Hydrological Processes*, 17, 1539-1560.
- (2007) Emergence of coherent flow structures over a gravel surface: A numerical experiment. *Water Resources Research*, 43.
- Hardy, R. J., S. N. Lane, M. R. Lawless, J. L. Best, L. Elliott and D. B. Ingham (2005) Development and testing of a numerical code for treatment of complex river channel topography in three-dimensional CFD models with structured grids. *Journal of Hydraulic Research*, 43, 468-480.
- Heald, J., I. McEwan and S. Tait (2004) Sediment transport over a flat bed in a unidirectional flow: simulations and validation. *Philosophical Transactions of the Royal Society of London Series A - Mathematical Physical and Engineering Sciences*, 362, 1973-1986.
- Higgitt, D. L. and J. Warburton (1999) Applications of differential GPS in upland fluvial geomorphology. *Geomorphology*, 29, 121-134.
- Hodge, R., J. Brasington and K. Richards (2009) In situ characterization of grain-scale fluvial morphology using Terrestrial Laser Scanning. *Earth Surface Processes and Landforms*, 34, 954-968.
- Hodge, R., K. Richards and J. Brasington (2007) A physically-based bedload transport model developed for 3-D reach-scale cellular modelling. *Geomorphology*, 90, 244-262.
- Hodge, R. A. (2007) *Grain-scale Approaches to Modelling and Measuring Fluvial Sedimentology and Bedload Transport*. PhD Thesis, University of Cambridge.
- Hodge, R. A., T. B. Hoey and S. Sklar (2011) Bed load transport in bedrock rivers: The role of sediment cover in grain entrainment, translation, and deposition. *Journal of Geophysical Research-Earth Surface*, 116.
- Hodkinson, A. (1996) Computational fluid dynamics as a tool for investigating separated flow in river bends. *Earth Surface Processes and Landforms*, 21, 993-1000.
- Huang, J. C., L. J. Weber and Y. G. Lai (2002) Three-dimensional numerical study of flows in open-channel junctions. *Journal of Hydraulic Engineering-Asce*, 128, 268-280.
- Hubbard, B. P., M. J. Sharp, I. C. Willis, M. K. Nielsen and C. C. Smart (1995) Borehole water-level variations and the structure of the subglacial hydrological system of Haut Glacier d'Arolla, Valais, Switzerland. *Journal of Glaciology*, 41, 572-583.
- Hunt, J. C. R. and F. Hussain (1991) A note on velocity, vorticity and helicity of inviscid fluid elements. *Journal of Fluid Mechanics*, 229, 569-587.
- Ibbeken, H. and R. Schleyer (1986) Photo-sieving - a method for grain-size analysis of coarse-grained, unconsolidated bedding surfaces. *Earth Surface Processes and Landforms*, 11, 59-77.
- Issa, R. I. (1986) Solution of the implicitly discretised fluid flow equations by operator-splitting. *Journal of Computational Physics*, 62, 40-65.

- Jones, W. P. and B. E. Launder (1972) The prediction of laminarization with a two-equation model of turbulence. *International Journal of Heat and Mass Transfer*, 15, 301-314.
- Keim, R. F., A. E. Skaugset and D. S. Bateman (1999) Digital terrain modeling of small stream channels with a total-station theodolite. *Advances in Water Resources*, 23, 41-48.
- Kelsey, A. (1996) Modelling the sediment transport process. In: *Advances in Fluvial Dynamics and Stratigraphy*, eds. P. A. Carling and M. R. Dawson, 229-261. Chichester: John Wiley and Sons.
- Kermack, K. A. and J. B. S. Haldane (1950) Organic Correlation and Allometry. *Biometrika*, 37, 30-41.
- Keylock, C. J., R. J. Hardy, D. R. Parsons, R. I. Ferguson, S. N. Lane and K. S. Richards (2005) The theoretical foundations and potential for large-eddy simulation (LES) in fluvial geomorphic and sedimentological research. *Earth-Science Reviews*, 71, 271-304.
- Keylock, C. J., K. Nishimura and J. Peinke (2012) A classification scheme for turbulence based on the velocity-intermittency structure with an application to near-wall flow and with implications for bed load transport. *Journal of Geophysical Research-Earth Surface*, 117.
- Kirkil, G. and G. Constantinescu (2009) Nature of flow and turbulence structure around an in-stream vertical plate in a shallow channel and the implications for sediment erosion. *Water Resources Research*, 45.
- Kirkman, R. D. and M. Metzger (2008) Sensitivity analysis of low Reynolds number channel flow using the finite volume method. *International Journal for Numerical Methods in Fluids*, 57, 1023-1045.
- Kondolf, G. M. (1997) Application of the pebble count: Notes on purpose, method, and variants. *Journal of the American Water Resources Association*, 33, 79-87.
- Kostaschuk, R., J. Best, P. Villard, J. Peakall and M. Franklin (2005) Measuring flow velocity and sediment transport with an acoustic Doppler current profiler. *Geomorphology*, 68, 25-37.
- Lamarre, H. and A. G. Roy (2008a) A field experiment on the development of sedimentary structures in a gravel-bed river. *Earth Surface Processes and Landforms*, 33, 1064-1081.
- (2008b) The role of morphology on the displacement of particles in a step-pool river system. *Geomorphology*, 99, 270-279.
- Lancaster, S. T., E. F. Underwood and W. T. Frueh (2010) Sediment reservoirs at mountain stream confluences: Dynamics and effects of tributaries dominated by debris-flow and fluvial processes. *Geological Society of America Bulletin*, 122, 1775-1786.
- Lane, S. N. (1998) Hydraulic modelling in hydrology and geomorphology: A review of high resolution approaches. *Hydrological Processes*, 12, 1131-1150.
- (2005) Roughness - time for a re-evaluation? *Earth Surface Processes and Landforms*, 30, 251-253.

- (2006) Approaching the system-scale understanding of braided river behaviour. In: *Braided Rivers: Process, Deposits, Ecology and Management*, eds. G. H. S. Smith, J. L. Best, C. S. Bristow and G. E. Petts, 107-135. Malden: Wiley-Blackwell.
- Lane, S. N., P. M. Biron, K. F. Bradbrook, J. B. Butler, J. H. Chandler, M. D. Crowell, S. J. McLelland, K. S. Richards and A. G. Roy (1998) Three-dimensional measurement of river channel flow processes using acoustic Doppler velocimetry. *Earth Surface Processes and Landforms*, 23, 1247-1267.
- Lane, S. N., K. F. Bradbrook, K. S. Richards, P. A. Biron and A. G. Roy (1999a) The application of computational fluid dynamics to natural river channels: three-dimensional versus two-dimensional approaches. *Geomorphology*, 29, 1-20.
- Lane, S. N., K. F. Bradbrook, K. S. Richards, P. M. Biron and A. G. Roy (1999b) Time-averaged flow structure in the central region of a stream confluence: A discussion. *Earth Surface Processes and Landforms*, 24, 361-367.
- (2000) Secondary circulation cells in river channel confluences: measurement artefacts or coherent flow structures? *Hydrological Processes*, 14, 2047-2071.
- Lane, S. N., J. H. Chandler and K. S. Richards (1994) Developments in Monitoring and Modeling Small-Scale River Bed Topography. *Earth Surface Processes and Landforms*, 19, 349-368.
- Lane, S. N., R. J. Hardy, L. Elliott and D. B. Ingham (2002) High-resolution numerical modelling of three-dimensional flows over complex river bed topography. *Hydrological Processes*, 16, 2261-2272.
- (2004) Numerical modeling of flow processes over gravelly surfaces using structured grids and a numerical porosity treatment. *Water Resources Research*, 40, 18.
- Lane, S. N., R. J. Hardy, R. I. Ferguson and D. R. Parsons (2005) A framework for model verification and validation of CFD schemes in natural open channel flows. In: *Computational Fluid Dynamics: Applications in Environmental Hydraulics*, eds. P. D. Bates, S. N. Lane and R. I. Ferguson, 169-192. Chichester: John Wiley and Sons.
- Lane, S. N., D. R. Parsons, J. L. Best, O. Orfeo, R. A. Kostaschuk and R. J. Hardy (2008) Causes of rapid mixing at a junction of two large rivers: Rio Parana and Rio Paraguay, Argentina. *Journal of Geophysical Research-Earth Surface*, 113.
- Lane, S. N. and K. S. Richards (1998) High resolution, two-dimensional spatial modelling of flow processes in a multi-thread channel. *Hydrological Processes*, 12, 1279-1298.
- Lane, S. N., K. S. Richards and J. H. Chandler (1995) Morphological estimation of the time-integrated bed-load transport rate. *Water Resources Research*, 31, 761-772.
- Lane, S. N., R. M. Westaway and D. M. Hicks (2003) Estimation of erosion and deposition volumes in a large, gravel-bed, braided river using synoptic remote sensing. *Earth Surface Processes and Landforms*, 28, 249-271.
- Laraque, A., J. L. Guyot and N. Filizola (2009) Mixing processes in the Amazon River at the confluences of the Negro and Solimoes Rivers, Encontro das Aguas, Manaus, Brazil. *Hydrological Processes*, 23, 3131-3140.



- Latham, J. P. and A. Munjiza (2004) The modelling of particle systems with real shapes. *Philosophical Transactions of the Royal Society of London Series A - Mathematical Physical and Engineering Sciences*, 362, 1953-1972.
- Lee, H. Y. and I. S. Hsu (1994) Investigation of saltating particle motions. *Journal of Hydraulic Engineering-Asce*, 120, 831-845.
- Leeder, M. R. (1983) On the Interactions between Turbulent Flow, Sediment Transport and Bedform Mechanics in Channelized Flows. In: *Modern and Ancient Fluvial Systems, International Association of Sedimentologists Special Publication 6*, eds. J. D. Collinson and J. Lewin, 5-18. Blackwell Publishing Ltd.
- Leica (2004a) *Leica GPS1200 User Manual Version 1.0*. Heerbrugg: Leica Geosystems AG.
- (2004b) *Leica TPS1200 User Manual Version 1.0*. Heerbrugg: Leica Geosystems AG.
- Leite Ribeiro, M., K. Blanckaert, A. G. Roy and A. J. Schleiss (2012) Flow and sediment dynamics in channel confluences. *Journal of Geophysical Research-Earth Surface*, 117.
- Lesser, G. R., J. A. Roelvink, J. van Kester and G. S. Stelling (2004) Development and validation of a three-dimensional morphological model. *Coastal Engineering*, 51, 883-915.
- Luettich, R. A. and J. W. Westerink (1994) Continental Shelf Scale Convergence Studies with a Barotropic Tidal Model. In: *Quantitative Skill Assessment for Coastal Ocean Models*, eds. D. R. Lynch and A. M. Davies. AGU Press.
- Lukerchenko, N., J. Dolansky and P. Vlasak (2012) Basset force in numerical models of saltation. *Journal of Hydrology and Hydromechanics*, 60, 277-287.
- Lukerchenko, N., S. Piatsevich, Z. Chara and P. Vlasak (2009) 3D numerical model of the spherical particle saltation in a channel with a rough fixed bed. *Journal of Hydrology and Hydromechanics*, 57, 100-112.
- Ma, L., P. J. Ashworth, J. L. Best, L. Elliot, D. B. Ingham and L. J. Whitcombe (2002) Computational fluid dynamics and the physical modelling of an upland urban river. *Geomorphology*, 44, 375-391.
- Mackay, J. R. (1970) Lateral mixing of the Liard and Mackenzie rivers downstream from their confluence. *Canadian Journal of Earth Sciences*, 7, 111-124.
- MacLeod, N. (2002) Geometric morphometrics and geological shape-classification systems. *Earth-Science Reviews*, 59, 27-47.
- MacVicar, B. J., E. Beaulieu, V. Champagne and A. G. Roy (2007) Measuring water velocity in highly turbulent flows: field tests of an electromagnetic current meter (ECM) and an acoustic Doppler velocimeter (ADV). *Earth Surface Processes and Landforms*, 32, 1412-1432.
- Maliska, C. R. and G. D. Raithby (1984) A method for computing three dimensional flows using non-orthogonal boundary-fitted co-ordinates. *International Journal for Numerical Methods in Fluids*, 4, 519-537.

- Marjoribanks, T. I., R. J. Hardy, S. N. Lane and D. R. Parsons (2012) Using high-resolution CFD results to improve representation of vegetative drag and blockage effects within reach-scale flow models. In: *Third International Symposium on Shallow Flows*. Iowa City, USA.
- McEwan, I. and J. Heald (2001) Discrete particle modeling of entrainment from flat uniformly sized sediment beds. *Journal of Hydraulic Engineering-Asce*, 127, 588-597.
- McEwan, I. K., B. J. Jefcoate and B. B. Willetts (1999) The grain-fluid interaction as a self-stabilizing mechanism in fluvial bed load transport. *Sedimentology*, 46, 407-416.
- Miori, S. (2008) *Dynamics of Bifurcations in Gravel-Bed Braided Streams*. PhD Thesis, Universita Degli Studi di Trento, Trento, Italy.
- Miori, S., R. J. Hardy and S. N. Lane (2012) Topographic forcing of flow partition and flow structures at river bifurcations. *Earth Surface Processes and Landforms*, 37, 666-679.
- Moreno, P. A. and F. A. Bombardelli (2012) 3D numerical simulation of particle-particle collisions in saltation mode near stream beds. *Acta Geophysica*, 60, 1661-1688.
- Mosley, M. P. (1976) Experimental Study of Channel Confluences. *Journal of Geology*, 84, 535-562.
- Murray, A. B. and C. Paola (1994) A cellular-model of braided rivers. *Nature*, 371, 54-57.
- (1997) Properties of a cellular braided-stream model. *Earth Surface Processes and Landforms*, 22, 1001-1025.
- Musselman, Z. A. (2011) The localized role of base level lowering on channel adjustment of tributary streams in the Trinity River basin downstream of Livingston Dam, Texas, USA. *Geomorphology*, 128, 42-56.
- Nardin, W. and S. Fagherazzi (2012) The effect of wind waves on the development of river mouth bars. *Geophysical Research Letters*, 39.
- Nash, J. E. and J. V. Sutcliffe (1970) River flow forecasting through conceptual models part I — A discussion of principles. *Journal of Hydrology*, 10, 282-290.
- Nicholas, A. P. (2001) Computational fluid dynamics modelling of boundary roughness in gravel-bed rivers: An investigation of the effects of random variability in bed elevation. *Earth Surface Processes and Landforms*, 26, 345-362.
- (2009) Reduced-complexity flow routing models for sinuous single-thread channels: intercomparison with a physically-based shallow-water equation model. *Earth Surface Processes and Landforms*, 34, 641-653.
- (2010) Reduced-complexity modeling of free bar morphodynamics in alluvial channels. *Journal of Geophysical Research-Earth Surface*, 115.
- Nicholas, A. P. and T. A. Quine (2007) Crossing the divide: Representation of channels and processes in reduced-complexity river models at reach and landscape scales. *Geomorphology*, 90, 318-339.

- Nicholas, A. P. and G. H. Sambrook Smith (1999) Numerical simulation of three-dimensional flow hydraulics in a braided channel. *Hydrological Processes*, 13, 913-929.
- Nicholas, A. P., S. D. Sandbach, P. J. Ashworth, M. L. Amsler, J. L. Best, R. J. Hardy, S. N. Lane, O. Orfeo, D. R. Parsons, A. J. H. Reesink, G. H. S. Smith and R. N. Szupiany (2012) Modelling hydrodynamics in the Rio Parana, Argentina: An evaluation and inter-comparison of reduced-complexity and physics based models applied to a large sand-bed river. *Geomorphology*, 169, 192-211.
- Nicholas, A. P., D. E. Walling, R. J. Sweet and X. Fang (2006) New strategies for upscaling high-resolution flow and overbank sedimentation models to quantify floodplain sediment storage at the catchment scale. *Journal of Hydrology*, 329, 577-594.
- Nienow, P., M. Sharp and I. Willis (1996) Temporal switching between englacial and subglacial drainage pathways: Dye tracer evidence from the Haut Glacier d'Arolla, Switzerland. *Geografiska Annaler Series A - Physical Geography*, 78A, 51-60.
- Nino, Y. and M. Garcia (1994) Gravel Saltation 2. Modeling. *Water Resources Research*, 30, 1915-1924.
- (1998) Using Lagrangian particle saltation observations for bedload sediment transport modelling. *Hydrological Processes*, 12, 1197-1218.
- Nino, Y., M. Garcia and L. Ayala (1994) Gravel Saltation 1. Experiments. *Water Resources Research*, 30, 1907-1914.
- NVIDIA (2013) CUDA C Programming Guide, viewed 14<sup>th</sup> June 2013, <<http://docs.nvidia.com/cuda/cuda-c-programming-guide/>>.
- Oberkampf, W. L. and T. G. Trucano (2002) Verification and validation in computational fluid dynamics. *Progress in Aerospace Sciences*, 38, 209-272.
- (2008) Verification and validation benchmarks. *Nuclear Engineering and Design*, 238, 716-743.
- Olsen, N. R. B. and S. Stokseth (1995) 3-Dimensional Numerical Modeling of Water Flow in a River with Large Bed Roughness. *Journal of Hydraulic Research*, 33, 571-581.
- Orfeo, O., D. R. Parsons, J. L. Best, S. N. Lane, R. J. Hardy, R. Kostaschuk, R. N. Szupiany and M. L. Amsler (2006) Morphology and flow structures in a large confluence-diffuence: Rio Parana, Argentina. In: *International Conference on Fluvial Hydraulics*, eds. R. M. L. Ferreira, C. T. L. Alves, G. A. B. Leal and A. H. Cardoso, 1277-1282. Lisbon, PORTUGAL: Taylor & Francis Ltd.
- Parsons, D. R. (2003) Discussion of "Three-dimensional numerical study of flows in open-channel junctions" by Jianchun Huang, Larry J. Weber, and Yong G. Lai. *Journal of Hydraulic Engineering-Asce*, 129, 822-823.
- Parsons, D. R., J. L. Best, S. N. Lane, R. J. Hardy, R. Kostaschuk, D. Shugar and O. Orfeo (2006) Morphology, flow and sediment transport over a natural 3D dune field: Rio Parana, Argentina. In: *International Conference on Fluvial Hydraulics*, eds. R. M. L. Ferreira, C. T. L. Alves, G. A. B. Leal and A. H. Cardoso, 997-1004. Lisbon, PORTUGAL: Taylor & Francis Ltd.

- Parsons, D. R., J. L. Best, S. N. Lane, R. Kostachuk, R. J. Hardy, O. Orfeo, M. L. Amsler and R. N. Szupiany (2008) Large River Channel Confluences. In: *River Confluences, Tributaries and the Fluvial Network*, eds. S. P. Rice, B. L. Rhoads and A. G. Roy. Chichester: John Wiley and Sons.
- Parsons, D. R., J. L. Best, S. N. Lane, O. Orfeo, R. J. Hardy and R. Kostaschuk (2007) Form roughness and the absence of secondary flow in a large confluence-difffluence, Rio Parana, Argentina. *Earth Surface Processes and Landforms*, 32, 155-162.
- Patankar, S. V. (1980) *Numerical Heat Transfer and Fluid Flow*. New York: Hemisphere Publishing Corporation, Taylor & Francis Group.
- (1981) A calculation procedure for two-dimensional elliptic situations. *Numerical Heat Transfer*, 4, 409-425.
- Patankar, S. V. and D. B. Spalding (1972) A Calculation Procedure for Heat, Mass and Momentum Transfer in Three-Dimensional Parabolic Flows. *International Journal of Heat and Mass Transfer*, 15, 1787-1806.
- Powers, M. C. (1953) A New Roundness Scale for Sedimentary Particles. *Journal of Sedimentary Petrology*, 23, 117-119.
- Rameshwaran, P., P. S. Naden and M. Lawless (2011) Flow modelling in gravel-bed rivers: rethinking the bottom boundary condition. *Earth Surface Processes and Landforms*, 36, 1350-1366.
- Ransing, R. S., R. W. Lewis and D. T. Gethin (2004) Using a deformable discrete-element technique to model the compaction behaviour of mixed ductile and brittle particulate systems. *Philosophical Transactions of the Royal Society of London Series A - Mathematical Physical and Engineering Sciences*, 362, 1867-1884.
- Rennie, C. D. and F. Rainville (2006) Case study of precision of GPS differential correction strategies: Influence on aDcp velocity and discharge estimates. *Journal of Hydraulic Engineering-Asce*, 132, 225-234.
- Rhoads, B. L. and S. T. Kenworthy (1995) Flow structure at an asymmetrical stream confluence. *Geomorphology*, 11, 273-293.
- (1998) Time-averaged flow structure in the central region of a stream confluence. *Earth Surface Processes and Landforms*, 23, 171-191.
- (1999) On secondary circulation, helical motion and Rozovskii-based analysis of time-averaged two-dimensional velocity fields at confluences. *Earth Surface Processes and Landforms*, 24, 369-375.
- Rhoads, B. L., J. D. Riley and D. R. Mayer (2009) Response of bed morphology and bed material texture to hydrological conditions at an asymmetrical stream confluence. *Geomorphology*, 109, 161-173.
- Rhoads, B. L. and A. N. Sukhodolov (2001) Field investigation of three-dimensional flow structure at stream confluences: 1. Thermal mixing and time-averaged velocities. *Water Resources Research*, 37, 2393-2410.
- (2004) Spatial and temporal structure of shear layer turbulence at a stream confluence. *Water Resources Research*, 40.

- (2008) Lateral momentum flux and the spatial evolution of flow within a confluence mixing interface. *Water Resources Research*, 44.
- Rice, S. (1998) Which tributaries disrupt downstream fining along gravel-bed rivers? *Geomorphology*, 22, 39-56.
- Rice, S. P. (2008) Introduction to Part II: Tributary-Stem Interactions. In: *River Confluences, Tributaries and the Fluvial Network*, eds. S. P. Rice, B. L. Rhoads and A. G. Roy. Chichester: John Wiley and Sons.
- Rice, S. and M. Church (1996) Sampling surficial fluvial gravels; the precision of size distribution percentile sediments. *Journal of Sedimentary Research*, 66, 654-665.
- Rice, S. P., B. L. Rhoads and A. G. Roy. (2008) Introduction: River Confluences, Tributaries and the Fluvial Network. In: *River Confluences, Tributaries and the Fluvial Network*, eds. S. P. Rice, B. L. Rhoads and A. G. Roy. Chichester: John Wiley and Sons.
- Richards, K., M. Bithell, M. Dove and R. Hodge (2004) Discrete-element modelling: methods and applications in the environmental sciences. *Philosophical Transactions of the Royal Society of London Series A - Mathematical Physical and Engineering Sciences*, 362, 1797-1816.
- Roache, P. J. (1994) Perspective - A Method for Uniform Reporting of Grid Refinement Studies. *Journal of Fluids Engineering-Transactions of the Asme*, 116, 405-413.
- (1997) Quantification of uncertainty in computational fluid dynamics. *Annual Review of Fluid Mechanics*, 29, 123-160.
- (1998) *Verification and Validation in Computational Science and Engineering*. Albuquerque, NM: Hermosa.
- Robert, A. (2003) *River Processes: An Introduction to Fluvial Dynamics*. London: Arnold Publishers.
- Robert, A., A. G. Roy and B. De Serres (1996) Turbulence at a roughness transition in a depth limited flow over a gravel bed. *Geomorphology*, 16, 175-187.
- Robert, A., A. G. Roy and B. Deserres (1992) Changes in velocity profiles at roughness transitions in coarse-grained channels. *Sedimentology*, 39, 725-735.
- Rodriguez, A., A. Sanchez-Arcilla, J. M. Redondo and C. Mosso (1999) Macroturbulence measurements with electromagnetic and ultrasonic sensors: a comparison under high-turbulent flows. *Experiments in Fluids*, 27, 31-42.
- Rodriguez, J. F., F. A. Bombardelli, M. H. Garcia, K. M. Frothingham, B. L. Rhoads and J. D. Abad (2004) High-resolution numerical simulation of flow through a highly sinuous river reach. *Water Resources Management*, 18, 177-199.
- Rogallo, R. S. and P. Moin (1984) Numerical Simulation of Turbulent Flows. *Annual Review of Fluid Mechanics*, 16, 99-137.
- Roy, A. G. 2008. Introduction to Part I: River Channel Confluences. In: *River Confluences, Tributaries and the Fluvial Network*, eds. S. P. Rice, B. L. Rhoads and A. G. Roy. Chichester: John Wiley and Sons.

- Roy, A. G. and N. Bergeron (1990) Flow and particle paths at a natural river confluence with coarse bed material. *Geomorphology*, 3, 99-112.
- Roy, A. G., P. M. Biron, T. Buffin-Belanger and M. Levasseur (1999) Combined visual and quantitative techniques in the study of natural turbulent flows. *Water Resources Research*, 35, 871-877.
- Roy, C. J. (2005) Review of code and solution verification procedures for computational simulation. *Journal of Computational Physics*, 205, 131-156.
- Ruether, N., J. M. Singh, N. R. B. Olsen and E. Atkinson (2005) 3-D computation of sediment transport at water intakes. *Proceedings of the Institution of Civil Engineers-Water Management*, 158, 1-7.
- Ruggiero, P., D. J. R. Walstra, G. Gelfenbaum and M. van Ormondt (2009) Seasonal-scale nearshore morphological evolution: Field observations and numerical modeling. *Coastal Engineering*, 56, 1153-1172.
- Rumsby, B. T., J. Brasington, J. A. Langham, S. J. McLelland, R. Middleton and G. Rollinson (2008) Monitoring and modelling particle and reach-scale morphological change in gravel-bed rivers: Applications and challenges. *Geomorphology*, 93, 40-54.
- Rüther, N. and N. R. B. Olsen (2007) Modelling free-forming meander evolution in a laboratory channel using three-dimensional computational fluid dynamics. *Geomorphology*, 89, 308-319.
- Sandbach, S. D., S. N. Lane, R. J. Hardy, M. L. Amsler, P. J. Ashworth, J. L. Best, A. P. Nicholas, O. Orfeo, D. R. Parsons, A. J. H. Reesink and R. N. Szupiany (2012) Application of a roughness-length representation to parameterize energy loss in 3-D numerical simulations of large rivers. *Water Resources Research*, 48.
- Schmeeckle, M. W. and J. M. Nelson (2003) Direct numerical simulation of bedload transport using a local, dynamic boundary condition. *Sedimentology*, 50, 279-301.
- Schmeeckle, M. W., J. M. Nelson and R. L. Shreve (2007) Forces on stationary particles in near-bed turbulent flows. *Journal of Geophysical Research-Earth Surface*, 112, 21.
- Sear, D. A. (1996) Sediment transport processes in pool-riffle sequences. *Earth Surface Processes and Landforms*, 21, 241-262.
- Sekine, M. and H. Kikkawa (1992) Mechanics of saltating grains 2. *Journal of Hydraulic Engineering-Asce*, 118, 536-558.
- Sharp, M., K. Richards, I. Willis, N. Arnold, P. Nienow, W. Lawson and J. L. Tison (1993) Geometry, bed topography and drainage system structure of the Haut Glacier d'Arolla, Switzerland. *Earth Surface Processes and Landforms*, 18, 557-571.
- Shields, F. D., S. S. Knight, S. Testa and C. M. Cooper (2003) Use of acoustic Doppler current profilers to describe velocity distributions at the reach scale. *Journal of the American Water Resources Association*, 39, 1397-1408.
- Sime, L. C. and R. I. Ferguson (2003) Information on grain sizes in gravel-bed rivers by automated image analysis. *Journal of Sedimentary Research*, 73, 630-636.

- Sime, L. C., R. I. Ferguson and M. Church (2007) Estimating shear stress from moving boat acoustic Doppler velocity measurements in a large gravel bed river. *Water Resources Research*, 43.
- Singh, A., F. Porte-Agel and E. Foufoula-Georgiou (2010) On the influence of gravel bed dynamics on velocity power spectra. *Water Resources Research*, 46.
- Siviglia, A., G. Stecca, D. Vanzo, G. Zolezzi, E. F. Toro and M. Tubino (2013) Numerical modelling of two-dimensional morphodynamics with applications to river bars and bifurcations. *Advances in Water Resources*, 52, 243-260.
- Sloff, K. and E. Mosselman (2012) Bifurcation modelling in a meandering gravel-sand bed river. *Earth Surface Processes and Landforms*, 37, 1556-1566.
- Sokal, R. R. and F. J. Rohlf (1995) *Biometry: The principles and Practice of Statistics in Biological Research*. New York: WH Freeman and Company.
- Sotiropoulos, F. (2005) Introduction to statistical turbulence modelling for hydraulic engineering flows. In: *Computational Fluid Dynamics: Applications in Environmental Hydraulics*, eds. P. D. Bates, S. N. Lane and R. I. Ferguson, 91-120.
- Spalding, D. B. (1980) Mathematical Modelling of Fluid Mechanics, Heat Transfer and Mass Transfer Processes. In: *Mechanical Engineering Department Technical Report HTS-80-1*. London: Imperial College of Science, Technology and Medicine.
- (1985) The Computation of Flow Around Ships with Allowance for Free-Surface and Density-Gradient Effects. In: *Maritime Simulation*, ed. M. Heller, 101-113. Springer, Berlin.
- Stern, F., R. Wilson and J. Shao (2006) Quantitative V&V of CFD simulations and certification of CFD codes. *International Journal for Numerical Methods in Fluids*, 50, 1335-1355.
- Stoesser, T., W. Rodi and G. H. Jirka (2004) Large-eddy simulation of flow over rough channel beds. In: *River Flow 2004*, eds. M. Greco, A. Carravetta and R. Della Morte, 265-271. Taylor Francis Group.
- Storlazzi, C. D., E. Elias, M. E. Field and M. K. Presto (2011) Numerical modeling of the impact of sea-level rise on fringing coral reef hydrodynamics and sediment transport. *Coral Reefs*, 30, 83-96.
- Sukhodolov, A. N., I. Schnauder and W. S. J. Uijttewaalt (2010) Dynamics of shallow lateral shear layers: Experimental study in a river with a sandy bed. *Water Resources Research*, 46.
- Szupiany, R. N., M. L. Amsler, D. R. Parsons and J. L. Best (2009) Morphology, flow structure, and suspended bed sediment transport at two large braid-bar confluences. *Water Resources Research*, 45.
- Thomas, R. and A. P. Nicholas (2002) Simulation of braided river flow using a new cellular routing scheme. *Geomorphology*, 43, 179-195.
- Thompson, C. J., J. C. Croke and D. Purvis-Smith (2011) Floodplain sediment disconnectivity at a tributary junction and valley constriction site in the Fitzroy River basin, Queensland, Australia. *Geomorphology*, 125, 293-304.

- Tritthart, M. and D. Gutknecht (2007) 3-D computation of flood processes in sharp river bends. *Proceedings of the Institution of Civil Engineers-Water Management*, 160, 233-247.
- Turowski, J. M., D. Rickenmann and S. J. Dadson (2010) The partitioning of the total sediment load of a river into suspended load and bedload: a review of empirical data. *Sedimentology*, 57, 1126-1146.
- Uijttewaal, W. S. J. and R. Booij (2000) Effects of shallowness on the development of free-surface mixing layers. *Physics of Fluids*, 12, 392-402.
- Unde, M. G. and S. Dhakal (2009) Sediment characteristics at river confluences: a case study of the Mula-Kas confluence, Maharashtra, India. *Progress in Physical Geography*, 33, 208-223.
- Valeport (2011) *Valeport Model 801 Datasheet*, viewed 21<sup>st</sup> November 2013, <[http://www.valeport.co.uk/Portals/0/Docs/Datasheets/Valeport\\_Model801\\_v2a.pdf](http://www.valeport.co.uk/Portals/0/Docs/Datasheets/Valeport_Model801_v2a.pdf)>.
- Van De Wiel, M. J., T. J. Coulthard, M. G. Macklin and J. Lewin (2007) Embedding reach-scale fluvial dynamics within the CAESAR cellular automaton landscape evolution model. *Geomorphology*, 90, 283-301.
- Verdu, J. M., R. J. Batalla and J. A. Martinez-Casasnovas (2005) High-resolution grain-size characterisation of gravel bars using imagery analysis and geo-statistics. *Geomorphology*, 72, 73-93.
- Vermaas, D. A., W. S. J. Uijttewaal and A. J. F. Hoitink (2011) Lateral transfer of streamwise momentum caused by a roughness transition across a shallow channel. *Water Resources Research*, 47.
- Vetsch, D., D. Ehrbar, S. Peter, P. Rousselot, C. Volz, L. Vonwiller, R. Faeh, D. Farshi, R. Mueller and R. Veprek (2013) *System Manuals of BASEMENT, Version 2.3*. Laboratory of Hydraulics, Glaciology and Hydrology, ETH Zurich.
- Villaret, C., J.-M. Hervouet, R. Kopmann, U. Merkel and A. G. Davies (2013) Morphodynamic modeling using the Telemac finite-element system. *Computers and Geosciences*, 53, 105-113.
- Wallis, E., R. Mac Nally and P. S. Lake (2008) A Bayesian analysis of physical habitat changes at tributary confluences in cobble-bed upland streams of the Acheron River basin, Australia. *Water Resources Research*, 44.
- Wang, H.-W., H.-Y. Lee and P.-N. Lee (2009) Three-dimensional saltating processes of multiple sediment particles. *International Journal of Sediment Research*, 24, 16-32.
- Warburton, J. (1990) An Alpine Proglacial Fluvial Sediment Budget. *Geografiska Annaler Series A - Physical Geography*, 72, 261-272.
- (1992) Observations of bed-load transport and channel bed changes in a proglacial mountain stream. *Arctic and Alpine Research*, 24, 195-203.
- (1994) Channel change in relation to meltwater flooding, Bas Glacier d'Arolla, Switzerland. *Geomorphology*, 11, 141-149.



- Warrick, J. A., D. M. Rubin, P. Ruggiero, J. N. Harney, A. E. Draut and D. Buscombe (2009) Cobble cam: grain-size measurements of sand to boulder from digital photographs and autocorrelation analyses. *Earth Surface Processes and Landforms*, 34, 1811-1821.
- Weerakoon, S. B., N. Tamai and Y. Kawahara (2003) Depth-averaged flow computation at a river confluence. *Proceedings of the Institution of Civil Engineers-Water and Maritime Engineering*, 156, 73-83.
- Weitbrecht, V., G. Kuhn and G. H. Jirka (2002) Large scale PIV-measurements at the surface of shallow water flows. *Flow Measurement and Instrumentation*, 13, 237-245.
- Westaway, R. M., S. N. Lane and D. M. Hicks (2001) Remote sensing of clear-water, shallow, gravel-bed rivers using digital photogrammetry. *Photogrammetric Engineering and Remote Sensing*, 67, 1271-1281.
- Wiberg, P. L. and J. D. Smith (1985) A Theoretical Model for Saltating Grains in Water. *Journal of Geophysical Research-Oceans*, 90, 7341-7354.
- Wilcock, P. R. (1996) Estimating local bed shear stress from velocity observations. *Water Resources Research*, 32, 3361-3366.
- Yakhot, V. and S. A. Orszag (1986) Renormalization-group analysis of turbulence. *Physical Review Letters*, 57, 1722-1724.